Proceedings of the XLIII International Symposium on Multiparticle Dynamics

Edited by
Sergei Chekanov and Zack Sullivan

Illinois Institute of Technology
IIT Press

Proceedings of the XLIII International Symposium on
Multiparticle Dynamics

Illinois Institute of Technology, Chicago, Illinois

15-20 September 2013

Edited by Sergei Chekanov and Zack Sullivan

Published by:
IIT Press
10 W. 35th St., 7D7-1
Chicago, IL 60616

ISBN: 978-1-61597-002-5

2013 Committees

Chairs

Zack Sullivan, Illinois Institute of Technology
Sergei Chekanov, Argonne National Laboratory

Local Organizing Committee

R. Russell Betts, Illinois Institute of Technology
Edmond L. Berger, Argonne National Laboratory
Radja Boughezal, Argonne National Laboratory
Sergei Chekanov, Argonne National Laboratory
Malcolm Derrick, Argonne National Laboratory
Frank Petriello, Northwestern University
James Proudfoot, Argonne National Laboratory
Zack Sullivan, Illinois Institute of Technology
Rik Yoshida, Argonne National Laboratory

Secretaries

Sharon Grant, Illinois Institute of Technology
Nancy Rezek, Argonne National Laboratory

ISMD International Advisory Committee

Andrzej Bialas, Jagiellonian University, Poland
Francesco Becattini, Dipartimento di Fisica Universita di Firenze, Italy
Jean-Paul Blaizot, Institute de Physique Theorique, CEA-Saclay, France
Markus Bleicher, Institut fur Theoretische Physik, J. Wolfgang Goethe-Universitat, Germany
Peter Braun-Munzinger, Wissenschaftliche Geschaeftsfuehrung, Darmstadt, Germany
Wojciech Broniowski, University of Kielce, Poland
Wit Busza, Massachusetts Institute of Technology, Cambridge, USA
Tamas Csörgö, Columbia University, USA
Igor Dremin, Lebedev Physical Institute, Russia
Krzysztof Fialkowski, Jagiellonian University, Poland
William Gary, University of California, Riverside, USA
Mark Gorenstein, National Academy of Sciences, Ukraine
Gosta Gustafson, Lund University, Sweden
Yogiro Hama, University of Sao Paulo, Brazil
Tetsuo Hatsuda, Nishina Center, Japan
Vecheslav Kuvshinov, National Academy of Science, Belarus
Hannes Jung, University of Antwerp, Belgium
Dmitri Kharzeev, State University of New York, Stony Brook, USA
Danuta Kisielewska, AGH-University of Science and Technology, Poland
Peter Levai Hungarian Academy of Sciences, Hungary
Larry McLerran, Brookhaven National Laboratory, USA
Wes Metzger, Radboud University Nijmegen, Netherlands
Berndt Mueller, Duke University, USA
Atsushi Nakamura, Hiroshima University, Japan
Carlos Pajares, Universidad Santiago de Compostela, Spain
Robi Peschanski, University of Saclay, France
Jan Pluta, Warsaw University of Technology, Poland
Krzysztof Redlich, Wroclaw University, Poland
Gunther Roland, Massachusetts Institute of Technology, USA
Peter Seyboth, Max Planck Institut fur Physik, Germany
Michal Sumbera, Czech Acadademy of Sciences, Czech Republic
Tom Trainor, University of Washington, USA
Georg Wolschin, Institut fur Theoretische Physik at Heidelberg, Germany
Yuanfang Wu, Huazhong University, Wuhan, China
Nu Xu, Lawrence Berkeley National Laboratory, USA
Agnieszka Zalewska, CERN, Switzerland

Physics sessions and conveners

Hadronic final states in high-p_T QCD
Chunhui Chen and Davison Soper

Higgs and related topics
Radja Boughezal and Bruce Mellado

Multiparticle dynamics in soft QCD and correlations
Rick Field and Nick Van Remortel

Proton structure, small- and large-X physics
Cynthia Keppel and Anna Stasto

Forward physics and Diffraction
Katarzyna Wichmann, Laszlo Jenkovszky, and Alan White

High p_T QCD calculations and particle production
Michael Schmitt and Alexander Paramonov

Phase diagrams of strongly interacting matter
Owe Philipsen and Nu Xu

Multiparticle aspects of high-density systems in heavy ion collisions
Piotr Bozek and Edward Sarkisyan-Grinbaum

Multiparticle aspects of physics beyond the Standard Model
LianTao Wang, Simona Rolli, and Eva Halkiadakis

Heavy-ion collisions
David Hofman, Thorsten Renk, and Nestor Armesto

Particle astrophysics
Francis Halzen and Salman Habib

Contents

Preface

This Proceedings of the XLIII International Symposium on Multiparticle Dynamics (ISMD 2013) contains summaries of some of the outstanding research presented at the 2013 meeting. The 2013 Symposium was held at the Illinois Institute of Technology (IIT) in Chicago, Illinois over September 15–20. The Symposium was jointly organized by the IIT College of Science and the High Energy Physics Division of Argonne National Laboratory. More than 100 participants from nearly 20 countries participated in the Symposium to review progress and discuss upcoming issues in the fields of high-energy physics, nuclear physics and astrophysics.

The International Symposium on Multiparticle Dynamics (ISMD) is a major international high-energy conference which attracts participants with a common interest in reactions involving a large number of particles. From the beginning, the goal was to bring experimentalists and theorists together to discuss all aspects multiparticle dynamics, from new analysis techniques to the latest discoveries.

ISMD 2013 is the latest in a series of Symposia with a long and well established history. The meeting started more than forty years ago in Paris, with a goal of understanding inelastic collisions with several hadrons in the final state. Before that first conference the attention in the field had mainly concentrated on elastic collisions, but the presence of "background" inelastic events with several low-p_T hadrons in the final state was fairly sizable and puzzling. There were very few theoretical models at the time explaining multi-hadron production. One of the popular descriptions was the longitudinal phase-space model by L. Van Hove, which attempted to describe the existing experimental data. In those days, Polish and Russian groups were active in analysis of inelastic data. Therefore, the goal of that first meeting was to set up a dedicated international conference to discuss multi-hadron production in QCD. The plan was to alternate the Symposium's location between Eastern and Western countries, which were divided at that time by the Iron Curtain.

After forty years of increasing energy and instantaneous luminosity in both high energy and nuclear experiments, final states with tens of thousands of hadrons have become commonplace. The numbers of identified jets at the Large Hadron Collider (LHC) at CERN can be as high as the multiplicities of hadrons measured some twenty or thirty years ago. Thus,

one can apply similar statistical techniques to analyze jets as those used for hadrons a few decades ago. Experimental research has become more theory-dependent as we have entered an era of precision measurements of the Standard Model which were once buried by QCD backgrounds. Theory has advanced to incorporate non-perturbative and perturbative QCD calculations up to next-to-next-to-leading order, analytical perturbative QCD through modified leading-log approximations, and the local parton-hadron duality hypothesis that relates parton spectra with observed hadrons. Detailed Monte Carlo models also became available, embedding various phenomenological approaches for soft QCD and experimental data into a numerical simulation for simulation of physics on an event-by-event basis.

Essentially, every aspect of multiparticle dynamics in elementary-particle and heavy-ion collisions was discussed at ISMD 2013. Between the all-day plenary sessions and the Monday evening poster session, the Symposium covered a number of topics, including underlying event studies, aspects of jet measurements (inclusive jets, inter-jet activity, multijet production), searches involving multi-object final states, and boosted jet techniques. A special session was dedicated to heavy ion collisions, which look very similar to the busy pp-collisions expected at future high-luminosity LHC runs. In addition, there were talks on multiparticle dynamics in astrophysics — an area of continually growing interest as large data sets become common.

Along with general discussions of multiparticle phenomena, several new experimental results were presented from the LHC experiments at CERN, as well as from Fermilab's Tevatron, the HERA collider at DESY, Jefferson Lab, the Relativistic Heavy-Ion Collider at Brookhaven, and the BaBar experiment at SLAC. In addition, several talks covered recent progress in theoretical QCD calculations, including Monte Carlo simulations, attempts to model and control the underlying event, searches for exotic processes using boosted jet techniques, multiparticle correlations, diffractive physics, and searches beyond the Standard Model using multi-object final states.

A primary theme that emerged from discussions at ISMD this year is the striking similarity between proton-proton collisions and heavy-ion collisions. This similarity, which exhibits itself in the high detector-occupancy of proton-proton collision events, presents significant challenges for future high-precision physics. A critical question for the next decade will be how to maintain energy resolution and reconstruction with a large contribution from multiple proton-proton interactions (pileup). Many participants expressed their concern that continued access to low-p_T jet physics is essential for future of the field.

The Symposium concluded with two views of the future of multiparticle dynamics. Chip Brock of Michigan State University discussed the conclusions of the Snowmass series of planning meetings that took place in the US

throughout 2012-2013. James Bjorken of SLAC concluded with a historic perspective of QCD. He considered the connections between outstanding issues that span nuclear physics, high-energy physics and cosmology, and encouraged a broad examination across the subdisciplines for answers.

The Symposium was mainly focused on testable predictions and precision measurements of Standard Model physics. The organizers provided an example of successful prediction by purchasing umbrellas for the participants one month in advance of the conference. The prediction of a rainy September in Chicago was confirmed in record fashion on the third day of the conference. The organizers wish similar success for all of the predictions discussed at the meeting.

The success of ISMD 2013 could not have occurred without the dedicated work of the International Advisory Committee, the Local Organizing Committee, the session Chairs, the secretaries, and the vocal and excited participants. We thank everyone involved, and are grateful for financial support from the U.S. Department of Energy, the National Science Foundation, the European Organization for Nuclear Research, the Deutsches Elektronen-Synchrotron and Research Centre of the Helmholtz Association, and the Illinois Institute of Technology College of Science. We now invite the reader to explore the summaries of research presented at the XLIII International Symposium on Multiparticle Dynamics.

Sergei Chekanov
Zack Sullivan
March 31, 2014

Overview of Higgs results from CMS

Petra Merkel for the CMS collaboration
Purdue University, Department of Physics,
525 Northwestern Avenue, 47906 West Lafayette, IN, USA

In this article we present an overview of Higgs boson results from the CMS Collaboration as presented at the ISMD13 conference.

1. Introduction

With the discovery of the Higgs boson by the CMS and ATLAS collaborations [1] new questions have arisen that need to be addressed. In particular, we need to measure if the new boson couples to the standard model (SM) particles at appropriate levels. Are the signal strengths, where observed, at the correct SM levels? Is the new boson a scalar, and not a pseudo-scalar or a tensor? We need to understand if this is the only new boson, and not one of several, and we need to measure if it couples to itself. Luckily, its mass of about 125 GeV allows us to answer many of these questions experimentally. In this article we present the current status of the ongoing analyses that contribute to these answers. We will show results for the dominant gluon-gluon fusion production process, as well as for vector boson fusion and associated production. The measurements are pursued in various decay channels, both in Higgs decays to vector bosons as well as fermions. Unless otherwise stated, the results are based on the full dataset from Run1 of the LHC, about 25 fb^{-1}.

2. Couplings to vector bosons

2.1. $\text{H} \to \text{ZZ} \to 4\ell$

The cleanest channel with the best Higgs mass resolution is the decay of the Higgs to a pair of Z bosons, which in turn decay to two electrons or muons each [2]. Figure 1 shows the four lepton invariant mass spectrum. The data from the full dataset are overlaid with background expectations from $\text{Z}\gamma^*$ and ZZ as well as inclusive Z production. Contributions from single Z decay to four leptons can be around the Z mass, while the SM process of on-shell ZZ production is found around 200 GeV and above. A

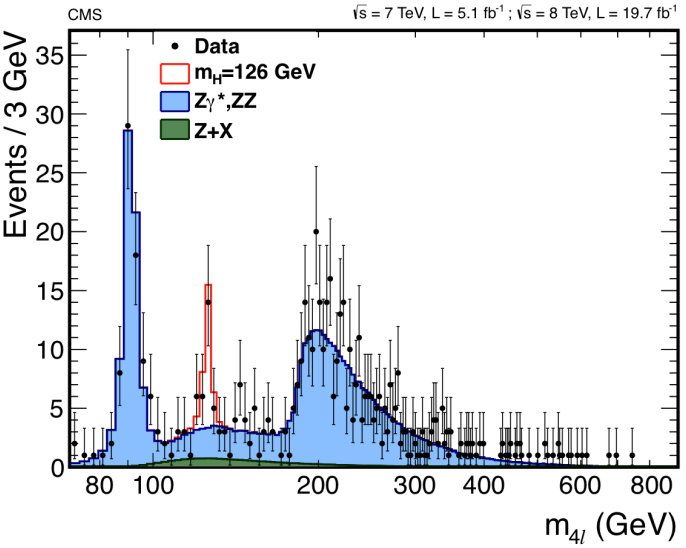

Fig. 1. Data from the H → ZZ → 4ℓ search channel are shown overlaid with SM background expectations. A simulated SM Higgs signal at 126 GeV is indicated as well.

clear excess of events above background expectations can be seen around 126 GeV, consistent with a SM Higgs signal.

The Higgs boson is observed as a narrow resonance with a local significance of 6.7 standard deviations, at a measured mass of $m_{\mathrm{H}} = 125.8 \pm 0.5(\mathrm{stat.}) \pm 0.2(\mathrm{syst.})$ GeV. The production cross section of the new boson times the branching fraction to four leptons is measured to be $0.91^{+0.30}_{-0.24}$ times that predicted by the SM (signal strength). Its spin-parity properties are found to be consistent with the expectations for the SM Higgs boson. The hypothesis of a pseudo-scalar and all the tested spin-one boson hypotheses are excluded at a 99% confidence level or higher. All the tested spin-two boson hypotheses are excluded at a 95% confidence level or higher.

2.2. H → WW → ℓνℓν

In the channel where the Higgs decays to a pair of W bosons, which subsequently each decay into a lepton and a neutrino [3], CMS sees a broad enhancement in data compared to the background only hypothesis, which is consistent with the SM Higgs boson of mass around 125 GeV and has a statistical significance of 4 standard deviations for this mass, see Figure 2. This result provides evidence for a Higgs-like particle decaying to $\mathrm{W^+W^-}$. Additional SM Higgs-like bosons are excluded in the mass range 128 – 600

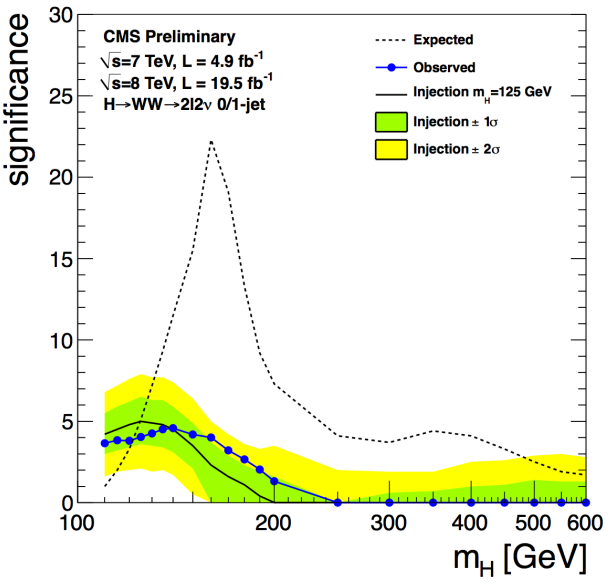

Fig. 2. Expected and observed significances are shown in the Higgs mass range of $110 - 600$ GeV for the $\mathrm{H} \to \mathrm{WW} \to \ell\nu\ell\nu$ search channel. A simulated SM Higgs signal with a Higgs mass of 125 GeV is indicated for comparison as well.

GeV at 95% confidence level.

The best fit value of the signal strength for $m_{\mathrm{H}} = 125$ GeV is found to be 0.76 ± 0.21. The hypothesis of the SM Higgs boson for quantum numbers and couplings is tested against the spin-2 hypothesis of a narrow resonance produced through gluon-gluon fusion and with minimal couplings to the $\mathrm{W^+W^-}$ pair. Assuming the best fit value of the signal strength obtained for the individual hypotheses, the observed separation is 0.5 and 1.3 standard deviations away from the expected values for the SM Higgs hypothesis and the spin-2 hypothesis, respectively.

2.3. $\mathrm{H} \to \gamma\gamma$

One of the discovery channels is where the Higgs boson decays to a pair of photons [4]. Despite a large cross section times branching ratio this channel is very challenging because of a large SM background. Figure 3 shows the measured 95% exclusion on the signal strength compared to the SM expectation and to the background-only hypothesis.

The signal strength at $m_{\mathrm{H}} = 125$ GeV is measured to be $0.78^{+0.28}_{-0.26}$. The significance of the signal in this channel alone is exceeding 3σ. A fit to the

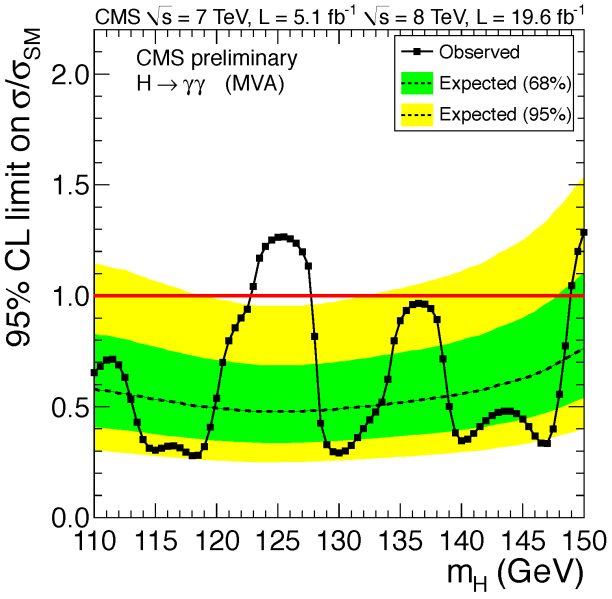

Fig. 3. The 95% upper limit on the signal strength of a Higgs boson decaying to two photons. The symbol $\sigma/\sigma_{\mathrm{SM}}$ denotes the production cross section times the relevant branching fractions, relative to the SM expectation. The background-only expectations are represented by their median (dashed line) and by the 68% and 95% CL bands.

di-photon invariant mass distribution in data results in a measured mass of $m_{\mathrm{H}} = 125.4 \pm 0.5(\mathrm{stat.}) \pm 0.6(\mathrm{syst.})$ GeV.

3. Couplings to fermions

3.1. $\mathrm{H} \to \mathrm{b\bar{b}}$

Due to the very large SM background in the gluon fusion production of this channel, we are presenting measurements only in the associated production and vector boson fusion. In the associated production, where the Higgs boson is created in addition to a vector boson, a W or a Z, which then decays subsequently into leptons, while the Higgs decays into a pair of b-quarks [6], the following channels have been taken into account: $\mathrm{W}(\to \mu\nu)\mathrm{H}(\to \mathrm{b\bar{b}})$, $\mathrm{W}(\to \mathrm{e}\nu)\mathrm{H}(\to \mathrm{b\bar{b}})$, $\mathrm{W}(\to \tau\nu)\mathrm{H}(\to \mathrm{b\bar{b}})$, $\mathrm{Z}(\to \mu\mu)\mathrm{H}(\to \mathrm{b\bar{b}})$, $\mathrm{Z}(\to \mathrm{ee})\mathrm{H}(\to \mathrm{b\bar{b}})$ and $\mathrm{Z}(\to \nu\nu)\mathrm{H}(\to \mathrm{b\bar{b}})$. We observe a broad excess of events compared to background expectations consistent with the production of the SM Higgs boson. Figure 4 shows the simulated background-subtracted invariant mass distribution, $m_{\mathrm{b\bar{b}}}$, for the combination of these production and decay

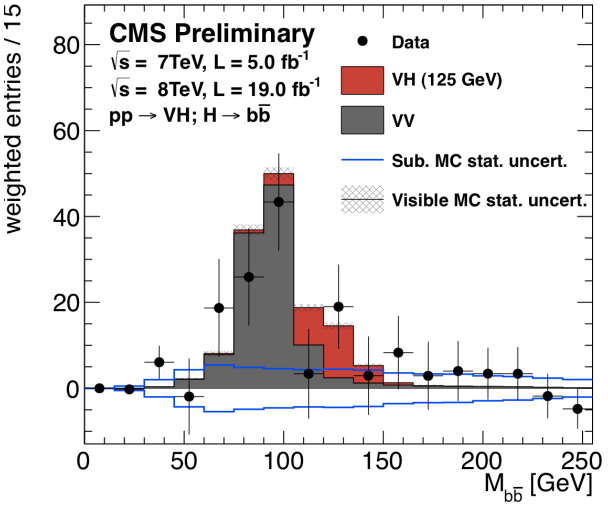

Fig. 4. Weighted $b\bar{b}$ invariant mass distribution, combined for all channels. All backgrounds, except di-boson processes, are subtracted.

channels. A combined significance for $m_{\mathrm{H}} = 125$ GeV is derived to be 2.1 standard deviations, while the signal strength is measured to be 1.0 ± 0.5 times the SM expectation.

In the vector boson fusion production we present a first measurement by using two forward jets to tag the events [7]. No excess is yet being observed in this channel alone.

3.2. $\mathrm{H} \rightarrow \tau\tau$

We are presenting results using the full Run1 dataset and by combining gluon fusion and vector boson fusion production modes using the following final states: eμ, $\mu\mu$, eτ_h, $\mu\tau_h$ and $\tau_h\tau_h$, as well as associated production modes, WH and ZH, with the following final states: $\ell\nu\ell\tau_h$, $\ell\nu\tau_h\tau_h$ and $\ell\ell\tau_h\tau_h$ [8]. An emerging signal can be seen in Figure 5, which shows the invariant mass of the τ-pairs for a subset of the above mentioned channels.

The observed signal above background for $m_{\mathrm{H}} = 125$ GeV is 2.9 standard deviations for all $\mathrm{H} \rightarrow \tau\tau$ decays under study. When combining this result with the $\mathrm{H} \rightarrow \mathrm{bb}$ measurements, we obtain an evidence for the Higgs boson coupling to fermions of 3.4 standard deviations.

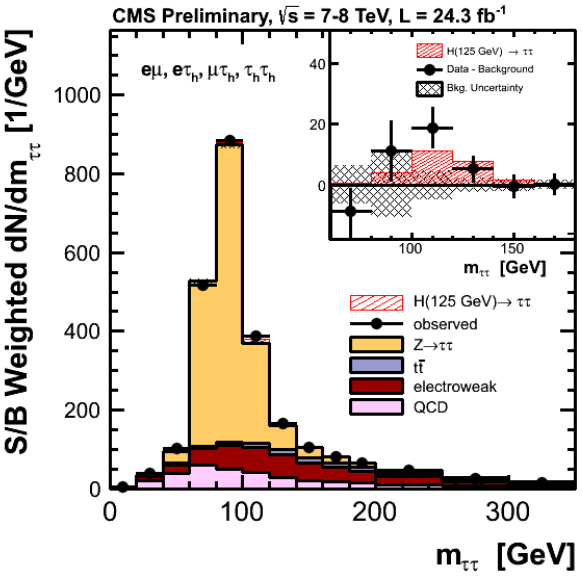

Fig. 5. Combined observed and expected $m_{\tau\tau}$ distribution for the $\mu\tau_h$, eτ_h, eμ and $\tau_h\tau_h$ channels. The distributions obtained in each category of each channel are weighted by the ratio between the expected signal and background yields in the category. The insert shows the corresponding difference between the observed data and expected background distributions, together with the expected signal distribution for a SM Higgs signal at $m_{\mathrm{H}} = 125$ GeV, with a focus on the signal region.

4. Standard model combination

We have combined the SM Higgs measurements in the various channels with each other [10]. The signal strength is measured and found compatible in a multitude of production and decay channels as summarized in Figure 6. All channels are found compatible with the SM Higgs hypothesis. The sensitivity of the measurements will be vastly improved in Run2 of the LHC.

The mass of the observed state has been measured to be $m_{\mathrm{H}} = 125.7 \pm 0.3(\mathrm{stat.}) \pm 0.3(\mathrm{syst.}) = 125.7 \pm 0.4$ GeV. We derive the coupling strength to fermions and vector bosons and find that the combined results are compatible within 1.5 standard deviations with the SM Higgs boson.

In order to determine the spin and tensor structure of the newly observed boson, several alternative models have been tested against the SM Higgs hypothesis of 0^+, such as 0^-, 1^+, 1^- and 2^+, and the preferred solution has been found to be the SM one.

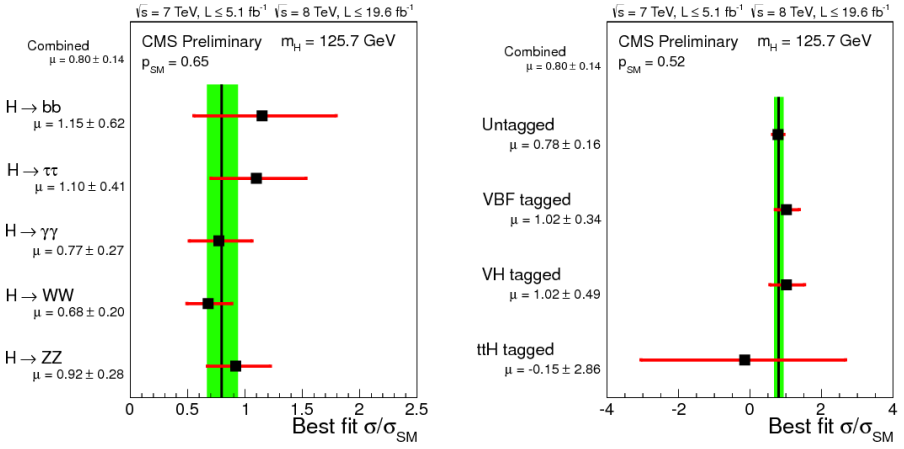

Fig. 6. Values of $\mu = \sigma/\sigma_{\mathrm{SM}}$ for the combination (solid vertical line) and for sub-combinations (points). The vertical band shows the overall μ value 0.80 ± 0.14. The horizontal bars indicate the $\pm 1\sigma$ uncertainties on the μ values for individual channels; they include both statistical and systematic uncertainties. Left: grouped by decay mode. Right: grouped by signature enhancing specific production mechanisms.

5. Beyond the standard model

There are many possibilities that change the precise predictions of the minimal Higgs sector of the SM. There could be a fourth, heavy, generation of fermions (SM4), which would modify the Higgs couplings and enhance the SM4 Higgs cross section over the SM one. This has already been ruled out over the entire parameter space with the 7 TeV data alone. The Higgs boson could be fermiophobic, which means that the mass of the fermions has a different origin than the Higgs. This would change the low mass Higgs production and decays dramatically and has also been ruled out for the newly observed boson at 125 GeV [11]. One conceivable expansion of the SM Higgs could be the two Higgs doublet model (2HDM), in which multiple Higgs bosons exist: three neutral and two charged ones, as required for example by the minimal supersymmetric models (MSSM). There are other models with even more Higgs bosons. Within the Run1 dataset collected by the CMS experiment we are looking for additional Higgs bosons, preliminary results have been presented [12, 13]. An additional SM-like Higgs boson is excluded for masses up to 1 TeV.

6. Summary

We have seen an impressive performance of the LHC and the CMS detector during the Run1 data taking period. The CMS collaboration successfully covered a large Higgs program over the past years [14]. The observation of the new boson was confirmed by the latest data. Everything points to a standard model-like Higgs boson. We are currently preparing for the new data to come in Run2, which will be the starting point of a new era: precision measurements of Higgs properties and new channels, searches beyond the standard model, and many more.

References

[1] CMS and ATLAS collaborations, Phys. Lett. B **716**, 30 (2012).
[2] CMS Collaboration, public analysis summary CMS-HIG-13-002.
[3] CMS Collaboration, public analysis summary CMS-HIG-13-003.
[4] CMS Collaboration, public analysis summary CMS-HIG-13-001.
[5] CMS Collaboration, public analysis summary CMS-HIG-13-006 and arXiv:1307.5515.
[6] CMS Collaboration, public analysis summary CMS-HIG-13-012.
[7] CMS Collaboration, public analysis summary CMS-HIG-13-011.
[8] CMS Collaboration, public analysis summary CMS-HIG-13-004.
[9] CMS Collaboration, public analysis summary CMS-HIG-13-019.
[10] CMS Collaboration, public analysis summary CMS-HIG-13-005.
[11] CMS Collaboration, Phys. Lett. B **725**, 36 (2013).
[12] CMS Collaboration, Eur. Phys. J. C **73**, 2469 (2013).
[13] CMS Collaboration, Eur. Phys. J. C **72**, 2189 (2012).
[14] http://cms.web.cern.ch/org/cms-higgs/results.

Boosted heavy particles and jet substructure with the CMS detector

Ivan Marchesini on behalf of the CMS Collaboration

University of Hamburg, Germany

In the last years, the understanding of jets and jet substructure has become increasingly important, in particular in the context of new physics searches. Many new physics models involve highly boosted hadronically-decaying particles, which result in jet-like objects with large masses and an intrinsic substructure. Discrimination of these heavy jets from ordinary quark and gluon jets is possible through a plethora of new techniques. The understanding of jets can be exploited also for the identification of pileup jets and for the discrimination between quark jets and gluon jets. A sampling of these techniques is discussed together with their validation on collider data recorded in proton-proton collisions at $\sqrt{s} = 8\,\text{TeV}$ with the CMS detector in the year 2012. The commissioning in the boosted regime of algorithms used to identify jets originating from bottom quarks is also discussed. Many studies have highlighted the potential of using jet substructure techniques to improve the sensitivity in physics searches. An overview of recent CMS results employing these techniques is presented.

1. Introduction

The LHC has crossed new energy frontiers in particle physics, where searches for new physics beyond the Standard Model (SM) typically involve objects with very large transverse momenta (p_T). In this regime the resulting decay products for hadronic decays of heavy particles tend to be collimated and can fall within a single jet ("fat-jet"). In this case, selections based on multiple jet searches cannot be applied and jet substructure is necessary to identify ("tag") the particle initiating the jet.

Jets are reconstructed at CMS [1] by clustering the objects ("candidates") reconstructed using a particle flow (PF) approach [2, 3]. The list of neutral and charged particle candidates produced by the PF reconstruction are typically clustered using an anti-kT algorithm of radius R=0.5 (AK5) [4]. For some studies, jets are reconstructed with the Cambridge-Aachen algorithm, either of radius R=0.8 (CA8) or R=1.5 (CA15) [5].

The performance of jet substructure observables used to identify merged hadronic decays of W bosons (W-jets) has been extensively studied at

CMS [6]. Section 2 discusses the results achieved. An algorithm developed to reconstruct highly boosted, hadronically-decaying top quarks [7] is described in Section 3. A wide range of physics processes is characterized by jets arising from the hadronization of bottom quarks (b-jets) and the ability to identify b-jets (b-tagging) is a fundamental prerequisite for several analyses. Section 4 summarizes a first study at CMS, dedicated to the commissioning of b-tagging algorithms in boosted topologies [8]. Two benchmark topologies are considered, with boosted tops and with boosted Higgs decaying to $b\bar{b}$. Section 5 discusses the use of jet shape information to reduce the incidence of jets from pileup (PU) [9]. A likelihood discriminator based on a similar concept, capable of distinguishing between jets originating from quarks and from gluons, is presented in Section 6. Finally, several of the presented tools have already been used in searches for physics beyond the SM, as shown in Section 7.

2. Identification of hadronically decaying W bosons

To study the discrimination of W-jets from gluon- and quark-initiated jets (referred to as QCD jets), a number of topologies are considered. A semileptonic $t\bar{t}$-enriched sample provides a source of W-jets in data. To study the misidentification of W-jets two topologies are analyzed, namely dijet and W+jet, where the W decays leptonically [10, 11].

The main observable to identify W-jets is the CA8 jet mass, which can be improved by grooming methods such as pruning [12, 13]. A good W-tagging performance is achieved selecting pruned jet masses between $60\,\mathrm{GeV}/c^2$ and $100\,\mathrm{GeV}/c^2$. Possible improvements can be achieved by exploiting additional information from jet substructure, such as the mass drop μ [14] or the N-subjettiness τ_N [15]. The performance of various substructure observables combined with the pruned jet mass requirement is shown in Fig. 1 (left). The most performing variable is the N-subjettiness τ_2/τ_1. A combination of the observables in a Likelihood and a Multi-layer Perceptron Neural Network (MLP) multi-variate discriminant is also shown.

A general good agreement between data and Monte Carlo is observed for the substructure variables considered. Small discrepancies in the W-tagging performance between data and simulation can be taken into account applying to simulation scale factors (SF). The SF extraction is done estimating the W-tagging selection efficiency in data and simulation, based on a $t\bar{t}$ control sample. For a W-tagger based on a τ_2/τ_1 requirement and on a pruned jet mass selection the computed scale factor is 0.905 ± 0.08. The pruned jet mass distribution is shown in Fig. 1 (right).

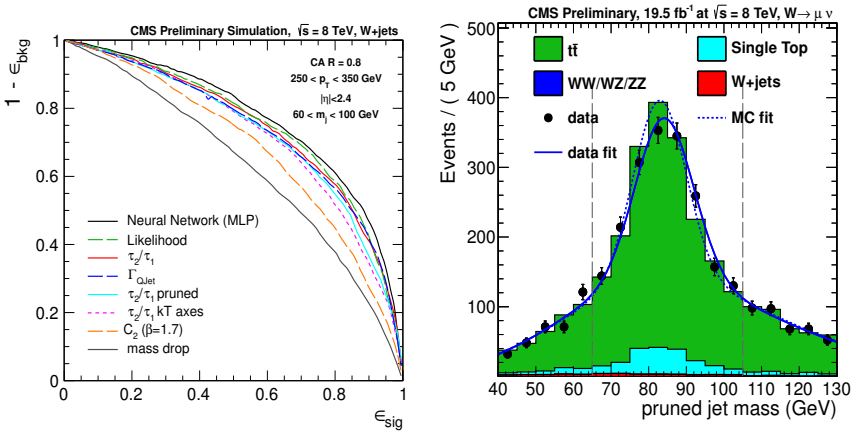

Fig. 1. Left: W-tagging performance for various discriminant observables in a low jet p_T region, 250-350 GeV/c. Right: Pruned jet mass distribution in a semi-leptonic $t\bar{t}$ sample, for jets satisfying a τ_2/τ_1 requirement.

3. Boosted top jet tagging

The CMS top-tagger is based on the algorithm developed by Kaplan et al. [16] and uses CA8 jets. The algorithm seeks the subjets of the top fat-jet reversing the clustering sequence. With a first primary decomposition the algorithm attempts to split the jet into two subclusters. A following secondary decomposition attempts to split the clusters found by the primary decomposition. The three highest p_T subjets found are examined pairwise and the invariant mass of each pair is calculated. The jet is identified as top if the jet mass is close to the top quark mass, at least three subjets are found and the minimum pairwise mass is greater than $50\,\mathrm{GeV}/c^2$. Good performances are achieved for jets with $p_T > 400\,\mathrm{GeV}/c$, when the decay products are collimated enough to be clustered in a single jet (Fig. 2, left).

The performance of the CMS top-tagger is evaluated in [17], using a semileptonic $t\bar{t}$ control sample and obtaining a data-to-simulation SF$=0.926 \pm 0.03$. The misidentification probability is measured using an anti-tag and probe method. Events with two or more jets are selected, with the two leading jets having $p_T > 400$ GeV/c. One jet is required to fulfill all the top-tagging requirements, except from asking the minimum pairwise mass to be lower than $30\,\mathrm{GeV}/c^2$, enriching the sample in QCD events. The top-tagging efficiency on the second jet with $p_T > 400$ GeV/c gives a measurement of the misidentification probability (Fig. 2, right).

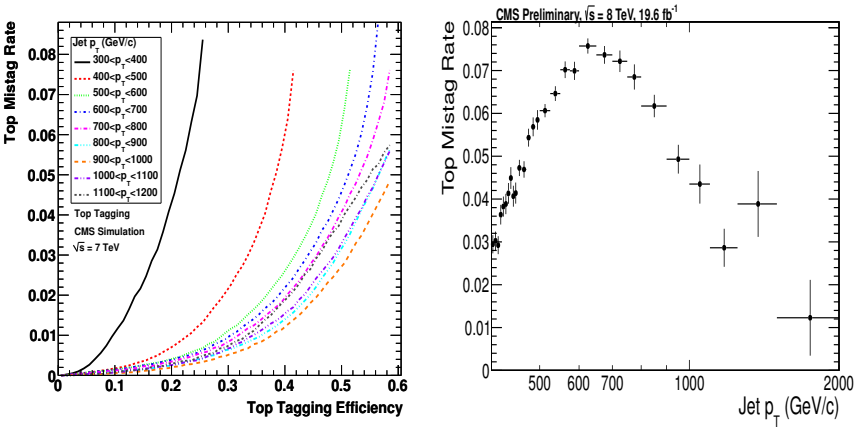

Fig. 2. Left: Simulated mistag rate versus efficiency for the CMS-top-tagger. The efficiency is calculated on seven $Z' \to t\bar{t}$ samples with Z′ masses between 750 GeV/c and 4 TeV/c. The mistag rate is calculated on a QCD dijet sample. Right: Mistag rate of the CMS-top-tagger as a function of jet p_T, measured in data using an anti-tag and probe method.

4. B-tagging in boosted topologies

The b-tagging performance in event topologies with boosted top quarks is studied in samples of simulated $T'\overline{T}' \to tH\overline{t}H$ events with a T′ mass of 1 TeV/c^2. Merged hadronic decays of top quarks are selected using the `HEPTopTagger` algorithm [18], which is based on CA15 jets and produces three subjets. Event topologies with boosted Higgs bosons are studied in samples of simulated $B'\overline{B}' \to bH\bar{b}H$ events with a B′ mass of 1 TeV/c^2 and 1.5 TeV/c^2. Smaller CA8 jets are used in this case and two subjets are clustered using the pruning technique. For both channels the Combined Secondary Vertex (CSV) b-tagging algorithm is adopted [8].

Two b-tagging approaches are considered: (i) application of b-tagging to fat-jets, (ii) application of b-tagging to subjets, which are reconstructed within fat-jets. As exemplified in Fig. 3 (left) for the top channel, subjet b-tagging overall outperforms the fat-jet tagging. Dedicated studies using suitably defined control samples have been performed to validate b-tagging in the boosted environment. The level of agreement present in the boosted regime is found to be as good as in the non-boosted regime for isolated AK5 jets. The SF for the non-boosted and for the boosted regimes are found to be in perfect agreement.

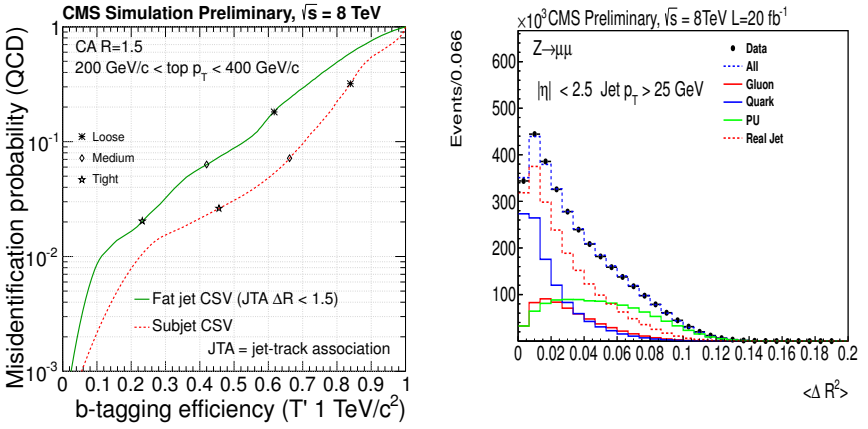

Fig. 3. Left: Performance of the CSV algorithm in simulation on CA15 fat-jets and on subjets of the same jets. The misidentification probability on inclusive QCD jets is shown versus the b-tagging efficiency on top quarks from a pair-produced $T' \rightarrow tH$ sample. Right: $\langle \Delta R^2 \rangle$ for jets with $p_T > 25\,\text{GeV}/c$ and $\eta < 2.5$.

5. Pileup jet identification

Identification of PU jets is performed in two ways at CMS, either using vertex information or through the use of jet shape information. As some fraction of charged particles in PU jets is typically not pointing to the vertex of the primary proton-proton interaction, the removal of PU based on vertex information is highly efficient. However, it can only be applied in the central region of the detector, where tracking is available. Jet shape information can be exploited to extend the identification of PU jets beyond the tracker acceptance. The most discriminating variable is shown in Fig. 3 (right), given by the radial extension of the jet, with respect to the jet axis: $\langle \Delta R^2 \rangle = \sum_i \Delta R_i^2 p_{Ti}^2 / \sum_i p_{Ti}^2$, where i runs over the jet PF-candidates.

Shape and tracking information are combined using a boosted decision tree, known as PU-jet multivariate analysis (MVA). The performance of the MVA is evaluated in simulated $Z \rightarrow \mu\mu$ events and on data using a control sample of $Z(\rightarrow \mu\mu)$+jets, where the jet recoiling against the Z is used as probe. For central jets the performance is excellent and signal efficiencies up to 99% can be achieved for PU rejections of 90-95% (85%) for $30\,\text{GeV} < p_T < 50\,\text{GeV}$ ($20\,\text{GeV} < p_T < 30\,\text{GeV}$). The performance degrades for large $|\eta|$ values, but still the fraction of PU jets can be significantly reduced. The agreement between data and simulation is generally good, with maximum discrepancies up to ∼20% in the forward region.

6. Quark-gluon discrimination

Hadronic jets initiated by gluons exhibit a different behaviour with respect to jets from light-flavor quarks. They are characterized by a higher charged particle multiplicity, by a softer fragmentation function and are less collimated. Observables sensitive to these differences can be combined in a multivariate analysis to develop a quark-/gluon-jet discriminator. This is useful for analyses reconstructing hadronic final states with a specific number of jets from light-quarks or to reduce combinatorial backgrounds in the mass reconstruction of heavy particles decaying into distinct jets.

The first discriminating variable is the multiplicity of the charged PF candidates. The jet width is quantified by the minor axis of the ellipse approximating the $\eta - \phi$ jet shape. Finally, a variable sensitive to the fragmentation function is defined as: $\sqrt{\sum_i p_{T,i}^2 / \sum_i p_{T,i}}$, where the index i runs over the PF jet candidates. The performance of the likelihood-product discriminator of these observables is shown in Fig. 4 (left).

The validation on data is performed on two samples: Z+jets events, which are quark-enriched, and dijet events, which are gluon-enriched. While the quark efficiency is simulated with a 5% precision, the discriminating performance of gluons is worse in data by up to 15%.

7. Searches employing substructure

Several searches at CMS have highlighted the potential of substructure. The CMS top-tagger has been used in searches for $t\bar{t}$ resonances, manifesting themselves in an enhancement of the invariant mass distribution $m_{t\bar{t}}$ of the $t\bar{t}$ system [19]. Several extensions of the SM suggest the existence of such resonances, for instance Kaluza-Klein excitations of particles or additional heavy gauge bosons, referred to as Z′, decaying predominantly to $t\bar{t}$. The fully hadronic final state is selected requiring two top-tagged jets with large p_T. No excess of events above the yield expected from the SM is observed and limits on the production cross section times branching fraction are set (Fig. 4, right). Depending on the specific model, non-SM resonances with masses below 2.1-2.7 TeV/c^2 are excluded at the 95% CL.

In explaining the features of electroweak symmetry breaking for scenarios beyond the SM, boosted final states with vector-like heavy quarks are typically present. In [20] an inclusive search for the pair production of vector-like bottom quark partners B′ that decay into tW, bZ or bH final states is performed. To select highly boosted W, Z or Higgs bosons that are merged into a single jet, a tagger is employed based on the pruned jet mass and on the mass drop observable. No significant excess of events is observed with respect to the SM expectations. A 95% CL limits between

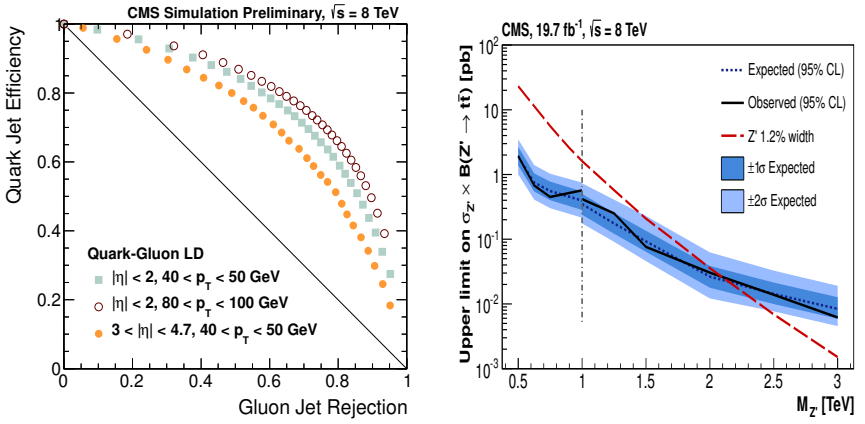

Fig. 4. Left: discrimination performance curves of the quark-gluon tagger, for different p_T and η regions. Right: The 95% CL upper limits on the production cross section times branching fraction as a function of the $t\bar{t}$ invariant mass for Z′ resonances with $\Gamma(Z')/M(Z')=1.2\%$ compared to theory predictions.

582 GeV/c^2 and 732 GeV/c^2 are set on the B′ mass for various decay branching ratios. In [21] a search for the production of heavy partners of the top quark with charge 5/3 is performed, assuming 100% braching ratio to tW. Both top-tagging and W-tagging are exploited by this study, which sets a lower limit on the mass of the heavy quark of 770 GeV/c^2 at the 95% CL. A search for an heavy partner of the top quark with charge 2/3 has been also performed [22], scanning all the possible branching ratios between three assumed decay modes: bW, tZ, and tH. The search in a final state with a single lepton has been performed using a multivariate analysis, exploiting both W- and top-tagging. Limits between 687 GeV/c^2 and 782 GeV/c^2 at the 95% CL are quoted for the heavy quark mass.

N-subjettiness and the pruned jet mass substructure variables are employed in [23, 24] to select final states with boosted hadronic decays of W and Z bosons, predicted by several models of physics beyond the SM. For instance, a Randall-Sundrum graviton decaying to WW or ZZ or a heavy partner of the SM W boson W′ which decays to WZ. Limits are set on the mass of the heavy particle, depending on the model. A heavy W′ decaying to WZ is excluded for masses up to 1.73 TeV/c^2 at the 95% CL.

8. Conclusions

Jet substructure techniques are discussed, developed for the identification of boosted hadronically decaying particles and for the discrimination

of jets with different flavors or not coming from the primary proton-proton collision. These tools are tested against data collected at the CMS experiment, observing extremely good performances, in particular in the context of new physics searches.

References

[1] S. Chatrchyan *et al.* (CMS Collaboration), JINST **3**, S08004 (2008).
[2] CMS Collaboration, CMS-PAS-PFT-09-001.
[3] CMS Collaboration, CMS-PAS-PFT-10-002.
[4] M. Cacciari, G.P. Salam, and G. Soyez, J. High Energy Phys. **04**, 063 (2008).
[5] Y.L. Dokshitzer, G.D. Leder, S. Moretti, and B.R. Webber, J. High Energy Phys. **08**, 001 (1997).
[6] CMS Collaboration, CMS-PAS-JME-13-006.
[7] CMS Collaboration, CMS-PAS-JME-10-013.
[8] CMS Collaboration, CMS-PAS-BTV-13-001.
[9] CMS Collaboration, CMS-PAS-JME-13-005.
[10] CMS Collaboration, CMS-PAS-EXO-12-024.
[11] CMS Collaboration, CMS-PAS-HIG-13-008.
[12] S.D. Ellis, C.K. Vermilion, and J.R. Walsh, Phys. Rev. D **80**, 051501 (2009).
[13] S.D. Ellis, C.K. Vermilion, and J.R. Walsh, Phys. Rev. D **81**, 094023 (2010).
[14] J.M. Butterworth, A.R. Davison, M. Rubin, and G.P. Salam, Phys. Rev. Lett. **100**, 242001 (2008).
[15] J. Thaler and K. Van Tilburg, J. High Energy Phys. **03**, 015 (2011).
[16] D.E. Kaplan, K. Rehermann, M.D. Schwartz, and B. Tweedie, Phys. Rev. Lett. **101**, 142001 (2008).
[17] CMS Collaboration, CMS-PAS-B2G-12-005.
[18] T. Plehn and M. Spannowsky, J. Phys. G **39**, 083001 (2012).
[19] S. Chatrchyan *et al.* (CMS Collaboration), arXiv:1309.2030 [hep-ex].
[20] CMS Collaboration, CMS-PAS-B2G-12-019.
[21] CMS Collaboration, CMS-PAS-B2G-12-012.
[22] CMS Collaboration, CMS-PAS-B2G-12-015.
[23] CMS Collaboration, CMS-PAS-EXO-12-021.
[24] CMS Collaboration, CMS-PAS-EXO-12-024.

Hadronic final states in high-p_T QCD at CDF

Keith Matera, on behalf of the CDF collaboration

University of Illinois at Urbana-Champaign

The heavy quark content associated with gauge boson production is of great interest to studies of QCD. These events probe the gluon and heavy-quark parton distribution functions of the proton, and also provide a measurement of the rate of final state gluon splitting to heavy flavor. In addition, gauge boson plus heavy quark events are representative of backgrounds to Higgs, single top, and supersymmetric particle searches. Recent work with the CDF II detector at the Fermilab Tevatron has measured the cross-section of several gauge boson plus heavy flavor production processes, including the first Tevatron observation of specific charm process $p\bar{p} \to W + c$. Results are found to be in agreement with NLO predictions that include an enhanced rate of $g \to c\bar{c}/b\bar{b}$ splitting. Lastly, a new analysis promises to probe a lower $p_T(c)$ region than has yet been explored, by fully reconstructing $D^* \to D^0(K\pi)\pi$ decays in the full CDF dataset (9.7 fb^{-1}).

1. Introduction

The study of gauge boson ($\gamma/W/Z$) plus heavy quark Q (b and c) production in hadronic collisions provides valuable information about the nature of QCD in accelerator events.

Measurements of these events are sensitive to the gluon and heavy-quark parton distribution functions of the proton. While convention assumes that charm and bottom quarks in the proton arise only from gluon splitting, there are other models that allow for intrinsic heavy quarks in the proton [1]. Measuring the cross-sections of $p\bar{p} \to \gamma/W/Z{+}b/c$ production tests these models, as well as measuring the rate of final-state gluon splitting to heavy quarks [2, 3]. Previous work has suggested that the rate of final-state gluon splitting to heavy quarks is roughly twice as large as that predicted by PYTHIA simulations [4–6].

Careful measurement of gauge boson plus heavy flavor cross-sections could also lead to a better understanding of other processes. The final state of $p\bar{p} \to \gamma/W/Z{+}b/c$ events are similar to the final states of neutral and charged Higgs boson production, single top production, and supersymmetric top quark production.

The CDF II detector at the Fermilab Tevatron [7] is well-suited to search for these events. The CDF II is a cylindrical detector with approximate azimuthal and forward-backward asymmetry. Three separate silicon microstrip detectors near the beampipe allow vertex reconstruction of prompt decays with a resolution of 30 μm in the transverse direction (60 μm along the beamline). The central outer tracker (COT), an open-cell drift chamber, provides excellent track resolution from a radius of $40 - 137$ cm. The COT and silicon detectors are immersed in a 1.4 T magnetic field parallel to the beamline, sourced by a solenoid outside of the COT. This field provides charge identification through track curvature. Electromagnetic calorimeters outside of the solenoid provide photon and electron identification, while hadronic calorimeters and muon chambers allow the identification of neutral hadrons and muons, respectively. A three-layer trigger system identifies events of interest, including those with secondary vertices (such as charm and bottom events), and those with high-p_T photon or lepton candidates (such as gauge-boson events).

In this paper, we first discuss recent CDF measurements of $\gamma+b/c$ cross-sections [8], and then move onto observations of $W/Z+b/c$ events [9, 10]. We conclude with a new approach at CDF for identifying $W/Z + c$ events [11].

2. Prompt photon + heavy flavor

We begin by discussing a recent CDF analysis of $\gamma+b/c$ cross-sections [8]. Direct photon production in association with heavy flavor is dominated by $gQ \to \gamma Q$ for $E_T^\gamma < 100$ GeV/c. At higher E_T^γ, production is dominated by quark-antiquark annihilation $q\bar{q} \to \gamma g \to \gamma Q\bar{Q}$ [12].

To identify these events, a photon candidate must first be identified which satisfies $E_T^\gamma > 30$ GeV/c and $\eta < 1.04$. An artificial neural network, constructed from isolation variables and calorimeter- and strip-chambers-shape information, is used to reduce background among the candidates [13].

Once a photon candidate has been tagged, jets are reconstructed using the JETCLU algorithm with cone radius $R = \sqrt{(\Delta\phi)^2 + (\Delta\eta)^2} < 0.4$. At least one jet with $E_T > 20$ GeV and $|\eta| < 1.5$ must be classified as a heavy-flavor jet using a secondary-vertex tagger [14], and this jet must be reconstructed in a volume outside of the $R = 0.4$ cone surrounding the photon candidate. If multiple jets pass these cuts, the jet with the highest E_T is selected for further analysis.

The invariant mass M_{SecVtx} of the system of charged particles originating at the secondary vertex is then calculated, assuming that all particles are pions. The M_{SecVtx} distribution is fit using templates for b-, c-, and light quark jets constructed with PYTHIA [15].

Results, reported as a differential cross-section, are compared to Monte

Carlo predictions (Figure 1). The NLO pQCD predictions agree with data for low E_T^γ, but do not well describe the data for $E_T^\gamma > 70$ GeV. This is true for both the charm- and bottom-jet cross-sections. This can be explained by noting that in this high-E_T^γ regime, the dominant production process is $q\bar{q} \to \gamma g \to \gamma Q\bar{Q}$, which is present only to leading order in NLO predictions.

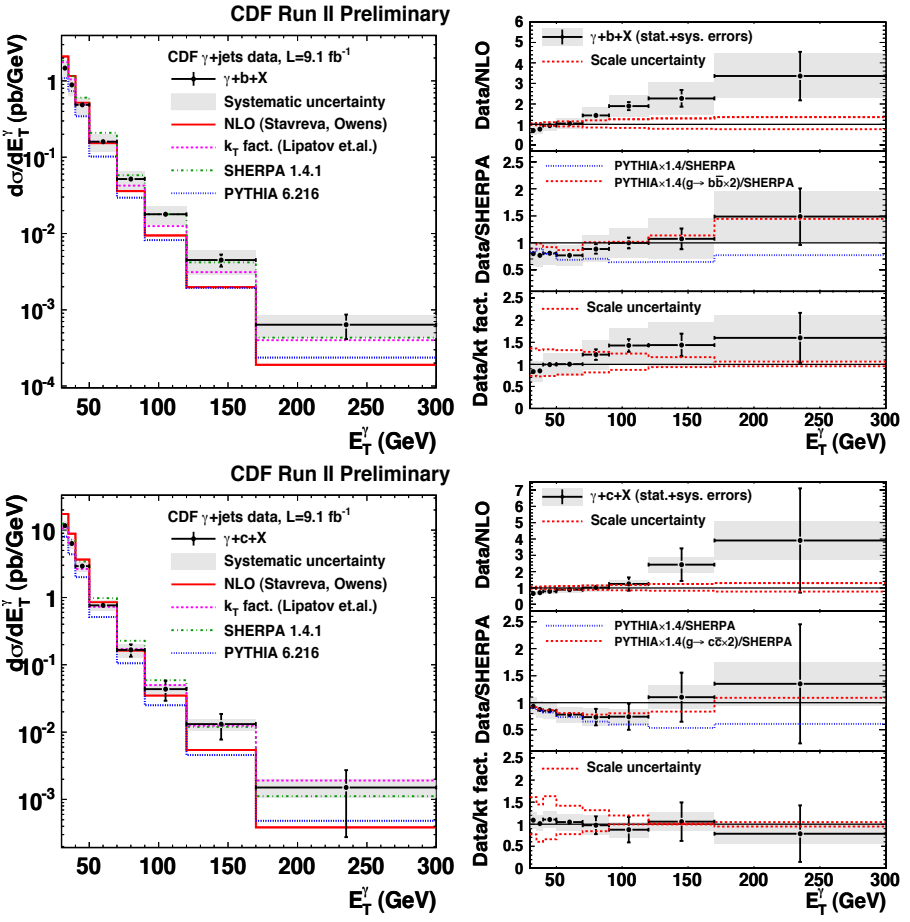

Fig. 1. Measured differential cross-sections compared with theoretical predictions. The left plots show absolute comparisons. The right plots show the ratios of data to theoretical predictions, with PYTHIA predictions scaled by 1.4. Scale uncertainties are shown for the NLO and k_T-factorization predictions.

The k_T -factorizations and SHERPA are in agreement with the measured cross-sections. PYTHIA can be made to agree well with data by doubling the rate for $g \to b\bar{b}/c\bar{c}$, and scaling the prediction by a factor of 1.4.

3. $W + c$ production

We now consider a recent CDF search [9] for the specific charm production process $p\bar{p} \to Wc$. To first order, this process proceeds as $gq \to Wc$, where q is a d, s, or b quark. In $p\bar{p}$ collisions, the larger d quark PDF is overridden by the small quark-mixing Cabibbo-Kobayashi-Maskawa (CKM) matrix element $|V_{cd}|$, such that about 80% of Wc production is due to strange-quark gluon fusion. Therefore, $p\bar{p} \to Wc$ production is sensitive to the s and g PDFs of the proton [2, 3], as well as CKM matrix element $|V_{cd}|$.

In this search [9], the W boson is identified through leptonic decay by looking for an electron (muon) with $E_T > 20$ GeV ($p_T > 20$ GeV/c), in events with missing energy $\not\!\!E_T > 25$ GeV. The charm quark is identified by looking for semi-leptonic decays of the charm hadron: an electron or muon candidate within a jet ($E_T^{jet} > 20$ GeV and $|\eta^{jet}| < 2.0$). This is referred to as "soft lepton tagging" or "SLT$_\ell$" [16–19].

Charge conservation in the process $p\bar{p} \to W + c$ allows only final states in which the W and c are oppositely charged. As such, the final state must involve two oppositely-signed leptons. The $p\bar{p} \to W + c$ production cross-section is found as

$$\sigma_{Wc} = \frac{N_{\rm tot}^{\rm OS\text{-}SS} - N_{\rm bkg}^{\rm OS\text{-}SS}}{SA \int Ldt} \tag{1}$$

where $N_{\rm tot}^{\rm OS\text{-}SS}$ ($N_{\rm bkg}^{\rm OS\text{-}SS}$) is the difference in the number of OS and SS events in data (background). A is the acceptance times efficiency for identifying Wc events, and $S = (N_{\rm Wc}^{\rm OS} - N_{\rm Wc}^{\rm SS})/(N_{\rm Wc}^{\rm OS} + N_{\rm Wc}^{\rm SS})$ accounts for the charge asymmetry of the real reconstructed Wc events. Both A and S are derived from a Monte Carlo simulation of Wc events and the CDF detector.

Accounting for background, the final result yields $\sigma_{WC} \times B(W \to \ell\nu) = 13.6 \pm 2.2({\rm stat})^{+2.3}_{-1.9}({\rm syst}) \pm 1.1({\rm lum}){\rm pb} = 13.6^{+3.4}_{-3.1}{\rm pb}$ for $p_{Tc} > 20$ GeV/c, $|\eta_c| < 1.5$. This agrees with a NLO calculation over the same phase space of 11.4 ± 1.3 pb [9]. Figure 2 shows the measured SLT muon and electron p_T distribution spectra as measured in data.

4. $Z + b$ production

Another CDF search [10] measures the production cross section of b jets with a Z boson, using 9.1 fb^{-1} of data. An artificial neural network is used to improve lepton identification efficiency for leptonic decays $Z \to \mu\mu/ee$. Jets are identified using the MidPoint algorithm with a cone size of $R = 0.7$, and a merging/splitting fraction set to 0.75. Jets are required to have corrected $p_T \geq 20$GeV/c and $|Y| \leq 1.5$. To be considered a b jet candidate,

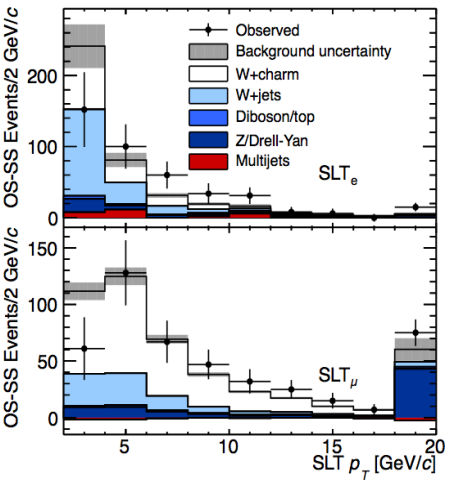

Fig. 2. The soft muon and soft electron p_T distributions. The Wc contribution shown is normalized to the measured cross section.

a jet must also have a reconstructed secondary vertex within a cone of 0.4 with respect to the jet axis.

As in [8], the fraction of jets that contain bottom hadron decays is found by fitting the M_{SecVtx} distribution of these reconstructed secondary vertices with b, c, and light flavor jets templates. The fraction of inclusive Z that are produced in association with a b jet is found to be $\sigma_{Z+bjet}/\sigma_Z = 0.261 \pm 0.023(\text{stat}) \pm 0.029(\text{syst})\%$. The fraction of Z + jet events with at least one bottom jet is found to be $\sigma_{Z+bjet}/\sigma_{Z+jet} = 2.08 \pm 0.18(\text{stat}) \pm 0.27(\text{syst})\%$. These measured cross-section ratios are found to be larger than those of the ALPGEN prediction by a factor of 1.6 [10], but are in agreement with MCFM within uncertainty (Table 1).

Table 1. Cross section ratios as calculated by MCFM. Within uncertainty, these results agree with measurements in data.

	NLO $Q^2 = m_Z^2 + p_{T,Z}^2$	NLO $Q^2 =< p_{T,jet}^2 >$
$\frac{\sigma(Z+b)}{\sigma(Z)}$	2.3×10^{-3}	2.9×10^{-3}
$\frac{\sigma(Z+b)}{\sigma(Z+jet)}$	1.8×10^{-3}	2.2×10^{-3}

The differential cross section measurements for Z+b jet production as a function of jet p_T is shown in Figure 3. These measurements have a large statistical uncertainty ($\sim$16%), but are in good agreement with NLO theory evaluated with MCFM predictions.

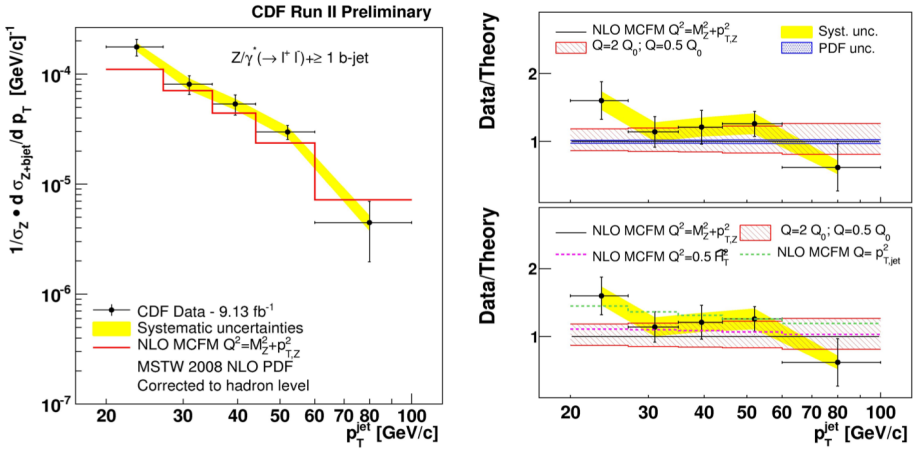

Fig. 3. The left panel displays the measured Z+b jet differential cross section with respect to the inclusive Z differential cross section, as a function of b jet p_T. The right panel shows the ratios of data to theoretical predictions at different renormalization and factorization scales.

5. A new approach to $W/Z + c$ at the Tevatron

Bottom and charm production in W/Z events at the Tevatron has, to date, been measured primarily by identifying heavy flavor in W/Z plus jet events. The standard procedure is to find candidate jets with a secondary vertex and $E_T^{jet} > 15$ or 20 GeV, and to fit the mass distribution of the secondary vertex M_{SecVtx} with b-, c-, and light-jet templates (as in [8, 10]).

A new CDF analysis [11] seeks instead to identify charm content in W/Z+c events in which the charm quark hadronizes as $c \to D^*(2010)$. First, W/Z events are selected with standard cuts of event $\not\!\!E_T > 25$ (20) GeV and $E_T > 25$ GeV ($p_T > 20$ GeV) for electron (muon) objects with low relative isolation ($\mathrm{Iso}_\ell < 0.1$). Vertex fitting is then used to reconstruct the decay $D^{*+} \to D^0\pi^+$ with $D^0 \to K^-\pi^+$. After cuts on track kinematics and the mass of the reconstructed D^0 vertex, the vertex mass difference $\Delta m = m(K\pi\pi) - m(K\pi)$ of remaining candidates is binned. The Δm values of real D^* will produce a signal peak above background near $\Delta m = 0.1455\mathrm{GeV}/c$. This can be fit with a signal plus background hypothesis in order to count the number of $D^{*+} \to D^0(\to K^-\pi^+)\pi^+$ events in the sample.

This is the first application at the Tevatron of this D^* tagging technique in a search for $W/Z + c$ events. This approach explores a kinematic regime with much lower average charm momentum ($\sim$ 10 GeV) [11] than the regime explored by jet-based studies: secondary-vertex tagging in jet events generally considers only events with $E_T^{b,cjet} > 15$ or 20 GeV.

Thus far, this search has identified both $W(\rightarrow \ell\nu) + D^*$ and $Z(\rightarrow (\ell^+\ell^-) + D^*$ events in the full CDF high-p_T muon and electron datasets (9.7fb^{-1}) (Figure 4). As of the writing of this paper, the work is ongoing.

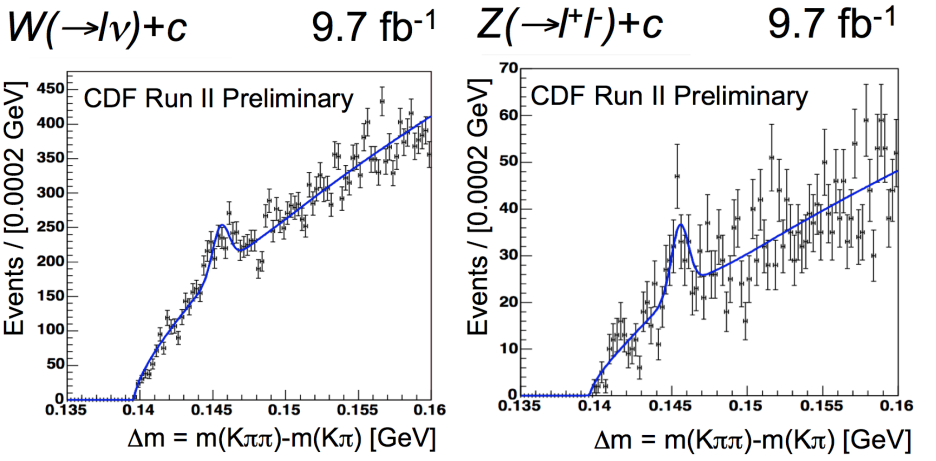

Fig. 4. Plots of discriminant $\Delta m = m(K\pi\pi) - m(K\pi)$ as used to identify $D^{*+} \rightarrow D^0(K^-\pi^+)\pi$ decays in W/Z events. Each plot is fit to a signal plus background hypothesis. Signal can be seen above background near $\Delta m = 0.1455$ GeV/c.

6. Summary

This is an exciting time for electroweak gauge boson plus heavy flavor physics. Results continue to support charm and bottom event production that may be higher than NLO predictions, highlighting the importance of heavy flavor work in modeling data. In addition, CDF is now probing new kinematic regimes in W/Z plus heavy flavor studies by exploring low $p_T(D^*)$ produced in association with W/Z. Further extensions in complementary kinematic regions may soon be made with higher statistics at the Large Hadron Collider. This growing improvement to the state of $W/Z/\gamma$ plus heavy flavor knowledge will benefit future analyses by both furthering our understanding of heavy flavor production, and by serving as a model for background in increasingly-sensitive measurements of Higgs, single top and supersymmetric particle searches.

Acknowledgments

We thank the Fermilab staff and the technical staffs of the participating institutions for their vital contributions. This work was supported by the U.S. Department of Energy and National Science Foundation; the Italian Istituto Nazionale di Fisica Nucleare; the Ministry of Education, Culture,

Sports, Science and Technology of Japan; the Natural Sciences and Engineering Research Council of Canada; the National Science Council of the Republic of China; the Swiss National Science Foundation; the A.P. Sloan Foundation; the Bundesministerium für Bildung und Forschung, Germany; the Korean World Class University Program, the National Research Foundation of Korea; the Science and Technology Facilities Council and the Royal Society, United Kingdom; the Russian Foundation for Basic Research; the Ministerio de Ciencia e Innovación, and Programa Consolider-Ingenio 2010, Spain; the Slovak R&D Agency; the Academy of Finland; the Australian Research Council (ARC); and the EU community Marie Curie Fellowship Contract No. 302103.

References

[1] T.P. Stavreva and J.F. Owens, Phys. Rev. D **79**, 054017 (2009).
[2] U. Baur, F. Halzen, S. Keller, M.L. Mangano, and K. Riesselmann, Phys. Lett. B **318**, 544 (1993).
[3] H.L. Lai, P. Nadolsky, J. Pumplin, D. Stump, W. Tung, and C. Yuan, J. High Energy Phys. **4**, 089 (2007).
[4] B. Abbott *et al.* (D0 Collaboration), Phys. Lett. B **487**, 264 (2000).
[5] D. Acosta *et al.* (CDF Collaboration) Phys. Rev. D **71**, 092001 (2005).
[6] T. Aaltonen *et al.* (CDF Collaboration), Phys. Rev. D **78**, 072005 (2008).
[7] D. Acosta *et al.* (CDF Collaboration), Phys. Rev. D **71**, 052003 (2005).
[8] T. Aaltonen *et al.* (CDF Collaboration), Phys. Rev. Lett. **111**, 042003 (2013).
[9] T. Aaltonen *et al.* (CDF Collaboration), Phys. Rev. Lett. **110**, 071801 (2013).
[10] T. Aaltonen *et al.* (CDF Collaboration), CDF note 10594 (2012).
[11] T. Aaltonen *et al.* (CDF Collaboration), CDF note 11032 (2013).
[12] T.P. Stavreva and J.F. Owens, Phys. Rev. D **79**, 054017 (2009).
[13] T. Aaltonen *et al.* (CDF Collaboration), Phys. Rev. Lett. **108**, 011801 (2012).
[14] D. Acosta *et al.* (CDF Collaboration), Phys. Rev. D **71**, 052003 (2005).
[15] T. Sjostrand, S. Mrenna, and P.Z. Skands, J. High Energy Phys. **05**, 026 (2006).
[16] D. Acosta *et al.* (CDF Collaboration), Phys. Rev. D **79**, 052007 (2009).
[17] D. Acosta *et al.* (CDF Collaboration), Phys. Rev. D **72**, 032002 (2005).
[18] D. Acosta *et al.* (CDF Collaboration), Phys. Rev. D **81**, 092002 (2010).
[19] J.P. Chou, PhD thesis, Harvard University, FERMILAB-THESIS-2008-93 (2008).

Particle production at large momentum transfer

V.P. Gonçalves, Werner K. Sauter†
High and Medium Energy Group
Instituto de Física e Matematica
Universidade Federal de Pelotas, Rio Grande do Sul, Brasil

Diffractive particle production in ep collisions and coherent pp interactions is studied assuming that the color singlet t channel exchange carries large momentum transfer. The differential and total cross sections for vector meson and photon production are calculated using the non-forward solution of the LO and NLO BFKL equation at high energy and large momentum transfer and the predictions are compared with the DESY HERA data. Moreover, we estimate the rapidity distributions and total cross section for the J/Ψ and ρ production in coherent pp interactions at LHC energies. We predict large rates, which implies that the experimental identification can be feasible at the LHC.

1. Introduction

The description of exclusive diffractive processes has been proposed as a probe of the Quantum Chromodynamics (QCD) dynamics in the high energy limit (For a recent review c.f. Ref. [1]). It is expected that the study of these processes provide insight into the parton dynamics of diffractive exchange when a hard scale is present. In particular, the diffractive vector meson and photon production at large momentum transfer is expected to probe the QCD Pomeron, which is described by the Balitsky, Fadin, Kuraev, and Lipatov (BFKL) equation [2, 3, 4, 5]. In this contribution, we present a brief summary of the results obtained in Refs. [6, 7, 8], where the vector meson and photon production at large momentum transfer were studied considering the non-forward solution of the BFKL equation at leading order (LO) and next-to-leading order (NLO). In particular, we have estimated the cross sections for the ρ, J/Ψ and γ production at large-t in ep collisions at HERA energy which can represented by the diagram presented in Fig. 1 (left panel). Moreover, we have studied vector meson production at large-t in coherent pp interactions as represented in Fig. 1 (right panel), which is an alternative way to study QCD dynamics at high energies.

† Speaker.

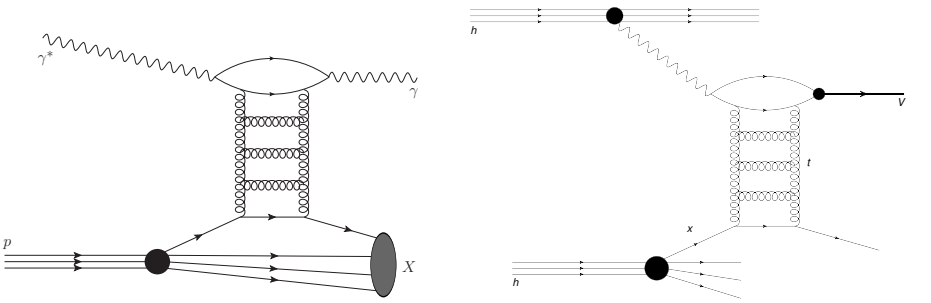

Fig. 1. The exclusive photon and vector meson production at large-t in ep collisions (left panel) and coherent pp interactions (right panel).

This contribution is organized as follows. In the next section we summarize the formalism used in the calculation. Our results are presented in Section 3 and the main conclusions are discussed in Section 4.

2. Formalism

The differential and total cross sections for diffractive particle photoproduction at large momentum transfer reads

$$\frac{d\sigma_{\gamma h\to YX}}{dt} = \int_{x_{\min}}^{1} dx_j \; \frac{d\sigma}{dt dx_j}, \quad \sigma_{\rm tot} = \int_{t_{\min}}^{t_{\max}} dt \; \frac{d\sigma_{\gamma h\to YX}}{dt}\,, \tag{1}$$

where h denotes a hadron, Y the produced particle ($J/\psi, \Upsilon, \rho$ and γ), X the hadron fragments and

$$\frac{d\sigma}{dt dx_j} = \left[\frac{81}{16} G(x_j,|t|) + \sum_j (q_j(x_j,|t|) + \bar{q}_j(x_j,|t|))\right] \frac{d\hat{\sigma}}{dt}. \tag{2}$$

Moreover, G, q and $\bar{q}$ are parton distribution functions (we are using CTEQ6L parametrization). The partonic cross section for vector meson production is given by

$$\frac{d\hat{\sigma}}{dt}(\gamma q \to Vq) = \frac{1}{16\pi} |\mathcal{A}_V(s,t)|^2. \tag{3}$$

and for photon production,

$$\frac{d\hat{\sigma}}{dt}(\gamma^* q \to \gamma q) = \frac{1}{16\pi} \left\{ |\mathcal{A}_{(+,+)}(s,t)|^2 + |\mathcal{A}_{(+,-)}(s,t)|^2 \right\}. \tag{4}$$

The amplitudes, in both cases, have a general expression (for details, see [7, 8]),

$$\mathcal{A} \propto \int d\nu \; G_{V,\gamma}(\nu) \left(\frac{s}{\Lambda^2}\right)^{\omega(\nu)} I_{\gamma/V,\gamma}(\nu) I_{q,q}(\nu) \,, \tag{5}$$

where G depends on the produced particle, $\omega(\nu) = \bar{\alpha}_s \chi(1/2 + i\nu)$ is the BFKL characteristic function and I are related with the impact factors for the transitions $\gamma \to (V, \gamma)$ and $q \to q$.

At leading order the BFKL function $\chi(\gamma)$ is given by

$$\chi^{\rm LO}(\gamma) = 2\psi(1) - \psi(\gamma) - \psi(1-\gamma) \,, \tag{6}$$

where $\psi(z)$ is the digamma function. In what follows this expression is used in our calculations of the vector meson production at large-t. Several shortcomings are present in a leading order calculation: the energy scale Λ is arbitrary; α_s is not running at LO BFKL and the power growth with energy violates s-channel unitarity at large rapidities. Some of these shortcomings are reduced if we consider the NLO corrections for the BFKL kernel obtained originally in Refs. [9, 10]. In this case, we have that

$$\chi(\gamma) = \chi^{\rm LO}(\gamma) + \overline{\alpha}_s \chi^{\rm NLO}(\gamma), \quad \bar{\alpha}_s = N_c \alpha_s/\pi, \tag{7}$$

with the $\chi^{\rm NLO}$ function being given by

$$\begin{aligned}
\chi^{\rm NLO}(\gamma) \; = \; & \mathcal{C}\chi^{\rm LO}(\gamma) + \frac{1}{4}\left[\psi''(\gamma) + \psi''(1-\gamma)\right] - \frac{1}{4}\left[\phi(\gamma) + \phi(1-\gamma)\right] \\
& - \frac{\pi^2 \cos(\pi\gamma)}{4\sin^2(\pi\gamma)(1-2\gamma)} \left\{ 3 + \left(1 + \frac{N_f}{N_c^3}\right) \frac{(2+3\gamma(1-\gamma))}{(3-2\gamma)(1+2\gamma)} \right\} \\
& + \frac{3}{2}\zeta(3) - \frac{\beta_0}{8N_c}\left(\chi^{\rm LO}(\gamma)\right)^2 ,
\end{aligned} \tag{8}$$

with $\mathcal{C} = \left(4 - \pi^2 + 5\beta_0/N_c\right)/12$, $\beta_0 = (11N_c - 2N_f)/3$ is the leading coefficient of the QCD β function, N_f is the number of flavours, $\psi^{(n)}(z)$ is the poligamma function, $\zeta(n)$ is the Riemann zeta-function and

$$\phi(\gamma) + \phi(1-\gamma) = \sum_{m=0}^{\infty} \left[\frac{1}{\gamma+m} + \frac{1}{1-\gamma+m}\right] \left[\psi'(\frac{2+m}{2}) - \psi'(\frac{1+m}{2})\right]. \tag{9}$$

However, there are several problems associated with these corrections (c.f. Ref. [11]). Among of them exist problems associated to the choice of energy scale, the renormalization scheme and related ambiguities.

An alternative is to use the ω-expansion, developed to resum collinear effects at all orders in a systematic way. This approach was revisited in

Ref. [12] obtaining an expression for the collinearly improved BFKL kernel characteristic function, denoted All-poles hereafter, given by

$$\omega_{\text{All-poles}} = \overline{\alpha}_s \chi^{\text{LO}}(\gamma) + \overline{\alpha}_s^2 \chi^{\text{NLO}}(\gamma) +$$

$$+ \sum_{m=0}^{\infty} \left[\left(\sum_{n=0}^{\infty} \frac{(-1)^n (2n)!}{2^n n!(n+1)!} \frac{(\overline{\alpha}_s + a\overline{\alpha}_s^2)^{n+1}}{(\gamma + m - b\overline{\alpha}_s)^{2n+1}} \right) - \frac{\overline{\alpha}_s}{\gamma + m} - \right.$$

$$\left. - \overline{\alpha}_s^2 \left(\frac{a}{\gamma + m} + \frac{b}{(\gamma + m)^2} - \frac{1}{2(\gamma + m)^3} \right) \right] + \{\gamma \to 1 - \gamma\}, \qquad (10)$$

where

$$a = \frac{5\beta_0}{12N_c} - \frac{13N_f}{36N_c^3} - \frac{55}{36}, \quad b = -\frac{\beta_0}{8N_c} - \frac{N_f}{6N_c^3} - \frac{11}{12}. \qquad (11)$$

Another alternative to solve the problems present in the original NLO kernel was proposed in Ref. [13]. To solve the energy scale ambiguity, the Brodsky-Lepage-Mackenzie (BLM) optimal scale setting [14] and the momentum space subtraction (MOM) scheme of renormalization were used to obtain the following BFKL characteristic function,

$$\omega_{\text{BLM}}^{\text{MOM}} = \chi^{\text{LO}}(\gamma) \frac{\alpha_{\text{MOM}}(\hat{Q}^2) N_c}{\pi} \left[1 + \hat{r}(\nu) \frac{\alpha_{\text{MOM}}(\hat{Q}^2)}{\pi} \right], \qquad (12)$$

where α_{MOM} is the coupling constant in the MOM scheme,

$$\alpha_{\text{MOM}} = \alpha_s \left[1 + \frac{\alpha_s}{\pi} T_{\text{MOM}} \right], \qquad (13)$$

with T being a function of number of colors, number of flavors and of a gauge parameter. Moreover, the function $\hat{Q}$ is the BLM optimal scale, which is given by

$$\hat{Q}^2(\nu) = Q^2 \exp\left[\frac{1}{2} \chi^{\text{LO}}(\gamma) - \frac{5}{3} + 2\left(1 + \frac{2}{3}\varrho \right) \right], \qquad (14)$$

with $\varrho \approx 2.3439$. Finally, $\hat{r}$ is the NLO coefficient of the characteristic function,

$$\hat{r}(\nu) = -\frac{\beta_0}{4} \left[\frac{\chi^{\text{LO}}(\nu)}{2} - \frac{5}{3} \right] - \frac{N_c}{4\chi^{\text{LO}}(\nu)} \left\{ \frac{\pi^2 \sinh(\pi\nu)}{2\nu \cosh^2(\pi\nu)} \right.$$

$$\times \left[3 + \left(1 + \frac{N_f}{N_c^3} \right) \frac{11 + 12\nu^2}{16(1 + \nu^2)} \right] - \chi''^{\text{LO}}(\nu) + \frac{\pi^2 - 4}{3} \chi^{\text{LO}}(\nu)$$

$$\left. - \frac{\pi^3}{\cosh(\pi\nu)} - 6\zeta(3) + 4\tilde{\phi}(\nu) \right\} + 7.471 - 1.281\beta_0, \qquad (15)$$

with

$$\tilde{\phi}(\nu) = 2\int_0^1 dx\, \frac{\cos(\nu \ln(x))}{(1+x)\sqrt{x}} \left[\frac{\pi^2}{6} - \mathrm{Li}_2(x)\right], \tag{16}$$

where $\mathrm{Li}_2(x)$ is the Euler dilogarithm or Spence function.

3. Results

The results strongly depend on the coupling constant and the choice of energy scale Λ. In Refs. [6, 7] we have performed an detailed study of these choices in the predictions. We assumed a fixed coupling constant ($\alpha_s = 0.21$) and that the energy scale for vector mesons can be expressed by $\Lambda^2 = \beta M_V^2 + \gamma|t|$, following [15], where β and γ are free parameters to be fixed by the data. Our results are presented in Fig. 2, where we demonstrated that LO BFKL formalism is able to describe the HERA data[16, 17, 18].

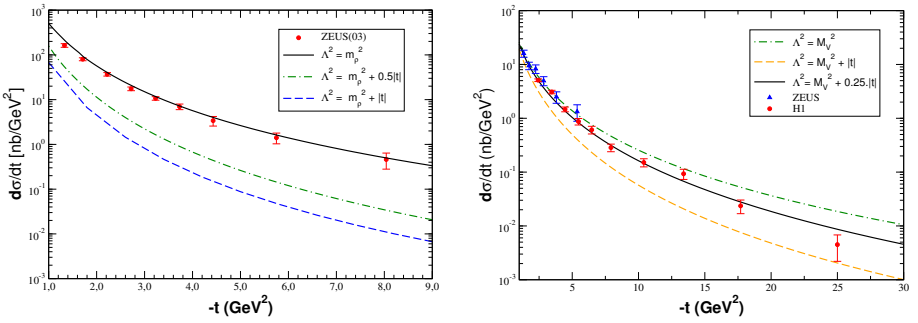

Fig. 2. Cross section for the exclusive production of vector mesons at large-t in ep collisions. Left: ρ production. Right: J/ψ production. Data from HERA[16, 17, 18].

In the case of photon production at large-t, we assumed that the scale can be expressed by $\Lambda^2 = \gamma'|t|$, with γ' depending on the BFKL function (see [8]). The results for the differential and total cross sections are presented in Fig. 3. In this case, we analyze the effects of change the BFKL dynamics, using distinct analytically forms for the NLO BFKL kernel as well as the LO one. We have obtained a reasonable agreement with the HERA experimental data. This results must be taken as an educated estimate, due the fact that we have used the impact factors of the transition $\gamma^* \to \gamma$ at leading order. The NLO expression was obtained recently in Ref. [23].

Let's now consider vector meson production at large-t in coherent pp collisions. The cross section in a coherent hadron-hadron collision is given

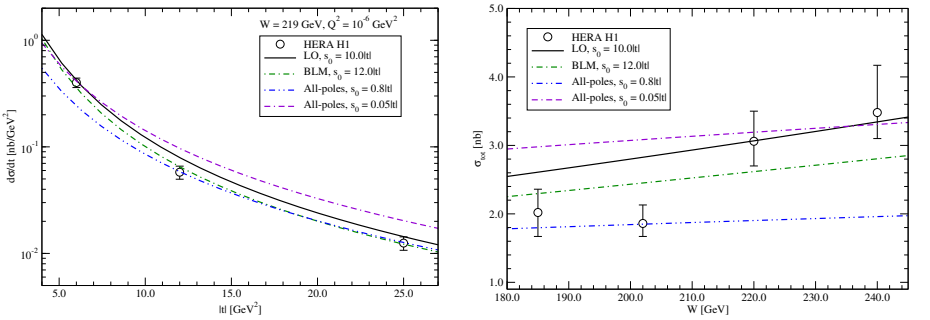

Fig. 3. Exclusive photon production at large-t in ep collisions. Data from HERA[22].

by

$$\frac{d\sigma\ [h_1 + h_2 \to h_1 \otimes Y \otimes X]}{dy} = \int_{t_{\rm min}}^{t_{\rm max}} dt\ \omega \frac{dN_\gamma(\omega)}{d\omega}\ \frac{d\sigma_{\gamma h \to YX}}{dt}\ (\omega)\ , \qquad (17)$$

where $dN_\gamma(\omega)/d\omega$ is the equivalent photon flux as a function of photon energy ω. In our calculations we have used the photon flux proposed in Ref. [20] for the proton and in Ref. [21] for the nucleus. Our predictions for the rapidity distributions for ρ and J/Ψ production are shown in Fig. 4 considering different t-ranges. In Ref. [7] we also have calculated Υ production. In Table 1, we present our predictions for the event rates at LHC energy. Our results indicate that experimental identification of these processes can be feasible at the LHC.

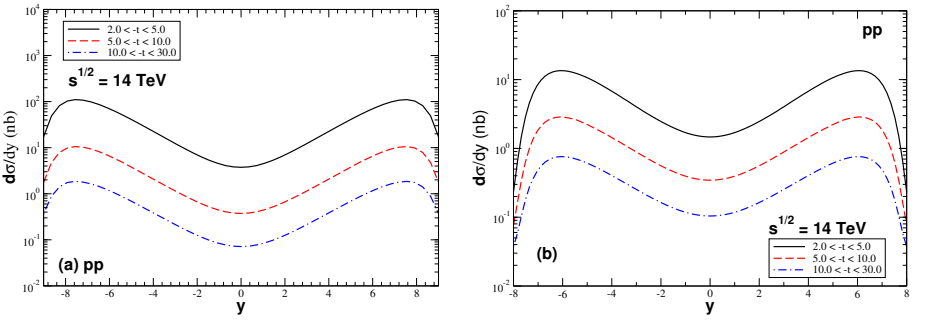

Fig. 4. Rapidity distribution for the ρ (left panel) and J/Ψ (right panel) production in coherent pp interactions at LHC energy.

Table 1. The integrated cross section (event rates/second) for diffractive vector meson photoproduction at large momentum transfer in pp and $PbPb$ collisions at LHC.

Meson	t range	pp	$PbPb$
ρ	$2.0 < \|t\| < 5.0$	751.0 nb (7510.0)	20.0 mb (8.4)
	$5.0 < \|t\| < 10.0$	71.0 nb (710.0)	2.2 mb (0.9)
	$10.0 < \|t\| < 30.0$	12.0 nb (120.0)	0.4 mb (0.17)
J/ψ	$2.0 < \|t\| < 5.0$	97.0 nb (970.0)	3.0 mb (13.0)
	$5.0 < \|t\| < 10.0$	21.0 nb (210.0)	0.9 mb (0.38)
	$10.0 < \|t\| < 30.0$	6.0 nb (60.0)	0.3 mb (0.12)
Υ	$2.0 < \|t\| < 5.0$	0.8 nb (8.0)	0.26 mb (0.1)
	$5.0 < \|t\| < 10.0$	0.4 nb (4.0)	0.17 mb (0.07)
	$10.0 < \|t\| < 30.0$	0.3 nb (3.0)	0.16 mb (0.06)

4. Conclusions and perspectives

The description of the high energy limit of Quantum Chromodynamics (QCD) is an important open question in the Standard Model. During the last decades several approaches were developed in order to improve our understanding from a fundamental perspective. In particular, after a huge theoretical effort, now we have available the NLO corrections for the BFKL characteristic function, which allow us to improve the analysis of the exclusive vector meson and photon production at large-t which are expected to probe the underlying QCD dynamics. Our results for vector meson and photon production in ep collisions at HERA demonstrated that the BFKL formalism is able to describe the current experimental data. Moreover, our estimates for vector meson production in coherent pp interactions at LHC demonstrated that the study of this process can constrain QCD dynamics. It is important to emphasize that our results are complementary to the recent theoretical and phenomenological studies that use NLO BFKL Pomeron [24, 25, 26, 27]. Presently, we are performing a more accurate analysis on the choice of the energies scales in exclusive production using the principle of maximum conformality in NLO BFKL Pomeron[28].

Acknowledgments

This work is supported by FAPERGS, CNPq and CAPES.

References

[1] L. Schoeffel, Prog. Part. Nucl. Phys. **65**, 9 (2010).

[2] L.N. Lipatov, Sov. J. Nucl. Phys. **23**, 338 (1976).

[3] E.A. Kuraev, L.N. Lipatov, and V.S. Fadin, Sov. Phys. JETP **44**, 443 (1976).

[4] E.A. Kuraev, L.N. Lipatov, and V.S. Fadin, Sov. Phys. JETP **45**, 199 (1977).

[5] I.I. Balitsky, L.N. Lipatov, Sov. J. Nucl. Phys. **28**, 822 (1978).

[6] V.P. Goncalves and W.K. Sauter, Phys. Rev. D **81**, 074028 (2010).

[7] V.P. Goncalves and W.K. Sauter, Eur. Phys. J. A **47**, 117 (2011).

[8] V.P. Goncalves and W.K. Sauter, Phys. Rev. D **87**, 054035 (2013).

[9] V.S. Fadin and L.N. Lipatov, Phys. Lett. B **429**, 127 (1998).

[10] M. Ciafaloni and G. Camici, Phys. Lett. B **430**, 349 (1998).

[11] D.A. Ross, Phys. Lett. B **431**, 161 (1998).

[12] A. Sabio Vera, Nucl. Phys. B **722**, 65 (2005).

[13] S.J. Brodsky, V.S. Fadin, V.T. Kim, L.N. Lipatov, and G.B. Pivovarov, JETP Lett. **70**, 155 (1999).

[14] S.J. Brodsky, G.P. Lepage, and P.B. Mackenzie, Phys. Rev. D **28**, 228 (1983).

[15] J.R. Forshaw and G. Poludniowski, Eur. Phys. J. C **26**, 411 (2003).

[16] S. Chekanov *et al.* (ZEUS Collaboration), Eur. Phys. J. C **26**, 389 (2003).

[17] A. Aktas *et al.* (H1 Collaboration), Phys. Lett. B **568**, 205 (2003).

[18] S. Chekanov *et al.* (ZEUS Collaboration), Eur. Phys. J. C **26**, 389 (2003).

[19] S. Frixione, M.L. Mangano, P. Nason, and G. Ridolfi, Phys. Lett. B **319**, 339 (1993).

[20] M. Drees and D. Zeppenfeld, Phys. Rev. D **39**, 2536 (1989).

[21] G. Baur, K. Hencken, D. Trautmann, S. Sadovsky, and Y. Kharlov, Phys. Rep. **364**, 359 (2002); C.A. Bertulani, S.R. Klein, and J. Nystrand, Ann. Rev. Nucl. Part. Sci. **55**, 271 (2005); K. Hencken *et al.*, Phys. Rept. **458**, 1 (2008).

[22] F.D. Aaron *et al.* (H1 Collaboration), Phys. Lett. B **672**, 219 (2009).

[23] I. Balitsky and G.A. Chirilli, Phys. Rev. D **87**, 014013 (2013).

[24] M. Hentschinski, A.S. Vera, and C. Salas, Phys. Rev. Lett. **110**, 041601 (2013).

[25] M. Hentschinski, A. Sabio Vera, and C. Salas, Phys. Rev. D **87**, 076005 (2013).

[26] D. Colferai, F. Schwennsen, L. Szymanowski, and S. Wallon, J. High Energy Phys. **12**, 026 (2010).

[27] B. Duclou, L. Szymanowski, and S. Wallon, arXiv:1309.3229 [hep-ph].

[28] X.-C. Zheng, X.-G. Wu, S.-Q. Wang, J.-M. Shen, and Q.-L. Zhang, arXiv:1308.2381 [hep-ph].

Searching for W' bosons at LHC with single top production

Daniel Duffty, Zack Sullivan

Department of Physics, Illinois Institute of Technology,
Chicago, Illinois 60616-3793, USA

One of the strengths of the LHC is its capacity for the discovery of new physics. As a consequence of many BSM theories, W' bosons make an ideal particle to search for to constrain many models. One mode in particular has relatively low background: Single top quark production mediated by a W' boson. For W' masses less than 1500 GeV, all the decay products of the top quark are visible, and the strongest channel is the top's decay into an electron or muon, with the associated neutrino and a bottom jet. As the W' mass increases, the decay products from the highly boosted top and bottom quarks from the W' appear as fat jets; boosted top tagging algorithms abound, and we propose a boosted bottom tag to set an exclusion limit of 2750 GeV for standard model-like couplings with existing 8 TeV data.

1. Introduction

The Large Hadron Collider is the best tool for discovering new particle resonances in existence today. Resonance searches can be used as a powerful tool for constraining many new theories; few are as powerful as the W' particle. A model independent search for the W' can reveal restrict many theories, from $\mathrm{SU}(3)_L$ x $\mathrm{SU}(3)_R$ to extra dimensions. A W' search through the top-bottom decay channel is accessible for all unexcluded masses, most theoretical couplings, and both chirailties (the lepton-neutrino channel cannot detect right-handed W's without right-handed neutrinos). For our analyses, we use the general Lagrangian [1, 2]:

$$\mathcal{L} = \frac{g'}{2\sqrt{2}} V'_{ij} W'_{\mu} \bar{f}^i \gamma^{\mu} (1 \pm \gamma_5) f^j + \text{H.c.}\,, \tag{1}$$

When analyzing decays including top quarks, there are two important regimes to be studied. In a non-boosted regime with relatively low-mass W's ($m_{W'} < 1.5$ TeV), the most efficient method is to look at the leptonic decay channel of the top quark, discussed thoroughly in Ref. [3]. For more highly boosted channels ($m_{W'} > 1.5$ TeV), leptons fail isolation cuts, and

using a boosted top tagging algorithm is better (Ref. [4]). For optimal signal to background, an additional cut must be placed to restrict the dijet background. A b-tag is normally the best way to reduce a light jet background, but for high-mass W's the traditional secondary vertex tagger will fail due to highly suppressed decay angle. To combat this, we propose to use a "boosted bottom tag" to suppress the light jet background. The most effective way to do this is restricting the $\Delta R_{\mu,\text{jet}}$ and the muon p_T.

We use the MadGraph and MadEvent [5] programs for event simulations. For our non-boosted regime analysis, we also used the PYTHIA program [6] for showering and PGS [7] for detector simulation. A MCFM [8] analysis was also done to calculate K-factors at next leading order. For the boosted regime, we use top and bottom tags on the MadEvent output. The top tag simulates the CMS top tagger [9] algorithm, looking for three subjets in a R=1 Cambridge-Aachen jet. The boosted b tag was developed by analyzing b decays through PYTHIA and PGS. We propose using bbj data to extract the tagging efficiencies in situ.

2. Non-boosted Regime

To analyze the non-boosted regime for W' decay, we choose to look at the $bblv$ final state. The final state in the detector from the top decay should be an electron or muon, a b tagged jet, and missing energy; there should also be a highly energetic recoiling jet, which may or may not be b-tagged with a traditional b tag. The best way to reduce background is to reconstruct the top quark; using the known W mass, missing energy, and the lepton four-vector to reconstruct the W, then adding the tagged b jet to reconstruct the top quark.

There are strong differences in shape between both positive and negative W's, as well as between left- and right-handed W's. The jet from the top-decay tends to have a larger E_T when coming from the left-handed decay. The differences between positive and negative W's are twofold. The recoiling high energy jet will tend to be more central in a W'^- decay, whereas the W'^+ has a double-peaked structure in pseudorapidity. Conversely, the leptons from W'^- top decays tends to be more central than those from W'^+.

The cuts used include transverse energy (E_T) cuts on the primary and secondary jets, as well as cuts on the lepton and missing energy. The lead jet, assumed to be the recoiling b, is required to have $E_T > 0.2m_{W'}$. The secondary jet is required to be b-tagged and have $E_T > 20$ GeV. The lepton is required to pass isolation cuts and have $p_T > 20$ GeV, and the missing transverse energy (MET) greater than 20 GeV. Finally, all jets and leptons used must have a pseudorapidity (η) less than 2.5 ($|\eta| < 2.5$). Using the missing energy and the lepton four-momentum, if we assume the W to be

produced on-shell, we can reconstruct the neutrino four-momentum up to a twofold ambiguity. Choosing the smallest rapidity solution for the neutrino, we can then fully reconstruct the 'top quark'; we apply an upper cut on $M_{l\nu b} < 200$ GeV. Finally we fit to a mass window of $0.75m_{W'} < M_{l\nu bj} < 1.1m_{W'}$. With all the cuts in place, the maximum detectable mass would be at approximately 1800 GeV, which agrees with the results of the CMS [10] and ATLAS [11] collaborations.

3. Interference

When modeling left-handed W's, the effect of interference should not be ignored. Depending on the model, the interference can be constructive or destructive. To retain generality, we present left-handed results as a band in the mass-coupling parameter space. We show that the effects of interference are predominantly just a rescaling of the shape of the cross-section curve at low masses if a search is done, but shrinks considerably if a narrow resonance search is done. At high masses the interference effects and the large widths produce small changes in the exclusion limits for left-handed W', with the destructive interference with the standard model process slightly reducing the significance for the corresponding signal (the only reason interference has an effect is that at high coupling, the peak is wide enough to interfere with the relatively low-mass SM W peak). For low to moderate mass W's ($m_{W'} < 2500$ GeV) however, the effect of interference is negligible, to the order of a few percent change on the resultant cross-section.

4. Boosted Regime

As the W' mass increases, the lepton is forced closer to the jet. This will prevent the lepton from being properly reconstructed due to failing isolation criteria. If instead we analyze top decays, it is possible to use jet substructure to tag the boosted top as a whole, instead of looking at the individual final state objects. This will unfortunately introduce a massive dijet background, which needs to be reduced through other methods even after using the top tagging algorithm on it. Commonly ignored backgrounds for top tagging algorithms are the Wjj and Zjj backgrounds; if one of the jets falls within the large jet radius of the tagging algorithm, all that remains is to pass a loose top mass cut for the jet to be accepted as a boosted-top jet.

When analyzing the Wjj and Zjj backgrounds to top tags, NLO radiation could significantly affect the amount of radiation near the vector boson (see Fig. 1). To model this effect, Wjj and $Wjjj$ events were compared in MCFM; they are found to be very different, with NLO effects being similar

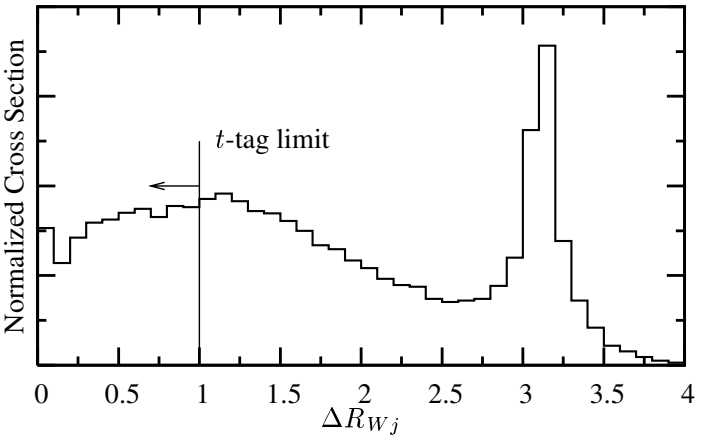

Fig. 1. The distance between the W and the nearest jet in Wjj events. Anytime the $\Delta R < 1$, the Wj combination has a chance of passing a top tag.

magnitude to leading order effects. This background will need to be carefully studied in experiment to accurately account for backgrounds to most single top-production processes.

A boosted top tagging algorithm to tag top jets is by itself very useful. This tag combined with a simple mass cut on the 'resonance' is enough to match the results from the non-boosted regime as described above. To truly gain an advantage over the non-boosted analysis, however, a cut must be placed on the recoil jet, which will be a b quark upwards of 99% of the time. Since a traditional b tagging algorithm relies heavily on vertex tagging, its effectiveness is greatly reduced as the energy of the jet increases. As the jet energy approaches 1000 GeV, it is unlikely the secondary vertex will be seen due to angle suppression of the decay products from the initial meson. This can be an advantage, however, when we look at the particulars of the B decay. While most of the decay products of the B will be quark matter, approximately 20% of B quarks will decay directly, or through an intermediate D meson, to a muon with additional quark radiation. Since muons are produced only rarely in light jet decays, the characteristics of this muon can be a large boon to salvaging a boosted-b tag.

We show that for high energy b jets, optimal cuts can be placed with the minimum muon $p_T > 20$ GeV, and a maximum $\Delta R_{\mu,j}$ of 0.1. This gives an ultimate b tagging rate of approximately 20% for high energy b jets, with lower tagging efficiencies for lower energy jets, as shown in Table 1. It can be shown through simple kinematic arguments that for a 20 GeV muon, the maximum radius of decay from a B meson is approximately 0.12

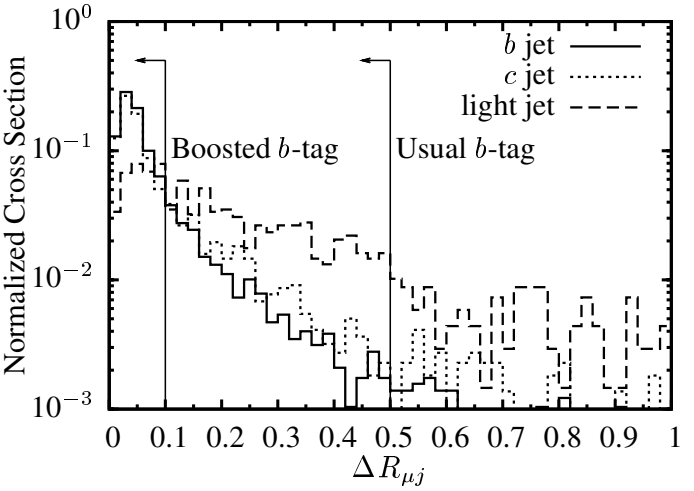

Fig. 2. The distance between muon energy and jet energy for b jets, charm jets, and light jets. Muons from heavy jets have a much higher chance of being central than light-quark initiated jets.

radians (shown in Fig. 2). The implications of this are that these cuts are synergistic with each other, and only occasionally will a muon with the specified criteria appear inside a light jet with these properties. Ultimately, although the acceptance rate is considerably lower, the tag to mistag ratio is comparable if not better than the standard secondary vertex tag, as long as the b is boosted enough.

Table 1. Boosted-bottom jet efficiencies using a muon tag with $p_{T\mu} > 20$ GeV and $\Delta R_{\mu j} < 0.1$ for b jets, c jets, and light jets j as a function of jet E_T.

Type	$E_{Tj} = 100$ GeV	400 GeV	1000 GeV
b	4.8%	11.8%	15.0%
c	2.1%	5.5%	7.5%
j	0.1%	0.4%	0.6%

With both the boosted top and boosted bottom tags in effect, the boosted object analysis can reach up to 750 GeV higher in mass than looking at isolated decay products. The ultimate limit of this method comes not from lack of signal or cut inefficiency, but from the characteristics of the signal itself. For W' masses above 2500 GeV (which require large couplings to identify), the width of the resonance becomes very large, approaching the mass. By g'/g=5 ($m_{W'}$=3 TeV), the width of the resonance required for detection is approximately 1000 GeV; the effect of this broadening means that

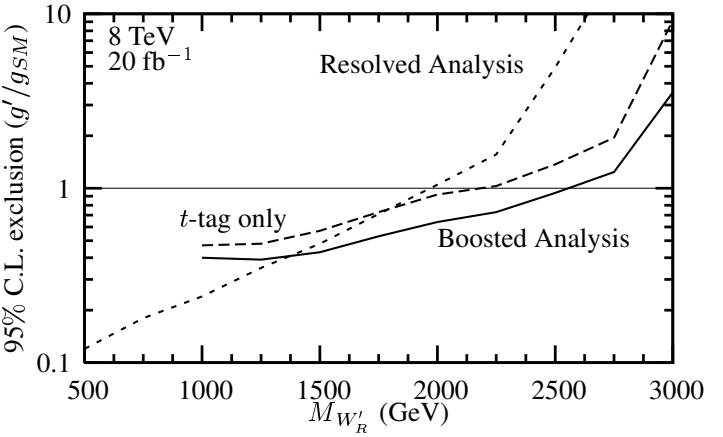

Fig. 3. 95% C.L. limit on the effective coupling g'_R relative to g_{SM} as a function of right-handed W'_R mass. Curves show the reach from current resolved-top quark analysis (dashed), the boosted-top analysis (dotted), and after adding a boosted-bottom tag (solid).

a simple peak search will fail due to the significantly more of the signal falling outside of the 'peak' region. The alternative, widening the search window, will introduce more background than signal for a broad peak, worsening the significance. Finally, the initial state parton luminosity falls rapidly for $m_{W'} > 3$ TeV, setting this as an approximate limit on any $m_{W'}$ search regardless of method, due to loss of signal.

5. Results

After making use of the cuts for the resolved (non-boosted) analysis, a $m_{W'}$ limit can be set at approximately 1800 GeV for both left and right handed W's at SM-like coupling. While some models can support greater than larger than SM couplings, even those are certainly ruled out by 2500 GeV, where g'/g =5 for exclusion.

Using the boosted analysis has advantages and disadvantages compared to the resolved analysis. The most obvious is at low $m_{W'}$ ($m_{W'}$ <1500), the coupling limit in the boosted analysis is less effective due to the low tagging efficiencies of tops and bottoms at low energies. The primary advantage is the higher reach of the analysis ($m_{W'}$ >2750 GeV) for SM-like couplings. In the mid-range regime, both analyses are competitive with each other, but the boosted analysis is the more powerful of the two for most masses, as long as the boosted b algorithm is used, otherwise the boosted analysis is only more powerful for excluding theories that allow for $g'/g > 1$.

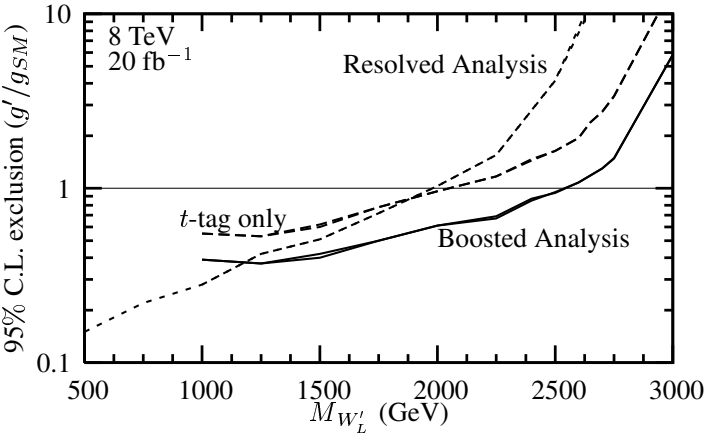

Fig. 4. 95% C.L. limit on the effective coupling g'_L relative to g_{SM} as a function of left-handed W'_L mass. Bands show the reach from current resolved-top quark analysis (dashed), the boosted-top analysis (dotted), and after adding a boosted-bottom tag (solid).

6. Outlook

By using the tb decay channel to its fullest extent, left handed W' bosons can approach the exclusion limits set by $W' > l\nu$ channel (the $l\nu$ final state will not appear for right-handed W's). The strength of the tb channel is twofold: Not only is it the only visible decay channel that will detect right-handed W's, but greater information could be gleaned about any potential signal due to the lack of missing energy in the boosted analysis, and the ability to fully reconstruct the mass resonance in the resolved analysis.

The boosted analysis will not be greatly affected by increases in pileup events, which is good for the LHC moving forward. The reason for this that high energy jets will be the least-effected by pileup (as opposed to light jets, which will suffer a larger percentage change in their energy due to pileup radiation). While large jet areas will suffer from more pileup than smaller jets, the jet substructure algorithms used in t tags will allow for significantly reduced excess energy in the 'fat' top jets. There is no reason this same analysis could not be used when the LHC turns back on at 14 TeV.

Acknowledgments

This work is supported by the U.S. Department of Energy under Contract No. DE-SC0008347.

References

[1] Zack Sullivan, Phys. Rev. D **66**, 075011 (2002).

[2] Yaofu Zhou and Zack Sullivan, "Modeling W' bosons for use with model independent studies," paper in production.

[3] Daniel Duffty and Zack Sullivan, Phys. Rev. D **86**, 075018 (2012).

[4] D. Duffty and Z. Sullivan, arXiv:1307.1820 [hep-ph].

[5] J. Alwall *et al.*, J. High Energy Phys. **09**, 028 (2007).

[6] T. Sjostrand, S. Mrenna, and P.Z. Skands, J. High Energy Phys. **05**, 026 (2006).

[7] J. Conway *et al.*, http://www.physics.ucdavis.edu/∼conway/research/software/pgs/pgs.html.

[8] J.M. Campbell and R.K. Ellis, Nucl. Phys. Proc. Suppl. **205-206**, 10 (2010).

[9] CMS Collaboration, CMS-PAS-JME-09-001.

[10] S. Chatrchyan *et al.* (CMS Collaboration), Phys. Lett. B **718**, 1229 (2013).

[11] G. Aad *et al.* (ATLAS Collaboration), Phys. Rev. Lett. **109**, 081801 (2012).

Study of *pp* interactions at high multiplicity at U-70

A. Aleev, V. Avdeichikov, V. Balandin, Yu. Borzunov, Yu. Chencov, V. Dunin, N. Furmanec, G. Kekelidze, V. Kireev, E. Kokoulina, V. Ladygin, V. Myalkovsky, V. Nikitin, V. Peshehonov, Yu. Petukhov, I. Rufanov, A. Yukaev, N. Zhidkov

JINR, VBLHE, Dubna, Moscow region, Russia, 141980

S. Basiladze, G. Bogdanova, I. Erofeeva, N. Grishin, Ya. Grishkevich, D. Karmanov, V. Kramarenko, A. Leflat, M. Merkin, V. Popov, L. Tihonova, A. Vishnevskaya, V. Volkov,A. Voronin, E. Zverev

Lomonosov Moscow State University Scobeltsyn Institute of Nuclear Physics, Russia, 110000

E. Ardashev, A. Afonin, V. Golovkin, S. Golovnya, S. Gorokhov, A. Kholodenko, A. Kiryakov, L. Kurchaniniv, I.Lobanov, E. Lobanova, G. Mitrofanov, V.Petrov, A. Pleskach, M. Polkovnikov, V. Ronzhin, V. Ryadovikov, V. Senko, M. Soldatov, N. Shalanda,Yu. Tsyupa, A. Vorobiev, V. Yakimchuk, V. Zapolsky,

IHEP, Protvino, Russia, 142281

A. Kutov

DM Komi SC UrD RAS, Syktyvkar, Russia 167982

The E190 Experiment is aimed at the search for collective phenomena in a quark-gluon system and a hadron system. It is carried out at U-70 in IHEP, Protvino. The evidence of Bose-Einstein condensation of pions has been confirmed with a twofold increasing of sampling at a level of 7 standard deviations. We study soft photon (smaller than 60 MeV) yield by using of an electromagnetic calorimeter with low energy threshold. In the gluon dominance model we explain multiparticle production by the active gluons. In this model the estimation of the contribution of charge exchange has been obtained.

1. Introduction

Our SVD-2 Collaboration carries out the experiment E-190 at the U-70 accelerator of IHEP [1] in Protvino city near Moscow. There are three main participants: Lomonosov MSU SINP, IHEP, and JINR. Our project is aimed at studying of pp interactions with 50 GeV/c proton beam. We are interested in investigation of high multiplicity (HM) events. HM is considerably higher than average multiplicity. We tend to reach the kinematical limit. The kinematical limit is defined by a condition of the transformation of the whole kinetic energy into mass of secondary pions. Pions are copiously formed at the U-70 energies 50–70 GeV.

Almost all Monte Carlo event generators are mistaken when they make predictions for HM region. PYTHIA underestimates two orders of magnetude topological cross section at $N_{ch} = 18$ (the Mirabelle Collaboration data) [1]. Models give diverse predictions too [1]. We believe that the HM study will give the deeper understanding of multi particle production mechanism.

Section 2 is devoted to HM phenomenology. The description of this region is carried out in the framework of the gluon dominance model (GDM) [3]. This model improves description of topological cross sections in this region, estimates the charge exchange contribution. The evidence of pion condensate formation is presented in section 3. The preparation for soft photon yield study is presented in section 4. Section 5 states the conclusions.

2. Phenomenology of high multiplicity

We carry out studies at the Spectrometer with Vertex Detector (SVD) setup [1] which consists of a hydrogen target, a high multiplicity trigger, a vertex detector, a drift tube chamber, a magnetic spectrometer (magnet and proportional chambers) and an electromagnetic calorimeter (ECal). We can register both charged and neutral particles. To measure of soft photons we included in the SVD setup a soft photon electromagnetic calorimeter (SPEC).

To suppress the registration of low multiplicity events the scintillator hodoscope or HM trigger has been manufactured. At trigger level $l =$ 4, 6, 8, 10, 12 we register events with multiplicity no less than the given level [2]. One million events have been processed at $l = 8$ with taking into account corrections obtained by a Monte-Carlo simulation. Topological cross sections and average multiplicity have been obtained [1].

To describe previous data and make predictions in the HM region we have developed a gluon dominance model (GDM) [3–6]. This model has appeared from the two stage model describing multiplicity distributions in e^+e^- annihilation at high energies by two stages [7]. The first stage is based

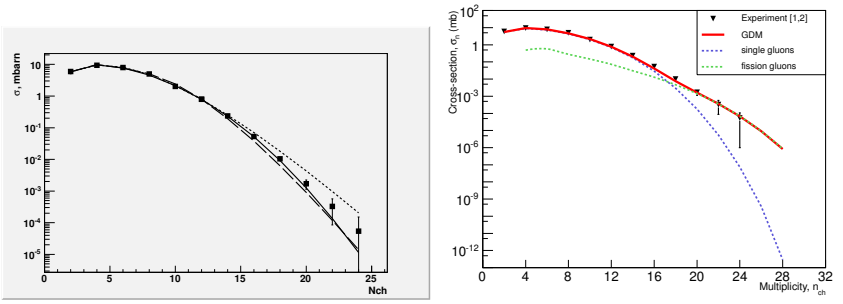

Fig. 1. Left panel: Experimental topological cross sections and the predictions of IHEP model [9], NBD and GDM. Right panel: Topological cross section versus charged multiplicity in GDM [3]. The dashed blue line describes the contribution of single sources, the green line – sources consisted of two gluons of fission, the solid red line is the sum both of contributions.

on QCD quark-gluon cascade: gluon bremsstrahlung by quarks and gluon fission. This stage is described by negative binomial distribution (NBD). The second stage (hadronization) is based on the phenomenological scheme with use of a binomial distribution.

Convolution of the two stages gives good agreement with the data in the region from 10 up to 200 GeV. The main result of that description is constancy of hadronization parameter $\overline{n}_g^h$. It defines the average number of charged particles nascent from one gluon source through itself passing of the hadronization stage. Such behavior is the evidence of the fragmentation mechanism of hadronization in e^+e^- annihilation: one parton — one hadron [8].

It has been shown in the framework of GDM that initial quarks are staying in leading particles and multi particle production is realized by active gluons. Two scheme were proposed with and without inclusion of a gluon fission. Gluon branching is described by a Farry distribution. In both schemes parameters of hadronization grow and become more than 1. We observe their growth from 1.5 at 50 GeV/c, U-70, up to 3.3 at 62 GeV, ISR. In the scheme with fission some gluons do not turn into hadrons (about 50 %) and stay in a quark-gluon system. They can be the sources of anomalous soft photons. GDM describes and predicts topological cross sections of pp ($p\overline{p}$) interactions in HM region. Topological cross sections and their model descriptions are shown in the left panel of Fig.1. The model of IHEP [9] (a dashed line) and GDM (a solid line) describe data well, NBD (a dotted line) overestimates of them slightly in HM area.

In double-logarithmic approximation the emission of two gluons can ex-

plain the angle broadening [10]. One of them is a product of fission. At U-70 this fission can occur. In the right panel of Fig. 2 contributions of two types of sources is shown. The blue dashed line describes contribution of single gluon sources, the green dashed line — double gluon sources nascent as a result of fission of single gluons and the red solid line is the superposition both contributions. The accounting of gluon fission improves the description of HM tail.

In the framework of GDM one can estimate the charge exchange contribution at $n_{ch} = 2$. One of the two protons can pass its charge to a neutral meson with turning it into a charged meson

$$p + p \to p + \pi^+ + n + N_\pi. \tag{1}$$

The cross section $\sigma_{2\to 2}$ consists of elastic and inelastic cross sections: $\sigma_{2\to 2} = \sigma_{2,el} + \sigma_{2,inel}$, where $\sigma_{2,inel}$ in turn consists of two summands, one of them is responsible for the charge exchange ($\sigma_2^{(+ch)}$), the second one ($\sigma_2^{(-ch)}$) for the inelastic cross section without it. GDM does not take into account the charge exchange. So we express $\sigma_{2,inel}$ through parameter P: $\sigma_{2,inel} = P \cdot \sigma_2^{(-ch)}$, as we know how $\sigma_2^{(-ch)}$ is calculated in GDM. Then we describe data by GDM in the whole multiplicity region, find GDM's parameters and P. Hence we estimate the charge exchange coefficient as $q = \sigma_2^{(+ch)}/\sigma_{2,inel} \cdot 100\%$ It approximates $50\pm$ 5%. This value is comparable with the data [11].

3. Search for collective phenomena at U-70

V. Begun and M. Gorenstein have predicted the conditions of the Bose-Einstein Condensate (BEC) formation for *pp* interactions at U-70 at high total multiplicity, $N_{tot} = N_{ch} + N_0$, in the framework of the ideal pion gas model [12]. N_0 is a number of neutral pions. The growth of total multiplicity leads to decrease of the pion system temperature. Pions are bosons and can fall out in pion condensate at high multiplicity.

The indication at the BEC formation is a growth of neutral pion number fluctuations. Begun and Gorenstein have proposed to measure the scaled variance. The scaled variance is calculated by the definition

$$\omega = D/ < N_0 >,$$

where $D =< (N_0 - < N_0 >)^2 >$ is a variance of neutral meson number, $N_{tot} = N_{ch} + N_0$ is fixed. $\omega = 1$ in the case of Poisson distribution. They have predicted [12] that the fluctuations of π^0 and $\pi^\pm$ number increases dramatically and abruptly when the system approaches the BEC line at the thermodynamic limit and $\omega \to \infty$. In the system of limited size a scaled variance grows to the certain constant value. The BEC temperature for

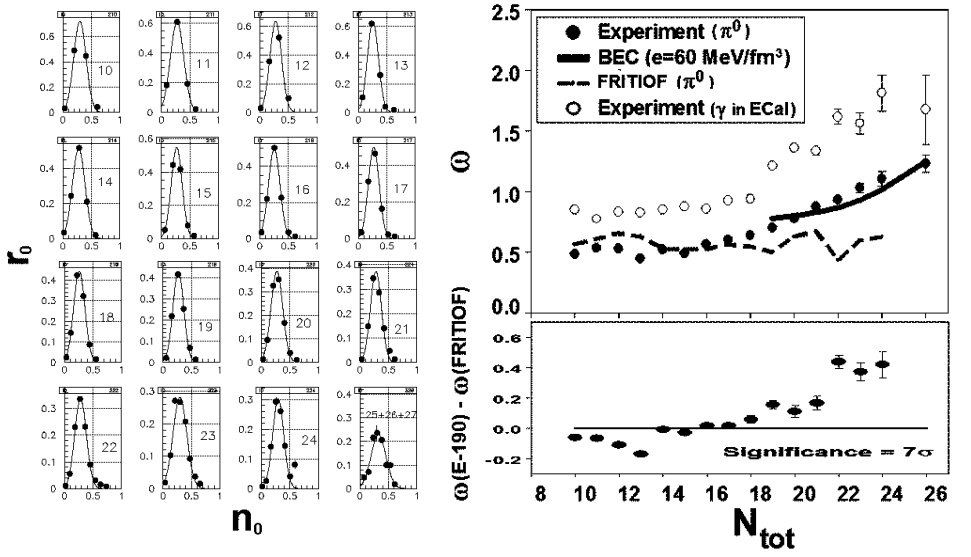

Fig. 2. Left panel. Multiplicity distributions of π^0-mesons versus the scaled total multiplicity at different total multiplicity. Right panel. (Top) The measured scaled variance ω versus N_{tot} for π^0-mesons (•), photons (◦), MC code FRITIOF7.02 (the dashed curve) and theoretical prediction (solid curve) [12] for the energy density ε =60 MeV/fm^3. $N_{tot} = N_{ch} + N_0$ for π^0-mesons and $N_{tot} = N_{ch} + N_\gamma$ for photons. (Bottom) The difference of experimental and Monte Carlo simulated ω for π^0-mesons [14, 15].

a pion system is considerably more than for a nuclear system as radius of nuclei is considerably bigger pion size [13].

Owing to the improved method of the photon registration the multiplicity distributions of π^0-mesons have been restored. To compare their at different values of total number of pions the scaled multiplicity n_0 is used. It is determined by the ratio $n_0 = N_0/N_{tot}$ and variates in the region $0 \leq n_0 \leq 1$. The distributions of neutral pions, $r_0(n_0, N_{tot})$ are presented in the left panel of Fig. 2. The experimental values of the scaled variance have shown the growth about seven standard deviations to a comparison with Monte-Carlo generators. It is seen in the right panel of Fig. 2. The same growth we observe for scaled variance versus a variable $N_{tot} = N_{ch} + N_\gamma$.

An interesting explanation of the connection between BEC and excess of soft photon yield has been proposed by S. Barshay [16].

4. Study of Soft Photon yield

Photons interact with nuclear matter only electromagnetically, and therefore they bear the information on properties of the environment during the interaction. The direct photons are not decay products of any known particles. In accordance with quantum electrodynamics they may be emitted in the process of charged particle scattering – bremsstrahlung at a hadron or parton cascade. In particular, $q + g \to q + \gamma$ parton interactions lead to photon emission. The higher the density and the longer the system lifetime, the more direct photons should be emitted. These photons are useful probes to investigate nuclear matter at all stages of the interaction.

Special attention is devoted to low energy direct soft photons (SP) which yield surpasses the theoretical predictions [17–19]. This excess is observed in K^+p, $\pi^\pm p$, $p\overline{p}$ and pA interactions from 10 GeV up to 450 GeV. Experimental and theoretical studies of the direct photon production in hadronic collisions essentially expand our insights into multi particle production [20]. SP have low transverse and longitudinal momenta $p_T < 0.1$ GeV/c and $|x| < 0.01$. In this domain their yield exceeds the theoretical estimates by 5–8 [17, 18] times and even 17 for neutral pions [19]. The phenomenological models try to explain this excess. Until now, no model was able to explain the experimental data well as a whole, especially in a kinematic range where the effect is most prominent [21].

SVD Collaboration has manufactured SPEC with low energy threshold. The main feature is its capability to register low energy deposit $E \leq 1$ MeV. Up to now none of the known experiments has reached such low value of the photon energy detection. It is presented in the left panel of Fig. 3. The calorimeter is the matrix of 49 scintillator counters. Every counter consists of BGO crystal. The crystal size is equal to $30\times30\times180$ mm^3. Photomultipliers (PMT) of type 9106SB (ET Enterprizes) look over the end face of every scintillator. PMT have 7 dynodes and green extended quantum efficiency. The diameter of photocathode is 25 mm, the diameter of the bulb is not more than 29.5 mm. The bulb has integrated permalloy shield. The PMT is fixing on the crystal by optic glue EPO-TEK 301.

The preliminary amplifier is manufactured on the current feedback (CFB) operational amplifier (OA) Ad8014. The signals from PMT is given to the inverting entry of OA. The maximum value of signal to noise ratio (SNR) is reached by minimal input capacitance on the OA input. This capacitance is defined by dynode-anode gap and assembling capacitance and is about 6 pF. The dynamic range of signals is more than 66 dB.

The front and back sides of the intermediate transitional plates are connected between themselves by two stubs of cables. One of them is placed into the box with crystals, another — out of the box. The low voltage bias

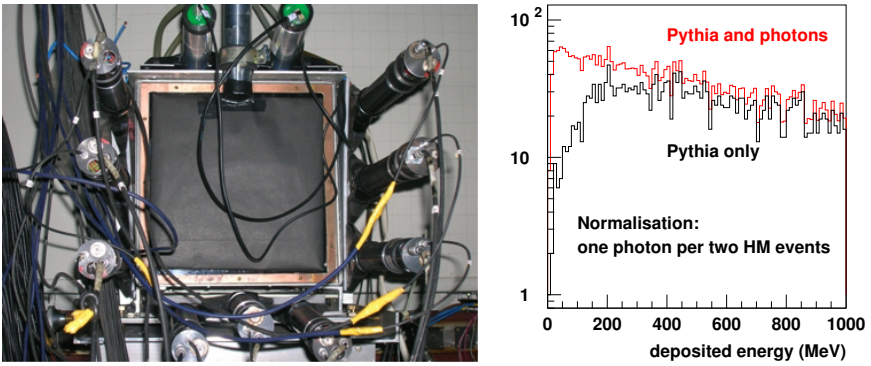

Fig. 3. Left panel: Soft photon electromagnetic calorimeter (SPEC). Right panel: Monte-Carlo energy spectra of photons in *pp* interactions.

(+6 V and -6 V) for the preamplifiers and HV (400-600 V) for PMT are generating on the distributive mother board .

High voltage can regulate on the external plate for every column of assembly (seven elements). The internal plate connects with back wall of calorimeter shield with using of three stubs. The commutations of counters with signal cable lines leading to electronics is carried out by these stubs and located at the control panel of setup.

The feeding of SPEC is realized by two sources +12 V and - 12 V. At the current of consumption smaller than 1 A (+12 V) and 50 mA (-12 V). PMT have been included in scheme with grounded photocathode. Such inclusion is explained by the maximum density of the packing of crystals. The signals is acquired from amplifiers arrive to amplifier inputs through cable lanes which are located on the control desk next to the data acquisition system electronics. After inversion every signal is divided into two and is digitized. One channel is direct, second – observable. The attenuation coefficient is 1:1.5. There are 112 output channels. The calorimeter is placed into the thermo-statical box. The thermal stabilization is realized by Huber 006B setup. The temperature is chosen 18 °C. The calorimeter is surrounded with scintillator counters of a guard system and a passive neutron protection by 8 cm-thickness polyethylene.

The Monte-Carlo simulation of assembly with all crystals is shown in the left panel of Fig. 3. The black line presents the simulation by PYTHIA without SP contribution, the red line takes into account SP contribution by Low formula, $d\sigma/dp \sim 1/p$.

We had a test run this year. The new calorimeter has been put near ECal under 2–6 ° and at the distance of 11 m from a hydrogen target. In the right panel of Fig. 3 the signal spectra in the calorimeter is presented. It has

been obtained at the next conditions: there is no signal in the veto system; there are no signals in counters of the external layer. The signals in the internal part of assembly (3×3 crystals) were summed up on all 9 channels with weight coefficients definite at the calibration. The soft photon spectra has been obtained. Its analysis is in progress. Now we plan to transfer SP study at Nuclotron, JINR.

Acknowledgments

We appreciate all participants of the SVD-2 Collaboration for their active and fruitful work.

References

[1] V.N. Ryadovikov, Phys. Atom. Nucl. **75**, 315 (2012).
[2] E. Kokoulina, A. Kutov, V. Nikitin, Y. Petukhov, and V. Popov, Proceedings of the 40th ISMD, Antwerpen University, 115 (2011).
[3] E.S. Kokoulina, Acta Phys. Pol. B **35**, 295 (2004).
[4] E.S. Kokoulina and A.A. Nikitin, Proc. of the 17th ISHEPP: Dubna, Russia, 319 (2006).
[5] P.F. Ermolov *et al.*, Proc. of the 17th ISHEPP, Dubna, Russia, 327 (2006).
[6] E.S. Kokoulina, AIP Conference proceeding, **828**, 81 (2006).
[7] E.S. Kokoulina, XXXII ISMD, Alushta, Ukraine, W. Sc. 340 (2002).
[8] B. Muller, Nucl. Phys. A **750**, 84 (2005).
[9] S.V. Semenov *et al.*, Sov. J. Nucl. Phys. **22**, 410 (1975).
[10] E.A. Kuraev, S. Bakmaev, and E.S. Kokoulina, Nucl. Phys. B **851**, 551 (2011).
[11] S. Bascovich *et al.*, Yad. Phys. (Russian) **27**, 1225 (1978).
[12] V.V. Begun and M.I. Gorenstein, Phys. Lett. B **653**, 190 (2007).
[13] V.V. Begun and M.I. Gorenstein, Phys.Rev. C **78**, 024904 (2008).
[14] E.S. Kokoulina, Prog. Theor. Phys. Suppl. **193**, 306 (2011).
[15] A.G. Afonin *et al.*, Eur. Phys. J. Web Conf. **37**, 06002 (2012); E. Kokoulina, PoS ICHEP2012, 259 (2013); E.S. Kokoulina *et al.*, PoS Baldin-ISHEPP-XXI, 007 (2012).
[16] S. Barshay, Phys. Lett. B **227**, 279 (1989).
[17] P.V. Chliapnikov *et al.*, Phys. Lett. B **141**, 276 (1984).
[18] A. Belogianni *et al.*, Phys. Lett. B **548**, 129 (2002).
[19] J. Abdallah *et al.*, Eur. Phys. J. C **67**, 343 (2010).
[20] http://theor.jinr.ru/twiki-cgi/view/NICA/NICAWhitePaper.
[21] P. Lichard, Phys. Rev. D **50**, 6824 (1994).

The Tevatron energy scan: Findings & surprises

Rick Field (for the CDF Collaboration)
Department of Physics, University of Florida Gainesville, Florida, 32611, USA

At CDF we study charged particle production ($p_T > 0.5$ GeV/c, $|\eta| < 0.8$) in proton-antiproton collisions at 300 GeV, 900 GeV, and 1.96 TeV. The 300 GeV and 900 GeV data are a result of the "Tevatron Energy Scan" which was performed just before the Tevatron was shut down. We use the direction of the leading charged particle in each event, PTmax, to define three regions of η-ϕ space; "toward," "away," and "transverse." The "transverse" region is further divided into the "transMAX" and "transMIN" contributions. The "transMIN" region is very sensitive to the multiple parton interaction component (MPI) of the "underlying event," while the "transDIF" ("transMAX" minus "transMIN") is very sensitive to the initial and final-state radiation. This CDF analysis together with LHC data provides a detailed study the energy dependence of the various components of the "underlying event" in hadronic collisions.

Min-bias (MB) is a generic term which refers to events that are selected with a "loose" trigger that accepts a large fraction of the overall inelastic cross section. The CDF MB trigger requires at least one charged particle in the forward region $3.2 < \eta < 5.9$ and simultaneously at least one charged particle in the backward region $-5.9 < \eta < -3.2$, where the pseudo-rapidity $\eta = -\log(\tan(\theta_{cm}/2))$ and θ_{cm} is the center-of-mass polar scattering angle. The underlying event (UE) consists of the beam-beam remnants (BBR) and the multiple parton interactions (MPI) that accompany a hard scattering. The UE is an unavoidable background to hard-scattering collider events. To study the UE we use MB data, however, MB and UE are not the same object. The majority of MB collisions are "soft," while the UE is studied in events in which a hard-scattering has occurred. One uses the structure of the hard hadron-hadron collision to experimentally study the UE. As illustrated in Fig. 1, on an event-by-event bases, a "leading object" is used to define regions of η-ϕ space, where η is the pseudo-rapidity and ϕ is the azimuthal angle [1, 2]. Here we use the highest transverse momentum charged particle in the event, PTmax, as the leading object. On an event by event basis, we define "transMAX" ("transMIN") to be the maximum (minimum) number of charged particles or the *scalar* p_T sum of charged particles in the two "transverse" regions, $60^\circ < \Delta\phi < 120^\circ$, $|\eta| < \eta_{\rm cut}$ and $60^\circ < -\Delta\phi < 120^\circ$,

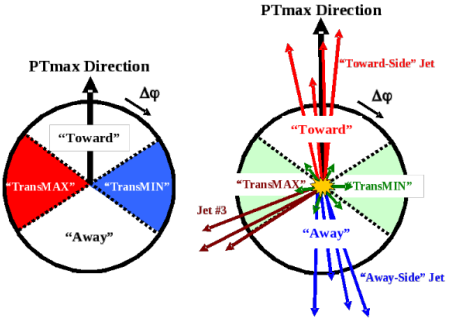

Fig. 1. (left) Illustration of correlations in azimuthal angle $\Delta\phi$ relative to the direction of the leading charged particle in the event, PTmax. The relative angle $\Delta\phi = \phi - \phi_{\rm MAX}$, where $\phi_{\rm MAX}$ is the azimuthal angle of PTmax and ϕ is the azimuthal angle of a charged particle. On an event by event basis, we define "transMAX" ("transMIN") to be the maximum (minimum) of the two "transverse" regions, $60^\circ < \Delta\phi < 120^\circ$, $|\eta| < \eta_{\rm cut}$ and $60^\circ < -\Delta\phi < 120^\circ$, $|\eta| < \eta_{\rm cut}$, where we take $\eta_{\rm cut} = 0.8$. The overall "transverse" region (i.e., "transAVE") is the average of the "transMAX" and the "transMIN" regions. (right) Illustration of the topology of a hadron-hadron collision in which a "hard" parton-parton collision has occurred. The "toward" region contains the leading "jet," while the "away" region, on the average, contains the "away-side jet." For events with large initial or final-state radiation the "transMAX" region contains the third jet, while both the "transMAX" and "transMIN" regions receive contributions from the MPI and beam-beam remnants. Thus, the "transMIN" region is very sensitive to the MPI and beam-beam remnants, while the "transMAX" minus the "transMIN" (i.e., "transDIF") is very sensitive to initial and final-state radiation.

$|\eta| < \eta_{\rm cut}$. Densities are then formed by dividing by the area in η-ϕ space. "TransMAX" and "transMIN" each have an area of $\Delta\eta\Delta\phi = 2\eta_{\rm cut} \times 2\pi/6$, where we take $\eta_{\rm cut} = 0.8$. The overall "transverse" region (i.e., "transAVE") is the average of the "transMAX" and the "transMIN" regions.

Figure 1 illustrates the topology of a hadron-hadron collision in which a "hard" parton-parton collision has occurred. The "toward" region contains the leading "jet," while the "away" region, on the average, contains the "away-side jet." For events with large initial or final-state radiation the "transMAX" region contains the third jet, while both the "transMAX" and "transMIN" regions receive contributions from the MPI and beam-beam remnants. Thus, the "transMIN" region is very sensitive to the MPI and beam-beam remnants, while "transDIF" ("transMAX" minus the "transMIN") is very sensitive to initial and final-state radiation [3].

Figures 2–4 show the preliminary CDF data at 1.96 TeV, 900 GeV, and

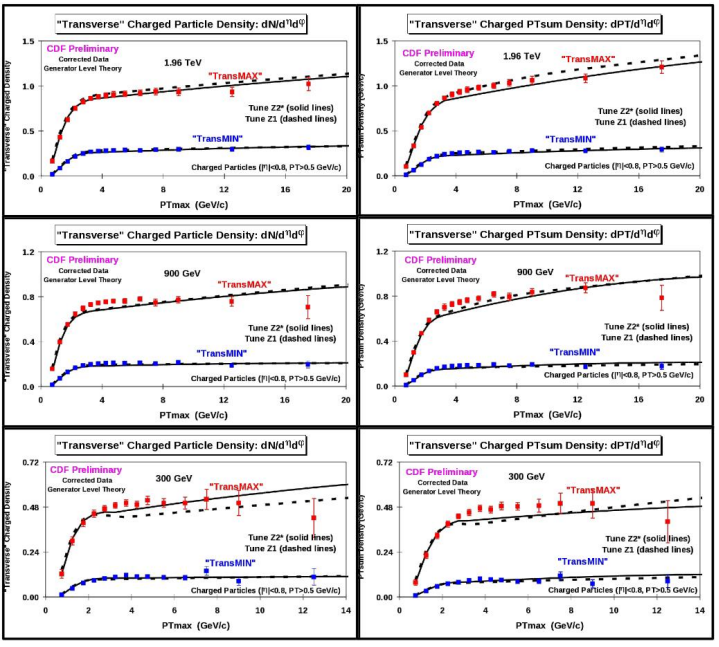

Fig. 2. Preliminary CDF data at 1.96 TeV (top row), 900 GeV (middle row), and 300 GeV (bottom row) on the "transMAX" and "transMIN" charged particle density (left column) and the "transMAX" and "transMIN" charged PTsum density (right column) as defined by the leading charged particle, PTmax, as a function of PTmax. The charged particles have $p_T > 0.5$ GeV and $|\eta| < 0.8$. The data are corrected to the particle level with errors that include both the statistical error and the systematic uncertainty and are compared with PYTHIA 6.4 Tune Z1 and Tune Z2* at the generator level.

300 GeV on the "transMAX," "transMIN," "transAVE," and "transDIF" charged particle and PTsum densities as defined by the leading charged particle, PTmax, as a function of PTmax. The charged particles have $p_T > 0.5$ GeV and $|\eta| < 0.8$. The data are corrected to the particle level with errors that include both the statistical error and the systematic uncertainty and are compared with PYTHIA 6.4 Tune Z1 and Tune Z2* at the generator level. QCD Monte-Carlo generators such as PYTHIA [4] have parameters which may be adjusted to control the behavior of their event modeling. A specified set of these parameters that has been adjusted to better fit some aspects of the data is referred to as a "tune" [5, 6]. Tune Z1 (CTEQ5L) and Tune Z2* (CTEQ6L) are PYTHIA 6.4 tunes that were constructed by fitting CMS UE data at 900 GeV and 7 TeV [7, 8]. Both tunes do a fairly good (although not perfect) job in describing the CDF UE data at 1.96

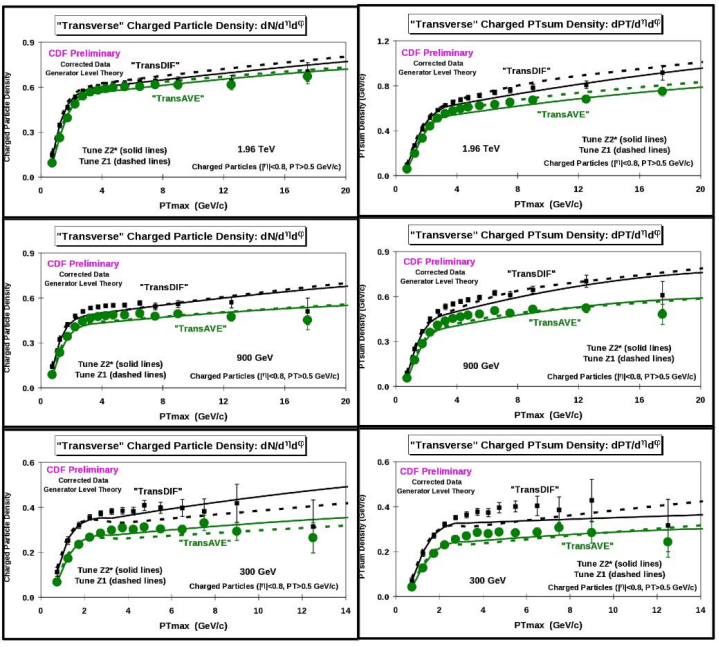

Fig. 3. Preliminary CDF data at 1.96 TeV (top row), 900 GeV (middle row), and 300 GeV (bottom row) on the "transAVE" and "transDIF" charged particle density (left column) and the "transAVE" and "transDIF" charged PTsum density (right column) as defined by the leading charged particle, PTmax, as a function of PTmax. The "transAVE" density is equal to the average of the "transMAX" density and the "transMIN" density (i.e., overall "transverse" density). The "transDIF" density is equal to the "transMAX" density minus the "transMIN" density. The charged particles have $p_T > 0.5$ GeV and $|\eta| < 0.8$. The data are corrected to the particle level with errors that include both the statistical error and the systematic uncertainty and are compared with PYTHIA 6.4 Tune Z1 and Tune Z2* at the generator level.

TeV, 900 GeV, and 300 GeV.

Figure 5 shows preliminary CMS data [9] at 7 TeV together with preliminary CDF data at 1.96 TeV, 900 GeV, and 300 GeV for the "transAVE" charged particle and PTsum densities as defined by the leading charged particle, PTmax, as a function of PTmax. The "transAVE" density is equal to the average of the "transMAX" density and the "transMIN" density (i.e., overall "transverse" density). Figure 6 shows preliminary CMS data [9] at 7 TeV and 900 GeV together with CDF data at 1.96 TeV, 900 GeV, and 300 GeV for the "transAVE" charged particle and PTsum densities as defined by the leading charged particle, PTmax, for 5.0 < PTmax < 6.0 GeV/c

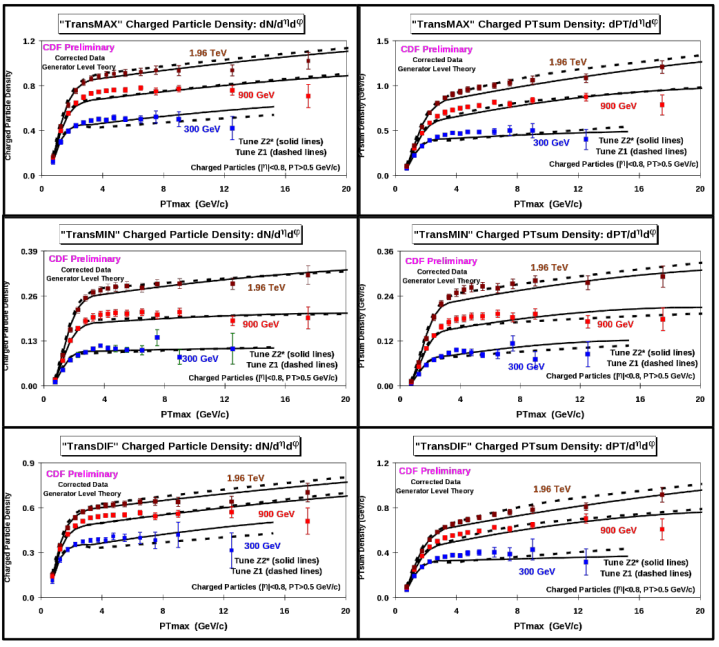

Fig. 4. Preliminary CDF data at 1.96 TeV, 900 GeV, and 300 GeV on the "transMAX" charged particle density (top left), the "transMAX" charged PTsum density (top right), the "transMIN" charged particle density (middle left), the "transMIN" charged PTsum density (middle right), the "transDIF" charged particle density (bottom left), and the "transDIF" charged PTsum density (bottom right) as defined by the leading charged particle, PTmax, as a function of PTmax. The "transDIF" density is equal to the "transMAX" density minus the "transMIN" density. The charged particles have $p_T > 0.5$ GeV and $|\eta| < 0.8$. The data are corrected to the particle level with errors that include both the statistical error and the systematic uncertainty and are compared with PYTHIA 6.4 Tune Z1 and Tune Z2* at the generator level.

versus the center-of-mass energy. Figure 6 also shows the ratio of the data to the corresponding value at 300 GeV for the "transAVE" charged particle and PTsum densities. The "transAVE" charge particle density increases by a factor of about 3.0 in going from 300 GeV to 7 TeV, while the PTsum density increase by a factor of about 3.5. This is a reflection of the fact that the "transverse" average p_T of the charged particles is increasing. Both Tune Z1 and Tune Z2* do a fairly good (although not perfect) job in describing the energy dependence of "transAVE."

Figure 7 shows the energy dependence of the "transMIN" and "transDIF" components. The "transMIN" density (more sensitive to MPI & BBR)

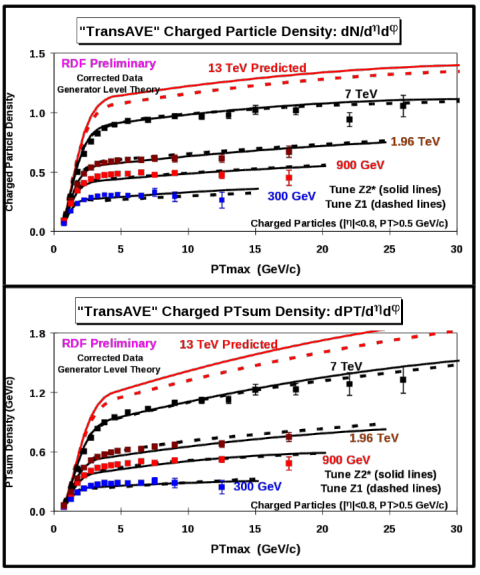

Fig. 5. Preliminary CMS data [9] at 7 TeV and preliminary CDF data at 1.96 TeV, 900 GeV, and 300 GeV on the "transAVE" charged particle density (top) and the "transAVE" charged PTsum density (bottom) as defined by the leading charged particle, PTmax, as a function of PTmax. The "transAVE" density is equal to the average of the "transMAX" density and the "transMIN" density (i.e., overall "transverse" density). The charged particles have $p_T > 0.5$ GeV and $|\eta| < 0.8$. The data are corrected to the particle level with errors that include both the statistical error and the systematic uncertainty and are compared with PYTHIA 6.4 Tune Z1 and Tune Z2* at the generator level. The predictions at 13 TeV are also shown.

increases much faster with center-of-mass energy than does the "transDIF" density (more sensitive to ISR & FSR). The MPI increases like a power of the center-of-mass energy, while the ISR & FSR increase logarithmically. Tune Z2* predicts that the "transMIN" charged particle density increases by factor of around 6.6 in going from 300 GeV to 13 TeV, while the "transDIF" charged particle density is predicted to increase by only a factor of around 2.5. This is the first time we have seen the different energy dependencies of these two components. Previously we only had information on the energy dependence of the "transAVE" charged particle density. Both Tune Z1 and Tune Z2* do a fairly good (although not perfect) job in describing the energy dependence of "transMIN" and "transDIF." What we are learning will allow for a deeper understanding of the BBR and MPI which will result in better Monte-Carlo model tunes and more precise predictions at the future LHC energies of 13 and 14 TeV.

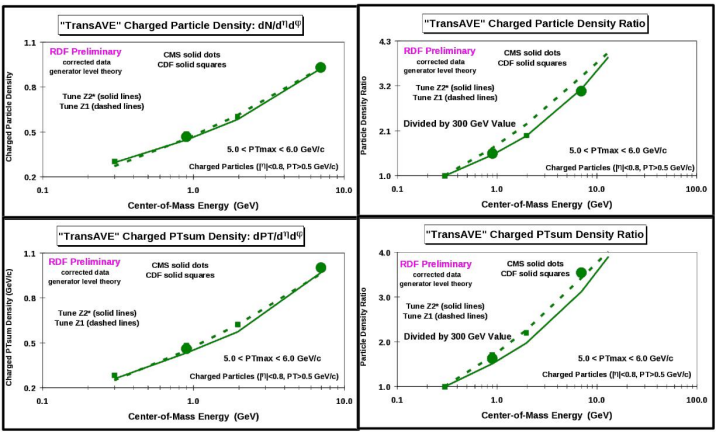

Fig. 6. (left column) Preliminary CMS data protect[9] at 7 TeV and 900 GeV (solid squares) and preliminary CDF data at 1.96 TeV, 900 GeV, and 300 GeV (solid dots) on the "transAVE" charged particle density (top) and the "transAVE" charged PTsum density (bottom) as defined by the leading charged particle, PTmax, for $5.0 < \text{PTmax} < 6.0$ GeV/c versus the center-of-mass energy (log scale). The "transAVE" density is equal to the average of the "transMAX" density and the "transMIN" density (i.e., overall "transverse" density). (right column) Ratio of the data to the corresponding value at 300 GeV for the "transAVE" charged particle density (top) and the "transAVE" charged PTsum density (bottom) as defined by the leading charged particle, PTmax, for $5.0 < \text{PTmax} < 6.0$ GeV/c versus the center-of-mass energy (log scale). The charged particles have $p_T > 0.5$ GeV and $|\eta| < 0.8$. The data are corrected to the particle level with errors that include both the statistical error and the systematic uncertainty and are compared with PYTHIA 6.4 Tune Z1 and Tune Z2* at the generator level extrapolated to 13 TeV (right column).

References

[1] CDF Collaboration, Phys. Rev. D **65**, 092002 (2002).

[2] R. Field, Ann. Rev. of Nucl. and Part. Sci. **62**, 427-457 (2012).

[3] Using "transMAX" and "transMIN" was first suggested by Bryan Webber and implemented in a paper by Jon Pumplin, Phys. Rev. D **57**, 5787 (1998).

[4] T. Sjöstrand, Phys. Lett. B **157**, 321 (1985); M. Bengtsson, T. Sjöstrand, and M. van Zijl, Z. Phys. C **32**, 67 (1986); T. Sjöstrand and M. van Zijl, Phys. Rev. D **36**, 2019 (1987); T. Sjöstrand, P. Eden, C. Friberg, L. Lonnblad, G. Miu, S. Mrenna, and E. Norrbin, Comput. Phys. Commun. **135**, 238 (2001).

[5] R. Field, arXiv:hep-ph/0610012.

[6] P. Skands, The Perugia Tunes, 2009, arXiv:0905.3418.

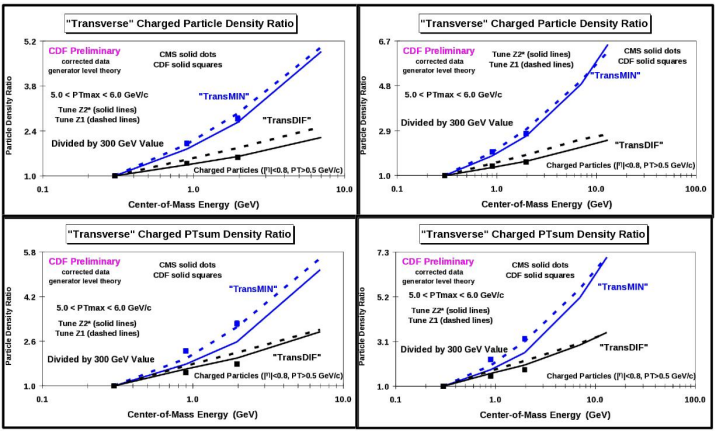

Fig. 7. Preliminary CDF data at 1.96 TeV, 900 GeV, and 300 GeV on the "transMIN" and "transDIF" charged particle density (top row) and the "transMIN" and "transDIF" charged PTsum density (bottom row) as defined by the leading charged particle, PTmax, for $5.0 < \mathrm{PTmax} < 6.0$ GeV/c versus the center-of-mass energy (log scale). The plots show the ratio of the data to the corresponding value at 300 GeV. The charged particles have $p_T > 0.5$ GeV and $|\eta| < 0.8$. The data are corrected to the particle level with errors that include both the statistical error and the systematic uncertainty and are compared with PYTHIA 6.4 Tune Z1 and Tune Z2* at the generator level extrapolated to 7 TeV (left column) and 13 TeV (right column).

[7] CMS Collaboration, J. High Energy Phys. **09**, 109 (2011).

[8] R. Field, arXiv:1110.5530; *Proceedings of the 51st Cracow School of Theoretical Physics: The Soft Side of the LHC*, Zakopane, Acta Phys. Pol. B **42**, 2631 (2011).

[9] CMS Collaboration, Technical Report No. CMS PAS FSQ-12-020, CERN, Geneva, 2012.

Improved isolation of the p-p underlying event based on minimum-bias trigger-associated hadron correlations

Thomas A. Trainor and Duncan J. Prindle

CENPA 354290, University of Washington, Seattle, USA

Some aspects of hadron production in *p-p* collisions remain unresolved, including the low-hadron-momentum structure of high-parton-energy dijets, separation of triggered dijets from the *underlying event* (UE), the systematics of multiple parton interactions and possible systematic underestimation of dijet contributions to high-energy nuclear collisions. In this study we apply a minimum-bias *trigger-associated* (TA) correlation analysis to *p-p* collisions. We extract a hard component from TA correlations that can be compared with measured jet fragment systematics derived from e^+-e^- collisions. The kinematic limits on jet fragment production may be determined. The same method may be extended to A-A collisions where the role of minimum-bias jets in spectra and correlations is strongly contested.

1. Introduction

Several open issues for hadron production in *p-p* collisions relate to dijet production, both the frequency of hard parton scattering and the subsequent fragmentation to jets. In this study we infer the hard scattering rate from the two-component multiplicity systematics of single-particle spectra and introduce a trigger-associated correlation analysis to extract minimum-bias jet fragment distributions. We wish to determine the momentum correlation structure of minimum-bias jets down to the kinematic limits.

2. Two-component model of p-p single-particle y_t spectra

The two-component model of single-particle (SP) spectra is defined by [1]

$$dn_{ch}/y_t dy_t \Delta\eta \;=\; \rho_s(n_{ch})S_0(y_t) + \rho_h(n_{ch})H_0(y_t), \tag{1}$$

where n_{ch} is integrated within some acceptance $\Delta\eta$ and $\rho_x = n_x/\Delta\eta$. Figure 1 (first) shows rescaled y_t spectra for seven multiplicity classes with $n_{ch}/\Delta\eta \approx 1.7, \ldots, 19$. Fixed soft-component model S_0 is the asymptotic limit of spectra scaled by soft-component multiplicity n_s. Subtraction of S_0 and a second rescaling reveals hard components $H(y_t, n_{ch})$ scaled by

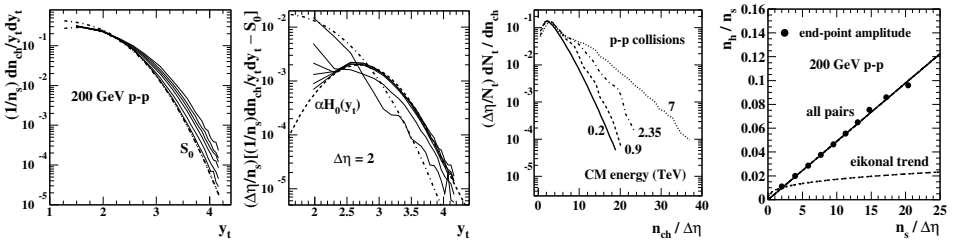

Fig. 1. First: Single-particle spectra for seven n_{ch} classes; Second: Scaled spectrum hard components $H(y_t, n_{ch})$; Third: Event distributions on n_{ch} for several energies; Fourth: Hard-component multiplicity n_h (dijet) trend on soft component n_s. n_h is the integral (end-point amplitude) of measured $H(y_t, n_{ch})$ independent of shape.

$(n_s/\Delta\eta)^2$ (second panel) nearly independent of n_{ch} approximated by fixed hard-component model $H_0(y_t)$. Soft-component multiplicity n_s may serve as a proxy for *participant partons* (low-x gluons) with substantial event-wise fluctuations (third panel). We observe (fourth panel) that $n_h \propto n_s^2$ (points), a trend inconsistent with that expected for the *eikonal model* (dashed curve $\propto n_s^{4/3}$) typically invoked in *p-p* Monte Carlo models [2,3]. These 1D spectrum results provide the model functions and dijet systematics required to analyze and interpret the trigger-associated correlations presented below.

3. Systematics of minimum-bias p-p angular correlations

Combinatoric minimum-bias (MB) angular correlations on angle differences $\eta_\Delta = \eta_1 - \eta_2$ and $\phi_\Delta = \phi_1 - \phi_2$ accepting all particle pairs (no p_t cuts) can be described by a 2D model function including only a few elements [4–6]. The principal correlation components are jet-related same-side (SS) 2D peak and away-side (AS) 1D peak on azimuth (back-to-back jets) and nonjet (NJ) quadrupole $\cos(2\phi_\Delta)$. Figure 2 (first, second) shows angular correlations for

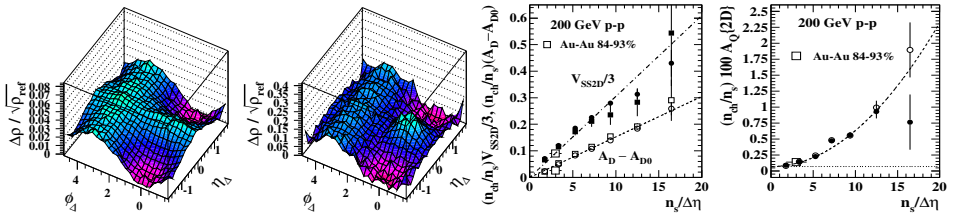

Fig. 2. First, second: Jet-related and non-jet quadrupole angular correlations for multiplicity classes $n = 1$ and 6; Third: Scaled amplitudes of jet-related structure vs soft multiplicity n_s; Fourth: Scaled nonjet quadrupole amplitude vs n_s

multiplicity classes $n = 1$ and 6. Minor elements of the 2D model fits (proton fragment correlations, Bose-Einstein correlations, conversion electron

pairs) have been subtracted leaving the jet-related components and the NJ quadrupole. The third panel shows trends on n_s for jet-related amplitudes consistent with dijet number $n_j = 0.03(n_s/2.5)^2$ (within $\Delta\eta = 2$) corresponding to pQCD dijet total cross section $\sigma_{dijet} = 2.5$ mb [7]. The *p-p* NJ quadrupole trend on n_s can be predicted. The observed centrality trend for Au-Au collisions is $A_Q(b) \equiv \rho_0(b)v_2^2(b) \approx B\, N_{bin}(b)\epsilon^2_{optical}(b)$ [8]. For the non-eikonal *p-p* case $N_{bin} \to N^2_{part}$ and impact parameter b is not an observable, so $n_{ch}A_Q(b) \propto N_{part}N_{bin}\langle\epsilon^2_{optical}\rangle \propto N^3_{part} \propto n_s^3$. Based on *p-p* dijet systematics we expect $(n_{ch}/n_s)A_Q(n_s) \propto n_s^2$, which is confirmed in the fourth panel.

4. Trigger-associated (TA) two-component model (TCM)

Based on *p-p* SP spectrum and 2D MB dijet angular correlation systematics we can construct a TCM for trigger-associated correlations [9]. For each *p-p* collision *event type* (soft or hard) the hadron with the highest transverse rapidity y_{tt} is the *trigger* particle. All other hadrons are *associated*, with rapidities y_{ta}. Definition of the TA TCM is an exercise in compound probabilities. The unit-normal 1D trigger spectrum for multiplicity class n_{ch} denoted by $T(y_{tt}, n_{ch}) \equiv [1/N_{evt}(n_{ch})]dn_{trig}/y_{tt}dy_{tt}$ is modeled by

$$T(y_{tt}, n_{ch}) \;=\; P_s(n_{ch})G_s(y_{tt})\, n_{ch}F_s(y_{tt}) + P_h(n_{ch})G_h(y_{tt})\, n_{ch}F_h(y_{tt}), \quad (2)$$

where $P_x(n_{ch})$ is an event-type probability, $G_x(y_{tt})$ is a void (above y_{tt}) probability and $F_x(y_{tt})$ is a unit-normal SP spectrum for event-type $x = s$ (soft, no dijets) or h (hard, at least one dijet), with $G_x(y_{tt})\, n_{ch}F_x(y_{tt}) \equiv T_x(y_{tt}, n_{ch})$. The Poisson event-type probabilities are defined by $P_s = \exp(-n_j)$ and $P_h = 1 - P_s$. The void probabilities are defined by $G_x = \exp(-n_{x\Sigma})$, where $n_{x\Sigma}$ is the appropriate spectrum integral above y_{tt}. Figure 3

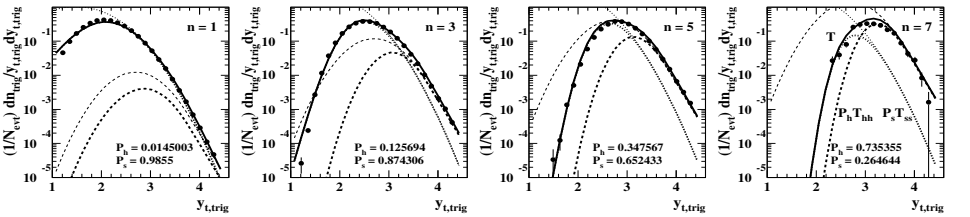

Fig. 3. Trigger spectrum data (points) and TCM (curves) for n = 1, 3, 5, 7.

shows trigger spectra (points) for four multiplicity classes. Solid curves $T(y_{tt}, n_{ch})$ are defined by Eq. (2). The other curves refer to TCM trigger-spectrum components. The TCM describes the trigger spectra well.

The unit-normal 2D TA distribution for event-type x and multiplicity class n_{ch} is *joint probability* $F_x(y_{ta}, y_{tt}) \equiv T_x(y_{tt})A_x(y_{ta}|y_{tt})$, where the *chain*

rule for compound probabilities has been invoked. $A_x(y_{ta}|y_{tt})$ is the *conditional probability* that an associated particle is emitted at y_{ta} in an event of type x given a trigger at y_{tt} with probability $T_x(y_{tt})$. The TA TCM is then

$$F(y_{ta}, y_{tt}, n_{ch}) \;=\; P_s(n_{ch})T_s(y_{tt})A_s(y_{ta}|y_{tt}) + P_h(n_{ch})T_h(y_{tt})A_h(y_{ta}|y_{tt}), \quad (3)$$

where the TCM A_x are formed from the SP-spectrum TCM elements with certain marginal constraints [9]. Hard component $H_h(y_{ta}|y_{tt})$ of $A_h(y_{ta}|y_{tt})$ represents the sought-after momentum correlation structure of MB jets.

5. Measured trigger-associated correlations

Trigger-associated correlations can be presented both as joint probabilities $F(y_{ta}, y_{tt}, n_{ch})$ and as conditional probabilities $A(y_{ta}|y_{tt}, n_{ch}) = F/T$ using the chain rule for joint probabilities. Figure 4 (left) shows the mea-

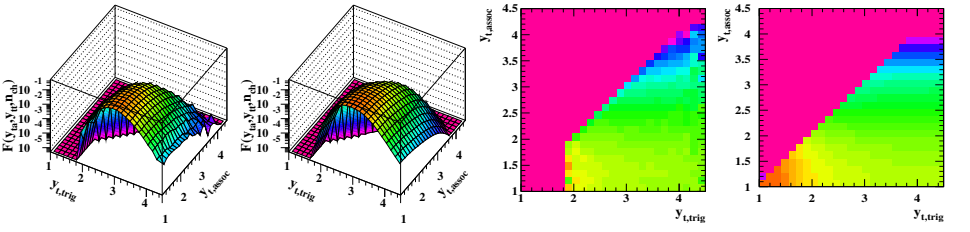

Fig. 4. Left: TA correlations F for multiplicity class $n = 6$ and for data and TCM (first and second respectively); Right: Same for conditional correlations $A = F/T$.

sured joint distribution F for $n = 6$ (first) and its corresponding TCM (second). Figure 4 (right) shows the measured conditional distribution A (third) and its TCM (fourth). In both cases the agreement is good below $y_{ta} \approx 2.5$. TCM hard component H_0' is based on a simple factorization approximation and plays no role in extraction of the data hard components described below. The jet-related hard component dominates TA structure for y_{ta}, $y_{tt} > 2.5$. The data and TCM hard components differ substantially.

6. Extracting the TA hard component

Dividing Eq. (3) by Eq. (2) we obtain the total conditional distribution

$$A(y_{ta}|y_{tt}, n_{ch}) \;=\; R_s(y_{tt}, n_{ch})A_s(y_{ta}|y_{tt}) + R_h(y_{tt}, n_{ch})A_h(y_{ta}|y_{tt}), \quad (4)$$

where the $R_x \leq 1$ are *trigger fractions*. The TCM conditional distributions are $A_s = S_0''$ and $A_h = p_s'S_0' + p_h'H_0'$ for $y_{ta} < y_{tt}$, with primes on X_0' denoting the effects of marginal constraints as described in Ref. [9], and

$p'_x = n'_x/(n_{ch}-1)$. Given that expression we can isolate the hard component of the TA conditional distribution by subtracting the TCM soft components

$$H'_h(y_{ta}|y_{tt},n_{ch}) = \frac{n_{ch}-1}{R_h}[A(y_{ta}|y_{tt}) - R_s S''_0(y_{ta}|y_{tt}) - R_h p'_s S'_0(y_{ta}|y_{tt})], \quad (5)$$

the hard component (dijet momentum structure) per hard event. All subtractions use the same soft-component models derived from SP spectra.

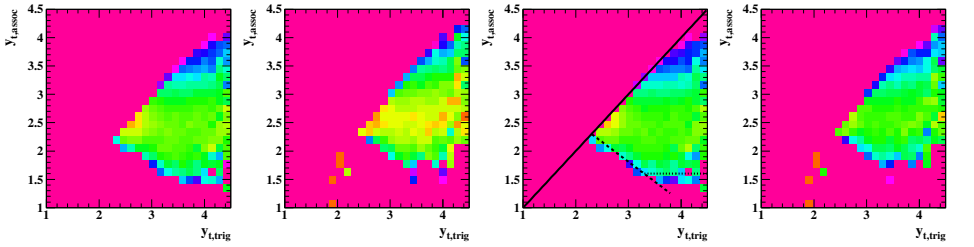

Fig. 5. Left: Per-hard-event hard component $H'_h(y_{ta}|y_{tt},n_{ch})$ for multiplicity classes $n = 2$ and 6; Right: The same data scaled by number of dijets per hard event n_j/P_h to yield the per-dijet hard component. Lines are discussed in the text.

Figure 5 (left) shows hard components $H'_h(y_{ta}|y_{tt})$ for multiplicity classes $n = 2$, 6 (first and second respectively). The jet structure *per hard event* increases substantially with n_{ch} because the probability that one or more additional dijets accompanies a triggered dijet (multiple parton interactions or MPI) becomes substantial. We can divide the left panels by the number of dijets per hard event n_j/P_h to obtain the right panels. The resulting *per-dijet* structure appears to be approximately independent of n_{ch} (universal). Universality is consistent with the $n_j(n_s)$ trend inferred from SP spectra.

7. TA azimuth dependence and the transverse region or TR

The azimuth structure of TA correlations relative to the trigger direction is of interest for several reasons including "underlying event" (UE) studies. Figure 6 (first) shows the conventional azimuth partition relative to trigger direction (arrow) into three equal regions: "toward" (T), "transverse" (TR) and "away" (A). In some studies the A region is split into two parts A_1 and A_2 as shown. In conventional UE analysis it is assumed that the triggered dijet does not contribute to the TR, which region should therefore permit unbiased access to the UE *complementary to the triggered dijet* [10, 11].

Figure 6 (second, third, fourth) shows TA hard components per hard event for T, TR and A regions respectively, averaged over lower multiplicity classes $n = 2$, 3, 4 to reduce dijet pileup (MPI) to less than 15%. Those data averaged over azimuth are equivalent to Fig. 5 (right). Most notable is the

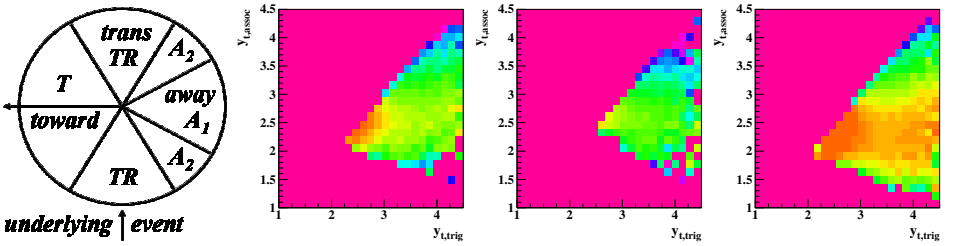

Fig. 6. First: Conventional definition of azimuth regions for underlying event analysis; Second, Third, Fourth: TA hard components for toward T, transverse TR and away A averaged over multiplicity classes $n = 2$, 3, 4 to minimize MPI.

substantial triggered-dijet contribution to the TR region (third panel), contradicting a common UE assumption. Compared to the T region (second) the A region (fourth) is both significantly softer *and* harder. The A region must be harder on average to compensate the trigger particle excluded from conditional distribution A in the T region. The A region is also softer on average because of trigger bias to lower-energy jets due to initial-state k_t effects and toward a softer fragmentation cascade within those jets.

8. The underlying event and multiple parton interactions

Other issues emerge for conventional UE analysis. Based on MB dijet angular correlations as in Fig. 2 (left) we expect a substantial contribution to the TR from any dijet [13]. Figure 7 (first) shows a projection onto azimuth of the model fit to Fig. 2 (first) approximating MB jet structure from non-single-diffractive p-p collisions. There is a substantial overlap of SS and AS jet peaks and resulting strong jet contribution to the TR. Figure 7 (second) shows $N_\perp$ spectra from the TR described by the TCM of Eq. (1) with the amplitude of (jet) hard-component H as expected for hard (triggered) events. Fig. 2 (third) shows the TR $N_\perp$ density vs trigger condition $y_{t,trig}$. The increase to a saturation value is conventionally attributed to MPI. However, a study based on the TCM for SP spectra reveals that the $N_\perp$ increase results from a dijet contribution to the TR for hard events with low ($\approx$ NSD) multiplicities where the incidence of MPI is negligible [13]. Fig. 2 (fourth) shows the calculated dijet number per hard event vs multiplicity. For NSD p-p collisions ($n_{ch}/\Delta\eta \approx 2.5$) the MPI rate is only a few percent. From TA and angular-correlation analysis we conclude that application of a trigger $y_{t,trig}$ (jet) condition in UE analysis selects for jets within mainly low-multiplicity ($\approx$ NSD) hard events. Applying an n_{ch} condition instead would select for multiple MB dijets (MPI) in higher-multiplicity events.

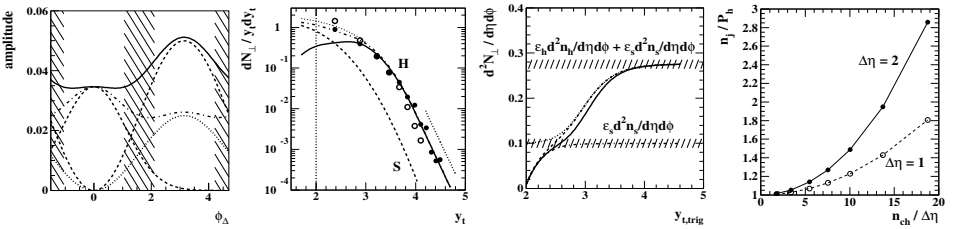

Fig. 7. First: Model fit to 2D MB jet angular correlations (curves) projected onto 1D azimuth showing substantial jet contribution to the TR (hatched); Second: Spectrum of $N_\perp$ yield in the TR (points, [10]) showing jet-related hard component (curve H); Third: Simulated $N_\perp$ density vs jet trigger condition showing increase to saturation due to selection of low-multiplicity hard events [13]; Fourth: Number of jets per hard event n_j/P_h vs n_{ch} inferred from SP spectrum systematics [1,13].

9. Kinematic limits on physical MB jet fragment production

The results in Figs. 5 (lines in third) and 6 (second and fourth panels) reveal the kinematic limits of minimum-bias jet fragment production: Trigger hadrons extend down to ≈ 1 GeV/c ($y_{tt} \approx 2.7$), and associated hadrons extend down to ≈ 0.35 GeV/c (AS, $y_{ta} \approx 1.5$) or 0.5 GeV/c (SS, $y_{ta} \approx 2$). We conjecture that this also represents the low-hadron-momentum (and large-angle) structure of high-parton-energy jets, the common base of any dijet. Higher-energy jets contain a few additional high-momentum hadrons located close to the dijet axis and therefore outside the TR. TA correlation analysis could be extended to A-A collisions to verify the strong contribution from MB jets (minijets) even in more-central Au-Au collisions [6, 7, 14].

These TA results are consistent with measured FFs from LEP, HERA and CDF and with a pQCD parton spectrum that predicts measured dijet production [12, 13] and the shape of the MB spectrum hard component [7]. The MB-jet-related SS 2D peak volume is also consistent with pQCD predictions [14]. Conventional trigger-associated p_t *cuts* invoked in A-A dihadron correlation analysis accept only a small fraction of the actual dijet number and jet fragments and, combined with so-called ZYAM subtraction of a combinatorial background, produce an unphysical picture of dijets in nuclear collisions in which jet structure is minimized and distorted [15].

10. Summary

The two-component (soft + hard) model (TCM) of hadron production in high-energy nuclear collisions works remarkably well. Based on various comparisons with theory the soft component represents fragments from projectile nucleons (their gluon constituents), and the hard component represents dijet fragments from large-angle-scattered partons (gluons).

In this study the TCM has been applied to MB trigger-associated (TA) correlations for several charge multiplicity classes of 200 GeV p-p collisions. A conditional hard component $H_h(y_{ta}|y_{tt})$ has been extracted by analogy with TCM analysis of single-particle spectra. The TA hard component reveals the kinematic limits of jet fragment production and is directly comparable with measured jet fragmentation functions from e^+-e^- collisions.

These TA correlation results have implications for underlying-event (UE) analysis. Consistent with MB angular-correlation analysis the TA results confirm that the triggered dijets make a strong contribution to the transverse region or TR, contradicting conventional UE assumptions. The increase of the $N_\perp$ charge multiplicity in the TR with jet trigger $y_{t,trig}$ results not from multiple parton interactions (MPI) but from increased probability of low-multiplicity hard events including only a single dijet. The MPI rate is increased by selecting instead higher event multiplicities n_{ch}. The physical UE is then the MPI rate determined by n_{ch} plus the TCM soft component.

This work was supported in part by the Office of Science of the U.S. DOE under grant DE-FG03-97ER41020.

References

[1] J. Adams *et al.* (STAR Collaboration), Phys. Rev. D **74**, 032006 (2006).

[2] T. Sjöstrand and M. van Zijl, Phys. Rev. D **36**, 2019 (1987); T. Sjöstrand, Comput. Phys. Commun. **82**, 74 (1994); T. Sjöstrand, L. Lönnblad, S. Mrenna and P. Skands, hep-ph/0308153.

[3] M. Bahr, S. Gieseke, M.A. Gigg, D. Grellscheid, K. Hamilton, O. Latunde-Dada, S. Platzer, P. Richardson *et al.*, Eur. Phys. J. C **58**, 639 (2008).

[4] R.J. Porter and T.A. Trainor (STAR Collaboration), J. Phys. Conf. Ser. **27**, 98 (2005).

[5] R.J. Porter and T.A. Trainor (STAR Collaboration), PoS C **FRNC2006**, 004 (2006).

[6] G. Agakishiev *et al.* (STAR Collaboration), Phys. Rev. C **86**, 064902 (2012).

[7] T.A. Trainor, Phys. Rev. C **80**, 044901 (2009).

[8] D.T. Kettler (STAR collaboration), Eur. Phys. J. C **62**, 175 (2009).

[9] T.A. Trainor and D.J. Prindle, arXiv:1307.1819.

[10] T. Affolder *et al.* (CDF Collaboration), Phys. Rev. D **65**, 092002 (2002).

[11] R. Field, Acta Phys. Polon. B **42**, 2631 (2011).

[12] T.A. Trainor and D.T. Kettler, Phys. Rev. D **74**, 034012 (2006).

[13] T.A. Trainor, Phys. Rev. D **87**, 054005 (2013).

[14] T.A. Trainor and D.T. Kettler, Phys. Rev. C **83**, 034903 (2011).

[15] T.A. Trainor, Phys. Rev. C **81**, 014905 (2010).

Color reconnection and its effects on precise measurements at the LHC

Torbjörn Sjöstrand

Department of Astronomy and Theoretical Physics, Lund University,
Sölvegatan 14A, SE-223 62 Lund, Sweden

There is experimental evidence for the occurrence of color reconnection, but the mechanisms involved are far from understood. Previous reconnection studies are briefly summarized, and some potential implications for LHC physics are outlined.

1. Introduction

LHC events have a complicated structure, which involves many physics components, the main ones being hard-process matrix elements, parton distribution functions, multiple parton interactions (MPIs), initial-state radiation (ISR), final-state radiation (FSR), beam remnants, hadronization and decays. All of these contain challenges, but are still understood individually, to some extent. When combined, additional sources of uncertainty appear, however. Foremost among these, color reconnection (CR) represents the uncertainty induced by the high density of color charges, that may interact in a nontrivial nonlinear manner.

To put numbers on the challenge, about ten charged particles are produced per unit of rapidity for LHC events at around $y = 0$. These come from around ten primary hadrons, which in their turn come from ten color strings [1] crossing $y = 0$, according to Pythia [2] simulations. The distributions are very widely spread around this average, so much higher densities are common. The string density is largely driven by the MPI component, where each gluon–gluon scattering may lead to two strings crossing $y = 0$, but it also receives contributions from ISR and FSR. The string width is the same as that of a hadron, the two being dictated by the same confinement physics, and most of the strings are produced and evolve within the transverse area of the original proton–proton collision. Therefore many strings overlap in space and time, potentially leading to nonlinear effects. Furthermore, the small number of colors, $N_C = 3$, inherently leads to ambiguities which partons belong together in separate color singlets.

One approach to this issue would be modify or abandon existing hadronization models, color ropes [3] being an example of the former and quark–gluon plasma of the latter. Less dramatic is the CR road, where hadronization as such is unmodified and the nonlinear effects are introduced via models that "only" reassign colors among partons. In the following we will study such models and some of their consequences.

2. Historical overview

The idea that color assignments provided by perturbation theory could be modified by nonperturbative effects was around already soon after the birth of QCD. The color octet production mechanism $g^* \to c\overline{c} \to J/\psi$ [4] is an early example. Such color rearrangement effects were studied more systematically for B decay [5], and the sequence $B \to J/\psi \to \ell^+\ell^-$ was proposed as an especially convenient test [6]. Indeed the $B \to J/\psi$ branching ratio suggests a non-negligible but not dominant fraction of the $b \to cW^- \to c\overline{c}s$ rate, kinematical restrictions taken into account [7].

Color reconnection in minimum-bias hadronic physics was first introduced [8] to explain the rising trend of $\langle p_\perp \rangle (n_{\rm ch})$ observed by UA1 [9]. The starting point here is that large charged-particle multiplicities predominantly come from having a large MPI activity, rather than from high-$p_\perp$ jets, say. If each such MPI produces particles more-or-less independently of each other, then the $\langle p_\perp \rangle$ should be independent of the number of MPIs, and hence of $n_{\rm ch}$. The alternative is that each further MPI brings less and less additional $n_{\rm ch}$, while still providing an equally big $p_\perp$ kick from the (semi-)hard interaction itself, to be shared among the produced hadrons. This is possible in scenarios with CR, if reconnections tend to reduce the total string length λ [10],

$$\lambda \approx \sum_{i,j} \ln\left(\frac{m_{ij}^2}{m_0^2}\right) \ , \tag{1}$$

where i, j runs over all color-string-connected parton pairs and $m_0 \approx 1$ GeV is a reference scale of a typical hadronic mass.

As an aside, other aspects (well modeled in generators) drive the rise of $\langle p_\perp \rangle (n_{\rm ch})$ at small $n_{\rm ch}$. Furthermore, the absolute normalization of $\langle p_\perp \rangle$ in this region comes straight from tunes of hadronization to e^+e^- data, supporting the notion that beam-remnant hadronization is no different from that of jets so long as the string density is low.

W pair production at LEP 2 was expected to offer an interesting test bed for such concepts, i.e. whether the $q\overline{q}$ pair produced in each W decay would hadronize separately or whether e.g. the q from one W could hadronize

together with the $\overline{q}$ from the other. Notably, this could mess up W mass determinations. Unfortunately, results were not conclusive.

- Perturbative effects are suppressed for a number of reasons, notably that hard-gluon exchanges would force the W propagators off-shell, giving a negligible uncertainty $\langle \delta M_W \rangle \leq 5$ MeV [11].
- Several nonperturbative CR models predicted large effects and could promptly be ruled out. More conservative ones [11] could not be excluded, but were not favored [12], and gave $\langle \delta M_W \rangle \sim 40$ MeV.
- Additionally Bose-Einstein effects, i.e. that the wave function of identical integer-spin hadrons should be symmetrized, could affect the separate identities of the W^+ and W^- decay products. Effects on $\langle \delta M_W \rangle$ could be as large as 100 MeV, but again more likely around 40 MeV [13]. An effect of the latter magnitude is disfavored by data, but again not fully ruled out [14].

Given the clean LEP environment, it was feasible to trace the space–time evolution of the strings [11], and use that to decide if and where a reconnection would occur. Two alternative scenarios were inspired by Type II and Type I superconductors. In the former, narrow vortex lines at the core of the strings carry the topological information, and so it was assumed that strings could reconnect only if and where these cores crossed. In the latter, strings are viewed as elongated bags with no marked internal structure, and therefore the reconnection probability was related to the integrated space–time overlap of these bags. In both cases reconnections that reduced the total string length could be favored.

A future high-luminosity e^+e^- collider for the study of Higgs production would, as a by-product, provide much larger W^+W^- samples and thereby allow more precise tests. Assuming an effect is found, its energy and angular-orientation dependence could constrain the range of allowed models [15].

The observation of diffractive event topologies in Deeply Inelastic Scattering at HERA has also been interpreted as a consequence of CR [16]. This offers an alternative to the Ingelman–Schlein picture [17] of scattering on a Pomeron (or glueball, in modern language) component inside the proton. Both approaches can be tuned to give comparable phenomenology, so there is no clear winner at HERA. Nevertheless, HERA, Tevatron and LHC diffractive data can provide significant constraints on any universal model of color reconnection. This also includes topics such as diffractive jet, W and Higgs production. Diffraction and models for diffraction is such a major topic in its own right [18] that it is impossible to cover it here.

It is also plausible that both CR and Pomeron mechanisms contribute to the appearance of rapidity gaps. To exemplify, a rapidity gap between two high-$p_\perp$ jets likely is dominated by reconnection, whereas small-mass diffraction comes more naturally in a traditional Pomeron language.

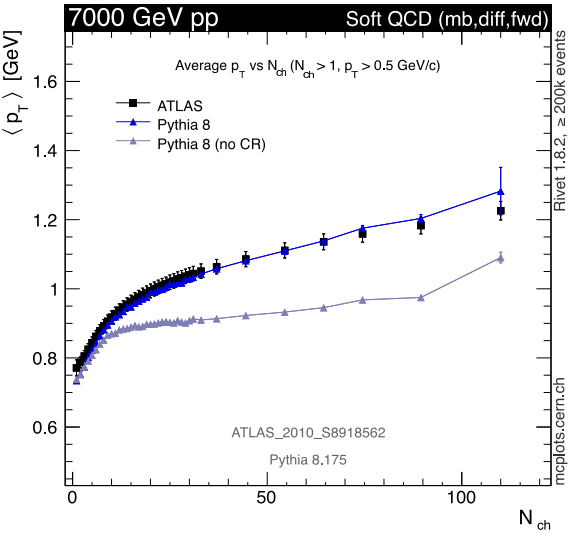

Fig. 1. $\langle p_\perp \rangle (n_{\mathrm{ch}})$ with the default PYTHIA 8 Tune 4C [21], and the same with CR switched off, compared with ATLAS data [22].

3. Status at the LHC

While most of the basic ideas for MPI modeling existed a long time ago [8], gradually models have become more sophisticated. One key example is the handling of beam remnants [19]. As a starting point, the color flow in each separate MPI, including its associated ISR and FSR, is traced in the $N_C \to \infty$ limit [20]. (This limit gives a well-defined color topology, as needed for the string hadronization model.) But any color coming into an MPI must be compensated by a corresponding anticolor left behind in a remnant, which for $N_C \to \infty$ leads to a remnant momentum to be shared between a multitude of string endpoints. Such a scenario is not ruled out, since essentially no data exists on how the remnant structure changes as a function of the central multiplicity, and since a modeling could introduce many free tuning parameters, but neither is it plausible.

Instead it is likely that the $N_c = 3$ reality leads to a smaller remnant color charge, as the initial color of one MPI often compensates the anticolor of another, thereby correlating the color flow of these two MPIs right up to the final state. Such correlations means that fewer strings need to be drawn out to the beam remnants for high MPI multiplicities, offering a mechanism for a rising $\langle p_\perp \rangle (n_{\mathrm{ch}})$, but nowhere near enough. Thus, also with modern models, LHC data reconfirm the need for a further mechanism, such as CR. This is illustrated in Fig. 1.

The almost perfect agreement in Fig. 1 is fortuitous, and it looks less impressive with other selection criteria [22, 23], even if the qualitative features still are reproduced. So there is room for improvements of the CR modeling, or for other physics mechanisms.

Over the years, PYTHIA 6.4 has come to contain a dozen of CR scenarios, many closely related. Unlike the above-mentioned e^+e^- scenarios there is no attempt to trace a space–time evolution. Instead the guiding principle is to reduce the total string length, as defined by the λ measure of Eq. (1) or, alternatively, by the $\sum_{i,j} m_{ij}^2$ (GAL, Generalized Area Law [24]). Typically an algorithm may go something like [25]

- Calculate a reconnection probability $P_{\rm rec} = 1-(1-\chi)^{n_{\rm MPI}}$, where $n_{\rm MPI}$ is the number of MPIs in the current event and χ is a free reconnection strength parameter.
- Each string piece is chosen to be a candidate for reconnection with a probability $P_{\rm rec}$.
- Use a simulated annealing algorithm to perform reconnections between the candidates picked in the previous step, favoring a reduced λ.

By contrast, currently PYTHIA 8.1 only contains one scenario, where either all or none of the final-state partons of a MPI system are attached to the string pieces of a higher-$p_\perp$ system, in a way so as to keep λ minimal. The lower the $p_\perp$ scale of an MPI, and the larger the number of other MPIs, the more likely it is to be disassembled by CR.

Also the other standard LHC generators face similar issues. The inclusion of CR into HERWIG/HERWIG++ [26] is of fairly recent date [27]. CR is necessary not only to to describe $\langle p_\perp \rangle (n_{\rm ch})$ but also, for example, the $\mathrm{d}n_{\rm ch}/\mathrm{d}\eta$ distribution. Again a simulated annealing approach is used to reduce $\sum m^2$, where the sum runs over all clusters, akin to the GAL above. SHERPA [28] currently has an MPI model based on the PYTHIA one, but without any color reconnection. Therefore it also fails to describe the $\langle p_\perp \rangle (n_{\rm ch})$ distribution. A new model for minimum-bias and underlying events is in preparation [29] that should address it.

4. The mass of unstable colored particles

Confinement leads to ambiguous masses for colored particles, since they cannot be studied in isolation. Short-lived colored particles, like the top, do not even form hadrons with well-defined masses. For the kinematics of production and decay, an event generator therefore have to use its own mass definition, that is close to but not necessarily identical with the pole mass. This inherently leads to ambiguities in a translation of a generator-assisted top mass measurement into a corresponding $\overline{\rm MS}$ mass.

Furthermore the top quark, as well as the W and Z gauge bosons, travel a distance $c\tau \approx 0.1$ fm before they decay, i.e. significantly less than a proton radius. Therefore their decays take place right in the middle of the showering/hadronization region, and so quarks (and gluons) produced in the decays are subject to the CR issues already discussed. That is, in a decay $t \to bu\overline{d}$ the b for sure is color-connected somewhere else, giving mass ambiguities, but additionally the $u\overline{d}$ system may or may not remain as a separate singlet, further contributing to the uncertainty.

Studies with Pythia 6.4 for the Tevatron suggested a total uncertainty approaching 1 GeV [25] when comparing different tunes. Of this a large part comes from the description of the perturbative stage, i.e. ISR and FSR uncertainties, which should have shrunk considerably since, with the advent of more sophisticated matching/merging techniques. But up to 0.5 GeV remains as a potential error related to CR issues. To put this in context, current top mass measurements at the Tevatron and the LHC now have statistical errors of the order 0.5 GeV, and quote systematic errors below 1 GeV [30].

Clearly this issue needs to be studied further, to try to constrain the possible magnitude of effects from data itself. CR effects should depend on the event kinematics, which would allow to test and constrain models. Such studies have already begun in CMS [31], although statistics does not yet allow any conclusions to be drawn.

As already mentioned, Pythia 8.1 does not yet have a range of CR scenarios to contrast, but CR on or off gives a shift of ≈ 0.15 GeV. Unfortunately this difference does not vary dramatically as a function of some obvious kinematical variables, but further studies are planned.

In top decays to leptons, $t \to b\ell^+\nu_\ell$, the lepton $p_\perp$ spectrum offers a CR-independent observable, that may allow an alternative route. It will face other challenges, however.

5. Summary and outlook

Color reconnection as such is well established, e.g. from $B \to J/\psi$. Given the high string and particle densities involved in a high-energy pp collision, it is hard to imagine that it would *not* play a prominent role also there.

This does not mean that what we today ascribe to CR could not be a much richer mixture of high-density effects, such as color ropes or collective flow. The particle composition as a function of $p_\perp$ is one example of LHC distributions not well described by Pythia simulations, and where thus some further mechanism may be at play. There is a twist to this story, however, in that CR in pp events can give some of the observed effects similar to the collective flow of heavy-ion collisions [32], by a combination

of two factors. Firstly, a string piece moving with some transverse velocity tends to transfer that velocity to the particles produced from it, albeit with large fluctuations, thereby giving larger transverse momenta to heavier hadrons. Secondly, a string piece has a larger transverse velocity the closer to each other the two endpoint partons are moving, which is precisely what is favored by CR scenarios intended to reduce the string length.

In the near future, the intention is to implement new CR models for *pp* collisions into Pythia 8, partly to offer a broader spectrum of possibilities, partly to add further physics aspects, such as the space–time and color structure, to provide more realistic scenarios. Other generator authors will also offer their schemes. When systematically confronted with a broad spectrum of data the hope is to see a pattern emerge, where some approaches are more favored than others. It would be foolish to promise that a unique answer will be found, however; we will have to live with CR uncertainties in many precision measurements. The top mass is the obvious example, but others are likely to emerge as LHC exploration continues.

In the far future, a high-luminosity e^+e^- Higgs factory would offer a second chance to study CR and related effects in W^+W^- events.

Acknowledgments

Work supported in part by the Swedish Research Council, contract number 621-2010-3326, and in part by the MCnetITN FP7 Marie Curie Initial Training Network, contract PITN-GA-2012-315877. Thanks to A. Karneyeu for providing Fig. 1, generated with MCPLOTS/Rivet [33].

References

[1] B. Andersson, G. Gustafson, G. Ingelman, and T. Sjöstrand, Phys. Rept. **97**, 31 (1983).

[2] T. Sjöstrand, S. Mrenna, and P.Z. Skands, JHEP **0605**, 026 (2006); Comput. Phys. Commun. **178**, 852 (2008).

[3] T.S. Biro, H.B. Nielsen, and J. Knoll, Nucl. Phys. B **245**, 449 (1984).

[4] H. Fritzsch, Phys. Lett. B **67**, 217 (1977).

[5] A. Ali, J.G. Körner, G. Kramer, and J. Willrodt, Z. Phys. C **1**, 269 (1979).

[6] H. Fritzsch, Phys. Lett. B **86**, 343 (1979).

[7] D. Eriksson, G. Ingelman, and J. Rathsman, Phys. Rev. D **79**, 014011 (2009).

[8] T. Sjöstrand and M. van Zijl, Phys. Rev. D **36**, 2019 (1987).

[9] UA1 Collaboration, Nucl. Phys. B **335**, 261 (1990).

[10] B. Andersson, G. Gustafson, and B. Söderberg, Nucl. Phys. B **264**, 29 (1986).

[11] T. Sjöstrand and V.A. Khoze, Z. Phys. C **62**, 281 (1994).

[12] L3 Collaboration, Phys. Lett. B **561**, 202 (2003);
OPAL Collaboration, Eur. Phys. J. C **45**, 291 (2006);
ALEPH Collaboration, Eur. Phys. J. C **47**, 309 (2006);
DELPHI Collaboration, Eur. Phys. J. C **51**, 249 (2007).

[13] L. Lönnblad and T. Sjöstrand, Phys. Lett. B **351**, 293 (1995); Eur. Phys. J. C **2**, 165 (1998).

[14] L3 Collaboration, Phys. Lett. B **547**, 139 (2002);
OPAL Collaboration, Eur. Phys. J. C **36**, 297 (2004);
ALEPH Collaboration, Phys. Lett. B **606**, 265 (2005);
DELPHI Collaboration, Eur. Phys. J. C **44**, 161 (2005).

[15] V.A. Khoze and T. Sjöstrand, Eur. Phys. J. C **2**, 1 (2000).

[16] W. Buchmuller and A. Hebecker, Phys. Lett. B **355**, 573 (1995);
A. Edin, G. Ingelman, and J. Rathsman, Phys. Lett. **366**, 371 (1996).

[17] G. Ingelman and P.E. Schlein, Phys. Lett. B **152**, 256 (1985).

[18] G. Ingelman, Int. J. Mod. Phys. A **21**, 1805 (2006).

[19] T. Sjöstrand and P.Z. Skands, J. High Energy Phys. **03**, 053 (2004).

[20] G. 't Hooft, Nucl. Phys. B **72**, 461 (1974).

[21] R. Corke and T. Sjöstrand, J. High Energy Phys. **03**, 032 (2011).

[22] ATLAS Collaboration, New J. Phys. **13**, 053033 (2011).

[23] CMS Collaboration, arXiv:1310.4554 [hep-ex].

[24] J. Rathsman, Phys. Lett. B **452**, 364 (1999).

[25] M. Sandhoff and P.Z. Skands, FERMILAB-CONF-05-518-T;
P.Z. Skands and D. Wicke, Eur. Phys. J. C **52**, 133 (2007);
D. Wicke and P.Z. Skands, Nuovo Cim. B **123**, S1 (2008).

[26] M. Bähr *et al.*, Eur. Phys. J. C **58**, 639 (2008).

[27] S. Gieseke, C. Röhr, and A. Siodmok, Eur. Phys. J. C **72**, 2225 (2012).

[28] T. Gleisberg *et al.*, J. High Energy Phys. **02**, 007 (2009).

[29] V.A. Khoze, F. Krauss, A.D. Martin, M.G. Ryskin, and K.C. Zapp, Eur. Phys. J. C **69**, 85 (2010).

[30] CDF and DO Collaborations, arXiv:1305.3929 [hep-ex];
CMS Collaboration, arXiv:1307.4617 [hep-ex].

[31] CMS Collaboration, CMS-PAS-TOP-12-029, CMS-PAS-TOP-13-007.

[32] A. Ortiz Velasquez, P. Christiansen, E. Cuautle Flores, I.A. Maldonado Cervantes, and G. Paić, Phys. Rev. Lett. **111** (2013) 042001.

[33] A. Karneyeu, L. Mijovic, S. Prestel, and P. Skands, arXiv:1306.3436 [hep-ph];
A. Buckley *et al.*, arXiv:1003.0694 [hep-ph].

Study of the helix model

Šárka Todorova-Nová

Institute of Particle and Nuclear Physics, Charles University, Prague

The quantum properties of a helix-like shaped QCD string are studied in the context of the semi-classical Lund fragmentation model. It is shown how simple quantization rules combined with the causality considerations in the string fragmentation process describe the mass hierarchy of light pseudoscalar mesons. The quantized helix string model predicts observable quantum effects related to the threshold behaviour of the intrinsic transverse momentum of hadrons, and of the minimal transverse momentum difference between adjacent hadrons.

1. Introduction

The concept of the QCD string with a helical structure has been introduced in [1] and some of its potential explored in [2]. The model has been shown to decribe the experimentally established correlations between the longitudinal and transverse momentum components of hadrons measured by DELPHI at LEP [3] and the azimuthal ordering of hadrons, recently observed by ATLAS at LHC ([4]).

The aim of this contribution is to discuss in some detail the space-time evolution of partons following a breakup of a QCD string with a helix structure. A concept of string quantization emerges from these considerations which has the merit to describe, in a consistent manner, several experimental observations.

2. Space-time properties of helical string model

In the transition from the 1-dimensional Lund string to a 3-dimensional helix-shaped string, it is necessary to reconsider some of the model properties. The basic assumption of a string modelling the confining QCD field with a constant string tension ($\kappa \sim 1$ GeV/fm) remains unchanged. However, the use of light-cone coordinates is no longer appropriate, as the trajectory of partons in the model is always bent by the interaction with the field.

In the case of slowly varying field, the string can be approximated by an ideal helix with radius R and constant pitch dΦ/dz, where Φ stands for the azimuthal angle (helix phase) and z is the space coordinate parallel to the string axis. Movement of a parton along the string can be thus described with the help of the longitudinal coordinate z and the folded transverse coordinate RΦ (Fig. 1).

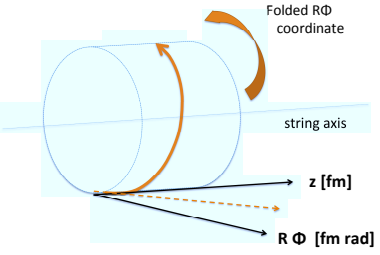

Fig. 1. The 2-dimensional coordinate system describing a helix-shaped string consists of the longitudinal string axis z and the folded transverse coordinate $R\Phi$, where R stands for radius of the helix and the Φ indicates the helix phase.

Following a string breakup at $[Re^{i\Phi_B}, z_B, t_B]$ into a pair of massless partons created at rest, the partons will move along the string and acquire the momentum

$$\begin{aligned} p_{||}(t) &= \pm\kappa\beta\ c\ (t - t_B) \\ p_T(t) &= \pm\kappa R(e^{i\omega c(t-t_B)} - e^{i\Phi_B}). \end{aligned} \tag{1}$$

The longitudinal velocity of partons β is related to the angular velocity ω

$$\beta = \sqrt{1 - (R\omega)^2}, \tag{2}$$

(the light-cone coordinates are recovered in the limit case $R\omega = 0$).

The momentum of a direct hadron created by adjacent string breakups at $[Re^{i\Phi_i}, z_i, t_i]$, $[Re^{i\Phi_j}, z_j, t_j]$ is

$$\begin{aligned} E_h &= \frac{\kappa}{\beta}|(z_i - z_j)| = \frac{\kappa}{\beta}|\Delta z|, \\ p_{h,||} &= \kappa\beta(t_i - t_j) = \kappa\beta\Delta t, \\ p_{h,T} &= \kappa R(e^{i\Phi_i} - e^{i\Phi_j}), \end{aligned} \tag{3}$$

and its mass is

$$m_h = \kappa\sqrt{(\Delta z/\beta)^2 - (\beta\Delta t)^2 - (2R\sin\Delta\Phi/2)^2}. \tag{4}$$

There is a fundamental difference (well illustrated by Eq. 4) between the helical string model and the standard Lund string model in what concerns the causality relation between breakup vertices. In the standard

Lund string model, the creation of a massive direct hadron requires a space-like distance between breakup vertices ($\beta = 1, m_h > 0 \Rightarrow |\Delta z| > |\Delta t|$). This implies some amount of magic has to be applied to make the hadrons emerge from the fragmentation with the correct mass. It turns out the problem of the on-shell birth is easily resolved in the helical string model, where a time-like distance between breakup vertices is possible.

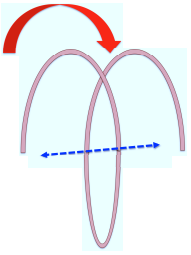

Fig. 2. The information about the string breakup propagates preferably along the string field, though a cross-talk between string loops is not excluded, either. The requirement of causal relation between breakups leads to an effective decoupling of the longitudinal and transverse component of the hadron momenta in the former case (see text).

In the following, the time-like distance between adjacent breakup vertices will be imposed - this is equivalent to the introduction of the causal relations in the Lund string fragmentation process. However, there is an ambiguity concerning the way the signal is allowed to propagate. If the information (about a breakup of the string at a given point) is allowed to pass along the string only, the space-time distance between adjacent vertices becomes negligible (to the extent we have neglected the parton masses) which means the propagating parton essentially triggers the following breakup and the mass of the outcoming hadron is (note that in this case $\Delta z = \beta \Delta t$)

$$m_S(\Delta\Phi) = \kappa R \sqrt{(\Delta\Phi)^2 - (2\sin\Delta\Phi/2)^2}. \tag{5}$$

It is interesting to see that the longitudinal momentum is factorized out from the equation and that the hadron mass depends on the transverse properties of the string shape only. To obtain a discrete mass spectrum, it is sufficient to introduce quantization of the transverse coordinate $\mathrm{R}\Phi$ (to be discussed in the following section).

There is of course also a possibility that the information about the breakup travels inside the string vortex (Fig. 2). To maintain the time-like difference between string breakups in such a case, the allowed time difference is then restricted to the interval

$$\sqrt{(\Delta z)^2 + (2R\sin\Delta\Phi/2)^2} \leq c\Delta t \leq \sqrt{(\Delta z)^2 + (R\Delta\Phi)^2} \tag{6}$$

and the outcoming hadron has a mass m_C in the range

$$m_S(\Delta\Phi) \leq m_C(\Delta\Phi) \leq m_S(\Delta\Phi)\sqrt{1+\beta^2} \tag{7}$$

(the subscripts S, C stand for "singular" and "continuous" mass solutions).

3. Mass spectra

Building on the causality requirements, we have obtained relations between the transverse string properties and the allowed hadron mass spectrum. It seems only natural to take a step further and to try to establish a quantization pattern for the string fragmentation which would match the measured discrete hadron mass spectra.

Let's assume the string quantization is realized through the quantization of the transverse coordinate

$$R\Phi \Rightarrow \mathrm{nR}\Delta\Phi = \mathrm{n}\xi, (\mathrm{n} = 1, 2, \ldots) \tag{8}$$

and that the n=1 case corresponds to the lightest hadron, the π meson.

Eq. 5 is particularly interesting for the study of light meson mass hierarchy because it describes the narrow pseudoscalar states (PS) decaying into an odd number of pions

$$\begin{aligned} PS &\rightarrow \mathrm{n}\pi,\ \mathrm{n} = (1), 3, 5, \ldots \\ m(PS) &= \kappa\sqrt{(\mathrm{n}\xi)^2 - (2\xi/\Delta\Phi)^2 \sin^2(\mathrm{n}\Delta\Phi/2)}. \end{aligned} \tag{9}$$

The results of the best fit matching the Eq. 9 to experimentally measured data [5] are listed in Table 1. Despite the fact that the simultaneous fit of 2 unknowns $(R, \Delta\Phi)$ from 3 hadronic states is overconstrained, a common solution describing the properties of the ground state is found. The π, $\eta(548)$ and $\eta'(958)$ masses are reproduced by Eq. 9 with precision better than 3% using $\xi = 0.192$ fm and $\Delta\Phi$=2.8 (for κ =1 GeV/fm).

$\kappa\xi$ [MeV]	κ R [MeV]	$\Delta\Phi$
192.5 ± 0.5	68 ± 2	2.82 ± 0.06
meson	PDG mass [MeV]	model estimate [MeV]
π	135 - 140	137
η	548	565
η'	958	958

Table 1. Best fit of the parameters of the pion ground state obtained from the mass spectrum of light pseudoscalar mesons. The η mass is reproduced within a 3% margin which serves as the base of uncertainty for $R, \Delta\Phi$ parameters.

Fig. 3 shows the dependence of the mass of PS mesons as a function of $\Delta\Phi$ in Eq.(9). With increasing $\Delta\Phi$, the predicted masses of η and η' reach the plateau (around $\Delta\Phi \sim 1.5$ rad) and lose sensitivity to the $\Delta\Phi$ value, but the mass of the π meson rises steadily till $\Delta\Phi \sim 5$ rad and effectively fixes the $\Delta\Phi$ value in the model.

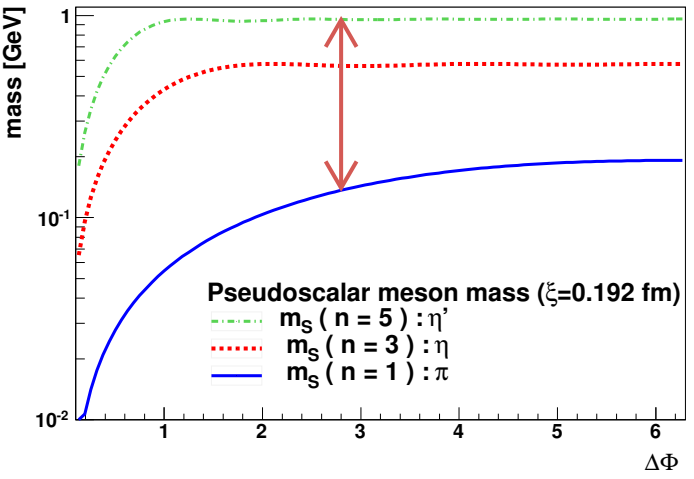

Fig. 3. The predicted masses of light pseudoscalar mesons as function of helix phase difference $\Delta\Phi$, for fixed $R\Delta\Phi$=0.192 fm rad.

The scalar nature of PS states is in agreement with the expectations of the quantization model: $m_T(PS) = \mathrm{n}\ m_T(\pi)$, thus the decay products of (η, η') have negligible (longitudinal) relative momentum in the rest frame of the mother resonance.

If the quantization model, in the first approximation, fits the mass spectra of light PS mesons, what can be said about the vector mesons (VM)?

The lightest vector mesons $\rho(770)$ and $\omega(782)$ can be interpreted as n=4 states decaying into m < n pions:

$$m_S(n = 4) = 0.76 \text{ GeV},$$

or n=3 states formed according to Eq. 7:

$$\sqrt{2}\ m_S(n = 3) \sim 0.79 \text{ GeV},$$

and their non-zero total angular momentum arises from the relative momentum of decay products (kinematically allowed since $m_T(VM) > \mathrm{m}\ m_T(\pi)$.

The mass of K*(890) and Φ(1020) mesons can be roughly associated with the mass of the $\rho(770)$ increased by the mass of the strange quark(s) (∼120 MeV). (The same reasoning would classify K meson as a $n = 2$ state.)

It is worth noticing that the quantization of the transverse component of the string is equivalent to the quantization of the angular momentum J stored in the string (proportional to the transverse area spanned by the string) and that the relation

$$J \simeq \kappa(R\Delta\Phi)^2 = m_T^2/\kappa \tag{10}$$

indicates that the spectra derived from the model will lie along Regge trajectories.

4. Transverse momentum threshold

The discretization of the mass spectrum is not the only quantum effect which can be observed in the string fragmentation. In fact, the current investigation of the properties of the helix string quantization was prompted by the study of the inclusive p_T spectra. In [2] it has been shown that the helix string model significantly improves the description of the inclusive low p_T region. It has been also shown that the strength of the azimuthal correlations between hadrons can be described by the model only if the helix string model is extended to the decay of short-lived resonances. However, it turns out that such an extension spoils the agreement between the LEP data and the helix model essentially because the resonance decay according to the helix shaped "field memory" produces way too many low p_T particles (Fig. 4).

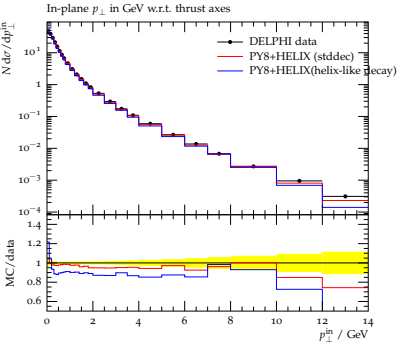

Fig. 4. Comparison of the helix string model predictions with the DELPHI data [3]. The production of low p_T charged particles is overestimated by the model when decay of short lived resonances is treated as a smooth continuation of the fragmentation of the helix string.

The effect cannot be tuned away as there are essentially no relevant free parameters left in the model. A careful study of the discrepancy and the gradients of the p_T spectra does not exclude existence of a natural p_T cutoff just below 0.2 GeV.

It is therefore encouraging to see - on the basis of results obtained in the previous section - that the production of soft pions with the $p \sim p_T < 0.14$ GeV should be supressed in the quantized model. This result has yet to be propagated through the entire fragmentation and decay chain but this particular model feature is expected to help the regularization of the soft particle production in the helix string model extended to the decay of resonances.

5. Momentum difference of adjacent hadrons

The quantization of the helix string implies a quantization of the momentum difference between adjacent hadrons. Since the local charge conservation forbids the production of adjacent like-sign charged hadron pairs in the fragmentation process, the quantum effects can play a large role in the correlation phenomena with a significant difference between particle pairs with like-sign and unlike-sign charge combination.

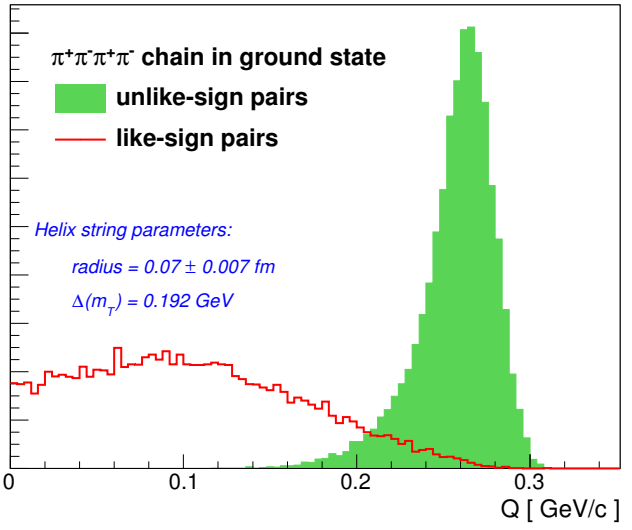

Fig. 5. The correlation pattern estimate for a chain of 4 charged pions in the ground state (Table 1). The longitudinal momentum differences are neglected, a variation of 10% is applied on the helix radius instead, in order to obtain a smooth spectra.

In the approximation of an ideal, or slowly varying helix string field, it is possible to make an estimate of the charge combination asymmetry induced by quantization. Consider a chain of adjacent charged pions in the ground state, for example from η' decay. The homogenity of the QCD field implies the difference between longitudinal momenta components of such pions is negligible. The momentum difference between pions along the chain is then given by the helix phase difference

$$\begin{aligned} Q &= \sqrt{-(p_i - p_j)^2} \approx 2p_T|\sin[0.5(\Phi_\mathrm{i} - \Phi_\mathrm{j})]| \\ &= 2p_T|\sin[0.5(\mathrm{j} - \mathrm{i})\Delta\Phi]|, \end{aligned} \tag{11}$$

where $p_T(\sim 0.14$ GeV) is the transverse momentum of the pion in the ground state, $i, j = 0, 1, 2, 3$ are integers corresponding to the rank of the hadron along the chain, and $\Delta\Phi(\sim 2.8)$ is the opening azimuthal angle between adjacent ground state pions. Fig. 5 shows the resulting correlation pattern with a marked separation of like-sign and unlike-sign pairs (the helix radius has been randomly varied by 10% in order to produce a smooth spectrum). The onset of excess of like-sign pairs occurs at $Q \sim 0.2$ GeV in the model. A large amount of experimental data provides evidence of an excess of like-sign hadron pair production in the low Q region. Most often, the data are studied from the perspective of the Handbury-Brown-Twiss model, i.e. as a signature of the incoherent particle production. The helix string model suggests an alternative point of view - such correlations may well be associated with fully coherent hadron production. In the specific case under study, due to the large opening angle $\Delta\Phi$, the quantized chain of ground state pions acquires properties reminiscent of Bose-Einstein condensate.

It should be possible to make a more precise experimental evaluation of the role of hadron 'chains' (and η' decay) in the correlation signal. Such a study may have a significant impact on the further development of the helix model, as it may confirm, or reject, the hypothesis of a strong link between resonance production and correlation phenomena.

6. Conclusions

The properties of the quantized helix string model have been investigated using a data driven simple quantization recipe. The model allows to introduce proper causal relations between the breakup vertices in the string fragmentation. The causality represents a strong constraint for the particle production and helps to understand the emergence of narrow hadronic resonant states. The fit of the light pseudoscalar mesons provides the parameters describing the ground hadronic state, and allows to make predictions concerning the threshold behaviour of relevant observables, to be verified with the help of experimental data.

References

[1] B. Andersson *et al.*, J. High Energy Phys. **09**, 014 (1998).
[2] Š. Todorova, Phys. Rev. D **86**, 034001 (2012).
[3] DELPHI Collaboration, Z. Phys. C **73**, 11 (1996).
[4] ATLAS Collaboration, Phys. Rev. D **86**, 052005 (2012).
[5] Particle Data Group, Phys. Rev. D **86**, 010001 (2012).

Measurement of the charged kaon correlations at small relative momentum in the SELEX experiment

Grigory Nigmatkulov on behalf of the SELEX Collaboration[†]

National Research Nuclear University "MEPhI", Moscow, Russia, 115409

We report the first measurement of charged kaon Bose–Einstein correlations produced by 600 GeV/c Σ^-, π^- and 540 GeV/c p beams in the SELEX experiment. The SELEX (E781) experiment at Fermilab is a fixed target three–stage magnetic spectrometer designed for study hadroproduction at high acceptance for forward interactions ($x_F \geq 0.1$).

One–dimensional charged kaon correlation functions were obtained for all three beams and three pair transverse momentum ranges. The femtoscopic parameters for the radii and correlation strength of the kaon source were extracted. The fit results show the decrease of the emission source radii with the increase of the pair transverse momentum.

1. Introduction

A measurement of the two-particle correlations at small relative momentum (also known as correlation femtoscopy) allows to measure spatio-temporal parameters of the particle-emitting source [1–4]. Previously correlation femtoscopy studies were performed for lepton-lepton [5], lepton- and hadron-hadron [6], and heavy ion collisions [7]. The high-statistics data from different experiments at powerful accelerators and development of theoretical formalism has expanded the information extracted from correlations from the original source size measurements to the extraction of the shape, extent and dynamical timescale of the emission region. These analyses usually study pions, however, measurements of heavier particles can complete the extracted information.

[†] SELEX Collaboration: Bogazici University, Carnegie-Mellon University, Centro Brasileiro de Pesquisas Físicas, Fermi National Accelerator Laboratory, Institute for High Energy Physics (Protvino), Institute of Theoretical and Experimental Physics Max-Planck-Institut für Kernphysik, Moscow State University, Petersburg Nuclear Physics Institute, Tel Aviv University, Universidad Autónoma de San Luis Potosí, University of Bristol, University of Iowa, University of Michigan-Flint, University of Rome "La Sapienza" and INFN, University of São Paulo, University of Trieste and INFN

In this paper, the preliminary results of study of pair transverse momentum dependencies of charged kaons emission source parameters for different initial state conditions in the SELEX experiment will be presented.

2. Data analysis

In this proceedings the most important features of the experimental setup used in current analysis will be listed. The detailed description of the SELEX experiment can be found elsewhere [8]. SELEX (E781) is a three-stage magnetic spectrometer, designed for hadroproduction study at forward interactions ($x_F \geq 0.1$). The negatively charged 600 GeV/c beam contains approximately equal fractions of Σ and π, meanwhile the positively charged beam contains 92% of protons and 8% of π. Beam particle was identified as a meson or a baryon by a transition radiation detector. Interactions were happen in a composite target (2 Cu and 3 C separated by 1.5 cm one by another), wich total thickness equals to 5% of an interaction length for protons. Downstream of the target 20 planes of vertex silicon strip detectors with about 5 μm space resolution were placed. A particle momentum was measured by deflection of the track position by two magnets M1 and M2 in a system of proportional wired chambers and silicon strip detectors. Momentum resolution of a typical 100 GeV/c track was $\sigma_p/p \approx 0.5\%$. Charged particle identification was performed with a Ring Imaging Cherenkov detector (RICH) [9], which separated kaons from pions in a wide momentum range up to 165 GeV/c. In current analysis we used only particles with momentum from 45 to 165 GeV/c, identified by the RICH detector as kaons, and distance of closest approach to the primary vertex less than 20 μm [10].

3. Correlation functions

Identified kaons from the same event were combined to the pairs in order to form the signal distribution A(Q) of relative momentum:

$$Q = \sqrt{(\vec{p_1} - \vec{p_2})^2 - (E_1 - E_2)^2}, \tag{1}$$

where $\vec{p_1}$, E_1 and $\vec{p_2}$, E_2 are momentum and energy of the first and the second particle respectively. Pairs combined from different events were used in order to construct uncorrelated background distribution B(Q) (also known as an event mixing technique). A correlation function is defined as a ratio:

$$C_2(Q) = \frac{A(Q)}{B(Q)} \cdot D(Q), \tag{2}$$

where $D(Q)$ is so-called correlation baseline that describes all non-femtoscopic correlations, for instance, the correlations caused by the momentum-energy conservation [11]. In the simplest case non-femtoscopic effects can be parameterized by a 2nd order polynomial:

$$D(Q) = 1 + aQ + bQ^2. \tag{3}$$

The correlation function of identical spinless bosons should increase at small relative momentum except for very small values where Coulomb interaction becomes dominant. In order to extract the size of the emission region one can use a Gaussian form:

$$C_2(Q) = N(1 - \lambda + K(Q)(\lambda e^{-R^2Q^2})) \cdot D(Q), \tag{4}$$

where N is a normalization parameter, λ – shows the fraction of particles emitted independently, R – radii of the emission source, and the factor $K(Q)$ is the Coulomb function [12, 13]. For the estimation of the baseline without Bose–Einstein correlations and final state interactions the Monte Carlo event generator PYTHIA-6.4.27 [15] with the Perugia 2011 tune [16] was used.

Current analysis was performed for Σ^-, π^- and p beam types, and for three pair transverse momentum ranges k_T: (0–0.3), (0.3–0.55), (0.55–0.85) GeV/c. Here the transverse momentum of a pair is defined as:

$$k_T = |\vec{p_{T1}} + \vec{p_{T2}}|/2, \tag{5}$$

where $\vec{p_{T1}}$ and $\vec{p_{T2}}$ are transverse momenta of the first and the second particle respectively.

Fig. 1 shows a comparison between experimental correlation functions and correlation functions obtained from the Pythia event generator using Perugia 2011 tune (blue open circles). It becomes clear, that simulated correlation functions (baseline) reproduce experimental for each beam type and k_T region, i.e. they describe all long-range correlations.

Due to the fact that Pythia does not contain Bose-Einstein correlations and final state interactions, but describes non-femtoscopic effects, it is necessary to correct experimental distributions on the simulated correlation functions. Fig. 2 represents the correlation functions obtained with this correction. Correlation functions were fitted by Eq. 4, where the Coulomb function $K(Q)$ was integrated over a spherical source of 1 fm.

Fig. 3 shows the source radii dependencies on pair transverse momentum k_T. The source radii decreases with k_T for all beam types. It can be also seen that the source radii is less for the meson than for the baryon beams.

The decrease of the source radii with k_T was previously measured in heavy ion collisions and interpreted as a collective hydrodynamic expansion

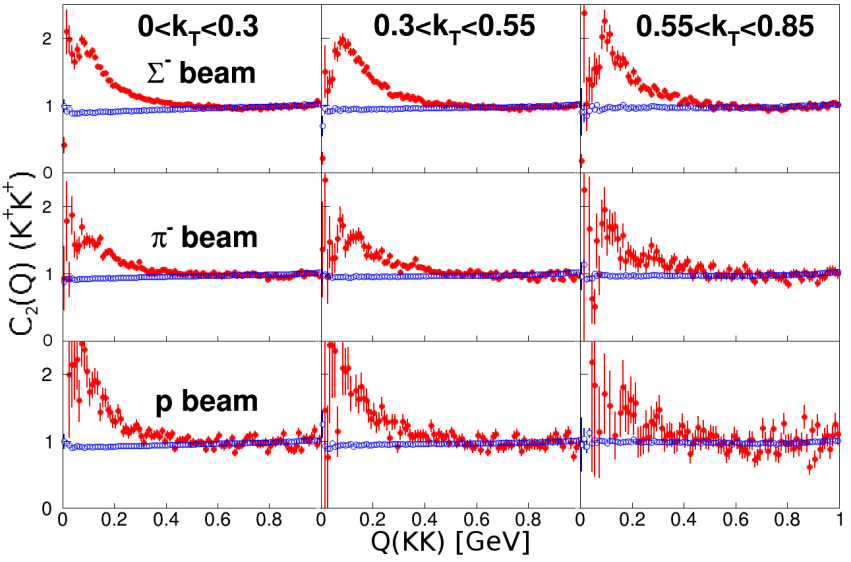

(a) Correlation functions of the K^+K^+ system

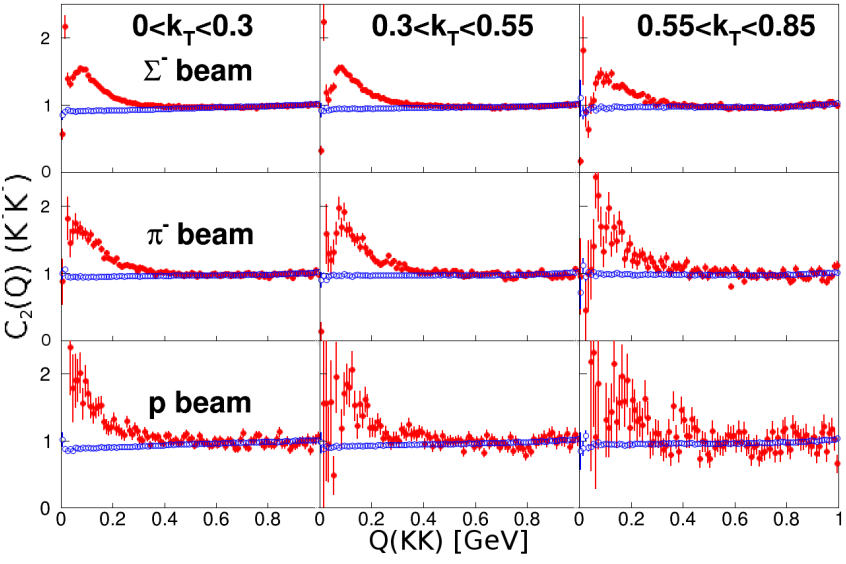

(b) Correlation functions of the K^-K^- system

Fig. 1: Comparison of experimental and simulated correlation functions obtained for three k_T bins: (0–0.3), (0.3–0.55), (0.55–0.85) [GeV/c]. From top to bottom rows represent Σ^-, π^- and p beams respectively. Solid circles show experimental correlation functions, open circles represent baselines obtained from Pythia.

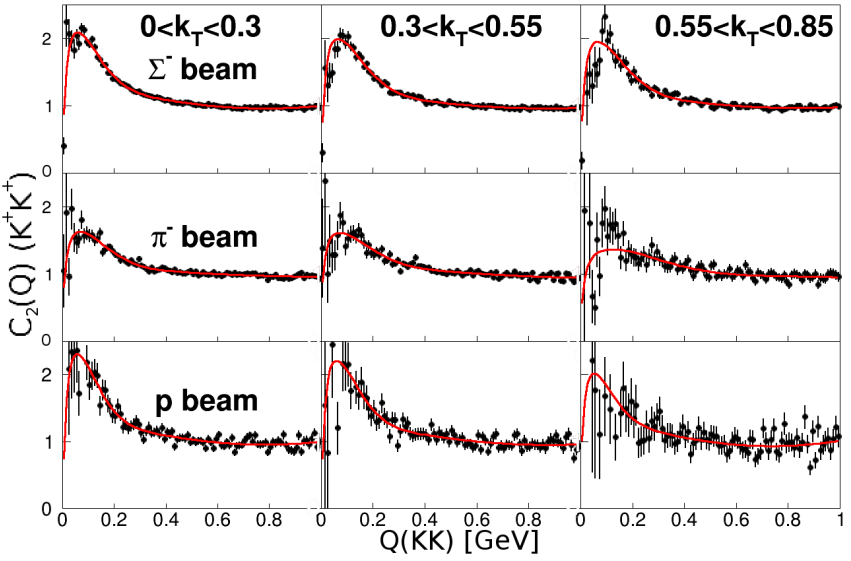

(a) K^+K^+ correlation functions

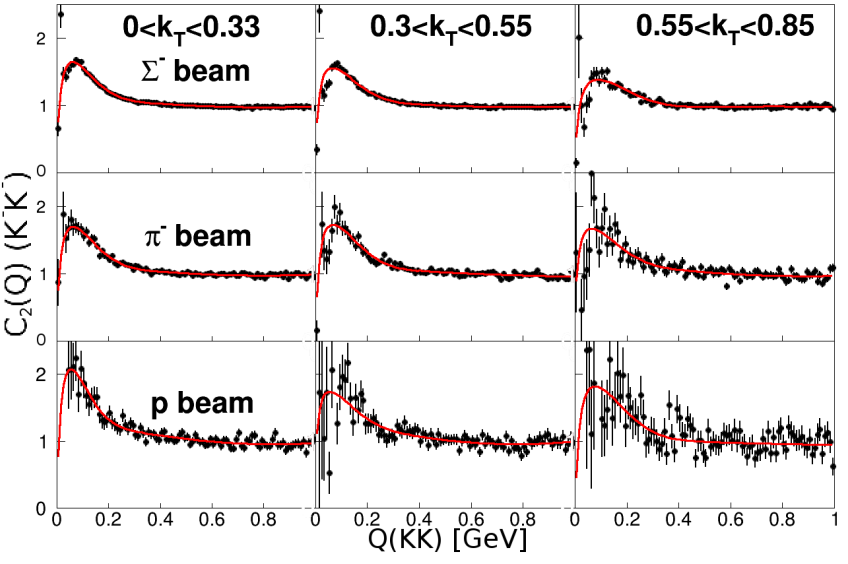

(b) K^-K^- correlation functions

Fig. 2: Correlation functions obtained after the correction on baselines for three k_T bins: (0–0.3), (0.3–0.55), (0.55–0.85) [GeV/c]. From top to bottom rows represent Σ^-, π^- and p beams respectively.

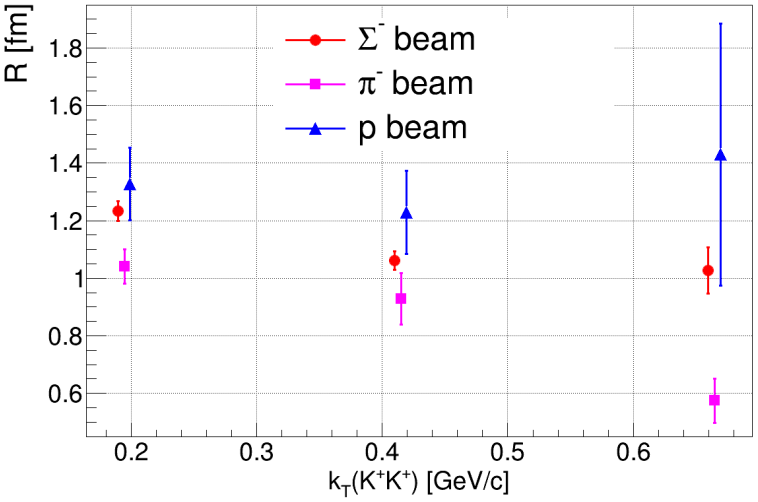

(a) K^+K^+ source parameters

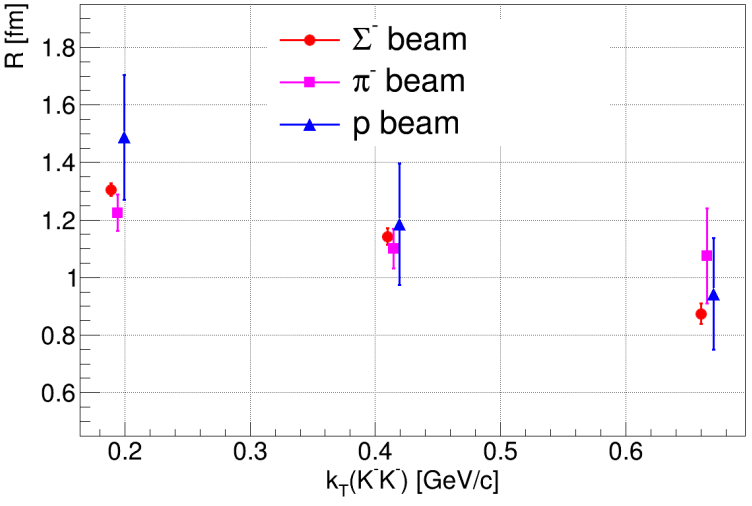

(b) K^-K^- source parameters

Fig. 3: k_T dependencies of the emission source radii. Red circles, magenta squares and blue triangles show the source radii obtained for Σ^-, π^- and p beams respectively.

of the created matter [7, 17]. The similar behavior was observed for pp collisions at RHIC and LHC, but it still lacks a firm interpretation for the events with low multiplicities. At high multiplicities hydrodynamic phase contribution is becoming more significant role and the experimental data have a better description by theory.

4. Summary

Charged kaons correlations at small relative momentum have been measured in the SELEX experiment for Σ^-, π^- and p beams and three k_T regions. The emission source radii parameters have been extracted. The decrease of the source radii for all beam types with the pair transverse momentum k_T has been observed.

Acknowledgments

The reported study was partially supported by RFBR, research project No. 11-02-01302a.

References

[1] G. Goldhaber, S. Goldhaber, W.Y. Lee, and A. Pais, Phys. Rev. **120**, 300 (1960).

[2] G.I. Kopylov and M.I. Podgoretsky, Sov. J. Nucl. Phys. **15**, 219 (1972).

[3] G.I. Kopylov and M.I. Podgoretsky, Phys. Lett. **50**, 472 (1974).

[4] G.I. Kopylov, V.L. Lyuboshits, and M.I. Podgoretsky, JINR-P2-8069.

[5] W. Kittel, Acta Phys. Polon. **32**, 3927 (2001).

[6] G. Alexander, Rept. Prog. Phys. **66**, 481 (2003).

[7] M. Lisa, S. Pratt, R. Soltz, and U. Wiedemann, Ann. Rev. Nucl. Part. Sci. **55**, 311 (2005).

[8] J.S. Russ *et al.* (SELEX Collaboration), ICHEP'98 Proc. Int. Con. on High Energy Physics, **II** 1259 (1998), hep-ex/9812031.

[9] J. Engelfried, I.S. Filimonov, J. Kilmer, A.P. Kozhevnikov, V.P. Kubarovsky, V.V. Molchanov, A.V. Nemitkin, E. Ramberg, V.I. Rud, and L. Stutte, Nucl. Instrum. Meth. A **502**, 285 (2003).

[10] G.V. Sinev and G.A. Nigmatkulov, Bull. Russ. Acad. Sci. Phys., **77**, 800 (2013); G.V. Sinev and G.A. Nigmatkulov, Izv. Ross. Akad. Nauk., **77**, 833 (2013).

[11] Z. Chajęcki and M. Lisa, Phys. Rev. C **78**, 064903 (2008); Phys. Rev. C **79**, 034908 (2009).

[12] M.G. Bowler, Phys. Lett. B **270**, 69 (1991).

[13] Y. Sinyukov, R. Lednicky, S.V. Akkelin, J. Plutta, and B. Erazmus, Phys. Lett. B **432**, 248 (1998).
[14] K. Aamodt *et al.* (ALICE Collaboration), arXiv:1212.5958.
[15] T. Sjostrand, S. Mrenna, and P. Skands, J. High Energy Phys. **05**, 026 (2006).
[16] P.Z. Skands, Phys. Rev. D **82**, 074018 (2010).
[17] S. Pratt, Phys. Rev. Lett. **53**, 1219 (1984).

Parton distributions and event generators

Stefano Carrazza, Stefano Forte

Dipartimento di Fisica, Università di Milano and INFN, Sezione di Milano, Via Celoria 16, I-20133 Milano, Italy

Juan Rojo

PH Department, TH Unit, CERN, CH-1211 Geneva 23, Switzerland

We present the implementation within the `Pythia8` event generator of a set of parton distributions based on NNPDF methodology. We construct a set of leading-order parton distributions with QED corrections, NNPDF2.3QED LO set, based on the same data as the previous NNPDF2.3 NLO and NNLO PDF sets. We compare this PDF set to its higher-order counterparts, we discuss its implementation as an internal set in `Pythia8`, and we use it to study some of the phenomenological implications of photon-initiated contributions for dilepton production at hadron colliders.

1. PDFs and event generators

The needs of physics at the LHC require an increasingly accurate control of the parton substructure of the nucleon: for example, this is a necessary ingredient in the accurate determination of Higgs couplings [1, 2], which in turn is essential both for precision determination of Standard Model parameters and for indirect searches for New Physics. Current sets of parton distributions [3] are based on increasingly refined theory, use an increasingly wide dataset (now also extended to LHC data) and attempt to arrive at an estimation of uncertainties which is as reliable as possible. An important ingredient in achieving all of these goals is the integration of parton distributions within Monte Carlo event generators [4]. Indeed, parton showering and hadronization are necessary in order to bridge perturbative QCD calculation with the quantities which are actually measured in experiments, all the more so as less inclusive observables are considered, even though also for observable which are in principle inclusive (such as the production of gauge bosons) comparisons are best made between theoretical predictions, and data collected in an experimental fiducial region.

Whereas next-to-leading (NLO) order Monte Carlo tools play an increasingly important role, leading-order (LO) Monte Carlo simulations are

still commonly used in a variety of applications. Furthermore, both LO and NLO Monte Carlo event generators typically rely on leading-order PDFs for the description of multiple-parton interactions and the underlying event, so that in fact generators which include a hadronization model, such as `Pythia` (and specifically its current version, `Pythia8` [5]) are tuned using one or more 'native' PDF sets

In this short contribution, we will discuss the NNPDF2.3QED LO PDF set, and its implementation within `Pythia8`: this is a PDF set which is based on the successful NNPDF methodology, which strives to minimize theoretical bias and construct statistically reliable parton distributions, recently used to produce a first global set of PDFs using LHC data, NNPDF2.3 [6]. This PDF set was subsequently used to construct a first set of PDFs with QED corrections and a photon distribution determined by experimental data, NNPDF2.3QED [7]. Recent general reviews of parton distributions are presented in Refs. [8, 9, 3].

2. The NNPDF2.3QED LO parton set

The NLO and NNLO NNPDF2.3QED PDF sets were recently presented in [7]. In these sets, the evolution of quark and gluon PDFs is consistently performed using combined QCD⊗QED evolution equations, and the photon PDF $\gamma(x, Q^2)$ is determined from LHC vector boson production and deep-inelastic scattering data. In order to construct a corresponding leading-order set, NNPDF2.3QED LO, we start from the NNPDF2.1LO PDF sets [10], with two different values of $\alpha_s(M_Z)$: 0.119 and 0.130. Note that in Ref. [10] further LO sets were constructed, NNPDF2.1 LO* in which the momentum sum rule was not imposed; however, this choice, sometimes advocated, did not turn out to be especially advantageous, hence we will not discuss these sets further.

The NNPDF2.3QED LO set is constructed by combining the PDFs from the NNPDF2.1 LO set with the photon PDF from the NNPDF2.3QED NLO set at $Q_0^2 = 2$ GeV^2, and then evolving upwards this boundary condition with combined LO QCD⊗QED evolution equations, including $O(\alpha_s)$ and $O(\alpha)$, but not $O(\alpha\alpha_s)$ terms. This procedure (which clearly retains LO QED+QCD accuracy) is justified because of the very mild correlation between the photon and the other PDFs, and the large uncertainty on the photon PDF itself [7]. The set of PDFs thus obtained is then also evolved down to $Q^2 = 1$ GeV^2: whereas leading-twist perturbative QCD might not be accurate in this region, low-scale PDFs are necessary for tunes of the underlying event and minimum bias physics in shower Monte Carlos.

The combined QCD⊗QED evolution has been performed with the `APFEL` package [11]. Among the various forms of the solution to the evolution

equation, differing by $O(\alpha\alpha_s)$ terms which are beyond our accuracy, we use the so-called `QECDS` [11] solution, which was also used for the construction of the NNPDF2.3QED NLO and NNLO sets. Strict positivity of all LO PDFs has been imposed in the relevant range of x and Q^2.

In Fig. 1 we show the gluon PDF in the LO, NLO and NNLO NNPDF2.3-QED fits. The much larger small-x gluon is a well-known feature of LO PDF sets, due to the need to compensate for missing NLO terms when fitting deep-inelastic structure function data. It is an important ingredient for tunes of soft QCD dynamics at hadron colliders.

In Fig. 2 we also show the photon PDF at $Q^2 = 10^4$ GeV^2, at LO, NLO and NNLO. The small differences seen arise due to the different evolution of quarks and gluons and their mixing with the photon through evolution equations.

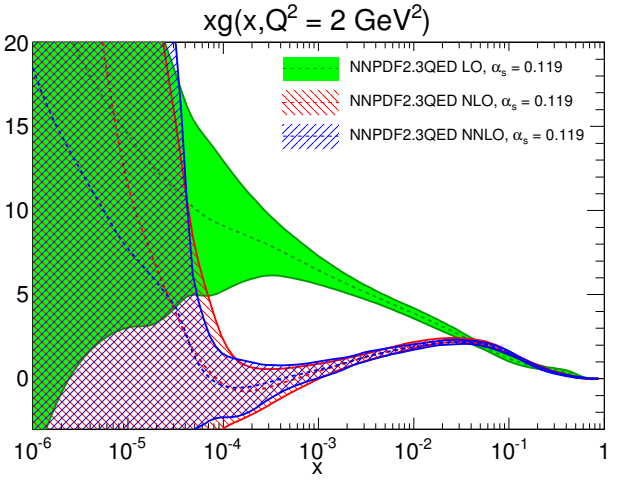

Fig. 1. The gluon PDF at LO, NLO and NNLO in the NNPDF2.3QED sets.

Finally, in Fig. 3 we compare the gluon PDF in the LO sets corresponding to the two different values of $\alpha_s(M_Z) = 0.119$ and 0.130: because of the slower running of α_s at LO, the smaller value is more accurate at higher scale, and the larger value at low scales. Reassuringly, in the small $x \leq 10^{-4}$, relevant for tunes of soft physics at hadron colliders, the two sets turn out to agree within their large uncertainties.

3. Implementation in `Pythia8` and phenomenological implications

The NNPDF2.3QED LO sets, with two different α_s values, together with their NLO and NNLO counterparts, have been implemented as internal

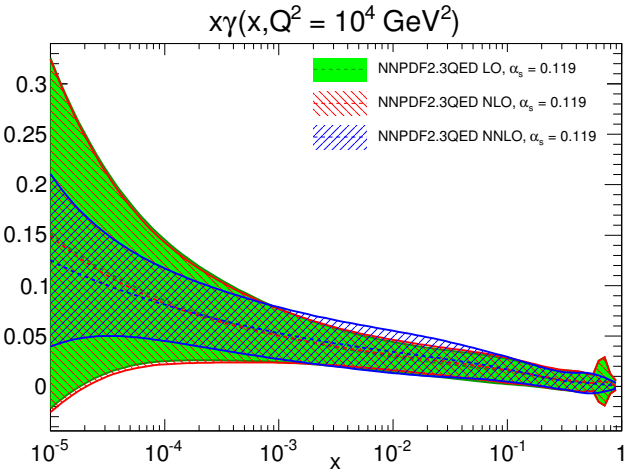

Fig. 2. The photon PDF at LO, NLO and NNLO in the NNPDF2.3QED sets.

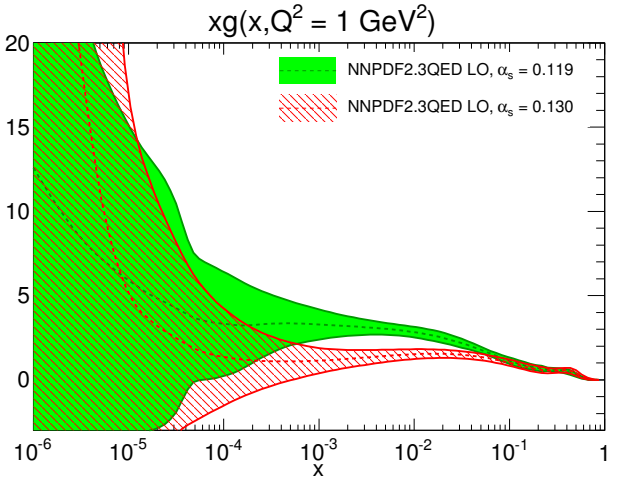

Fig. 3. The small-x gluon PDFs in the NNPDF2.3QED LO set for $\alpha_s = 0.119$ and 0.130.

PDF sets in `Pythia8` [5] starting with `v8.180`, and there is ongoing work by the `Pythia8` authors towards providing a complete new tune based on NNPDF2.3QED LO, including all the relevant constraints from LHC and previous lower-energy colliders [12].

For the time being, we will illustrate some of the phenomenological implications of the NNPDF2.3QED LO set by generating events with `Pythia8` for processes in which photon-initiated contributions are substantial. As a

case study, we consider dilepton production at the LHC 14TeV. Related studies were presented in the original NNPDF2.3QED paper [7] but were restricted to the parton level, while now we include the effects of the initial state parton shower and underlying event with the standard `Pythia8` tune. The QED shower option of `Pythia8` is turned off. We generate events for $q\bar{q} \to \gamma^*/Z \to l^+l^-$ and for $\gamma\gamma \to l^+l^-$, and compare the relative contributions of the two different initial states. We consider both electrons and muons in the final state.

The invariant mass distributions of the dilepton pair at the LHC 14 TeV, without any kinematical cut, is shown in Fig. 4, in the Z peak mass region. We shown separately the contributions from the $q\bar{q}$ and $\gamma\gamma$ initiated subprocesses (though experimentally they cannot be separated, as they lead to the same final state). Is clear that in this region the $q\bar{q}$ contribution is much larger, while the $\gamma\gamma$ contribution is at the permille level. The total (leading order) cross section, including branching fractions, is found to be around 3.2 nb, in agreement with MCFM when run with the same input PDF set. We conclude that photon-initiated contributions are generally not required in the Z peak region, except perhaps for high precision studies, such as the determination of the W boson mass, where a permille accuracy in the distributions is required [13].

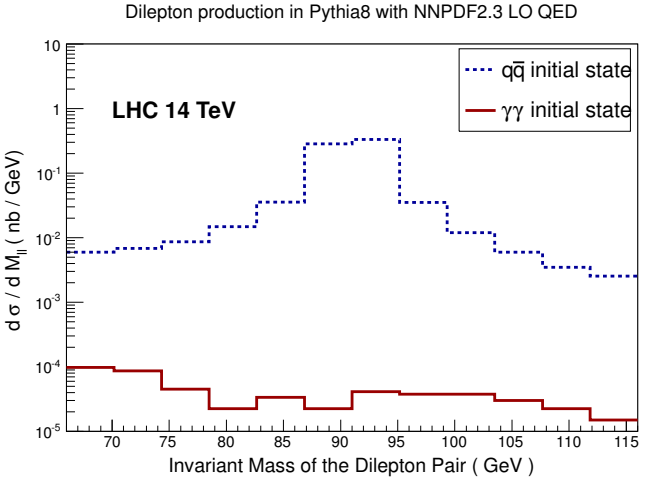

Fig. 4. Invariant mass distributions of the dilepton pair at the LHC 14 TeV, computed with NNPDF2.3QED LO and `Pythia8`. The contribution from the $q\bar{q}$ and $\gamma\gamma$ initiated subprocess are separately shown. No kinematical cuts have been applied.

The situation is quite different if we consider the high-mass tail. In Fig. 5

we show the region of dilepton invariant masses M_{ll} between 1 TeV and 2.5 TeV. We have applied realistic kinematical cuts based on the typical ATLAS and CMS acceptances, namely, we require $p_{T,l} \geq 25$ GeV and $|\eta_l| \leq 2.5$. It is clear that now the photon-initiated contributions to the event yields are rather more significant, ranging from 10% at low masses to up to 50% at high masses. Therefore, photon-induced contributions are an important background for New Physics searches in electroweak production at high invariant masses.

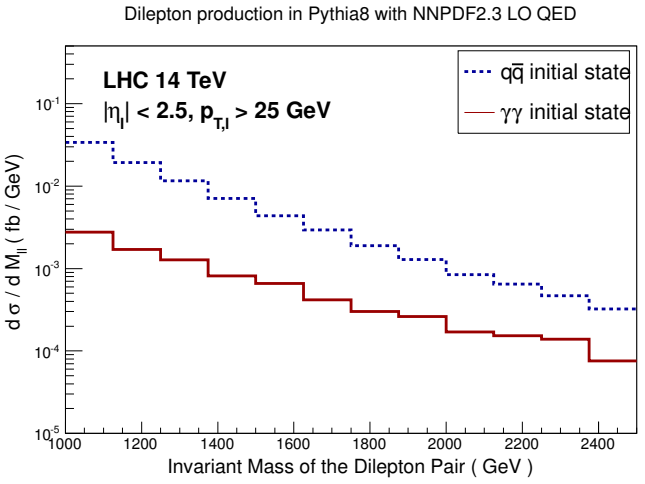

Fig. 5. Same as Fig. 4 but now in the high dilepton mass region. Realistic kinematical cuts have been applied to the events, see text.

In order to disentangle the two contributions, or to provide a measurement which is especially sensitive to the photon PDF, one may look at the rapidity distribution of the dilepton system. This is shown in Fig. 6 for fixed dilepton invariant mass of 2 TeV, at LHC 14 TeV, using the same kinematical cuts as before. It is clear that for a $q\bar{q}$ initial state, the dilepton system tends to be produced more centrally (due to the s-channel exchange of the Z boson) while for a $\gamma\gamma$ initial state, the system is more broadly distributed in rapidity (t-channel exchange). Indeed, for the bins with larger rapidity the contribution from $\gamma\gamma$ diagrams becomes larger than that of $q\bar{q}$ contributions.

All this suggest that a measurement of the rapidity distribution of high-mass Drell-Yan pairs, with a cut excluding the central region to enhance the $\gamma\gamma$ contribution, might be a good way to isolate and eventually pin down the photon contribution to gauge boson production.

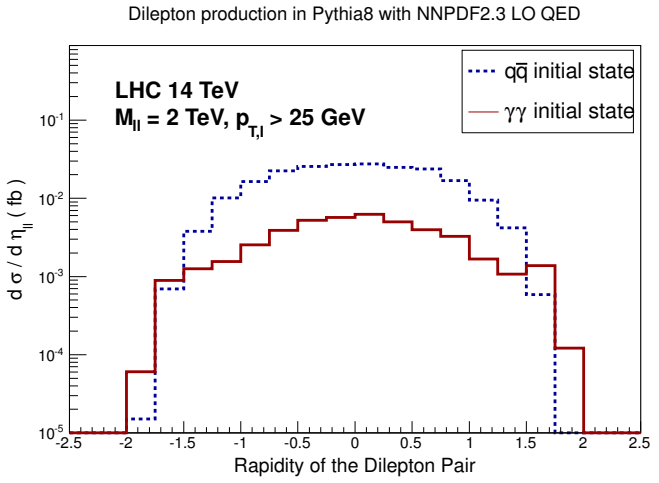

Fig. 6. The rapidity distribution of the dilepton system at LHC 14 TeV and for the same kinematical cuts as in Fig. 5.

4. Using the NNPDF2.3QED LO sets

The NNPDF2.3QED LO sets can be obtained from the NNPDF website

`http://nnpdf.hepforge.org/html/nnpdf23qed/nnpdf23qed.html`

together with the corresponding `C/C++` stand-alone code. They can be used together with the `LHAPDF5.9.0` interface, and they will also be available in a future release of `LHAPDF6`. They are now also available as an stand-alone internal PDF set in `Pythia8`. For consistency of notation, the NNPDF2.1LO PDF set (without QED corrections) will henceforth be equivalently referred to as NNPDF2.3 LO.

Acknowledgments: We are grateful to T. Sjostrand and P. Skands for their help with the implementation of the NNPDF2.3 sets in `Pythia8`.

References

[1] F. Petriello, *this Symposium.*

[2] D. Rebuzzi, *this Symposium.*

[3] S. Forte and G. Watt, Ann. Rev. Nucl. Part. Sci. **63**, 291 (2013).

[4] A. Buckley *et al.*, Phys. Rept. **504**, 145 (2011).

[5] T. Sjostrand, S. Mrenna, and P.Z. Skands, Comput. Phys. Commun. **178**, 852 (2008).

[6] R. D. Ball *et al.*, Nucl. Phys. B **867**, 244 (2013).

[7] R.D. Ball *et al.* (NNPDF Collaboration), Nucl. Phys. B **877**, no. 2, 290 (2013).
[8] A. De Roeck and R. S. Thorne, Prog. Part. Nucl. Phys. **66**, 727 (2011).
[9] E. Perez and E. Rizvi, Rep. Prog. Phys. **76**, 046201 (2013).
[10] R.D. Ball *et al.* (NNPDF Collaboration), Nucl. Phys. B **855**, 153 (2012).
[11] V. Bertone, S. Carrazza, and J. Rojo, arXiv:1310.1394 [hep-ph].
[12] T. Sjostrand, private communication.
[13] G. Bozzi, J. Rojo, and A. Vicini, Phys. Rev. D **83**, 113008 (2011).

Inclusive measurements at HERA from low to high x

Olaf Behnke, on behalf of the H1 and ZEUS Collaborations
DESY, Notkestrasse 85, Hamburg 22607, Germany

New inclusive Deep Inelastic Scattering (DIS) measurements are presented, obtained with the H1 and ZEUS detectors at HERA. The results comprise (flavour) inclusive DIS cross sections as well as inclusive charm production. In the area of inclusive DIS, both H1 and ZEUS completed last year their high Q^2 Neutral and Charged current measurements exploiting the large statistics from the HERA II running period. For inclusive charm production, H1 and ZEUS published a combination of numerous existing measurements based on various tagging methods. Among other things a precise determination of the running charm quark mass $m_c(m_c)$ was obtained from the combined data.

1. Introduction

Since more than 40 years one studies in Deep Inelastic Scattering (DIS) simultaneously the nucleon structure and the strong interactions as represented by the theory of Quantum Chromo Dynamics (QCD). HERA, the worldwide only *ep* collider, plays a crucial role in this field. Figure 1 (left) shows a typical DIS process at HERA. A highly virtual gauge boson, either a photon or a Z in Neutral Current (NC) reactions or a W boson in Charged Current (CC) interactions, is emitted from the lepton and knocks out a quark of the proton which is destroyed. One of the many possible higher order reactions of the strong interaction takes places: a hard gluon is emitted from the struck quark. The basic kinematics of the DIS scattering is described by the following observables:

- $Q^2 = -q^2$, the negative of the squared four-momentum vector q of the exchanged gauge boson.
- the inelasticity $y = qp/kp$, with k and p denoting the four-momentum vectors of the incident lepton and proton, respectively.
- the *Bjorken* x, defined as $x = Q^2/2pq$. In the quark parton model x specifies the longitudinal momentum fraction of the proton carried by the quark that is struck by the gauge boson.

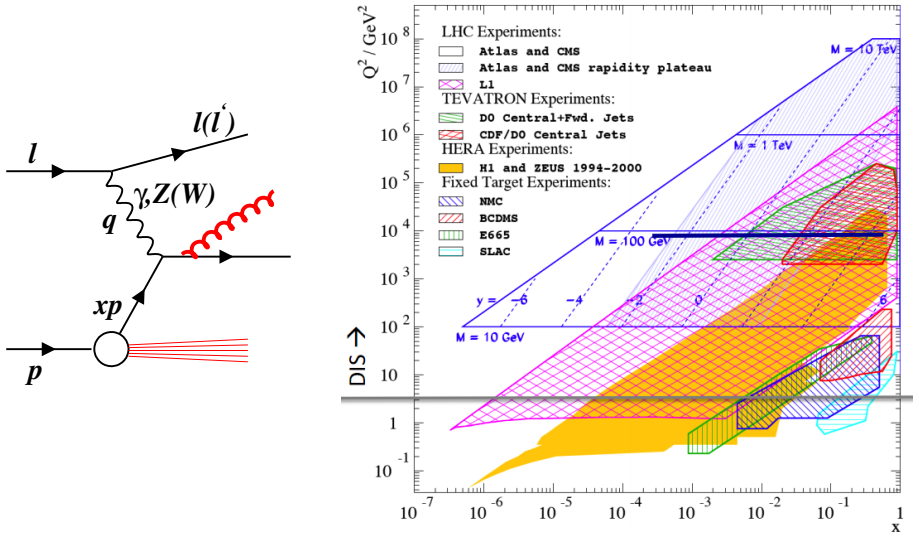

Fig. 1. Left: Sketch of an exemplary higher order DIS process. Right:DIS kinematic plane of Q^2 and x and coverage of various experiments.

The three variables are constrained by the relation $Q^2 = xys$, where s denotes the fixed squared centre-of-mass energy of the lepton-proton system.

Figure 1 (right) shows the kinematic plane in Q^2 and x, covered by various experiments in the past, present and future. The DIS region is defined by $Q^2 \geq$ few GeV^2, while the photoproduction region (exchange of quasi-real photons) is defined by $Q^2 < 1$ GeV^2. Decades ago fixed target experiments started the exploration of the nucleon structure from the region of large x and small Q^2. The H1 and ZEUS experiments at the HERA collider extended the phase space to the region of smallest $x \sim 0.000001$ and highest $Q^2 \sim 40000$ GeV^2. The coverage of the central detector experiments at the $p\bar{p}$ collider TEVATRON and the pp collider LHC is also indicated in Figure 1. It overlaps with HERA; this makes the proton structure information from HERA so crucial for obtaining predictions for many important reactions at the two hadron colliders (e.g. Higgs production at the LHC).

In the following we will discuss some selected highlights of new inclusive measurements from H1 and ZEUS, starting with inclusive DIS and moving to charm production. As a reminder, H1 and ZEUS collected each about 0.5 fb^{-1} of ep collisions; the first quarter was taken in the HERA I period and the other three in the HERA II period, where the lepton beams were polarised. About half of the data were taken with e^+p collisions and the other with e^-p collisions.

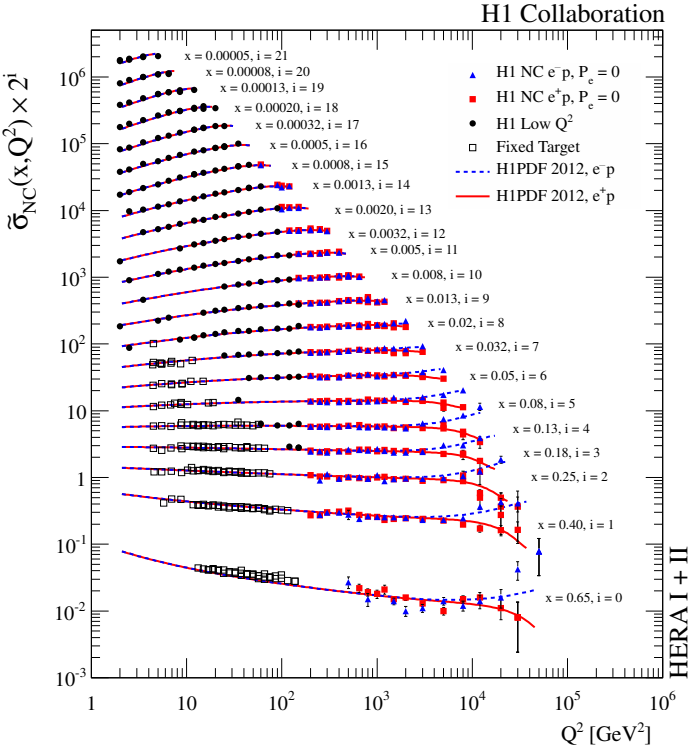

Fig. 2. Recent Neutral Current reduced cross section measurements from H1.

2. Inclusive DIS

Inclusive DIS means to count every DIS event in a given region of Q^2 and x. Recently the H1 and ZEUS experiments completed their inclusive DIS analyses by releasing the full high Q^2 data sets taken in the HERA II period. The H1 publication [1] contains the finalised inclusive $e^{\pm}p$ NC and CC data. The ZEUS paper [2] covers the last missing high Q^2 data set from ZEUS, the e^+p NC data.

Figure 2 shows the $e^{\pm}p$ NC reduced cross section[1] measurements by H1 [1] as a function of Q^2 for various values of x. The data were obtained from a weighted averaging of the HERA II high Q^2 inclusive DIS data, their HERA I counterparts and also the HERA I low Q^2 data. An excellent experimental precision of about 1.5% has been reached for a large region $Q^2 < 500$ GeV^2. In an Next-To-Leading Order (NLO) QCD analysis based

[1] The NC reduced cross section is in a large part of the HERA kinematic phase space approximately equal to the structure function F_2. In specific phase phase parts the structure functions F_L and F_3 also contribute significantly.

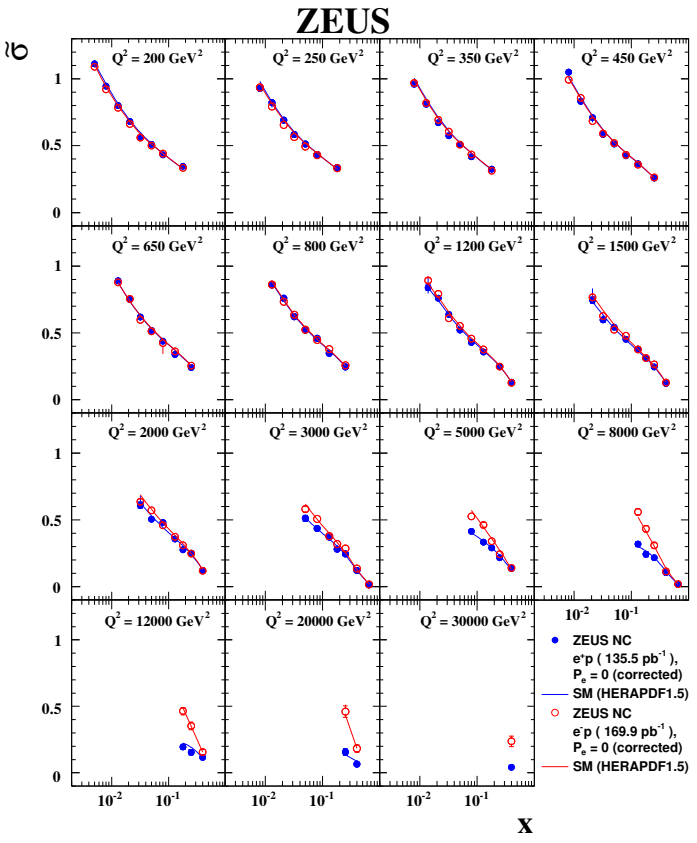

Fig. 3. Recent Neutral Current reduced cross section measurements from ZEUS.

on the DGLAP evolution equations, PDFs were fitted to the data. The fit function from the resulting PDF set "H1PDF2012," is also depicted in Figure 2. It provides a reasonable description of the data in the whole kinematic range. It was often hypothesised that one might find a prominent breakdown of the NLO DGLAP fit description at low Q^2 and low x due to uncontrollable higher order QCD effects, but there is at least no blatant evidence from this plot.

Figure 3 shows the $e^{\pm}p$ NC reduced cross sections by ZEUS [2], using the HERA II high Q^2 data sets. Here the data are plotted as a function of x for various fixed values of Q^2. A very good experimental precision is reached of about 1.5% in some lower Q^2 regions. Also shown is the prediction using the PDF set "HERAPDF1.5", which was obtained from an NLO DGLAP fit to specific subsets of the H1 and ZEUS inclusive data. As in the H1 case, the data are described well by the fit.

In the future it is planned to combine the finalised/new high Q^2 HERA II

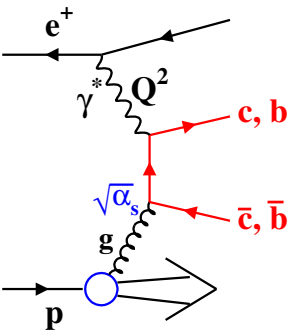

Fig. 4. Leading order BGF process for charm and beauty quark production at HERA.

inclusive DIS data from H1 and ZEUS together with the HERA I combined inclusive data in order to obtain the best available HERA data set to be used for QCD analyses and PDF determinations.

3. Charm production in DIS

The heavy charm and beauty quarks are produced at HERA mainly by boson gluon fusion (BGF) processes. The leading order diagram is shown in Figure 4. Due to the large gluon density in the proton, the BGF processes gives large contributions to DIS; charm production alone accounts at low x and high Q^2 for up to $\sim 35\%$ of the inclusive DIS cross section. Furthermore, the process provides direct sensitivity to the gluon density in the proton. There are different schemes to treat the heavy flavour production (for references consult [3]). At low Q^2, that is $Q^2 \sim m_c^2$, with m_c denoting the charm quark mass, there is no doubt that the *massive scheme* is correct. The scheme is rigorous quantum field theory in which the masses of the heavy quarks are fully taken into account in every part of the calculation. In this scheme, charm and beauty quarks can only be dynamically produced in the hard interaction. The proton PDFs contain only light quarks and gluons and hence the scheme is also called *Fixed-Flavour-Number Scheme* (FFNS). However, at very high virtualities $Q^2 \gg m_c^2$, it might be favourable to treat the charm quark (and similarly the beauty quark for $Q^2 \gg m_b^2$) as massless which is done in the *Zero-Mass-Variable-Flavour-Number Scheme (ZMVNFS)*. In this scheme, the charm and beauty quarks appear above some kinematic thresholds also as massless sea quarks in the proton. The nice feature of this scheme is that it allows to resum to all orders certain logarithmic terms appearing in the perturbative calculation related to collinear gluon radiation from the heavy quark lines. The

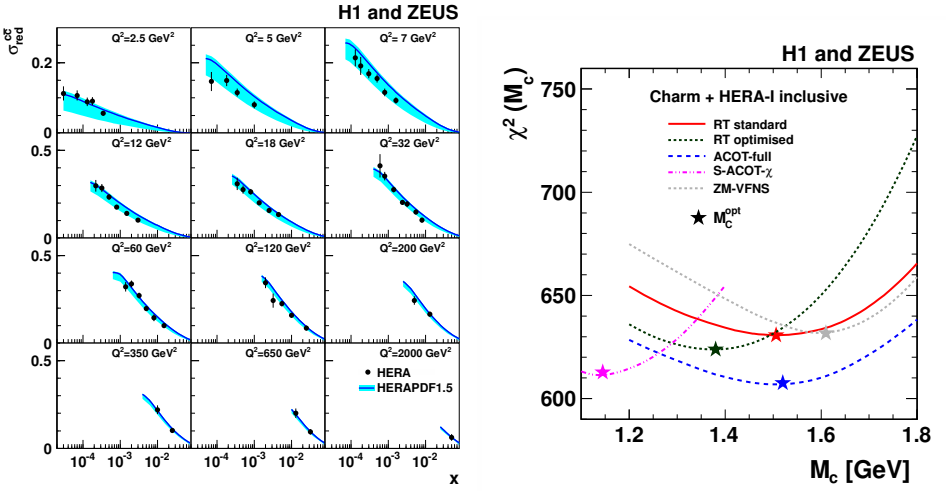

Fig. 5. Left: Reduced cross sections for charm production in DIS. The HERA combined data are compared to a GMVFNS prediction. Right: χ^2 of the PDF plus charm mass fit as a function of the charm mass parameter M_c — for further details see the main text.

General-Mass-Variable-Flavour-Number Schemes (GMVFNS) make use of the best of "both worlds": at low Q^2 the massive scheme is used and at high Q^2 the massless scheme, with a suitable interpolation in the intermediate region. However, what is a suitable interpolation is debated for a long time as well as many other details of the treatment of mass dependent terms in pQCD; in fact there are numerous GMVFNS variants on the market and used by the various PDF fitter groups in the world.

3.1. Charm combination and determination of the running charm mass

Recently, H1 and ZEUS published the combination of charm production data in DIS [3]. The data, based on various tagging methods such as full reconstruction of D^* mesons, D^+ mesons, semileptonic decays, or inclusive secondary vertex tagging, have been combined at the level of the so called reduced cross sections. This cross section is related to the total charm production cross section in a region of Q^2 and x. In the combination the correlated systematics is fully taken into account. The combined data reach a for charm production at HERA unprecedented best precision of about 5% in certain phase space regions. Figure 5 (left) shows the obtained combined reduced cross sections as a function of x for various values of Q^2. Also shown is the prediction based on the "HERAPDF1.5" PDF, using the GMVFNS in the "Robert Thorne standard" scheme variant (for proper references consult [3]). These PDFs were obtained from fitting only inclusive DIS data, without any knowledge of charm production data. The prediction

describes the charm data reasonably well which is a triumph for the QCD collinear factorisation approach used in the calculations: the gluon density in HERAPDF1.5, obtained from the scaling violations observed in inclusive DIS, is in agreement with the gluon density that is needed to describe the charm production data. The not so nice thing is the large theory uncertainty, as indicated by the error band, which is dominated by variations of the charm quark mass. Turning the tables, a simultaneous fit of PDFs plus the charm quark pole mass was performed in [3]. Both the HERA combined charm data and combined HERA I inclusive DIS data were used as input and various GMVFNS variants were tried out. Figure 5 (right) shows a χ^2 scan of this fit as a function of the charm mass parameter M_C. It can be seen that the fitted M_c values (called optimal mass "M_c^{opt}" in the plot) differ considerably between the various GMVFNS variants (e.g. "RT standard","S-ACOT-χ"). In fact, when using a fixed value $M_c = 1.4$ GeV, some of the schemes fail to describe (not shown here) the combined charm data in the lower Q^2 regions, while when using the optimal masses most of the schemes give a good description. What can we learn from this? The various GMVFNS interpolate differently between the massive and massless schemes and this leads to a different quality of the charm data description for a fixed charm mass; these deficiencies can be compensated by using the M_c^{opt} values. This has even broader ramifications as discussed in [3]. Using the specific M_c^{opt} value for each scheme stabilises the PDF mixture of the various quark flavours and of the gluon; in turn this stabilises predictions for W and Z production at the LHC which depend crucially on the flavour mixture.

The massive scheme predictions (not shown here) which are available at NLO plus partial NNLO, provide the best description of the HERA charm combined data. A simultaneous fit of PDFs and of the running charm quark mass has been performed with this scheme, yielding a value $m_c(m_c) = 1.26 \pm 0.06$; GeV, which is consistent with the world average value $m_c(m_c) = 1.275 \pm 0.025$ GeV [4].

At this conference two further brand new publications on charm production in DIS have been presented by ZEUS, based on the full reconstruction of D^* mesons [5] or D^+ mesons [6]. The data have good precision and are consistent with the HERA combined charm data; in the future they can be used to improve the combination.

Finally a general remark: the existing measurements of open charm and beauty quarks at HERA in DIS and also in photoproduction are described over the whole kinematic phase space, from smallest to largest transverse momenta or Q^2, by the NLO massive scheme calculations, so one could say that *the massive scheme prevails at HERA.*

4. Conclusions

Six years after the end of the HERA data taking there is still a continuous flow of new inclusive DIS precision results from the H1 and ZEUS experiments. Recently both experiments completed (and published) the analysis of the full high Q^2 data sets taken in the HERA II period. As a result, DIS data sets are now available spanning a huge phase space from smallest to highest Q^2 and x, with high precision up to Q^2 of a few 1000 GeV^2. Over the whole perturbative phasespace $Q^2 > 3.5$ GeV^2, the data are reasonably well described from smallest to largest x values by NLO DGLAP calculations.

The combination of H1 and ZEUS charm data in DIS provides a data set with (for charm production at HERA) unprecedented precisions of $\sim 5\%$. These data are a unique testing ground for the treatment of heavy quark mass dependent terms in pQCD. Among other things, a precise measurement of the running charm quark mass $m_c(m_c)$ was obtained, compatible with the world average value.

Acknowledgments

I want to thank the organisers for inviting me to this nice symposium, in particular Sergei Chekanov and Zack Sullivan for their marvellous organisational work. Special thanks go to Sharon Grant and Nancy Rezek for their excellent secretarial work and their kind help and guidance.

References

[1] H1 Collaboration, J. High Energy Phys. **09**, 061 (2012).

[2] ZEUS Collaboration, Phys. Rev. D **87**, 052014 (2013).

[3] H1 and ZEUS Collaborations, Eur. Phys. J. C **73**, 2311 (2013).

[4] K. Nakamura *et al.* (Particle Data Group Collaboration), J. Phys. G **37**, 075021 (2010).

[5] ZEUS Collaboration, J. High Energy Phys. **05**, 097 (2013).

[6] I. Abt *et al.* (ZEUS Collaboration), J. High Energy Phys. **05**, 023 (2013).

Polarised Drell-Yan physics at COMPASS

Celso Franco, on behalf of the COMPASS collaboration
LIP, Av. Elias Garcia 14 - 1 1000-149 Lisboa

The COMPASS experiment at CERN is one of the leading experiments studying the spin structure of the nucleon. Until now, the Parton Distribution Functions (PDFs) and the Transverse Momentum Dependent Parton Distribution Functions (TMD PDFs) of protons and deuterons have been studied in Semi-Inclusive Deep Inelastic Scattering (SIDIS) measurements. The polarised Drell-Yan (DY) process is a complementary way to access the TMD PDFs, as it allows us to measure convolutions of only PDFs without involving fragmentation functions (FFs). COMPASS aims to perform the first ever polarised DY experiment in the world, which is foreseen to start in late 2014. By detecting dimuons from DY events we will be able to extract azimuthal spin asymmetries, each containing a convolution of two TMD PDFs, one from a negative pion beam with a momentum of 190 GeV/c and the other one from a transversely polarised proton target (NH_3). After their disentangling we can access four of the eight TMD PDFs needed to describe the nucleon structure at leading twist, like the Sivers and the Boer-Mulders functions. The opportunity to study, in the same experiment, the TMD PDFs from both SIDIS and DY processes is unique at COMPASS. Therefore, we are in privileged conditions to confirm or to deny the expected sign change in Sivers and Boer-Mulders functions when accessed via DY or SIDIS processes. An overview of the preparation and future measurements of the polarised DY experiment will be provided.

1. Introduction

The main goal of the DY program of COMPASS is the study of the TMD PDFs of the proton [1]. The DY process consists in an electromagnetic annihilation of a quark-antiquark pair with the production of two leptons in the final state. The COMPASS case is represented in Fig. 1. A negative pion beam is used to study the valence up quarks of the proton. The experiment is focused on the dimuon channel to take advantage of the good muon reconstruction by the existing spectrometer. The idea of using the polarised DY process to study TMD PDFs comes from unpolarised DY experiments. In particular, it was found by two past experiments (NA10 [2] and E615 [3])

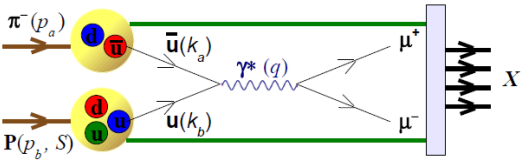

Fig. 1. The Drell-Yan process at COMPASS

that the intrinsic transverse momentum (k_T) of quarks is not a negligible quantity inside the proton. This conclusion was made by studying the angular dependence of the DY cross-section:

$$\frac{1}{\sigma}\frac{d\sigma}{d\Omega} = \frac{3}{4\pi}\frac{1}{\lambda+3}[1+\lambda\cos^2\theta+\eta\sin 2\theta\cos\phi+\frac{\nu}{2}\sin^2\theta\cos 2\phi]\,, \qquad (1)$$

where θ and ϕ are the polar and azimuthal angles of one of the produced leptons in the dilepton rest frame. In the case of $k_T = 0$ no azimuthal modulations are expected. However, the above mentioned experiments measured a $\cos 2\phi$ modulation up to 30%, which without a doubt point to the importance of k_T. Consequentely, instead of 3 collinear PDFs (unpolarised f_1, helicity g_1 and transversity h_1) a total of 8 TMD PDFs are needed to describe the nucleon structure at leading twist.

The key feature of the DY process, when compared with the SIDIS process, is the possibility to study convolutions of two TMD PDFs instead of a TMD PDF convoluted with a quark fragmentation function. Using a transversely polarised proton target and a π^- beam we are able to measure four azimuthal spin asymmetries, each containing a convolution of two TMD PDFs. Therefore, we can access 4 of the 8 leading twist TMD PDFs of the proton: $h_1(x, k_T^2)$ (which leads to transversity after integration over k_T), $h_1^\perp(x, k_T^2)$ (Boer-Mulders), $f_{1T}^\perp(x, k_T^2)$ (Sivers) and $h_{1T}^\perp(x, k_T^2)$ (pretzelosity). Of particular importance are the T-odd Sivers and Boer-Mulders functions. The former describes the transverse motion of quarks induced by the transverse spin of the nucleon and the latter describes the correlations between the transverse spin and transverse momentum of quarks in an unpolarised nucleon. By itself the Sivers function is extremely important because it contains information about the orbital angular momentum (OAM) of quarks. The OAM of quarks is one of the remaining unknowns of the so-called spin-puzzle of the nucleon, a puzzle which the scientific community has been trying to solve over the last 30 years. However, the main motivation to study $h_1^\perp(x, k_T^2)$ and $f_{1T}^\perp(x, k_T^2)$ via DY is the prediction that these two TMD PDFs must change sign when accessed via DY or SIDIS. This prediction is a crucial test of our current understanding of TMD PDFs.

It results from the fact that the re-summation of all soft gluons in a k_T dependent PDF is process dependent. This procedure, which is essential to provide the gauge invariance of a PDF, leads to the existence of the above mentioned T-odd functions. Therefore, the time invariance of the Sivers and Boer-Mulders functions is ensured if and only if they change sign between SIDIS and DY.

Up to now COMPASS has been studying the TMD PDFs of protons and deuterons via SIDIS processes of a polarised muon beam off a transversely polarised target. With our pioneering polarised DY experiment, which basically uses the same spectrometer, we are in privileged conditions to observe the sign change. In Fig. 2 we can confirm the existence of a phase-space overlap between the two COMPASS measurements.

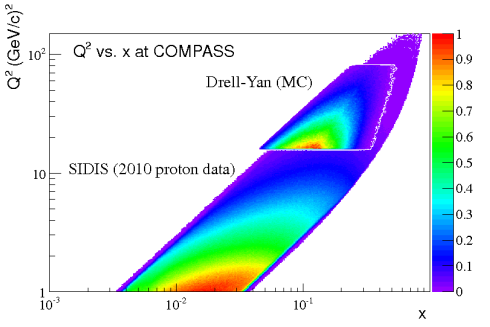

Fig. 2. Phase-space coverage of the SIDIS and DY measurements at COMPASS.

2. The COMPASS experiment

COMPASS is a fixed target experiment located in the CERN North Area, at the end of the M2 beam line of the **S**uper **P**roton **S**ynchrotron (SPS) accelerator. The M2 line provides either muon or hadron beams in a momentum range of 50 to 280 GeV/c. Detailed studies have shown that a π^- beam with 1×10^8 π^-/s and a 190 GeV/c momentum is the best choice for the DY measurement. The high intensity is required to counterbalance the low DY cross-section and it is only limited by the polarised target and by the performance of the M2 beam line. Concerning the target, it will be formed by two cells transversely polarised in opposite directions in order to allow us to measure the needed spin asymmetries for the extraction of the TMD PDFs. Using solid state ammonia as target material one can reach a polarisation of the order of 90%, with a fraction of polarisable material of 0.22.

Since the hadro-production cross section is much larger than the DY

one, the use of a hadron absorber is mandatory to prevent the hadronic products to overflood the detectors. The composition of the absorber is chosen to minimise the number of radiation lengths crossed by the muons (for a minimum multiple scattering), while maximising the number of pion interaction lengths. It will be a compound more than 2 meters long made of aluminum oxide, aluminum and stainless steel, placed immediately after the polarised target. A tungsten beam-plug will also be used as a beam-stopper in the central part of the absorber. Together with a vertex detector and a dimuon trigger, formed by two large area hodoscopes with target pointing features, these are the main modifications in the two-stage spectrometer of COMPASS. A complete description of the latter can be found in [4].

3. The extraction of azimuthal asymmetries

The general polarised DY cross-section was derived by Arnold et. al. [5]. For the special case of COMPASS, involving an unpolarised beam and a transversely polarised target, the cross-section can be written in LO as:

$$\frac{d\sigma}{d^4q d\Omega} = \frac{\alpha^2}{Fq^2}\hat{\sigma}_U\{(1 + D_{[\sin^2\theta]}\boxed{A_U^{\cos 2\phi}}\cos 2\phi) + |\vec{S}_T|[\boxed{A_T^{\sin \phi s}}\sin\phi_S \qquad (2)$$
$$+ D_{[\sin^2\theta]}(\boxed{A_T^{\sin(2\phi+\phi_S)}}\sin(2\phi+\phi_S) + \boxed{A_T^{\sin(2\phi-\phi_S)}}\sin(2\phi-\phi_S))]\}$$

where the azimuthal and polar angles, ϕ and θ, are defined in the Collins-Soper reference frame and ϕ_S is the angle between the transverse spin of the target and the transverse momentum of the virtual-photon (γ^*):

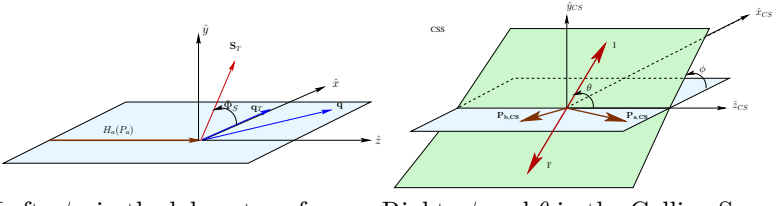

Fig. 3. Left: ϕ_S in the laboratory frame. Right: ϕ and θ in the Collins-Soper frame.

The quantity F is defined by $F = 4\sqrt{(p_\pi \cdot p_P)^2 - M_\pi^2 M_p^2}$, q is the four-momentum of the γ^*, $\hat{\sigma}_U$ is the part of the cross-section surviving the integration over the angles ϕ and θ, $|\vec{S}_T|$ is the target polarisation and $D_{[\sin^2\theta]}$ is the γ^* depolarisation factor.

The four highlighted asymmetries in Eq. 2 can be measured at COMPASS by fitting the corresponding azimuthal modulations of the dimuan pair. In non-perturbative QCD these asymmetries are interpreted as a ratio of 2 convolutions, each one containing 2 TMD PDFs. The TMD PDFs depending on spin appear in the numerator and they completely define the corresponding asymmetries. In this sense, each of the asymmetries is defined by the following convolutions:

- $A_U^{\cos 2\phi}$: the Boer-Mulders function of both hadrons ($h_1^\perp \otimes h_1^\perp$)
- $A_T^{\sin 2\phi}$: the density number function of the beam hadron with the Sivers function of the target nucleon ($f_1 \otimes f_{1T}^\perp$)
- $A_T^{\sin 2\phi+\phi_S}$: the Boer-Mulders function of the beam hadron with the pretzelosity function of the target nucleon ($h_1^\perp \otimes h_{1T}^\perp$)
- $A_T^{\sin 2\phi-\phi_S}$: the Boer-Mulders function of the beam hadron with the transversity function of the target nucleon ($h_1^\perp \otimes h_1$)

The proton's TMD PDFs $h_1^\perp(x, k_T^2)$, $f_{1T}^\perp(x, k_T^2)$, $h_{1T}^\perp(x, k_T^2)$ and $h_1(x, k_T^2)$ can be extracted from the measured asymmetries in global analyses.

4. Event rates and statistical errors

In COMPASS we are interested mostly in the so-called high mass region of the dimuon pair, i.e. $4 \leq M_{\mu\mu} < 9$ GeV/c^2. Despite the DY cross-section being quite low, amounting only to fractions of nanobarn, the main advantage of this mass region is that it is free from both combinatorial and physics backgrounds. The intermediate mass region of $2 \leq M_{\mu\mu} < 2.5$ GeV/c^2 has 5 times larger cross-section but it has also a huge contamination by the combinatorial background, at least as large as the signal, and an open charm contamination at the level of 15%. In addition to the high mass region, the J/Ψ resonance will also be investigated in detail due to the so-called DY-J/Ψ duality. Since the J/Ψ and γ are both vector particles, we can consider an analogous DY and J/Ψ production via quark-antiquark annihilation, which is believed to dominate at the COMPASS energy. In case of duality, we can use the much higher dimuon cross-section in the J/Ψ region to extract the TMD PDFs with much better precision. This can be confirmed in Table 1, where the expected precision is provided for

the 4 azimuthal asymmetries. These predictions are based on the use of a π^- beam with a $p = 190$ GeV/c momentum and an intensity of $I_{beam} = 6\times10^7 s^{-1}$, which allows us to achieve a luminosity of $L = 1.2\times10^{32} cm^{-2} s^{-1}$. With this luminosity we expect about 900 events/day in the high mass region, $4 \leq M_{\mu\mu} < 9$ GeV/c^2, 4300 events/day in $2 \leq M_{\mu\mu} < 2.5$ GeV/c^2 and 22500 events/day in the DY+J/Ψ mass region of $2.9 \leq M_{\mu\mu} < 3.2$ GeV/c^2. A total of 280 days of data taking is foreseen.

Table 1. Statistical uncertainty for the asymmetries in the high mass region.

Asymmetry uncertainty	Dimuon mass (GeV/c^2)		
	$2 < M_{\mu\mu} < 2.5$	$2.9 < M_{\mu\mu} < 3.2$	$4 < M_{\mu\mu} < 9$
$\delta A_U^{cos2\phi}$	0.0026	0.0014	0.0056
$\delta A_T^{sin\phi_S}$	0.0065	0.0036	0.0142
$\delta A_T^{sin(2\phi+\phi_S)}$	0.0131	0.0073	0.0284
$\delta A_T^{sin(2\phi-\phi_S)}$	0.0131	0.0073	0.0284

In Fig. 4 is shown a comparison between the expected precision of the measurements and the theoretical predictions for the azimuthal asymmetries. These predictions point to sizable asymmetries in the valence region of the proton and, as it is clearly seen from Fig 5, COMPASS has a large acceptance in that region.

5. Feasibility of the measurement

The feasibility of the measurement was proved by several beam tests performed in 2007, 2008, 2009 and 2012. In 2007 and 2008 an open spectrometer configuration (without a hadron absorber) was used. Using a π^- beam of 160 GeV/c momentum and an intensity up to $6.5 \times 10^6 \pi/s$, a high occupancy of the detectors closer to the target region was observed. This expected fact confirmed the necessity of using a hadron absorber in the future experiment. These first tests were important to verify the spectrometer response and the level of radiation in the experimental hall.

In 2009 a more important test was performed using a prototype hadron absorber. A π^- beam of 190 GeV/c momentum was used together with two target cells of polyethylene material, each one 40 cm in length and 5 cm in diameter, spaced by 20 cm. The absorber was made of two blocks of concrete and stainless steel, each one 100 cm in length and 80×80 cm^2 in transverse dimension. The beam test had a duration of only three days but it was enough to compare the J/Ψ signal with the expected yield. The obtained mass spectrum can be seen in Fig. 6. Good agreement was found with the expected number of J/Ψ's, which amounts to 3600 ± 600.

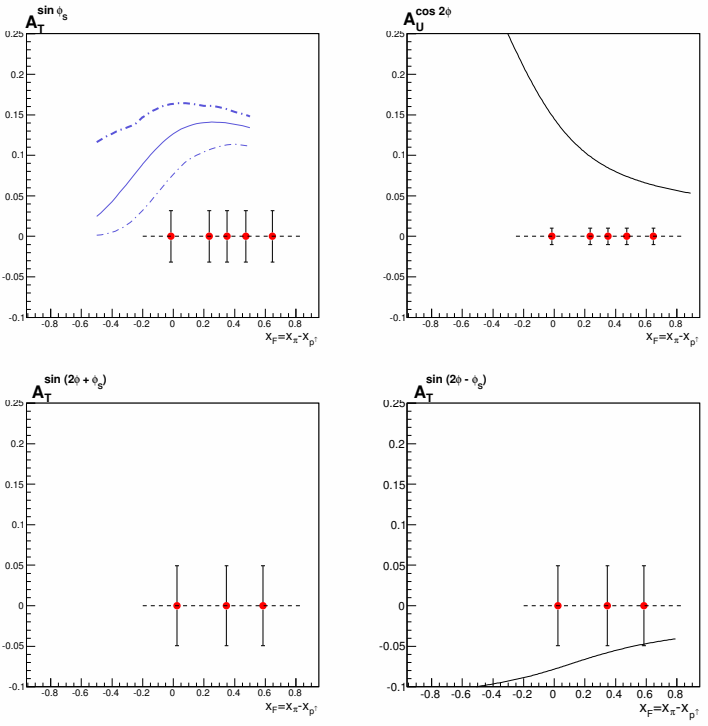

Fig. 4. Comparison between theory predictions and experimental precision for the 4 azimuthal asymmetries accessible at COMPASS.

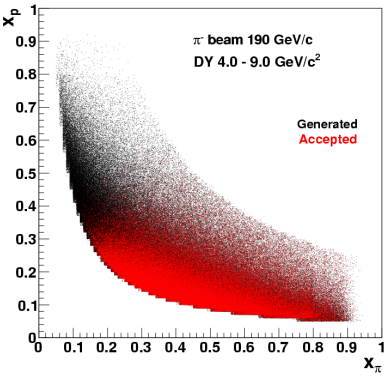

Fig. 5. COMPASS acceptance for DY in the high mass region.

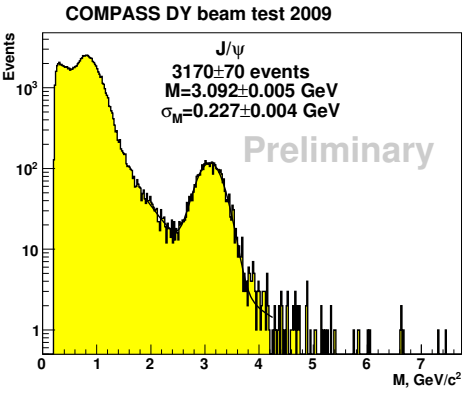

Fig. 6. Invariant mass spectrum of dimuons obtained with the 2009 DY beam test.

6. Summary

The experimental acceptance of COMPASS for DY events covers the valence quarks region, where TMD effects are expected to be sizable. The opportunity to study, with the same spectrometer, the TMD PDFs from both SIDIS and DY processes is unique at COMPASS. In particular, the sign change in the Sivers and Boer-Mulders functions when measuring in DY or in SIDIS will be checked. This verification is crucial for our current understanding of TMD PDFs. The feasibility of the measurement has been proven after a series of beam tests.

The polarised DY measurement is approved and will start by the end of 2014 with a short beam test. The physics run will take place in 2015. A second year of data taking is also planed, possibly in 2018. With 2 years of data we can study the TMD PDFs as a function of x_F and p_T.

Acknowledgments

This work is supported by Fundação para a Ciência e a Tecnologia.

References

[1] COMPASS Collaboration, COMPASS-II proposal, CERN-SPSC.2010-014, SPSC-P-340, 17 May 2010.

[2] S. Falciano *et al.* (NA10 Collaboration), Z. Phys. C **31**, 513 (1986).

[3] J.S. Conway *et al.* (E615 Collaboration), Phys. Rev. D **39**, 92 (1989).

[4] P. Abbon *et al.* (COMPASS Collaboration), Nucl. Inst. Meth. A **577**, 455 (2007).

[5] S. Arnold *et al.*, Phys. Rev. D **79**, 034005 (2009).

Large x physics: recent results and future plans

Roy J. Holt

Physics Division, Argonne National Laboratory, Argonne, IL, 60439

The valence region is exceedingly important in hadron physics since this region not only defines a hadron but also is an excellent discriminator of nucleon structure models. Present uncertainties in light quark distribution functions at high x could also impact high energy physics. Here we will describe a new generation of experiments at Jefferson Lab that is aimed at the high x region of the nucleon. It is noted that the proposed Electron Ion Collider could explore the high x regime.

1. Introduction

During the past four decades there has been an enormous effort to determine the parton distribution functions (PDFs) of the most stable hadrons: neutron, proton and pion [1]. The behavior of the PDFs on the far valence region (Bjorken-$x > 0.5$) is of particular interest because this domain defines a hadron. Recognizing the importance of the far valence region, a new generation of experiments, focused on $x \gtrsim 0.5$, is planned at the Thomas Jefferson National Accelerator Facility (JLab), and under examination in connection with Drell-Yan studies at the Fermi National Accelerator Facility (FNAL) [2] and a possible Electron Ion Collider (EIC), in China or the USA. Theoretical calculations [3–6] have moved far beyond the simple parameterization of PDFs. These computations have emphasized the importance of nonperturbative QCD. The importance of these calculations was illustrated by the pion's valence-quark PDF, $u_v^\pi(x)$, where a failure of QCD was suggested following a leading-order analysis of πN Drell-Yan measurements [7] and with a lack of soft gluon resummation corrections [8]. On the other hand, a series of QCD-connected calculations [8–11] subsequently established that the leading-order analysis was misleading, so that $u_v^\pi(x)$ may now be seen as a success for the nonperturbative approach in QCD. Finally, the high-x region could impact high energy physics since low momentum transfer and high x evolves to high momentum transfer and low x. This talk will focus on three main areas of high-x research at JLab: First, the planned measurements of the F_2^n/F_2^p and d/u ratios as well as present status; Secondly, measurements of the longitudinal spin asymmetries for

the proton and neutron, while the third, the planned measurements of the transversity distributions of the nucleons.

2. Experimental Status

2.1. F_2^n/F_2^p and d/u ratios

There is considerable theoretical interest in the ratio of F_2^n/F_2^p and d/u at very high x. The ratio as $x \to 1$ is sensitive to the model of the nucleon. One can see from the right side of Fig. 1 that the F_2^n/F_2^p or d/u ratio varies substantially among the models. The ratio of the neutron structure function, F_2^n, to the proton structure function, F_2^p, is particularly interesting. Within the parton model at very high x:

$$\frac{F_2^n}{F_2^p} \overset{x\cong 1}{=} \frac{1+4(d_v/u_v)}{4+(d_v/u_v)}. \tag{1}$$

Thus a measurement of the neutron and proton structure functions at large-x provides a determination of the d_v/u_v ratio. However, while proton and deuteron DIS data are well measured at reasonably high x, the extraction of the neutron structure function at very high x from DIS data on the deuteron is problematic. The central difficulty is that the extraction of F_2^n/F_2^p at high x is sensitive to the poorly known high-momentum components of the deuteron wave function [12].

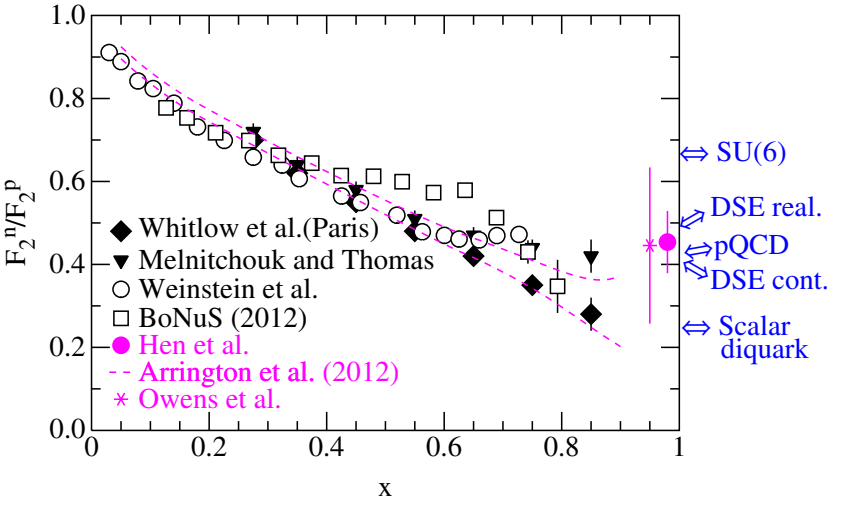

Fig. 1. F_2^n/F_2^p as a function of x. Results from five extraction methods are shown [13–19] along with selected predictions. Adapted from Ref. [3].

To see this, we note that many extractions of the neutron-proton structure function ratios have been performed [13–19]. They are summarised in Fig. 1, with the three most recent inferences indicated by the points with error bars near $x = 1$: there is a large uncertainty in the ratio for $x \gtrsim 0.6$. (See also Fig. 25 in Ref. [1].) New experimental methods are necessary in order to place tighter constraints on the far valence domain. A primary goal is to empirically eliminate two of the three quite different theoretical predictions.

Two new experiments [20, 21] should provide data up to $x \approx 0.85$. Since much of the uncertainty can be traced to the poorly known short-range part of the deuteron wave function, the JLab BoNuS Collaboration has performed [22] an experiment where a very low energy spectator proton from the deuteron can be detected in coincidence with a DIS event from the neutron in the deuteron. In this way, one can restrict the data to a region where the well-known long-range part of the deuteron wave function dominates the process. The central difficulty with this experiment is detecting the very low energy proton of about 150 MeV/c or less. This requires extremely thin target and detector components. An interesting variant of this approach is to use an EIC with, e.g., an 8 GeV electron beam impinging on a deuteron beam of 30 GeV/nucleon. The forward going energetic proton would be detected at very small angles in coincidence with a DIS event from the neutron. Simulations suggest that this should be feasible [Accardi *et al.*Accardi, Keppel, and Ent].

Another method is to perform deep inelastic scattering from the mirror nuclei ^{3}He and ^{3}H over a broad range in x [21, 23–26]. Theoretical calculations indicate that nuclear effects cancel to a high degree in extracting the F_2^n/F_2^p ratio from these two nuclei. This experiment would also be useful in determining the EMC effect in the mass-three system [27]. Although providing a tritium target for JLab is straightforward [28], it is not trivial.

Finally, parity violating DIS can avoid the problem encountered with neutrons bound in nuclei. Parity-violating DIS from the proton is sensitive to the d/u ratio [29]. Plans include measuring the d/u ratio up to an x of 0.7.

2.2. Longitudinally polarized deep inelastic scattering

It is evident from right side of Fig.2 that measurements of the longitudinal asymmetries in DIS provide an important constraint on models of nucleon structure. Numerous experiments and extractions aimed at determining nucleon longitudinal spin structure functions have been performed [30].

Existing measurements of A_1^p are summarised in Fig. 2. Unfortunately,

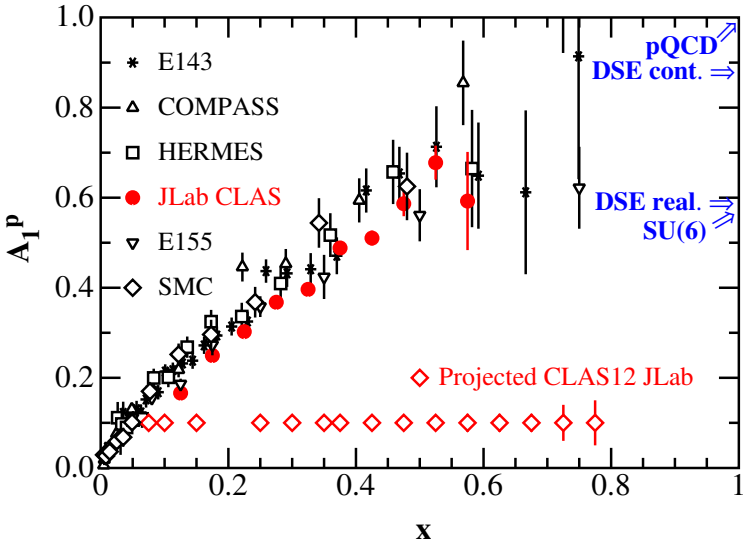

Fig. 2. Existing and projected measurements of the proton's longitudinal spin asymmetry as a function of x (statistical errors only), along with selected predictions. Adapted from Ref. [3].

these data are not of sufficient accuracy and high enough x to discriminate among the models. As indicated in Fig. 2, however, a new JLab experiment [31] will extend the results up to $x \approx 0.8$ with a projected error that promises a significant constraint on the models.

The status of existing data for A_1^n is shown in Fig. 3. The data extend only to $x \approx 0.6$ and place little constraint on descriptions of the nucleon. New experiments proposed at JLab [32, 33] are expected to provide results up to $x \approx 0.75$, as indicated in Fig. 3. These new results should permit discrimination between the pQCD model and other predictions.

2.3. Transversity distributions

The transversity distribution function is a chiral odd, T-even function that is accessible in Drell-Yan interactions and in semi-inclusive DIS (SIDIS). The transversity is a measure of the quark transverse polarization in a transversely polarized nucleon. A feature of the transversity distribution function is that the quark-antiquark and gluon seas do not contribute. The nucleon tensor charge, an intrinsic property such as axial or vector charge, can be determined from the transversity distribution function, $h_1(x)$. The tensor charges are important for calculation a permanent electric dipole moment of a nucleon. In SIDIS, the asymmetry arises from the product $h_1(x)$

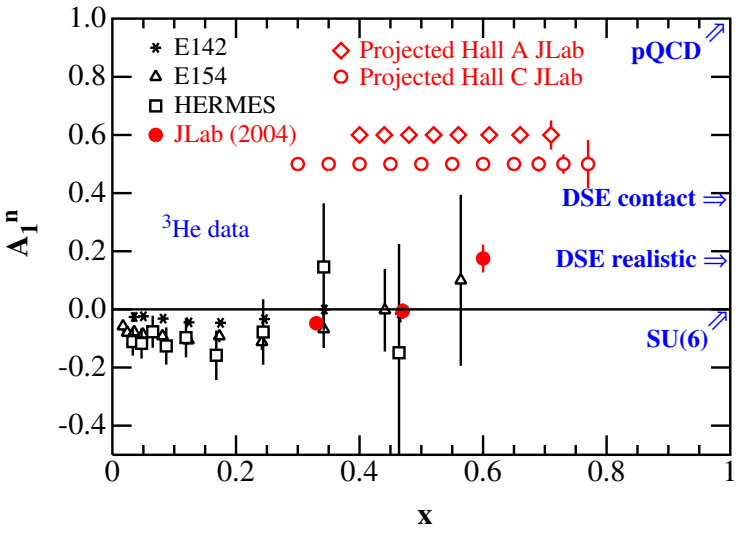

Fig. 3. Existing and projected measurements of the neutron's longitudinal spin asymmetry as a function of x (statistical errors only), along with selected predictions. N.B. We only display A_1^n data obtained from polarised ^{3}He targets. Adapted from Ref. [3].

and the Collins fragmentation function, $H_1^\perp(x)$. Fortunately, the Collins fragmentation function has been measured at Belle so that the $h_1(x)$ can be isolated. A recent analysis [34] of all transversity and Collins fragmentation function data has been performed and the tensor charges have been determined [35]. At present the extracted value of the u-quark tensor charge is $0.39^{+0.18}_{-0.12}$ and the d-quark tensor charge: $-0.25^{+0.30}_{-0.10}$. The uncertainties in these values are generally too large to discriminate among the models. However, a new generation of experiments would be expected to reduce these uncertainties by about an order of magnitude. Transversity experiments for the proton [36, 37] using a polarized hydrogen target and for the neutron [38, 39] *via* transversely polarized ^{3}He targets have been planned for JLab at 12 GeV. Data of such accuracy would add an important constraint on the available models. An important recent finding is that within the framework of DSE, the inclusion of an axial diquark has a pronounced effect on the u-quark tensor charge.

3. Summary

An understanding of hadrons in terms of QCD is an essential goal of nuclear physics and would be a great contribution to science in general. A

vigorous program aimed at the high x domain is planned at JLab at 12 GeV. The goal of this program is to provide new data for the d/u ratio and the longitudinal spin asymmetries at very high x as well as for the tensor charges of the nucleons. These new results will provide unprecedented constraints on the models of the nucleon.

Acknowledgments

I am grateful to C. D. Roberts, J. Arrington, C. Keppel, S. Kuhn and X. Zheng for fruitful discussions. This work was funded by the Department of Energy, Office of Nuclear Physics, contract no. DE-AC02-06CH11357.

References

[1] R.J. Holt and C.D. Roberts, Rev. Mod. Phys. **82**, 2991 (2010).

[2] P. Reimer, D. Geesaman, *et al.* (Fermilab E906/Drell-Yan), E906: Fermilab Proposal 906, 2006.

[3] C.D. Roberts, R.J. Holt, and S.M. Schmidt, `arXiv:1308.1236`.

[4] L. Chang *et al.*, Phys. Rev. Lett. **110**, 132001 (2013).

[5] I.C. Cloët, L. Chang, C.D. Roberts, S.M. Schmidt, and P.C. Tandy, arXiv:1306.2645 [nucl-th], Phys. Rev. Lett. *in press*.

[6] L. Chang, I.C. Cloët, C.D. Roberts, S.M. Schmidt, and P.C. Tandy, arXiv:1307.0026 [nucl-th].

[7] J.S. Conway *et al.*, Phys. Rev. D **39**, 92 (1989).

[8] M. Aicher, A. Schafer, and W. Vogelsang, Phys. Rev. Lett. **105**, 252003 (2010).

[9] M.B. Hecht, C.D. Roberts, and S.M. Schmidt, Phys. Rev. C **63**, 025213 (2001).

[10] K. Wijesooriya, P.E. Reimer, and R.J. Holt, Phys. Rev. C **72**, 065203 (2005).

[11] T. Nguyen, A. Bashir, C.D. Roberts, and P.C. Tandy, Phys. Rev. C **83**, 062201(R) (2011).

[12] J. Arrington, D.W. Higinbotham, G. Rosner, and M. Sargsian, Prog. Part. Nucl. Phys. **67**, 898 (2012).

[13] L. Whitlow, E. Riordan, S. Dasu, S. Rock, and A. Bodek, Phys. Lett. B **282**, 475 (1992).

[14] W. Melnitchouk and A.W. Thomas, Phys. Lett. B **377**, 11 (1996).

[15] J. Arrington, F. Coester, R.J. Holt, and T.S.H. Lee, J. Phys. G **36**, 025005 (2009).

[16] L. Weinstein, E. Piasetzky, D. Higinbotham, J. Gomez, O. Hen, *et al.*, Phys. Rev. Lett. **106**, 052301 (2011).

[17] O. Hen, A. Accardi, W. Melnitchouk, and E. Piasetzky, Phys. Rev. D **84**, 117501 (2011).

[18] J. Arrington, J. Rubin, and W. Melnitchouk, Phys. Rev. Lett. **108**, 252001 (2012).

[19] J. Owens, A. Accardi, and W. Melnitchouk, Phys. Rev. D **87**, 094012 (2013).

[20] S. Bueltmann *et al.* (BoNuS Collaboration), *The Structure of the Free Neutron at Large x-Bjorken*, JLab Experiment E12-06-113.

[21] G. Petratos *et al.* (MARATHON Collaboration), *Measurement of the F_2^n/F_2^p, d/u Ratios and the $A = 3$ EMC Effect in Deep Inelastic Scattering off the Tritium and Helium Mirror Nuclei*, JLab Experiment E12-06-118.

[22] N. Baillie *et al.* (CLAS Collaboration), Phys. Rev. Lett. **108**, 199902 (2012).

[Accardi *et al.*Accardi, Keppel, and Ent] A. Accardi, C. Keppel, and R. Ent (2010), presentation at the "Workshop on Nuclear Chromodynamics with an EIC", Argonne National Laboratory (2010).

[23] I.R. Afnan *et al.*, Phys. Lett. B **493**, 36 (2000).

[24] F.R.P. Bissey, A.W. Thomas, and I.R. Afnan, Phys. Rev. C **64**, 024004 (2001).

[25] I.R. Afnan *et al.*, Phys. Rev. C **68**, 035201 (2003).

[26] R.J. Holt and G.G. Petratos, AIP Conf.Proc. **1369**, 106 (2011).

[27] O. Hen, D. Higinbotham, G. Miller, E. Piasetzky, and L. Weinstein, Int. J. Mod. Phys. E. **22**, 1330017 (2013).

[28] B. Brajuskovic, T. O'Connor, R.J. Holt, J. Reneker, D. Meekin, *et al.* (2013).

[29] P. Souder *et al.* (SoLID Collaboration), *Precision Measurement of Parity Violation in Deep Inelastic Scattering over a Broad Kinematic Range*, JLab Experiment E10-007.

[30] C.A. Aidala, S.D. Bass, D. Hasch, and G.K. Mallot, Rev. Mod. Phys. **85**, 655 (2013).

[31] S. Khun *et al.* (CLAS Collaboration), *The Longitudinal Spin Structure of the Nucleon*, JLab Experiment E12-06-109.

[32] X. Zheng *et al.* (E12-06-110 Collaboration), *Measurement of Neutron Spin Asymmetry A_1^n in the Valence Quark Region using an 11 GeV Beam and a Polarized ^{3}He Target in Hall C*, JLab Experiment E12-06-110.

[33] N. Liyanage *et al.* (E12-06-122 Collaboration), *Measurement of Neutron Spin Asymmetry A_1^n in the Valence Quark Region using 8.8 and 6.6 GeV Beam Energies and Bigbite Spectrometer in Hall A*, JLab Experiment E12-06-122.

[34] M. Anselmino, M. Boglione, U. D'Alesio, S. Melis, F. Murgia, *et al.*, Phys. Rev. D **87**, 094019 (2013).

[35] A. Prokudin, PoS **CD12**, 082 (2013).

[36] H. Avakian *et al.* (Hall B Collaboration), *Transverse Spin Effects in SIDIS at 11 GeV with a Transversely Polarized Target using the CLAS12 Detector*, JLab Experiment E12-11-111.

[37] H. Gao *et al.* (SoLID Collaboration), *Target single spin asymmetry in semi-inclusive Deep-inelastic (e,e'$\pi^{\pm}$) Reaction on a Transversely Polarized Proton Target*, JLab Experiment E12-11-108.

[38] G. Cates *et al.* (Hall A Collaboration), *Measurement of Semi-inclusive Pion and Kaon Electroproduction in the DIS Regime on a Transversely Polarized ^{3}He Target using the Super BigBite and BigBite Spectrometers in Hall A*, JLab Experiment E12-09-018.

[39] H. Gao *et al.* (SoLID Collaboration), *Target Single Spin Asymmetry in Semi-inclusive Deep-inelastic Electro-pion Production on a Transversely Polarized ^{3}He Target at 8.8 and 11 GeV*, JLab Experiment E12-10-006.

HERAFitter - an open source QCD fit framework

Pavel Starovitov
on behalf of the HERAFitter team

DESY (Deutsches Elektronen-Synchrotron)
Notkestrasse, 85, 22607 Hamburg, Germany

The patron distribution functions (PDFs) describe the parton content of the proton. They cannot be calculated from the first principle and are to be determined empirically by fitting experimental observables to quantum chromodynamics (QCD) predictions. The HERAFitter project aims to provide a framework for QCD analyses of proton structure at leading order (LO), next-to-leading order (NLO) and next-to-next-to-leading (NNLO) orders in perturbative QCD. The framework includes various modules and interfaces enabling a large number of theoretical and methodological options. It also allows to study the impact of the new experimental data on the PDFs from ep, pp and $p\bar{p}$ scattering processes. The fast development of the project involves active communication with theorists and experimentalist as well as a close collaboration with the main PDF fitting groups. Full information about the project, downloads and documentation can be found in http://herafitter.org.

1. HERAFitter project

The hard-scattering cross section is a convolution of the parton distribution functions, coupling constant and the perturbatively calculable matrix elements of a hard scattering process. PDFs, which cannot be derived from the theory and are to be determined by a fit of predictions to experimental observables using the DGLAP evolution equation [1]. HERAFitter project is an open source QCD fit framework designed for the extraction of parton distribution functions of the proton. The framework includes a large number of theoretical models and allows to study the impact of the new experimental data on the PDFs. A schematic structure of the HERAFitter framework is illustrated in Figure 1 and explained below. Further information about the project with available releases and documentation (manual and release notes) can be found in http://herafitter.org.

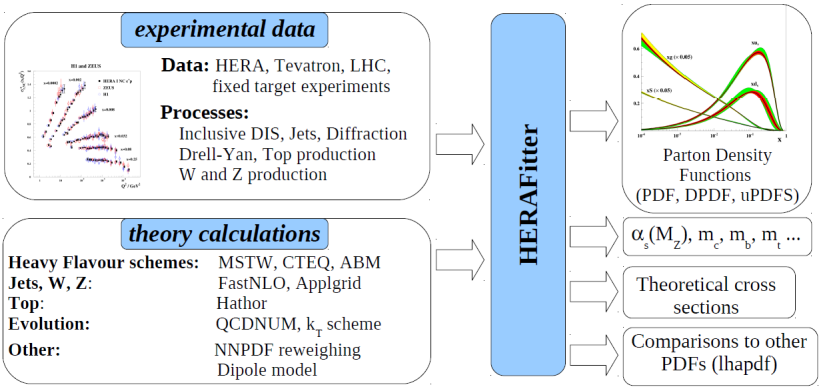

Fig. 1. Schematic structure of the `HERAFitter` program: The "experimental data" block illustrates variety of processes which can be included into the framework and are matched to the corresponding theoretical calculation illustrated in the block below; after the QCD fit is performed the resulting PDFs together with theoretical cross sections are provided as shown on the right side of the figure.

2. Functionality

The procedure to determine PDFs in the `HERAFitter` framework is the following. First, the PDFs are parametrized at the starting scale Q_0^2 chosen to be below the charm mass threshold. Then, the fits to the experimental data are performed using DGLAP evolution in the $\overline{MS}$ scheme as implemented in the QCDNUM [2] package. The evolution is available at leading (LO), next-to-leading (NLO) or next-to-next-to-leading (NNLO) orders.

During the fitting procedure, the measured and predicted cross sections together with their corresponding errors are used to build a χ^2 and determine the parameters of the PDF model. The main functionality of the code which includes the treatment of the experimental data, calculation of the theory predictions, χ^2 minimization, parametrization and optional tools are summarized below.

All the main experimental data sets relevant for PDFs can be fitted within the `HERAFitter` framework: inclusive deep inelastic scattering (DIS) cross sections from HERA and fixed target experiments, Drell-Yan cross sections, inclusive jet production data (ep, pp and $p\bar{p}$) and heavy quark structure functions. The DIS structure functions may be computed in a variety of heavy quark schemes including the fixed-flavor (FFN) and variable flavor number (VFN) schemes. VFN schemes with various treatments for the heavy quark thresholds include the Thorne Roberts (TR) scheme at LO, NLO and NNLO [3, 4] as provided by the MSTW group, the ACOT scheme at LO and NLO as provided by the CTEQ group. The QCDNUM

also provides the calculations of the DIS structure functions in the zero-mass FFN schemes. The FFN scheme is alternatively available via the OPENQCDRAD [7] interface in which the running mass definition [8] is implemented.

The calculations of production cross sections at hadron colliders with NLO accuracy require a huge amount CPU time in order to reach a high statistical precision of the result. To facilitate the use of NLO calculations in the fitting framework the grid methods were adopted by the `HERAFitter` team. These techniques rely on the factorization theorem. It decouples the hard scattering coefficients from PDFs and stores them on the grid allowing a fast recalculation of the cross section in every fit iteration. APPLGRID [9] (or FastNLO [10]) technique is used as a fast interface to jet [6] and electroweak [5] cross sections calculators. An independent treatment for the electro-weak corrections is applied as k-factors, using external packages such as SANC or FEWZ to calculate them.

The predictions of Drell Yan production in $pp(\bar{p})$-collisions can be provided using two independent implementations. The first one uses calculations at the LO which and is extendable to NLO by applying a k-factors. Alternatively, one can obtain the full NLO predictions directly from the NLO calculations as implemented in MCFM [5] by interfacing it to APPLGRID library. Any of two methods can be chosen by a framework user.

The program HATHOR [11] interfaced to `HERAFitter` provides the calculation of the total $t\bar{t}$ cross section at $p\bar{p}$ and pp colliders up to approximate NNLO accuracy. Various definitions of χ^2 can be chosen in the `HERAFitter` for the minimization procedure which are based on the use of nuisance parameters or on the full covariance matrix. For a single data set, the χ^2 function is defined in a simple form

$$\chi^2 = \sum_i \frac{\left[m^i - \sum_j \gamma_j^i m^i b_j - \mu^i\right]^2}{\left(\delta_{i,\mathrm{stat}} m^i\right)^2 + \left(\delta_{i,\mathrm{uncor}}\, m^i\right)^2} + \sum_j b_j^2, \tag{1}$$

or can be evolved to the so called "scaled" form:

$$\chi^2 = \sum_i \frac{\left[m^i - \sum_j \gamma_j^i m^i b_j - \mu^i\right]^2}{\delta_{i,\mathrm{stat}}^2 \mu^i \left(m^i - \sum_j \gamma_j^i m^i b_j\right) + \left(\delta_{i,\mathrm{uncor}}\, m^i\right)^2} + \sum_j b_j^2. \tag{2}$$

Here μ^i is the measured central value at a point i with relative statistical $\delta_{i,stat}$ and relative uncorrelated systematic $\delta_{i,unc}$ uncertainties, the quantity m^i is the theoretical prediction, γ_j^i represents relative correlated systematic uncertainties and b_j – their shifts. In the case of the covariance matrix, the

χ^2 function takes the form

$$\chi^2 = \sum_{ij} (m^i - \mu^i) C^{-1}_{\text{tot } ij} (m^j - \mu^j), \tag{3}$$

where the $C^{-1}_{\text{tot } ij}$ is the total covariance matrix given by the sum of the statistical and systematic covariance matrices. In addition, the different approaches can be combined together, e.g. some systematic uncertainties can be treated using the matrix method, others can be treated using nuisance parameters.

Several different parametrization forms for the PDFs at the staring scale can be chosen in the `HERAFitter`. First, the standard functional form can be used to parameterize PDFs, second, the bi-log normal functional form is available and third, forms based on generalized polynomials such as the Chebyshev can be used.

The best way to see the impact of the measurement on the PDFs is to perform a QCD fit. As an alternative to the PDF fit, a Bayesian reweighting technique can be used to study the impact of experimental data on PDFs. Bayesian reweighting can be used with Monte Carlo method as first employed by the NNPDF Collaboration [12] or using the Hessian Eigenvector Method as proposed in [13].

The `HERAFitter` provides PDFs in a standard LHAPDF format which can be used by theoretical calculation and Monte Carlo simulation programs. Basic plotting tools and several examples of the fits are included in the `HERAFitter` package.

3. Latest developments (HERAFitter-0.3.1)

The latest developments which are included in the newest `HERAFitter` release (HERAFitter-0.3.1 beta) are summarized below:

- improved treatment of the experimental data uncertainties which can be treated as asymmetric (using Toy MC method), as Offset method (the minimization is performed without taking into account correlated uncertainty sources but nuisance parameters are shifted by ± 1 in the uncertainty determination) and using the covariance matrix representation for data sets which have uncertainties reported in this form;

- the possibility to study the bias introduced by the parametrization form, a flexible PDF parametrization and MC method now can be employed. There are two regularization techniques, data driven and external regularization based on the χ^2 penalty term, which can be used to estimate parametrization induced biases;

- PDF Bayesian reweighting based on eigenvectors (Hessian method) as explained in the section above,
- unintegrated PDFs based on the k_T factorization (CCFM) evolution as an alternative approach to colinear DGLAP evolution;
- a Bartels-Golec-Kowalski(BGK) [14] dipole model which takes into account the effects of DGLAP evolution;
- inclusion of additional data sets from LHC and Tevatron and other updates like upgraded interface format to FastNLO and newer electroweak DIS program.

4. Results obtained using HERAFitter

The HERAFitter framework is actively used by HERA and LHC experiments. At HERA, the results of QCD analyses using HERAFitter are published in the recent combination of charm production measurements in DIS [15] and inclusive H1 measurements at high Q^2 with longitudinally polarized lepton beams [16]. The HERAFitter framework has been used in the QCD studies with Z and W cross sections measured by the ATLAS Collaboration to determine the strange quark density of the proton [17] as depicted in Figure 2. It was shown that the Z and W measurements introduce a novel sensitivity to the strange quark density at $x \sim 0.01$. The ratio of the strange to the down sea quark density is found to be $r_s = 1.00^{+0.25}_{-0.28}$ at Bjorken $x = 0.023$ and the initial scale of the QCD fit $Q_0^2 = 1.9$ GeV^2.

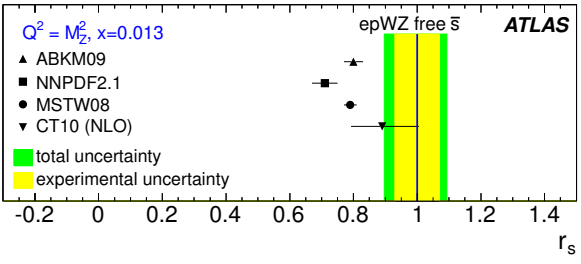

Fig. 2. Predictions obtained from NNLO pQCD analyses of the ratio $r_s = 0.5(s + \bar{s})/\bar{d}$, at $Q^2 = M_Z^2$ and $x = 0.013$. Points: Global fit analyzes using the PDF uncertainties as quoted in [17]; Bands: ATLAS measurement [17]; inner yellow band — experimental uncertainty; outer green band — total uncertainty.

Another QCD analysis using the HERAFitter framework was performed on the inclusive ATLAS jet data at $\sqrt{s} = 2.76$ TeV and $\sqrt{s} = 7$ TeV [18].

It was demonstrated that by including the ATLAS jet data, a harder gluon distribution and a softer sea-quark distribution in the high Bjorken-x region are obtained with respect to the fit of HERA data only. The results are presented in Figure 3.

At CMS, there are several analyses which use `HERAFitter` for PDF constraints, i.e. Drell-Yan, W+charm, W asymmetry data and inclusive jets. The combined analysis of HERA I data and CMS W asymmetry measurement [20] shows that CMS data change the central values of the light valence quark PDFs and decreases its uncertainties (see Figure 4).

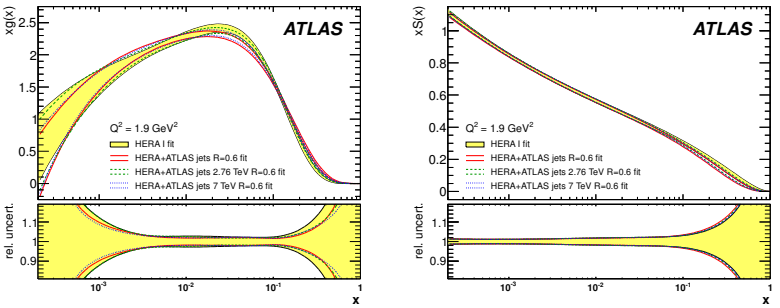

Fig. 3. Momentum distributions of the gluon, $xg(x)$, (left) and total sea, $xS(x)$,(right) together with their relative experimental uncertainty as a function of x for $Q^2 = 1.9$ GeV^2. The filled area indicates a fit to HERA data only. The bands show fits to HERA data in combination with both ATLAS jet data sets, and with the individual ATLAS jet data sets separately, each for jets of $R = 0.6$ size. For each fit the uncertainty in the PDF is centered on unity.

Adding the CMS jet data [19] to the HERA I data set (see Figure 5) results in a harder gluon distribution in high Bjorken-x region in agreement with ATLAS analysis [18].

From the theory side, the work is ongoing on updating the ACOT scheme module (in collaboration with CTEQ group members), inclusion of photon PDF in QCDNUM (on former a publication is foreseen). The QCD studies of LHeC data have been also performed with `HERAFitter` and published in [21].

5. Summary

`HERAFitter` contains all necessary ingredients to study the proton PDFs, it incorporates variety of different data processes and theory calculations, contains many useful tools and is an optimal platform for various benchmarking studies. `HERAFitter` is the first open source package to perform

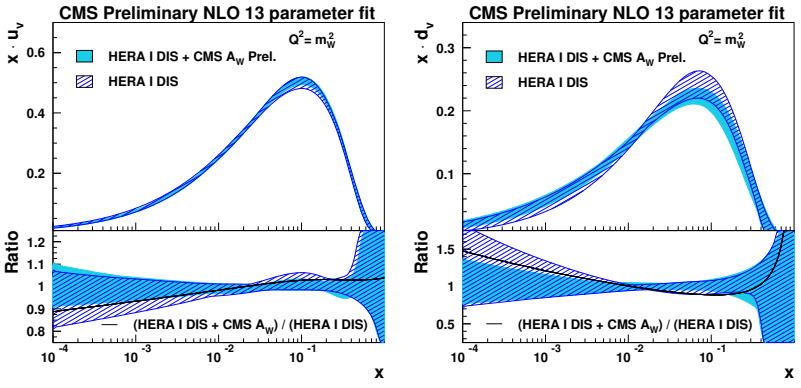

Fig. 4. Distributions of u-valence (left) and d-valence (right) quarks as a function of x at the scale. The results of the 13-parameter fixed strangeness fit to the HERA I DIS data and CMS muon asymmetry measurements (shaded band), and to HERA only (hashed band) are compared.

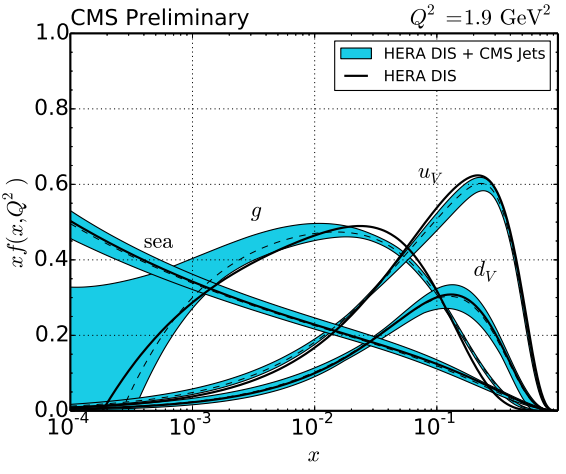

Fig. 5. Overview of the gluon, sea $\Sigma = 2(\bar{u}+\bar{d}+\bar{s})$, u valence, and d valence PDFs before (full line) and after (dashed line) including the CMS jet data into the fit. The PDFs are shown at the starting scale $Q^2 = 1.9$ GeV^2. In addition the total uncertainty including the CMS jet data is shown as a band around the central fit.

PDF fits and is actively used by experimental and theoretical high energy physics communities.

References

[1] V.N. Gribov and L.N. Lipatov, Sov. J. Nucl. Phys. **15**, 438, 675 (1972); G. Altarelli and G. Parisi, Nucl. Phys. B 126, 298 (1977); G. Curci, W. Furmanski, and R. Petronzio, Nucl. Phys. B **175**, 27 (1980); W. Furmanski and R. Petronzio, Nucl. Phys. B **97**, 473 (1980); S. Moch, J. Vermaseren, and A. Vogt, Nucl. Phys. B **688**, 101 (2004); A. Vogt, S. Moch, and J. Vermaseren, Nucl. Phys. B **691**, 129 (2004).

[2] M. Botje, http://www.nikef.nl/h24/qcdnum/index.html.

[3] R.S. Thorne and R.G. Roberts, Phys. Rev. D **57**, 6871 (1998).

[4] R.S. Thorne, Phys. Rev. D **73**, 054019 (2006).

[5] J. Campbell, K. Ellis, C. Williams, MCFM - Monte Carlo for FeMtobarn processes, a program description and the code are available via: http://mcfm.fnal.gov.

[6] Z. Nagy, NLOJet++, a program description and the code are available via: http://www.desy.de/∼znagy/Site/NLOJet++.html.

[7] S. Alekhin, OPENQCDRAD, a program description and the code are available via: http://www-zeuthen.desy.de/∼alekhin/OPENQCDRAD.

[8] S. Alekhin and S. Moch, Phys. Lett. B **699**, 345 (2011).

[9] T. Carli *et al.*, Eur. Phys. J C **66**, 503 (2010).

[10] D. Britzger, K. Rabbertz, F. Stober, and M. Wobisch, "New features in version 2 of the fastNLO project," in the proceedings of the XX International Workshop on Deep Inelastic Scattering (DIS12), 26–30th March 2012, hep-ph/1208.3641; http://fastnlo.hepforge.org/.

[11] M. Aliev *et al.*, Comput. Phys. Commun. **182**, 1034 (2011).

[12] R.D. Ball *et al.*, Nucl. Phys. B **855**, 608 (2012);R.D. Ball *et al.* (NNPDF Collaboration), Nucl. Phys. B **849**, 112 (2011).

[13] G. Watt and R. Thorne, J. High Energy Phys. **08**, 052 (2012).

[14] J. Bartels, K. Golec-Biernat, and H. Kowalski, Phys. Rev. D **66**, 014001 (2002).

[15] H. Abramowicz *et al.* (H1 and ZEUS Collaborations), Eur. Phys. J C **73**, 2311 (2013).

[16] F. Aaron *et al.* (H1 Collaboration), J. High Energy Phys. **09**, 061 (2012).

[17] Georges Aad *et al.* (ATLAS Collaboration), Phys. Rev. Lett. **109**, 012001 (2012).

[18] Georges Aad *et al.* (ATLAS Collaboration), Eur. Phys. J C **73**, 2509 (2013).

[19] CMS Collaboration, Technical Report No. CMS-PAS-SMP-12-028, CERN, Geneva, 2013.

[20] CMS Collaboration, Technical Report No. CMS-PAS-SMP-12-021, CERN, Geneva, 2013.

[21] J. L. Abelleira Fernandez *et al.* (LHeC Study Group), J. Phys. G. **39**, 075001 (2012).

Proton structure from multiparticle contribution to elastic pp-scattering at 7 TeV

I.M. Dremin

Lebedev Physical Institute, Moscow 119991, Russia

The parton content of protons gets strong peripheral contribution at 1 fm from multiparticle dynamics as revealed by the overlap function in the unitarity condition for elastic pp-scattering at 7 TeV.

It is well known that parton (quark, gluon) densities and the share of low-x partons rise with increasing energies of colliding hadrons. Less attention has been paid to the analysis of the spatial distribution of the parton content inside them and its evolution with energy. This can be done by studying the structure of the overlap function in the unitarity condition for the elastic scattering amplitude in the impact parameter representation at different energies of colliding protons. The very first analyses [1, 2, 3] have lead to extremely interesting conclusions about the increasing peripherality of protons within the rather narrow interval of ISR energies. Later, this was confirmed and strengthened at somewhat higher energies by the S$p\bar{p}$S data [4]. It was shown that while the increase of the overlap function at the proton periphery is quite modest in the ISR energy range (about 4%), it becomes much stronger (about 12%) if S$p\bar{p}$S energies are included. However, no sizable change of the proton blackness was noticed at small distances in this energy interval. The similar effect at HERA energies was discussed in [5] for the vector meson production process in the framework of the dipole-proton scattering model.

That is why we attempt to learn if peripheral regions of protons become even more active at LHC energies and the central region is activated as well. The striking, but not at all unexpected, result is that this increase persists and extends to smaller impact parameters now. It amounts to about 40% of edge corrections at distances about 1 fm. The main parton content in the overall region of inelastic collisions remains relatively constant and below the unitarity bound in the central region of impact parameters less than about 0.5 fm but also indicates some increase of opacity compared to lower energies.

We proceed by using the approach adopted in [3]. First of all, the TOTEM data on the differential cross section of elastic pp-scattering at 7

TeV [6] are fitted by the formula (1) for the elastic scattering amplitude $f(s,t)$ (which depends on the center-of-mass energy $\sqrt{s}$ and the transferred momentum $\sqrt{|t|}$) proposed in [7]:

$$f(s,t) = i\alpha[A_1 \exp(0.5b_1\alpha t) + A_2 \exp(0.5b_2\alpha t)] - iA_3 \exp(0.5b_3 t), \quad (1)$$

where $\alpha(s)$ is complex and is given by

$$\alpha(s) = [\sigma_t(s)/\sigma_t(23.5\text{GeV})](1 - i\rho_0(s)). \quad (2)$$

Even though this parametrization has no theoretical foundation, it provides in a wide energy interval good phenomenological fits of differential cross sections[1] defined as

$$\frac{d\sigma}{dt} = |f(s,t)|^2. \quad (3)$$

The normalization at the optical point is

$$\sigma_t(s) = \sqrt{16\pi}\text{Im}f(s,0). \quad (4)$$

We shall also use the ratio of the real to imaginary parts of the amplitude

$$\rho(s,t) = \frac{\text{Re}f(s,t)}{\text{Im}f(s,t)}. \quad (5)$$

The following values of the parameters have been fixed by the fit to the experimental points of the differential cross section at the energy 7 TeV in the range $0.0052 < |t| < 2.44$ GeV^2:

$$A_1^2 = 55.09\text{mb/GeV}^2, \quad A_2^2 = 3.46\text{mb/GeV}^2, \quad A_3^2 = 1.47\text{mb/GeV}^2,$$
$$b_1 = 8.31\text{GeV}^{-2}, \quad b_2 = 4.58\text{GeV}^{-2}, \quad b_3 = 4.70\text{GeV}^{-2}. \quad (6)$$

We have also used $\sigma_t(7\text{ TeV}) = 98.58$ mb and $\rho_0(7\text{ TeV}) = 0.14$. The normalization of $|f(s,t)|^2$ in mb/GeV^2 allows direct comparison with [3].

The good quality of the fit with these values is seen in Fig. 1. With some adjustment of parameters A_i, b_i, the fit is also satisfactory if one adopts the value of $\rho_0 = 0.107$ favored by the recent results of the TOTEM collaboration [13].

The real and imaginary parts of the amplitude are shown in Fig. 2. Each of them has one zero. The evolution of their ratio $\rho(s,t)$ with the transferred momentum t is mainly prescribed by the last term in this formula with the negative sign in front of it and small exponential b_3. It is also shown in Fig. 2. It is small and can be neglected everywhere except near the point where the imaginary part is equal to zero.

[1] There are many others (albeit with larger number of adjustable and hidden parameters) reviewed in [8] and recently published [9, 10, 11, 12].

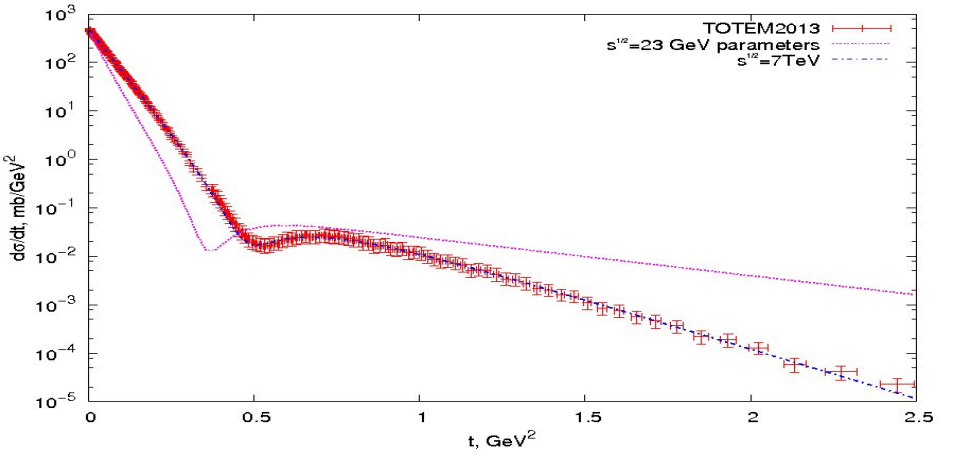

Fig. 1. Fit of the TOTEM data – dash-dotted curve. Dotted curve is calculated with parameters from [3] and with $\rho_0 = 0.14$.

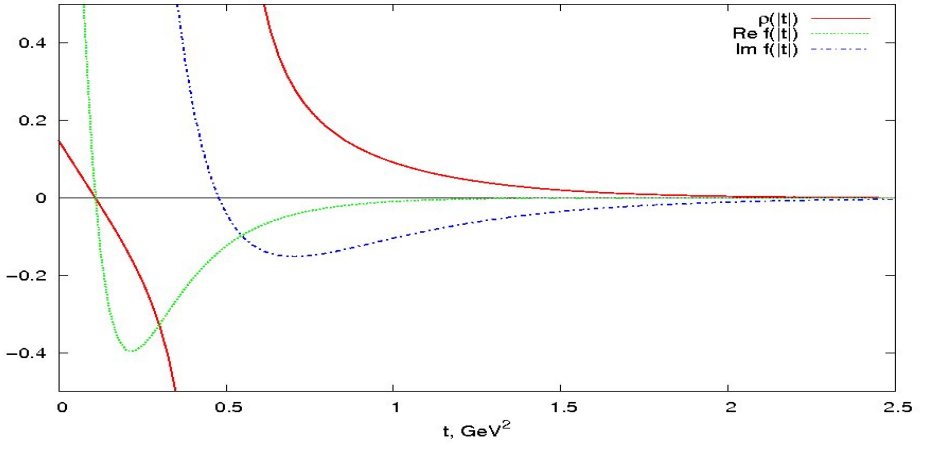

Fig. 2. Real (dotted curve) and imaginary (dash-dotted curve) parts of the amplitude and their ratio (solid curve).

The new feature seen in Fig. 2 is the difference in values of $\rho(s,t)$ in the Orear region for the two choices of ρ_0. It becomes of the order of 1 for $\rho_0 = 0.107$. Note that in both cases it strongly differs from its average value about -2 required by the fit according to the solution of the unitarity equation [14]. The solution [15] predicts the exponential of $\sqrt{|t|}$-behavior of the amplitude. It poses an interesting problem which has not yet been

resolved. This ratio can change the sign if more zeros of either imaginary or real parts of the amplitude appear. For example, this happens in the model of [11]. It incorporates phenomenologically the Orear type behavior of the amplitude at larger transferred momenta (albeit in a way somewhat different from [15]) and predicts two zeros of the real part. The ratio reaches large negative values at high transferred momenta. The somewhat smaller values at large $|t|$ are also predicted in the model using the inverse of polynomials [9] as described in [11]. The analysis of [11] clearly shows that the proper description of the amplitude at larger transferred momenta can change our conclusions about the behavior of this ratio there.

To reveal the space structure of proton interactions, the amplitude $f(s,t)$ must be rewritten in the impact parameter space. By applying the Fourier-Bessel transformation, we define the profile function

$$i\Gamma(s,b) = \frac{1}{\sqrt{\pi}} \int_0^\infty dqqf(s,t)J_0(qb). \tag{7}$$

Here, the variable b, called the impact parameter, describes the vector joining the centers of colliding protons at the moment of their collision, $q = \sqrt{-t}$, and J_0 is the Bessel function of zero order.

The amplitude $f(s,t)$ must satisfy the unitarity condition. If written in the impact parameter representation (7) it is

$$2\mathrm{Re}\Gamma(s,b) = |\Gamma(s,b)|^2 + G(s,b), \tag{8}$$

where G is called the overlap function in the impact parameter space.

The smallness of the real part of $f(t)$ corresponding to small $\mathrm{Im}\Gamma(s,b)$ implies that one can compute G approximately as

$$G(s,b) \approx 2\mathrm{Re}\Gamma(s,b) - (\mathrm{Re}\Gamma(s,b))^2. \tag{9}$$

The physics meaning of these relations is very simple. The overlap function G describes the kinematical overlap of two cones filled in by the inelastically produced secondary particles in the momentum space expressed in terms of the proton structure at a given impact parameter b. In other words, it corresponds to the particle distribution $d\sigma/db$ in the impact parameter space. One may treat it as a parton distribution if one-to-one correspondence of particles and partons is assumed.

The overlap function at 7 TeV has a form shown in Fig. 3 by the upper dash-dotted curve. Its dependence on $\rho(s,0)$ is so weak that can be neglected. However, as we see, it strongly differs from the corresponding function at ISR energy 23.5 GeV (shown by the lower solid curve), especially at the very edge of the distribution. The overlap function at 7 TeV declines steeply but there is no sharp cutoff at large impact parameters. At $b = 0$,

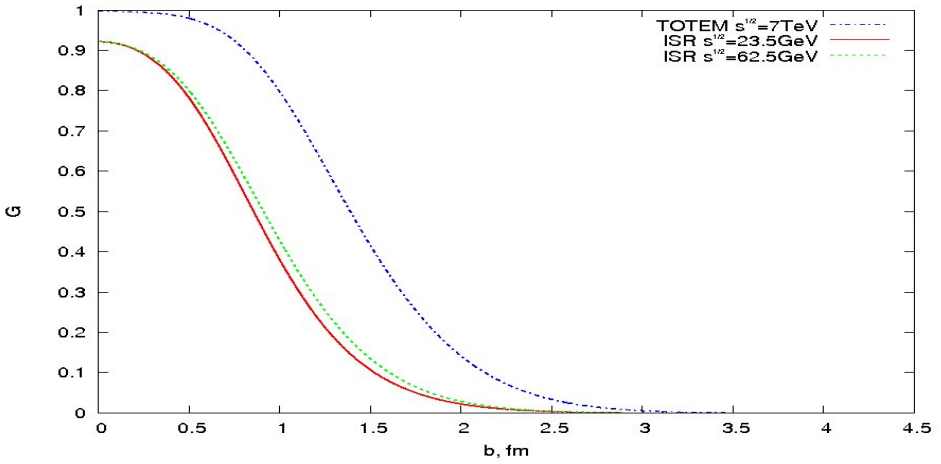

Fig. 3. The overlap functions at 23.5 GeV (solid curve), 62.5 GeV (dotted curve) and 7 TeV (dash-dotted curve).

it approaches the unitarity limit corresponding to the complete blackness. This is a clear manifestation of the parton saturation effect.

The difference between the two functions $\Delta G(b) = G(s_1, b) - G(s_2, b)$ ($\sqrt{s_1} =$ 7 TeV, $\sqrt{s_2} = 23.5$ GeV) results because of the increase of the elastic cross section and shrinkage of the diffraction cone with energy. In other words, it demonstrates the increase of the opacity since the ratio σ_{el}/σ_t increases also, and it is proportional to the opacity.

In Fig. 4, we demonstrate the difference between these two distributions (the upper curve). It is mainly concentrated at the periphery of the proton at the distance about 1 fm. This feature is stable against the variations of ρ_0. It shows that, at higher energies, the peripheral region becomes more populated by partons, and they play more active role in particle production.

It is tempting to ascribe the peripheral nature of this effect to two features of inelastic processes observed already at LHC. First, the collisions with impact parameters about 1 fm lead to the almond-shaped overlap region. Therefore, due to increase of the parton density they become responsible for the ridge-effect visible in high multiplicity pp-processes at LHC but not observed at lower energies. Second, the more peripheral collisions with larger impact parameters would lead to strong increase of the cross section of the inelastic diffraction with large masses and high multiplicities which can hardly be separated by the gap criteria from the minimum bias events. This is especially interesting because the cross section of the low-mass diffraction is rather small at 7 TeV [16] and surprisingly close to its values at ISR energies. The stronger absorption in the peripheral region at

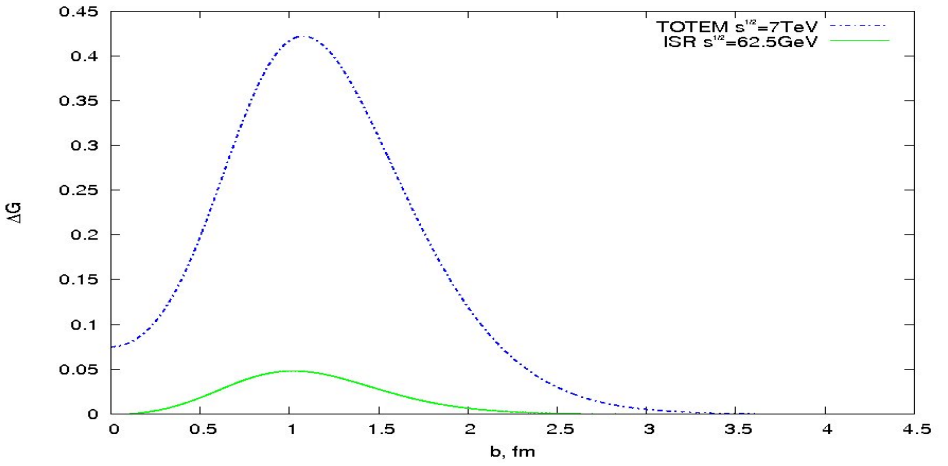

Fig. 4. The difference between the overlap functions. Dash-dotted curve is for 7 TeV and 23.5 GeV energies, solid curve is for 62.5 GeV and 23.5 GeV energies. Conclusion: The parton density at the periphery increases strongly!

7 TeV results in the suppression of the low-mass inelastic diffraction processes. It looks as if it is necessary to include the states of the continuum spectrum beside the discrete bare eigenstates in the traditional approach [17].

We note that the Regge-type models of inelastic diffraction [18] do not agree with the observed decrease below 1 at 7 TeV of the parameter $Z = 4\pi B/\sigma_t$ studied in [8] because they predict that this parameter is equal to $1 + \sigma_{in}^D/\sigma_{el}$ greater than 1 (where σ_{in}^D is the cross section of the low-mass inelastic diffraction). It has been pointed out in [15] that this parameter defines the slope of $d\sigma/dt$ beyond the diffraction cone in the Orear region. Its further decrease with energy would result [19] in first signatures of the approach to the black disk limit to appear just in there.

Another new feature, seen in Fig. 4, is the quite large (about 0.08) value of $\Delta G(b)$ at small impact parameters that reveals a stronger blackness of the disk at higher energies and is related to the rise of the cross section of the main bulk of inelastic processes. No signs of this effect have been found at lower energies. These observations are tightly related to the visible violation of geometric scaling even in the diffraction cone at LHC energies [20] because of the dual correspondence of the transferred momenta t and the impact parameters b. Probably, they correspond also to disagreement between experimental data at 7 TeV and predictions of Monte Carlo models seen in high multiplicity events [21].

In the same Figure, the lower curve corresponds to the similar (albeit

much smaller!) difference $\Delta G(b)$ within the quite narrow ISR energy interval (23.5 - 62.5 GeV). It was stressed in [3] that this difference is negligibly small at low impact parameters while showing some statistically significant excess about 4% at the periphery[2].

Comparison of the curves in Fig. 4 leads to the conclusion that the size of the proton as well as its blackness increase with energy. The protons become more black both in the central region, where they almost reach the saturation of the unitarity condition, and, especially, at the periphery, where the parton density strongly increases. Multiparticle dynamics is in charge of these effects.

References

[1] R. Henzi and P. Valin, Phys. Lett. B **48**, 119 (1974).

[2] F.S. Henyey, R.H. Tuan, and G.L. Kane, Nucl. Phys. B **70**,445 (1974).

[3] U. Amaldi and K.R. Schubert, Nucl. Phys. B **166**, 301 (1980).

[4] U. Amaldi, arXiv:1206.3954.

[5] S. Munier, A.M. Stasto, and A.H. Mueller, Nucl. Phys. B **603**, 427 (2001).

[6] G. Antchev *et al.* (TOTEM Collaboration), Europhys. Lett. **101**, 21004 (2013).

[7] E. Nagy *et al.*, Nucl. Phys. B **150**, 221 (1979).

[8] I.M. Dremin, Physics-Uspekhi **56**, 3 (2013).

[9] C. Bourrely, J.M. Myers, J. Soffer, and T.T. Wu, Phys. Rev. D **85**, 096009 (2012).

[10] D.A. Fagundes, E.G.S. Luna, M.J. Menon, and A.A. Natale, Nucl. Phys. A **886**, 48 (2012).

[11] A.K. Kohara, F. Ferreira, and T. Kodama, Eur. Phys. J. C **73**, 2326 (2013).

[12] A.K. Kohara, F. Ferreira, and T. Kodama, Phys. Rev. D **87**, 054024 (2013).

[13] K. Österberg, talk at EPS-HEP 2013 conference, Stockholm.

[14] I.M. Dremin and V.A. Nechitailo, Phys. Rev. D **85**, 074009 (2012).

[15] I.V. Andreev and I.M. Dremin, ZhETF Pis'ma **6**, 810 (1967).

[16] G. Antchev *et al.* (TOTEM Collaboration), Europhys. Lett. **101**, 21003 (2013).

[17] M.L. Good and W.D. Walker, Phys. Rev. **120**, 1854 (1960).

[18] A.B. Kaidalov, Phys. Rep. **50**, 157 (1979).

[19] I.M. Dremin, Nucl. Phys. A **888**, 1 (2012).

[20] I.M. Dremin, V.A. Nechitailo, Phys. Lett. B **720**, 177 (2013).

[21] S. Chatrchyan *et al.* (CMS Collaboration), Eur. Phys. J. C **73**, 2674 (2013).

[2] This curve differs slightly from that of [3] because we did not use the interpolation procedure adopted there but subtracted directly two overlap functions at 62.5 GeV and 23.5 GeV.

Diffraction at the LHC

M. Csanád

Eötvös University, Budapest, Hungary

Proton-proton collisions at the LHC can be classified as elastic, non-diffractive, and diffractive. In this paper we discuss various measurements of these above processes at various LHC experiments. We report about the total proton-proton cross-section measurements, about the analysis of diffractive events and also about the pseudorapidity distribution in inelastic events.

1. Introduction

High energy proton-proton collisions are observed at the Large Hadron Collider of CERN. A large fraction of these collisions are events where color degrees of freedom are exchanged between the two protons, and new particles are created throughout the phase-space spanned by longitudinal pseudorapidity, defined as $\eta = 0.5 \ln[(p+p_z)/(p-p_z)]$ and azimuth angle defined as $\phi = \arctan(p_y/p_x)$. However, a substantial fraction of the total pp cross section is due to diffractive processes, where protons remain intact or dissociate into a mixture of particles with a low diffractive mass (compared to the original energy of the proton). These events can be characterized by a colorless momentum exchange of the two protons, via the Pomeron, carrying the quantum numbers of the vacuum. A significant number of elastic events are also observed at the LHC, where Pomeron exchange governs the deflection of the protons, both of which remain intact, and no new particles are created (i.e. the kinetic energy is retained in the collision).

A summary of diffractive p+p event classes is shown in Fig. 1. The particles in the final state are separated by a large ($\gtrsim 3$) rapidity gap $\Delta\eta$[1] The rapidity gap size is related to the diffractive mass of the dissociated system, M_X. In case of single diffraction, $\Delta\eta \approx \ln \xi$, with $\xi = \Delta p/p$, being the momentum loss of the proton, also equal $\xi = M_X^2/s$ where $s = (p_1 + p_2)^2$, i.e. the total center of mass energy squared. In order to experimentally classify these events, one needs to identify the rapidity gap in particle production, with detectors covering a large rapidity region.

[1] E.g. in single diffraction, a rapidity gap means no particles in a pseudorapidity region defined by $\Delta\eta$ between the leading proton and the diffractive system.

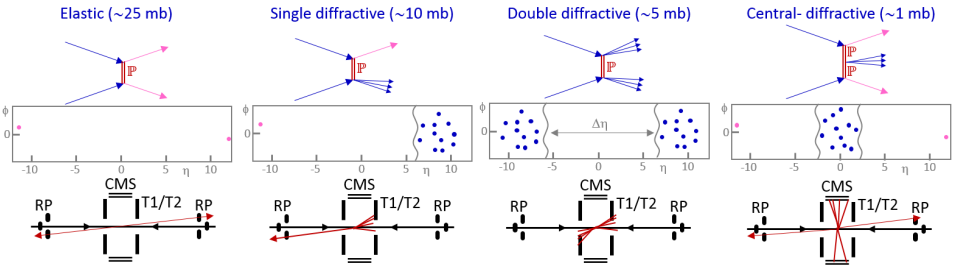

Fig. 1. Event classification in the TOTEM+CMS detector system. In elastic pp events, only momentum is exchanged (by colorless particles), while in diffractive events, particles are produced either through the dissociation of one or both of the protons, or through the interaction of the exchanged Pomeron.

The LHC TOTEM experiment detects the leading protons with a system of Roman Pots (RP). There are four RP stations, ±147 and ±220 meters from the Interaction Point (IP5), with two units at each location. A unit consists of two vertical and one horizontal edgeless Si strip detector [1], reaching to a distance of a few millimeters from the beam. RP's allow TOTEM to track protons which were deflected by a few microradians only (in elastic, single diffractive or central diffractive events). Two tracking detectors at a smaller pseudorapidity allow TOTEM to track almost the entirety of diffractive dissociation. These are the T1 and T2 telescopes, covering $3.1 < |\eta| < 4.7$ and $5.3 < |\eta| < 6.5$ respectively.

Located also at IP5, CMS also has a set of forward calorimeters which can be used in observing single, double or central diffractive events. The Hadron Forward calorimeter (HF) is at $3< |\eta| <5$, while the CASTOR calorimeter is located only on one side of the IP, at $-6.6 < |\eta| < -5.2$.

At ATLAS, there are forward calorimeters outside the tracking system. A highly segmented electromagnetic (EM) liquid argon sampling calorimeter covers the range $|\eta| < 3.2$. The Hadronic End-cap Calorimeter (HEC) covers $1.5 < |\eta| < 3.2$, while the Forward Calorimeter (FCal) covers $3.1 < |\eta| < 4.9$. For triggering, ATLAS uses Minimum Bias Trigger Scintillators (MBTS, $2.1 < |\eta| < 3.8$), placed on the inner face of the HEC. For the analysis of rapidity gaps, only calorimeter information is used in the region $2.5 < |\eta| < 4.9$, beyond the acceptance of the inner detector.

2. Cross-section measurements

Cross-section of pp collisions is a particularly interesting, since the total cross-section rises with increasing total center of mass energy ($\sqrt{s}$), which

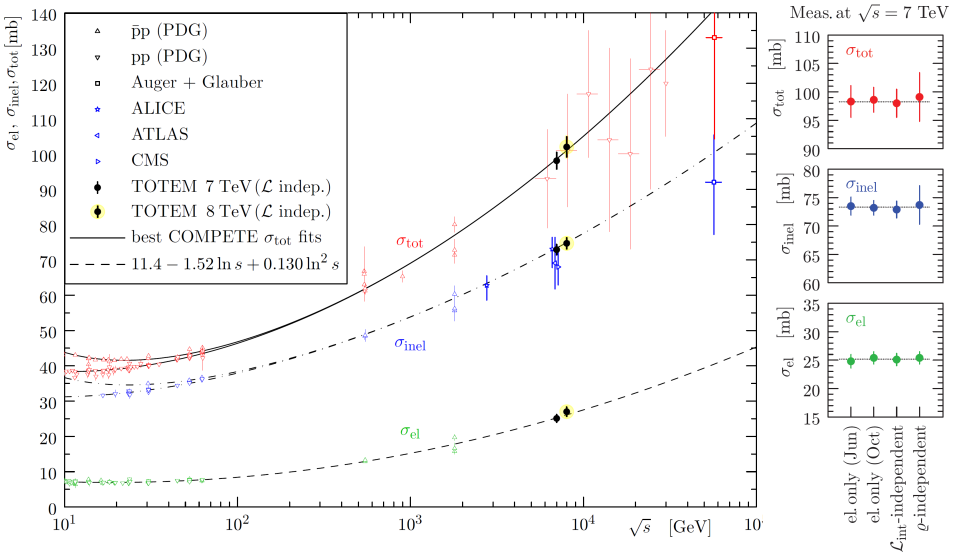

Fig. 2. TOTEM luminosity-independent p+p cross-section measurements with world cross-section data as a function of $\sqrt{s}$. On the right, comparison of the TOTEM measurements obtained with different analysis methods are shown.

can only be explained in terms of the Regge theory with the exchange of Pomerons. Measurements of $\sigma_{\rm tot}$ at LHC energies were available only in high uncertainty cosmic-ray data. TOTEM has now measured the total, elastic and inelastic pp cross-sections with a very high precision, with several independent methods (see Fig. 2 and Refs. [2, 3, 4, 5, 6]):

a) The basic method is to measure the number of elastic and inelastic events ($N_{\rm el,inel}$), and using luminosity $\mathcal{L}$[2]: $\sigma_{\rm tot} = (N_{\rm el} + N_{\rm inel})/\mathcal{L}$.

b) There is also a method which does not require the knowledge of the number of inelastic events, but is based instead of the optical theorem: $\sigma^2_{\rm tot} = 16\pi(\hbar c)^2/(1+\rho^2) \times \mathcal{L}^{-1} \times dN_{\rm el}/dt|_{t=0}$, where $-t$ is the momentum exchange squared, while ρ is the real over imaginary part of the forward scattering amplitude.

c) The third, luminosity independent method can be summarized as $\sigma_{\rm tot} = 16\pi(\hbar c)^2/(1+\rho^2) \times (dN_{\rm el}/dt|_{t=0})/(N_{\rm el} + N_{\rm inel})$.

As described in the previous paragraph, for the total cross-section measurement, differential measurements of $d\sigma/dt$ are needed at small t values. The minimum reachable t by TOTEM depends on the accelerator optics (described by β^*, the betatron amplitude taken at the interaction point).

[2] Luminosity is the number of interactions per effective area and per second

If $\beta^* = 3.5$ m, the range of $|t| > 0.36$ GeV^2 can be measured, while with a special, $\beta^* = 90$ m optics, ranges of $|t| > 0.005$ GeV^2 can be seen. With these measurements [3, 7], extrapolation to $t \to 0$ is possible. TOTEM has performed also a measurement at $\beta^* = 1000$ m, which allowed to reach $|t| = 6 \cdot 10^{-4}$ GeV^2 where the Coulomb-nuclear interference can be studied [8].

In ATLAS, inelastic cross-sections are measured as a function of the accessible ξ range [9]. Determined by the η acceptance, a $\xi > 5 \cdot 10^{-6}$ range is accessible. Event selection is based on triggering via the MBTS. This way a measurement with the integrated luminosity of 20.3 μb was performed, and an inelastic cross-section of $60.3 \pm 0.5(\text{syst}) \pm 2.1(\text{lumi})$ mb was measured [10], for $\xi > 5 \cdot 10^{-6}$, corresponding to the diffractive mass being larger than 15.7 GeV. A dependence on ξ_{cut} has also been analyzed, from which (via extrapolation) $\sigma_{\text{inel}} = 69.4 \pm 2.4(\text{exp}) \pm 6.9(\text{extr})$ mb was extracted [9]. Measurement of total inelastic cross-sections was also performed at ALICE [11]. The 2.76 TeV result is $62.8^{+2.4}_{-4.0}(\text{model}) \pm 1.2(\text{lumi})$, while the 7 TeV result, as shown in Fig. 2, is $73.2^{+2.0}_{-4.6}(\text{model}) \pm 2.6(\text{lumi})$. For $\xi > 5 \cdot 10^{-6}$, ALICE obtained $62.1^{+1.0}_{-0.9}(\text{model}) \pm 2.2(\text{lumi})$. The results of all LHC experiments are consistent with each other.

3. Single diffraction

TOTEM measures single diffractive events with a large rapidity gap between the outgoing proton and the dissociative hadronic system [12]. The final goal of this preliminary measurement is to determine the integrated cross-section and the differential $d\sigma/dt$ distribution in each mass range. Event selection is done via the RP's and the Telescopes, requiring one proton and a rapidity gap in T2 on the side of the proton, and tracks in the opposite side. The correspondence of the gap size to the diffractive mass is given in Table 1. Raw rates have to be corrected for efficiency and acceptance, and backgrounds have to be subtracted. The main background source is the pileup of a proton in RP from the beam halo with an independent non-diffractive event in T2. Preliminary results in the $3.4 - 1100$ GeV diffractive mass region indicate $\sigma_{SD} = 6.5 \pm 1.3$ mb for both arms, while differential cross-section exponential slopes are estimated to be $B = 10.1, 8.5$ and 6.8 GeV^{-2} for the first three mass ranges, respectively.

CMS has measured single diffractive dijet production [13], where one of the protons remains intact or is excited into a low-mass state, while the other participates in a hard scattering with a Pomeron from the non-dissociating proton. CMS measures the cross section for dijet production as a function of an evaluation of ξ (CMS has no direct access to the momentum loss of the undissociated proton), based on events with at least two jets with

Table 1. Single diffraction event classes in TOTEM

Event class	Event topology	Mass range	Mom. loss (ξ)
Low mass	RP, opposite T2	3.4 – 8 GeV	$2 \cdot 10^{-7}$ – 10^{-6}
Medium mass	RP, opp. T2, opp. T1	8 – 350 GeV	10^{-6} – 0.25%
High mass	RP, opp. T2, same T1	0.35 – 1.1 TeV	0.25% – 2.5%
Very high mass	RP, opp. T2, same T2	1.1 TeV –	2.5% –

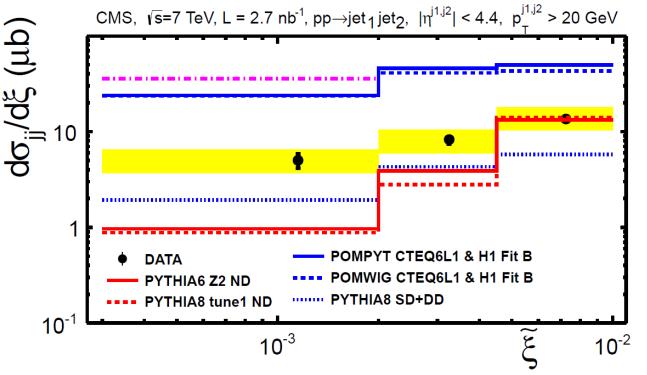

Fig. 3. The differential cross section for inclusive dijet production from Ref. [13]. The points are plotted at the center of the bins. The error bars indicate the statistical uncertainty and the band represents the systematic uncertainties added in quadrature. See text and Ref. [13] for details.

a transverse momentum of $p_t^{j1,j2} > 20$ GeV in the pseudorapidity region $|\eta^{j1,j2}| < 4.4$. The results are compared to diffractive and non-diffractive MC models (see Fig. 3). The low-ξ data show a significant contribution from diffractive dijet production, observed for the first time at the LHC. POMPYT and POMWIG, based on dPDFs from HERA, overestimate the measured cross section by a factor of 5. This factor can be interpreted as the effect of the rapidity gap survival probability.

4. Double and central diffraction

TOTEM has measured the double diffractive cross-section in the very forward region at 7 TeV. With the T1 and T2 telescopes a clean sample of double diffractive events could be extracted. The event topology was defined as no tracks in the T1 detectors (to ensure that no particles are present at low η), and valid tracks in both T2 arms, which selected events that have

Table 2. Double diffractive cross-section measurements in the forward region. Both visible and true η_{min} corrected cross-sections are given. There were two subregions defined; (1): $4.7 < |\eta|_{\min} < 5.9$ and (2): $5.9 < |\eta|_{\min} < 6.5$. D_{ij} requires then $|\eta|_{\min}$ to be in region i on the + side and in region j on the − side.

σ_{DD} [μb]	Total	D_{11}	D_{22}	D_{12}	D_{21}
Visible	131±22	58±14	20±8	31±5	34±5
True η_{min}	116±25	65±20	12±5	26±5	27±5
Pythia true η_{min}	159	70	17	36	36
Phojet true η_{min}	101	44	12	23	23

two diffractive systems having particles with a minimal pseudorapidity in the $4.7 < |\eta| < 6.5$ range. These events make up only roughly 3% of the total double diffractive cross-section, they however provide a pure selection of such events. The cross-section in the total region was estimated to be $\sigma_{\rm DD} = (116 \pm 25)\ \mu$b [14]. To access further experimental details, the above η range was divided into two sub-regions on each side, by cutting at $|\eta| = 5.9$. In each measurement category, the selected sample had to be corrected for trigger-efficiency, pile-up and T1 multiplicity, and also the background had to be estimated. The visible cross-section was then determined by correcting the raw rate for acceptance and detection efficiency. Lastly, the visible cross-section had to be corrected so that both diffractive systems have a minimal pseudorapidity in the $4.7 < |\eta| < 6.5$ range. See results in Table 2. In order to determine the background, three event classes were considered: non-diffractive (ND), single diffractive (SD) and central diffractive (CD). A data-driven background estimation was used, where the values of the background estimates were calculated iteratively (see details in Ref. [14]).

CMS has measured single and double diffractive events with the experimental topologies of a large rapidity gap [15]. Event types were defined as SD1 (gap on + side), SD2 (gap on − side) and DD (central gap). Both SD1 and SD2 event topologies (defined as $\eta_{\min} > -1$ and $\eta_{\max} < 1$, respectively) contain SD and DD events, with the second hadronic system being outside the central region. For the SD2 topology, CASTOR was used for tagging to select a DD enhanced event sample and to calculate SD and DD cross-section, using a $\Delta\eta^0 > 3$ selection. Since there is no similar detector on the + side, the SD1 sample was treated as a control sample. The differential SD cross-section was then measured as a function of ξ, in the $-5.5 < \log_{10}\xi < -2.5$ range, while the DD cross-section was measured in events in which a hadronic system is detected in the central arm ($12 < M_X < 394$ GeV) and the other in CASTOR ($3.2 < M_Y < 12$ GeV), in the $\xi_X = M_X^2/s$ range of $-5.5 < \log_{10}\xi < -2.5$. The DD cross-section was

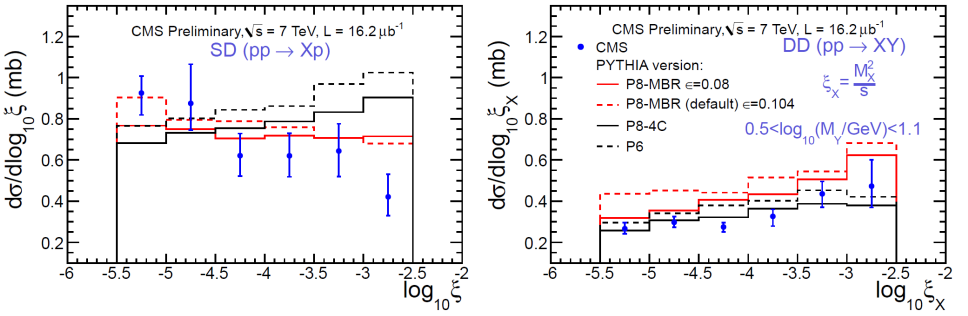

Fig. 4. The SD (left) and DD (right) cross sections as a function of ξ, compared to several MC predictions.

also measured differentially as a function of the central pseudorapidity gap $\Delta\eta$. Results were compared to predictions of theoretical models, as shown in Fig. 4 (see details in Ref. [15]). In total, a $\sigma_{SD}^{\rm vis} = 4.27 \pm 0.04({\rm stat.})^{+0.65}_{-0.58}({\rm syst.})$ mb integrated cross-section was measured (multiplied by two to account for both side processes). Note also, that for all the above event types, the forward rapidity gap cross-section $d\sigma/d\Delta\eta^F$ was measured both at CMS and at ATLAS. At small $\Delta\eta^F$, the cross-sections are dominated by non-diffractive events, exponentially suppressed as $\Delta\eta^F$ increases. For $\Delta\eta^F > 3$, cross-section per unit rapidity gap weakly changes with $\Delta\eta^F$, taking the value of $d\sigma/\Delta\eta^F \approx 1.0$ mb [9]. The large η range comparison between data and MCs allows to tune the relative fraction of the different components in the models. CMS extends the ATLAS measurement by 0.4 unit of rapidity gap size, and the two measurements agree within uncertainties [9, 15].

Central diffractive events are also measured at TOTEM, defined by the event topology of protons in both RP arms and tracks in the T2 telescopes. The background of this selection is mainly elastic events and inelastic events with pile-up of beam-halo. Since during data taking the RP distance to the beam was greater than $11\sigma_{\rm beam}$, it was found that beam halo contribution is negligible. Elastic event events can rejected via anti-elastic cuts in the RP's, or by selecting non-elastic topologies (e.g. protons being in the top RP's on both sides). Single-arm differential event rate was then measured and a preliminary exponential slope parameter of $B = -7.8 \pm 1.4$ GeV^2 was extracted via a MC fit on the t_y distribution. The preliminary cross-section estimate of TOTEM is $\sigma_{CD} \approx 1$ mb. CMS and TOTEM are also working on a common central diffraction measurement, where the diffractive central mass can be measured by both experiments: using the proton tracks by TOTEM (via $M_X^2 = \xi_1\xi_2 s$) and directly by CMS. This will provide a result with an unprecedented rapidity coverage.

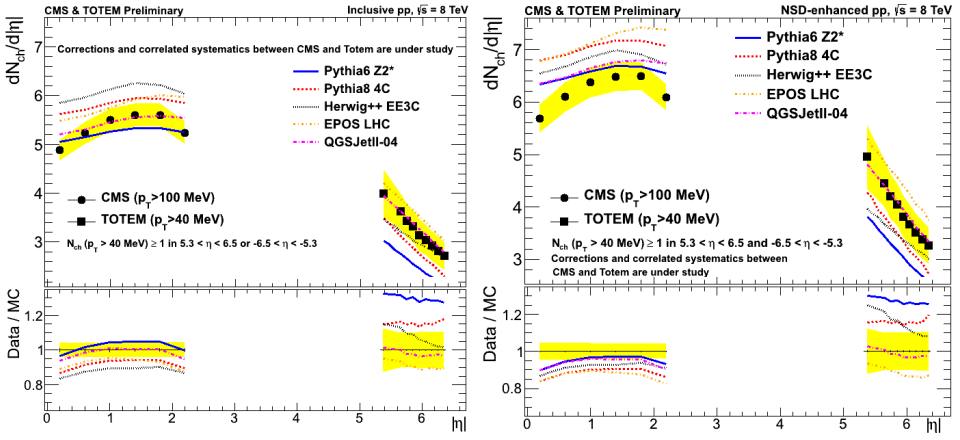

Fig. 5. Charged particle pseudorapidity density distribution as measured by the CMS tracker in the central region and TOTEM T2 in the forward region for the same events with one charged particle with $p_t > 40$ MeV/c, for both the inclusive and the non-single diffractive enhanced sample, with comparisons to various MC tunes (see details in [16]).

5. Inelastic pseudorapidity distributions

A measurement of the pseudorapidity density ($\mathrm{d}N_{ch}/\mathrm{d}\eta$) of forward charged particles in inelastic events was also performed by TOTEM with the T2 detectors [17]. The measurement refers to events with at least one charged particle with $p_t \geq 40$ MeV/c and with a mean lifetime $\tau > 0.3 \times 10^{-10}$ s, directly produced in pp interactions or in subsequent decays of particles having a shorter lifetime. Results of this measurement were compared to MC expectations: none of the theoretical models has been found to fully describe the data. The cosmic ray MC generators (e.g. QGSJETII, see a review of event generators in Ref. [18]) show a better agreement for the slope. The TOTEM experiment has also measured the pseudorapidity density of charged particles with $p_t \geq 40$ MeV/c in pp collisions at 8 TeV for $5.3 < |\eta| < 6.4$ in a low intensity run with common data taking with the CMS experiment [16, 19]. This represents the extension of the analogous measurement described in the beginning of this paragraph. The analysis was performed on 3 different events categories: an inclusive one with at least one charged particle in either $-6.5 < \eta < 5.3$ or $5.3 < \eta < 6.5$, a non-single diffractive enhanced one with at least one charged particle in both $-6.5 < \eta < 5.3$ and $5.3 < \eta < 6.5$ and a single diffractive enhanced one with at least one charged particle in $-6.5 < \eta < 5.3$ and none in $5.3 < \eta < 6.5$ or vice-versa. A minimum bias trigger was provided by the TOTEM T2 tele-

scope and contributed to the CMS Global Trigger decision to initiate the simultaneous read out of both CMS and TOTEM detectors. The event data from TOTEM and CMS were then combined offline in a common data analysis activity. The visible cross section for events triggered by T2 has been estimated to be about 95% of the total inelastic cross section: more than 99% of all non-diffractive events and all single and double diffractive events having at least one diffractive mass larger than ≈ 3.6 GeV/c^2. See results in Fig. 5, and details about the compared event generators in Refs. [16, 19].

Acknowledgments

M.C. would like to thank the Organizers of ISMD 2013 for organizing an inspiring conference. The author is also thankful for Marco Bozzo and the TOTEM Editorial Board for their help in improving the manuscript. The work presented in this paper was done by the TOTEM, CMS and ATLAS collaborations. The participation of the author at ISMD was supported by the Hungarian OTKA grant NK 101438.

References

[1] G. Ruggiero *et al.*, Nucl. Instrum. Meth. A **604**, 242 (2009).
[2] G. Antchev *et al.*, Europhys. Lett. **96**, 21002 (2011).
[3] G. Antchev *et al.*, Europhys. Lett. **101**, 21002 (2013).
[4] G. Antchev *et al.*, Europhys. Lett. **101**, 21004 (2013).
[5] G. Antchev *et al.*, Europhys. Lett. **101**, 21003 (2013).
[6] G. Antchev *et al.*, Phys. Rev. Lett. **111**, 012001 (2013).
[7] G. Antchev *et al.*, Europhys. Lett. **95**, 41001 (2011).
[8] J. Kaspar, arXiv:1310.3178.
[9] G. Aad *et al.*, Eur. Phys. J. C **72**, 1926 (2012).
[10] G. Aad *et al.*, Nature Commun. **2**, 463 (2011).
[11] B. I. Abelev *et al.*, Eur. Phys. J. C **73**, 2456 (2013).
[12] F. Oljemark, arXiv:1310.4305.
[13] S. Chatrchyan *et al.*, Phys. Rev. D **87**, 012006 (2013).
[14] G. Antchev *et al.*, arXiv:1308.6722.
[15] CMS Collaboration, CMS-PAS-FSQ-12-005 (unpublished).
[16] TOTEM Collaboration, CERN-TOTEM-NOTE-2013-001 (unpublished).
[17] G. Antchev *et al.*, Europhys. Lett. **98**, 31002 (2012).
[18] D. d'Enterria *et al.*, Astropart. Phys. **35**, 98 (2011).
[19] CMS Collaboration, CMS-PAS-FSQ-12-026 (unpublished).

Central exclusive production and the Durham diffractive program

L.A. Harland–Lang†, V.A. Khoze

Institute for Particle Physics Phenomenology, University of Durham, Durham, DH1 3LE

M.G. Ryskin

Petersburg Nuclear Physics Institute, NRC Kurchatov Institute, Gatchina, St. Petersburg, 188300, Russia

Recent results in central exclusive production within the Durham model are presented. A wide range of processes are considered, and their theoretical and phenomenological interest is discussed.

1. Introduction

Central exclusive production (CEP) processes of the type

$$pp(\bar{p}) \to p + X + p(\bar{p}) \,, \tag{1}$$

can significantly extend the physics program at hadron colliders. Here X represents a system of invariant mass M_X, and the '+' signs denote the presence of large rapidity gaps. Such reactions represent an experimentally very clean signal and provide a very promising way to investigate both QCD dynamics and new physics in hadron collisions. The study of such processes is becoming particularly topical at the current time due to the range of exclusive measurements proposed and underway at the LHC; as such this forms an important part of the LHC working group on forward physics and diffraction, see for example [1].

We will present here the latest phenomenological results with the so–called 'Durham' model of CEP, see for example [2] for an early paper, and [3] for a more recent discussion. We will discuss some of the most topical and interesting of such exclusive processes, considering both their theoretical interest and the existing measurements and future experimental possibilities at the LHC and elsewhere.

† Speaker

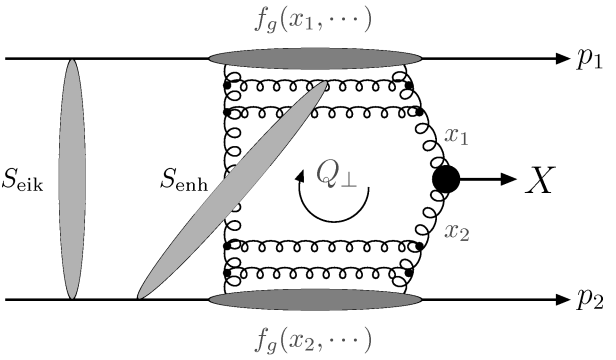

Fig. 1. The perturbative mechanism for the exclusive process $pp \to p + X + p$, with the eikonal and enhanced survival factors shown symbolically.

2. The Durham Model

The perturbative mechanism for CEP, is shown schematically in Fig. 1. The subprocess $gg \to X$ initiated by gluon–gluon fusion and the second t–channel gluon needed to screen the color flow across the rapidity gap intervals. It is given by

$$T \;=\; \pi^2 \int \frac{d^2\mathbf{Q}_\perp \,\mathcal{M}}{\mathbf{Q}_\perp^2 (\mathbf{Q}_\perp - \mathbf{p}_{1_\perp})^2 (\mathbf{Q}_\perp + \mathbf{p}_{2_\perp})^2} \times f_g(x_1, x_1', Q_1^2, \mu^2; t_1) f_g(x_2, x_2', Q_2^2, \mu^2; t_2) \;, \qquad (2)$$

where the 'skewed' PDFs f_g couple the t–channel gg state to the proton

$$f_g(x, x', Q^2, \mu^2) = \frac{\partial}{\partial \ln(\mathbf{Q}_\perp^2)} \left[R_g \left(x g(x, Q^2) \right) \sqrt{T(\mathbf{Q}_\perp, \mu^2)} \right] \;, \qquad (3)$$

where $\mu \sim M_X$. A crucial ingredient in the calculation of this amplitude is the correct inclusion of the Sudakov factor $T(\mathbf{Q}_\perp, \mu^2)$, representing the probability of no gluon emission from the fusing t–channel gluons. The form that this factor takes in the amplitude is largely dictated by requiring all leading and next–to–leading logarithms in $M_X/Q_\perp$ to be correctly resummed, see for example [4] for a detailed discussion of this. In this way a reliable result, which is largely insensitive to the region of low gluon transverse momentum, $Q_\perp$, is achieved. In the kinematic regime relevant to CEP, the skewed PDFs are related via Eq. (3) to the conventional PDFs, with the R_g factor encoding the degree to which these differ; typically we have $R_g \sim 1.2 - 1.4$. In [5] the importance of including the Q^2 dependence of this factor (which was commonly ignored in previous calculations) was highlighted, and a simple technique for doing so was demonstrated.

While the discussion above concerns the hard process, that is the probability for producing such an exclusive configuration in a short–distance interaction, we must in general also include the possibility that the protons may interact quite independently of this hard scatter, that is via non-perturbative rescattering, which may also lead to the production of additional particles. The probability that this does not occur is known as the (eikonal) survival factor $\left\langle S^2_{\rm eik}\right\rangle$, and it must be modeled phenomenologically and fitted to the available soft hadronic data. An up–to–date model, including the $\sqrt{s} = 7$ TeV TOTEM measurements is found in [6]: typically this suppression is sizable, with $\left\langle S^2_{\rm eik}\right\rangle \sim 1$ %. An additional factor due to the rescattering of the protons and the partons which initiate the hard process, the so–called 'enhanced' survival factor $\left\langle S^2_{\rm enh}\right\rangle$, should also be included, although the suppression due to this is not nearly as large, see [7].

A final important feature of interest in this production mechanism is the dynamical selection rule which operates for CEP. In particular, in the limit that the outgoing protons scatter with zero $p_\perp$, the only transverse momentum of the fusing gluons is provided by the loop momentum $Q_\perp$, and thus the gluons must have equal and opposite transverse momenta. It can readily be shown that, in terms of the $gg \to X$ production subprocess, where for $Q^2_\perp \ll M^2_X$ the gluons are quasi–on–shell, this translates into a correlation between the helicities of the gluons, with only an even parity combination of $J_z = 0$ (i.e. $++$ or $--$ along the gg axis) helicities contributing. This is in complete contrast to the usual inclusive case, where all gluon helicities contribute, and as we will see leads to some very non–trivial predictions. In general, the outgoing protons may have some small non–zero $p_\perp$, and so this selection rule is only approximate, but an explicit calculation shows that the production non–$J^P_z = 0^+$ states are strongly suppressed by about two orders of magnitude.

Finally, we note that from the experimental point of view the best way to select exclusive events is to actually measure the outgoing intact protons via proton tagging detectors installed near to the beam pipe (such detectors are proposed at the LHC, see e.g. [8] and references therein). However, if this is not possible, dominantly exclusive data can also be selected by simply vetoing on additional hadronic activity (i.e. other than the object X of interest) over a large enough rapidity region. Although here there will be some background from the case that one or both proton dissociates, if the rapidity region is large enough this will be small.

3. Heavy quarkonium production

The first cross section predictions for the CEP of χ_{q0} quarkonium ($q = c, b$) were presented in [9], while in [10] this was extended to include all three

$J = 0, 1, 2$ spin states. Exclusively, we have the non–trivial prediction that the χ_{c0} should be strongly dominant. For the χ_{q1} the coupling of this vector state to two quasi–on–shell (boson) gluons is strongly suppressed due to the Landau–Yang theorem, while χ_{q2} production is suppressed due the $J_z = 0$ selection rule, as in the non–relativistic quarkonium approximation the coupling of the χ_{q2} to two gluons in a $J_z = 0$ state vanishes, and so this state can only be produced for the (strongly suppressed) case that the gluons are in a $|J_z| = 2$ configuration.

However, when for example χ_c production was observed via the $\chi_c \to J/\psi\gamma$ decay channel by CDF [11], with insufficient photon energy resolution to distinguish the three spin states, it cannot be naively assumed that only the χ_{c0} will contribute, as in this case the much larger branching ratios for the $\chi_{c(1,2)}$ states decays may compensate the suppression in their exclusive production cross sections. This was demonstrated explicitly in [10], where it was predicted that the contribution of these higher spin states to the $\chi_c \to J/\psi\gamma$ cross section will be of a similar size to the χ_{c0}. This was supported by a subsequent preliminary measurement by LHCb of exclusive χ_c production [12]. The production of all three spin states was observed, with the measured cross sections in good agreement with the Durham predictions for the $\chi_{c(0,1)}$ states, and somewhat higher for the χ_{c2}. The source of this discrepancy may be due to the non–exclusive component of this data, or to additional theoretical corrections needed for the production of these lower mass states, see [13] for more discussion. Other observables, such as χ_b and $\eta_{c,b}$ production are discussed in detail in [3].

A further, and so far relatively unexplored, possibility is to observe the CEP of the 'exotic' XYZ charmonium–like states which have been discovered over the past 10 years, see for example [14] for a review. To give one topical example, we may consider the well–known $X(3872)$, the quantum numbers of which have recently been established to be $J^{PC} = 1^{++}$ by LHCb [15], an assignment which leaves both the more exotic (e.g. as a $D^0\overline{D}^{*0}$ molecule) and a conventional $\chi_{c1}(2^3P_1)$ interpretation in principle available. The observation of *exclusive* $X(3872)$ production would immediately provide clear evidence, so–far lacking, of a direct (i.e. not due to feed–down from the decay of higher mass states) production channel $gg \to X$. Moreover, if as discussed in [16], in the case of a molecular $D^0\overline{D}^{*0}$ interpretation the hadroproduction of such a state with the size of cross section observed inclusively, must in general take place in an environment where additional particles are emitted, than the observation of exclusive production would strongly disfavor such a purely molecular interpretation. On the other hand, if the $X(3872)$ is simply a conventional $\chi_{c1}(2^3P_1)$ state, then the ratio of the CEP cross sections $\sigma(\chi_{c1}(2P))/\sigma(\chi_{c1}(1P))$ is predicted to first approximation (ignoring reasonably small corrections due to the different masses,

relativistic effects etc) to be simply given by the ratio of the respective squared wavefunctions at the origin $|\phi'_P(0)|^2$. That is, we will expect them to be of comparable sizes. More generally, the $X(3872)$ may be a mixture of a $\chi_{c1}(2P)$ and a molecular $D^0\overline{D}^{*0}$ state, and so the CEP process may shed light on the size of each component, see [13] for a more detailed discussion.

4. Production of light meson pairs

Cross sections for the exclusive production of light meson pairs, M_3, M_4, were first calculated within the Durham model in [17], with the $gg \to M_3M_4$ subprocess modeled using the 'hard exclusive' formalism described in [18]: the full amplitude is calculated in terms of the parton–level process, $gg \to q\overline{q}q\overline{q}$, where the outgoing partons are collinear with the parent meson and have the correct color and spin quantum numbers, and a 'distribution amplitude' $\phi(x)$, representing the (non–perturbative) probability for the partons to form the meson state.

This approach led to quite unexpected predictions for flavor–singlet and non–singlet mesons, with the former expected to be strongly enhanced. This was due to the different contributing parton–level amplitudes in the two cases, with an additional 'ladder–type' set of diagrams shown in Fig. 2 (right), being possible for flavor–singlet mesons, but vanishing due to isospin conservation for flavor–non–singlets, where only the diagram type shown in Fig. 2 (left) contributes. Crucially, it was found that for $J_z = 0$ incoming gluons, it was only the contribution from these ladder–type diagrams which was non–vanishing, and thus we expect a strong suppression in the production of flavor–non–singlet meson pairs ($\pi\pi$, KK) at sufficiently high transverse momentum $p_\perp$ that this perturbative approach (both the Durham model and hard exclusive formalism) can be reliably applied. This prediction was supported by the CDF [19] observation of exclusive $\gamma\gamma$ production, for which the contamination caused by $\pi^0\pi^0$ production was determined experimentally to be very small, and consistent with zero (finding $N(\pi^0\pi^0)/N(\gamma\gamma) < 0.35$, at 95% C.L.). Without this additional $J_z = 0$ suppression discussed above, we would naively expect $N(\pi^0\pi^0)/N(\gamma\gamma) \sim 1$.

In [20] this approach was extended to include a gg valence component for the case of the flavor–singlet η' (and also, through mixing, η) mesons. This will contribute at the same (leading) order to the $q\overline{q}$ component, via the parton–level $gg \to gggg$ and $gg \to ggq\overline{q}$ processes, and an explicit calculation showed that any sizable gg component of the η' (and η) can have a strong effect on the CEP cross section, increasing (or decreasing) it by up to $\sim$ an order of magnitude, depending on the specific size and sign of the gg component. Thus by observing the CEP of $\eta(')\eta(')$ meson pairs, we may shed light on the size of such a gg component, a question which so

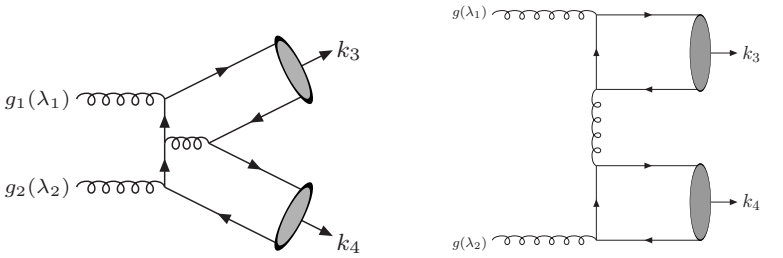

Fig. 2. (Left) A typical diagram for the $gg \to M\overline{M}$ process. (Right) Representative 'ladder' diagram, which contributes to the production of flavor–singlet mesons.

far remains unresolved, see [20] for more discussion.

5. Exclusive jet production and the Higgs Boson

The observation of exclusive dijet production (with $X = jj$ in (1)) was reported by CDF in 2008 [21] and D0 in [22]. The CDF data was found to be in quite good agreement with the `ExHuME` Monte Carlo implementation [23] of the Durham model, with the inclusion of the Sudakov factor as in (3) essential to describe the invariant mass M_{jj} and transverse energy $E_\perp^j$ distributions. Using the existing CMS+TOTEM detectors, some limited preliminary data for central jet production has been taken at the LHC during low luminosity runs [24], with plans to take further such measurements currently under discussion. The possibilities for performing such measurements at higher luminosity using the proposed forward tagging AFP and PPS detectors at ATLAS and CMS, are also being considered [8].

For the case of exclusive jet production, the CEP $J_z = 0$ selection rule leads to some non–trivial predictions which are not observed in the standard inclusive production process. In particular, as the leading–order $gg \to q\overline{q}$ amplitude for massless quarks and $J_z = 0$ incoming gluons vanishes, we expect exclusive gg jets to be strongly dominant. This therefore presents the potentially unique possibility of a clean observation of isolated gluon jets at a hadron collider, and thus of a probe of the QCD predictions for gluon jet properties (particle multiplicity, correlations etc). In the three jet case, this leads to a suppression in $gq\overline{q}$ production as the gluon become soft or collinear to the quark/anti–quark, and thus we expect a relative enhancement in such a final–state with the jets in a well–separated 'Mercedes' configuration. A detailed quantitative study and comparison of the the exclusive three–jet topologies for ggg and $gq\overline{q}$ production would provide an interesting test of the underlying theory.

Another interesting possibility, which has thus far not been observed, is the exclusive production of the Higgs Boson. Although the expected cross sections are quite low, this would in principle be possible with the proposed forward tagging AFP and PPS detectors at ATLAS and CMS, see e.g. [8] and references therein. A particularly interesting result in the case of exclusive $H \to b\bar{b}$, is that, as discussed above, the leading order QCD background $gg \to b\bar{b}$ is strongly dynamically suppressed, making an observation via this channel with $S/B \sim 1$ in principle possible: in the inclusive case, the signal is typically swamped by the direct QCD process. A further interesting point is that any CP–odd term in the $gg \to H$ vertex (possible if the Higgs state is in fact not purely CP–even, an issue which will take some time to clarify experimentally) will show up as an asymmetry in the distribution with respect to ϕ, the azimuthal angle between the outgoing protons. Further details and discussion can be found in [13].

6. Conclusion

CEP provides a very promising and potentially unique framework, complementary to more standard inclusive channels, in which to study SM and BSM signals. These processes therefore offer a rich phenomenology at high–energy colliders, with a detailed program of theoretical work ongoing and a wide range of experimental measurements being explored at the LHC.

LHL thanks the organizers for support and for a very interesting and productive conference.

References

[1] O. Kepka, `arXiv:1310.7374`.

[2] V.A. Khoze, A.D. Martin, and M. G. Ryskin, Eur. Phys. J. C **23**, 311 (2002).

[3] L.A. Harland-Lang, V.A. Khoze, M.G. Ryskin, and W.J. Stirling, Eur. Phys. J. C **69**, 179 (2010).

[4] T. Coughlin and J. Forshaw, J. High Energy Phys. **1001**, 121 (2010).

[5] L. Harland-Lang, Phys. Rev. D **88**, 034029 (2013).

[6] V.A. Khoze, A.D. Martin, and M.G. Ryskin, Eur. Phys. J. C **73**, 2503 (2013).

[7] M.G. Ryskin, A.D. Martin, and V.A. Khoze, Eur. Phys. J. C **60**, 265 (2009).

[8] M. Albrow, `arXiv:1310.7047`.

[9] V.A. Khoze, A.D. Martin, M.G. Ryskin, and W.J. Stirling, Eur. Phys. J. C **35**, 211 (2004).

[10] L.A. Harland-Lang, V.A. Khoze, M.G. Ryskin, and W.J. Stirling, Eur. Phys. J. C **65**, 433 (2010).

[11] T. Aaltonen *et al.* (CDF Collaboration), Phys. Rev. Lett. **102**, 242001 (2009).

[12] Paula Collins, talk at the Workshop: "Results and Prospects of Forward Physics at the LHC," CERN, Feb. 11–13, 2013.

[13] L.A. Harland-Lang, V.A. Khoze, M.G. Ryskin, and W.J. Stirling, `arXiv:1301.2552`.

[14] N. Brambilla, S. Eidelman, B. Heltsley, R. Vogt, G. Bodwin, *et al.*, Eur. Phys. J. C **71**, 1534 (2011).

[15] R. Aaij *et al.* (LHCb collaboration), Phys. Rev. Lett. **110**, 222001 (2013).

[16] C. Bignamini, B. Grinstein, F. Piccinini, A. Polosa, and C. Sabelli, Phys. Rev. Lett. **103**, 162001 (2009).

[17] L.A. Harland-Lang, V.A. Khoze, M.G. Ryskin, and W.J. Stirling, Eur. Phys. J. C **71**, 1714 (2011).

[18] S.J. Brodsky and G.P. Lepage, Phys. Rev. D **24**, 1808 (1981).

[19] T. Aaltonen *et al.* (CDF Collaboration), Phys. Rev. Lett. **108**, 081801 (2012).

[20] L.A. Harland-Lang, V.A. Khoze, M.G. Ryskin, and W.J. Stirling, Eur. Phys. J. C **73**, 2429 (2013).

[21] T. Aaltonen *et al.* (CDF Collaboration), Phys. Rev. D **77**, 052004 (2008).

[22] V.M. Abazov *et al.* (D0 Collaboration), Phys. Lett. B **705**, 193 (2011).

[23] J. Monk and A. Pilkington, Comput. Phys. Commun. **175**, 232 (2006).

[24] Máté Csanád, this conference.

Diffractive cross sections implemented in PYTHIA8-MBR vs LHC results

Konstantin Goulianos

The Rockefeller University, 1230 York Avenue, New York, NY 10065, USA

Diffractive cross sections implemented in the PYTHIA8-MBR Monte Carlo simulation are reviewed and compared to results obtained at the Large Hadron Collider.

1. Introduction

Measurements at the LHC have shown that there are sizable disagreements among Monte Carlo (MC) implementations of "soft" processes based on cross sections proposed by various physics models, and that it is not possible to reliably predict all such processes, or even all aspects of a given process, using a single model [1, 2, 3]. In the CDF studies of diffraction at the Tevatron, all processes are well modeled by the MBR (Minimum Bias Rockefeller) MC simulation, which is a stand-alone simulation based on a unitarized Regge-theory model, RENORM [4], employing inclusive nucleon parton distribution functions (PDF's) and QCD color factors. The RENORM model was updated in a presentation at EDS-2009 [5] to include a unique unitarization prescription for predicting the total pp cross section at high energies, and that update has been included as an MBR option for simulating diffractive processes in PYTHIA8 since version PYTHIA8.165 [6], to be referred here-forth as PYTHIA8-MBR. In this paper, we briefly review the cross sections [7] implemented in this option of PYTHIA8 and compare them with LHC measurements.

The PYTHIA8-MBR option includes a full simulation of the hadronization of the implemented diffraction dissociation processes: single, double, and central diffraction. In the original MBR simulation used in CDF, the hadronization of the final state(s) was based on a data-driven phenomenological model of multiplicities and p_t distributions calibrated using S$\bar{p}p$S and Fermilab fixed-target results. Later, the model was successfully tested against Tevatron MB and diffraction data. However, only $\pi^{\pm}$ and π^0 particles were produced in the final state, with multiplicities obeying a statistical model of a modified Gamma distribution function that provided good fits

to experimental data [8]. This model could not be used to predict specific-particle final states. In the PYTHIA8-MBR implementation, hadronization is performed by PYTHIA8 tuned to reproduce final-state distributions in agreement with MBR's, with hadronization done in the PYTHIA8 framework. Thus, all final-state particles are now automatically produced, greatly enhancing the horizon of applicability of tPYTHIA8-MBR.

2. Cross sections

The following diffraction dissociation processes are considered in PYTHIA8-MBR:

$$\begin{aligned} \text{SD} \quad & pp \to Xp \quad \text{Single Diffraction (or Single Dissociation),} && (1)\\ \text{or} \quad & pp \to pY \quad \text{(the other proton survives)} \\ \text{DD} \quad & pp \to XY \quad \text{Double Diffraction (or Double Dissociation),} && (2)\\ \text{CD/DPE} \quad & pp \to pXp \quad \text{Central Diffraction/Double Pomeron Exchange.} && (3) \end{aligned}$$

The RENORM predictions are expressed as unitarized Regge-theory formulas, in which the unitarization is achieved by a renormalization scheme where the Pomeron ($I\!P$) flux is interpreted as the probability for forming a diffractive (non-exponentially suppressed) rapidity gap and thereby its integral over all phase space saturates at the energy where it reaches unity. Differential cross sections are expressed in terms of the $I\!P$-trajectory, $\alpha(t) = 1 + \epsilon + \alpha' t = 1.104 + 0.25\ (\text{GeV}^{-2}) \cdot t$, the $I\!P$-p coupling, $\beta(t)$, and the ratio of the triple-$I\!P$ to the $I\!P$-p couplings, $\kappa \equiv g(t)/\beta(0)$. For large rapidity gaps, $\Delta y \geq 3$, for which $I\!P$-exchange dominates, the cross sections may be written as,

$$\frac{d^2\sigma_{SD}}{dt d\Delta y} = \frac{1}{N_{\text{gap}}(s)} \left[\frac{\beta^2(t)}{16\pi} e^{2[\alpha(t)-1]\Delta y} \right] \cdot \left\{ \kappa\beta^2(0) \left(\frac{s'}{s_0} \right)^{\epsilon} \right\}, \quad (4)$$

$$\frac{d^3\sigma_{DD}}{dt d\Delta y dy_0} = \frac{1}{N_{\text{gap}}(s)} \left[\frac{\kappa\beta^2(0)}{16\pi} e^{2[\alpha(t)-1]\Delta y} \right] \cdot \left\{ \kappa\beta^2(0) \left(\frac{s'}{s_0} \right)^{\epsilon} \right\}, \quad (5)$$

$$\frac{d^4\sigma_{DPE}}{dt_1 dt_2 d\Delta y dy_c} = \frac{1}{N_{\text{gap}}(s)} \left[\Pi_i \frac{\beta^2(t_i)}{16\pi} e^{2[\alpha(t_i)-1]\Delta y_i} \right] \cdot \kappa \left\{ \kappa\beta^2(0) \left(\frac{s'}{s_0} \right)^{\epsilon} \right\}, \quad (6)$$

where t is the 4-momentum-transfer squared at the proton vertex, Δy the rapidity-gap width, and y_0 the center of the rapidity gap. In Eq. (6), the subscript $i = 1, 2$ enumerates Pomerons in a DPE event, $\Delta y = \Delta y_1 + \Delta y_2$ is the total rapidity gap (sum of two gaps) in the event, and y_c is the center in η of the centrally-produced hadronic system.

The total cross section ($\sigma_{\rm tot}$) is expressed as:

$$\sigma_{\rm tot}^{p^{\pm}p} = 16.79 s^{0.104} + 60.81 s^{-0.32} \mp 31.68 s^{-0.54} \quad \text{for } \sqrt{s} \leq 1.8 \text{ TeV}, \quad (7)$$

$$\sigma_{\rm tot}^{p^{\pm}p} = \sigma_{\rm tot}^{\rm CDF} + \frac{\pi}{s_0}\left[\left(\ln\frac{s}{s_F}\right)^2 - \left(\ln\frac{s^{\rm CDF}}{s_F}\right)^2\right] \quad \text{for } \sqrt{s} \geq 1.8 \text{ TeV}, \quad (8)$$

where s_0 and s_F are energy and the Pomeron flux saturation scales, respectively [7]. For $\sqrt{s} \leq 1.8$ TeV, where there are Reggeon contributions, we use the global fit expression [9], while for $\sqrt{s} \geq 1.8$ TeV, where Reggeon contributions are negligible, we employ the Froissart-Martin formula [10, 11, 12]. The two expressions are smoothly matched at $\sqrt{s} \sim 1.8$ TeV.

The elastic cross section is obtained from the global fit [9] for $\sqrt{s} \leq 1.8$ TeV, while for $1.8 < \sqrt{s} \leq 50$ TeV we use an extrapolation of the global-fit ratio of $\sigma_{\rm el}/\sigma_{\rm tot}$, which is slowly varying with $\sqrt{s}$, multiplied by σ_{tot}. The total non-diffractive cross section is then calculated as $\sigma_{\rm ND} = (\sigma_{\rm tot} - \sigma_{\rm el}) - (2\sigma_{\rm SD} + \sigma_{\rm DD} + \sigma_{\rm CD})$.

3. Results

In this section, we present as examples of the predictive power of the RENORM model some results reported by the TOTEM, CMS, and ALICE collaborations for pp collisions at $\sqrt{s} = 7$ TeV, which can be directly compared with RENORM formulas without using the PYTHIA8-MBR simulation. Figure 1 (left) shows a comparison of the TOTEM total, elastic, and total-inelastic cross sections, along with results from other experiments fitted by the COMPETE Collaboration [13]; the RENORM predictions, displayed as filled (green) squares, are in excellent agreement with the TOTEM results. Similarly, in Fig. 1 (right), good agreement is observed between the ALICE [14] and CMS [15] total-inelastic cross sections and the RENORM prediction.

The uncertainty shown in the RENORM prediction of $\sigma_{\rm tot}$ in Fig. 1 (left) is dominated by that in the scale parameter s_0. The latter can be reduced by a factor of ~ 4 if $\sqrt{s_0}$ is interpreted as the mean value of the glue-ball-like object discussed in [16] and the data shown in Fig. 8 of [16] are used to determine its value. Work is in progress to finalize the details of this interpretation.

Another example of the predictive power of RENORM is shown in Fig. 2, which displays the total SD (left) and total DD (right) cross sections for $\xi < 0.05$, after extrapolation into the low mass region from the measured CMS cross sections at higher mass regions, presented in [17], using RENORM.

The justification for using the RENORM model for the extrapolation into the low mass region is presented in Fig. 3, in which the measured diffractive cross sections within a wide (albeit limited) pseudorpidity regions are

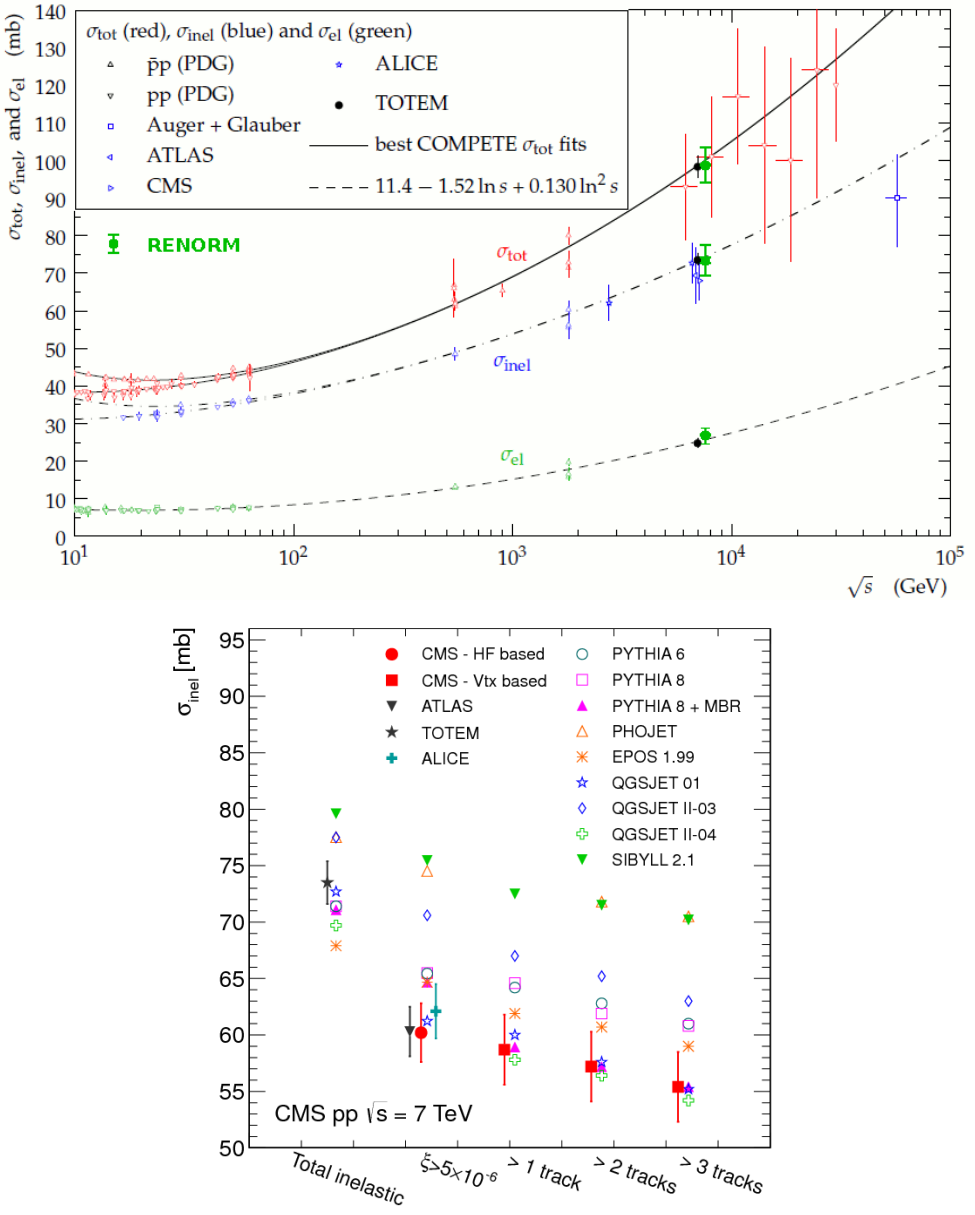

Fig. 1. (top) TOTEM measurements of the total, total-inelastic, and elastic *pp* cross sections at $\sqrt{s} = 7$ TeV shown with best COMPETE fits [13] and RENORM predictions; (bottom) ALICE [14] and CMS [15] measurements of the total inelastic cross section at $\sqrt{s}$ =7 TeV compared to RENORM prediction (PYTHIA8-MBR).

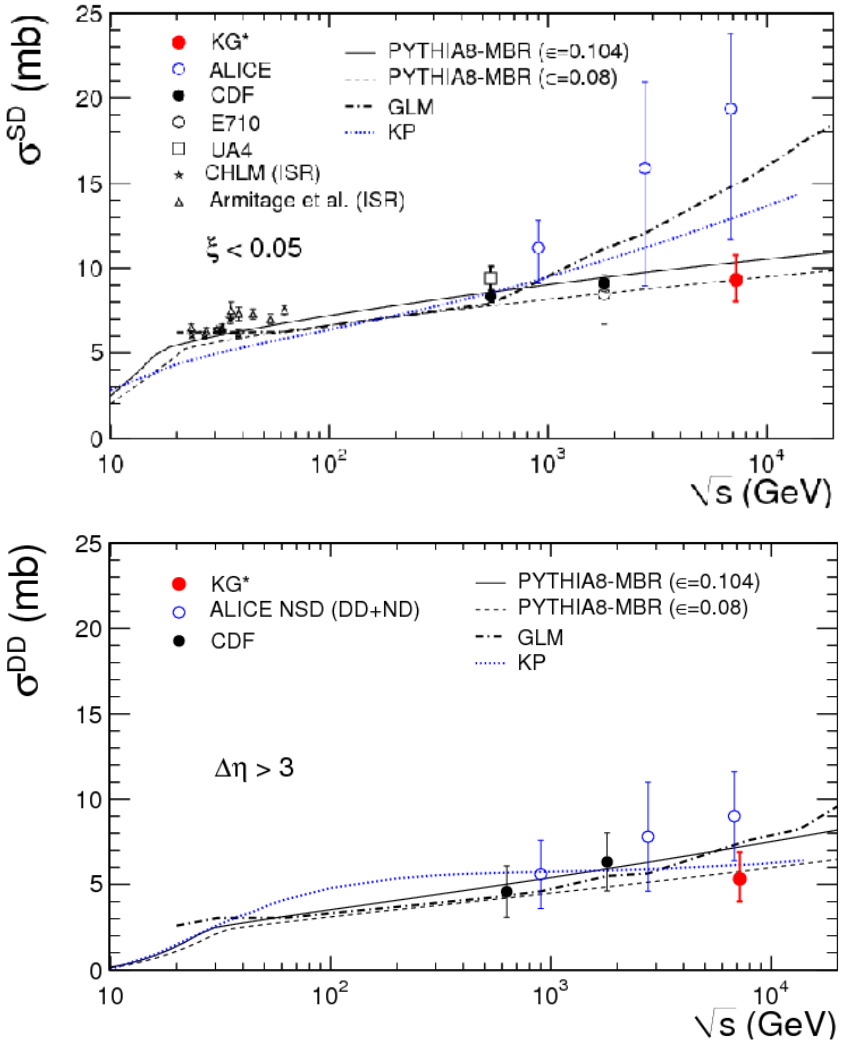

KG*: the value of this entry was obtained by extrapolating from the measured CMS cross sections [17] to the low mass region using the MBR model.

Fig. 2. Measured SD (left) and DD (right) cross sections for $\xi < 0.05$ compared with theoretical predictions; the model embedded in PYTHIA8-MBR provides a good description of all data.

compared with predictions. In Figs. 3 (top-left and top-middle), the predictions of PYTHIA8-MBR are shown for two values of the ϵ parameter of the Pomeron trajectory ($\alpha(t) = 1 + \epsilon + \alpha' t$), $\epsilon = 0.08$ and $\epsilon = 0.104$. Both values describe the measured SD cross section within uncertainties, while the DD data favor the smaller value of ϵ, which is consistent with low mass CDF data. The predictions of PYTHIA8-4C and PYTHIA6 describe well the measured DD cross section, but fail to describe the falling behavior of the data (see details in [17]). The total SD cross cross section integrated over the region $-5.5 < \log_{10}\xi < -2.5$ ($12 < M_X < 394$ GeV) was measured to be $\sigma_{vis}^{SD} = 4.27 \pm 0.04(\text{stat.})^{+0.65}_{-0.58}(\text{syst.})$ mb (dissociation of either proton).

The event sample after the $\Delta\eta^0 > 3$ selection, was used to extract the differential DD cross section as a function of the central-gap width, $\Delta\eta$. The cross section for $\Delta\eta > 3$, $M_X > 10$ GeV and $M_Y > 10$ GeV is presented in Fig. 3 (right). The total DD cross cross section integrated over this region was measured to be $\sigma_{vis}^{DD} = 0.93 \pm 0.01(\text{stat.})^{+0.26}_{-0.22}(\text{syst.})$ mb.

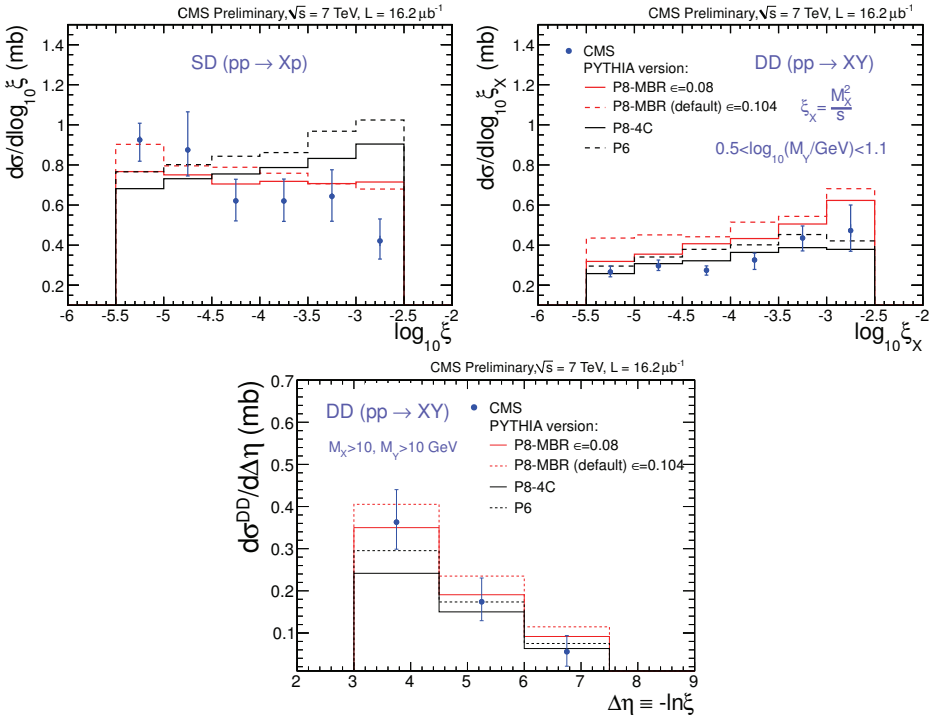

Fig. 3. SD (top) and DD (middle) cross sections vs ξ, and DD cross section vs $\Delta\eta$ (bottom), compared to PYTHIA6, PYTHIA8-4C and PYTHIA8-MBR. Errors are dominated by systematics (HF energy scale, and hadronization/diffraction model).

4. Summary

We reviewed our pre-LHC predictions for the total, elastic, total-inelastic, and diffractive components of the proton-proton cross section at high energies, which are based on a special parton-model approach to diffraction employing inclusive proton parton distribution functions and QCD color factors. We discuss single diffraction/dissociation, double diffraction/dissociation, and central diffraction or double-Pomeron exchange, comparing predictions with LHC measurements. Agreement is found in all cases.

Acknowledgments

I would like to thank Robert Ciesielski, my colleage at Rockefeller and collaborator in the implementation of the MBR simulation into PYTHIA8, and the Office of Science of the Department of Energy for supporting the Rockefeller experimental diffraction physics programs at Fermilab and LHC on which this research is anchored.

References

[1] K. Goulianos, *Predictions of Diffractive Cross Sections in Proton-Proton Collisions*, in proceedings of *Diffraction 2012: International Workshop on Diffraction in High Energy Physics, 10-15 September 2012*, AIP Conf. Proc. 1523, pp. 107-110 (2013).

[2] See models presented by various authors in proceedings of *Diffraction 2012*, AIP Conf. Proc. **1523**.

[3] K. Goulianos, *Predictions of Diffractive, Elastic, Total, and Total-Inelastic pp Cross Sections vs LHC Measurements*, to appear in proceedings of *XXI International Workshop on Deep-Inelastic Scattering and Related Subject - DIS2013, 22-26 April 2013, Marseilles, France*.

[4] K. Goulianos, *Hadronic Diffraction: Where do we Stand?*, in proceedings of *Les Rencontres de Physique de la Vallee d'Aoste: Results and Perspectives in Particle Physics, La Thuile, Italy, February 27 - March 6, 2004*, Frascati Physics Series, Special 34 Issue, edited by Mario Greco, hep-ph/0407035.

[5] K. Goulianos, *Diffractive and Total pp Cross Sections at* LHC, in proceedings of *13th International Conference on Elastic and Diffractive Scattering (Blois Workshop) - Moving Forward into the LHC Era, CERN, Geneva, Switzerland, June 29-July 3, 2009*, CERN-Proceedings-2010-02, edited by Mario Deile, arXiv:1002.3527v2.

[6] T. Sjöstrand, S. Mrenna and P. Skands, J. High Enegy Phys. **05**, 026 (2006), Comput. Phys. Comm. **178**, 852 (2008).

[7] R. Ciesielski and K. Goulianos, *MBR Monte Carlo Simulation in PYTHIA8*, arXiv:1205.1446.

[8] K. Goulianos, Phys. Lett. B **193**, 151 (1987).

[9] R.J.M. Covolan, J. Montanha and K. Goulianos, Phys. Lett. B **389**, 176 (1996).

[10] M. Froissart, Phys. Rev. **3**, 123 (1961).

[11] A. Martin, Nuovo Cimento **42**, 930 (1966).

[12] A. Martin, Phys. Rev. D **80**, 065013 (2009).

[13] M. Deile (TOTEM Collaboration), *Measurements of Proton-Proton and Total Cross Section at the LHC by TOTEM*, in proceedings of DIFFRACTION *2012* (figure from talk presented at the Conference).

[14] B. Abelev *et al.* (ALICE Collaboration), Eur. Phys. J. C **73**, 2456 (2013).

[15] S. Chatrchyan *et al.* (CMS Collaboration), Phys. Lett. B **722**, 5 (2013).

[16] M.G. Albrow, T.D. Coughlin and J.R. Forshaw, Prog. Part. Nucl. Phys **65**, 149 (2010).

[17] R. Ciesielski (CMS Collaboration), *Measurements of diffraction in p-p collisions in CMS*, in proceedings of *XXI International Workshop on Deep-Inelastic Scattering and Related Subject -DIS2013, 22-26 April 2013, Marseilles,France.*

Recent results on vector boson production in association with jets with the CMS detector

Tom Cornelis, for the CMS collaboration

Department of Elementary Particle Physics, University of Antwerp, Groenenborgerlaan 171, 2020 Antwerp, Belgium

The production of weak vector bosons in association with jets and their properties are intensively studied using proton-proton collision data collected with the CMS detector. In this proceedings, we will show the cross section measurement of the electroweak production of a Z boson in association with 2 jets at $\sqrt{s} = 8$ TeV, including a new data-driven approach and studies on the hadronic activity in the region between the two tagging jets. The azimuthal correlations and event shapes in Z + jets events at $\sqrt{s} = 7$ TeV are also presented.

1. Azimuthal correlations and event shapes in Z plus jet events

Azimuthal correlations in Z plus at least one jet events were studied [1] in pp collisions at $\sqrt{s} = 7$ TeV, using 5 fb^{-1} of data recorded with the CMS detector [2]. Events were selected by requiring an oppositely charged electron or muon pair with an invariant mass within a window of 20 GeV around the Z boson mass. Both leptons satisfy $p_T > 20$ GeV and $|\eta| < 2.4$ and fulfill quality and isolation criteria. Jets with $p_T > 50$ GeV and $|\eta| < 2.5$ were used, clustered using the anti-k_T algorithm with size parameter of 0.5.

1.1. Azimuthal angles

Figure 1 shows the azimuthal angle between the Z boson and the leading jet, either for all Z bosons or in a subset of events with $p_T^Z > 150$ GeV, a region which is critical in searches for new phenomena. The results agree within uncertainties with the MadGraph [3] prediction. In $Z+ \geq 1$ jet events, the Sherpa [4] prediction is about 10% too low whereas Powheg [5, 6, 7, 8] overestimates the distribution by about 10%. The Z boson and leading jet are completely correlated for $N_{jets} = 1$, as $\Delta\phi(Z, j_1)$ tends to π. If $\Delta\phi(Z, j_1) < \frac{\pi}{2}$, the leading jet and Z boson are in the same hemisphere and therefore balanced by subleading jets in the opposite hemisphere which results in a more isotropic $\Delta\phi(Z, j_1)$ distribution for larger inclusive jet multiplicities.

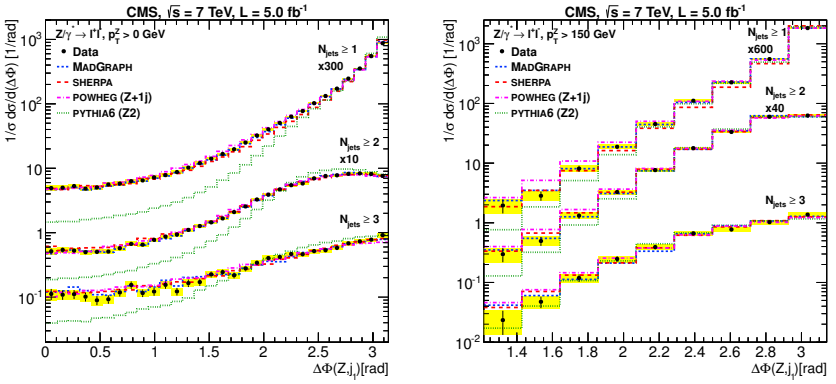

Fig. 1. Normalized $\Delta\phi(Z, j_1)$ distributions categorized as a function of jet multiplicity. The yellow band shows the sum of statistical and systematic errors on the data. *(left)* All p_T^Z *(right)* $p_T^Z > 150$ GeV.

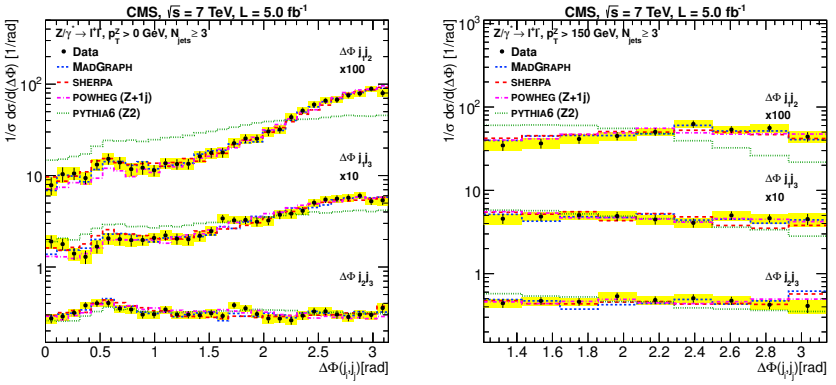

Fig. 2. Normalized $\Delta\phi(j_i, j_j)$ distributions for the inclusive $N_{jets} > 3$ multiplicity bin. The yellow band shows the sum of statistical and systematic errors on the data. *(left)* All p_T^Z *(right)* $p_T^Z > 150$ GeV.

There is good agreement between MADGRAPH, SHERPA and PYTHIA [9] predictions, and the data for the azimuthal angles among the three leading jets, shown in Figure 2. For higher p_T^Z, these angles decorrelate.

1.2. Transverse thrust

The properties of Z plus jet events have also been studied using the transverse thrust τ_{T}, defined as $\tau_{\mathrm{T}} \equiv 1 - \max_{\vec{n}_\tau} \frac{\sum_i |\vec{p}_{\mathrm{T},i} \cdot \vec{n}_\tau|}{\sum_i p_{\mathrm{T},i}}$ where the sum

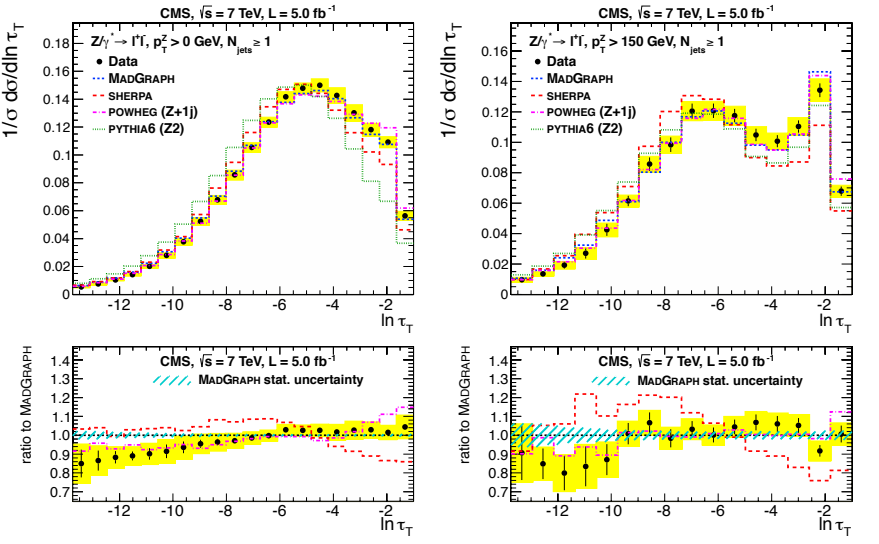

Fig. 3. Normalized distributions in ln τ_{T} for Z plus at least 1 jet events for *(left)* all p_T^Z *(right)* $p_T^Z > 150$ GeV. The yellow band shows the sum of statistical and systematic errors on the data.

over i runs over the Z and each accepted jet in the event. The sum is maximized by the unit vector $\vec{n}_\tau$, called the thrust axis. In the limit of a perfectly balanced Z plus one jet event, τ_{T} tends to zero (ln $\tau_{\mathrm{T}} \to -\infty$). In the limit of a homogeneously distributed event, the transverse thrust reaches $1 - \frac{\pi}{2}$ (ln $\tau_{\mathrm{T}} \to -1$), its maximum possible value. The ln τ_{T} distribution is shown in Figure 3. The data is best described by POWHEG and MADGRAPH, except at large negative values for the transverse thrust where an overestimation by MADGRAPH is seen. PYTHIA and SHERPA have larger discrepancies and predict also too small values for ln τ_{T}. The peak at ln $\tau_{\mathrm{T}} \approx -2$ in the boosted region corresponds with events where the Z is balanced by two or more jets.

2. Electroweak production of Z + 2 jets

Although most Zjj events at the LHC are produced by Drell-Yan (DY) processes, the the same final state could also be created only by electroweak interactions. Three classes of diagrams, shown in Figure 4, contribute to the electroweak Zjj production: bremsstrahlung, vector boson fusion (VBF) processes and multi-peripheral. There is great interest in the study of the VBF diagram, which establishes a foundation for the more general study of VBF processes which include Higgs boson studies and supersymmetry

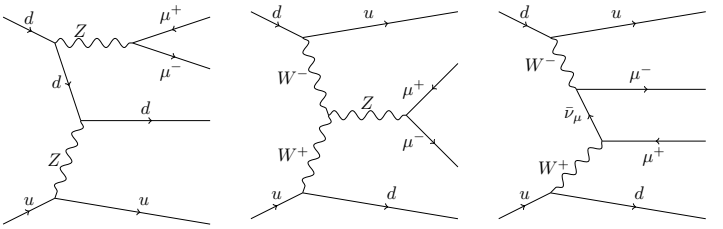

Fig. 4. Representative diagrams for the electroweak Zjj production processes.

searches. However, all three categories should be studied together, as large negative interference effects exists between the VBF process and the other two categories.

The pure electroweak cross section of a Z boson in association with two jets has already been measured with the CMS detector in pp collisions at $\sqrt{s} = 7$ TeV [10]. We will discuss now the first preliminary results using the $\sqrt{s} = 8$ TeV dataset (19.7 fb^{-1}) [11], which includes the addition of a data-driven method that models the DY background using γjj events.

Events are selected by requiring a muon or electron pair with opposite charge, in which both leptons satisfy a series of quality and isolation criteria, a transverse momentum of at least 20 GeV and $|\eta| < 2.4$. The Z bosons are reconstructed by taking events with a dilepton mass within the 15 GeV mass interval around the nominal Z boson mass. The two leading jets within $|\eta| < 4.7$ and exceeding $p_T^{j_1,j_2} > 50, 30$ GeV are selected as the tagging jets.

2.1. Cross section measurement

Because the signal is small compared with the main background, DY Zjj, a precise modeling of this background is necessary. However, the simulation is based on MadGraph and therefore lacks possible virtual corrections at higher order then the Born level. A first method, also used in the 7 TeV analysis, corrects the MadGraph simulation with dynamical k-factors derived from NLO predictions with mcfm for the dijet invariant mass and the $y^* = y_Z - 0.5(y_{j1} + y_{j2})$ variable. For the 8 TeV analysis, a data-driven approach is added. It is expected that the kinematics of dijet system in DY Zjj are similar to the dijet system in photon plus 2 jet events. A reweighting of the p_T of the photon to the p_T of the Z candidate is used to eliminate differences induced by specific γ or Z sample selections. Because the photon sample is at low p_T affected by multijet production and high trigger prescales, the p_T of the photon or Z is required to be larger than 50 GeV.

Both methods use multi variate analysis techniques. The signal cross

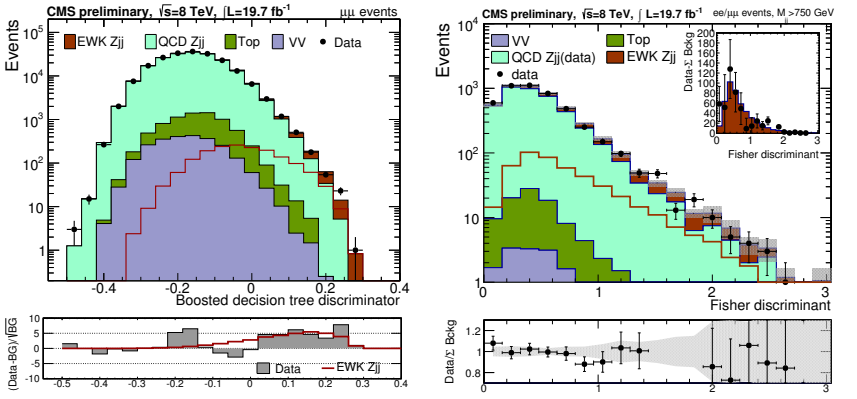

Fig. 5. Shape discriminators used for the signal cross section extraction *(left)* BDT using simulated background *(right)* dijet Fisher discriminator using data-driven background estimation

sections are extracted by fitting the output shapes for signal and background to the data (Figure 5). For the simulation based method, this is a boosted decision tree (BDT) built out of the following variables: the p_T of the tagging jets, the pseudorapidity separation between them, the invariant dijet mass, the y^* variable, the transverse momentum and rapidity of the dilepton system, the sum of the pseudorapidities of the two tagging jets and the difference between the azimuthal angles $(\phi_Z - \phi_{j1})$ and $(\phi_{j1} - \phi_{j2})$. The measured cross section with this method is $\sigma_{meas}^{EW\ \mu\mu jj} = 191 \pm 29\ (\text{stat}) \pm 39\ (\text{syst})$ fb. The cross section in the simulation based method is based only on the dimuon channel.

For the data-driven approach, a linear Fisher discriminant is constructed, only based on dijet kinematics: the pseudorapidity distance $\Delta\eta_{jj}$ between the two jets, the dijet invariant mass M_{jj} and the relative balance of the dijet system. The cross section, combining the dielectron and dimuon channels, is $\sigma_{meas}^{EW\ lljj} = 303 \pm 29\,(\text{stat}) \pm 57\,(\text{syst})$ fb.

Both methods are combined using the Best Linear Unbiased Estimator technique [12, 13] resulting in:

$$\sigma_{meas}^{EW\ lljj} = 226 \pm 26\,(\text{stat}) \pm 35\,(\text{syst})\ \text{fb}$$

which is in agreement with the theoretical NLO prediction of 239 pb computed with VBFNLO[14].

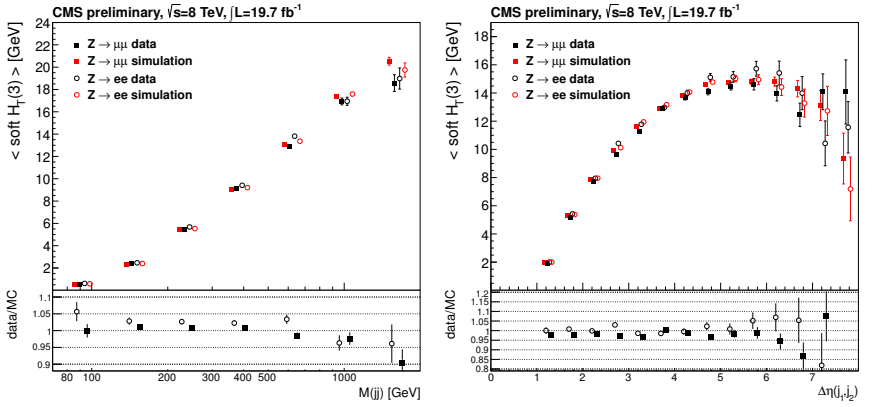

Fig. 6. Average H_T of the three leading soft track jets in the rapidity interval between the two leading jets with $p_T^{j_1,j_2} > 50, 30$ GeV in Zjj events versus *(left)* the dijet invariant mass *(right)* the pseudorapidity separation between the two tagging jets.

2.2. Central hadronic activity

Because there is no color flow between the two tagging jets in electroweak Zjj events, the hadronic activity between these jets is expected to be small. Although we do not use the hadronic activity to separate the EW Zjj from the backgrounds, studies have been done to test the agreement between data and simulation.

A first study makes use of soft track-jets. Tracks associated with the primary vertex and not associated with either of the two leptons or the two tagging jets are selected if they satisfy a high purity requirement and have a transverse momentum exceeding 300 MeV. These tracks are clustered into soft track jets with the anti-k_T algorithm with distance parameter of 0.5. This method gives us a collection of soft track-jets with energy as low as a few GeV which are not affected by the pileup.

In order to monitor the hadronic activity in the rapidity gap between the two tagging jets, only track-jets with pseudorapidity $\eta_{\min}^{\text{tag.jet}} + 0.5 < \eta < \eta_{\max}^{\text{tag.jet}} - 0.5$ are considered. The evolution of the average H_T as a function of the dijet invariant mass and the pseudorapidity separation between the two tagging jets is shown in Figure 6 and demonstrates a good agreement between data and simulation up to the highest regions of dijet invariant mass and pseudorapidity separation.

A second study is performed in a high purity region for which the dijet invariant mass is greater than 1250 GeV. This study makes use of jets with a

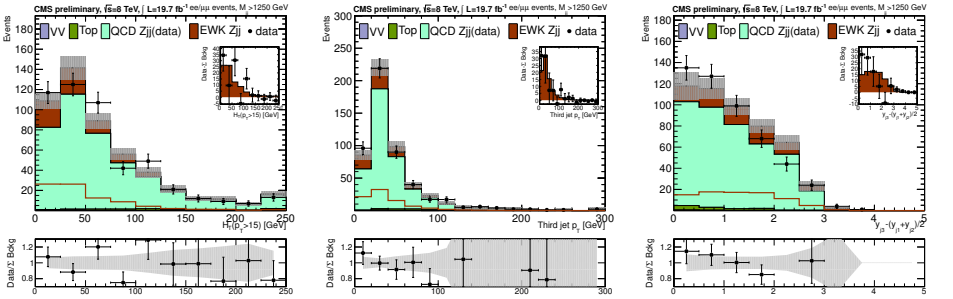

Fig. 7. Control distributions for the hadronic activity for events with $M_{jj} > 1250$ GeV *(left)* scalar sum of all jets with $p_T > 15$ GeV found in the pseudorapidity distance between the tagging jets *(middle)* p_T of the third jet *(right)* $y^*_{j_3}$

.

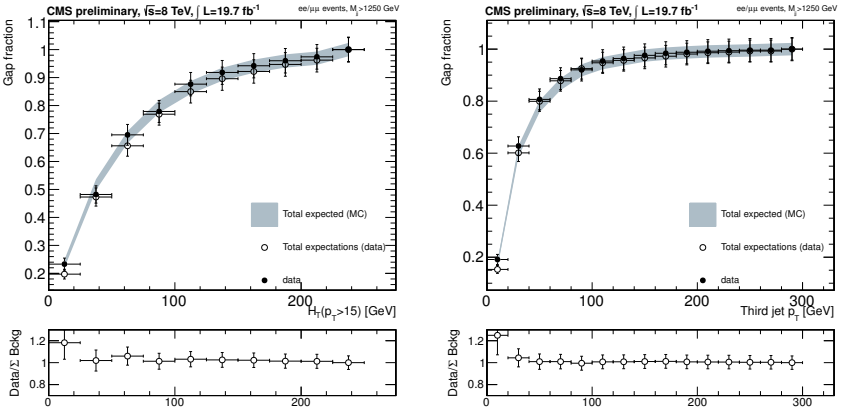

Fig. 8. Gap fraction versus *(left)* the scalar sum of the p_T of all jets *(right)* the p_T of the third jet.

$p_T > 15$ GeV, found in the pseudorapidity distance between the two tagging jets. The background prediction is modeled from the photon control sample. Figure 7 shows the scalar sum H_T of the p_T of these jets, the transverse momentum of the third jet, and its pseudorapidity measured in the dijet rest frame, which is slightly more central than expected. These distributions could be used to compute the efficiency of a hadronic veto either based on the transverse momentum of the third jet or on the H_T variable, as shown in Figure 8. The gap fraction corresponds to the fraction of events for which the tested variable does not exceed a given threshold and is calculated for data, simulation and the data-driven prediction.

3. Other results on vector boson production in association with jets

Besides the two analyses presented above, many other important benchmarks are recently achieved in V+jet studies using 7 TeV data. Recent results could be found on rapidity measurements in Z/γ plus jet events [15] and the study of double parton scattering in W plus 2 jet events [16]. Also the production of vector bosons in association with heavy flavor jets is studied, with measeruments which include the cross section of the production of Z plus one or two b jets [17, 19], the cross section and angular correlations for associated production of a Z boson with a b hadron [18], the cross section for W in association with 2 b jets [20], and the measurement of associated W plus charm production [21].

References

[1] CMS Collaboration, Phys. Lett. B **722**, 238 (2013).
[2] CMS Collaboration, J. Inst. **3**, S08004 (2008).
[3] J. Alwall *et al.*, J. High Energy Phys. **06**, 128 (2011).
[4] T. Gleisberg *et al.*, J. High Energy Phys. **02**, 007 (2009).
[5] P. Nason, J. High Energy Phys. **11**, 040 (2004).
[6] S. Frixione, P. Nason, and C. Oleari, J. High Energy Phys. **11**, 070 (2007).
[7] S. Alioli *et al.*, J. High Energy Phys. **06**, 043 (2010).
[8] S. Alioli *et al.*, J. High Energy Phys. **01**, 095 (2011).
[9] T. Sjostrand, S. Mrenna, and P.Z. Skands, J. High Energy Phys. **05**, 026 (2006).
[10] CMS Collaboration, J. High Energy Phys. **10**, 101 (2013).
[11] CMS Collaboration, CMS-PAS-FSQ-12-035 (2013).
[12] L. Lyons, D. Gibaut, and P. Clifford, Nucl. Instrum. Meth. A **270**, 110 (1988).
[13] L. Lyons, A.J. Martin, and D.H. Saxon, Phys. Rev. D **41**, 982 (1990).
[14] K. Arnold *et al.*, Comput. Phys. Commun. **180**, 1661 (2009).
[15] CMS Collaboration, CMS-PAS-SMP-12-004 (2013).
[16] CMS Collaboration, CMS-PAS-FSQ-12-028 (2013).
[17] CMS Collaboration, CMS-PAS-EWK-11-012 (2012).
[18] CMS Collaboration, CMS-PAS-EWK-11-015 (2013).
[19] CMS Collaboration, CMS-PAS-SMP-13-004 (2013).
[20] CMS Collaboration, CMS-PAS-SMP-12-026 (2013).
[21] CMS Collaboration, CMS-PAS-SMP-12-002 (2013).

Recent developments in Monte Carlo simulations

Jennifer M. Thompson

IPPP, South Road, University of Durham, UK

This talk outlines the current status of Monte Carlo simulations in particle physics. It demonstrates the implementation of automated NLO contributions to matrix elements. The matching methods MC@NLO and POWHEG are outlined and results using various NLO tools are presented. The first plots from POWHEG showing the matching of NNLO matrix elements to the parton shower are also presented.

1. Introduction

There is a current drive in the Monte Carlo community to include higher order perturbative corrections in computational simulations. The most recent developments in Monte Carlos has been to include NLO QCD corrections to the matrix element matched to the parton shower.

Motivations for this extension are the occurrence of large and non-flat K-factors (σ_{NLO}/σ_{LO}), indicating the need for a local K-factor. Also, NLO matrix element calculations exhibit a significant reduction in scale dependence. In a Monte Carlo, extending the matrix element calculation to NLO QCD allows a reasonable error estimate to be formed. Furthermore, the matching of the NLO prediction to the parton shower gives the distribution of the hardest emission to NLO accuracy [1].

Numerical fixed order NLO matrix elements are calculated by using a method such as Catani-Seymour subtraction [2]. Details on the subtraction method for numerical matrix element calculations can be found at Ref. [3]. Equation (1) relates the NLO cross section, σ_{NLO}, to the differential born (B), virtual (V) and real (R) cross sections. The subtraction term introduced here is denoted by $B \otimes \mathrm{d}S$ as it can be factorised into the underlying Born configuration and a splitting function.

$$\sigma_{NLO} = \int \mathrm{d}\Phi_B \left[B + \int \mathrm{d}\Phi_1 B \otimes \mathrm{d}S + V \right] + \int \mathrm{d}\Phi_R \left[R - B \otimes \mathrm{d}S \right] \qquad (1)$$

Equation (1) allows for the numerical calculation of NLO matrix elements. However, including a parton shower on top of this requires a matching method such as the POWHEG [4] and MC@NLO [5] method.

2. POWHEG

Here we will briefly look at the formalism (for a more involved treatment, see Ref. [4]) and see some example plots from using the POWHEG method. The POWHEG implementations considered are from POWHEG-BOX [6], HERWIG++ [7] and PYTHIA8 [8].

2.1. POWHEG formalism

In order to include a possible matrix element emission, the Sudakov form factor is modified in the POWHEG formalism by identifying the kernel with the ratio of the real matrix element and the underlying born term.

$$\Delta(\mu, \mu_0) = \exp\left[-\int_{\mu_0}^{\mu} \mathrm{d}\Phi_1 \frac{R(\Phi_B \otimes \Phi_1)}{B(\Phi_B)}\right] \tag{2}$$

Equation (2) is then included in the POWHEG master equation (equation (3)) to reweight the contribution from the matrix element.

$$\sigma_{\mathrm{POWHEG}} = \int \mathrm{d}\Phi_B \overline{B}(\Phi_B) \left[\Delta(\mu, \mu_0) + \int_{\mu_0}^{\mu} \mathrm{d}\Phi_1 \frac{R(\Phi_B \otimes \Phi_1)}{B(\Phi_B)} \Delta(k_T^2, \mu_0)\right] \tag{3}$$

This gives a modified Born term, $\overline{B}$, which is the calculation to NLO, and correctly accounts for a possible matrix element emission. The phase space can be divided into 2 regions by introducing a small parameter. It is divided such that should this introduced parameter be taken to 0, the equation above is recovered. The advantage of this is that the new parameter can be tuned to match NNLO distributions or data [9].

2.2. Results from POWHEG

Figure 1 compares CDF data to Monte Carlo simulation for diphoton production. The Monte Carlo used here is HERWIG++ with the POWHEG method implemented. This shows the difference between the LO calculation and the NLO QCD matched sample. There is a substantially improved modelling of data, especially in the $\Delta\Phi$ plot.

Figure 2 shows the importance of NLO calculations in searches for BSM physics, as the affect on the distribution is clearly shown in the difference in magnitude of the dijet invariant mass peak on graviton events.

Higgs processes often contain local K-factors. Figure 2 shows the locality of the K-factor in the p_T of the 3$^{\mathrm{rd}}$ hardest jet in H+jets events. The effect of including NLO corrections on the scale uncertainties can also be seen here.

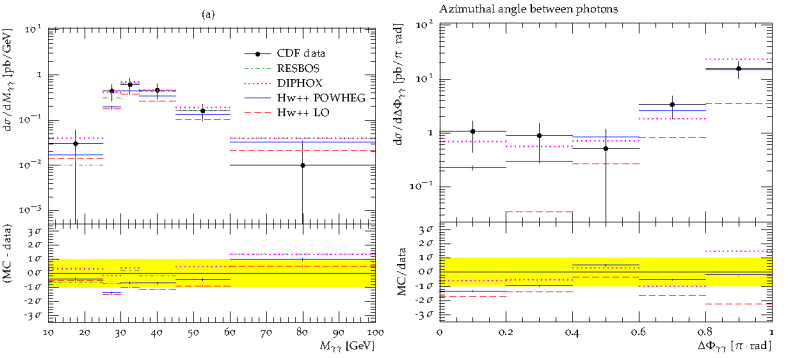

Fig. 1. The left hand plot shows the invariant mass of the photon pair with HERWIG+POWHEG compared to TeVatron data, and the right shows the $\Delta\Phi$ distribution of the pair. These plots are taken from Ref. [10].

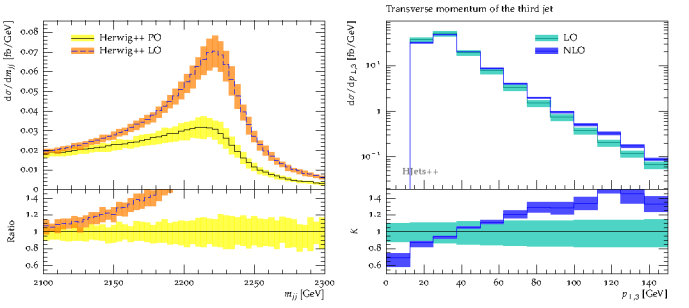

Fig. 2. The left hand plot shows the invariant mass of dijets in graviton production from Ref. [11], and the right hand plot shows the locality of the K-factor in the p_T distribution of the 3$^{\text{rd}}$ jet in Higgs production from Ref. [12].

3. MC@NLO

The MC@NLO method to match NLO matrix elements to a parton shower can be considered as a special case of a more general POWHEG method. For a detailed treatment, see Ref. [5]. In this section, some recent results using MC@NLO matching as implemented in aMC@NLO [13] and SHERPA [14] are presented.

3.1. MC@NLO formalism

This method extends the POWHEG master formula by splitting the real matrix element into a soft and a hard piece. The soft piece now contains the divergences of the matrix element, and the hard part represents the resolvable emission. The real contribution is formed from the sum of these

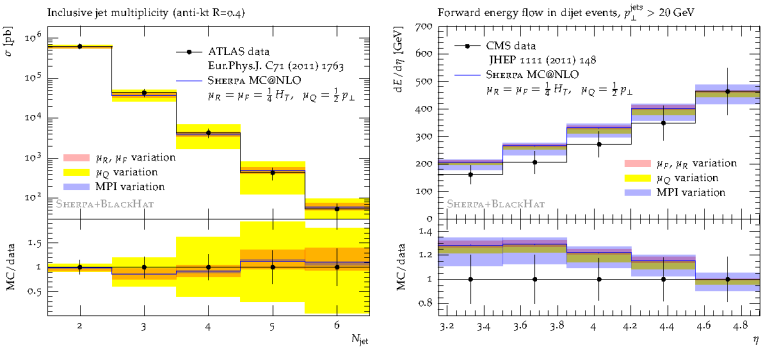

Fig. 3. This shows the a comparison of jet multiplicity in dijet events between SHERPA simulation and ATLAS (left) and of the forward energy flow in dijet events between SHERPA simulation and CMS (right). These plots are taken from Ref. [15]. The errors here are due to scale variation.

two pieces, $R = R^H + R^S$. R^H represents the hard piece and R^S represents the soft, divergent piece. This is then put back into the POWHEG master formula. This yields the MC@NLO master formula, Eq. (4).

$$\sigma_{\text{MC@NLO}} = \int \mathrm{d}\Phi_B \overline{B}(\Phi_B) \left[\Delta(\mu, \mu_0) + \int_{\mu_0}^{\mu} \mathrm{d}\Phi_1 \frac{R^S(\Phi_B \otimes \Phi_1)}{B(\Phi_B)} \Delta(k_T^2, \mu_0)\right] + \int \mathrm{d}\Phi_R R^H(\Phi_R) \quad (4)$$

The MC@NLO Sudakov form factor is

$$\Delta(\mu, \mu_0) = \exp\left[-\int_{\mu_0}^{\mu} \mathrm{d}\Phi_1 \frac{R^S(\Phi_B \otimes \Phi_1)}{B(\Phi_B)}\right] . \quad (5)$$

Equation (4) includes one additional term, which is the hard part of the real emission term. The modified matrix element is also altered by this separation. This introduces the possibility of negatively weighted events, which can introduce a small inefficiency. However, the splitting kernel in the Sudakov form factor can be used as the splitting kernel in the parton shower, making the transition from matrix element to parton shower natural. The MC@NLO method provides the hardest emission to NLO and introduces a local K-factor, similar to POWHEG.

3.2. MC@NLO Results

Figure 3 show ATLAS and CMS results for dijet events. The ATLAS jet multiplicity plot shows SHERPA+BLACKHAT [16] in good agreement with

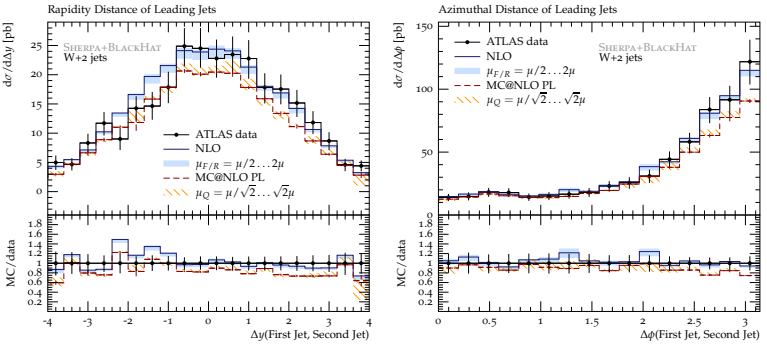

Fig. 4. These plots are from Ref. [17]. The distributions are of the hardest 2 jets in W boson production. The left hand plot is of Δy_{jj} and the right is of $\Delta\Phi_{jj}$.

the data, and the dominating uncertainty here comes from the variation in the resummation scale. The forward energy flow shows a prediction from SHERPA which is consistent with the data. Here the dominating error comes from the MPI.

Figure 4 uses SHERPA+BLACKHAT with W+2 jets production calculated with the MC@NLO method. This compares ATLAS data with NLO and MC@NLO simulations. The uncertainty on the fixed order prediction is given by a variation of renormalisation (μ_R) and fatorisation scale (μ_F) as $\frac{1}{2}\mu_{R/F} < \mu_{R/F} < 2\mu_{R/F}$. On the MC@NLO sample, the uncertainty is given by a variation of resummation scale, $\frac{1}{\sqrt{2}}\mu_Q < \mu_Q < \sqrt{2}\mu_Q$.

4. Merging methods

The matching methods considered above give the hardest emission correct to NLO. This can be considered alongside the merging methods, which better describe hard emissions than the parton shower, which becomes exact in the soft-collinear approximation. Merging methods are implemented in Monte Carlos at LO, and can be easily extended to NLO in principle, by a reweighting of all the contributing terms by a K-factor.

The merging methods considered here are MEPS@NLO [18], which is the implementation in SHERPA with MC@NLO, and MINLO [19], which is implemented with POWHEG.

4.1. Merging Results

This section presents results from merging NLO matrix elements together. Some of the plots show the improved modelling of the hard jets

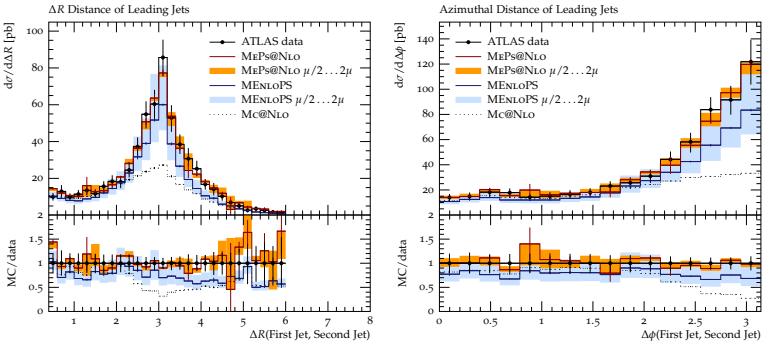

Fig. 5. These are SHERPA+BLACKHAT plots for the ΔR (left) and $\Delta\Phi$ (right) distributions between the hardest 2 jets in merged W+jets results from Ref. [20].

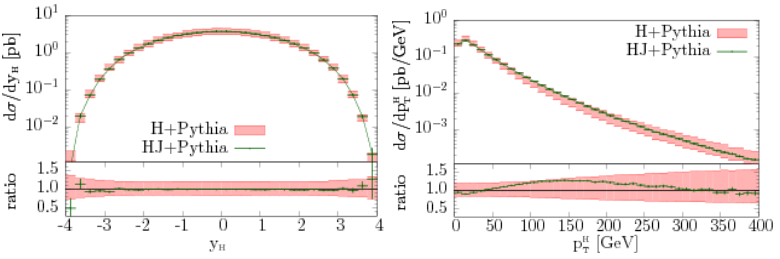

Fig. 6. The left hand plot shows the MINLO merged prediction for the Higgs rapidity, and the right hand plot shows the MINLO merged prediction for the p_T of the Higgs boson from Ref. [21].

that this achieves over simply a matching method. These improvements are most noticeable in observables sensitive to jets other than the hardest.

Figure 5, compares the different NLO techniques for ΔR and $\Delta\Phi$ distributions between the hardest 2 jets. The improvement as we move towards MEPS@NLO is very pronounced for these observables. This is due to how sensitive they are to the modelling of the second jet. MEPS@NLO is the only method which calculates this to NLO accuracy.

Figure 6 demonstrates the implementation of the MINLO method in PYTHIA with the POWHEG method. Figure 6 shows the difference between merging and POWHEG for the rapidity distribution of the Higgs boson in H+jets events. Here the first jet is merged in via the MINLO procedure. Figure 6 also shows the p_T distribution for the Higgs boson, again in H+jets events. Again, the comparison is made between POWHEG and the merging in of an additional jet.

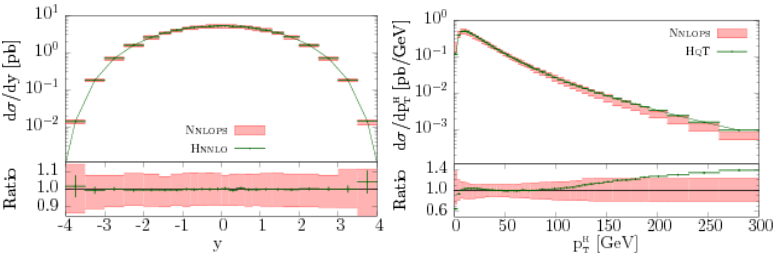

Fig. 7. The p_T and y of the Higgs boson is shown to NNLO matched to a parton shower. These plots are taken from Ref. [22].

5. NNLO matched to parton shower

POWHEG has recently released plots from the first instance of NNLO matrix elements being matched to parton shower [22]. These results are shown in Fig. 7, and are again for the rapidity and p_T of the Higgs boson in Higgs production processes. These can be compared with the POWHEG results for the same observables in Fig. 6. The uncertainties in Fig. 7 are greatly reduced, as compared with Fig. 6.

6. Future outlook and conclusions

In the near future, the NLO calculations performed in the Monte Carlo community will be compared with data once these become available, in order to fully verify our implementations of the NLO physics. Completing this leads naturally on to calculating higher order corrections on the longer term. This involves calculating NNLO QCD corrections, and also to begin to introduce NLO EW corrections which can become very large at the collider energies we are beginning to probe.

Another area of interest to the Monte Carlo physics community is to discuss observables which would help the community to properly understand what the Monte Carlo is doing in complicated regions of phase space, and for us to gain a deeper understanding of the physics involved in the processes we are modelling. To this end, the Monte Carlo community is discussing different measurements that we would like the experimentalists to complete.

The current status of Monte Carlo physics is the automation of NLO corrections to the vast majority of processes. These predictions have been compared to data in several cases, and even more are still being verified. The interfacing technology between the matrix element and the parton shower is now very well established.

Acknowledgments

This work is supported by STFC and MCnet. I would like to thank Dr. F. Krauss for his supervision and the University of Durham for their support. Also, I am grateful to the POWHEG-BOX and HERWIG++ Collaborations for providing some recent results.

References

[1] S. Höche, F. Krauss, M. Schönherr, and F. Siegert, J. High Energy Phys. **04**, 024 (2011).

[2] S. Catani and M. Seymour, Nucl. Phys. B **485**, 291 (1997).

[3] R.K. Ellis, D.A. Ross, and A.E. Terrano, Nucl. Phys. B **178**, 421 (1981).

[4] P. Nason, J. High Energy Phys. **11**, 042 (2004).

[5] S. Frixione and B. Webber, J. High Energy Phys. **06**, 029 (2002).

[6] P. Nason, arXiv:1001.2747.

[7] M. Bahr, *et al.*, arXiv:0803.0883.

[8] T. Sjöstrand, S. Mrenna, and P. Skands, arXiv:0710.3820.

[9] S. Alioli, P. Nason, C. Oleari, and E. Re, J. High Energy Phys. **04**, 002 (2009).

[10] L. D'Errico and P. Richardson, J. High Energy Phys. **02**, 130 (2011).

[11] A. Wilcock and P. Richardson, Eur. Phys. J. C **74**, 2713 (2014).

[12] F. Campanario, T.M. Figy, S. Plätzer, and M. Sjödahl, Phys. Rev. Lett. **111**, 211802 (2013).

[13] http://amcatnlo.cern.ch

[14] T. Gleisberg, *et al.*, J. High Energy Phys. **02**, 007 (2009).

[15] S. Höche and M. Schönherr, Phys. Rev. D **86**, 094042 (2012).

[16] C. Berger, *et al.*, Phys. Rev. D **78**, 036003 (2008).

[17] S. Höche, F. Krauss, M. Schönherr, and F. Siegert, Phys. Rev. Lett. **110**, 052001 (2013).

[18] S. Höche, F. Krauss, M. Schönherr, and F. Siegert, J. High Energy Phys. **04**, 027 (2013).

[19] K. Hamilton, P. Nason, and G. Zanderighi, J. High Energy Phys. **10**, 155 (2012).

[20] A. Höche, F. Krauss, M. Schönherr, and F. Siegert, J. High Energy Phys. **04**, 027 (2013).

[21] K. Hamilton, P. Nason, C. Oleari, and G. Zanderighi, J. High Energy Phys. **05**, 082 (2013).

[22] K. Hamilton, P. Nason, E. Re, and G. Zanderighi, J. High Energy Phys. **10**, 222 (2013).

Recent results from the search for the critical point of strongly interacting matter at the CERN SPS

Peter Seyboth

Max-Planck Institut für Physik, Munich, Germany
and
Jan Kochanowski University, Kielce, Poland

for the NA49 and NA61/SHINE collaborations

Recent searches at the CERN SPS for evidence of the critical point of strongly interacting matter are discussed. Experimental results on theroretically expected signatures, such as event-to-event fluctuations of the particle multiplicity and the average transverse momentum as well as intermittency in particle production are presented.

1. Introduction

Exploration of the phases of strongly interacting matter is the main purpose of the study of high energy heavy-ion collisions. Theoretical considerations [1] suggest that the phase boundary between confined hadrons at low and quasi-free quarks and gluons at high temperature and/or density is of the first order in systems with large net-baryon density (or equivalently baryochemical potential $\mu_B \gg 0$). Lattice QCD calculations [2] can provide quantitative predictions at zero net baryon density ($\mu_B = 0$) and find that the transition is a rapid crossover. Thus a critical point is expected as the endpoint of the first-order transition line. However, lattice QCD is not yet able to cope with $\mu_B > 0$ in a strict way. Predictions of the existence and location of the critical point (CP) in the phase diagram of T versus μ_B have to be obtained from extrapolations which arrive at conflicting results. Some find a CP in a region accessible to experiments at the SPS and the RHIC beam energy scan [3], others locate the CP at high μ_B where heavy-ion experiments are not able to produce the deconfined phase [4] or they find no CP at all [5]. Clearly it is important to address this issue by experimental studies.

At a CP the correlation length ξ diverges leading to a strong increase of suitable correlation measures such as event-to-event fluctuations of the multiplicity and average transverse momentum of produced particles [6] as

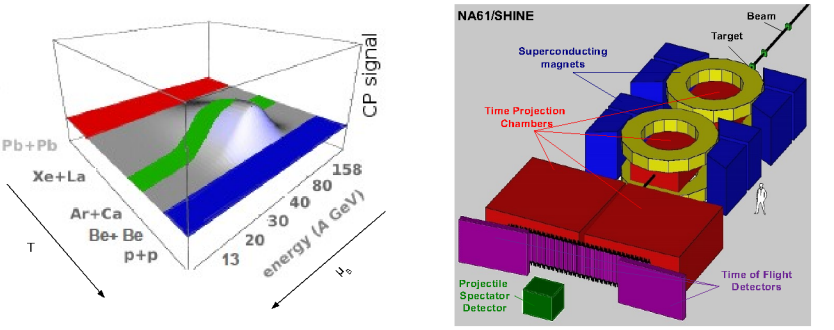

Fig. 1. Left: expected hill of fluctuations in a scan of the phase diagram with a critical point. Right: schematic view of the NA49/NA61 detector

well as local density fluctuations resulting in the appearance of intermittency in particle production [7]. Owing to the finite size and short lifetime of the fireballs produced in collisions of nuclei, ξ is expected not to exceed 3-6 fm in Pb+Pb collisions. Moreover, correlations may be diluted by rescattering of the produced particles before final freezeout.

A scan of the phase diagram by varying the sizes of colliding nuclei (change of rescattering probabilty) and energies of the collisions (change of μ_B) is a promising search strategy (see Fig. 1, left). A coinciding maximum of several fluctuation measures would indicate the existence and the location of the CP. This program was started by the NA49 collaboration [8] and is now pursued systematically by the NA61/SHINE experiment [9].

2. Detector and recorded data

The NA61 experiment, the successor of NA49, uses a fixed target spectrometer with particle identification, covering mainly the forward region in the center-of-mass rapidity. The schemtic view in Fig. 1 (right) shows the system of four large Time Projection Chambers for particle tracking and momentum measurement. The first two are placed inside superconducting magnets with combined bending power of 9 Tm. Particle identification is obtained by measuring the energy loss by ionisation in the gas of the TPCs with precision of about 4 % and the time-of-flight in scintillation counter walls with resolution of 60-80 ps. For the NA61 program the NA49 detector was upgraded by a new cellular zero degree calorimeter (Projectile Spectator Detector) with single beam nucleon energy resolution and a He filled beam pipe trough the TPCs to reduce beam induced δ-ray background. Finally, the digital part of the TPC readout was replaced resulting in a factor 10 increase of the data acquisition rate.

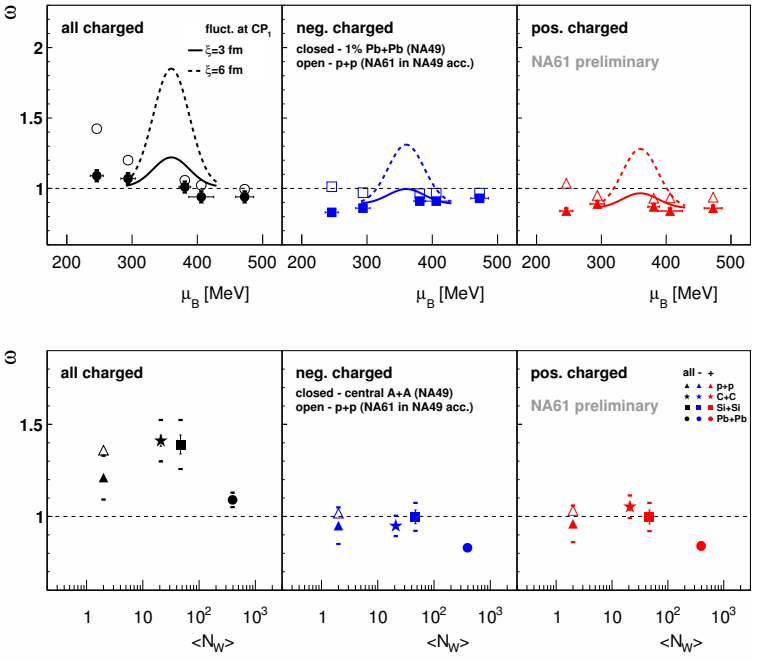

Fig. 2. Scaled variance ω of the multiplicity distribution of charged particles. Top: versus μ_B for the 1% most central Pb+Pb collisions and inelastic p+p reactions for $1.0 < y < y_{beam}$ (assuming the pion mass). Bottom: versus the number of wounded nucleons N_W in inelastic p+p ($1.1 < y < 2.6$) and the 1% most central C+C, Si+Si and Pb+Pb collisions at 158A GeV ($1.0 < y < y_{beam}$). Full symbols show results of NA49 [10], open symbols NA61 (preliminary).

NA49 recorded data on central Pb+Pb collisions at a set of energies (20A, 30A, 40A, 80A and 158A GeV) through the SPS energy range in the period 1994–2002. Additionally a smaller set of data was taken for C+C and Si+Si collisions at 40A and 158A GeV. NA61 expands this program and resumed in 2009 a comrehensive scan of energies (13A GeV + NA49 energies) and nuclear sizes (p+p, Be+Be, Ar+Ca, Xe+La, Pb+Pb) which has been completed for the lightest two systems.

3. Fluctuations of the particle multiplicity

The signature of a CP is expected to be primarily an increase of multiplicity fluctuations [6] which are usually quantified by the scaled variance $\omega = (\langle N^2 \rangle - \langle N \rangle^2)/\langle N \rangle$ of the distribution of particle multiplicities N produced in the collisions. The measure ω is "intensive", i.e., it is independent

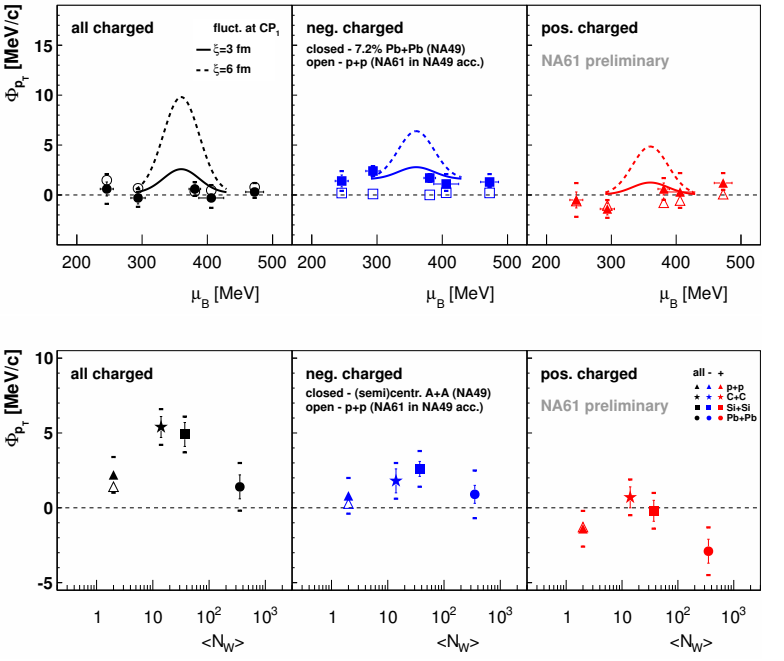

Fig. 3. Fluctuation measure Φ_{p_T} of the average transverse momentum of charged particles. Top: versus μ_B for the 7.2% most central Pb+Pb collisions (full symbols, NA49 [16]) and inelastic p+p reactions (open symbols, NA61 preliminary). Bottom: versus the number of wounded nucleons N_W in central C+C, Si+Si and Pb+Pb collisions at 158A GeV (NA49 [17]) and inelastic p+p reactions (NA61 preliminary). Results are for cms rapidity $1.1 < y < 2.6$ assuming the pion mass.

of the number of wounded nucleons N_W (size or volume) of the system in models which assume nucleus+nucleus collisions to be a superposition of nucleon+nucleon reactions. However, ω is sensitive to the unavoidable fluctuations of N_W [12]. Therefore the measurements were restricted to the 1 % most central collisions. Results for charged particles in Pb+Pb collisions (NA49 [10]) are shown in Fig. 2 (top) versus μ_B (obtained from statistical model fits to yields of different particle types at the various collision energies) and compared to preliminary NA61 results from p+p reactions. The data do not support a maximum as might be expected for a CP (see curves [11]). NA49 also obtained results for different size nuclei at the top SPS energy of 158A GeV (see Fig. 2 (bottom)). Here there may be an indication of a maximum for medium size nuclei. A new identification procedure (identity method [13]) allowed to measure the energy dependence of fluctu-

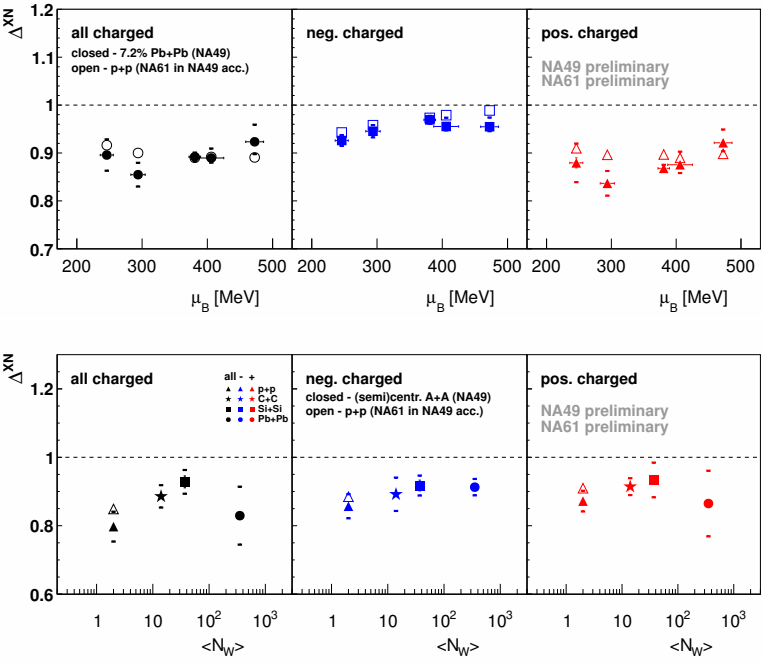

Fig. 4. Fluctuation measure $\Delta^{P_T,N}$ of the average transverse momentum of charged particles. Top: versus μ_B for the 7.2% most central Pb+Pb collisions (full symbols) and inelastic p+p reactions (open symbols). Bottom: versus the number of wounded nucleons N_W in inelastic p+p and central C+C, Si+Si and Pb+Pb collisions at 158A GeV. Results are for cms rapidity $1.1 < y < 2.6$ assuming the pion mass. (NA49 and NA61 preliminary).

ations of identified proton, kaon and pion multiplicities in p+p and Pb+Pb collisions. As in the case of charged particle multiplicities no indication of a CP is found. It was pointed out that higher moments of the multiplicity distributions are more sensitive to effects of the CP [14]. Unfortunately the systematic uncertainties of the measurements in NA49 and NA61 at present do not allow meaningful conclusions.

4. Fluctuations of the average transverse momentum

Enhanced fluctuations are also expected for the average transverse momentum p_T when the freezeout occurs close to the CP [6]. A suitable measure Φ_{p_T} was proposed in [15], which is "strongly intensive", i.e. independent of both N_W and its fluctuations. Results on the dependence of Φ_{p_T} on μ_B in central Pb+Pb (NA49 [16]) and inelastic p+p collisions (NA61

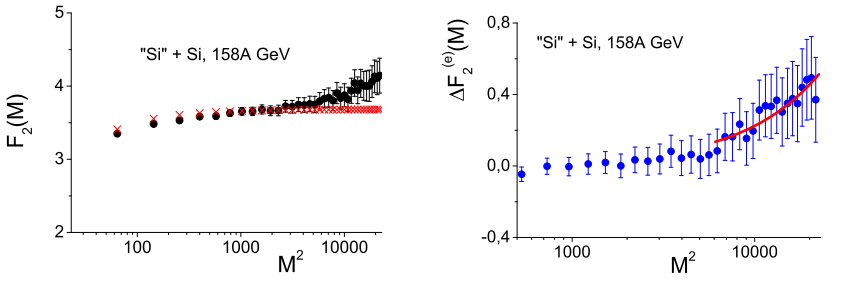

Fig. 5. Scaled factorial moments of protons in rapidity $|y| < 0.75$ for the 12.5% most central Si+Si collisions at 158A GeV (NA49 [20]). Left: $F_2(M)$ versus the number of cells M^2 in transverse momentum space. Dots show data, crosses the mixed event background. Right: $\Delta F_2(M)$ versus M^2; dots show background subtracted data, the curve the result of a power-law fit $\Delta F_2(M) \propto M^{2\Phi_2}$.

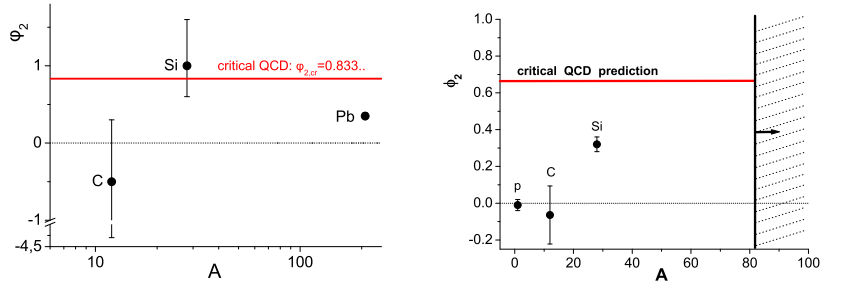

Fig. 6. Exponent Φ_2 obtained from power law fits to second scaled factorial moments of protons [18] (left) and low-mass $\pi^+\pi^-$ pairs [21] (right) for several collision systems at 158A GeV.

preliminary) are plotted in Fig. 3 (top) and compared to expectations for a CP (curves in Fig. 3 (top) [11]). Measurements for different size nuclei at the top SPS energy of 158A GeV are shown in Fig. 3 (bottom). As found for ω there is no evidence for a CP from the dependence of Φ_{p_T} on μ_B, but there may be a maximum for medium-size nuclei.

Recently a new class of strongly intensive measures was proposed in Ref. [12]. Whereas $\Sigma^{P_T,N}$ is closely related to Φ_{p_T} the quantity $\Delta^{P_T,N}$ is sensitive to fluctuations of p_T and N in a different combination. Results shown in Fig. 4 are inconclusive, in particular, as at present there are no predictions for the effect of a CP in this observable.

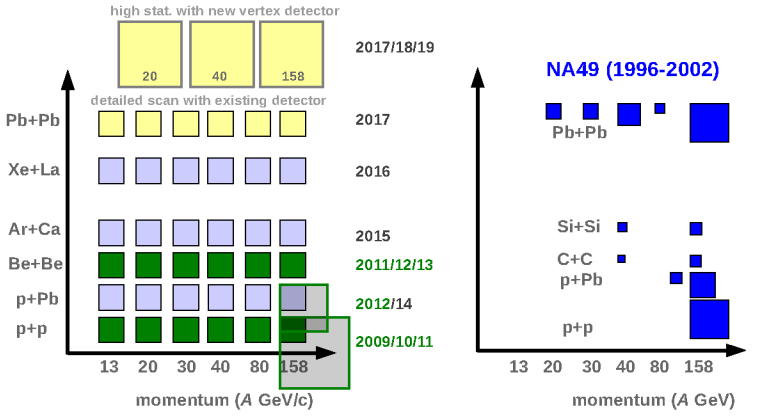

Fig. 7. Reactions and energies of the scan of the phase diagram by NA61 (left, in progress) and systems previously studied by NA49 (right).

5. Local density fluctuations of protons and low-mass $\pi^+\pi^-$ pairs

Theoretical investigations [7] predict near the CP the appearance of local density fluctuation for protons [18] and low-mass $\pi^+\pi^-$ pairs of power-law nature with known critical exponents [19]. These can be studied by the intermittency analysis method in transverse momentum space using second factorial moments $F_2(M)$, where M is the number of subdivisions in each p_T direction. After combinatorial background subtraction the exponents Φ_2 are obtained from a power-law fit to the corrected moments $\Delta F_2(M) \propto M^{2\Phi_2}$. The procedure is illustrated for protons in central Si+Si collisions in Fig. 5. The resulting values of Φ_2 obtained for central C+C, Si+Si and Pb+Pb collisions at 158A GeV [20] are plotted in Fig. 6 (left). Remarkably, Φ_2 seems to reach a maximum for Si+Si collisions which is consistent with the theoretical expectation for the CP. A similar conclusion was reached for low-mass $\pi^+\pi^-$ pairs [21] (see Fig. 6 (right)).

6. Conclusion

The continuing search in nucleus+nucleus collisions for the maximum of fluctuations predicted for a critical point of strongly interacting matter has

not yet turned up firm evidence in the CERN SPS energy range. Tantalising hints were found for medium-size nuclei in data from the NA49 experiment which strongly motivate the ongoing scan of the phase diagram by the NA61 experiment (see Fig. 7). A search for the CP is also in progress at the Brookhaven RHIC within the beam energy scan (BES) program.

Acknowledgments

I thank the organisers of ISMD2013 for giving me the opportunity to present this report and I am grateful to all members of the NA49 and NA61 collaborations for their hard work to obtain these experimental results.

References

[1] See e.g. E. Shuryak, Phys. Rep. **61**, 71 (1980).

[2] For a recent review see: O. Philipsen, Prog. Part. Nucl. Phys. **70**, 55 (2013).

[3] Z. Fodor and S. Katz, J. High Energy Phys. **04**, 50 (2004); S. Datta, R. Gavai, and S. Gupta, Nucl. Phys. A **905–906**, 883c (2013).

[4] A. Li, A. Alexandru, and K.-F. Liu, Phys. Rev. D **84**, 071503 (2011).

[5] Ph. de Forcrand and O. Philipsen, J. High Energy Phys. **11**, 12, (2008); G. Endrődi *et al.*, J. High Energy Phys. **04**, 1 (2011).

[6] M. Stephanov, K. Rajagopal, and E. Shuryak, Phys. Rev. D **60**, 114028 (1999).

[7] N. Antoniou *et al.*, Nucl. Phys. A **693**, 799 (2001); ibid **761**, 149 (2005).

[8] http://na49info.web.cern.ch/na49info/na49/

[9] https://na61.web.cern.ch/na61/

[10] C. Alt *et al.* (NA49 collaboration), Phys. Rev. C **78**, 034914 (2008).

[11] M. Stephanov, private communication; K. Grebieszkow (NA49 collaboration), Nucl. Phys. A **830**, 547c (2009).

[12] M. Gazdzicki and M. Gorenstein, Phys. Rev. C **84**, 014904 (2011).

[13] M. Gazdzicki *et al.*, Phys. Rev. C **83**, 054907 (2011); M. Gorenstein, Phys. Rev. C **84**, 024902 (2011).

[14] M. Stephanov, Phys. Rev. Lett. **102**, 032301 (2009).

[15] M. Gazdzicki and S. Mrowczynski, Z. Phys. C **54**, 127 (1992).

[16] T. Anticic *et al.* (NA49 collaboration), Phys. Rev. C **79**, 044904 (2009).

[17] T. Anticic *et al.* (NA49 collaboration), Phys. Rev. C **70**, 034902 (2004).

[18] Y. Hatta and M. Stephanov, Phys. Rev. Lett. **91**, 102003 (2003).

[19] N. Antoniou *et al.*, Phys. Rev. Lett. **97**, 032002 (2006).

[20] T. Anticic *et al.* (NA49 collaboration), arXiv:1208.5292.

[21] T. Anticic *et al.* (NA49 collaboration), Phys. Rev. C **81**, 064907 (2010).

The phase diagram of QCD from lattice simulations

Massimo D'Elia
Dipartimento di Fisica dell'Università di Pisa
and INFN - Sezione di Pisa, Largo Pontecorvo 3, I-56127 Pisa, Italy

Numerical simulations of Quantum Chromodynamics on a space-time lattice represent the best non-perturbative tool to explore the QCD phase diagram and the behavior of strong interactions under extreme conditions. We review the present status of the field and discuss some recent results.

1. Introduction

Many of the questions which are still open within the Standard Model of particle physics concern strong interactions. They are described by Quantum Chromodynamics (QCD). While we have a clear understanding of the theory in the high energy limit where, thanks to property of asymptotic freedom, it is perturbative, we still cannot solve the low energy regime, where the coupling is strong and the theory is non-perturbative. As a result, we still do not understand why quarks and gluons, the elementary colored degrees of freedom of QCD, are confined into hadrons. One would also like to know if color confinement is a permanent state of matter, or if in particular extreme conditions, characterized by high temperature, high baryon density or strong magnetic fields, different phases of strongly interacting matter can be found.

The possible presence of a high temperature deconfined Quark-Gluon plasma phase has been explored since long: it is of particular interest for cosmological and astrophysical reasons (think, e.g., of the early stages of evolution of the Universe), and it is experimentally probed by heavy ion collision experiments.

Numerical simulations of QCD discretized on a Euclidean space-time lattice represent the best available tool to explore strong interactions in the non-perturbative regime, starting from the first principles of the theory. In practice, one rewrites the QCD thermal partition function, formulated in the Feynman path integral formalism, as follows

$$Z(V,T) = \int \mathcal{D}U\mathcal{D}\psi\mathcal{D}\bar{\psi} e^{-(S_G[U]+\bar{\psi}M[U]\psi)} = \int \mathcal{D}U e^{-S_G[U]} \det M[U] \, ,$$

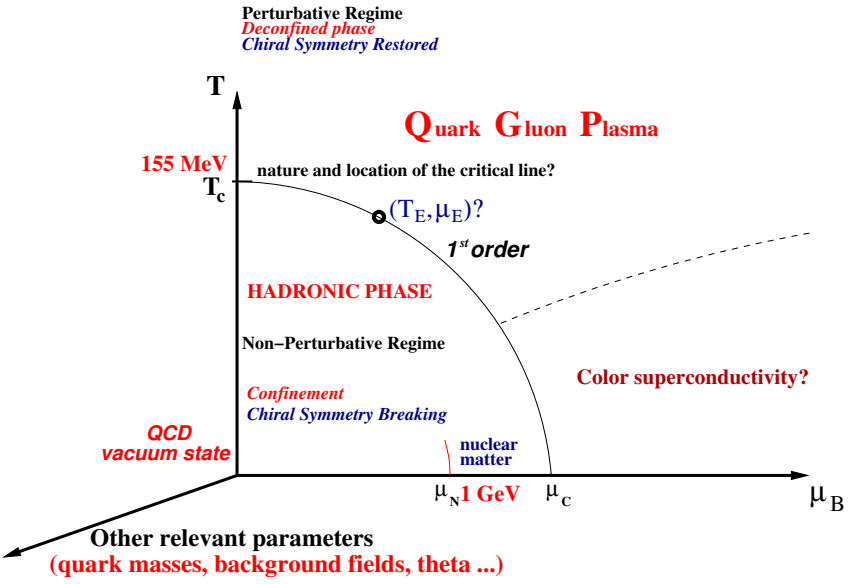

Fig. 1. Schematic view of the QCD phase diagram. The $T - \mu_B$ plane is shown in more detail, together with some questions that lattice simulations still leave open.

where U are the gauge link variables (elementary parallel transports) and $\bar{\psi} M \psi$ is a proper discretization of the quark action. The temperature T is related to the extension of the compactified Euclidean time dimension τ, $T = 1/\tau = 1/(N_t a)$ where a is the lattice spacing (we assume an isotropic cubic lattice) and N_t is the number of lattice sites in the time direction. $S_G[U]$ is the pure gauge action while $\det M$ encodes the contribution of dynamical fermions. Lattice simulations are ideally suited to compute equilibrium quantities, like

$$\langle O \rangle_T = \frac{\int \mathcal{D}U e^{-S_G[U]} \det M[U] O[U]}{\int \mathcal{D}U e^{-S_G[U]} \det M[U]} = \int \mathcal{D}U \mathcal{P}[U] O[U] \, ,$$

where O is a generic physical observable, via Monte-Carlo sampling. An obvious requirement is that the probability distribution over gauge configurations, $\mathcal{P}[U]$, be real and positive. In general, the correct inclusion of the fermion determinant in the probability distribution is the most demanding task in terms of computational power, especially when one tries to lower the values of the light quark masses towards their physical values.

Lattice simulations give us information, with a systematically increasable precision, about basic thermodynamical quantities, like the pressure and the

energy density, about equilibrium particle and quantum number distributions (e.g., quadratic and higher order susceptibilities of baryon number and electric charge) and on the location and the order of the transitions to the different phases of strongly interacting matter, i.e. about the QCD phase diagram, which is reported schematically in Fig. 1. Apart from temperature, one can think of many possible extensions of the phase diagram, representing external parameters of phenomenological relevance. Unfortunately, the important case of a baryonic chemical potential μ_B, which is necessary to consider QCD at finite density, is plagued by the so-called sign problem: the fermion determinant $\det M[\mu_B \neq 0]$ is complex, so that the path integral measure is not positive and Monte-Carlo methods are not directly usable. Approximate methods works well only in a limited region where $\mu_B/T \ll 1$, which is the case of the strongly interacting medium produced in heavy ion collisions at very high energies ($\mu_B/T \sim 10^{-2}$ at LHC).

2. Phase diagram at zero and non-zero baryon density

The liberation of color degrees of freedom at the deconfinement temperature is clearly visible, in lattice studies, from the sudden increase of approximate order parameters, like the Polyakov loop, and of various thermodynamical quantities, like the energy density, the pressure or the quark number susceptibilities. Roughly around the same temperature, the restoration of chiral symmetry, which is spontaneously broken at low T, takes place. There is now good agreement between different collaborations, adopting different discretizations schemes, regarding the location of this transition, which according to chiral symmetry restoration is placed around $T_c \sim 155$ MeV [1, 2].

The behavior of various susceptibilities is consistent with the absence of a true transition, i.e. no discontinuities seem to develop as the thermodynamical limit is approached [3]: that means that either the transition is extremely weak (hence not phenomenologically relevant) or deconfinement and chiral symmetry restoration correspond simply to a rapid change of physical properties.

Actually, this is the situation for physical values of the quark masses. In numerical simulations the quark mass spectrum can be changed at will and one can explore the nature of the transition as a function of u/d and s quark masses. The present outcome of such exploration is reported in Fig. 2, which is usually known as the Columbia plot. A true transition is present in the limit of very light or very heavy quark masses, where exact symmetries and order parameters can be found (chiral and center symmetry respectively). Unsettled issues exist regarding the chiral limit of the two flavor theory [4], where the transition could be first order or second order

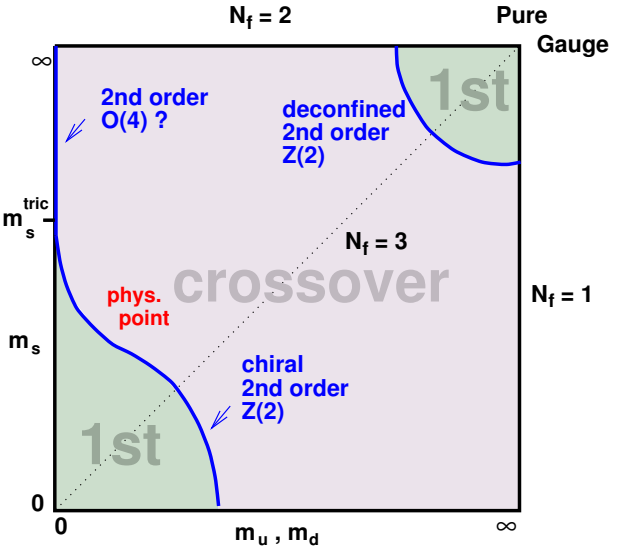

Fig. 2. Phase structure of $N_f = 2 + 1$ QCD as a function of the up/down and strange quark masses.

in the $O(4)$ universality class.

When one considers the various possible extensions of the phase diagram, like the inclusion of a baryon chemical potential μ_B, one would like to determine how T_c changes and if it corresponds to a true transition at some stage, for instance at a critical endpoint in the $T - \mu_B$ plane. For QCD at finite baryon density reliable numerical results can be obtained only in a restricted region of high T and small chemical potentials, where approximate solutions to the sign problem can be found, like reweighting techniques [5, 6], analytic continuation from imaginary chemical potentials [7–9] and Taylor expansion techniques [10, 11].

As an example, in Fig. 2 we report a comparison (see Ref. [12]) of the critical line $T_c(\mu_B)$ determined in the case of four degenerate flavors by different techniques (the pseudocritical temperature T_c is an increasing function of the pseudocritical coupling β_c, which is the quantity reported in the figure). Consistency among different determinations is good as long $\mu/T \leq 1$ (μ is the quark chemical potential, i.e. $\mu \equiv \mu_B/3$), meaning that the curvature of the pseudocritical line at $\mu = 0$ can be determined with good control over systematic uncertainties. In the physical case of 2 or 2+1 flavors one obtains values for the curvature of the critical line, $T_c(\mu)/T_c(0) = 1 - A\,(\mu/T)^2$, in the range $A \sim 0.05 - 0.07$ [8, 13–15]. Such values are smaller, by ap-

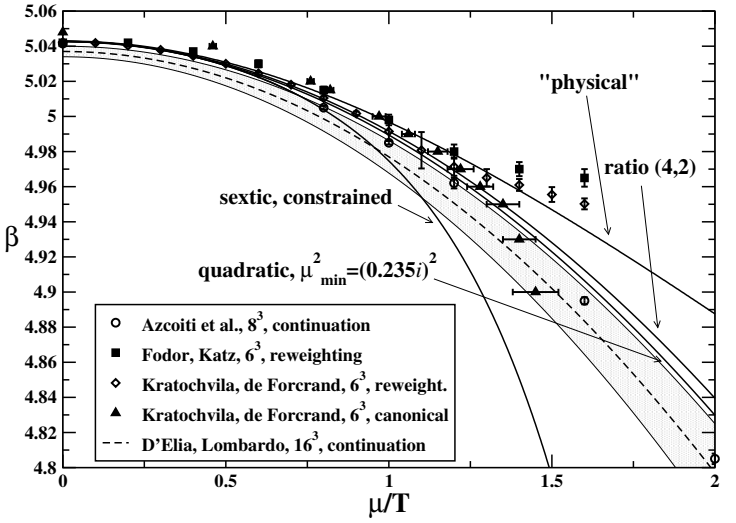

Fig. 3. Determination of the line of pseudo-critical couplings for deconfinement as a function of the quark chemical potential μ for $N_f = 4$ QCD. Various different methods are compared, including different extrapolations from simulations at imaginary chemical potentials.

proximately a factor 3, than those usually obtained for chemical freeze-out curves in heavy ion collisions. However a recent re-analysis of heavy-ion data, which takes better into account inelastic interactions after hadronization, seems to bring the freeze-out curves closer to lattice predictions for the pseudocritical line [16, 17].

Unfortunately the same techniques, working well for small baryon chemical potentials, have not provided, up to now, a clear and consistent evidence for the presence and the location of the critical endpoint in the $T-\mu_B$ plane, at which the pseudo-transition present at $\mu_B = 0$ would turn into a first order transition.

The general idea is that the introduction of non-zero μ_B would increase the strength of the transition, thus enlarging the low-mass first order region in Fig. 2 till the physical point is included into it. However, numerical simulations performed at imaginary chemical potential, i.e. negative μ_B^2, seem indicate that the effect of a a positive μ_B^2 is instead to decrease the strength of the transition [18]. This has been recently reinterpreted in terms of the general structure of the phase diagram at $\mu_B^2 < 0$, in particular in connection with the phase structure close to the so-called Roberge-Weiss endpoint [19, 20] and the related tricritical points. In Fig. 2 we show the

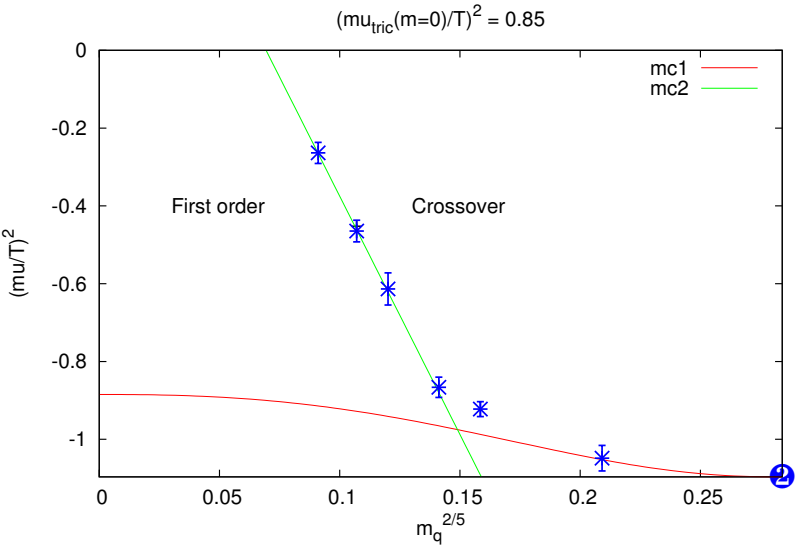

Fig. 4. Phase structure of $N_f = 2$ QCD in the bare quark mass - imaginary chemical potential plane. Imaginary chemical potentials correspond negative values of μ^2. The scale chosen for the quark mass axis permits to better appreciate the chiral extrapolation according to tricritical scaling (see Ref. [21]).

result of recent extensive studies regarding the order of the phase transition for the theory with two light flavors, $N_f = 2$ QCD, as a function of the bare quark mass and μ^2 [21]: the first order region clearly shrinks as μ^2 increases; moreover, present results suggest that the chiral limit at $\mu = 0$, i.e. the left-upper corner in Fig. 2, might be first order, in agreement also with the findings of Ref. [4].

3. Strongly interacting matter in strong magnetic fields

Quarks are also subject to electromagnetic interactions, which however are expected, in general, to bring small corrections to strong interaction physics. Nevertheless, the situation may be different in the presence of background fields whose strenght is at the QCD scale. The issue is of great phenomenological interest, since in some heavy ion collisions one has the highest magnetic fields ever created in a laboratory [22], reaching up to 10^{15} Tesla ($eB \sim 0.1$ GeV^2) at LHC, and even larger fields may have been created in the early stages of the Universe [23, 24].

That justifies the recent theoretical interest in the subject [25]. Contrary

to the case of a finite μ_B, the introduction of a magnetic background field does not encounter particular technical problems, such as a sign problem, so that various interesting questions can be conveniently approached and have been investigated by lattice QCD simulations in the last few years [26–43].

Lattice results show that T_c decreases as a function of the external field, with deconfinement and chiral symmetry breaking remaining entangled. The strength of the transition increases, in the sense that the rapid change of thermodynamical quantities becomes steeper and steeper, even if no evidence has been found till now for a critical endpoint in the $T - B$ plane where T_c becomes a true transition point.

Various studies have investigated the magnetic properties of strongly interacting matter. The outcome is that it behaves as a paramagnetic material [38–40, 43], with a magnetic susceptibility which steeply rises as one enters the deconfined Quark-Gluon Plasma phase, and is comparable to that of well known strong paramagnetic materials, such as liquid oxygen.

References

[1] S. Borsanyi *et al.*, J. High Energy Phys. **09**, 073 (2010).
[2] A. Bazavov *et al.*, Phys. Rev. D, **85**, 054503 (2012).
[3] Y. Aoki, Z. Fodor, S.D. Katz, and K. K. Szabo, Phys. Lett. B **643**, 46 (2006).
[4] M. D'Elia, A. Di Giacomo, and C. Pica, Phys. Rev. D **72**, 114510 (2005); G. Cossu, M. D'Elia, A. Di Giacomo, and C. Pica, arXiv:0706.4470 [hep-lat].
[5] I.M. Barbour *et al.*, Nucl. Phys. (Proc. Suppl.) A **60**, 220 (1998).
[6] Z. Fodor and S.D. Katz, Phys. Lett. B **534**, 87 (2002).
[7] M.G. Alford, A. Kapustin, and F. Wilczek, Phys. Rev. D **59**, 054502 (1999).
[8] P. de Forcrand and O. Philipsen, Nucl. Phys. B **642**, 290 (2002).
[9] M. D'Elia and M.P. Lombardo, Phys. Rev. D **67**, 014505 (2003).
[10] C.R. Allton *et al.*, Phys. Rev. D **66**, 074507 (2002).
[11] R.V. Gavai and S. Gupta, Phys. Rev. D **68**, 034506 (2003).
[12] P. Cea, L. Cosmai, M. D'Elia, and A. Papa, Phys. Rev. D **81**, 094502 (2010).
[13] O. Kaczmarek *et al.*, Phys. Rev. D **83**, 014504 (2011).
[14] G. Endrodi, Z. Fodor, S.D. Katz, and K.K. Szabo, J. High Energy Phys. **04**, 001 (2011).
[15] P. Cea *et al.*, Phys. Rev. D, **85**, 094512 (2012).
[16] F. Becattini *et al.*, Phys. Rev. C **85**, 044921 (2012).
[17] F. Becattini *et al.*, Phys. Rev. Lett. **111**, 082302 (2013).

[18] P. de Forcrand and O. Philipsen, J. High Energy Phys. **01**, 077 (2007); J. High Energy Phys. **11**, 012 (2008).
[19] A. Roberge and N. Weiss, Nucl. Phys. B **275**, 734 (1986).
[20] M. D'Elia and F. Sanfilippo, Phys. Rev. D **80**, 111501 (2009); P. de Forcrand and O. Philipsen, Phys. Rev. Lett. **105**, 152001 (2010); C. Bonati, G. Cossu, M. D'Elia, and F. Sanfilippo, Phys. Rev. D **83**, 054505 (2011).
[21] C. Bonati *et al.*, PoS LATTICE **2011**, 189 (2011); arXiv:1311.0473.
[22] V. Skokov, A.Y. .Illarionov and V. Toneev, Int. J. Mod. Phys. A **24**, 5925 (2009); V. Voronyuk *et al.*, Phys. Rev. C **83**, 054911 (2011); A. Bzdak and V. Skokov, W.-T. Deng and X.-G. Huang, Phys. Rev. C **85**, 044907 (2012).
[23] T. Vachaspati, Phys. Lett. B **265**, 258 (1991).
[24] D. Grasso and H.R. Rubinstein, Phys. Rept. **348**, 163 (2001).
[25] D. Kharzeev, K. Landsteiner, A. Schmitt, and H.-U. Yee, Lect. Notes Phys. **871**, 1 (2013).
[26] P. Cea and L. Cosmai, J. High Energy Phys. **08**, 079 (2005); P. Cea, L. Cosmai, and M. D'Elia, J. High Energy Phys. **12**, 097 (2007).
[27] P.V. Buividovich, M.N. Chernodub, E.V. Luschevskaya, and M.I. Polikarpov, Nucl. Phys. B **826**, 313 (2010).
[28] P.V. Buividovich, M.N. Chernodub, E.V. Luschevskaya, and M.I. Polikarpov, Phys. Rev. D **80**, 054503 (2009).
[29] M. Abramczyk, T. Blum, G. Petropoulos, and R. Zhou, PoS LAT **2009**, 181 (2009).
[30] P.V. Buividovich *et al.*, Phys. Rev. Lett. **105**, 132001 (2010).
[31] M. D'Elia, S. Mukherjee, F. Sanfilippo, Phys. Rev. D **82**, 051501 (2010).
[32] M. D'Elia and F. Negro, Phys. Rev. D **83**, 114028 (2011).
[33] V.V. Braguta *et al.*, Phys. Lett. B **718**, 667 (2012).
[34] E.-M. Ilgenfritz *et al.*, Phys. Rev. D **85**, 114504 (2012).
[35] G.S. Bali *et al.*, J. High Energy Phys. **02**, 044 (2012).
[36] G.S. Bali *et al.*, Phys. Rev. D **86**, 094512 (2012).
[37] G.S. Bali *et al.*, J. High Energy Phys. **04**, 130 (2013).
[38] C. Bonati *et al.*, Phys. Rev. Lett. **111**, 182001 (2013).
[39] C. Bonati *et al.*, arXiv:1310.8656 [hep-lat].
[40] L. Levkova and C. DeTar, arXiv:1309.1142 [hep-lat].
[41] M. D'Elia, M. Mariti, and F. Negro, Phys. Rev. Lett. **110**, 082002 (2013).
[42] E.-M. Ilgenfritz, M. Muller-Preussker, B. Petersson, and A. Schreiber, arXiv:1310.7876 [hep-lat].
[43] G.S. Bali, F. Bruckmann, G. Endrodi, and A. Schafer, arXiv:1310.8145 [hep-lat]; arXiv:1311.2559 [hep-lat].

Particle production sources in heavy ion collisions at RHIC and LHC

Georg Wolschin

Institut für Theoretische Physik der Universität Heidelberg, Philosophenweg 16, D-69120 Heidelberg, Germany, EU

A nonequilibrium statistical relativistic diffusion model (RDM) with three sources is applied to the analysis of charged-hadron distributions in Au–Au collisions at RHIC energies, in Pb–Pb collisions at the current LHC energy of 2.76 TeV, and in p–Pb at 5.02 TeV. The relative sizes of the particle production sources at RHIC and LHC energies are investigated in pseudorapidity space as functions of incident energy. The midrapidity source that arises mostly from gluon-gluon collisions becomes more important than the fragmentation sources as the energy increases from RHIC to LHC.

1. Introduction

Charged-hadron production in relativistic heavy ion collisions has been investigated in great detail at the Relativistic Heavy Ion Collider RHIC in Au–Au collisions, and more recently at the Large Hadron Collider LHC in Pb–Pb collisions. In particular, high-precision pseudorapidity distributions $dN_{ch}/d\eta$ of produced charged particles including their centrality dependence are now available in an energy range from $\sqrt{s_{NN}} = 0.019$ to 2.76 TeV [1, 2]. At RHIC energies these data include the fragmentation regions up to the values of the beam rapidities, whereas at the current LHC energy of 2.76 TeV corresponding to a beam rapidity of $y_{beam} = 7.99$ very precise ALICE data are available at $-5 < \eta < 5.5$ [2].

Theoretical descriptions of the underlying partonic processes often focus on gluon-gluon production, such as in many approaches based on the color glass condensate (see [3] as an example). Based on this mechanism particle and antiparticle distributions would, however, be identical – which is not the case experimentally, as found for example in π^+ and π^- distribution functions [4].

The relevance of the fragmentation sources from quark-gluon interactions has been investigated in a recent QCD-based study of net-baryon

distributions (baryons minus antibaryons). There the gluon-gluon source that is peaked at midrapidity cancels out such that only the fragmentation sources remain [5, 6], giving rise to two fragmentation peaks that are clearly seen in the data at high SPS and RHIC energies, and in the theoretical predictions at LHC energies. At low SPS energies the fragmentation peaks overlap in rapidity space and hence, are not directly visible in the data, but can still be extracted quite reliably [7].

For produced particles (rather than net baryons), the effect of the fragmentation sources is less obvious, but clearly has to be considered. In this note I propose to investigate the relative importance of gluon-gluon vs. fragmentation sources as a function of c.m. energy in collisions of heavy systems (Au–Au, Pb–Pb) using a phenomenological nonequilibrium-statistical model. This relativistic diffusion model (RDM) [8] has proven to be useful in the analysis of data and in predictions for asymmetric [9] and symmetric [10] systems. Its three sources correspond to the gluon-gluon and fragmentation sources of the available microscopic theories. In direct comparisons with data the RDM can be used to infer the relative sizes of these underlying components as functions of the incident energy.

In charged-hadron production at SPS and low RHIC energies up to $\sqrt{s_{NN}} \simeq 20$ GeV, the gluon-gluon source centered at midrapidity is expected – and has turned out – to be unimportant [11], and the measured pseudorapidity distributions are well reproduced from the fragmentation sources only. At these relatively low energies, the fragmentation sources are peaked close to midrapidity and hence, are influenced considerably by the Jacobian transformation from rapidity to pseudorapidity space. At higher energies, the fragmentation peaks move apart, and the central gluon-gluon source emerges. Then the Jacobian increasingly affects only the central source. Also, its overall effect becomes smaller with rising energy since it depends on $(\langle m \rangle / p_T)^2$. Still, a precise determination of the Jacobian is essential for the modeling of pseudorapidity distributions at LHC energies. The pronounced midrapidity dip that is seen in the recent ALICE Pb–Pb charged-hadron data is due to the interplay of fragmentation and central sources, plus the effect of the Jacobian on the central source.

A brief outline of the method used to determine the relative size and extent of the sources in $\eta-$space is given in the next section. Results for heavy systems at RHIC and LHC energies are presented in Sec. 3. The energy dependence of central and fragmentation sources is discussed in Sec. 4. A brief outlook on single-particle observables in p–Pb at 5.02 TeV is also given. The conclusions are drawn in Sec. 5.

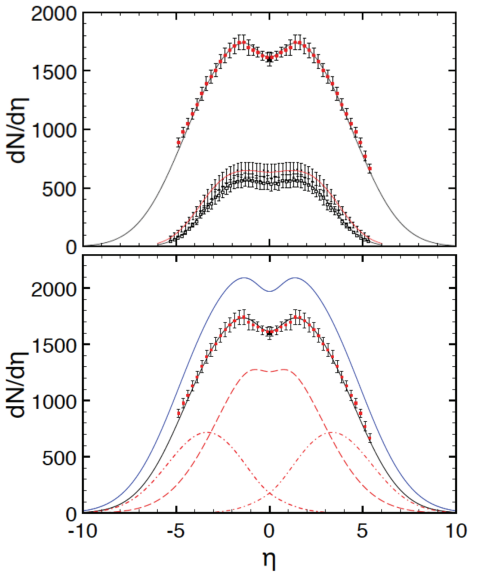

Fig. 1. (Color online) The RDM pseudorapidity distribution function for charged hadrons in central Pb–Pb collisions at LHC energies of 2.76 TeV, and central Au–Au at RHIC energies of 130 and 200 GeV with RDM parameters (Tab. 1) adjusted to the ALICE [12, 2] and PHOBOS [1] data, upper frame. In the bottom frame, the underlying theoretical distributions are shown for 2.76 TeV Pb–Pb. The shape of the midrapidity source is modified by the Jacobian. At LHC energies, the midrapidity value is mostly determined by particle production from gluon–gluon collisions. The upper curve is the RDM-prediction for 5.52 TeV. From Ref. [13].

2. Three sources model

In the three-sources version of the relativistic diffusion model, rapidity distributions of produced particles are calculated from an incoherent superposition of the fragmentation sources $R_{1,2}(y, t = \tau_{int})$ with charged-particle content N^1_{ch} (projectile-like), N^2_{ch} (target-like) and the midrapidity gluon-gluon source $R_{gg}(y, t = \tau_{int})$ with charged-particle content N^{gg}_{ch} as

$$\frac{dN_{ch}(y, t = \tau_{int})}{dy} = N^1_{ch} R_1(y, \tau_{int}) + N^2_{ch} R_2(y, \tau_{int}) + N^{gg}_{ch} R_{gg}(y, \tau_{int}) \ , \quad (1)$$

with the rapidity $y = 0.5 \cdot \ln((E + p)/(E - p))$, and the interaction time τ_{int} (total integration time of the underlying partial differential equation). In the linear version of the RDM [8], the macroscopic distribution functions

are solutions of the Fokker-Planck equation ($k = 1, 2, 3$)

$$\frac{\partial}{\partial t} R_k(y,t) = -\frac{1}{\tau_y}\frac{\partial}{\partial y}\Big[(y_{eq} - y)\cdot R_k(y,t)\Big] + D_y^k \frac{\partial^2}{\partial y^2} R_k(y,t). \qquad (2)$$

The consideration of the additive variable rapidity in the nonequilibrium-statistical Fokker-Planck framework has proven to be a useful approach in calculations and predictions of macroscopic distribution functions for produced particles. Integrating the equation with the initial conditions $R_{1,2}(y, t = 0) = \delta(y \pm y_{max})$, the absolute value of the beam rapidities y_{max}, and $R_{3=gg}(y, t = 0) = \delta(y - y_{eq})$ yields the exact solution as described in [13], and references therein.

Since the theoretical model is formulated in rapidity space, one has to transform the calculated distribution functions to pseudorapidity space, $\eta = -\ln[\tan(\theta/2)]$, in order to be able to compare with the available data, and perform χ^2-minimizations. The well-known Jacobian transformation

$$\frac{dN}{d\eta} = \frac{dN}{dy}\frac{dy}{d\eta} = J(\eta, m/p_T)\frac{dN}{dy}, \qquad (3)$$

$$J(\eta, m/p_T) = \cosh(\eta)\cdot[1 + (m/p_T)^2 + \sinh^2(\eta)]^{-1/2} \qquad (4)$$

depends on the squared ratio of the mass and the transverse momentum of the produced particles. Hence, its effect increases with the mass of the particles, and it is most pronounced at small transverse momenta. For reliable results one has to consider the full p_T-distribution, however. In [10, 13] it is outlined how this can be done approximately.

However, LHC data are still missing in the fragmentation region. We have therefore proposed in [10] to use the well-known limiting fragmentation scaling hypothesis [14] as an additional constraint: At sufficiently high energy, particle production in the fragmentation region becomes almost independent of the collision energy. Hence we use 0.2 TeV Au–Au results at RHIC – where data in the fragmentation region are available – to supplement the LHC 2.76 TeV Pb–Pb data in analogous centrality classes at large values of pseudorapidity as described in [10].

It should be noted that the data in pseudorapidity space appear to extend beyond the value of the beam rapidity, $y = 1/2 \cdot \ln(1 + \beta_{||})/(1 - \beta_{||})$ with $\beta_{||} \equiv \beta_{beam} = v_{beam}/c = (\exp(2y_{beam}) - 1)/(\exp(2y_{beam}) + 1)$ as seen clearly for 130 GeV Au–Au in Fig. 2. Although it is not excluded that this is to some extent a physical effect, it is most likely due to the transformation from pseudorapidity $\eta = -\ln(\tan(\theta/2))$ to rapidity y,

$$y = \frac{1}{2}\ln\frac{\sqrt{(m/p_T)^2 + \cosh^2 y} + \sinh\eta}{\sqrt{(m/p_T)^2 + \cosh^2 y} - \sinh\eta}, \qquad (5)$$

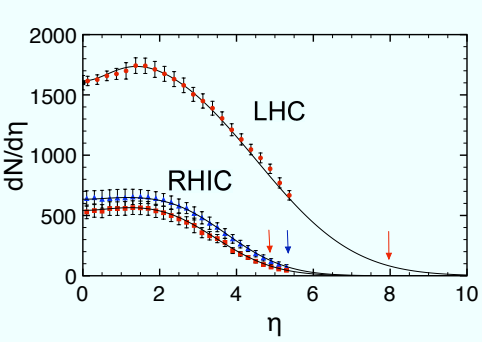

Fig. 2. (Color online) Pseudorapidity distributions for produced charged hadrons in central 130 and 200 GeV Au–Au, and 2.76 TeV Pb–Pb collisions. Calculated RDM distributions (solid curves) have been optimized in χ^2-fits with respect to the PHOBOS data from Ref. [1], and the ALICE data from [2]. The data tend to extend beyond the values of the beam rapidities (arrows).

where $y \to \eta - \ln(m/p_T)$ for $m \ll p_T$, and $y \to \eta$ for $p_T \ll m$.

In Pb–Pb at LHC energies, about 83% of the produced charged hadrons are pions, and for pions the limit $\eta \simeq y$ is reached at larger η values than for protons. Hence, the pion-dominated $dN/d\eta-$distribution extends beyond y_{beam} that is defined for protons.

3. Results

The result of the three-sources RDM calculation for the pseudorapidity distribution of produced charged hadrons 2.76 TeV Pb–Pb is shown in figure 1 together with recent ALICE data [2] for $0-5\%$ centrality in a χ^2 optimization. Parameters are given in Tab. 1. A prediction for the LHC design energy of 5.52 TeV Pb–Pb is also shown.

The relative size of the three sources in central 2.76 TeV Pb–Pb is displayed in the lower frame of figure 1. At this LHC energy, the midrapidity source already contains the largest fraction of produced charged hadrons. Its shape is significantly deformed by the Jacobian transformation from rapidity to pseudorapidity space, whereas the fragmentation sources are not much influenced by the transformation.

In the full distribution that arises from the incoherent superposition of the three sources, it is evident that the midrapidity dip is more pronounced at LHC energies as compared to RHIC energies, although the effect of the Jacobian tends to be smaller at the higher incident energy. This clearly indicates that there has to be a physical origin of the midrapidity dip in

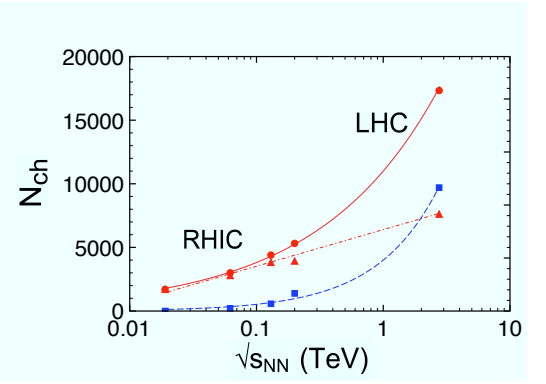

Fig. 3. (Color online) Number of produced charged hadrons as function of the c.m. energy $\sqrt{s_{NN}}$ from RDM-fits of the available data for central heavy ion collisions at 0.019, 0.062, 0.13, 0.2 TeV (RHIC, Au–Au), and 2.76 TeV (LHC, Pb–Pb). Circles are the total numbers, squares are hadrons produced from the midrapidity source, and triangles are particles from the fragmentation sources. The gluon-gluon source (dashed) becomes the main source of particle production between RHIC and LHC energies. From Ref. [13].

addition to the effect of the Jacobian.

The hypothesis promoted in this work is that the interplay of the three sources provides the observed effect. In 2.76 TeV Pb–Pb collisions, the fragmentation sources are peaked at large values ($< y_{1,2} >= 3.34$) of rapidity – whereas at 0.2 TeV RHIC energy, the center is at $< y_{1,2} >= 2.4$. Consequently, the midrapidity yield at LHC energies is essentially due to the central source, with only a small contribution from the fragmentation sources. Although the relative particle content in the central source is larger at LHC energies than at RHIC, this produces the observed midrapidity dip, together with the effect of the Jacobian on the central source.

4. Energy dependence of the hadron production sources

There are now sufficiently precise data on charged-hadron production at RHIC [1] and LHC [2] energies available in order to investigate the relative size of the three particle production sources as function of energy in heavy ion collisions (Au–Au at RHIC, Pb–Pb at LHC). I have displayed the energy dependence of the sources in figure 3, with parameters as shown in Tab. 1.

According to these results, the total charged-hadron production (circles) follows a power law $\propto s_{NN}^{0.23}$. The hadrons produced from the central source (squares) have an even stronger dependence on initial energy according to

Table 1. Three-sources RDM-parameters τ_{int}/τ_y, $\Gamma_{1,2}, \Gamma_{gg}$, and N_{gg}. N_{ch}^{1+2} is the total charged-particle number in the fragmentation sources, N_{gg} the number of charged particles produced in the central source. Parameters at 5.52 TeV denoted by * are extrapolated. From Ref. [13].

$\sqrt{s_{NN}}$ (TeV)	y_{beam}	τ_{int}/τ_y	$\Gamma_{1,2}$	Γ_{gg}	N_{ch}^{1+2}	N_{gg}	$\frac{dN}{d\eta}\|_{\eta\simeq 0}^{exp}$
0.019	$\mp$3.04	0.97	2.83	0	1704	-	314±23[1]
0.062	$\mp$4.20	0.89	3.24	2.05	2793	210	463±34[1]
0.13	$\mp$4.93	0.89	3.43	2.46	3826	572	579±23[1]
0.20	$\mp$5.36	0.82	3.48	3.28	3933	1382	655±49 [1]
2.76	$\mp$7.99	0.87	4.99	6.24	7624	9703	1601±60 [12]
5.52	$\mp$8.68	0.85*	5.16*	7.21*	8889*	13903*	1940*

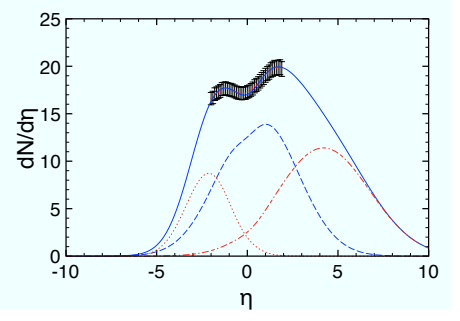

Fig. 4. (Color online) The RDM pseudorapidity distribution function for charged hadrons in minimum bias p–Pb collisions at LHC c.m. energy of 5.02 TeV shown here is adjusted in the mid-rapidity region to the ALICE data [15]. From Ref. [13].

$\propto s_{NN}^{0.44}$, whereas particles produced in the fragmentation sources have a weaker dependence $\propto \log(s_{NN}/s_0)$.

The strong rise of the particle production yield from the central (gluon-gluon induced) source is evidently due to the increasing gluon content of the system at high relativistic energies. In particular, the total particle production rate from the central source becomes larger than that from the two fragmentation sources at an incident energy between the highest RHIC energy (0.2 TeV), and the LHC regime. In view of the lack of data in this intermediate regime, the precise crossing point is, however, difficult to determine.

In central p–Pb collisions at 5.02 TeV, ALICE data [15] have also been used to compare with the analytical RDM-solutions, cf. figure 4. The RDM calculation exhibits a steeper slope on the proton-like side, as compared to the Pb-like side. Forthcoming LHC p–Pb large-η data could confirm this.

5. Conclusions

The particle content of fragmentation (valence quark–gluon) and midrapidity (gluon–gluon) sources for charged-hadron production in heavy ion collisions at high relativistic energies has been determined as function of c.m. energy in a phenomenological approach.

In turns out that particle production from the gluon–gluon source becomes more important than that from the fragmentation sources in the energy range between the maximum RHIC energy of 0.2 TeV, and the current LHC energy of 2.76 TeV.

Acknowledgments

I am grateful to ALICE for their data. Parts of this proceedings report (as indicated in the figure captions) have been published in [13].

References

[1] B. Alver *et al.* (PHOBOS Collaboration), Phys. Rev. C **83**, 024913 (2011).
[2] M. Guilbaud *et al.* (ALICE Collaboration), Nucl. Phys. A **904-905**, 381c (2013).
[3] J.L. Albacete, Phys. Rev. Lett. **99**, 262301 (2007).
[4] I.G. Bearden *et al.* (BRAHMS Collaboration), Phys. Rev. Lett. **87**, 112305 (2001).
[5] Y. Mehtar-Tani and G. Wolschin, Phys. Rev. Lett. **102**, 182301 (2009).
[6] Y. Mehtar-Tani and G. Wolschin, Phys. Rev. C **80**, 054905 (2009).
[7] Y. Mehtar-Tani and G. Wolschin, Euro Phys. Lett. **94**, 62003 (2011).
[8] G. Wolschin, Eur. Phys. J. A **5**, 85 (1999).
[9] G. Wolschin, M. Biyajima, T. Mizoguchi, and N. Suzuki, Phys. Lett. B **633**, 38 (2006).
[10] D. Röhrscheid and G. Wolschin, Phys. Rev. C **86**, 024902 (2012).
[11] R. Kuiper and G. Wolschin, Euro Phys. Lett. **78**, 2201 (2007).
[12] K. Aamodt *et al.* (ALICE Collaboration), Phys. Rev. Lett. **106**, 032301 (2011).
[13] G. Wolschin, J. Phys. G: Nucl. Part. Phys. **40**, 045104 (2013).
[14] J. Benecke, T. Chou, C. Yang, and E. Yen, Phys. Rev. **188**, 2159 (1969).
[15] B. Abelev *et al.* (ALICE Collaboration), Phys. Rev. Lett. **110**, 032301 (2013).

STAR Results from the RHIC Beam Energy Scan

Hui Wang for the STAR collaboration

RM 1-174, Building 510A, Brookhaven National Laboratory, Upton, NY, 11973

The Beam Energy Scan Program is launched by RHIC to study the QCD phase diagram. The goal is to explore the possible QCD phase boundary and search for possible QCD critical point. In 2010 and 2011, experiments collected data at $\sqrt{s_{\rm NN}}$=7.7,11.5,19.6,27,39 and 62.4 GeV, covering a wide range of baryon chemical potential from $\mu_{\rm B}$ 420 to 70 MeV. In this presentation, we will report some latest results of the Beam Energy Scan Program from the STAR collaboration.

1. Introduction

Current results from RHIC and LHC indicate the existence of a deconfined Quark Gluon Plasma (QGP) phase at high energy in A+A collisions. One major challenge, however, is to understand the structure of the QCD phase diagram. If the temperature is high and μ_B is relatively small, both lattice QCD and experimental data indicate this transition from hadronic matter to Quark Gluon Plasma is an analytical transition (cross-over) [1], while some theoretical calculations predict that the transition at lower temperatures and high μ_B is a first order phase transition [2]. If a phase transition exists at higher μ_B, with a cross-over at $\mu_B = 0$, the phase transition would end in a critical point at finite μ_B. However, due to the difficulty of lattice QCD calculations at finite μ_B, accurate predictions of the critical point location are still lacking [3]. Therefore it falls to experiment to search for traces of the existence of the critical point of QCD.

To further explore the QCD phase diagram, a Beam Energy Scan (BES) proposal was made by the STAR Collaboration [4], which aims to search for the turn-off of QGP signatures, signals for first order phase transition and the critical point. The first phase of the BES program was started in 2010 with collisions recorded at $\sqrt{s_{\rm NN}}$ = 7.7, 11.5, 39 GeV and finished in 2011 with collisions at $\sqrt{s_{\rm NN}}$=19.6 and 27 GeV. In this paper, a few selected results from the STAR BES program will be discussed.

2. Search for Turn-off of QGP Signatures

2.1. the Balance Function

The balance functions, which measure the correlation between the opposite sign charge pairs, are sensitive to the mechanisms of charge formation and the subsequent relative diffusion of the balancing charges [5]. Due to conservation laws like electric charge conservation, particles and their anti-particles are pair produced and correlated initially in coordinate space, if a delayed hadronization occurs, the lower temperature and less expansion and diffusion will result in a narrower charge balance function [5]. It has been reported that the balance function for $\Delta\eta$ narrows at top RHIC energies [6]. Thus the balance function could be used to probe the evolution of the system hadronization time vs. energy and search for possible turn-off of QGP at lower energies.

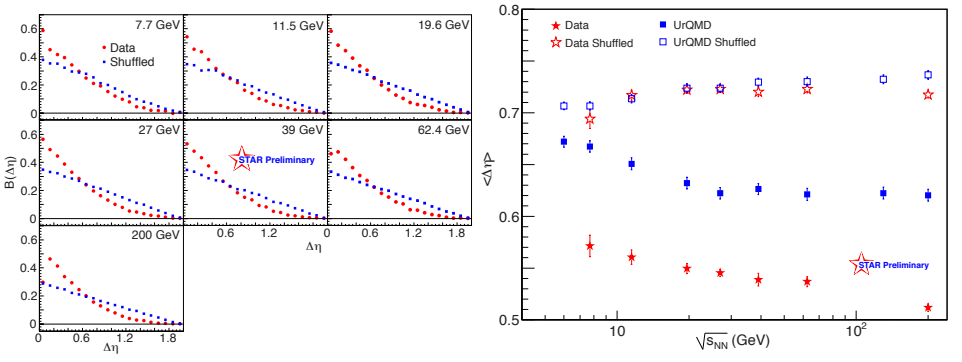

(a) The balance function in terms of $\Delta\eta$ for all charged particles.

(b) Energy dependence of the balance function width $\langle\Delta\eta\rangle$ for central Au+Au collisions (0-5%) compared with shuffled events.

Fig. 1: The balance function in terms of $\Delta\eta$ for all charged particles. Central events (0-5%) are shown here with $\sqrt{s_{\rm NN}}$ from 7.7 to 200 GeV.

For this analysis, we use all charged particles with the transverse momentum cut of $0.2 < p_t < 2.0$ GeV/c and the pseudorapidity cut of $|\eta| < 1.0$. Figure 1a shows the balance function in terms of $\Delta\eta$ for all charged particles. The most central events (0-5%) are shown for seven incident energies. The data in the figure are the balance function results from real data corrected by subtracting the balance function calculated using mixed events. We can see that, for all the energies shown here, the balance functions from data are narrower than the ones from shuffled events. To quantify the narrowing of balance function, figure 1b shows the energy dependence of the balance func-

tion width for central Au+Au collisions. The data show a smooth decrease of $\langle \Delta\eta \rangle$ with increasing energy. UrQMD calculations predict a similar trend but over predict the observed results. Since the balance function is sensitive to the hadronization time and relative diffusion after hadronization, this decrease in balance function width could mean a longer lived QGP phase at higher energies. The UrQMD model is a hadronic model that does not have a deconfined phase transition and has little flow. This early hadronization time combined with strong interaction between final particles leads to a wider balance function in UrQMD. In the same figure, the shuffled events from both data and UrQMD show a wider balance function that slightly increases with increasing energy.

2.2. Elliptic Flow

Elliptic flow is the second harmonic coefficient of the Fourier expansion

$$\frac{dN}{d\phi} \propto 1 + 2\sum_{n\geq 1} v_n \cos\left[n(\phi - \Psi_n)\right] \ , \tag{1}$$

where ϕ is the azimuthal angle of the particles and Ψ is the reconstructed event plane azimuthal angle. Elliptic flow would be generated by the initial pressure gradient created by non-central heavy ion collisions. One major line of evidence that a deconfined quark gluon plasma is produced in Au+Au collisions at $\sqrt{s_{NN}} = 200$ GeV is the number-of-constituent quark (NCQ) scaling of v_2 versus transverse momentum p_T for hadrons at intermediate p_T (2 to 5 GeV/c) [7, 8]. Deviations from such a scaling at lower beam energies could be an indication for the absence of the deconfined phase [9].

Figure 2 shows the differences in v_2 between particles X (p, Λ, Ξ^-, π^+, K^+) and corresponding anti-particles $\overline{X}$ ($\bar{p}$, $\overline{\Lambda}$, $\overline{\Xi}^+$, π^-, K^-) with $\sqrt{s_{NN}}$. Larger v_2 values are found for particles than for antiparticles, except for pions for which the opposite ordering is observed. The difference increases with decreasing beam energy and is larger for baryons compared to mesons [10].

As discussed previously, the universal NCQ scaling of v_2 at $\sqrt{s_{NN}} = 200$ GeV suggests strongly interacting partonic matter is produced. The observed difference in v_2 at lower beam energies demonstrates that this common NCQ scaling of particles and anti-particles splits. Such a breaking of the NCQ scaling could indicate increased contributions from hadronic interactions in the system evolution with decreasing beam energy, or could be related to the larger values of μ_B.

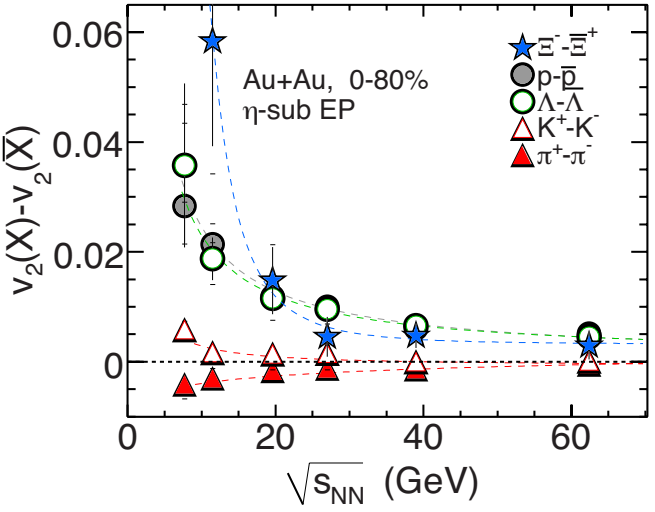

Fig. 2: The difference in v_2 between particles (X) and their corresponding anti-particles ($\overline{\mathrm{X}}$) (see legend) as a function of $\sqrt{s_{NN}}$ for 0–80% central Au+Au collisions. The dashed lines in the plot are fits with a power-law function [10].

3. Search for Critical Point

3.1. Particle Ratio Fluctuations

The energy dependence of particle-ratio fluctuations is also an interesting topic. Enhanced fluctuations are one of the possible signatures of a phase transition near a critical point [11]. The observable ν_{dyn} for kaons and pions can be written as

$$\nu_{\mathrm{dyn},K\pi} = \frac{< K(K-1) >}{< K >^2} + \frac{< \pi(\pi-1) >}{< \pi >^2} - \frac{2 < K\pi >}{< K >< \pi >} , \qquad (2)$$

Figure 3a shows the $\nu_{\mathrm{dyn},K\pi}$ results for 7.7–200 GeV [12, 13, 14]. STAR results are approximately independent of collision energy. This disagrees with NA49's results, which show a strong increase with decreasing incident energy. The same figure also shows model calculations. The points labeled STAR UrQMD represent UrQMD calculations with STAR acceptance cuts, which show little energy dependence and over predict the magnitude of the data. The HSD model predicts increased fluctuations at low energies and agrees with the NA49 measurements at the lowest energies but over predict

the data at higher energies. None of the models presented here can fully describe the incident energy dependence of the data.

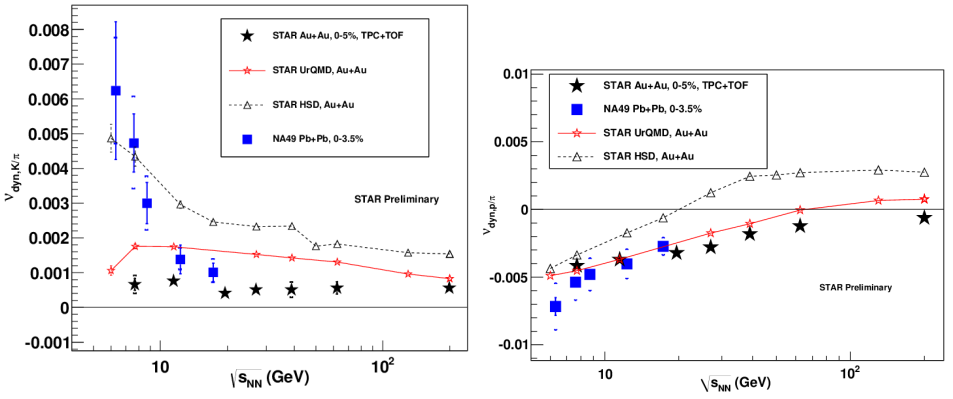

(a) K/π fluctuations. (b) p/π fluctuations.

Fig. 3: Energy dependence of K/π and p/π fluctuations expressed as $\nu_{\mathrm{dyn,p/\pi}}$. Only central events are shown here (0-5% for STAR Au+Au collisions, 0–3.5% for NA49 Pb+Pb collisions). UrQMD and HSD calculations are also shown.

Unlike the results for K/π fluctuations, the results for p/π fluctuations are affected by resonance correlations (e.g. Δ, Λ, Σ all decay to p, π). These correlations increase the cross-correlation terms of ν_{dyn} and produce a negative ν_{dyn} value. Figure 3b shows the incident energy dependence of $\nu_{\mathrm{dyn},p\pi}$. The STAR and NA49 results for p/π fluctuations show good agreement. They are both negative and increase with increasing collision energy. The UrQMD model describes the data well at SPS energies, which supports the resonance correlations interpretation because UrQMD is a hadronic transport model. However, UrQMD becomes positive and over predicts the data at higher energies.

p/K fluctuations, which are related to baryon-strangeness correlations, can be used as a tool to study the deconfinement phase transition. Figure 4a shows the incident energy dependence of $\nu_{\mathrm{dyn},Kp}$ results. The STAR data show a smooth decrease with decreasing collision energy and disagree with NA49 data at 7.7 GeV. Further study is still needed to understand the differences between the two experiments. A UrQMD calculation with the STAR acceptance filter is also shown in the same figure. UrQMD always over predicts fluctuations and becomes positive at high collision energies. The HSD model always predicts positive ν_{dyn} results.

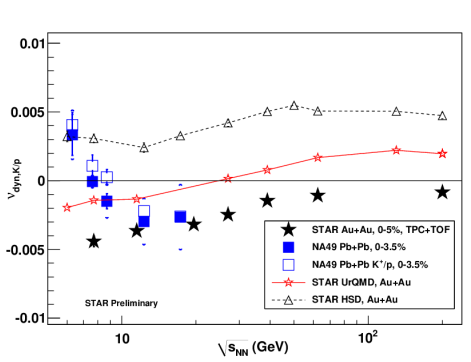

(a) Energy dependence of p/K fluctuations. UrQMD and HSD calculations are also shown.

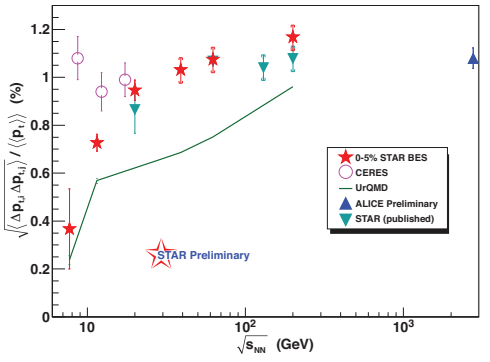

(b) $\sqrt{\langle \Delta p_{t,i} \Delta p_{t,j} \rangle} / \langle \langle p_t \rangle \rangle$ as a function of incident energy. UrQMD calculations are also shown in the same figure.

Fig. 4: Energy dependence of p/K fluctuations and p_t Fluctuations. Only central events are shown here.

3.2. p_t Fluctuations

The p_t fluctuations could also serve as a signal for the QCD critical point or the occurrence of thermalization and collectivity [15, 16]. One observable for the event-by-event two particle momentum correlation is defined [17] as

$$\langle \Delta p_{t,i} \Delta p_{t,j} \rangle = \frac{1}{N_{\text{event}}} \sum_{k=1}^{N_{\text{event}}} \frac{C_k}{N_k (N_k - 1)}, \tag{3}$$

where

$$C_k = \sum_{i=1}^{N_k} \sum_{j=1, i \neq j}^{N_k} (p_{t,i} - \langle \langle p_t \rangle \rangle) (p_{t,j} - \langle \langle p_t \rangle \rangle). \tag{4}$$

Figure 4b shows the incident energy dependence of p_t correlations. The STAR data shows a rapid increase from 7.7 to 62.4 GeV and then little energy dependence up to 2.76 TeV. UrQMD shows a similar increasing trend but under predicts the measured correlations. The CERES data deviates from STAR at lower energy. Effects due to different experimental acceptances are still under investigation.

4. Search for First Order Phase Transition

One important goal of the STAR BES program is to search for the evidence of a first order phase transition. The HBT technique can be used to

determine the freeze-out eccentricity ε_F. A non-monotonic behavior of ε_F as a function of energy could indicate a soft point in the equation of state [20]. Figure 5a shows the excitation function of the freeze-out eccentricity. The combined E895 and STAR data shows a smooth decrease of ε_F with energy. Also, the UrQMD model reproduces both E895 and STAR data. Overall, no non-monotonic behavior is observed in ε_F.

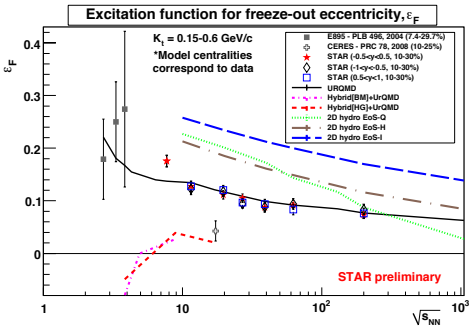

(a) Freeze-out eccentricity, ϵ_F , as a function of $\sqrt{s_{NN}}$ for data and models [19].

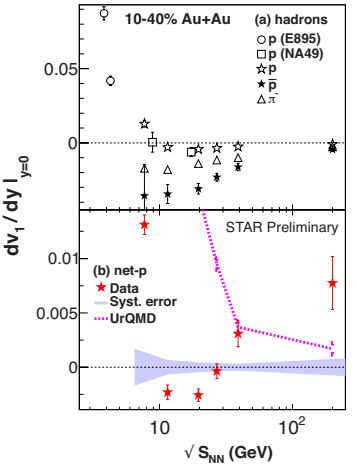

(b) Directed flow slope (dv_1/dy) near mid-rapidity as a function of beam energy for mid-central (10-40%) Au+Au collisions.

Fig. 5: Energy dependence of ϵ_F and dv_1/dy

Directed flow, which measures the "side-splash" motion of the collision products, is sensitive to the equation of state (EOS) and hence can be considered a first order phase transition signal [18]. Figure 5b shows the energy dependence of directed flow slope (dv_1/dy) near mid-rapidity for 10-40% central Au+Au collisions [21]. The v_1 slope for net protons is calculated via the relation $F_p = rF_{\bar{p}} + (1-r)F_{\mathrm{net-p}}$, where r is the observed ratio of antiprotons to protons among the analyzed tracks. The net proton v_1 slope changes sign twice and shows a minimum at $\sqrt{s_{NN}}$ =10 to 20 GeV. This result is qualitatively different from UrQMD and AMPT transport models, which both predict a monotonic trend throughout $\sqrt{s_{NN}}$ =7.7 to 200 GeV [21]. Further studies are needed to understand the current results and their implications for the Equation of State.

5. Summary

We have presented some of the latest results from the STAR BES Phase I program. Most results show a smooth change vs. incident energy. We do see significant differences in particle and anti-particle v_2, which indicates the breaking of the NCQ scaling. A possible minimum at $\sqrt{s_{NN}}$ =10–20 GeV is also observed for the net proton v_1 slope. More statistics are needed to confirm a few other interesting observables such as higher moments of net-protons distributions and ϕ-meson v_2. We are looking forward to the BES Phase II program with STAR iTPC upgrade and fixed-target mode [22].

References

[1] Y. Aoki *et al.*, Nature **443**, 675 (2006).

[2] S. Ejiri, Phys. Rev. D **78**, 074507 (2008).

[3] M.A. Stephanov PoS LAT2006:024 (2006).

[4] M.M. Aggarwal *et al.* (STAR Collaboration), arXiv:1007.2613v1.

[5] S.A. Bass, P. Danielewicz, and S. Pratt, Phys. Rev. Lett. **85**, 2689 (2000).

[6] B.I. Abelev *et al.* (STAR Collaboration), Phys. Rev. C **82**, 024905 (2010).

[7] J. Adams *et al.* (STAR Collaboration), Phys. Rev. Lett. **95**, 122301 (2005).

[8] B.I. Abelev *et al.* (STAR Collaboration), Phys. Rev. C **75**, 054906 (2007).

[9] M.M. Aggarwal *et al.* (STAR Collaboration), arXiv:1007.2613 [nucl-ex].

[10] L. Adamczyk *et al.* (STAR Collaboration), Phys. Rev. Lett. **110**, 142301 (2013).

[11] V. Koch, arXiv:0810.2520 [nucl-th].

[12] C. Alt *et al.*, Phys. Rev. C **79**, 044910 (2009).

[13] J. Adams *et al.* (STAR Collaboration), Phys. Rev. Lett. **103**, 092301 (2009).

[14] T.J. Tarnowsky (STAR Collaboration), arXiv:1110.2222 [nucl-ex]..

[15] M.A. Stephanov, K. Rajagopal, and E.V. Shuryak Phys. Rev. Lett. **81**, 4816 (1998).

[16] S. Gavin, Phys. Rev. Lett. **92**, 162301 (2004).

[17] J. Adams *et al.* (STAR Collaboration), Phys. Rev. C **72**, 044902 (2005).

[18] R. Snellings *et al.*, Phys. Rev. Lett. **84**, 2803 (2000); J. Brachmann *et al.*, Phys. Rev. C **61**, 024909 (2000); L.P. Csernai and D. Rohrich, Phys. Lett. B **458**, 454 (1999); H. Stoecker, Nucl. Phys. A **750**, 121 (2005).

[19] N. Shah (STAR Collaboration), arXiv:1210.5436 [nucl-ex].

[20] M. A. Lisa, E. Frodermann, G. Graef, M. Mitrovski, E. Mount, H. Petersen, and M. Bleicher, New J. Phys. **13**, 065006 (2011).

[21] Y. Pandit (STAR Collaboration), arXiv:1210.5315 [nucl-ex].

[22] RHIC Beam Use Request For Runs 13 and 14.

High-order cumulants from the 3D $O(1)$ and $O(4)$ spin models

Xue Pan, Yuanfang Wu

Key Laboratory of Quark and Lepton Physics (MOE) and Institute of Particle Physics, Central China Normal University, Wuhan 430079, China

X.S. Chen

Institute of Theoretial Physics, Chinese Academy of Sciences, Beijing 100190, China

Lizhu Chen

School of Physics and Optoelectronic Engineering, Nanjing University of Information Science and Technology, Nanjing 210044, China

We simulate the 3D $O(1)$ (Ising) and $O(4)$ spin models by the Monte Carlo method. Interesting high-order cumulants from the 3D Ising and $O(4)$ universality classes are presented and discussed. They all show the non-monotonic or sign change behavior. The critical behavior is instructive to that of the high-order cumulants of the net baryon number in the QCD phase transitions. Maybe it's difficult to distinguish the universality classes by the high-order cumulants in the heavy ion collisions.

1. Introduction

One of the primary goals of current ultra-relativistic heavy-ion collision experiments is to map the QCD phase diagram onto the T–μ_B plane [1]. The critical point is particularly interesting, because the divergent susceptibility and correlation length (ξ) are expected. But the expansion of ξ is limited as the finite evolution time and volume of relativistic heavy-ion collision system. So the more sensitive probes to locate the QCD critical point are needed. Recently, the high-order cumulants of the conserved charges are suggested, i.e., the net baryon number, net electric charge, and net strangeness [2, 3]. They are more sensitive to the correlation length and may change sign near the critical point based on the theory [4–7].

The net baryon number fluctuations have been studied by lattice QCD and QCD effective models [8–11]. However, owing to the difficulties of

the lattice calculations and model estimations, the study of the high-order cumulants of the net baryon number need to be continued anyway [12, 13].

The QCD critical point falls into the same universality class with the 3D Ising model [14, 15]. In the chiral limit, the chiral phase transition for 2-flavor QCD is expected to belong to the 3D $O(4)$ universality class [15]. Because of the universal properties of the critical phenomena, the relevant cumulants can be studied in the simple spin systems. The results should be instructive to a finite system formed in relativistic heavy-ion collisions.

The paper is organized as follows, firstly, the cumulants of order parameter and energy from the $O(N)$ spin models are derived in Sec. 2. Then, their relations to the net baryon number fluctuations are discussed. In Sec. 3, the high-order cumulants from the 3D Ising model and $O(4)$ spin model are presented and discussed. Finally, the summary and conclusions are given in Sec. 4.

2. Cumulants in the $O(N)$ spin models

The $O(N)$ spin models are defined as,

$$\beta\mathcal{H} = -J\sum_{\langle i,j\rangle}\vec{S}_i\cdot\vec{S}_j - \vec{H}\cdot\sum_i\vec{S}_i, \tag{1}$$

where $\mathcal{H}$ is the Hamiltonian, J is an interaction energy between nearest-neighbor spins $\langle i,j\rangle$, and $\vec{H}$ is the external magnetic field. J and $\vec{H}$ are both reduced quantities which already contain a factor $\beta = 1/T$. $\vec{S}_i$ is a unit vector of N-components at site i of a d-dimensional hyper-cubic lattice. It is usually decomposed into the longitudinal (parallel to the magnetic field $\vec{H}$) and the transverse component $\vec{S}_i = S_i^{\parallel}\vec{e}_H + \vec{S}_i^{\perp}$, where $\vec{e}_H = \vec{H}/H$. For the 3D Ising and $O(4)$ spin models, $d = 3$, $N = 1$ and 4, respectively.

The partition function is as follows,

$$Z = \int\prod_i d^N S_i\delta(\vec{S}_i^2 - 1)\exp(-\beta E + HVS^{\parallel}), \tag{2}$$

where $E = -\sum_{\langle i,j\rangle}\vec{S}_i\cdot\vec{S}_j$ is the energy of a spin configuration, $S^{\parallel} = \frac{1}{V}\sum_i S_i^{\parallel}$ is the lattice average of the longitudinal spin components, $V = L^3$ and L is the number of lattice points of each direction.

As we know, the cumulants of the order parameter are related to the derivatives of the free energy density, $f(T,H) = -\frac{1}{V}\ln Z$, with respect to H. They can be got from the generating function [16],

$$\kappa_n^S = \frac{d^n}{dx^n}\ln\langle e^{xS^{\parallel}}\rangle\Big|_{x=0}. \tag{3}$$

So the first, second, third, fourth and sixth order cumulants of the order parameter are as follows,

$$\begin{aligned}\kappa_1^S &= \langle S^{\|}\rangle,\ \ \kappa_2^S = \langle \delta S^{\|^2}\rangle,\ \ \kappa_3^S = \langle \delta S^{\|^3}\rangle,\ \ \kappa_4^S = \langle \delta S^{\|^4}\rangle - 3\langle \delta S^{\|^2}\rangle^2,\\ \kappa_6^S &= \langle \delta S^{\|^6}\rangle - 10\langle \delta S^{\|^3}\rangle^2 + 30\langle \delta S^{\|^2}\rangle^3 - 15\langle \delta S^{\|^4}\rangle\langle \delta S^{\|^2}\rangle, \end{aligned} \tag{4}$$

where $\delta S^{\|} = S^{\|} - \langle S^{\|}\rangle$, and κ_1^S is the magnetization (order parameter) of the system. At vanishing external magnetic field, due to the spatial rotation symmetry of the $O(N)$ groups, such defined order parameter is zero. In the case, an approximated order parameter definition is suggested as, $M = \langle|\frac{1}{V}\sum_i \vec{S}_i|\rangle$ [17].

The cumulants of the energy are related to the derivatives of the free energy density with respect to T. The forms of the formulas for the cumulants are the same as that in Eq. (4), where it just need to replace $S^{\|}$ by E.

In the vicinity of the critical point, the free energy density can be decomposed into two parts, the regular and singular parts. The critical related fluctuations are determined by the singular part. It has the scaling form $f_s(t,h) = l^{-d} f_s(l^{y_t}t, l^{y_h}h)$. Here $t = (T - T_c)/T_0$ and $h = H/H_0$ are reduced temperature and magnetic field, T_0 and H_0 are the normalized parameters. T_c is the critical temperature. y_t and y_h are universal critical exponents. In our simulation, we set $J = \beta$ and choose the approximate critical temperatures, T_c =4.51 [17] and 1.068 [18] for the 3D Ising and $O(4)$ spin models, respectively.

In order to map the result of the 3D Ising model to that of the QCD if the QCD critical point exists, the following linear ansatz is suggested [19–21],

$$t \approx T - T_{cp} + a(\mu - \mu_{cp}), \qquad h \approx \mu - \mu_{cp} + b(T - T_{cp}). \tag{5}$$

T_{cp} and μ_{cp} are the temperature and chemical potential at the QCD critical point, respectively. a and b are two undecided mixed parameters. The baryon-baryon correlation length diverges with the exponent y_t and exponent y_h when the critical point is approached along the t-direction and h-direction, respectively [9]. Because y_h (≈ 2.5) is larger than y_t (≈ 1.6) [22], the critical behavior of the net baryon number fluctuations is mainly controlled by the derivatives with respect to h, i.e., the fluctuations of the order parameter in the 3D Ising model.

The singular part of the free energy density for the chiral phase transition is suggested as [7]

$$\frac{f_s(T,\mu_q,h)}{T^4} = A h^{(1+1/\delta)} f_f(z), \qquad z = t/h^{1/\beta\delta}, \tag{6}$$

where β and δ are the universal critical exponents of the 3D $O(4)$ spin model. $f_f(z)$ is the scaling function. The reduced temperature t and external field h are expressed as follows,

$$t \equiv \frac{1}{t_0}(\frac{T-T_c}{T_c} + \kappa_\mu(\frac{\mu_q}{T})^2), \qquad h \equiv \frac{1}{h_0}\frac{m_q}{T_c}. \tag{7}$$

Here T_c is the critical temperature in the chiral limit. κ_μ is a parameter determined by QCD [23]. The net baryon number susceptibility is the derivative of free energy density with respect to the chemical potential μ_q. From Eqs. (6) and (7), it's clear that the form of the derivatives of the free energy density with respect to T and chemical potential $\hat{\mu}_q = \mu_q/T$ is similar. Particularly, The n-th order cumulant of the energy from the 3D $O(4)$ spin model is relevant to the $2n$-th (or n-th) order cumulant of the net baryon number at $\mu_q = 0$ (or $\mu_q \neq 0$) in the chiral phase transition.

3. Critical behavior of the high-order cumulants

The Monte Carlo simulations are performed by the Wolff algorithm with helical boundary conditions [24]. The typical size of an observable at a given magnetic field is determined by the saturation of size dependence, as shown in Ref. [25]. The system sizes in this work for each kind of cumulants at a given magnetic field and model are listed in Table 1.

Table 1. The typical system size for each kind of cumulant.

H	$\kappa_n^S(O(1))$	$\kappa_n^E(O(1))$	$\kappa_n^E(O(4))$
0	24	20	20
0.05	12	10	8
0.1	8	8	8

In order to compare the basic structure of the cumulants at different external fields, each cumulant is rescaled to unity by its maximum or minimum (except for the first order cumulant of the energy from the $O(4)$ spin model). For the Ising model, the cumulants of order parameter at $H = 0$ and $H \neq 0$ are quite different, so they are presented discretely.

The cumulants of energy from the 3D Ising model at $H = 0.1$, 0.05, and 0 are shown in the upper panel of Fig. 1. From each sub-figure, it's clear that the basic features of the cumulants, i.e., the patterns of the fluctuations, are not influenced by the magnitude of the external field. With the appearing or increasing of the external field, the whole critical region is amplified and shifted toward the higher temperature side. This is easy to understand that the cumulants are governed by universal functions that depend on the scaling variable $z = t/h^{1/\beta\delta}$.

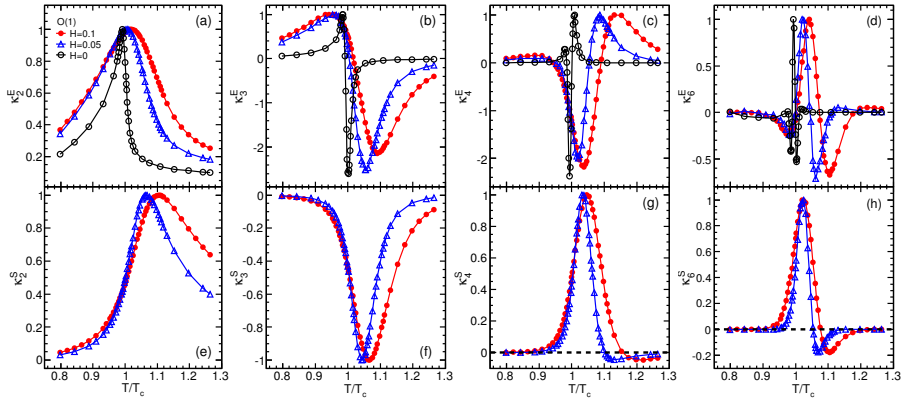

Fig. 1. (Color online) The 2nd, 3rd, 4th and 6th order cumulants of the energy (upper panel) and order parameter (lower panel) versus temperature for different H from the 3D Ising model.

In the vicinity of T_c, κ_2^E has a peak. κ_3^E oscillates and its sign changes from positive to negative when the temperature increases and passes the critical one. κ_4^E has two positive peaks locating at the two sides of T_c. The valley between the peaks is negative. In contrast to the κ_4^E, κ_6^E has two negative valleys and one positive peak in the vicinity of the critical temperature.

The cumulants of order parameter at $H = 0.1$ and 0.05 from the 3D Ising model are shown in the lower panel of Fig. 1. The influences of the external field are similar to those as discussed in the cumulants of the energy. In the vicinity of T_c, κ_2^S has a peak. κ_3^S has a negative valley and no sign change in the critical region. κ_4^S shows a obvious positive peak and a very small and negative valley when the temperature increases and passes the critical one. κ_6^S oscillates from positive to negative, and the negative valley is more obvious than that in κ_4^S.

Comparing the upper part and lower part of Fig. 1, it's clear that the generic structure of the same order cumulant of the energy is different from that of the order parameter, except for the second order one.

In Fig. 2, the high-order cumulants of the order parameter at $H = 0$ are shown. κ_2^S in Fig. 2(a) has a narrow and sharp peak near T_c. From Fig. 2(b) and (c), both κ_3^S and κ_4^S oscillate, but the former changes from negative to positive, while the latter changes from positive to negative with the increasing temperature. The generic structure of κ_6^S in Fig. 2(d) is similar to that of κ_4^E in Fig. 1(c). The behavior of the high-order cumulants at $H \neq 0$ and $H = 0$ is quite different. The sign change in the former case

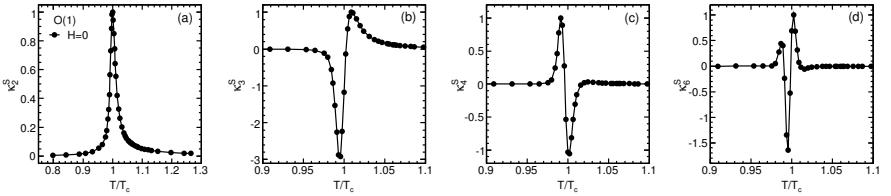

Fig. 2. The 2ed, 3rd, 4th and 6th order cumulants of the order parameter versus temperature at $H = 0$ from the 3D Ising model.

appears in the fourth order cumulant, while the third one in the later case.

The way of the sign change of κ_3^S at $H = 0$ as shown in Fig. 2(b) is consistent with the expectation from the effective model [5]. The qualitative features of κ_4^S as shown in Fig. 1(g) and Fig. 2(c) are consistent with that from the linear parametric model of the Ising universality class (see Fig. 1 in Ref. [6]). Especially at non-vanishing external field, the generic structure of κ_4^S in Fig. 1(g) is the same as Fig. 1(b) in Ref. [6]. When the critical point is approached from the higher temperature side, κ_4^S is negative. Based on the Ising universality class, the sixth order cumulant of the order parameter is also negative when approaching the critical point on the crossover side. And the negative valley is more obvious than that in the fourth order cumulant. Maybe the negative signal of the sixth order cumulant of the net baryon number is easier to be detected in the experiments.

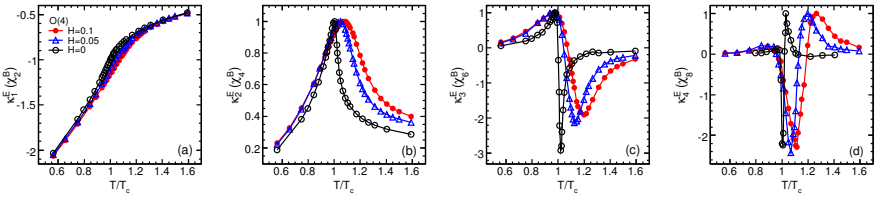

Fig. 3. (Color online) The 1st, 2ed, 3rd and 4th order cumulants of the energy versus temperature for different H from the 3D $O(4)$ spin model.

The cumulants of the energy from the 3D $O(4)$ spin model at $H = 0.1$, 0.05, and 0 are presented in Fig. 3. Again, the external field shows the similar influences as discussed above. κ_1^E increases with the temperature. κ_2^E, κ_3^E, and κ_4^E have a similar behavior with that from the Ising model.

As discussed in section 2, κ_1^E, κ_2^E, κ_3^E, and κ_4^E from the 3D $O(4)$ spin model are related to χ_2^B, χ_4^B, χ_6^B, and χ_8^B at $\mu_B = 0$ in the chiral phase transition. The positive peak of κ_2^E is consistent with χ_4^B from the lattice QCD calculations [8] and the estimations of QCD effective models [10, 11,

26]. The sign change of κ_3^E is also shown in χ_6^B from the Polyakov loop extended Quark-Meson (PQM) model [7, 11].

Based on the order parameter fluctuations from the Ising model at $H \neq 0$ and energy fluctuations from the $O(4)$ spin model, the generic structure of the fourth order cumulant of the net baryon number in the vicinity of the critical point and in the chiral phase transition at vanishing chemical potential is similar. Except for the small negative valley of the fourth order cumulant of the order parameter in the Ising model, they both have a obvious peak. The sixth order cumulant in the vicinity of the critical point is also similar to that in the chiral phase transition at vanishing chemical potential. It oscillates and has a sign change in the two cases. It's maybe difficult to distinguish the two universality classes by the high-order cumulants in the heavy ion collisions.

4. Summary

In this work, the behavior of the high-order cumulants of order parameter and energy in the 3D Ising model, and the cumulants of energy in the 3D $O(4)$ spin model at $H = 0.1$, 0.05, and 0 is presented, respectively. The external field does not influence the generic structure of the cumulants, except the cumulants of the order parameter from the 3D Ising model.

For the 3D Ising universality class, the generic structure of the high-order cumulants of energy are different from that of order parameter. But they all have the non-monotonic or sign change behavior. The fourth and sixth order cumulants of the order parameter at nonzero external field are both negative when approaching the critical point from the crossover side. But the negative signal is more obvious in the sixth order cumulant. Maybe it's easier to be detected in the experiment.

For the 3D $O(4)$ universality class, the behavior of the second to fourth order cumulants of energy is similar to that from the 3D Ising universality class. The net baryon number fluctuations based on the $O(4)$ spin model are qualitatively consistent with the calculations from the lattice QCD, and expectations from the QCD effective models. Our results also show that at vanishing chemical potential, the sixth order cumulant of the net baryon number is necessary in order to observe a sign change in the chiral phase transition.

Based on the order parameter fluctuations from the 3D Ising and energy fluctuations from the 3D $O(4)$ universality classes, maybe it's difficult to distinguish the different universality classes by the high-order cumulants in the heavy ion collisions.

Acknowledgments

This work was supported in part by the National Natural Science Foundation of China under Grant No. 10835005, 11221504, and MOE of China for doctoral site with project No. 20120144110001.

References

[1] H. Caines-for the STAR Collaboration, nucl-ex/0906.0305.
[2] Y. Hatta and M.A. Stephanov, Phys. Rev. Lett. **91**, 102003 (2003).
[3] V. Koch, nucl-th/0810.2520.
[4] M.A. Stephanov, Phys. Rev. Lett. **102**, 032301 (2009).
[5] M. Asakawa, S. Ejiri, and M. Kitazawa, Phys. Rev. Lett. **103**, 262301 (2009).
[6] M.A. Stephanov, Phys. Rev. Lett. **107**, 052301 (2011).
[7] B. Friman, F. Karsch, K. Redlich, and V. Skokov, Eur. Phys. J. C **71**, 1694 (2011).
[8] M. Cheng *et al.*, Phys. Rev. D **79**, 074505 (2009).
[9] R.V. Gavai and S. Gupta, Phys. Lett. B **696**, 459 (2011).
[10] W.J. Fu, Y.X. Liu, and Y.L. Wu, Phys. Rev. D **81**, 014028 (2010).
[11] S. Chatterjee and K.A. Mohan, Phys. Rev. D **86**, 114021 (2012).
[12] F. Karsch and K. Redlich, Phys. Rev. D **84**, 051504 (2011).
[13] S. Borsányi (for the Wuppertal-Budapest Collaboration), hep-lat/1210.6901.
[14] P. de Forcrand and O. Philipsen, Phys. Rev. Lett. **105**, 152001 (2010); M. Stephanov, K. Rajagopal, and E. Shuryak, Phys. Rev. Lett. **81**, 4816 (1998); M. Asakawa, J. Phys. G: Nucl. Part. Phys. **36**, 064042 (2009).
[15] R.D. Pisarski and F. Wilczek, Phys. Rev. D **29**, 338 (1984).
[16] C.f. S.L. Lauritzen, Thiele Pioneer in Statistics, Oxford University Press, 2002.
[17] A.L. Talapov and H.W.J. Blöte, J. Phys. A: Math. Gen. **29**, 5727 (1996).
[18] H.G. Ballesteros, L.A. Fernández, V. Marín-Mayor, A. Muñoz Sudupe, Phys. Lett. B **387**, 125 (1996).
[19] J.J. Rehr and N.D. Mermin, Phys. Rev. A **8**, 472 (1973).
[20] N. B Wilding, J. Phys.: Condens. Matter **9**, 585 (1997).
[21] C. Nonaka and M. Asakawa, Phys. Rev. C **71**, 044904 (2005).
[22] J. García and J.A. Gonzalo, Phys. A **326**, 464 (2003).
[23] O. Kaczmarek *et al.*, Phys. Rev. D **83**, 014504 (2011).
[24] U. Wolff, Phys. Rev. Lett. **62**, 361 (1989).
[25] M.A. York and G.D. Moore, hep-lat/1106.2535.
[26] V. Skokov, B. Friman, E. Nakano, K. Redlich, and B.-J. Schaefer, Phys. Rev. D **82**, 034029 (2010).

Minimum-bias angular and trigger-associated correlations from 200 GeV p-p collisions: jets, flows, centrality and the underlying event

D. Prindle for the STAR collaboration

CENPA 354290, University of Washington, Seattle, USA

The mechanisms leading to the hadronic final state of high-energy proton-proton collisions remain an unresolved issue at the RHIC and LHC. A substantial contribution to the hadronic final state from minimum-bias (MB) jets is dominated by non-perturbative processes and may provide the common base for any high-energy dijet. Observation of a same-side (on azimuth)"ridge" in LHC p-p collisions suggests to some that hydrodynamic flows may play a role in that small system at higher energies. The issue of p-p centrality vs triggered jets has emerged in the context of gluon transverse distributions in the proton inferred from DIS data. Attempts have been made to isolate and study the underlying event (UE) complementary to triggered dijets, and it is suggested that multiple parton interactions may contribute to the UE.

Reference [1] considered theoretical and experimental results for UE systematics and p-p centrality in the context of a two-component (soft+ hard) model derived from single-particle p_t spectrum n_{ch} systematics. The study concluded that there may be a substantial contribution to the UE from the triggered dijet and that p-p centrality is not controlled significantly by a jet trigger condition (if p-p centrality is relevant at all). Further study of two-particle correlations in p-p collisions was called for, particularly the n_{ch} dependence of MB correlations.

We report a comprehensive study of MB (no p_t cuts) angular correlations and trigger-associated (TA) y_t correlations (transverse rapidity $y_t = \ln[(m_t + p_t)/m_\pi]$) from 200 GeV p-p collisions. Angular correlations are characterized by 2D model fits that accurately distinguish among proton dissociation structure (soft), jet-related structure (hard) and a nonjet azimuth quadrupole. All angular correlations are simply represented by a (2+1)-component model. The hard and quadrupole component scale simply with the soft-component multiplicity n_s, clarifying the role of centrality and the eikonal model in p-p collisions. 2D TA correlations project to a marginal 1D trigger spectrum that can be simply predicted from p_t spectrum n_{ch} dependence. 2D TA distributions can then be processed to reveal MB jet fragment (hard component) systematics comparable to measured

fragmentation functions. Hard-component azimuth dependence relative to the trigger relates to UE studies. From TA analysis we can establish the kinematic limits of jet fragment production in p-p collisions.

1. Introduction

In this paper we present an analysis of particle production in proton-proton collisions at a center of mass energy of 200 GeV. The data were recorded by the STAR detector at RHIC in 2009 during a low luminosity running period which enabled an efficient minimum-bias (MB) trigger with very little, if any, pileup. We have enough statistics to divide the sample into six multiplicity bins ranging from a mean multiplicity of about two to 27 in two units of rapidity.

In Sec. 2 we recap a few features of the 1D two component spectrum model (TCM) that we use in understanding the MB two-particle angular correlations presented in Sec. 3. The angular correlations are described with a few components. In Sec. 4 we extend the 1D TCM to 2D trigger-associated (TA) correlations. The TA model describes the trigger spectra and associated soft component very well allowing us to subtract the TA model soft component and study the data hard component in detail. The hard component is discussed in Sec. 5, focusing on toward, transverse (trans) and away azimuth regions as conventionally defined in UE studies. We summarize in Sec. 6.

2. 1D Two-component model

The two-component spectrum model was developed to understand y_t (or p_t) spectra in proton-proton collisions.[1] It was observed that the spectrum shape can be decomposed into soft, $S_0(y_t)$, and hard, $H_0(y_t)$, components where the soft component is defined by the spectrum shape as the event multiplicity goes to zero. The component shapes are independent of multiplicity but the ratio of their amplitudes depends on multiplicity: $n_h/n_s \propto n_s \approx n_{ch}$ where n_s and n_h are the soft and hard components of n_{ch} within the acceptance $\Delta\eta$. In analogy with A-A collisions we can think of the soft component as being related to participants (low-x gluons for p-p) and the hard component to binary parton collisions. In a Glauber calculation of A-A collisions the numbers of participants and binary collisions depend on the impact parameter and we find $N_{bin} \propto N_{part}^{4/3}$. For proton-proton collisions we find $n_h \propto n_s^2$; a Glauber description doesn't work.

3. Angular correlations of particles produced in p-p collisions

We developed a MB method to analyze two particle angular correlations to study A-A collisions without imposing preconceived ideas.[2–5] In this method we take all pairs of particles and project out $\phi_1+\phi_2$ and $\eta_1+\eta_2$ which loses no information if we have rotational symmetry in ϕ (which is true) and translational symmetry in η (which is a reasonable approximation at mid-rapidity). Integrating over p_t we end up with a two dimensional correlation on $\phi_\Delta \equiv \phi_1 - \phi_2$ and $\eta_\Delta \equiv \eta_1 - \eta_2$. This analysis works for even very low multiplicity events so we can apply it to proton-proton collisions. In Fig. 1 we show the angular correlations for the lowest and highest multiplicity bins. In each case the upper left quadrant is the model, the upper right quadrant is the data and the lower left quadrant is the residuals. The model consists of a 2D Gaussian at the origin, a narrow 2D exponential at the origin, an away-side 1D azimuth dipole and a 1D Gaussian on η_Δ. There is a significant improvement in the fit when we include a nonjet quadrupole $\cos(2\phi_\Delta)$ component which is clearly required in A-A correlations. By examining the p_t and charge dependence of these components we find that the narrow 2D exponential is due to HBT and γ conversion to e^+e^- pairs, the 1D Gaussian on η_Δ is consistent with soft particle emission from the beam remnants and the same-side 2D Gaussian is due to intra-jet correlations while the away-side dipole is due to inter-jet correlations. The lower right quadrants show the data with the 1D Gaussian on η_Δ and the HBT/e^+e^- components removed leaving the jet structure and non-jet quadrupole.

In Fig. 2 we show the multiplicity dependence of the dijet amplitudes for the same-side 2D peak and the away-side dipole. The amplitudes of the dijet structures scale with the square of the multiplicity and are consistent with a QCD dijet total cross section $\sigma_{dijet} = 2.5$ mb [6]. The nonjet quadrupole component is interesting. In A-A collisions we find that $n_{ch}A_Q \propto N_{part}N_{bin}\varepsilon^2_{opt}$. We assume that in proton-proton collisions $\langle\varepsilon^2_{opt}\rangle$ is non-zero and note that $N_{bin} \propto N^2_{part}$. If the non-jet quadrupole in proton-proton collisions arises from the same mechanism as in A-A collisions we predict that

$$(n_{ch}/n_s)\, A_Q \propto n_s^2\,, \tag{1}$$

which indeed appears to be the case. This suggests that we should seriously consider if the non-jet quadrupole in proton-proton collisions is due to the same physics as in A-A collisions and is unrelated to hydrodynamic flows.

4. Trigger-associated analysis

We extend the 1D TCM to a 2D trigger-associated (TA) model to isolate the hard component in (y_{tt}, y_{ta}) as well as to connect with underlying event

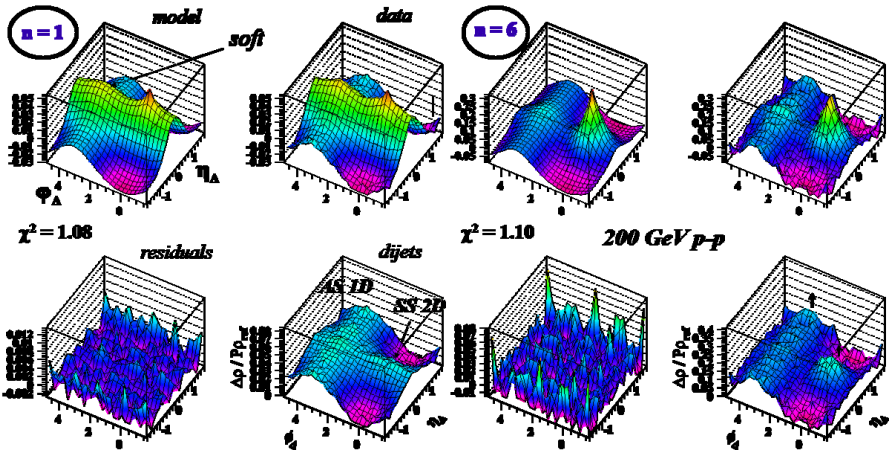

Fig. 1. MB angular correlations. The four panels on the left are for low multiplicity and the four panels on the right for high multiplicity events. In each group the upper left quadrant shows the model, the upper right quadrant shows the data and the lower left shows the residuals. In the lower right quadrant the 1D Gaussian and HBT/e^+e^- model components have been removed leaving the dijet and non-jet quadrupole components.

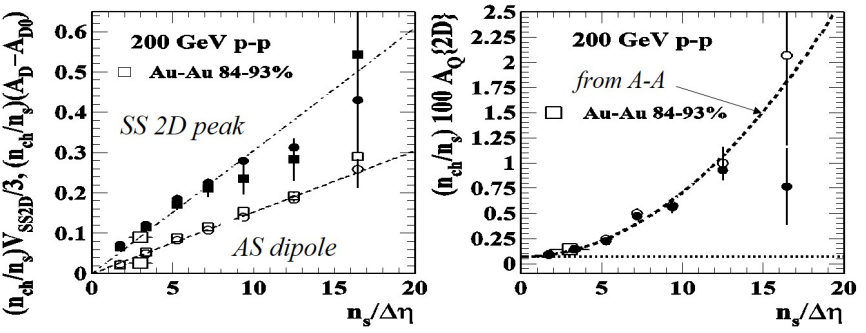

Fig. 2. The left panel shows the volume of the same-side 2D Gaussian (V_{SS2D}) and the away-side dipole amplitude, both scaled by n_{ch}/n_s. The away-side dipole amplitude has been adjusted by subtracting A_{D0} to account for global transverse momentum conservation. n_{ch} and n_s are the total multiplicity and soft component of the multiplicity within the acceptance, $\Delta\eta$. The right panel is the nonjet quadrupole amplitude, A_Q, also scaled by n_{ch}/n_s. We observe that n_{ch} times each dijet component amplitude is proportional to n_s^2 while $n_{ch}A_Q$ is proportional to n_s^3.

(UE) studies. Here y_{tt} is y_t of the trigger and y_{ta} is y_t of the associated particle. For a MB analysis we take the track with the highest y_t in the event as the trigger, all other tracks are associated. Thus we accept all pairs from all jets in the analysis. A useful constraint on the 2D TA model is that the projection onto the associated particle axis is the 1D single-particle spectrum minus the trigger spectrum.

The trigger particle may be from an event with no hard component (no dijet in the acceptance) in which case the spectrum is derived from the soft component only. If the event has a hard component (at least one jet) then the trigger can be due to the soft or hard component depending on which produced the highest y_t particle of the event. The void probability G is in either case the probability that no particle appears above y_{tt}.

$$\begin{aligned}\rho_{trig}(y_{tt}, n_{ch}) =& P_s(n_{ch})G_s(y_{tt}, n_{ch})S_o(y_{tt})+ \\ & P_h(n_{ch})G_h(y_{tt}, n_{ch})F_h(y_{tt}),\end{aligned} \tag{2}$$

where

$$F_h(y_{tt}, n_{ch}) = p'_s(n_{ch})S_0(y_{tt}) + p'_h(n_{ch})H_0(y_{tt})\,, \tag{3}$$

P_s and $P_h \equiv (1 - P_s)$ are probabilities for soft and hard events, p'_s and p'_h are the soft and hard probabilities given that there is a hard component, G_s and G_h are the void probabilities and S_0 and H_0 are the soft and hard components of the 1D TCM. All functions and probabilities are taken from the 1D TCM and the predicted trigger spectra are in excellent agreement with the measured trigger spectra.

The 2D TA distribution

$$F(y_{ta}, y_{tt}, n_{ch}) = T(y_{tt})A(y_{ta}|y_{tt})\,, \tag{4}$$

is the joint probability of a trigger, $T(y_{tt})$, and an associated particle, $A(y_{ta}|y_{tt})$, where A is the conditional probability of an associated particle being emitted at y_{ta} in an event with trigger y_{tt}. We combine soft and hard components for F according to the 1D TCM. Complete details are given in Ref. [7].

In the previous paragraphs we have sketched how we extend a 1D TCM spectrum model of proton-proton collisions to a 2D TA model. In Fig. 3 we compare the measured correlations (left panel) with the model (middle panel). These are for multiplicity bin 3 but other multiplicity bins show similar agreement. The $y_{t,trig}$ axis of these panels reflect the trigger spectrum. We are interested in the associated spectrum which we get by dividing the 2D TA correlations by the 1D trigger spectrum, $A \equiv F/T$. The third panel of Fig. 3 is the ratio of data and TA model for A. The soft component is described very well (ratio ≈ 1) for $y_{ta} < 2.5$. We subtract the TCM model soft component from the data to reveal the data hard component in detail.

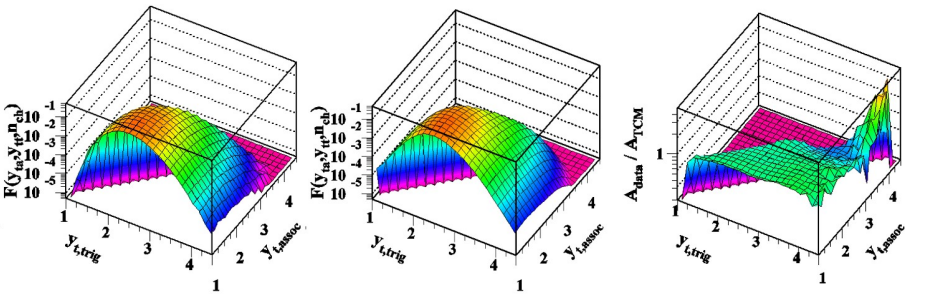

Fig. 3. The left panel contains TA correlations, the middle panel is the TA model based on the 1D spectrum TCM. The right panel is the data to TA model ratio of the associated spectrum (A) showing that the soft component is described very well (ratio ≈ 1) by the TA model for $y_{ta} < 2.5$. These are for multiplicity bin 3, the other multiplicity bins are equally well described.

5. Hard component of A

In Sec. 4 we discussed an extension of the 1D TCM spectrum model to 2D in order to describe MB TA correlations and we showed this accurately described the trigger spectrum and the soft part of the associated spectrum. This enables us to isolate the associated hard component of data by subtracting the model soft component. In Fig. 4 we show the hard component for like-sign and unlike-sign pairs in the toward ($\Delta\phi \leq \pi/3$), trans ($\pi/3 < \Delta\phi \leq 2\pi/3$) and away ($2\pi/3 < \Delta\phi$) regions. In UE studies the toward and away regions are usually assumed to be dominated by jets and the trans to be dominated by the UE. While the trans may have fewer jet-related particles than toward and away there are still a significant number that can't be ignored. The toward region shows a charge-ordering effect with more unlike-sign pairs than like-sign pairs [3]. The away-side is charge independent and the associated particles extend to lower y_t than the same-side. This can be understood as due to the initial k_t, for back to back particles of equal y_t one will be boosted to higher energy and become the trigger while the other will be reduced in energy.

6. Summary

We have analyzed a very clean sample of 200 GeV proton-proton collisions. To understand the data we reviewed the characteristics of the soft and hard components of the TCM developed to understand 1D y_t spectra. Then we extracted jet-like components and a non-jet quadrupole from the 2D angular correlations on $(\eta_\Delta, \phi_\Delta)$. We showed the non-jet quadrupole

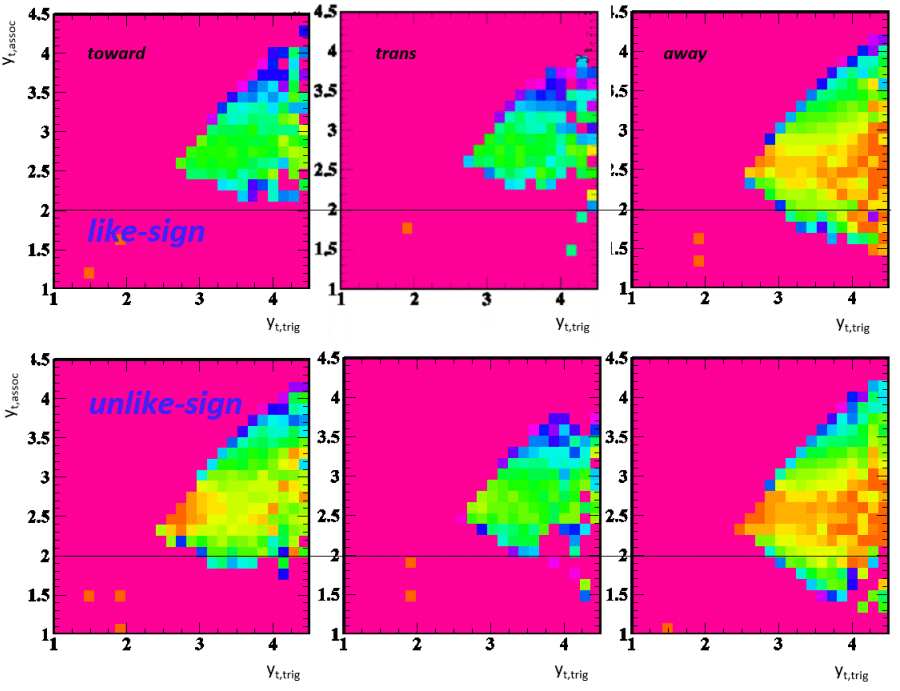

Fig. 4. Upper row are like-sign pairs of the hard component of the TA correlations. Lower row are unlike-sign pairs. Left column is toward ($\Delta\phi \leq \pi/3$), middle is trans ($\pi/3 < \Delta\phi \leq 2\pi/3$) and right is away ($2\pi/3 < \Delta\phi$). Toward shows charge ordering while the away is charge independent. There is a significant jet-related yield in trans.

may have the same origin in proton-proton collisions as it does in A-A collisions. We did a MB TA analysis where the highest y_t in the event is taken to be the trigger. To understand this we extended the TCM to a 2D TA model which describes the trigger spectrum and soft component of the data very well. Subtracting the TA model soft component we see that the remaining hard component exhibits charge ordering for the toward region but not the away region, as expected for jets. The trans region exhibits a significant jet structure.

Acknowledgments

This work is supported in part by the Office of Science in the U.S. DOE under grant DE-FG03-97ER41020.

References

[1] J. Adams *et al.*, Phys. Rev. D **74**, 032006 (2006).

[2] R.J. Porter and T.A. Trainor (STAR Collaboration), J. Phys. Conf. Ser. **27**, 98 (2005).

[3] R.J. Porter and T.A. Trainor (STAR Collaboration), PoS **CFRNC2006**, 004 (2006).

[4] J. Adams *et al.* (STAR Collaboration), Phys. Rev. C **73**, 064907 (2006).

[5] G. Agakishiev *et al.* (STAR Collaboration), Phys. Rev. C **86**, 064902 (2012).

[6] T.A. Trainor, Phys. Rev. C **80**, 044901 (2009).

[7] T.A. Trainor and D.J. Prindle, Phys. Rev. D **88**, 094018 (2013).

BSM searches in multi-objects final states in ATLAS

Thijs Cornelissen†

Bergische Universität Wuppertal, Wuppertal, Germany

Recent results on searches for new physics from Run 1 of the Large Hadron Collider are reported. The ATLAS experiment has already collected more than 20 fb^{-1} of integrated luminosity, allowing for a large number of new phenomena searches in many different final states. No deviations from the Standard Model expectations are found, and corresponding constraints on physics beyond the Standard Model are obtained.

1. Introduction

The Standard Model (SM) of particle physics is regarded as a highly successful theory. It provides a description of matter and forces in our universe. The predictions made by the SM have been verified by many experiments to date and so far no discrepancies have been found. In particular the recent discovery of a Higgs-like boson fits very well in the SM framework. However the SM is not a complete theory as it leaves several questions unanswered, e.g. the nature of dark matter, and the origin of the light Higgs mass. There are many new theories that attempt to address these issues, which are collectively called 'physics beyond the SM' (BSM). In this contribution, some of the most important searches for new physics at the ATLAS experiment [1] are summarized. The references to the relevant theory papers can be found in the corresponding ATLAS publications.

2. Exotic Phenomena Searches

The exotic searches in ATLAS cover a wide range of signatures and models by looking at various final states. We provide the limits in a model independent way on the visible production cross-section of the new physics processes, and translate them into limits on the particle masses in various new physics models.

† On behalf of the ATLAS collaboration

2.1. Search for heavy resonances decaying into semi-leptonic $t\bar{t}$ pairs

In this search [2], two event topologies were tested. In highly boosted events, the decay products of the hadronically decaying top quark are expected to be collimated so that they all fall within a single 'fat' jet (R = 1.0). Such events should also contain one small jet (R = 0.4) close to the lepton, at least one small jet tagged as b-quark and sizable E_T^{miss}. Further acceptance is gained by considering in addition the resolved event topology, that consists of four small jets (or three small jets if one of them has mass greater than 60 GeV), one of which is tagged as originating from a b-quark, a lepton and sizable E_T^{miss}. In both cases the invariant mass of the top pair is used as a discriminant (Fig. 1). In the boosted case, the longitudinal neutrino momentum p_z is obtained by imposing an on-shell mass of the leptonically decaying W boson candidate, whereas in the resolved case a χ^2 function is constructed to calculate the p_z and assign the jets to the top quarks. This search results in the exclusion of a leptophobic topcolor Z' boson [3] (assuming $\Gamma/m = 1.2\%$),

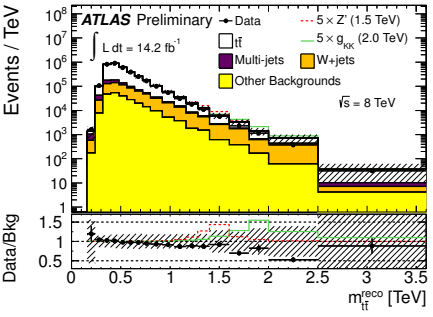

Fig. 1. The $t\bar{t}$ invariant mass spectrum, summing the spectra from the electron and muon channels and the two selection methods. The shaded areas indicate the total systematic uncertainties [2].

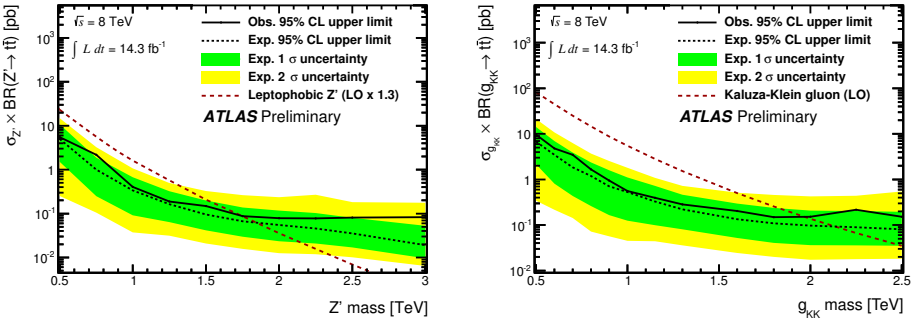

Fig. 2. Observed and expected upper cross section limits times the $t\bar{t}$ branching ratio on Z' bosons (left) and Kaluza-Klein gluons (right). The resolved and the boosted selections have been combined in the estimation of the limits. Both systematic and statistical uncertainties are included [2].

and a Kaluza-Klein gluon [4] (assuming $\Gamma/m = 15.3\%$), in the mass ranges 0.5 TeV $< m_{Z'} <$ 1.8 TeV and 0.5 TeV $< m_{g_{KK}} <$ 2.0 TeV (Fig. 2).

2.2. Search for vector-like quarks

Vector-like quarks are postulated by some models addressing the hierarchy problem, such as Little Higgs models and extra dimension models. The name refers to the feature that both chiralities transform in the same way under the weak symmetry group, which implies that they have no Yukawa coupling to the SM Higgs field.

The existence of the vector-like quarks would cause the cancellation of the quadratic divergences of the Higgs mass in the top loop. Vector-like quarks can appear with the SM charges (2/3, -1/3) or with exotic charges +5/3 and -4/3. They can form weak-isospin singlets, doublets and triplets. Pair production of these top partners is independent of their coupling to SM quarks.

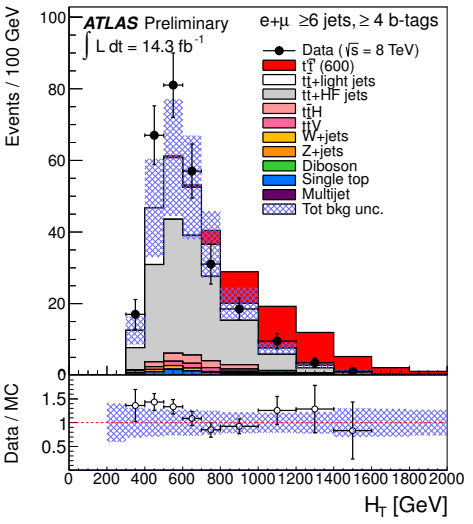

Fig. 3. Comparison between data and simulation for H_T in the combined e+jets and μ+jets channels with ≥ 6 jets and ≥ 4 b tags. Also shown is the expected $t'\bar{t}'$ signal corresponding to $m_{t'}$=600 GeV in the t' doublet scenario. The shaded area represents the total post-fit background uncertainty [7].

The final states are expected to include third generation particles. The signatures investigated by ATLAS include $T \to Wb$ [5], $T \to Zt$ [6], $T \to Ht$ [7], and same-sign dileptons [8] (from the decay $T^{+}_{5/3} \to W^{+}t \to W^{+}W^{+}b$). The Ht analysis requires a lepton, at least six jets of which at least two are b-tagged, and missing transverse energy. The discriminant variable used is the total transverse energy $H_T = \sum_j p_T^j + p_T^l + E_T^{\mathrm{miss}}$, which is shown in Fig. 3. The combined limits on the masses of vector-like T quarks are shown in Fig. 4.

3. Supersymmetry Searches

Supersymmetry (SUSY) is one of the most favored theories for physics beyond the SM. The theory introduces new particles (sparticles) for each

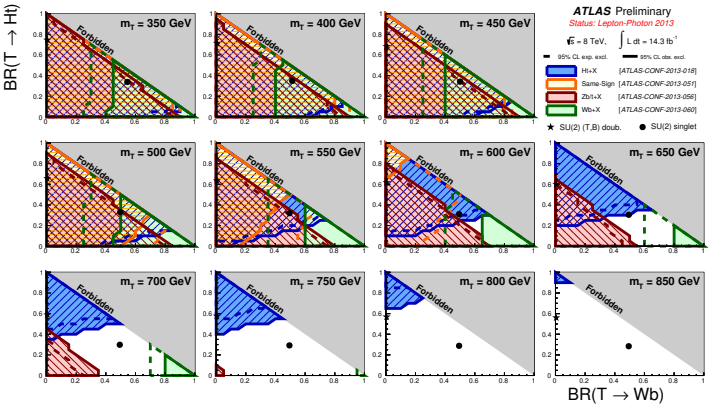

Fig. 4. Exclusion area in the branching ratio plane for individual signal mass point of vector-like T quarks [9].

SM particle that differ in spin by 1/2 from their SM counterparts. A new kind of symmetry called R-parity ($R = (-1)^{3(B-L)+2S}$) is an important part of many SUSY models. In R-parity conserving (RPC) scenarios, the sparticles are produced in pairs and the lightest SUSY particle (LSP) is stable and weakly interacting. In a large variety of models the LSP is the lightest neutralino ($\tilde{\chi}_1^0$), which escapes detection in the detector and leads to missing transverse energy E_T^{miss}. In R-parity violating (RPV) models, the LSP is no longer stable and decays into SM particles. The analyses presented here are studied in the context of both RPC and RPV scenarios.

3.1. Search for gluino mediated stop/sbottom production

The mixing between the squark eigenstates may be large for the third generation, leading to masses for the stop and sbottom eigenstates that are much lighter than for the other squarks. As a consequence, stops and sbottoms could be produced with relatively large cross-sections at the LHC, either directly in pairs, or through $\tilde{g}\tilde{g}$ production followed by $\tilde{g} \to b\tilde{b}$ or $\tilde{g} \to t\tilde{t}$ decays. These models are probed by requiring zero or one lepton, at least three b-tagged jets, and missing energy [10]. The list of selection variables used includes the inclusive effective mass $m_{\text{eff}}^{\text{incl}}$, defined as the scalar sum of the E_T^{miss} and the p_T of all jets with $p_T > 30$ GeV. In the 1-lepton channel, the p_T of the leading lepton and the transverse mass $m_T = \sqrt{2p_T E_T^{\text{miss}}(1 - \cos\Delta\phi(l, E_T^{\text{miss}}))}$ are also used. Figure 5 shows the effective mass distributions as well as the limits on the $\tilde{\chi}_1^0$ and $\tilde{g}$ masses in the so-called *Gtt* model, where $\tilde{g} \to tt\tilde{\chi}_1^0$ via an off-shell stop.

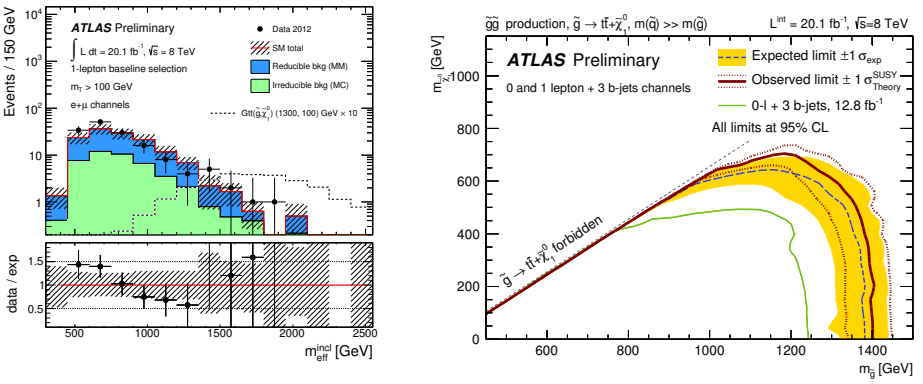

Fig. 5. (Left) The distribution of the inclusive effective mass for the baseline selection in the 1-lepton channel and after requiring $m_T > 100$ GeV, as observed in data together with the background prediction from the matrix method. The prediction for one signal point from the *Gtt* model is overlaid. (Right) Expected and observed exclusion limits in the $(m_{\tilde{g}}, m_{\tilde{\chi}_1^0})$ plane for the *Gtt* model [10].

3.2. Gluino pair production with many jets

The gluino pairs produced in RPC models may lead to cascade decays with many jets in the final state, e.g. $\tilde{g} \to \bar{q}+\tilde{q} \to \bar{q}+q'+\tilde{\chi}_1^{\pm} \to \bar{q}+q'+W+\tilde{\chi}_1^0$ (the 'gluino-squark model'). The search in Ref. [11] requires a large number (between 7 and 10) of jets, missing energy, as well as a veto against isolated leptons. Different signal regions are defined, e.g. requiring different number of b-tags, to provide sensitivity to models that predict either more or fewer b-jets than the SM background. A complementary set of signal regions clusters the 'standard' R=0.4 jets into large (R=1.0) composite jets, with cuts being placed on the scalar sum of masses of the composite jets. In all signal regions the final selection is $E_T^{\rm miss}/\sqrt{H_T} > 4$ GeV$^{1/2}$, where H_T is the scalar sum of transverse momenta of all jets with $p_T > 40$ GeV and $|\eta| < 2.8$. This selection variable has the property that its shape is approximately independent of the number of jets, thus the SM multijet background can be estimated from the lower jet multiplicity bins which are free of signal. Figure 6 shows the $E_T^{\rm miss}/\sqrt{H_T}$ distribution for one of the signal regions, as well as the combined limits on the $\tilde{\chi}_1^0$ and $\tilde{g}$ masses.

3.3. RPV decays with large jet multiplicities

In the context of RPV SUSY, both the gluino and neutralino can play the role of LSP. When they undergo decays with non-zero couplings of superfields of the type $\lambda''_{ijk}U_iD_jD_k$, the result would be 6-quark or 10-

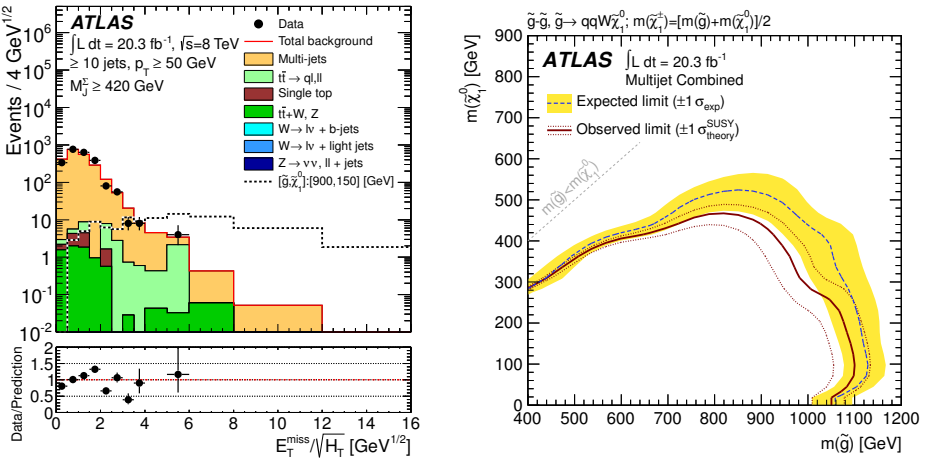

Fig. 6. (Left) $E_T^{\rm miss}/\sqrt{H_T}$ distribution for the signal region requiring at least 10 jets, and a scalar sum of composite jet masses larger than 420 GeV. Also shown is the expected signal corresponding to $m_{\tilde{g}} = 900$ GeV and $m_{\tilde{\chi}_1^0} = 150$ GeV, with $\tilde{g} \to t+\bar{t}+\tilde{\chi}_1^0$. (Right) 95% CL exclusion curve for the simplified gluino-squark (via $\tilde{\chi}_1^\pm$) model, for fixed $x = 1/2$, where $x = (m_{\tilde{\chi}_1^\pm} - m_{\tilde{\chi}_1^0})/(m_{\tilde{g}} - m_{\tilde{\chi}_1^0})$, and varying $\tilde{\chi}_1^0$ mass [11].

quark final states. Evidence of multijet events is probed by counting the number of high transverse momentum (at least 80 GeV) 6-jet and 7-jet events, with various b-tagging requirements added to enhance the sensitivity to couplings that favour decays to third generation quarks [12]. The number of jets, the p_T cut that is used to select jets, and the number of b-tags are optimised separately for each signal model taking into account experimental and theoretical uncertainties. The background yield in each of the signal regions is estimated by using a signal-depleted control region in data and then projecting into the signal region using a factor that is determined from multi-jet simulation. The distribution for one of the signal regions (6-jet) is shown in Fig. 7. No excess above SM background is seen and results are interpreted for all possible RPV branching fractions of gluino decays in the considered quark models. Figure 7 shows the obtained cross-section limits in one of the 6-quark models.

3.4. Search for long lived particles with displaced vertices

Several extensions to the SM posit the existence of heavy particles with lifetimes that can vary from picoseconds to nanoseconds. The decays of such particles form a unique signature of vertices that are displaced from the *pp*

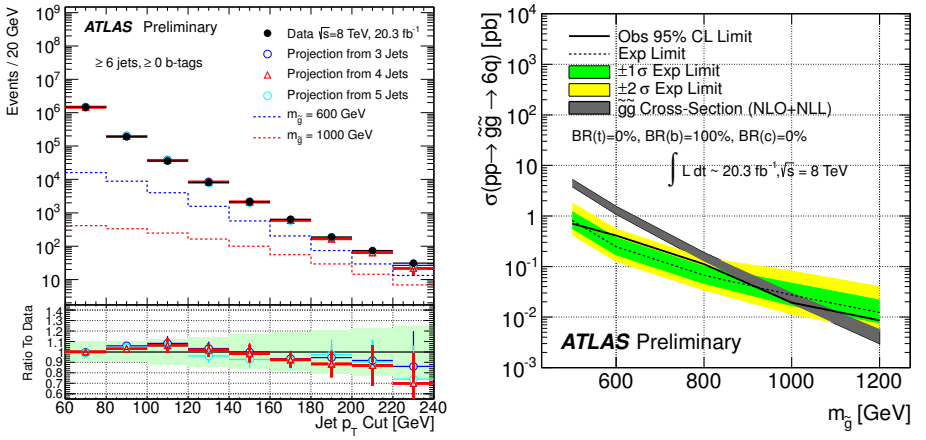

Fig. 7. (Left) The number of observed events with ≥6 jets is compared with two signal models, and with expectations that are determined by using Pythia to project the number of observed events from low-jet multiplicity control regions. In the ratio plots the green bands convey the background systematic uncertainties. (Right) Expected and observed cross-section limits for the 6-quark gluino model where every gluino decays into a b-quark in the final state [12].

interaction point. Such a search for the decay of a heavy particle, producing a multi-track vertex that contains a high p_T muon, at a distance between 0.4 cm to 18 cm from the pp interaction point has been carried out [13]. To reduce the background from hadronic interactions, the vertex is searched in a low density material region. The total background contribution is estimated to be very small (0.02 ± 0.02). No candidate events are observed in the data and the results are translated into limits in the context of a RPV scenario as shown in Fig. 8. The limits are reported as a function of the neutralino lifetime and for a range of neutralino masses and velocities. Branching ratios of 50% and 100% for the decay chain from squarks to neutralinos to muon-plus-quarks are considered.

4. Conclusions

The ATLAS experiment has carried out extensive studies in the search for physics beyond the Standard Model. So far, no evidence for new physics has been found. The investigation of the 7 and 8 TeV data continues, while the data from the upcoming LHC Run 2 will greatly extend the discovery reach of many analyses presented here.

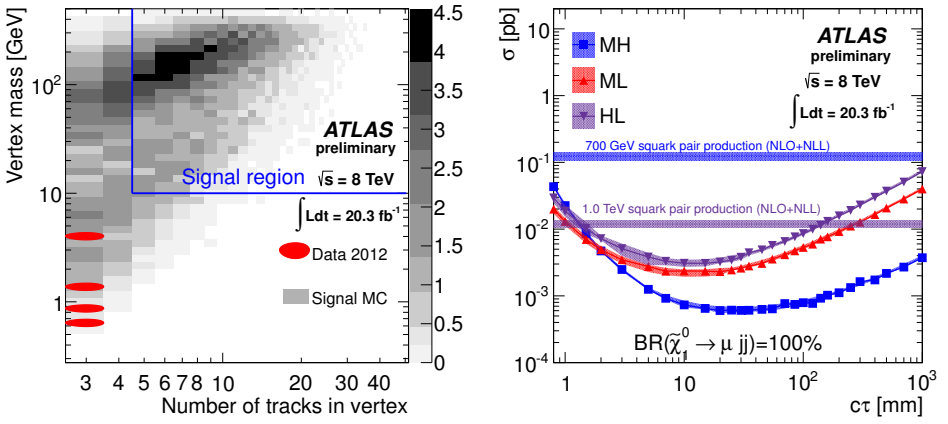

Fig. 8. (Left) Vertex mass vs track multiplicity for reconstructed displaced vertices in non-material regions, where all event, muon, and vertex selection requirements are satisfied. (Right) Upper limits at 95% CL on sigma vs neutralino lifetime for different combinations of squark and neutralino masses, based on the observation of zero events satisfying all criteria in a 20.3 fb^{-1} data sample, for the case where the branching ratio for the decay chain from squark to neutralino to muon-plus-jets is 100% [13].

References

[1] ATLAS Collaboration, J. Inst. **3**, S08003 (2008).
[2] ATLAS Collaboration, ATLAS-CONF-2013-052.
[3] R. M. Harris and S. Jain, Eur. Phys. J. C **72**, 2072 (2012).
[4] B. Lillie, L. Randall, and L.T. Wang, J. High Energy Phys. **09**, 074 (2007).
[5] ATLAS Collaboration, ATLAS-CONF-2013-060.
[6] ATLAS Collaboration, ATLAS-CONF-2013-056.
[7] ATLAS Collaboration, ATLAS-CONF-2013-018.
[8] ATLAS Collaboration, ATLAS-CONF-2013-051.
[9] ATLAS Collaboration, `https://twiki.cern.ch/twiki/pub/AtlasPublic/CombinedSummaryPlots/ATLAS_VLQ_TT_june2013_step4.png`.
[10] ATLAS Collaboration, ATLAS-CONF-2013-061.
[11] ATLAS Collaboration, J. High Energy Phys. **10**, 130 (2013).
[12] ATLAS Collaboration, ATLAS-CONF-2013-091.
[13] ATLAS Collaboration, ATLAS-CONF-2013-092.

Physics implications of correlation data from the RHIC and LHC heavy-ion programs

R. L. Ray

Department of Physics, University of Texas at Austin, Austin, TX 78712 USA

Two-dimensional angular correlation data from the STAR experiment at RHIC and from the LHC experiments provide critical information about dynamical processes in relativistic heavy-ion collisions. The principal correlation structures of interest are a broad jet-related peak at small relative azimuth (ϕ) extending to large relative pseudorapidity (η), the dijet ridge at large relative azimuth, and an independent double ridge on ϕ represented by a quadrupole function. The broad peak at small relative azimuth has been attributed, in large part, to initial-state fluctuations and hydrodynamic flow which produce higher-order harmonics on ϕ. That conjecture is challenged in this paper. It is shown that the net effect of additional higher harmonic model elements is to describe small, non-Gaussian (NG) shapes in the broad jet-related peak. The quadrupole correlation, which is also conventionally attributed to hydrodynamic flow, is considered within the Balitsky - Fadin - Kuraev - Lipatov (BFKL) Pomeron framework. Preliminary results using this model for the quadrupole correlation for particle production from 200 GeV $p + p$ collisions are shown to be consistent with recent data from STAR.

1. Introduction

One of the more interesting observations to emerge from the study of two-particle angular correlation data from heavy-ion collisions at the RHIC and the LHC is the appearance of a two-dimensional (2D) peak at small relative azimuth (same-side ϕ) which significantly increases in amplitude and in width along relative pseudorapidity for more-central collisions [1–4]. For minimum-bias $p+p$ collisions and for Au+Au collisions from peripheral to mid-centrality (50% of fractional cross section) at RHIC this correlation peak structure is consistent with perturbative quantum chromodynamics (pQCD) predictions for minimum-bias jets (those with no lower momentum cut) assuming binary nucleon-nucleon collision scaling [2, 5, 6]. The dynamical origin of the same-side peak for more-central collisions is not known. Alver and Roland [7] conjectured that the η-elongation is caused by triangu-

lar flow, a $\cos 3(\phi_1 - \phi_2)$ element or sextupole. Critical evaluations [2, 8–10] show that this sextupole is determined by the multipole decomposition of the azimuth projection of the same-side 2D peak, implying that the sextupole derives from that structure rather than from some other aspect of the data.

Another long-range η correlation is the quadrupole, a $\cos 2(\phi_1 - \phi_2)$ element, proportional to v_2^2 and conventionally attributed to elliptic flow. However, the simultaneous occurrence of pQCD minijets and large quadrupole in peripheral to mid-central 200 GeV Au+Au correlation data [2] calls into question the notion of a strongly interacting medium. Analysis of the quadrupole correlation systematics with respect to collision energy, transverse momentum (p_t), and centrality shows that its amplitude scales with the number of binary nucleon-nucleon collisions, $\log(\sqrt{s})$ and eccentricity implying that the quadrupole is generated in the initial state rather than via final-state scattering. The properties of the same-side 2D peak and the quadrupole correlation lead to a general consideration of long-range pseudorapidity correlations from heavy-ion collisions and the possibility that these structures can be understood within a pQCD framework.

2. Analysis method

For the correlations shown here sibling pairs (those from the same event) and mixed-event pair histograms for all charged particles in the STAR TPC acceptance ($p_t > 0.15$ GeV/c, $|\eta| < 1$ and 2π azimuth) are filled on relative azimuth $\phi_\Delta = \phi_1 - \phi_2$ and pseudorapidity $\eta_\Delta = \eta_1 - \eta_2$. There is no "trigger" particle; all pairs are used. A per-particle normalization is used which eliminates the trivial combinatoric $1/N_{ch}$ dependence. The measured quantity reported in [2] is

$$\frac{\Delta\rho}{\sqrt{\rho_{\rm ref}}} \equiv \sqrt{\rho_{\rm ref}}\frac{\rho_{\rm sib} - \rho_{\rm mix}}{\rho_{\rm mix}}, \tag{1}$$

where $\sqrt{\rho_{\rm ref}} = d^2N_{\rm ch}/d\eta d\phi$ is the single charged particle density.

The principal correlation structures are well described with a same-side 2D Gaussian, an away-side ($|\phi_\Delta| > \pi/2$) dipole, a quadrupole, and a same-side 2D exponential which describes conversion electrons and quantum correlations. The standard fitting model is defined in [2, 8]. No additional model elements are required to describe the minimum-bias p_t-integral 2D angular correlation data from STAR. An added sextupole term would have the form $2A_{\rm S}\cos(3\phi_\Delta)$.

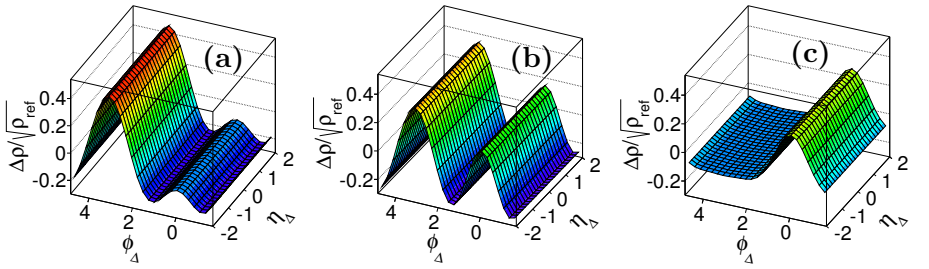

Fig. 1. (Color online) Multipoles from fits to the 200 GeV Au+Au 9-18% centrality data [2] showing: (a) Fitted dipole + quadrupole. (b) Fitted dipole + quadrupole + sextupole. (c) Difference (b) - (a).

3. Same-side 2D peak results

The standard model function accurately describes the η_Δ-independent structure in the away-side correlation data [1, 2]. Including a sextupole forces the dipole and quadrupole terms to adjust to maintain a good fit. The net difference is shown in Fig. 1 for model fits to more-central Au+Au correlation data. The right-most panel shows the quantity $[A'_{\rm D}\cos(\phi_\Delta - \pi)/2 + 2A'_{\rm Q}\cos(2\phi_\Delta) + 2A'_{\rm S}\cos(3\phi_\Delta) - A_{\rm D}\cos(\phi_\Delta - \pi)/2 - 2A_{\rm Q}\cos(2\phi_\Delta)]$ where primes indicate fitting parameters obtained with an included sextupole. The net structural difference is a narrow, same-side 1D peak (effective ridge) on azimuth [2, 8–10] which is accurately represented as a periodic 1D Gaussian. Fitting the data with an added sextupole element is statistically equivalent to fitting the data with an additional 1D same-side azimuth Gaussian (SSG) whose width is approximately 0.7.

The combination of an azimuth ridge and a 2D Gaussian produces a NG 2D peak. Projections of the same-side correlation data onto η_Δ are consistent with a 1D Gaussian within statistics. However, including small NG dependence improves the χ^2 [8]. Two-dimensional NG fitting models [8] are therefore considered further. NG modifications to the standard fitting model included: (i) replacing both exponents in the SS 2D Gaussian with fit parameters; (ii) replacing the η_Δ-dependent Gaussian with a power series through terms of order η_Δ^4; (iii) same as (ii) but allowing the exponent of the ϕ_Δ-dependent Gaussian to vary; (iv) adding quartic η_Δ^4 and ϕ_Δ^4 terms in the argument of the exponential. The functional forms are given in [8] . The sextupole term was excluded from fits which included these NG functions.

These five NG fitting models plus the standard model function with and without the sextupole were used to fit the angular correlation data for 200 GeV minimum-bias Au+Au collisions from STAR [2]. The best-fit values

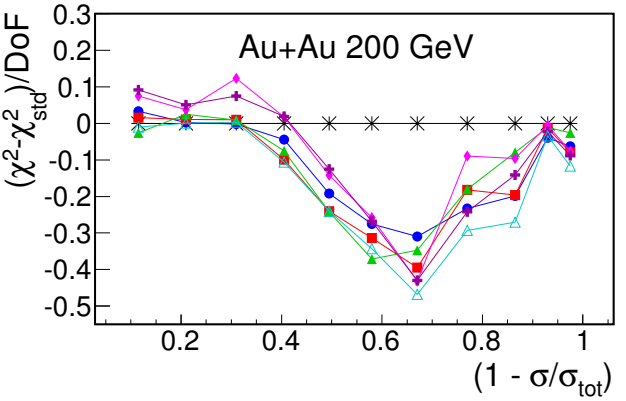

Fig. 2. (Color online) Differences between the χ^2/DoF for the six NG models and the standard model function versus centrality. Lines connect corresponding model results. The symbols denote each model as follows (see Ref. [8]): (1) black stars, standard, (2) solid blue circles, sextupole, (3) solid red squares, SSG, (4) solid green triangles, NG exponents, (5) solid magenta diamonds, η_Δ polynomial, (6) solid purple "plus" symbols, η_Δ polynomial with NG ϕ_Δ exponent, (7) open cyan triangles, quartic.

of χ^2 per degree-of-freedom (DoF) for all models and collision centralities are plotted in Fig. 2. Centrality is represented by the fraction of total cross section $\sigma/\sigma_{\rm tot}$, where results for peripheral collisions are shown on the left-hand side. From these results we find that all of the NG models reduce the χ^2/DoF for the mid- to more-central collision data from $(1-\sigma/\sigma_{\rm tot}) = 0.4$ to 0.9. The sextupole model is not special in that regard. For the NG models studied here the quartic model produces the best overall χ^2/DoF.

Correlation measurements with higher p_t cuts and for the higher collision energies attained at the LHC [4] provide strong evidence for NG dependence in the same-side 2D peak. It should not be surprising if a small NG dependence exists for same-side p_t-integral correlations at RHIC energies. Such occurrence would not exclude the possibility that the same-side correlation peak is dominated by pQCD jets with modified fragmentation [5, 6, 11]. While none of the NG fitting models considered here are excluded, it seems more plausible for possible NG structure in these data to originate locally in relative azimuth rather than arising from the combination of a same-side peaked structure with global angle correlations, such as $m > 2$ harmonics.

4. Perturbative QCD models of the quadrupole correlation

The scaling properties of the quadrupole correlation suggest that it may originate in the initial state via pQCD processes. Several authors recently presented pQCD based models in which a quadrupole correlation is generated by coherent gluon radiation from either BFKL Pomeron ladders [12], color dipoles [13], or glasma [14]. Reference [12] provides explicit calculations which facilitate comparisons to data. Results from that paper are used here.

In Ref. [12] the BFKL-Pomeron diagram in Fig. 3 results in quantum interference among the outgoing gluons such that the singles distribution contains a term proportional to $\cos 2\phi$ where ϕ is measured relative to the N-N Pomeron momentum transfer $\vec{Q}_T$. The two-gluon density is

$$\frac{d\sigma}{dy_1 dy_2 d^2p_{t1} d^2p_{t2}} \;=\; \mathcal{N}\left(1+\frac{1}{2}p_{t1}^2 p_{t2}^2 \langle\langle Q_T^4\rangle\rangle \langle q^{-4}\rangle^2 (2+\cos 2\phi_\Delta)\right), \quad (2)$$

where $\mathcal{N}$ is proportional to the product of the single gluon distributions times the probability $N_{I\!P h}^2(Q_T^2)$ of producing a two-Pomeron parton shower in a hadron-hadron collision. The momentum integrals were estimated in Ref. [12] assuming a gluon saturation model with saturation scale Q_S^2, however, the unknown probability $N_{I\!P h}^2(Q_T^2)$ was not estimated.

Each parton shower is assumed to produce a Poisson distribution with an average charged particle multiplicity $\bar{N}_{\rm ch}$ equal to the minimum-bias average multiplicity [12] which is $2.5/\Delta\eta$ for $p+p$ at $\sqrt{s} = 200$ GeV [15]. The relative probability that each $p+p$ collision in a minimum-bias ensemble produces 1, 2, etc. parton showers is defined in this paper as P_n, $n \in [1, 2, \cdots]$. In addition there is a finite probability of producing a hard-scattering process [15] in each $p+p$ collision. These factors were combined in a model of the minimum-bias $p+p$ multiplicity frequency distribution, where the data are described with a negative binomial distribution (NBD). Fits to the latter provide estimates of P_n.

The hard-scattering component of multiplicity in minimum-bias $p+p$ collisions at 200 GeV was studied in [15]. Defining the soft and hard particle multiplicities as $n_{\rm s}$ and $n_{\rm h}$, where the total charged particle multiplicity $n_{\rm ch} = n_{\rm s} + n_{\rm h}$, it was found that

$$n_{\rm h}/n_{\rm s} \;=\; \alpha n_{\rm ch}\,, \quad (3)$$

where $\alpha = 0.005$ and

$$n_{\rm h} \;=\; \alpha n_{\rm s}^2/(1-\alpha n_{\rm s}). \quad (4)$$

The frequency distribution on $n_{\rm s}$ in this model is $\sum_{n=1} P_n \mathcal{P}(n_{\rm s}, n\bar{N}_{\rm ch})$ where $\mathcal{P}(x,\bar{x})$ is the Poisson distribution on x for mean $\bar{x}$. The hard component

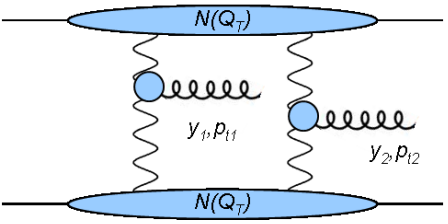

Fig. 3. BFKL Pomeron diagrams with interfering gluon emission [12].

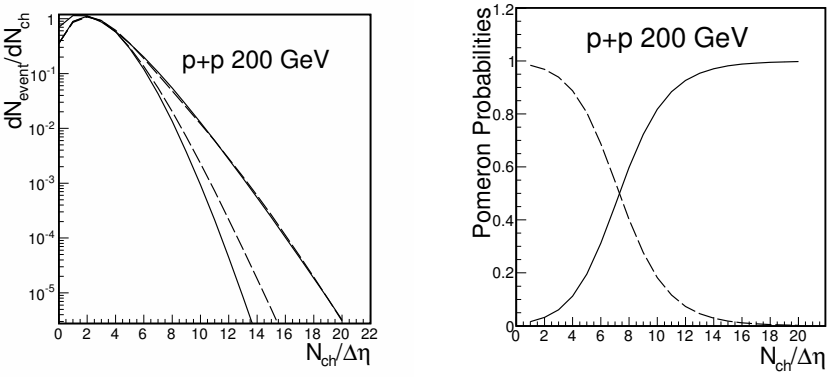

Fig. 4. Left panel: One- and two-Pomeron shower distributions fitted to the 200 GeV $p+p$ minimum-bias frequency distribution for $|\eta| < 0.5$. Right panel: Probabilities for one-Pomeron (dashed curve) and two-Pomeron (solid curve) showers.

distribution depends on $n_{\rm s}$ and is proportional to $\mathcal{P}(n_{\rm h}, \alpha n_{\rm s}^2/(1-\alpha n_{\rm s}))$. The joint probability distribution on total charge $n_{\rm ch}$ is

$$\frac{1}{N_{\rm event}}\frac{dN_{\rm event}}{dn_{\rm ch}} = \sum_{n_{\rm s}} \mathcal{P}(n_{\rm ch}-n_{\rm s}, \alpha n_{\rm s}^2/(1-\alpha n_{\rm s})) \sum_{n=1} P_n \mathcal{P}(n_{\rm s}, n\bar{N}_{\rm ch}). \quad (5)$$

Fits to the data, shown in the left panel of Fig. 4, obtain $P_1 = 0.91$, $P_2 = 0.09$ and $P_{n>2} = 0$ for the minimum-bias average. The NBD representation of the data is shown by the upper solid curve. Distributions for one-Pomeron shower, one-Pomeron shower plus hard component, and the one- and two-Pomeron showers plus hard component fit are shown by the lower solid curve, lower dashed curve and upper dashed curve, respectively. The one-Pomeron (dashed) and two-Pomeron (solid) probabilities as a function of $n_{\rm ch}$ are shown in the right-hand panel of Fig. 4.

The minimum-bias average quadrupole amplitude from Ref. [12] is

$$A_Q \;=\; \frac{\bar{N}_{\rm ch}}{2\pi\Delta\eta}\frac{P_2}{P_1+4P_2}\langle p_t^2\rangle^2\langle\langle Q_T^4\rangle\rangle\langle q^{-4}\rangle^2\,, \qquad (6)$$

for $p+p$ collisions where only one- or two-Pomeron showers occur. Mean p_t^2 was estimated from spectrum data and equals 0.19 $(\mathrm{GeV}/c)^2$. The momentum integrals were estimated in Ref. [12] as Q_S^{-4} in the fully saturated limit and as $m^4/(15Q_S^8)$ in the semi-saturated domain where Q_S^2 is assumed to be 0.6 $(\mathrm{GeV}/c)^2$ and the dipole cut-off mass m^2 was assumed to be between 0.8 and 1.6 GeV^2. The quadrupole amplitude is predicted to be between 0.0003 and 0.003 [16] depending on the assumed gluon saturation model. The measured 200 GeV $p+p$ minimum-bias quadrupole reported by the STAR experiment at this conference [17] is 0.002 corresponding to azimuth asymmetry parameter $v_2 = 0.072$, a large value compared to typical p_t-integral v_2 values for Au+Au collisions.

The $n_{\rm ch}$-dependent quadrupole amplitude is similarly predicted to be

$$A_Q \;=\; P_2(n_{\rm ch})\frac{n_{\rm ch}-1}{8\pi\Delta\eta}\langle p_t^2\rangle^2\langle\langle Q_T^4\rangle\rangle\langle q^{-4}\rangle^2\,. \qquad (7)$$

The BFKL predicted quadrupole amplitude should increase with event multiplicity owing to the increasing 2-Pomeron probability shown in Fig. 4.

Application of this model to proton + nucleus and nucleus + nucleus collisions can be done assuming a Glauber superposition approach. The total number of correlated pairs in quantity $\Delta\rho$ for the quadrupole structure is an incoherent sum of those corresponding pairs from each nucleon + nucleon collision. If individual 2-Pomeron momentum transfer vectors $\vec{Q}_T$ are aligned via the initial overlap geometry of the colliding ions, then the total p+A and A+A quadrupole amplitudes will be further enhanced.

5. Summary and Conclusions

The physics implications of two-particle angular correlations from the RHIC and the LHC heavy-ion programs are intriguing. Most of the current interest concerns two major structures − a jet related peak with its accompanying away-side dijet ridge, and a quadrupole. Recent descriptions of the 2D angular correlation data, which are motivated by flow models, invoke higher harmonics ($m > 2$) to describe these data. In this work and in Ref. [8] it was shown that the net effect of the $m > 2$ multipoles is to produce small, marginally significant NG dependence in the same-side peak's η_Δ-dependent structure. In my opinion the present results motivate a study of NG structure in the same-side 2D peak based on the fragmentation of minimum-bias jets in heavy-ion collisions.

The simultaneous appearance of approximately unperturbed minijets and large quadrupole correlations combined with the latter's initial-state scaling properties suggest that an underlying pQCD mechanism may be responsible for the quadrupole correlation. The BFKL Pomeron model of Levin and Rezaeian [12] was shown to provide a predicted magnitude for 200 GeV minimum-bias $p + p$ collisions which is in reasonable agreement with recent STAR data.

Acknowledgments

This work was supported in part by the U.S. Dept. of Energy contract No. DE-FG02-94ER40845.

References

[1] J. Adams *et al.* (STAR Collaboration), Phys. Rev. C **73**, 064907 (2006).
[2] G. Agakishiev *et al.* (STAR Collaboration), Phys. Rev. C **86**, 064902 (2012).
[3] B. Abelev *et al.* (STAR Collaboration), Phys. Rev. C **80**, 064912 (2009).
[4] G. Aad *et al.* (ATLAS Collaboration), Phys. Rev. C **86**, 014907 (2012).
[5] T.A. Trainor and D.T. Kettler, Phys. Rev. C **83**, 034903 (2011).
[6] T.A. Trainor, Phys. Rev. C **80**, 044901 (2009).
[7] B. Alver and G. Roland, Phys. Rev. C **81**, 054905 (2010).
[8] R.L. Ray, D.J. Prindle, and T.A. Trainor, Phys. Rev. C **88**, 044920 (2013).
[9] T.A. Trainor, arXiv:1109.2540v1.
[10] T.A. Trainor, D.J. Prindle, and R.L. Ray, Phys. Rev. C **86**, 064905 (2012).
[11] N. Borghini and U.A. Wiedemann, PoS **EPS-HEP**, 026 (2009).
[12] E. Levin and A.H. Rezaeian, Phys. Rev. D **84**, 034031 (2011).
[13] B.Z. Kopeliovich, A.H. Rezaeian, and I. Schmidt, Phys. Rev. D **78**, 114009 (2008).
[14] K. Dusling and R. Venugopalan, Phys. Rev. D **87**, 094034 (2013).
[15] J. Adams *et al.* (STAR Collaboration), Phys. Rev. D **74**, 032006 (2006).
[16] The quadrupole values reported here are smaller than that presented during the conference due to an omitted factor of $1/2\pi$.
[17] D. Prindle, poster presented at the XLIII Int. Symp. on Multiparticle Dynamics, Illinois Institute of Technology, Chicago, IL, 2013.

Recent Results from RHIC

O. Evdokimov
Department of Physics, University of Illinois at Chicago,
Chicago, IL 60607, USA

The Relativistic Heavy Ion Collider (RHIC) has opened a new era in experimental nuclear physics. Among the most important discoveries of this new era are the jet quenching phenomenon, the energy loss suffered by a hard scattered parton traversing the medium, and the collective flow, approaching the limit of ideal hydrodynamics. RHIC experiments have introduced a number of novel correlation methods for studies of jets and jet-medium interactions in the high multiplicity environment of ultra-relativistic heavy ion collisions. The di- and multi-hadron correlation techniques have since been quintessential to the understanding of the properties of the created medium in many complementary ways. In this work selected recent results are presented for the RHIC's top energy collisions at 200 GeV. Di-hadron correlation measurements from Au–Au collisions, illuminating the properties of the hot nuclear medium, are confronted with the recent findings from d–Au data at the same energy. Understanding of initial state properties and collision evolution is tested by unexpected similarities in the di-hadron correlation measurements between the two systems.

1. Introduction

Quantum Chromodynamics (QCD) predicts a transition from ordinary (hadronic) matter to a deconfined state of quarks and gluons, the Quark Gluon Plasma (QGP), at sufficiently high energy densities. The RHIC facility was originally conceived as a heavy ion collider dedicated to production and experimental studies of such deconfied state of matter. Within the first few years of RHIC experimental operations a number of discoveries, both expected and unexpected, has been made, advancing our understanding of QCD. For obvious reasons, the QGP phase could not be studied directly, but most of its properties have to be inferred from the final state observables. There is, perhaps, no single experimental measurement that could undoubtedly prove the creation of a deconfined matter in heavy ion collisions; nevertheless mounting amount of evidence supports the discovery of the partonic medium with "Perfect Liquid" properties [1]. In recent years,

the RHIC physics program has evolved in a number of different directions. The polarized *pp* collisions at 200 and 500 GeV provided a new ground for studies of nucleon spin structure. Flexibility of the collider facility has allowed a change of the center-of-mass energies of the delivered ion beams by more than an order of magnitude, leading to the successful start of the Beam Energy Scan (BES) program. This ongoing program carries out systematic studies of the QCD phase diagram in search for the tri-critical point on the phase boundary [2] and the on-set of deconfinement. At the higher end of RHIC energies the systematic studies of the QGP medium are continuing with new beam species. The p, d, Cu, Au, and U beams, delivered by RHIC facility, have allowed studies of the system size and initial state geometry effects on medium properties.

The discovery of jet-quenching effect has brought new attention to the hard sector probes, that were traditionally not a focus for nuclear experiments. Physics interest in rare processes (high transverse momentum (p_T) particles, jets, heavy flavor hadrons) put new demands on both the collider facility, reaching for higher integrated luminosities, and the experiments, putting forward suitable detector upgrades to advance such measurements.

Of the original four, there are two experimental collaborations continuing operations at RHIC: PHENIX [3] and STAR [4]. Each of the two detectors consists of multiple sub-systems that allow to study a variety of physics observables simultaneously. The main parts of the PHENIX detector include Drift, Pad, and Time-Extension Chambers; RICH detector and Electro-Magnetic Calorimeters. These collectively called "Central Arms" detectors provide tracking and particle identification at mid-rapidity within two 90-degree-wide azimuthal slices. The total pseudorapidity (η) coverage of the Central Arms is 0.7 units. Another set of detectors provides the forward region coverage for PHENIX. The forward Muon Arm Detectors provide measurements in $1.2 < |\eta| < 2.2$ and $3 < |\eta| < 4$ ranges within the full azimuth. Additionally, PHENIX experiment has recently installed a new silicon detector for higher precision reconstruction of primary and secondary vertices and thus enhancement of PHENIX capabilities for heavy flavor studies.

The STAR detector set-up has a distinctly different layout and acceptance. The main workhorse of STAR is a large gas-filled Time Projection Chamber, that provides mid-rapidity tracking, momentum measurements and particle identification capabilities across full azimuth with a uniform acceptance in $|\eta| < 1$. The Electro-Magnetic Calorimeters (EMC) compliment charged particle measurements, provided by the TPC, and cover pseudorapidity range of $-1 < \eta < 4$. The EMC measurements and triggering capabilities greatly enhance the hard sector studies for STAR. Recently added Muon Telescope detector and the ongoing Heavy Flavor tracking up-

grade will substantially advance the heavy flavor studies in the near future.

Both experiments have dedicated significant efforts to systematic studies of medium properties and jet-medium interactions via di-hadron correlations. In this report recent results from correlation measurements in Au–Au collisions at 200 GeV assessing the systematic trends of azimuthal anisotropies in heavy ion events are presented. These results are put in the context with a new and surprising observation of similar correlation structures from d–Au data at the same energy. Until recently the d–Au collisions were mostly sought after to provide a reference measurement for the cold nuclear mater effects. Unexpected similarities in di-hadron correlations from both systems challenge mainstream concepts of the heavy ion physics and may shed new light on the initial state properties of the collisions studied.

2. Precision studies of medium properties

In the first few years of RHIC operations it has been established experimentally that the matter created in the high energy Au–Au collisions is dense, strongly interacting, and exhibiting multiple unusual features. Among the main findings from this period, summarized in four experimental "Whitepapers" [5], are strong partonic collectivity of the explosive system with an unexpectedly short mean free path. The system created in these collisions was found to be highly opaque to the propagating partons, leading to the quenching phenomenon at high p_T due to in-medium energy loss. The collective properties of the created medium were evident in the magnitude of the elliptic flow, the second order (elliptical) modulation of the azimuthal distributions with respect to reaction plane. Strong elliptic flow has been observed for multiple hadron species, including strange and multi-strange hadrons. The magnitude of v_2, the second coefficient of the Fourier expansion, was found in a good agreement with the ideal hydrodynamic calculations for the soft sector particles (below 2 GeV/c), yielding the concepts of medium thermalization (across u, d, s flavors) and "Perfect fluid." At intermediate momenta, the mass-dependent ordering of the identified hadron v_2 was found taken over by the constituent quark scaling behavior – specific grouping of the observed v_2 trends for mesons and baryons separately – further supporting the partonic collectivity idea.

It has been since realized that the initial state density and/or geometry fluctuations can leave an imprint on the final state distributions resulting in significant magnitudes of higher order Fourier terms [6, 7]. This idea has been confirmed experimentally in the precision measurements of multiple v_n harmonics. Compilation of recent RHIC results from [8] is presented in Fig. 1. Significant amplitudes of Fourier coefficients up to the 5th order were observed by both STAR [9] and PHENIX [10] experiments. The

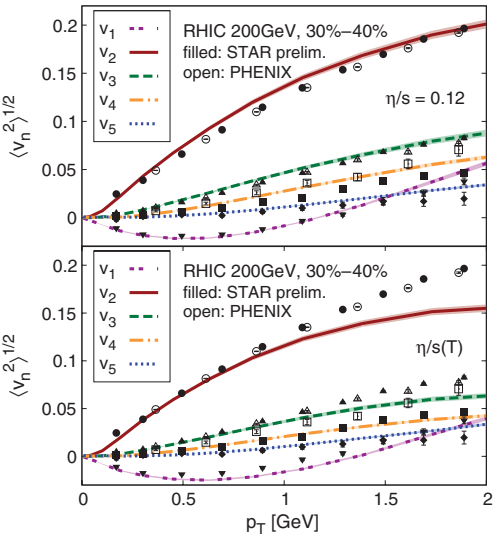

Fig. 1. Transverse momentum dependence of azimuthal anisotropies measured for charged hadrons by STAR [9] (open symbols) and PHENIX [10] (filled symbols). The compilation of data and theoretical calculations are from [8].

transverse momentum, energy and centrality dependence of the Fourier harmonics constrain the shear viscosity over entropy density ratio (η/s) for the evolving medium. The v_2 measurements along, while consistently described in hydrodynamic calculations with low viscosity values [11], are the least sensitive to the viscous effects. Different sensitivities of the higher order terms are illustrated in Fig. 1 by comparing the data with two viscous hydrodynamic calculations within IP-Glasma model [8]. Within this model the RHIC data are found to be best described by the η/s value of 0.12.

3. Di-hadron correlations in the d–Au collisions

The extent of the azimuthal anisotropies observed in heavy ion collisions goes far beyond the soft sector, the commonly accepted applicability range of hydrodynamic description. At high-p_T these anisotropies are attributed to the effects of jet quenching, where path-length dependence of the parton energy loss produces the correlation of the hard-scattering products with the reaction plane. At RHIC the di-hadron correlation measurements with high-p_T particles (leading hadrons or "triggers") have become a well-recognized tool for studies not only of the collective effects but of jet properties and the jet-medium interactions. However, the interpretation of such di-hadron correlations in heavy ion collisions is complicated by the variety of corre-

lated signals, from both soft and hard processes, that could be intertwined through mutual correlation with reaction plane.

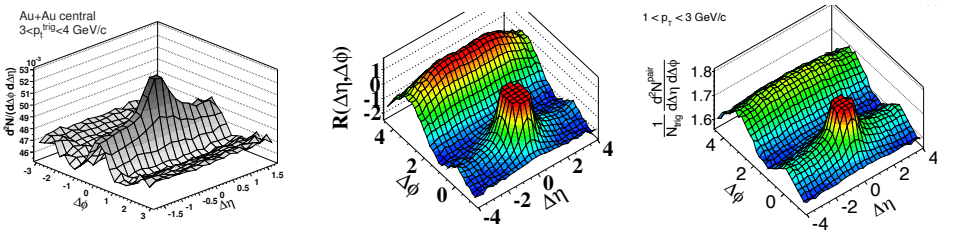

Fig. 2. Ridge in di-hadron correlations from high multiplicity events. Left: central 200 GeV Au–Au collisions from STAR/RHIC experiment. Middle: di-hadron correlations from high multiplicity *pp* collisions at 2.76 TeV reported by the CMS experiment at LHC. Right: di-hadron correlations from high multiplicity p–Pb collisions at 5.02 TeV measured by CMS/LHC.

To quantify the effects of the medium on propagating partons, the jet-like correlations from heavy ion collisions are compared with the reference, created from either *pp* or d–Au data, where no QGP medium was expected to be formed. To separate the collective effects, described in previous section, the initial analysis of di-hadron correlations in relative azimuth ($\Delta\phi$) was later expanded by adding the second dimension on relative pseudorapidity ($\Delta\eta$). The first 2D angular correlation data from [12] is shown in the left panel of Fig. 2. A novel feature, the *ridge*, discovered for the first time at RHIC in that study, could be seen in the figure on the near side of the trigger particle (small $\Delta\phi$), extending to large relative pseudorapidities. The correlation visually splits into a small-angles peak, resembling the jet structures from the elementary collisions, and a long-range η-independent part, that has not been seen before. The short-range correlations contain the majority of jet-related contributions, but also may include HBT effects and products of resonance decays. The later contributions are expected to be negligible for high-p_T triggers. The ridge-like η-independent part of the correlated signal was commonly attributed in recent years to the higher order flow harmonics, specifically, the triangular flow v_3. New experimental results from the CMS experiment at LHC have uncovered a similar ridge structure first in the very-high multiplicity *pp* collisions at 2.76 TeV [13], see middle panel of Fig. 2. Last year another ridge discovery has been reported by CMS Collaboration (Fig. 2, right), this time in high multiplicity p–Pb data at 5.02 TeV [14], which was also confirmed by ALICE and ATLAS experiments [15, 16]. The Fourier analysis of the long-range correlations from the p–Pb data yielded magnitudes for the second and third harmonics comparable to those measured in Pb–Pb events of similar multiplicity.

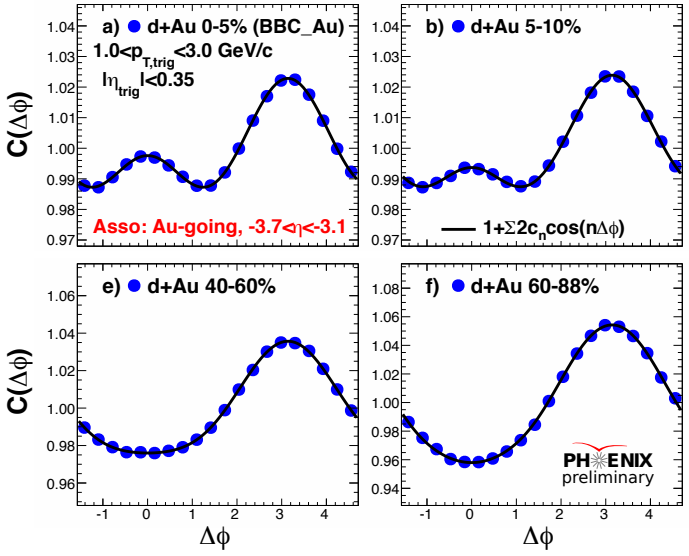

Fig. 3. Azimuthal projections of long-range di-hadron correlations for different multiplicity classes of 200 GeV d–Au collisions from PHENIX. Mid-rapidity hadrons with transverse momentum above 1 GeV/c were selected as triggers. The correlations are then constructed with forward (Au-going) hadrons in the rapidity region of -3.7< η <-3.1. Fourier fits to the data are shown as solid lines.

In light of these discoveries the long-range correlation measurements were revisited for 200 GeV d–Au collisions with a new larger data set recorded at RHIC in the year 2008. For the PHENIX experiment, this new data set has also allowed to take advantage of the newly commissioned Muon Piston detectors, providing charged track measurements at forward(backward) rapidities at $3.1 < |\eta| < 3.7$ (3.9). The hadrons reconstructed in the Central Arms and the Muon Piston detectors have an significant rapidity gap, suppressing the jet-like contributions to the di-hadron correlations constructed between them. The analysis has been performed for various event multiplicities, and separately for d- and Au-going directions [17]. In most central (high multiplicity) d–Au events a ridge-like structure at small $\Delta\phi$ angles has been reported as shown in Fig. 3, while no such feature was seen in lower multiplicity events or in the d-going direction. The STAR experiment is in the process of analyzing the long-range correlations from the new d–Au data as well. At the moment the preliminary STAR data do not show significant ridge-like yield on the near side of the trigger hadron [18]. A direct comparison of correlation structures for two

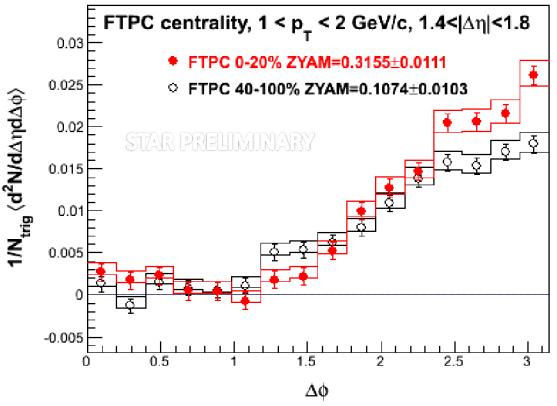

Fig. 4. Long-range di-hadron correlations from 20% most central (filled symbols) and 50-100% most peripheral (open symbols) 200 GeV d–Au collisions from STAR. The kinematic selection is indicated on the figure; the random combinatoric background is subtracted with a zero-yield-at-minimum method.

multiplicity bins (20% central and 50-100% peripheral) of d–Au collisions from STAR experiment is shown in Fig. 4: no appreciable difference can be seen on the near-side for the events selected.

The discovery of the ridge in high multiplicity *pp* and p–Pb collisions at LHC, and in d–Au collisions at RHIC (if confirmed) challenge the understanding of a phase structure of nuclear matter. The flow-attributed correlation features were unanticipated for the cold nuclear matter, where neither phase transition nor thermalization were predicted to happen. Despite this, theoretical calculation describing the RHIC and LHC observations of the flow-like behavior in the p–Pb and d–Au data within hydrodynamic approach have quickly followed [19, 20]. An alternative interpretation has also been put forward, in which the ridge-like correlations observed in the final state are linked to the initial state color field fluctuations in the incoming nucleons [21]. Detailed systematic investigation of the newly observed phenomenon is necessary to differentiate between these (and other possible) descriptions.

4. Summary

In this work recent di-hadron correlation measurements for RHIC has been discussed. Collective dynamics studies illuminated importance of the higher order azimuthal anisotropies in the final state hadron measurements. The precision measurements of corresponding higher order Fourier harmon-

ics have been carried out, providing experimental constraints on the initial state properties of the system and the value of shear viscosity over entropy density ratio for the created medium. Unexpected long-range correlation structures have been reported by PHENIX experiment in the high multiplicity d–Au collisions at 200 GeV. Even more surprisingly, the systematic trends of the second and third Fourier harmonics extracted from the d–Au correlation analysis are found similar to those in heavy ion data. Additional studies are underway to help discriminate between the theoretical interpretations that are put forward to explain the new phenomenon.

References

[1] H. Song, S. Bass, U. Heinz, T. Hirano, and C. Shen, Phys. Rev. Lett. **106**, 192301 (2011).

[2] M. Stephanov, PoS **LAT2006**, 024 (2006).

[3] PHENIX Collaboration, `http://www.phenix.bnl.gov`.

[4] STAR Collaboration, `http://www.star.bnl.gov`.

[5] J. Adams *et al.*, Nucl. Phys. A **757**, 102 (2005); K. Adcox *et al.*, Nucl. Phys. A **757**, 184 (2005); B.B. Back *et al.*, Nucl. Phys. A **757**, 28 (2005); I. Arsene *et al.*, Nucl. Phys. A **757**, 1 (2005).

[6] B. Alver and G. Roland, Phys. Rev. C **81**, 054905 (2010).

[7] J. Xu and C. M. Ko, Phys. Rev. C **84**, 014903 (2011).

[8] C. Gale, S. Jeon, B. Schenke, P. Tribedy, and R. Venugopalan, Phys. Rev. Lett. **110**, 012302 (2013).

[9] Y. Pandit *et al.*, Nucl. Phys. A **904-905**, 357 (2013).

[10] A. Adare *et al.*, Phys. Rev. Lett. **107**, 252301 (2011).

[11] S. A. Voloshin, A. M. Poskanzer and R. Snellings, Landolt-Brnstein Database "Relativistic Heavy Ion Physics," Vol. **23**, 5 (2010).

[12] B. Abelev *et al.*, Phys. Rev. C **80**, 064912 (2009).

[13] V. Khachatryan *et al.*, J. High Enegy Phys. **1009**, 091 (2010).

[14] S. Chatrchyan *et al.*, Phys. Lett. B **718**, 795 (2013).

[15] B. Abelev, *et al.*, Phys. Lett. B **719**, 29 (2013).

[16] G. Aad, *et al.*, Phys. Rev. Lett. **110**, 182302 (2013).

[17] A. Sickles, arXiv:1310.4388.

[18] F. Wang, *Jet Quenching at RHIC vs LHC*, RIKEN BNL Workshop (2013).

[19] G. Qin and B. Mller, arXiv:1306.3439.

[20] P. Bozek, Phys. Rev. C **85**, 014911 (2012).

[21] K. Dusling, R. Venugopalan, Phys. Rev. D **87**, 054014 (2013).

Collective dynamics of the p-Pb collisions at the LHC

Wojciech Broniowski[1,2], Piotr Bożek[2,3]

[1] Institute of Physics, Jan Kochanowski University, 25-406 Kielce, Poland
[2] The H. Niewodniczański Institute of Nuclear Physics, Polish Academy of Sciences, 31-342 Kraków, Poland
[3] AGH University of Science and Technology, Faculty of Physics and Applied Computer Science, 30-059 Krakow, Poland

We review the signatures for the soft collective dynamics in highest-multiplicity ultrarelativistic p-Pb collisions and show that the effects are well described in a three-stage model, consisting of the event-by-event Glauber initial conditions, viscous 3+1D hydrodynamics, and statistical hadronization. In particular, we discuss the ridges in two-particle correlations in the relative azimuth and pseudorapidity, the elliptic and triangular flow coefficients, and the mass hierarchy of observables sensitive to flow.

1. Introduction

This talk is based on Refs. [1–3], where the details and more complete lists of references can be found (see also the mini-review [4]). We wish to address here the most intriguing physics questions concerning the topic:

- Are the highest-multiplicity p-Pb collisions *collective?*
- What is the nature of the initial state and correlations therein?
- What are the limits in conditions on applicability of hydrodynamics?

Recall that the *collective flow* is one of the principal signatures of the strongly-interacting Quark-Gluon Plasma formed in ultra-relativistic A-A collisions at RHIC and the LHC. It manifests itself in harmonic components in the momentum spectra v_n, in specific structures in the correlation data *(ridges)*, in *mass hierarchy* of the p_T spectra and v_n's of identified particles, as well as in certain features of interferometry (femtoscopy). Since 1) the ridges were found experimentally at the LHC in p-Pb collisions [5], 2) large elliptic and triangular flow was measured in p-Pb [8], 3) strong mass hierarchy was recently detected in p-Pb [10], there are clear analogies between the "collective" A-A system and the "small" p-A system. Below we present

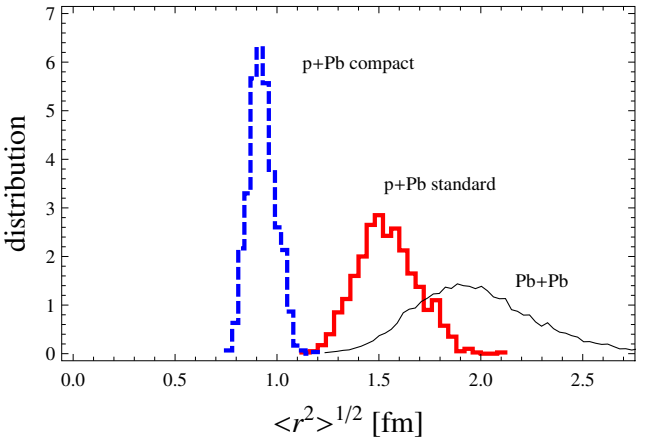

Fig. 1. Event-by-event distribution of the rms size of the Glauber initial conditions for the *fixed* number of participants, $N_p = 18$, for the standard source in p-Pb (thick solid line) obtained by placing the sources at the centers of participants, the compact source (dashed line), obtained by placing the sources in the center-of-mass of the colliding pair [18], and for the peripheral Pb-Pb collisions (thin solid line). The p-Pb sizes are not more that twice smaller from the Pb-Pb sizes. At the same time, the p-Pb system is more dense. This allows to analyze the p-Pb system with viscous hydrodynamics [4].

the evidence for the collective interpretation of the highest-multiplicity p-A collisions.

2. Three-stage approach

To place our argumentation on a quantitative level, we use the three stage approach consisting of 1) modeling of the initial phase with the Glauber approach as implemented in GLISSANDO [13], 2) applying event-by-event 3+1D viscous hydrodynamics [15] to the intermediate evolution, and 3) carrying out statistical hadronization at freezeout with THERMINATOR [16]. The details can be found in Refs. [1, 2]. Here we only wish to point out the similarity of the initial conditions in high-multiplicity p-A collisions to those in peripheral A-A collisions, as seen from Fig. 1. This indicates that our approach should work with similar accuracy for the most central p-Pb collisions as it worked for the Pb-Pb collisions at centralities $\sim 70\%$.

Fig. 2. Creation of the near-side ridge: The surfers' motion is correlated even when they are widely separated along the shore.

3. The ridge

The emergence of the ridges in the two-particle correlations in the relative azimuth and pseudorapidity, $C(\Delta\eta, \Delta\phi) = N^{\text{pairs}}_{\text{phys}}(\Delta\eta, \Delta\phi)/N^{\text{pairs}}_{\text{mixed}}(\Delta\eta)$, finds a natural explanation in correlated collective flow orientation within a long pseudorapidity span. This is cartooned in Fig. 2. Numerical calculation in our approach yields fair agreement with the data, as indicated in Fig. 3, providing alternative explanation to the color-glass approach [19]. As shown below, the event-by-event hydrodynamics also yields the proper magnitude of the triangular component of the flow in a natural way.

4. Harmonic flow

The structure of the correlation data (similar to the top panel of Fig. 3) indicates that one may get rid of most of the nonflow effects by excluding the central peak from the analysis, simply using pairs with $|\Delta\eta > 2|$. The flow coefficients ($v_n\{2, |\Delta\eta > 2|\}$) obtained that way from the experiment and from our model simulations are compared in Figs. 4 and 5. We note a very fair agreement with the data for the highest-multiplicity events. As the system becomes smaller, the simulations depart from the experiment, indicating that the dissipative effects or the direct production from the corona are becoming important.

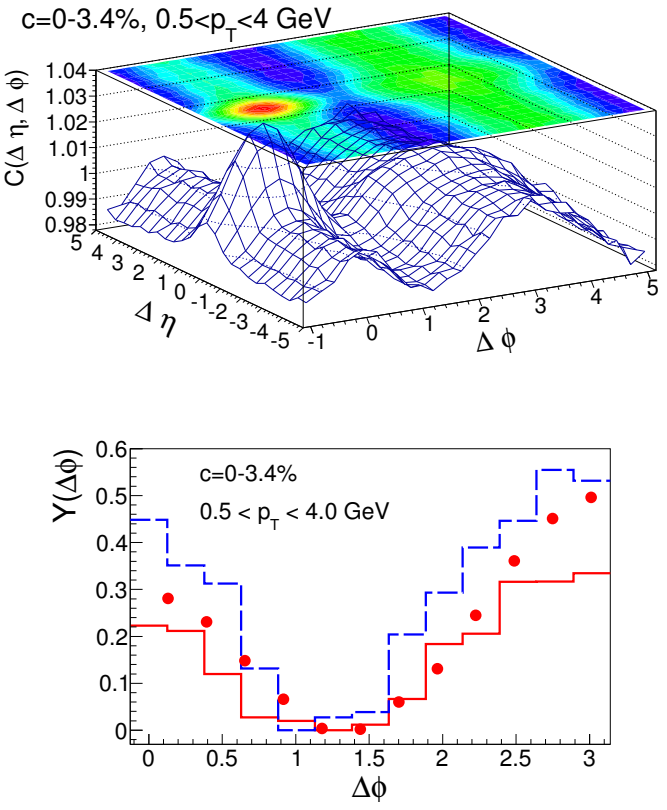

Fig. 3. Correlation functions in the ATLAS kinematic conditions. Top: $C(\Delta\phi, \Delta\eta)$. Bottom: the projected ($2 \leq |\Delta\eta| \leq 5$) per-trigger correlation function $Y(\Delta\phi) = \int B(\Delta\phi)d(\Delta\phi)C(\Delta\phi)/N - b_{\mathrm{ZYAM}}$, compared to the ATLAS data. The solid (dashed) lines correspond to the standard (compact) source.

5. Mass hierarchy

A very important effect of the presence of collective flow is the emergent mass hierarchy in certain heavy-ion observables [3, 21]. The effect is kinematic: hadrons emitted from a moving fluid element acquire more momentum when they are more massive. For that reason, for instance, the average transverse momentum of the protons is significantly higher than for the kaons, which in turn is higher than for the pions. The results, showing agreement of our approach with the data, are presented in Fig. 6(a). As a benchmark with no flow, we show in Fig. 6(b) the results of the HIJING simulations, exhibiting much smaller splitting.

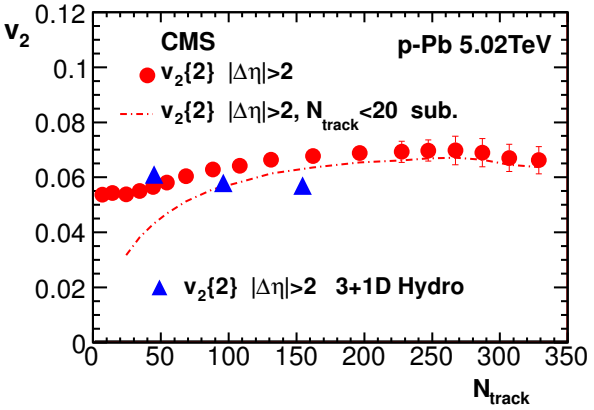

Fig. 4. The elliptic flow coefficient $v_2\{2, |\Delta\eta > 2|\}$ from our model (points) compared to the CMS data.

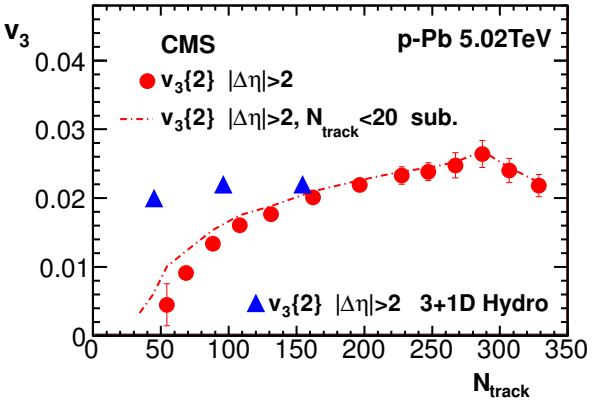

Fig. 5. Same as Fig. 4 but for the triangular flow $v_3\{2, |\Delta\eta > 2|\}$. The departure of the model from the experiment for lower centrality classes indicates the limits of validity of the collective approach.

A proper pattern in the differential identified-particle elliptic flow is also found, as seen from Fig. 7. We note that a very general argument in favor collectivity, based on failure of superposition in the p-A spectra, has been brought up in Ref. [22].

6. Conclusions

The numerous experimental data from the LHC for the p-Pb collisions of highest multiplicity are compatible with the collective expansion scenario: the formation of the two ridges, large elliptic and triangular flow, and the mass hierarchy found in the average transverse momentum and in the differential elliptic flow [3, 21]. Thus the p-Pb system can be used as a test

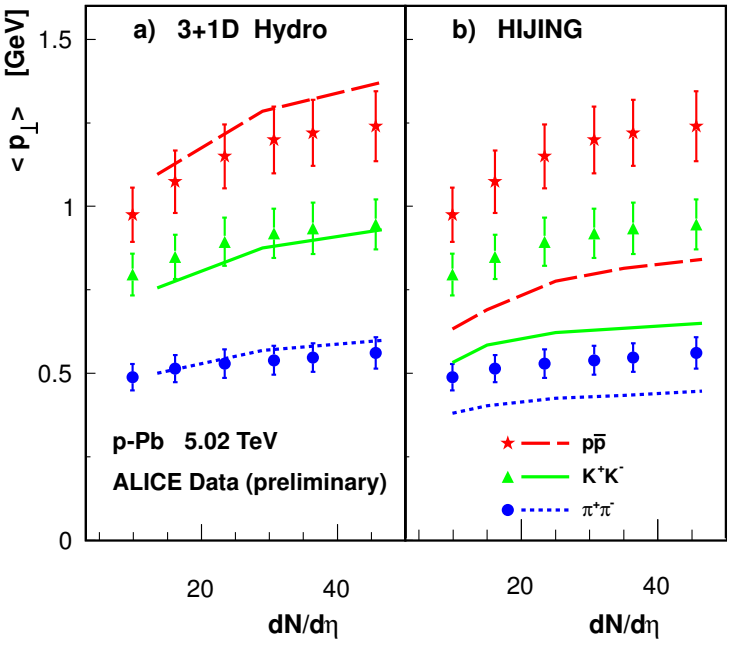

Fig. 6. Mean transverse momentum of identified particles produced in the p-Pb collisions, plotted as a function of the charged particle density. (a) our model, and for comparison (b) HIJING 2.1, where no collective effects are present. The lines correspond to the model calculations, while the data points come from Ref. [12].

ground for the onset of collective dynamics. Certainly, lower multiplicity events are "contaminated" with other effects, e.g., the production from the corona nucleons and their modeling must be more involved. Another signature of collectivity would be provided by the interferometric radii, where the model calculation for p+Pb place the results closer to the A+A lines and farther from the p+p lines [23].

Acknowledgments

This work was supported by the Polish National Science Centre, grants DEC-2012/06/A/ST2/00390 and DEC-2011/01/D/ST2/00772, and PL-Grid infrastructure.

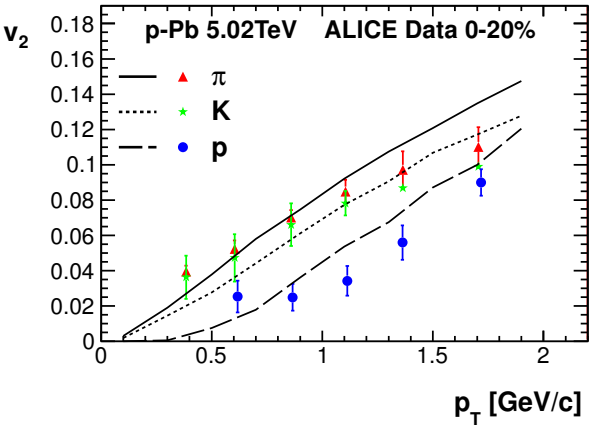

Fig. 7. $v_2\{2\}$ for pions, kaons and protons in p-Pb collisions calculated in our model, plotted as a function of the transverse momentum. The data come from Ref. [11].

References

[1] P. Bożek and W. Broniowski, Phys. Lett. B **718**, 1557 (2013).

[2] P. Bożek and W. Broniowski, Phys. Rev. C **88**, 014903 (2013).

[3] P. Bożek, W. Broniowski, and G. Torrieri, Phys. Rev. Lett. **111**, 172303 (2013).

[4] P. Bożek, W. Broniowski, and G. Torrieri, `arXiv:1309.7782`.

[5] S. Chatrchyan *et al.* (CMS Collaboration), Phys. Lett. B **718**, 795 (2013).

[6] B. Abelev *et al.* (ALICE Collaboration), Phys. Lett. B **719**, 29 (2013).

[7] G. Aad *et al.* (ATLAS Collaboration), Phys. Rev. Lett. **110**, 182302 (2013).

[8] G. Aad *et al.* (ATLAS Collaboration), Phys. Lett. B **725**, 60 (2013).

[9] S. Chatrchyan *et al.* (CMS Collaboration), Phys. Lett. B **724**, 213 (2013).

[10] S. Chatrchyan *et al.* (CMS Collaboration), `arXiv:1307.3442`.

[11] B. B. Abelev *et al.* (ALICE Collaboration), Phys. Lett. B **726**, 164 (2013).

[12] B. B. Abelev *et al.* (ALICE Collaboration), `arXiv:1307.1094`.

[13] W. Broniowski, M. Rybczyński, and P. Bożek, Comput. Phys. Commun. **180**, 69 (2009).

[14] M. Rybczynski, G. Stefanek, W. Broniowski, and P. Bozek, arXiv:1310.5475.
[15] P. Bożek, Phys. Rev. C **85**, 034901 (2012).
[16] A. Kisiel, T. Tałuć, W. Broniowski, and W. Florkowski, Comput. Phys. Commun. **174**, 669 (2006).
[17] M. Chojnacki, A. Kisiel, W. Florkowski, and W. Broniowski, Comput. Phys. Commun. **183**, 746 (2012).
[18] A. Bzdak, B. Schenke, P. Tribedy, and R. Venugopalan, Phys. Rev. C **87**, 064906 (2013).
[19] K. Dusling and R. Venugopalan, Phys. Rev. Lett. **108**, 262001 (2012).
[20] K. Dusling and R. Venugopalan, Phys. Rev. D **87**, 094034 (2013).
[21] K. Werner, M. Bleicher, B. Guiot, I. Karpenko, and T. Pierog, arXiv:1307.4379.
[22] A. Bzdak and V. Skokov, Phys. Lett. B **726**, 408 (2013).
[23] P. Bożek and W. Broniowski, Phys. Lett. B **720**, 250 (2013).

Kaon Freeze-out Dynamics in $\sqrt{s_{NN}}$=200 GeV Au+Au Collisions at RHIC

Michal Šumbera for the STAR Collaboration

Nuclear Physics Institute ASCR, 250 68 Řež, Czech Republic

Measurements of three-dimensional correlation functions of like-sign low transverse momentum kaon pairs from Au+Au collisions at top RHIC energy $\sqrt{s_{NN}}$=200 GeV are presented. The extracted kaon source function is narrower than the pion one and does not have the long tail along the pair transverse momentum direction. This indicates a much smaller role of long-lived resonance decays and/or of the emission duration on kaon emission. Three-dimensional Gaussian shape of the kaon source function can be adequately reproduced by Therminator simulations with resonance contributions taken into account. Comparison to pion data at the same energy reveals that the kaon Gaussian radii in the outward and sideward directions scale with the transverse mass m_{T}. In the longitudinal direction, unlike at lower SPS energies, the Gaussian radii do not seem to follow the exact m_{T} scaling between kaons and pions.

1. Introduction

The momentum correlations of particles at small relative momenta in their center-of-mass system contain an important information about space-time characteristics of the production process on a femtometer scale, so serving as a correlation femtoscopy tool (see, e.g., [1, 2] and references therein). For non-interacting identical particles, like photons, these correlations result from the interference of the production amplitudes due to symmetrization requirement of quantum statistics (QS). Additional important source of femtoscopic correlations comes from Coulomb and strong final state interaction (FSI). It provides an important information on coalescence femtoscopy and correlation femtoscopy with unlike particles, including the studies of space-time asymmetries in particle production and strong interaction between specific particles [1].

In heavy ion experiments two-particle interferometry with identical charged hadrons has been for a long time used as a reliable technique to extract the space-time characteristics of the hot expanding fireball [1, 3]. Object of study is three-dimensional (3D) correlation function $C(\mathbf{q})$, where $2\mathbf{q}$ is the difference between the momenta of the two particles in the pair

center-of-mass system (PCMS). The correlation function is defined as the ratio of the 3D relative momentum distribution of particle pairs from the same event to pairs constructed from mixed events. In the following a right-handed Cartesian coordinate system with z (*long*) parallel to the beam direction, x (*out*) pointing in the direction of the pair total transverse momentum and y (*side*) perpendicular to x and z will be used. $C(\mathbf{q})$ is related to the probability $S(\mathbf{r})$ to emitt a pair of particles with a pair separation vector $\mathbf{r}$ in the PCMS via Koonin-Pratt equation [3]:

$$C(\mathbf{q}) - 1 \equiv R(\mathbf{q}) = \int d\mathbf{r} K(\mathbf{q},\mathbf{r}) S(\mathbf{r}), \quad K(\mathbf{q},\mathbf{r}) \equiv |\phi(\mathbf{q},\mathbf{r})|^2 - 1. \quad (1)$$

The wave function of relative motion of two particle $\phi(\mathbf{q},\mathbf{r})$ incorporates both QS and FSI effects. The bias arising from the frequently used Gaussian assumption on the source shape [1, 3] can be avoided if we directly extract $S(\mathbf{r})$ inverting Eq. (1) numerically [4, 5]. No assumption on the source shape is thus needed.

In [6] data on femtoscopic correlations of like-sign charged pions from 20% most central Au+Au collisions at $\sqrt{s_{NN}}$=200 GeV were analysed exploiting expansion of the source function $S(\mathbf{r})$ into a Cartesian harmonic basis [5, 7]:

$$S(\mathbf{r}) = \sum_{l,\alpha_1 \ldots \alpha_l} S^l_{\alpha_1 \ldots \alpha_l}(r) A^l_{\alpha_1 \ldots \alpha_l}(\Omega_{\mathbf{r}}), \quad (2)$$

where $l = 0, 1, 2, \ldots$, $\alpha_i = x, y$ or z, $A^l_{\alpha_1 \ldots \alpha_l}(\Omega_{\mathbf{q}})$ are Cartesian harmonic basis elements and $\Omega_{\mathbf{q}}$ is the solid angle in $\mathbf{q}$ space. Significant non-Gaussian features including a long range tail in *out* and *long* directions in the pion source function were found. Model comparisons were used to study lifetime and emission duration of expanding fireball. Sizeable emission time differences between emitted pions were required to allow models to be successfully matched to these tails. However, an interpretation of pion correlations in terms of pure hydrodynamic evolution is complicated by significant contributions from later stages of the reaction, such as decays of long-lived resonances and anomalous diffusion from rescattering [8].

A purer probe of the fireball decay could be obtained with kaons which have less contribution from long life-time resonances and suffer less rescattering than pions. Their lower yields, however, make it difficult to carry out a detailed 3D source shape analysis. A one-dimensional kaon source image measurement for the same colliding system as in Ref. [6] was reported by the PHENIX collaboration [10]. The measurement corresponds to a fairly broad range of the pair transverse momentum $2k_{\mathrm{T}}$, which makes the interpretation more ambiguous. In particular, information about the transverse expansion of the system contained in the k_{T}-dependence of the emission radii is lost. The one-dimensional nature of the measurement also less constrains the model predictions than would be available from a 3D measurement. A different aspect of the fireball expansion can be addressed

by studying the $k_{\rm T}$-dependence of the source size. Data at SPS energies [9], as well as at RHIC [10] at relatively higher $k_{\rm T}$ values, showed a scaling behaviour between pions and kaons, as expected from perfect hydrodynamics [11].

In this contribution we present recent STAR 3D analyses [12] of the shape and $k_{\rm T}$-dependent size of the kaon source at mid-rapidity using low transverse momentum like-sign kaon pairs produced in $\sqrt{s_{NN}}$=200 GeV central Au+Au collisions.

2. Data analysis

The kaon source shape was analyzed using 4.6 million 0–20% central events from 2004, and 16 million 0–20% central events from 2007. The $k_{\rm T}$–dependent analysis was carried out using 6.6 million 0–30% central events from 2004. The STAR Time Projection Chamber was used to select charged kaons with rapidity $|y| < 0.5$ and transverse momenta $0.1<p_{\rm T}<1.0$ GeV/c. Only pairs with $0.2<k_{\rm T}<0.36$ GeV/c were accepted. In the $k_{\rm T}$–dependent analysis, kaon pairs were collected in two bins: $0.2<k_{\rm T}<0.36$ GeV/c and $0.36<k_{\rm T}<0.48$ GeV/c. The 3D correlation function $C(\mathbf{q})$ defined via Eq. (1) was constructed as a ratio of the $N_{\rm same}(\mathbf{q})$, for K^+K^+ and K^-K^- pairs in the same event to $N_{\rm mixed}(\mathbf{q})$. $C(\mathbf{q})$ is flat and normalized to unity over $60< |\mathbf{q}| <100$ MeV/c. For further experimental details see Ref. [12].

From the measured 3D correlation function correlation moments

$$R^l_{\alpha_1\ldots\alpha_l}(q) = \frac{(2l+1)!!}{l!}\int \frac{d\Omega_{\mathbf{q}}}{4\pi} A^l_{\alpha_1\ldots\alpha_l}(\Omega_{\mathbf{q}})\, R(\mathbf{q}) \qquad (3)$$

were extracted. The lowest correlation moment R^0 agrees with the direction independent correlation function $R(q)$ within statistical errors. Even moments with $l > 4$ were found to be consistent with zero within statistical uncertainty. As expected from symmetry considerations, the same was also found for odd moments. Therefore in this analysis, the sum in Eq. (2) is truncated at $l = 4$ and expressed in terms of independent moments only. Up to order 4, there are 6 independent moments: R^0, R^2_{xx}, R^2_{yy}, R^4_{xxxx}, R^4_{yyyy} and R^4_{xxyy}. Dependent moments are obtained from independent ones [5, 7].

Fitting the truncated series to the measured 3D correlation function with a 3D Gaussian,

$$S^G(r_x, r_y, r_z) = \frac{\lambda}{(2\sqrt{\pi})^3 R_x R_y R_z} \exp[-(\frac{r_x^2}{4R_x^2} + \frac{r_y^2}{4R_y^2} + \frac{r_z^2}{4R_z^2})], \qquad (4)$$

has yielded the independent moments as a function of q. In Eq.(4) R_x, R_y and R_z are the characteristic radii of the source in the *out*, *side* and *long* directions, and λ represents the overall correlation strength. While λ may be sensitive to feed-down from long-lived resonance decays, remainder sample

contamination or track splitting/merging not removed by purity and track quality cuts, the radii are virtually independent of these effects. Technically, the fit is carried out as a simultaneous fit on the even independent moments up to l=4, yielding χ^2/ndf=1.7 in the source shape analysis, χ^2/ndf=1.1 and χ^2/ndf=1.3 in the $0.2<k_{\rm T}<0.36$ GeV/c and $0.36<k_{\rm T}<0.48$ GeV/c bins in the $k_{\rm T}$-dependent analysis, respectively. The three Gaussian radii and the amplitude obtained from this fit are listed in Table 1.

Table 1. Parameters obtained from the 3D Gaussian source function fits for the different datasets. The first errors are statistical, the second errors are systematic.

Year	2004+2007	2004	
Centrality	0%–20%	0%–30%	
$k_{\rm T}$ [GeV/c]	0.2–0.36	0.2–0.36	0.36–0.48
R_x [fm]	4.8±0.1±0.2	4.3±0.1±0.4	4.5±0.2±0.3
R_y [fm]	4.3±0.1±0.1	4.0±0.1±0.3	3.7±0.1±0.1
R_z [fm]	4.7±0.1±0.2	4.3±0.2±0.4	3.6±0.2±0.3
λ	0.49±0.02±0.05	0.39±0.01±0.09	0.27±0.01±0.04

The shape assumption was tested using a double Gaussian trial function and by pushing the fit parameters to the edges of their errors. Other systematic errors were obtained under varying conditions including magnetic field, data collection periods, charge and various sample purity selections. The systematic errors are largely governed by the limited statistics available.

3. Results

The source function profiles in the x, y and z directions are shown on the left panel of Figure 1 (circles). The two solid curves around the Gaussian source function profiles represent the error band arising from the statistical and systematic errors on the 3D Gaussian fit. Note that the latter becomes important for large r values only. The 3D pion source functions from PHENIX [6] are shown for comparison purposes (squares). While the Gaussian radii are similar, there is a strinking difference between the source shapes of the two particle species, especially in the *out* direction. Note that the PHENIX and STAR pion measurements are fully consistent [14]. We have used the STAR tune of the Therminator Blast-Wave model (solid triangles) [15, 16] to gain a better understanding of this difference. The simulation reproduces the source function profiles with emission duration $\Delta\tau$=0 (solid upward-pointing triangles). However, with resonance contribution switched off, Therminator gives a distribution that is narrower than the measurement (empty triangles). Also note that the pion source function is reproduced with Therminator only when non-zero emission duration

is assumed [6]. Recent simulations of the kaon source function [17] with the hydrokinetic model (HKM) [18] show a good agreement in the *side* direction, although it is slightly over the measurements at larger radii in *out* and *long* (downward-pointing triangles).

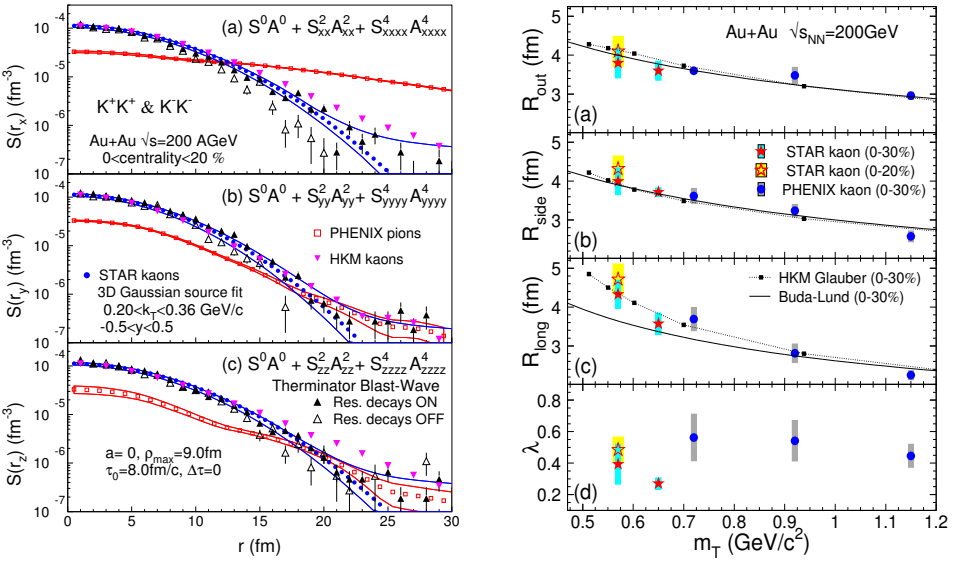

Fig. 1. (Color online) Left: Kaon source function profiles extracted from the data (solid circles) compared to 3D pion source function (squares) from PHENIX [6], and to the Therminator (triangles pointing upwards) and HKM (triangles pointing downwards) models. Right: Transverse mass dependence of Gaussian radii and the λ for the 30% most central Au+Au collisions (solid stars). PHENIX data are also plotted (dots). Squares are HKM, solid curves are Buda-Lund model calculations. The 20% most central data are also shown for comparison (open stars).

The right panel of Figure 1 shows the dependence of the Gaussian radii in the longitudinally co-moving system (LCMS) ($R_{out}=R_x/\gamma$, $R_{side}=R_y$ and $R_{long}=R_z$; γ is the Lorentz boost in the outward direction from the LCMS to the PCMS frame) as a function of the transverse mass $m_{\rm T} = (m^2+k_{\rm T}^2)^{1/2}$. PHENIX kaon data [10] are also shown. The perfect fluid hydrodynamics calculations from the Buda-Lund model [11] and the hydrokinetic model (HKM) [18] with Glauber initial conditions are plotted for comparison purposes. While pions are well described by the Buda Lund model in the whole interval shown [11], low-$k_{\rm T}$ kaons in the *long* direction seem to favour HKM over the Buda-Lund model, suggesting that that contrary to lower SPS energies [9] the $m_{\rm T}$-scaling in the *long* direction is broken at RHIC.

4. Summary

We have presented the first model-independent extraction of the 3D kaon source by the STAR Collaboration [12], at mid-rapidity in $\sqrt{s_{NN}}$=200 GeV central Au+Au collisions, using low-k_{T} kaon pair correlations and the Cartesian surface-spherical harmonic decomposition technique. No significant non-Gaussian tail has been observed. Comparison with the Therminator model calculations indicates that, although the transverse extent of the source is similar to pions, the shape and the size in the longitudinal direction is very different. This can be attributed to resonance decays, but also indicates that kaons and pions may be subject to different freeze-out dynamics. Although the Gaussian radii follow m_{T}-scaling in the outward and sideward directions, the scaling appears to be broken in the longitudinal direction. Thus the hydro-kinetic predictions [18] are favoured over pure hydrodynamical model calculations.

Acknowledgments

This research was supported by the grant LA09013 of the Ministry of Education of the Czech Republic.

References

[1] R. Lednicky, Nucl. Phys. A **774**, 189 (2006).
[2] R. Lednicky, J. Phys. G **35**, 125109 (2008); Phys. Part. Nucl. **40**, 307 (2009).
[3] M.A. Lisa *et al.*, Ann. Rev. Nucl. Part. Sci. **55**, 357 (2005).
[4] D.A. Brown and P. Danielewicz, Phys. Lett. B **398**, 252 (1997).
[5] P. Danielewicz and S. Pratt, Phys. Lett. B **618**, 60 (2005).
[6] S. Afanasiev *et al.* (PHENIX Collaboration), Phys. Rev. Lett. **100**, 232301 (2008).
[7] P. Danielewicz and S. Pratt, Phys. Rev. C **75**, 034907 (2007).
[8] M. Csanád, T. Csörgő and M. Nagy, Braz. J. Phys. **37**, 1002 (2007).
[9] S.V. Afanasiev *et al.* (NA49 Collaboration), Phys. Lett. B **557**, 157 (2003).
[10] S. Afanasiev *et al.* (PHENIX Collaboration), Phys. Rev. Lett. **103**, 142301 (2009).
[11] M. Csanád and T. Csörgő, Acta Phys. Polon. Supp. **1**, 521 (2008).
[12] L. Adamczyk *et al.* (STAR Collaboration), Phys. Rev. C **88**, 034906 (2013).
[13] B.I. Abelev *et al.* (STAR Collaboration), Phys. Rev. C **74**, 054902 (2006).
[14] P. Chung (STAR Collaboration), Phys. Part. Nucl. Lett. **8**, 1019 (2011).
[15] A. Kisiel *et al.*, Comput. Phys. Commun. **174**, 669 (2006).
[16] A. Kisiel *et al.*, Phys. Rev. C **73**, 064902 (2006).
[17] V.M. Shapoval, Y.M. Sinyukov and I.A. Karpenko, arXiv:1308.6272.
[18] I.A. Karpenko and Y.M. Sinyukov, Phys. Rev. C **81**, 054903 (2010).

Influence of the target on multiparticle production in the forward domain in p+Pb collisions at 158 GeV

Maciej Rybczyński (for the NA49 Collaboration)
Institute of Physics, Jan Kochanowski University, PL-25406 Kielce, Poland

In this talk we show the influence of the target on multiparticle production in the forward hemisphere in p+Pb collisions at top SPS energy. The multiplicity distributions appear to be almost target independent in the projectile fragmentation domain and the effect of fluctuations of the number of target participants is not seen in the projectile fragmentation region. We compare the obtained results with those for p+p interactions and predictions of models.

1. Introduction

The NA49 Collaboration reported [1] large multiplicity fluctuations in the forward rapidity domain of non-central Pb+Pb collisions at beam momentum of 158 GeV/c per nucleon at a fixed number of participating nucleons from the projectile. There is no commonly accepted explanation of the phenomenon but it was observed [2] that even at fixed number of projectile participants, the number of target participants fluctuates and it was suggested that the observed large multiplicity fluctuations in the forward rapidity domain of Pb+Pb collisions are due to the fluctuating number of participants from the target. Such a mechanism, however, assumes that the target (projectile) participants contribute to the projectile (target) fragmentation region, i.e. that the domains of projectile and target fragmentation overlap. A model assuming such a mechanism is called by the authors of Ref. [2] the *mixing* model to be distinguished from the *transparency* model where the projectile participants only contribute to the projectile fragmentation domain and the target participants only to the target fragmentation domain. The transparency model is compatible with the limiting fragmentation hypothesis [3][1] while the mixing model contradicts it. Both models

[1] Hypothesis of limiting fragmentation states that for a sufficiently high collision energy particle production becomes target and energy independent in the projectile (target) fragmentation domain corresponding to the rapidities close to that of the projectile (target).

should obviously be treated as idealizations. The analysis of d+Au collisions at RHIC [4] shows that in reality we have both mixing and transparency. Our objective here is to study the importance of the mechanism of mixing in p+Pb collisions where the number of participants from the target fluctuates but the number of projectile participants is always one.

As a measure of multiplicity fluctuations we use here, as in the study described in ref.[1], the scaled variance $\omega = \mathrm{Var}(N)/\langle N \rangle$ of the multiplicity distribution where $\mathrm{Var}(N)$ is the variance and $\langle N \rangle$ the mean value of the distribution. We analyze minimum bias p+Pb collisions and confront the results with those from p+p interactions at the same collision energy.

2. The NA49 Experiment

The NA49 experiment is a large acceptance hadron spectrometer situated in the H2 beam line at the CERN SPS accelerator complex which was used to study the hadronic final states produced in collisions of protons with a variety of fixed targets. [5]. The main tracking devices are four large volume Time Projection Chambers (TPCs). Two of them, the Vertex TPCs (VTPC-1 and VTPC-2), are located inside the magnetic field of two super-conducting dipole magnets (1.5 and 1.1 T, respectively) and two others (MTPC-L and MTPC-R) are positioned downstream of the magnets symmetrically to the beam line.

Interactions of protons in the target are selected by anti-coincidence of the incoming beam particle with a signal in a small scintillation counter S4 placed on the beam trajectory between the two vertex magnets. For p+p interactions at 158 GeV/c this counter selects a (trigger) cross section of 28.23 mb out of 31.78 mb of the total inelastic cross section [6].

Details of the NA49 detector set-up and performance of the tracking software are described in [5]. The parts of the NA49 experiment specific to the study of p+Pb interactions are described in [7].

2.1. Data sets, detector acceptance, and event and particle selection

In this contribution we show the results of the analysis of 125,000 minimum bias p+Pb collisions and 320,000 p+p interactions both at beam momentum of 158 GeV/c. Although the NA49 detector was designed for a large acceptance in the forward hemisphere [5], the geometrical acceptance is not complete in this region. The acceptance limits in transverse momentum p_T at given azimuthal angle ϕ are parametrized by the function

$$p_T(\phi) = \frac{1}{A + \frac{\phi^2}{C}} + B, \tag{1}$$

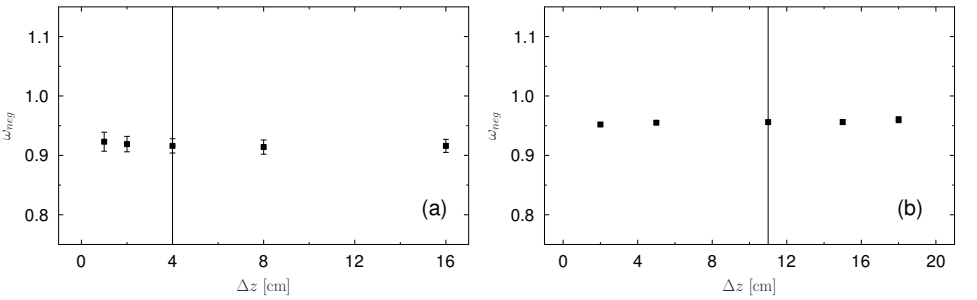

Fig. 1. The scaled variance of the uncorrected multiplicity distribution of negatively charged particles produced in minimum bias p+Pb collisions (panel (a)) and p+p interactions (panel (b)) as a function of the maximally allowed difference Δz between the reconstructed main vertex and the actual target position. The vertical line indicates the value used in the analysis.

where the values of A, B and C depend on the rapidity (see ref.[8]). Only particles within the curves given by Eq. 1 are used in this analysis. Additionally, the particle's transverse momentum is required to obey $0.005 < p_T < 1.5$ GeV/c. This well defined acceptance is essential for later comparison of the results with models and other experiments.

Several event selection criteria are applied to reduce contamination from non-target collisions. The primary vertex was reconstructed by fitting the intersection point of the measured particle trajectories. Only events with a proper quality and position of the reconstructed vertex are accepted for further analysis. The vertex coordinate z along the beam has to satisfy $|z - z_0| < \Delta z$, where the nominal vertex position z_0 and cut parameter Δz values are: -579.5 and 5.5 cm, -581 and 2 cm for p+p and minimum bias p+Pb collisions, respectively. In Fig. 1 we show the stability of the scaled variance of the uncorrected multiplicity distribution of negatively charged particles produced in minimum bias p+Pb and p+p interactions with respect to the maximally allowed difference Δz between the reconstructed main vertex and the actual target position. As seen, the results are stable.

In order to reduce the contamination by poorly reconstructed tracks and particles from secondary interactions and other sources of non-vertex tracks, several track cuts were applied. The accepted particles are required to have measured points in at least one of the Vertex TPCs and the potential number of points (calculated on the basis of the geometry of the track) in the detector has to exceed 30. Moreover, the ratio of the number of points on a track to the potential number of points has to be higher than 0.5 to

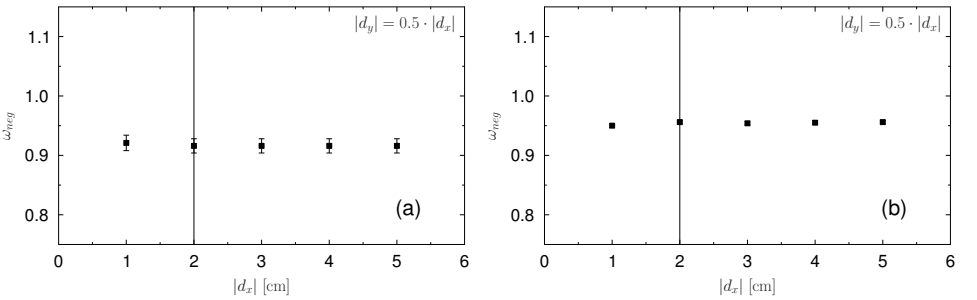

Fig. 2. The scaled variance of the uncorrected multiplicity distribution of negatively charged particles produced in minimum bias p+Pb collisions (panel (a)) and p+p interactions (panel (b)) as a function of the maximally allowed distance between the reconstructed primary vertex and the back-extrapolated track in the target plane $|d_x|$. Simultaneously the deviation in $|d_y|$ is required to be below $0.5|d_x|$. The vertical line indicates the value used in the analysis.

avoid split tracks (double counting). A cut on the extrapolated distance of closest approach (dca) to the fitted vertex of the particle at the vertex plane is applied ($|d_x| < 2$ cm and $|d_y| < 1$ cm) in order to reduce the contribution from weak decay daughters (feeddown). To estimate the effect on the multiplicity fluctuations, the maximally accepted dca was varied. Fig. 2 shows the result for ω and demonstrates that the scaled variance is stable with respect to the cut.

2.2. Corrections for multiplicity distributions based on the VENUS event gereator and detector simulation

In this subsection we describe the VENUS 4.12 [9] simulation of p+Pb minimum bias collisions and p+p interactions used to derive corrections applied later to measured multiplicity distributions. The NA49 apparatus was simulated by using GEANT 3 [10]. The multiplicity distributions were calculated for *pure* VENUS and *accepted* VENUS events, both with acceptance filter of Eq. 1 turned on. *Pure* VENUS results correspond to all charged particles produced in the primary interaction. *Accepted* VENUS results were obtained from GEANT/detector simulated and reconstructed VENUS events applying event and track cuts as for real data. Thus these results correspond to all reconstructed particles which are consistent with originating from the reconstruced event vertex, i.e. particles produced in the primary interaction as some contribution from secondary interactions

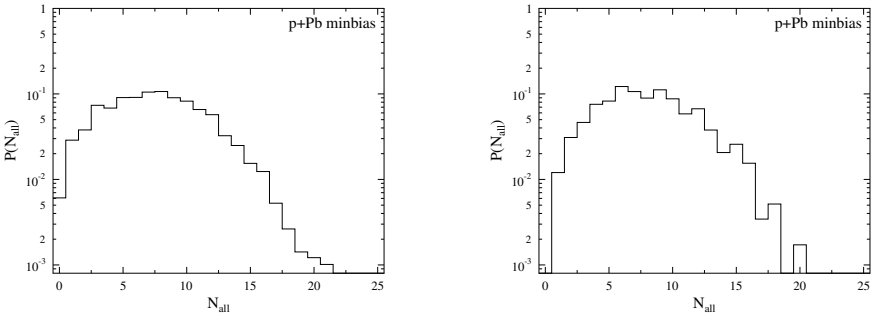

Fig. 3. Multiplicity distributions of all charged particles obtained from *pure* VENUS events of p+Pb minimum bias collisions. Left panel: *good* events for which all measured particles miss the S4 counter. Right panel: *lost* events for which at least one measured particle hits the S4 counter.

and feeddown from decays. The pion mass was assumed for the calculation of the rapidity y in both *pure* and *accepted* VENUS events. Based on the simulation results the unfolding method [11, 12, 13] provided by the ROOT [14] TUnfold class [15] was used to obtain the corrected results.

2.3. Correction for the S4 trigger bias

In this subsection we estimate the effect of a trigger bias caused by the fact that some of the particles produced in an interaction can hit the S4 counter and cause a false veto. All charged particles simulated in full phase-space from each *pure* VENUS p+p and p+Pb minimum bias event were tracked down to the position of the S4 counter: $S4_x = -1.5\ cm$, $S4_y = 0.0\ cm$ and $S4_z = -201\ cm$ in the NA49 detector coordinate system. If all charged particles from a given event miss the S4 counter then the event is treated as *good*. In the left panel of Fig. 3 we show the corresponding multiplicity distribution of *good* events of p+Pb minimum bias collisions. If a charged particle from an event hits S4 then the event is treated as *lost*. In the right panel of Fig. 3 we show the corresponding multiplicity distribution of *lost* events. The fraction of *lost* events amounts to 10.5%. This number is in good agreement with previous calculations [6, 7]. The *lost* events were excluded from the sample of *accepted* VENUS events used to obtain corrections to the multiplicity distributions.

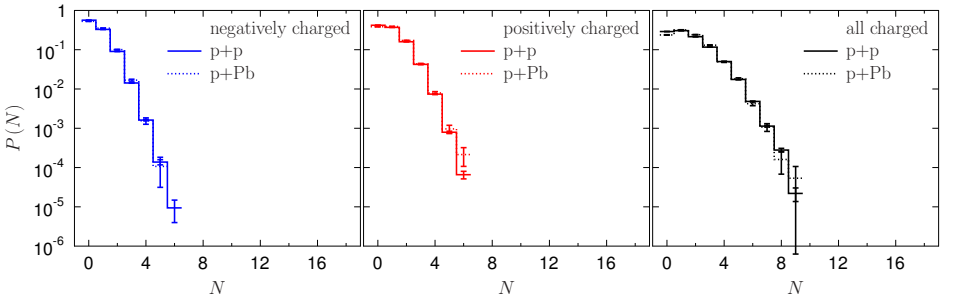

Fig. 4. Uncorrected multiplicity distributions of negatively (left panel), positively (middle panel) and all (right panel) charged particles produced in minimum bias p+Pb collisions (dotted) as well as in p+p interactions (continuous lines).

Table 1. Scaled variance of the corrected multiplicity distributions of particles produced in minimum bias p+Pb collisions and p+p interactions. The errors are statistical only.

Data Set	ω_{neg}	ω_{pos}	ω_{all}
p+p	0.989 ± 0.003	1.002 ± 0.003	1.31 ± 0.004
p+Pb	0.929 ± 0.012	0.924 ± 0.011	1.13 ± 0.013

3. Results

We now proceed to the central subject of our study, the multiplicity fluctuations in the projectile fragmentation region. Results refer to all production (inelastic) reactions in minimum bias p+Pb and inelastic p+p interactions both at beam momentum of 158 GeV/c and to charged hadrons produced in the primary interactions. Figure 4 shows the uncorrected multiplicity distributions of negatively, positively and all charged particles produced in the rapidity interval $4 < y < 5.5$. The distributions in p+Pb and p+p interactions are seen to be very similar again suggesting the validity of the limiting fragmentation hypothesis. In Table 1 we collect the numerical values of the scaled variances ω of the corrected multiplicity distributions. As seen, the second moments of the multiplicity distributions in both classes of collisions are very close to each other. The multiplicity distributions are approximately Poissonian as the scaled variances are close to unity. It is also worth noting that the multiplicity distributions in p+p interactions tend to be broader than those in the p+Pb collisions.

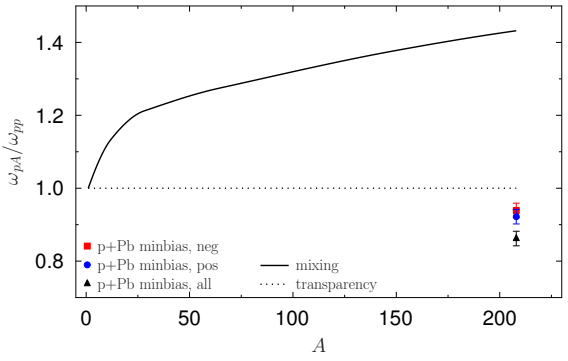

Fig. 5. Scaled variance of the corrected multiplicity distributions of negatively (squares), positively (circles) and all (triangles) charged particles produced in minimum bias p+Pb collisions divided by the respective number from the p+p interactions. The data are plotted as function of atomic mass of target nucleus to show the difference of the mixing (solid line) and transparency (dotted line) models [2].

4. Summary and discussion

We studied particle production in the projectile fragmentation region of minimum bias p+Pb collisions at beam momentum of 158 GeV/c. The results were compared to those from p+p interactions at the same collision energy. The multiplicity distributions appear to be almost target independent in the projectile fragmentation domain. As mentioned in the Introduction, our specific motivation was to test the mixing model proposed in ref.[2]. In Fig. 5 we confront the results on the scaled variance from minimum bias p+Pb collisions with the model predictions. As seen, the transparency model describes the data quite well but the mixing model seems to be excluded. The effect of fluctuating number of target participants is not seen in the projectile fragmentation region. Obviously, the mechanism of Pb+Pb collisions might be rather different from that of p+Pb collisions and thus the mixing model is not ruled out. Nevertheless our results show that there is no strong mixing of the projectile and target fragmentation regions at least in the proton-nucleus collisions.

Acknowledgments

I thank the organisers of ISMD2013 for giving me the opportunity to present this report. This research was supported by the National Science Center (NCN) under contract no. 2011/03/B/ST2/02617.

References

[1] C. Alt *et al.* (NA49 Collaboration), Phys. Rev. C **75**, 064904 (2007).

[2] M. Gazdzicki and M. I. Gorenstein, Phys. Lett. B **640**, 155 (2006).

[3] J. Benecke *et al.* Phys. Rev. **188**, 2159 (1969).

[4] A. Bialas and W. Czyz, Acta Phys. Polon. B **36**, 905 (2005).

[5] S. Afanasiev *et al.* (NA49 Collaboration), Nucl. Instrum. Meth. A **430**, 210 (1999).

[6] C. Alt *et al.* (NA49 Collaboration), Eur. Phys. J. C **45**, 343 (2006).

[7] C. Alt *et al.* (NA49 Collaboration), Eur. Phys. J. C **49**, 897 (2007).

[8] T. Anticic *et al.* (NA49 Collaboration), Phys. Rev. C **70**, 034902 (2004).

[9] K. Werner, Phys. Rept. **232**, 87 (1993).

[10] See http://wwwinfo.cern.ch/asdoc/pdfdir/geant.pdf

[11] P. C. Hansen, in Computational Inverse Problems in Electrocardiology, ed. P. Johnston, Advances in Computational Bioengineering, WIT Press (2000).

[12] P. C. Hansen, Rank-Deficient and Discrete Ill-posed Problems, Siam (1998).

[13] J. Kaipio and E. Somersalo, Statistical and Computational Inverse problems, Springer (2005).

[14] R. Brun *et al.*, Root Users Guide 5.16, CERN (2007).

[15] See http://root.cern.ch/root/html/TUnfold.html

Measurement of anisotropic radial flow rapidity

Yuanfang Wu, Lin Li

Key Laboratory of Quark and Lepton Physics (MOE) and Institute of Particle Physics, Central China Normal University, Wuhan 430079, China

Na Li

Hua-Zhong University of Science and Technology, 430074, China

Using the sample of Au + Au collisions at 200 GeV generated by the AMPT with string melting model, the anisotropic amplitudes of azimuthal distributions of total transverse momentum, mean radial (transverse) momentum, and multiplicity are first presented and compared. It shows that the azimuthal distribution of mean radial momentum well characterizes the radial expansion. So a measurement of the azimuthal distribution of mean transverse (radial) rapidity of final state particles is suggested. We further show that the isotropic part of the suggested distribution is the combination of isotropic radial expansion and thermal motion. The anisotropic amplitude characterizes the anisotropic radial flow, and coincides with the parameter of anisotropic radial flow rapidity extracted from a generalized blast-wave parametrization.

1. Introduction

The observation of large elliptic flow at RHIC is considered as one of the most important signatures of the formation of the strongly interacting Quark Gluon Plasma (sQGP) [1, 2]. The flow harmonics are Fourier coefficients of the azimuthal multiplicity distribution of final state hadrons [3]. One common feature of flow harmonics is their mass ordering in the low transverse momentum region [4]. This phenomena can be well understood by hydrodynamics with a set of kinetic freeze-out constraints, i.e., the temperature, the radial flow, and the source deformation [5]. The radial flow is usually described by 2 parameters. The first is the isotropic radial velocity (or rapidity, related by $v_{\mathrm{T}} = \tanh y_{\mathrm{T}}$). It presents the surface profile of isotropic transverse expansion of the source at kinetic freeze-out.

The other parameter is the anisotropic radial velocity (i.e., the azimuthal dependent radial velocity). It measures the difference of the radial flow strength in and out of the reaction plane. It is introduced to account for

the anisotropic radial flow field which arises in *non-central* collisions. The observed elliptic flow can be generated by anisotropic radial flow [5, 6]. Moreover, the shear tension of viscosity in hydrodynamics is supposed to be proportional to the gradient of radial velocity along the azimuthal direction [7], which is directly related to anisotropic radial velocity. The proportionality constant is the shear viscosity.

In hydrodynamic models [8, 9, 10], these parameters are not independent. They are related by the initial conditions and the equation of state. Their determination is crucial for theoretical calculations.

It has been shown that the azimuthal distribution of mean transverse momentum directly measures the transverse motion of the source at kinetic freeze-out [11]. So we suggest the measurement of the azimuthal distribution of the mean transverse rapidity of final state hadrons ($\langle y_{\rm T}(\phi)\rangle$). It should be helpful in determining the parameters of the anisotropic radial rapidity.

As we know, $\langle y_{\rm T}(\phi)\rangle$ contains three parts: average isotropic radial rapidity, average anisotropic radial rapidity, and average thermal motion rapidity [4]. Since both thermal and radial motions contribute to the isotropic rapidity of the distribution, the isotropic radial rapidity itself can not be directly obtained from the distribution. Conventionally, the radial flow parameters are extracted from the $p_{\rm T}$ spectra of the hadrons [12, 13], or dileptons [14, 15], by a generalized blast-wave parametrization [5, 6]. The obtained parameters are an approximate description of the radial flow; they are model dependent. A model independent measure is called for.

Fortunately, the thermal motion is isotropic. As such, it does not contribute to the anisotropic radial flow. The azimuthal amplitude of the mean transverse rapidity distribution should correspond directly to the anisotropic radial rapidity. It is interesting to see the features of the azimuthal distribution of mean transverse rapidity, and how its azimuthal amplitude relates to the parameters of anisotropic radial rapidity extracted by a generalized blast-wave parametrization.

In this paper, using a sample generated by the AMPT model with string melting [16, 17], we first compare the anisotropic amplitudes of three azimuthal distributions of total transverse momentum, the mean radial (transverse) momentum, and multiplicity in section II. It shows that the azimuthal distribution of mean radial momentum, or rapidity, is a good measure of radial expansion. In section III, we further demonstrate the measured physics of isotropic and anisotropic amplitudes of the suggested distribution. They behave indeed as the expected radial flow (with a random thermal component), and anisotropic radial flow, respectively. In section IV, it is further shown that the parameter of anisotropic radial flow rapidity is just the anisotropic amplitude of the suggested distribution. Finally, the summary and conclusions are given in section V.

2. Measurements of radial expansion

Conventionally, the azimuthal distribution of the multiplicity of final state particles is presented by

$$\frac{dN}{d\phi} \propto 1 + \sum_{n=1}^{\infty} 2v_n(N)\cos(n\phi), \tag{1}$$

where ϕ is the azimuthal angle between the transverse momentum of the particle and the reaction plane. The coefficients of the Fourier expansion are [18],

$$v_n(N) = \langle \cos(n\phi) \rangle, \tag{2}$$

where $\langle \dots \rangle$ is an average over all particles in all events. The second harmonic coefficient $v_2(N)$ is the so-called elliptic flow parameter. It represents the anisotropy of the colliding system and has the biggest value in relativistic heavy ion collisions [19].

However, the multiplicity distribution only counts the number of particle emissions in a certain azimuthal angle. The initial anisotropy in coordinate space in non-central collisions makes the formed system expand in a perpendicular almond shape in momentum space. The expansion of the system generates not only the anisotropy of multiplicity distribution but also their associate radial (transverse) momentum. The total radial momentum at a given azimuthal angle is the combination of them. Therefore, the azimuthal distribution of radial momentum is a good measure of the anisotropic expansion. The total transverse momentum in the mth azimuthal bin can be defined as

$$\langle P_{\mathrm{t}}(\phi_m) \rangle = \frac{1}{N_{\mathrm{event}}} \sum_{j=1}^{N_{\mathrm{event}}} \left(\sum_{i=1}^{N_m} p_{\mathrm{T},i}(\phi_m) \right). \tag{3}$$

Where $p_{\mathrm{T},i}$ is the transverse momentum of the ith particle, N_m is the total number of particles, and $\langle \dots \rangle$ denotes the average over all events.

In order to see the contributions of radial expansion alone, the mean radial momentum in the mth azimuthal bin can be defined accordingly as,

$$\langle \langle p_{\mathrm{T}}(\phi_m) \rangle \rangle = \frac{1}{N_{\mathrm{event}}} \sum_{j=1}^{N_{\mathrm{event}}} \left(\frac{1}{N_m} \sum_{i=1}^{N_m} p_{\mathrm{T},i}(\phi_m) \right). \tag{4}$$

Here, the averages $\langle \langle \dots \rangle \rangle$ are over all particles in the mth angle bin and all events. This records only the contributions from the transverse momentum of final particles. In contrast to the azimuthal multiplicity distribution, the multiplicity effect is eliminated by the average over the number of particles in the mth bin.

The anisotropic parameters of all those azimuthal distributions can be directly obtained from their Fourier expansions,

$$\frac{d\langle P_{\rm t}\rangle}{d\phi} \propto \ 1+\sum_{n=1}^{\infty} 2v_n(\langle P_{\rm t}\rangle)\cos(n\phi), \tag{5}$$

and

$$\frac{d\langle\langle p_{\rm T}\rangle\rangle}{d\phi} \propto \ 1+\sum_{n=1}^{\infty} 2v_n(\langle\langle p_{\rm T}\rangle\rangle)\cos(n\phi). \tag{6}$$

$\frac{d\langle P_{\rm t}\rangle}{d\phi}$ and $\frac{d\langle\langle p_{\rm T}\rangle\rangle}{d\phi}$ are the azimuthal distribution functions of total radial momentum and mean radial momentum. $v_n(\langle P_{\rm t}\rangle)$ and $v_n(\langle\langle p_{\rm T}\rangle\rangle)$ are their anisotropic parameters, respectively.

In order to see the contributions of those anisotropic flows in a real system, we simulate the Au + Au collisions at 200 GeV by AMPT with string melting model [16, 17]. A partonic phase is implemented in the model and the elliptic flow data from RHIC are well reproduced by the model [20]. We generate 1.6 millions minimum bias events. Their centrality dependencies are presented in Fig. 1. The red stars, the blue triangles, and the black solid circles are the anisotropic amplitudes of total transverse momentum $v_2(P_t)$, multiplicity $v_2(N)$, and mean transverse momentum $v_2(\langle\langle p_t\rangle\rangle)$, respectively.

Figure 1 shows that they have similar centrality dependence, small at peripheral and central collisions, and largest at mid-central collisions. But their anisotropies are different. The anisotropy of mean transverse momentum is the smallest, the anisotropy of multiplicity is in the middle, and the anisotropy of total transverse momentum is the largest, as it counts the anisotropy from both multiplicity and transverse momentum distributions, as we discussed in their definitions.

So the azimuthal distribution of mean transverse momentum can measure the anisotropy of radial expansion, in additional to the multiplicity distribution. We suggest the measurement of azimuthal distribution of mean transverse rapidity. Usually, the transverse rapidity of a final state hadron is considered as a good approximation of its transverse rapidity at kinetic freeze-out [21]. It is defined similarly to that of mean transverse momentum.

$$y_{\rm T} = \ln(\frac{m_{\rm T}+p_{\rm T}}{m_0}) \ , \tag{7}$$

where m_0 is the particle mass in the rest frame, $p_{\rm T}$ is transverse momentum, and $m_{\rm T} = \sqrt{m_0^2+p_{\rm T}^2}$ is the transverse mass.

The mean transverse rapidity in a given azimuthal angle bin is defined as the summation of all particles' rapidities divided by the total number of

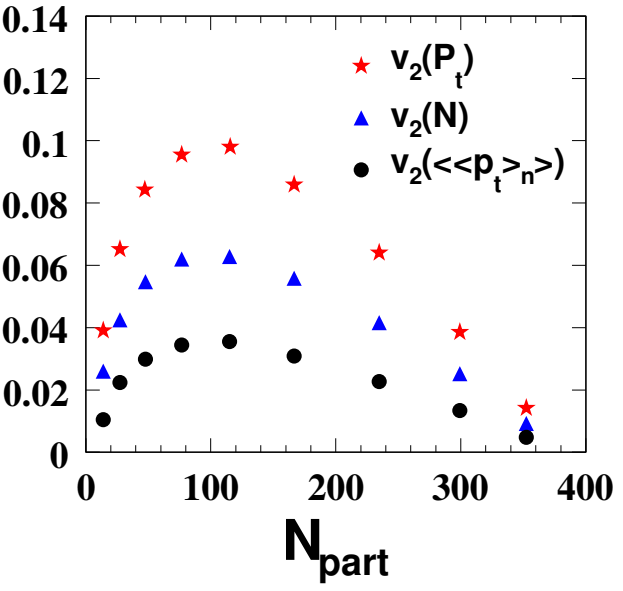

Fig. 1. (Color online) The centrality dependence of elliptic flow parameters deduced from azimuthal distributions of radial momentum (red stars), mean radial momentum (black solid circles), and multiplicity (blue solid triangles) for the sample of Au+Au collisions at $\sqrt{s_{NN}} = 200$ GeV generated by AMPT with string melting.

particles, i.e.,

$$\langle y_{\rm T}(\phi_m - \psi_r)\rangle = \frac{1}{N_{\rm event}} \sum_{e=1}^{N_{\rm event}} \frac{1}{N_m^e} \sum_{i=1}^{N_m^e} y_{{\rm T},i}^e(\phi_m - \psi_r), \tag{8}$$

where the transverse rapidity of final state particle with mass m_0 is determined by its transverse momentum. Rapidity is more convenient in boost transformations. It should directly relate to the radial flow parameters that we are interested in.

The distribution of mean transverse rapidity in a minimum bias sample is shown in Fig. 2(a). We can see it is a periodic function of azimuthal angle, and consists of two parts. The isotropic constant, $y_{T0} = 1.3371 \pm 0.0001$, and azimuthal dependent part $y_{T2} = 0.0334 \pm 0.0002$.

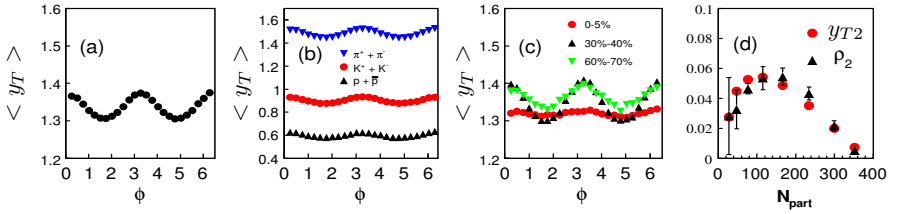

Fig. 2. (Color online) (a): $\langle y_T(\phi)\rangle$ for centrality $0-70\%$, (b): $\langle y_T(\phi)\rangle$ for 3 different mass particles, (c): $\langle y_T(\phi)\rangle$ at three different centralities, $0-5\%$ (red points), $30\%-40\%$ (black triangles), and $60\%-70\%$ (green down triangles), (d): The centrality dependence of y_{T2} (red points), and ρ_2 (black triangles).

3. Physics of the suggested measurement

The isotropic part of the suggested distribution contains both isotropic radial expansion and thermal motion. In order to see the features of the isotropic part, we study the mass dependence of the suggested distributions.

The suggested distributions of three different particles, pion (blue triangles), kaon (red points), and proton (black triangles) are given in Fig. 2(b). It shows that the distribution of the lightest pion is at the top with the largest isotropic rapidity, while the distribution of the heaviest proton is at bottom with the smallest isotropic rapidity, and the distribution of kaons with intermediate mass is between them with intermediate isotropic rapidity.

As we know, the thermal motion is mainly determined by the temperature and particle mass. At fixed temperature, the particles with small mass should have larger thermal velocity. So the isotropic part of the suggested distribution is just ordered as expected by thermal motion.

The features of the anisotropic part, the suggested distribution, at three typical centralities, 0-5% (red points For the most central collisions), 30%-40% (black up triangles for the middle-central collisions), and 60%-70% (green down triangles for the peripheral collisions), are given in Fig. 2(c).

It shows that the distribution is almost flat and azimuthal angle independent in central collisions, but azimuthal angle dependent in non-central collisions. It also shows the large anisotropy in mid-central collisions, and small anisotropy in peripheral collisions.

This centrality dependence is consistent with the fact that anisotropic radial flow appears in non-central collisions, and is the largest in mid-central collisions.

So the suggested distribution well represents the characters of radial

flow. Since we can not separate the thermal motion, the parameter of isotropic radial rapidity can not be obtained from the measurement. However, the thermal motion is isotropic, and has no contribution to the anisotropic part. The azimuthal dependent part, y_{T2}, should correspond to the parameter of anisotropic radial flow rapidity.

4. Measured anisotropic amplitude and extracted parameter of anisotropic radial flow rapidity

It is interesting to check if the measured anisotropic part corresponds to the extracted parameter of anisotropic radial flow rapidity.

The blast-wave model is currently the only model that simply includes the radial flow parameters. It is motivated from hydrodynamics with the kinetic freeze-out parameters [6, 12, 22, 24, 25, 26]. It is assumed that the longitudinal expansion is boost invariant [27]. The single-particle spectrum is given by the Cooper-Frye formalism (as in hydrodynamics) [28],

$$E\frac{d^3N}{d^3p} \propto \frac{1}{(2\pi)^3}\int_{\Sigma_f} p^\mu d\sigma_\mu(x) f(x,p), \tag{9}$$

where $f(x,p)$ is the momentum distribution at space-time point x. Eq. (4) is an integral over a freeze-out hyper-surface, and sums over the contributions from all space-time points.

Originally, local thermal equilibrium is assumed to be reached at kinetic freeze-out and a Boltzman distribution of the momentum is applied [12]. It has been shown recently that a Tsallis distribution provides an even better description for all p_{T} spectra from elementary to nuclear collisions [29, 30]. So, we use the Tsallis distribution for $f(x,p)$, i.e.,

$$f(x,p) = \left[1 + \frac{q-1}{T(x)}\Big(p\cdot u(x) - \mu(x)\Big)\right]^{-\frac{1}{q-1}}, \tag{10}$$

where q is the parameter characterizing the degree of non-equilibrium, and T is the kinetic freeze-out temperature. Thus the transverse momentum spectrum can be given by [31],

$$\frac{dN}{p_{\rm T}dp_{\rm T}d\phi} \propto \int_0^{2\pi} d\phi_s \int_{-y_b}^{y_b} dy e^{\sqrt{y_b^2-y^2}} \cosh y \int_0^R m_{\rm T} r dr \left[1+\frac{q-1}{T}\Big(m_{\rm T}\cosh y\cosh\rho - p_{\rm T}\sinh\rho\cos(\phi_b-\phi)\Big)\right]^{-\frac{1}{q-1}}, \quad (11)$$

where $m_{\rm T}$ and $p_{\rm T}$ are transverse mass and transverse momentum of the particle, respectively, and $y_b = \ln(\sqrt{s_{NN}}/m_N)$ is the beam rapidity [32].

According to the generalized blast-wave parametrization, the radial flow rapidity which controls the magnitude of the transverse expansion velocity is [6, 22, 33, 34],

$$\rho = \widetilde{r}\big(\rho_0 + \rho_2\cos(2\phi_b)\big) , \quad (12)$$

where $\widetilde{r} = \sqrt{(r\cos(\phi_s)/R_X)^2 + (r\sin(\phi_s)/R_Y)^2}$. ρ_0 and ρ_2 are the parameters of isotropic radial flow rapidity and the amplitude of anisotropic radial flow rapidity, respectively. The greater the magnitude of ρ_2, the larger the momentum-space anisotropy. Here, ϕ_s is the azimuthal angle in coordinate space and ϕ_b is the azimuthal angle of the boost source element defined with respect to the reaction plane. They are related by $\tan(\phi_b) = (R_X/R_Y)^2\tan(\phi_s)$.

There are 5 undetermined parameters: the temperature (T), isotropic radial flow rapidity (ρ_0) and anisotropic radial flow rapidity (ρ_2), q of the Tsallis distribution, and R_X/R_Y. Since all the particles are assumed to move with a common radial flow velocity, the mean kinetic freeze-out parameters are usually obtained by the simultaneous fitting of spectra from several hadrons [23, 24] and elliptic flow [6]. Elliptic flow, $v_2(p_{\rm T})$, is the second coefficient of the Fourier expansion of azimuthal multiplicity distribution [35, 18], and defined as,

$$v_2(p_{\rm T}) = \frac{\int_{-y_b}^{y_b} dy \int_0^{2\pi} d\phi \cos(2\phi)\frac{dN}{p_{\rm T}dp_{\rm T}dyd\phi}}{\int_{-y_b}^{y_b} dy \int_0^{2\pi} d\phi \frac{dN}{p_{\rm T}dp_{\rm T}dyd\phi}} . \quad (13)$$

In Fig. 3, the $p_{\rm T}$ spectra of six particles, $\pi^{\pm}$, $K^{\pm}$, $\overline{p}$, and p, of the *same* sample, are presented by red solid circles. The differential elliptic flow $v_2(p_{\rm T})$ of pions, kaons, and protons are presented in Fig. 4 by black triangles, red solid circles and blue triangles, respectively. The error bars only include statistical errors. They are very small in comparison with the

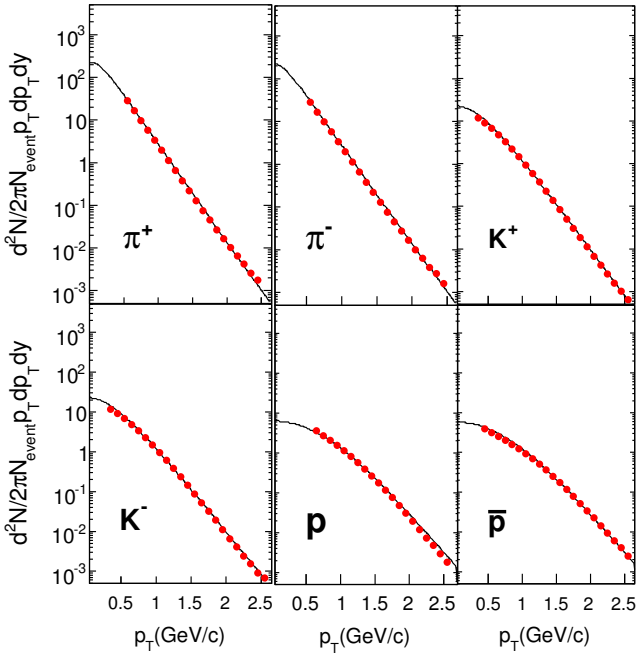

Fig. 3. (Color online) The transverse momentum spectra for $\pi^{\pm}$, $K^{\pm}$, $\bar{p}$ and p within $|y_{\rm L}| < 0.1$ at centrality $0-70\%$ for the sample of Au+Au collisions at $\sqrt{s_{NN}} = 200$ GeV generated by the AMPT model with string melting.

experimental data [22]. Typically, the systematic errors are considered to be 5% when fitting the simulated data [36]. Due to resonance decays in the low momentum region of pions [23], the data points in the low $p_{\rm T}$ regions of the spectra are excluded in this fitting.

Using Eqs. (6) and (8), the fitting curves in each plots of Fig. 3 and 4 are drawn. They describe well the corresponding data points of the $p_{\rm T}$ spectra and elliptic flow. The fitting parameters are $T = 102 \pm 1$ MeV, $\rho_0 = 0.67 \pm 0.01$, and $\rho_2 = 0.036 \pm 0.002$. This temperature is the same magnitude as that given by hydrodynamics [5, 10], and experimental data [22]. The parameter of anisotropic radial flow rapidity, ρ_2, is very close to the azimuthal amplitude of the suggested distribution, $y_{\rm T2} = 0.0343 \pm 0.0002$.

The centrality dependence of ρ_2 is shown in Fig. 2(d) by black triangles. We can see that at each centrality, ρ_2 is very close to $y_{\rm T2}$. The azimuthal amplitude of the suggested distribution coincides with the parameter of anisotropic radial flow rapidity extracted from a generalized

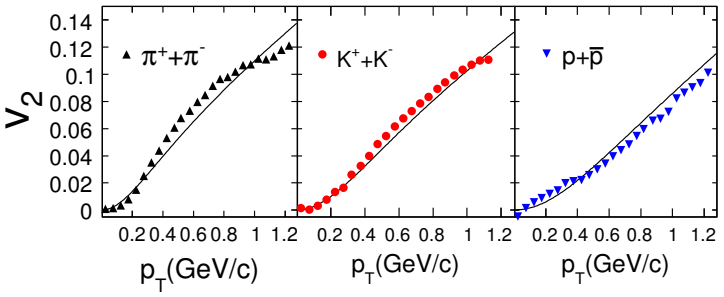

Fig. 4. (Color online) The differential elliptic flow $v_2(p_T)$ for different particle species within $|y_{\rm L}| < 0.1$ at centrality $0-70\%$ for the sample of Au+Au collisions at $\sqrt{s_{NN}} = 200$ GeV generated by the AMPT model with string melting.

blast-wave parametrization. So they are consistent.

5. Summary

We suggest a measurement for the azimuthal distribution of mean transverse rapidity. It consists of two parts: isotropic, and anisotropic mean transverse rapidity. The isotropic part is the combination of isotropic radial expansion and thermal motion. It is demonstrated to be consistent with expected the mass ordering. The anisotropic part presents the anisotropic radial expansion. Its centrality dependence is shown to be consistent with extracted the parameter of anisotropic radial flow rapidity. The suggested distribution provides a model independent way to get the parameter of anisotropic radial flow rapidity. It is helpful for hydrodynamic calculations, and a model independent determination of shear viscosity [37].

Acknowledgments

This work is supported in part by the Major State Basic Research Development Program of China under Grant No. 2014CB845402, the NSFC of China with project No. 11221504, and the MOE of China for doctoral site with project No. 20120144110001.

References

[1] K. Adcox *et al.* (PHENIX Collaboration), Nucl. Phys. A **757**, 184 (2005); J. Adams *et al.* (STAR Collaboration), Nucl. Phys. A **757**, 102 (2005);

B.B. Back *et al.* (PHOBOS Collaboration), Nucl. Phys. A **757**, 28(2005); I. Arsene *et al.* (BRAHMS Collaboration), Nucl. Phys. A **757**, 1 (2005).

[2] M. Gyulassy, L. McLerran, Nucl. Phys. A **750** 30 (2005); B. Müller, Annu. Rev. Nucl. and Part. Phys. **1** (2006).

[3] J.Y. Ollitrault, Phys. Rev. D **46**, 229 (1992); H. Sorge, Phys. Rev. Lett. **78**, 2309 (1997); K.H. Ackermann *et al.* (STAR Collaboration), Phys. Rev. Lett. **86**, 402 (2001); Adams *et al.* (STAR Collaboration), Phys. Rev. Lett. **92**, 052302 (2004).

[4] S.A. Voloshin, A.M. Poskanzer, and R. Snellings, arXiv:0809.2949.

[5] P. Huovinen, P.F. Kolb, U. Heinz, P.V. Ruuskanen, and S. Voloshin, Phys. Lett. B **503**, 58 (2001).

[6] F. Retiere and M.A. Lisa, Phys. Rev. C **70**, 044907 (2004).

[7] L.D. Landau, E.M. Lifschitz, Fluid Mechanics, Insti- tute of Physical Problems, U.S.S.R. Academy of Sci- ences, Volume 6, Course of Theoretical Physics.

[8] P.F. Kolb, J. Sollfrank, U. Heinz, Phys. Lett. B **459**, 667 (1999).

[9] P. Huovinen and P.V. Ruuskanen, Ann. Rev. Nucl. Part. Sci. **56**, 163 (2006); D.A. Teaney, arXiv:0905.2433.

[10] Huichao Song, arXiv:0908.3656.

[11] Li Lin, Li Na, and Wu Yuanfang, Chinese Physics C **36**, 423 (2012).

[12] E. Schnedermann, J. Sollfrank, and U.W. Heinz, Phys. Rev. C **48**, 2462 (1993).

[13] W. Broniowski and W. Florkowski, Phys. Rev. Lett. **87**, 272302 (2001).

[14] J.K. Nayak and Jan-e Alam, Phys. Rev. C **80**, 064906 (2009).

[15] P. Mohanty, J.K. Nayak, Jan-e Alam, and S. K. Das, arXiv:0910:4856.

[16] B. Zhang, C.M. Ko, B.A. Li, and Z.W. Lin, Phys. Rev. C **61**, 067901 (2000).

[17] Zi-Wei Lin, Che Ming Ko, Bao-An Li, Bin Zhang, and Subrata Pal, Phys. Rev. C **72**, 064901 (2005).

[18] S. Voloshin, Y. Zhang, Z. Phys. C **70**, 665 (1996).

[19] S.A. Voloshin, A.M. Poskanzer, and R. Snellings, arXiv:0809.2949.

[20] Z.W. Lin and C.M. Ko, Phys. Rev. C **65**, 034904 (2002).

[21] P. Braun-Munzinger and J. Stachel, Nature **448** Issue 7151, 302 (2007).

[22] J. Adams *et al.* (STAR Collaboration), Phys. Rev. C **72**, 014904 (2005).

[23] B.I. Abelev *et al.* (STAR Collaboration) Phys. Rev. C **79**, 034909 (2009).

[24] J. Adams *et al.*, Phys. Rev. Lett. **92**, 112301 (2004).

[25] W. Broniowski, A. Baran, and W. Florkowski, AIP Conf. Proc. **660**, 185 (2003) [nucl-th/0212053].

[26] P.J. Siemens and J.O. Rasmussen, Phys. Rev. Lett. **42**, 880 (1979).

[27] J.D. Bjorken, Phys. Rev. D **27**, 140 (1983).

[28] F. Cooper and G. Frye, Phys. Rev. D **10**, 186 (1974).

[29] C. Tsallis, J. Stat. Phys. **52**, 479 (1988).

[30] Ming Shao, Li Yi, Zebo Tang, Hongfang Chen *et al.*, J. Phys. G **37**, 085104 (2010).

[31] Zebo Tang *et al.*, arXiv:1101.1912.

[32] C.-Y. Wong, Phys. Rev. C **78**, 054902 (2008).

[33] A.M. Poskanzer, J. Phys. G **30**, S1225 (2004).

[34] Yongseok Oh, Zi-Wei Lin, Che Ming Ko, Phys. Rev. C **80**, 064902 (2009).

[35] J.-Y. Ollitrault, Phys. Rev. D **46**, 229 (1992).

[36] Shan Lianqiang, J. Phys. G: Nucl. Part. Phys. **36**, 055003 (2009).

[37] Wang Meijuan, Li Lin, Liu Lianshou, and Wu Yuanfang, J. Phys. G: Nucl. Part. Phys. **36**, 064070 (2009).

The potential importance of low luminosity and high energy at the LHC

Alan R. White

Argonne National Laboratory, Argonne, Illinois 60439, USA

Low luminosity runs at higher LHC energy could provide definitive evidence for an electroweak scale sextet quark sector of QCD that produces electroweak symmetry breaking and dark matter within the bound-state S-Matrix of QUD - a massless, weak coupling, infra-red fixed-point, SU(5) field theory that might underly and unify the full Standard Model.

1. Introduction

The "nightmare scenario" seems to be emerging at the LHC. A resonance has been discovered that looks a lot like a Standard Model Higgs boson, but no other new physics is seen! In particular, the much anticipated manifestation of supersymmetry has not happened. Theoretical inconsistency implies there must be more, but there is no indication what to look for and there is much concern that the current theoretical framework for new physics searches may be seriously misdirected.

QUD[1] is a massless, weak coupling, infra-red fixed-point, SU(5) field theory that I have discovered as having a massive bound-state S-Matrix that is generated by infra-red chirality transition anomalies and that, uniquely, contains the unitary Critical Pomeron. Unbelievably (almost!), QUD might also underly and unify the S-Matrix of the full Standard Model. Moreover, unitarity may require the presence of a Higgs-like boson resonance.

If the QUD S-Matrix is the origin[2] of the Standard Model then, in addition to small neutrino masses, the only "new physics" is an electroweak scale, strongly interacting, sextet quark sector of QCD that provides electroweak symmetry breaking and dark matter, but is hard to isolate at large $p_\perp$. The dynamics is conceptually radical (within today's theory paradigm), and a calculational procedure has still to be developed. Nevertheless, the implications of QUD's existence are overwhelming. Suggestive evidence already exists and low luminosity runs at higher LHC energy could be definitive.

[1] Quantum Uno/Unification/Unique/Unitary/Underlying Dynamics

[2] The Standard Model could be reproducing the "Unique Unitary S-Matrix."

2. The Critical Pomeron and the Formulation of QUD

The Reggeon Field Theory Critical Pomeron is the only known description of rising total cross-sections[3] that satisfies full multiparticle t-channel unitarity and all s-channel unitarity constraints. The supercritical phase occurs *uniquely* in superconducting QCD, and the critical behavior appears when asymptotic freedom is saturated. Saturation is achieved with 6 color triplet quarks and 2 color sextet quarks and is physically realistic if "sextet pions" produce electroweak symmetry breaking!

QCD sextet quarks with the right electroweak quantum numbers, plus the electroweak interaction, embed uniquely (with asymptotic freedom and no anomaly) in QUD, i.e., SU(5) gauge theory with left-handed massless fermions in the $5\oplus15\oplus40\oplus45^*$ representation. Under $SU(3)\otimes SU(2)\otimes U(1)$

$$5 = (3,1,-\frac{1}{3}) + (1,2,\frac{1}{2}) \ , \qquad 15 = (1,3,1) + (3,2,\frac{1}{6}) + (6,1,-\frac{2}{3}) \ ,$$

$$40 = (1,2,-\frac{3}{2}) + (3,2,\frac{1}{6}) + (3^*,1,-\frac{2}{3}) + (3^*,3,-\frac{2}{3}) + (6^*,2,\frac{1}{6}) + (8,1,1) \ ,$$

$$45^* = (1,2,-\frac{1}{2}) + (3^*,1,\frac{1}{3}) + (3^*,3,\frac{1}{3}) + (3,1,-\frac{4}{3}) + (3,2,\frac{7}{6}) + (6,1,\frac{1}{3}) + (8,2,-\frac{1}{2})$$

Astonishingly, there are 3 "generations" of both leptons and triplet quarks, and QUD is vector-like wrt SU(3)xU(1)$_{em}$. SU(2)xU(1) is not quite right, but if the anomaly-dominated S-Matrix can be constructed via multi-regge theory, as I have outlined [1], all elementary fermions are confined and Standard Model interactions and states emerge.

3. QUD Multi-Regge Theory

In multi-regge limits, infinite momentum bound-states and interactions can be studied using $k\perp$ reggeon diagrams. The removal of fermion masses introduces "anomaly vertices" and after the (crucially ordered) removal of gauge boson masses and a cut-off $k_\perp^\lambda$, an overall divergence[4] produces a "wee parton vacuum" of universal anomalous wee gauge bosons (SU(5) adjoint $C\neq\tau$) as illustrated in Fig. 1. The surviving interactions couple via anomalies and preserve the vector SU(3)xU(1) symmetry. They are

1. *Even Signature Critical Pomeron ≈ SU(3) gluon reggeon + wee gauge bosons. No BFKL pomeron and no odderon.*
2. *Odd Signature Photon ≈ U(1)$_{em}$ gauge boson + wee gauge bosons.*
3. *Electroweak Interaction ≈ left-handed gauge boson, mixed with sextet pion (via anomalies), + wee gauge bosons.*

Anomaly color factors, in wee gauge boson infinite sums, enhance couplings — hopefully to Standard Model values ($\alpha_{QCD} \gg \alpha_{QUD} \sim \frac{1}{120}$).

[3] A necessity to match with an asymptotically-free gauge theory at short distances.

[4] After elaborate cancelations of reggeization of infra-red divergences.

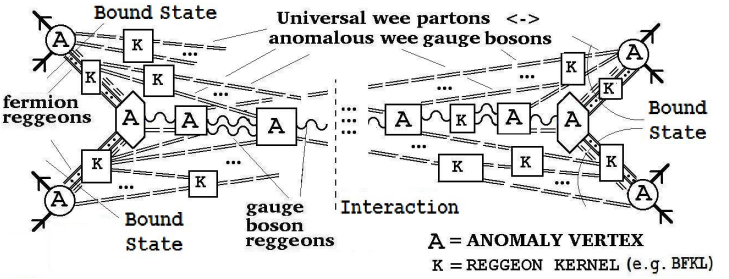

Fig. 1. The general form of divergent Reggeon diagrams.

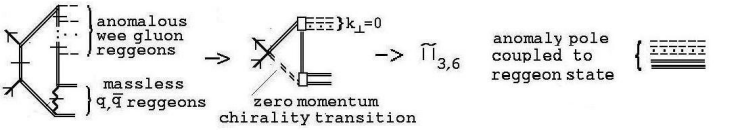

Fig. 2. The anomaly pole Goldstone pion.

Bound-states involve anomaly poles due to chirality transitions, e.g., Goldstone pions in QCD as illustrated in Fig. 2. Within QCD, confinement and chiral symmetry breaking coexist with a "parton model."

- *Bound-states are triplet or sextet quark mesons and baryons. The proton and neuson ("dark matter" sextet neutron) are stable. There are no hybrids and no glueballs.*
- *Sextet anomaly color factors are much larger than triplets and so (electroweak scale) sextet masses are correspondingly larger.*
- *Wee gluon color factors give large pomeron couplings to sextet states, producing large high-energy x-sections and large couplings to (pomeron producing) high-multiplicity hadron states.*

Within QUD, ultra-violet octet quark anomaly poles produce Standard Model generations of physical hadrons and leptons. Lepton bound states contain three elementary leptons:

- $(e^-,\nu) \leftrightarrow (1,2,-\frac{1}{2})\times\{(1,2,-\frac{1}{2})(1,2,\frac{1}{2})\}_{AP}\times\{(8,1,1)(8,2,-\frac{1}{2})\}_{UV}$
- $(\mu^-,\nu) \leftrightarrow (1,2,\frac{1}{2})\times\{(1,2,-\frac{1}{2})(1,2,-\frac{1}{2})\}_{AP}\times\{(8,1,1)(8,2,-\frac{1}{2})\}_{UV}$
- $(\tau^-,\nu) \leftrightarrow (1,2,-\frac{3}{2})\times\{(1,2,\frac{1}{2})(1,2,\frac{1}{2})\}_{AP}\times\{(8,1,1)(8,2,-\frac{1}{2})\}_{UV}$

Anomaly interactions imply $M_{hadrons} \gg M_{leptons} \gg M_{\nu's} \sim \alpha_{QUD}$. The electron is almost elementary (the anomaly pole is, effectively, a minimal disturbance of the Dirac sea). The muon has the same constituents in a more massive dynamical configuration!

4. "Top" and "Higgs" Physics

The primary decay of the "sextet η" is $\eta_6 \to W^+\,W^-Z^0 \;\to\; W^+\,W^-\,b\bar{b}$ (cf. $\eta \to \pi^+\pi^-\pi^0$). Since this is the dominant Standard Model $t\bar{t}$ decay mode, the η_6 resonance produces events that are experimentally hard to distinguish from Standard Model top physics. However, it is the sextet quark mass scale that is involved, and not a "bizarrely large" triplet quark mass!

Two QUD triplet quark generations give Standard Model hadrons. The third is $(3, -\frac{1}{3}) \;\equiv\; [3, 1, -\frac{1}{3}] \;\in 5,\; (3, \frac{2}{3}) \;\in [3, 2, \frac{7}{6}] \;\in 45^*$. The physical b quark is a mixture of all three QUD generations. However, there are two "exotic" triplet quarks with charges -4/3 and 5/3 that have no chiral symmetry and so do not produce light (anomaly pole) bound-states. The left-handed "top quark" (t_{QL}) forms an electroweak doublet with one of the exotic quarks and so will not appear in low mass states. (The electroweak interaction is enhanced, at high energy, by the sextet quark sector.) The $\eta_t \approx t_{QR}\bar{t}_{QL}$ remains as a "constituent t_Q state." Mixing with the sextet η gives two mixed-parity scalars — the η_6 with electroweak scale mass and the η_3, with a mass between triplet and sextet scales that, could be ~ 125 GeV! If so, the "QUD Higgs" is predominantly a "top/anti-top" resonance.

Because QUD interactions are reggeized, intermediate state cancelations must occur that are equivalent to the "tree-unitarity" condition determining electroweak Higgs couplings in the Standard Model. Consequently, the combined $\hat{\eta}_3$ and $\hat{\eta}_6$ couplings should reproduce Standard Model couplings and disparities between the 125 GeV resonance and the Standard Model Higgs should be accounted for by the η_6.

5. At the LHC ?

The most direct evidence for QUD is the appearance of the η_6 resonance, in the Z-pair cross section, at the "$t\bar{t}$" threshold. As can be seen from Fig. 3, it is most visible in the lower luminosity 7 GeV data. Is ultra-high luminosity missing QUD cross sections (as we will suggest often in the following)?

Large pomeron couplings to π_6's ($\equiv$ longitudinal W's/Z's) implies large rapidity-gap cross sections for multiple W's/Z's (i.e. sextet isospin conserving WW, ZZ, WWZ, ZZZ, ...) above the EW scale, including a large double-pomeron cross section for Z^0Z^0 and W^+W^- pairs (some of these events might be identified, partially or fully, via jets). There should also be (correlated) much larger, cross sections for multiple W's/Z's, over a wide range of rapidities, with high associated hadron multiplicity — that are the intermediate states of the pomeron. At higher energies, multiple sextet baryons — "neusons" (dark matter) and "prosons" will be similarly produced. Growing cross sections, coupling pomeron and electroweak physics

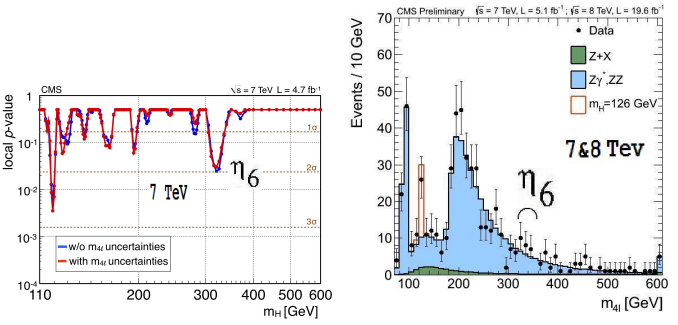

Fig. 3. The η_6 at the LHC.

are clearly what should be looked for at the highest LHC energy. However, *low luminosity is essential!*

Existing evidence, appropriately interpreted, includes

1. *"Heavy Ion" UHE cosmic rays are dark matter neusons.*
2. *The spectrum knee is due to arriving/produced neuson thresholds.*
3. *Enhancement of high multiplicities and small $p_\perp$ at the LHC reflects a sextet anomaly generated triple pomeron coupling.*
4. *"Top quark events" are due to the η_6 resonance — interference with the background produces the Tevatron asymmetry.*
5. *W^+W^- and Z^0Z^0 pairs have high mass excess cross sections, with the η_6 resonance appearing at the "$t\bar{t}$ threshold".*
6. *The 125 GeV Higgs is the QUD ($t_R\bar{t}_L$ + η_6) resonance.*
7. *The AMS e^+/e^- ratio reflects EW scale CR production of W's and Z's (+ neuson/antineuson annihilation?)*
8. *Low luminosity Tevatron/LHC events with a Z pair + high multiplicity of small $p_\perp$ particles, could be QUD (not Standard Model) events.*
9. *TOTEM+CMS missing momentum events could be $ZZ \rightarrow \nu$'s*

6. The Low Luminosity Events

Interesting events were seen with initial low luminosity at the Tevatron and the LHC, and also in the recent TOTEM-CMS low luminosity run.

The first CDF Z^0Z^0 event, shown in Fig. 4, was recorded in 2004 — before pile-up! It was first counted as a Z^0Z^0 event, then rejected because one electron was insufficiently isolated, and finally counted. It has some remarkable features. A cut-off $E_T > 500$ MeV leaves only a few extra particles, but with $E_T > 100$ MeV, many more (> 70) fill the rapidity

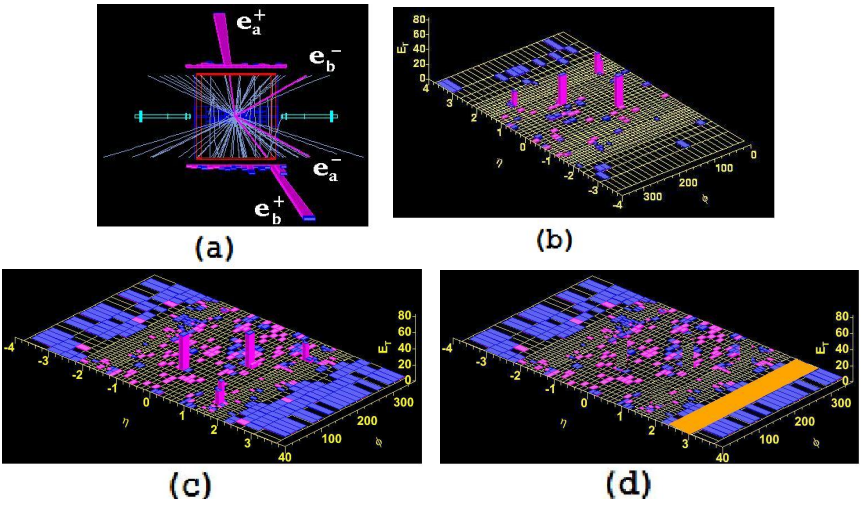

Fig. 4. (a) $p_\perp > 200$ MeV, (b) $E_T > 500$ MeV, (c) $E_T > 100$ MeV (d) Z^0Z^0 production region.

axis away from the very forward Z^0Z^0 production region which, as shown in Fig. 4(d), is almost out of the detector. While this is *just what would be expected for QUD events*, a 4 electron event would have been very rare in the Standard Model with the very small accumulated luminosity. Also, the very high hadron multiplicity (which was discovered serendipitously) is unexpected in the Standard Model. Unfortunately, pile-up made looking for similar events at the Tevatron impossible. So, was this event part of a (QUD predicted) forward cross section that was almost entirely missed?

The first CMS Z^0Z^0 event (4 $\mu's$), shown in Fig. 5, was recorded when the accumulated luminosity was ∼2-3 pb^{-1}. Therefore, naively, from ∼25 fb^{-1} we might expect ∼ 10,000 Z^0Z^0 events, yet only ∼ 400 have been seen! It is a remarkably clean event; with $p_\perp > 1$ GeV there are only two extra particles. With no cut-off there are twenty additional particles which all have momenta in one or the other of the two forward directions. Also $< n >$ *and* $< p_\perp >$ are close to minimum bias. Moreover, both Z^0's are very central and $p_\perp$(ZZ) is unusually low ∼ 3 GeV. Clearly, this does not look like a Standard Model hard scattering event! Could it also have been part of a QUD cross section, containing Z^0 pair events distributed over a wide range of rapidities, that were largely unseen because of pile-up?

A CMS 4e event with pile-up is shown in Fig. 6. The line of scattering vertices is clear. Not only is it obviously impossible to determine any properties of associated soft hadrons produced with the Z^0 pair, also more forward-going leptons and photons will surely be very difficult to isolate!

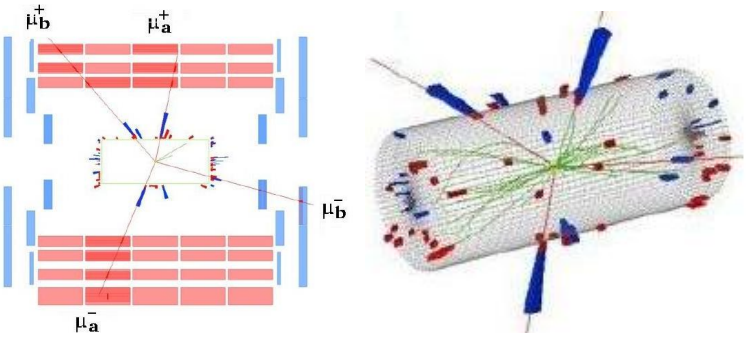

Fig. 5. The first CMS Z^0Z^0 event.

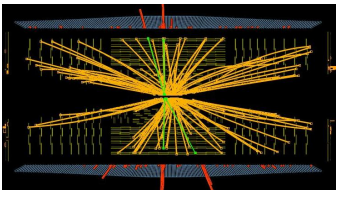

Fig. 6. A CMS Z^0Z^0 event with pile-up.

In the recent CMS-TOTEM special run, the rapidity coverage was

$$\text{CMS: } |\eta| < 5.5,\ \text{T1: } 3.1 < |\eta| < 4.7,\ \text{T2: } 5.3 < |\eta| < 6.5,\ \text{FSC: } 6 < |\eta| < 8$$

For events with clearly isolated forward-going protons, and with rapidity gaps imposed outside of T2, the central M_{TOT} calculated from TOTEM Roman pot measurements was compared with M_{CMS} measured in the central CMS detector. In events where $M_{CMS} \ll M_{TOT}$ corresponding additional tracks were generally seen in the TOTEM T2 detector. However, in some events no additional tracks were seen and in a few the missing mass was as high as O(400) GeV. Could these events include $Z^0Z^0 \longrightarrow 4\nu$'s, as part of the large rapidity QUD Z^0Z^0 cross section?

7. The Low Luminosity Future?

QUD cross sections should increase with energy, but increased high luminosity could still hide signals and, moreover, low luminosity runs will be short and focus on small $p_\perp$ physics. However, CMS-TOTEM is working well — with beautiful double-pomeron multi-jet event displays and also "missing mass" events recorded. Assuming a major part of the cross section has been missed at high luminosity, as I have argued, then some Z^0Z^0 and W^+W^- pairs could be seen in the CMS detector, even at low luminosity.

The unprecedented wide rapidity coverage of rapidity gaps and hadron multiplicities suggests that direct evidence for the link between pomeron and electroweak physics, that I have described could be seen!

If the "nightmare scenario" persists after extensive high luminosity running, and significant evidence of new phenomena is seen in brief low luminosity runs, we might hope (very optimistically) that, eventually, there could be a transition to full-time low luminosity — with modified detectors? If it is present, QUD physics would provide a rich and exciting program with a wide variety of phenomena.

8. Some QUD Virtues

- QUD is self-contained and is either entirely right, or simply wrong!
- The scientific and aesthetic importance of an underlying massless field theory for the Standard Model can not be exaggerated.

If hard evidence of an electroweak scale strong interaction appears, supporting the existence of QUD, there will be a *(perhaps needed?)* radical redirection of the field, from the pursuit of rare, elusive, probably nonexistent, short-distance physics, to the full-scale study of novel high-energy, unexpectedly large cross section, long-distance physics.

Assuming the QUD S-Matrix can be derived as I have outlined, then

1. *The only new physics is a high mass sector of the strong interaction that gives electroweak symmetry breaking and dark matter.*
2. *Parity properties of the strong, electromagnetic, and weak interactions are naturally explained.*
3. *The massless photon partners the "massless" Critical Pomeron.*
4. *Anomaly vertices mix the Reggeon states. Color factors could produce the wide range of Standard Model scales and masses, with small Majorana neutrino masses due to the very small QUD coupling.*
5. *Particles and fields are truly distinct. Physical hadrons and leptons have equal status.*
6. *Symmetries and masses are S-Matrix properties. There are no off-shell amplitudes and there is no Higgs field.*
7. *As a massless, asymptotically free, fixed-point theory, QUD induces Einstein gravity with zero cosmological constant.*

References

[1] Considerable background, including references, is provided in a series of papers by A.R. White, arXiv:1106.5662; arXiv:1009.4850; arXiv:0803.1151; arXiv:0708.1306; arXiv:1206.0192; arXiv:1301.5628.

Measurement of the strong coupling α_S from the 3-jet rate in e^+e^- annihilation using JADE data

S. Kluth

Max-Planck-Institut für Physik, Föhringer Ring 6, 80805 Munich, Germany

for J. Schieck, S. Bethke, SK, C. Pahl, Z. Trócsányi, and the JADE Collaboration

We describe a measurement of the strong coupling $\alpha_S(M_{Z^0})$ from the 3-jet rate in hadronic final states of e^+e^- annihilation recorded with the JADE detector at centre-of-mass energies of 14 to 44 GeV. The jets are reconstructed with the Durham jet clustering algorithm. The JADE 3-jet rate data are compared with QCD predictions in NNLO combined with resummed calculations. We find good agreement between the data and the prediction and extract

$\alpha_S(M_{Z^0}) = 0.1199 \pm 0.0010(\text{stat.}) \pm 0.0021(\text{exp.}) \pm 0.0054(\text{had.}) \pm 0.0007(\text{theo.})$.

1. Introduction

We report on a precision measurement of $\alpha_S(M_{Z^0})$ from the 3-jet rate R_3 in hadron production in e^+e^- annihilation[1]. The data were recorded with the JADE experiment at the PETRA e^+e^- collider operated at DESY from 1979 to 1986. The jets are defined with the Durham algorithm and the data for the R_3 are compared with combined next-to-next-leading-order (NNLO) and next-to-leading-log (NLLA) QCD calculations [2]. The first measurement of α_S from R_3 with NNLO QCD calculations was shown in [3].

Even though the data for this analysis was recorded more than 27 years ago the results of this study are still valuable. Firstly, we obtain a precision determination of the strong coupling constant. Secondly, we can provide strong consistency checks of the recent QCD calculations based on theoretical progress also relevant for predictions for the LHC experiments.

2. JADE detector and data

The JADE detector was a universal and hermetic detector covering a solid angle of almost 4π. The interaction point was surrounded by a large

[1] This article is a revised version of [1].

tracking detector (jet chamber) of 1.6 m diameter and 2.4 m length inside a solenoid magnet coil with a magnetic field of 0.48 T. Outside of the magnetic coil was the electromagnetic calorimeter consisting of 2520 lead glass blocks in the barrel section and 96 lead glass blocks in each endcap with a total acceptance of 90% of 4π. The measurement of hadronic final states relies mainly on these two detector systems. More details can be found e.g. in [4]. A technical drawing of the JADE detector is shown in figure 1.

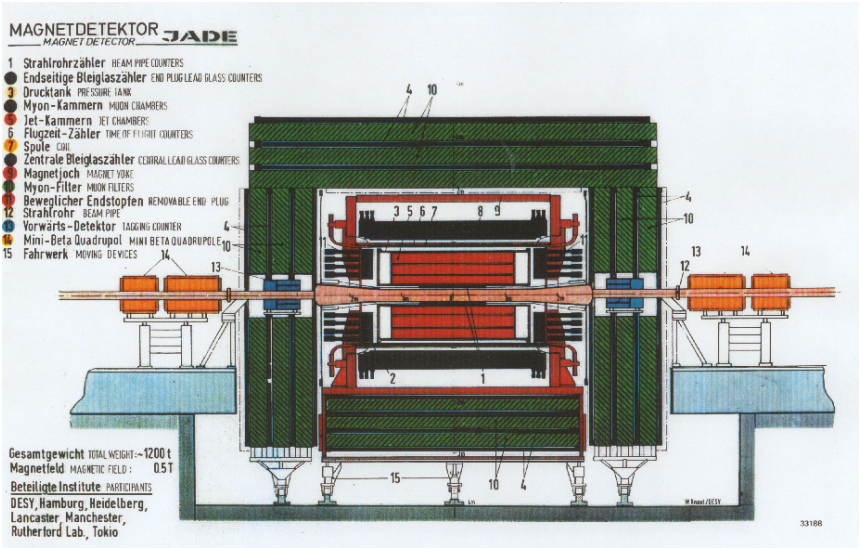

Fig. 1. The JADE detector.

The data used in the analysis are from the JADE experiment which operated at the PETRA e^+e^- collider at DESY in Hamburg, Germany, from 1979 to 1986. The main data samples were collected at centre-of-mass (cms) energies of 14, 22, 35, 38 and 44 GeV. The integrated luminosities range from about 1/pb at 14 and 22 GeV to about 100/pb at 35 GeV and correspond to sample sizes of $O(10^3)$ events at 14, 22, 38 and 44 GeV and $O(10^5)$ events at 35 GeV.

3. QCD predictions

The Durham jet clustering algorithm [5] defines $y_{ij} = 2\min(E_i, E_j)^2(1-\cos\theta_{ij})/s$ as distance in phase space between a pair of particles or jets i and j with energies E_i, E_j and angle θ_{ij} between them. The pair with the smallest y_{ij} is combined by adding their 4-vectors, the particles or jets i, j are removed and the combined 4-vector is added. This procedure is repeated

until all $y_{ij} > y_{\rm cut}$. The 3-jet rate for a given value of $y_{\rm cut}$ at a cms energy $Q = \sqrt{s}$ is defined as $R_3(y_{\rm cut}, Q) = N_{3-jet}(y_{\rm cut}, Q)/N(Q)$, where N_{3-jet} is the number of 3-jet events and N is the total number of events in the sample. The 3-jet rate is a measurement of $\sigma_{3-jet}(y_{\rm cut}, Q)/\sigma_{had}(Q)$ where $\sigma_{3-jet}(y_{\rm cut}, Q)$ is the exclusive 3-jet cross section and $\sigma_{had}(Q)$ is the total hadronic cross section.

The NNLO QCD prediction [6, 7] can be written as:

$$R_{3,NNLO}(y_{\rm cut}, Q) = A(y_{\rm cut})\hat{\alpha}_{\rm S}(Q) + B(y_{\rm cut})\hat{\alpha}_{\rm S}^2(Q) + C(y_{\rm cut})\hat{\alpha}_{\rm S}^3(Q) \quad (1)$$

with $\hat{\alpha}_{\rm S}(Q) = \alpha_{\rm S}(Q)/(2\pi)$. The coefficient functions $A(y_{\rm cut})$, $B(y_{\rm cut})$ and $C(y_{\rm cut})$ are obtained by numerical integration of the QCD matrix elements in LO, NLO or NNLO. The resummed NLLA calculations use an improved resummation scheme [8] including the so-called K-term to take some subleading logarithmic terms into account and are matched to the NNLO prediction [2]. Figure 2 (left) shows these QCD predictions as black band with theory uncertainties defined by changing the renormalisation scale of the theory μ by a factor of 1/2 or 2. The other bands show NLO and NLO+NLLA+K predictions for comparison. The theoretical uncertainties of the NNLO+NLLA+K prediction are significantly smaller compared to the less advanced predictions.

4. Data analysis

The data from the JADE experiment for the 3-jet rate R_3 are corrected for the effects of detector resolution and acceptance and for photon initial state radiation to the so-called hadron-level using samples of simulated events. The expected contributions from $\mathrm{e^+e^-} \to \mathrm{b\bar{b}}$ events are subtracted. The Monte Carlo generators PYTHIA 5.7, HERWIG 6.2 or ARIADNE 4.11 with parameter settings from OPAL are used to produce the simulated events together with a full simulation of the JADE detector. The corrected data for R_3 are well described by the simulations.

The QCD predictions have to be corrected for effects of the transition from the partons (quarks and gluons) of the theory to the particles of the hadronic final state. These so-called hadronisation corrections are taken from the samples of simulated events by comparing R_3 values after the parton shower has stopped (parton-level) and the hadron-level consisting of all particles with a lifetime larger than 300 ps. OPAL has compared for the observable [2] y_{23} the parton-level predictions of the NNLO+NLLA theory and the simulations and found agreement within the differences between the three simulations [9]. Thus it is justified to use the simulations to derive the

[2] The distribution of y_{ij} values for which events change from 2 jets to 3 jets.

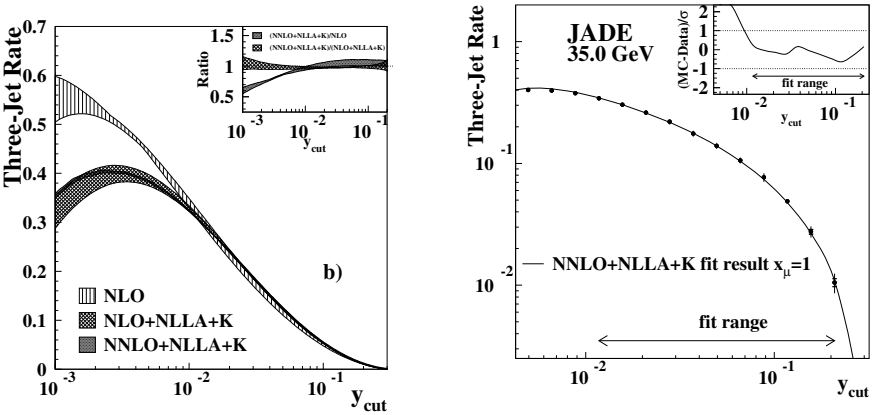

Fig. 2. (left) QCD predictions for R_3 in NLO, NLO+NLLA+K and NNLO+NLLA+K are shown by bands as indicated on the figure. The widths of the bands reflect the renormalisation scale uncertainty. (right) Fit of the NNLO+NLLA+K prediction to the R_3 data at $\sqrt{s} = 35$ GeV corrected for experimental effects. The data points included in the fit are indicated by the horizontal arrow. The insert shows the difference between data and fitted QCD prediction divided by the combined statistical and experimental error [2].

hadronisation corrections, since the hadronisation systematic uncertainty evaluated by comparing the three simulations covers any discrepancies.

The theory is compared with the data using a χ^2-fit with α_S as a free parameter. The statistical correlations between the data points for $R_3(y_{\rm cut})$ are taken into account. Only data points within a restricted range of $y_{\rm cut}$ are used in the fits to ensure that the experimental and hadronisation corrections are under control and that the QCD predictions are reliable.

Several sources of systematic uncertainty are investigated. Experimental uncertainties are evaluated by repeating the analysis with different event selection cuts, reconstruction calibration versions, samples of simulated events to derive the corrections for experimental effects, and with different fit ranges. The experimental uncertainties are dominated by the different detector calibrations and the experimental corrections based on PYTHIA or HERWIG. Hadronisation uncertainties are estimated by changing the Monte Carlo generator for hadronisation corrections from PYTHIA to HERWIG or ARIADNE. The differences between PYHTIA and HERWIG determine this uncertainty. Theoretical systematic uncertainties are found by repeating the fits with the renormalisation scale factor $x_\mu = \mu/Q$ changed from $x_\mu = 1$ to 0.5 or 2.

5. Results

The fit of the NNLO+NLLA+K QCD prediction to the 3-jet rate data at $\sqrt{s} = 35$ GeV is shown in figure 2 (right). The fitted prediction agrees well with the data corrected to the hadron-level within the fit range. The extrapolation to the other data points also gives a good description of the data. For this fit based on statistical errors we find $\chi^2/\text{d.o.f.} = 1.2$. The fits at the other cms energies are similar with $1.2 < \chi^2/\text{d.o.f.} < 4.1$ except at $\sqrt{s} = 14$ GeV where we have $\chi^2/\text{d.o.f.} = 6.3$. At the lowest cms energy the hadronisation corrections are significantly larger compared to the other cms energies. The individual fit results for α_S are shown in figure 3 (left) as a function of the cms energy where they were obtained.

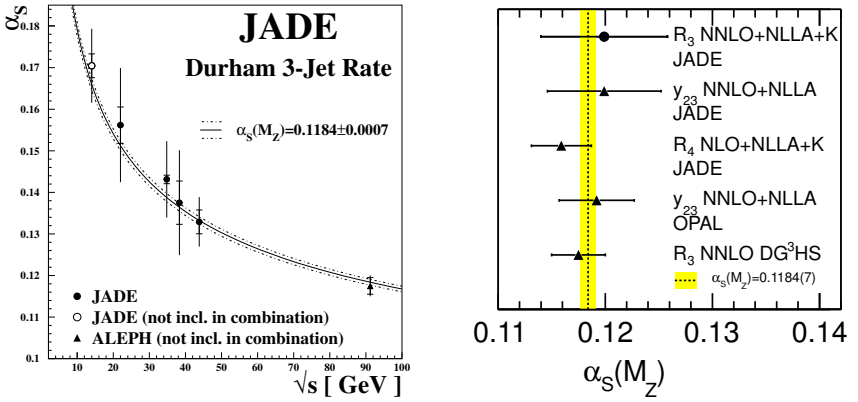

Fig. 3. (left) Results for α_S from the JADE energy points are shown. The lines give the prediction from the 3-loop QCD evolution with uncertainties for the value of $\alpha_S(M_{Z^0})$ as indicated on the figure. (right) The result for $\alpha_S(M_{Z^0})$ from this analysis (solid point) is compared with results from [10, 11, 9, 3] (solid triangles) and the current world average value [12, 13, 14]. The error bars show total errors.

The individual results for α_S are evolved to $\alpha_S(M_{Z^0})$ using the 3-loop evolution equations. Then they are combined into a single value taking account of correlated experiental, hadronisation and theory uncertainties as described in [2]. The result from $\sqrt{s} = 14$ GeV is excluded from the combined value since it has a much larger value of $\chi^2/\text{d.o.f.}$ and larger hadronisation corrections compared to the other results. The combined value is

$$\begin{aligned}\alpha_S(M_{Z^0}) \;=\; & 0.1199 \pm 0.0010(\text{stat.}) \pm 0.0021(\text{exp.}) \pm 0.0054(\text{had.}) \\ & \pm 0.0007(\text{theo.})\,. \end{aligned} \tag{2}$$

The errors are dominated by the hadronisation correction uncertainties.

As a cross check the analysis is repeated with NNLO QCD predictions using the same fit ranges with $x_\mu = 1$. We find larger values of χ^2/d.o.f., a less satisfactory description of the R_3 data and larger uncertainties from variations of the fit ranges compared to the NNLO+NLLA+K fits. The NNLO predictions do not reproduce the slope of the $R_3(y_{\mathrm{cut}})$ data as well as the NNLO+NLLA+K predictions. A similar observation can be made in the analysis of [3].

In figure 3 (right) the result of this analysis is compared with other measurements of $\alpha_{\mathrm{S}}(M_{\mathrm{Z}^0})$ using the 3-jet or 4-jet rate based on the Durham algorithm. The JADE measurement with y_{23} is highly correlated with our measurement using R_3 and the good agreement of the results is a strong consistency check. The agreement with the other results and with the world average value is also satisfactory within the uncertainties.

6. Conclusion

We have shown the first measurement of $\alpha_{\mathrm{S}}(M_{\mathrm{Z}^0})$ using the 3-jet rate with the Durham algorithm and matched NNLO+NLLA+K QCD calculations and data from the JADE experiment. The agreement between data and the NNLO+NLLA+K QCD prediction is improved compared to less advanced predictions. The errors are dominated by the hadronisation correction uncertainties as expected at the low cms energies of the JADE experiment. However, the data of the JADE experiment at comparatively small cms energies can now be analysed with rather good precision thanks to the progress in perturbative QCD calculations and Monte Carlo simulations made since the data were recorded. Our analysis provides an independent and strong cross check on those recent QCD calculations made for the LHC which have related Feynman diagrams or share calculation techniques.

The author would like to thank the organisers of the ISMD 2013 conference for the opportunity to present these results and for a stimulating and fruitful meeting.

References

[1] S. Kluth, arXiv:1206.0065, contribution to "47th Rencontres de Moriond: QCD and High Energy Interactions" (2012).

[2] J. Schieck, S. Bethke, S. Kluth, C. Pahl, Z. Trocsanyi, and the JADE Collaboration, Eur. Phys. J. C **73**, 2332 (2013).

[3] G. Dissertori, A. Gehrmann-De Ridder, T. Gehrmann, E.W.N. Glover, G. Heinrich *et al.*, Phys. Rev. Lett. **104**, 072002 (2010).

[4] B. Naroska, Phys. Rep. **148**, 67 (1987).

[5] S. Catani *et al.*, Phys. Lett. B **269**, 432 (1991).

[6] A. Gehrmann-De Ridder, T. Gehrmann, E.W.N. Glover, and G. Heinrich, Phys. Rev. Lett. **100**, 172001 (2008).

[7] S. Weinzierl, J. High Energy Phys. **0906**, 041 (2009).

[8] Z. Nagy and Z. Trocsanyi, Nucl. Phys. Proc. Suppl. **74**, 44 (1999).

[9] G. Abbiendi *et al.* (OPAL Collaboration), Eur. Phys. J. C **71**, 1733 (2011).

[10] S. Bethke, S. Kluth, C. Pahl, and J. Schieck (JADE Collaboration), Eur. Phys. J. C **64**, 351 (2009).

[11] J. Schieck *et al.* (JADE Collaboration), Eur. Phys. J. C **48**, 3 (2006), Erratum, *ibid.* C **50**, 769 (2007).

[12] S. Bethke, Eur. Phys. J. C **64**, 689 (2009).

[13] K. Nakamura *et al.* (PDG Collaboration), J. Phys. G **37**, 075021 (2010).

[14] J. Beringer *et al.* (PDG Collaboration), Phys. Rev. D **86**, 010001 (2012).

Measurement of hadron production in Deep Inelastic Scattering

H. Jung (on behalf of the H1 Collaboration)
Deutsches Elektronen Synchrotron, D-22603 Hamburg,
Elementaire Deeltjes Fysica, Universiteit Antwerpen, B 2020 Antwerpen

Measurements of charged particle densities and K^0_s and Λ production in deep inelastic scattering at HERA are presented and compared to Monte Carlo event generator predictions. The measurements provide sensitive tests for the initial state parton radiation process as well as for the hadronization process.

1. Introduction

In deep inelastic scattering (DIS) at the *ep* collider HERA small values of Bjorken-x can be accessed where the interaction with the virtual photon may originate from a cascade of partons as illustrated in Fig. 1(left). The transverse momentum spectrum of charged particles measured in deep inelastic scattering is a sensitive probe to parton radiation at the high p_T tail of the spectrum while at small p_T the contribution from hadronization becomes significant. The measurement of strange particle production provides additional information on the hadronization process.

2. Charged Particle Spectra

The charged particle spectra [1] are presented in the hadronic centre-of-mass frame (HCM), to minimize the effect of the transverse boost from the virtual photon. Particles with $\eta^* > 0$ belong to the current hemisphere and particles with $\eta^* < 0$ originate from the target (proton remnant) hemisphere (Fig.1 right).

The charged particle densities as a function of η^* are shown separately for $p_T < 1$ GeV and for $1 < p_T < 10$ GeV in Fig. 2. The sensitivity to hadronization effects obtained with RAPGAP [2] (based on the DGLAP shower evolution) with three sets of fragmentation parameters are compared to the data in Fig. 2: parameters tuned by ALEPH [3], by the Professor collaboration [4] and from default PYTHIA6.424 [5]. Significant differences are visible in the soft p_T region: the data are best described by the ALEPH

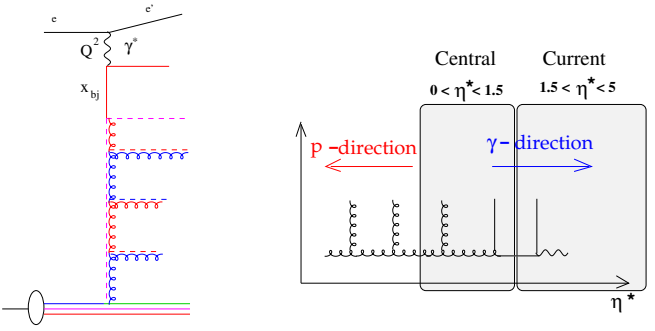

Fig. 1. Left: Schematic diagram for DIS at small x. Right: pseudorapidity regions relevant for charged particle spectra

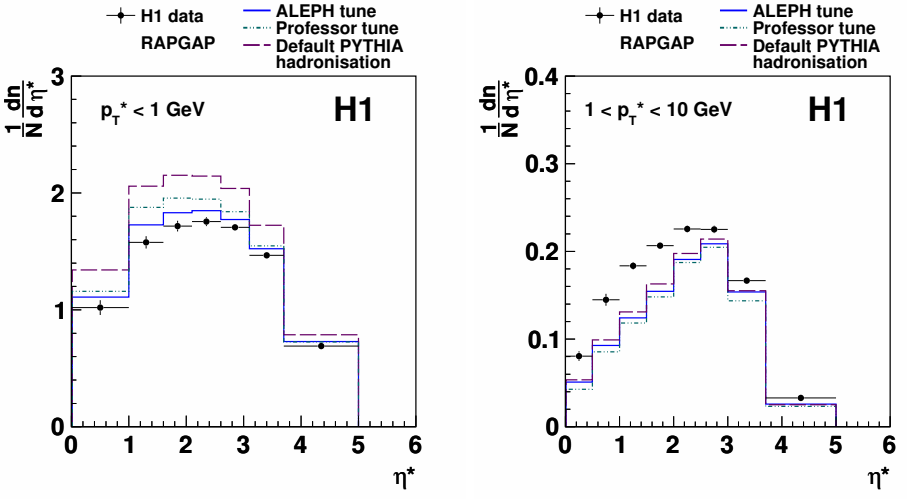

Fig. 2. Charged particle density as a function of η^* compared to RAPGAP predictions for three different sets of fragmentation parameters. The predictions are obtained using CTEQ6L(LO) PDF.

tune. At large transverse momenta none of the fragmentation parameter sets describes the data. In Fig. 3 the charged particle densities are shown as a function of η^* in (x, Q^2) intervals for the range $1 < p_T < 10$ GeV. The shape of the distributions changes with x and Q^2. At small values of x and Q^2 the measured distributions are less dependent on η^* compared to the region at high x and Q^2. However, none of the models describes all aspects of the data. The prediction of CASCADE [6] (based on CCFM) agrees reasonably well with the measurement at low x and Q^2, but overshoots the

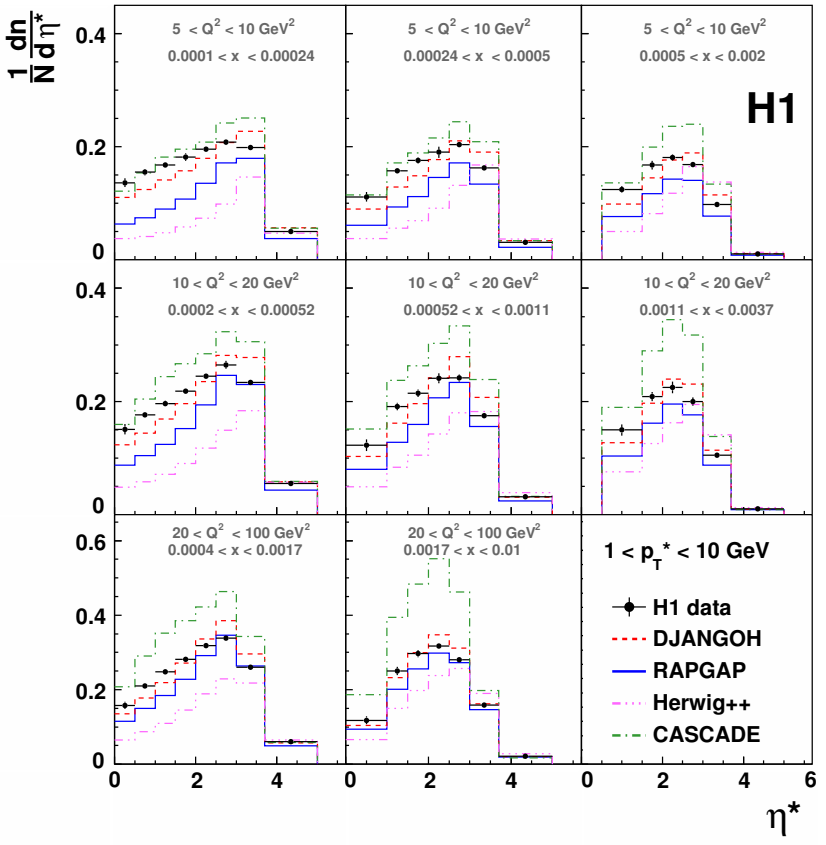

Fig. 3. Charged particle density as a function of η^* for $1 < p_T < 10$ GeV for eight intervals of Q^2 and x compared to different Monte Carlo generator predictions.

data significantly as x or Q^2 increases.

In Fig. 4 the charged particle densities are shown for two pseudorapidity intervals, $0 < \eta^* < 1.5$ (central) and $1.5 < \eta^* < 5$ (current) as a function p_T. The shapes of the distributions in the two pseudorapidity ranges are similar. Only DJANGOH [7] (based on the Color Dipole Model) describes reasonably well the data but shows deviations from the measurements at high pt in the current region. The other models fail to describe the data, with the strongest deviations being observed in the central region. CASCADE in general produces higher particle densities than measured. In summary, at small p_T , the data are reasonably well described by DJANGOH, as well as by RAPGAP. At high p_T and at low η^*, RAPGAP severely undershoots the data. The differences are most pronounced at lowest x and Q^2, and decrease

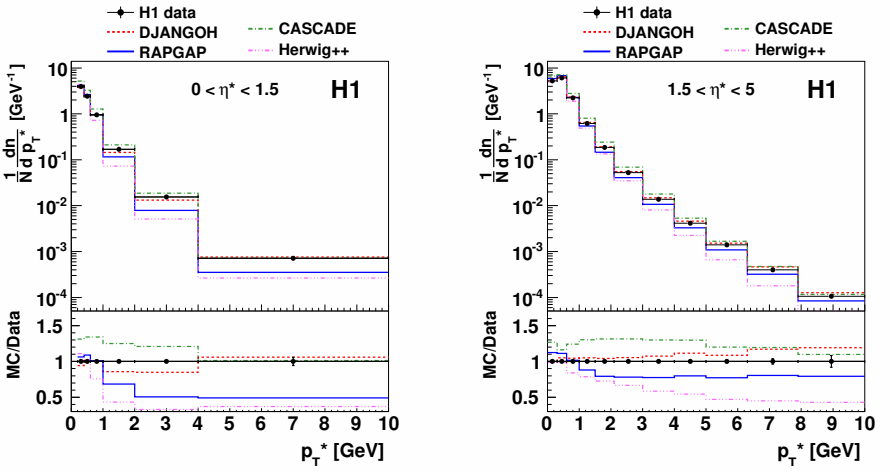

Fig. 4. Charged particle density as a function of p_T for different η^* ranges compared to different Monte Carlo generator predictions.

with increasing x and Q^2 values. CASCADE gives a reasonable description only at the lowest x and Q^2, but overall predicts higher charged particle densities than observed in data. The Color Dipole Model implemented in DJANGOH is the best among the considered models and provides a reasonable description of the data.

3. Measurement of K_s^0 and Λ Baryons

In DIS at HERA strange quarks may be created in the hard sub-process by originating directly from the strange sea of the proton in a quark-parton-model (QPM) like interaction, from boson-gluon-fusion or from the decays of heavy flavored hadrons. The dominant source for strange hadron production, however, is the creation of an $s\bar{s}$ pair in the non-perturbative fragmentation process. In the modeling of the fragmentation process strange quarks are suppressed compared to the production of light quarks, controlled by the strangeness suppression factor λ_s.

The K_s^0 mesons are measured by the kinematic reconstruction of its decay $K_s^0 \to \pi^+\pi^-$ in $7 < Q^2 < 100$ GeV^2, $0.1 < y < 0.6$. The ratio of the differential cross section for K_s^0 [8] production to inclusive charged particle production is shown in Fig. 5 as a function of η and p_T compared to DJANGOH using three different values of the suppression factor λ_s ranging from 0.220 to 0.35. The ratio as a function of η is well described and a high sensitivity on the value of λ_s is observed. However, the shape in p_T is not

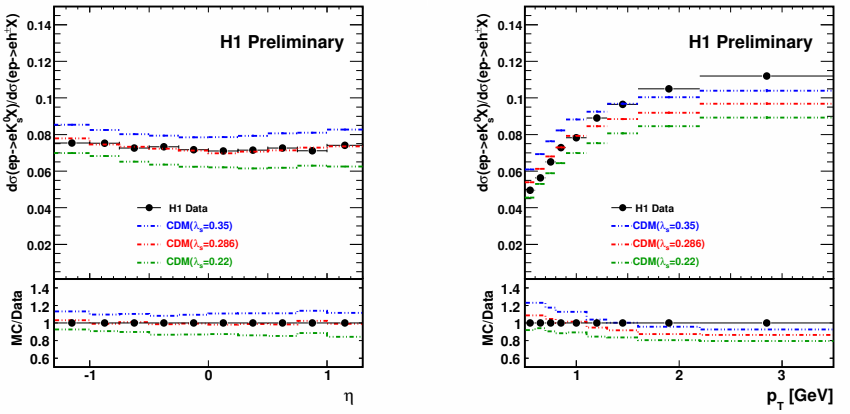

Fig. 5. Ratio of K_s^0 to charged particle production as a function of η and p_T in comparison to DJANGOH (CDM) for three different values of λ_s.

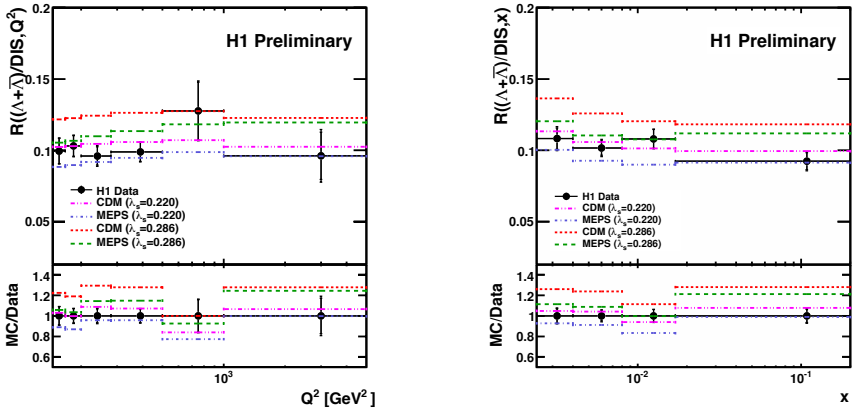

Fig. 6. Ratio R(DIS) of Λ production to the inclusive DIS cross section as a function of (left) the photon virtuality squared Q^2 and (right) Bjorken scaling variable x in comparison to RAPGAP (MEPS) and DJANGOH (CDM) with two different values of λ_s.

well reproduced.

Λ baryons are measured by their decay $\Lambda \to p\pi^-$ in $145 < Q^2 < 20000$ GeV^2, $0.2 < y < 0.6$. In Fig. 6 the ratio of Λ production to inclusive DIS [9] is shown as a function of x and Q^2 and compared to the expectations from RAPGAP and DJANGOH for $\lambda_s = 0.286$ and $\lambda_s = 0.220$. The best

description is provided by DJANGHO using $\lambda_s = 0.220$, different to what is observed for K^0_s production, where the best description is for $\lambda_s = 0.286$.

4. Summary

Charged particle densities in ep collisions have been measured and compared to Monte Carlo event generators. While at small p_T hadronization is dominant and the parameters can be tuned to describe the measurements, at larger p_T hadronization plays little role and parton radiation from the initial state becomes dominant. None of the Monte Carlo generators studied is able to describe the spectrum of charged particles over the full kinematic range.

Strange particle production in DIS is sensitive to the hadronization process and the measurements can be used to determine the suppression of strange particle production compared to pions. The suppression factors which best describe the measurements are different for K^0_s and Λ baryons, indicating that the modeling of strange particle production is more complicated than implemented in the investigated models.

It is important to note, that charged and strange particle production in DIS does not suffer from contributions of multiparton interactions compared to hadron-hadron collisions at the LHC.

Acknowledgments

The author thanks the organizers for this interesting workshop.

References

[1] C. Alexa *et al.* (H1 Collaboration), Eur. Phys. J. C **73**, 2406 (2013).
[2] H. Jung, Comput. Phys. Commun. **86**, 147 (1995).
[3] S. Schael *et al.* (ALEPH Collaboration), Phys. Lett. B **606**, 265 (2005).
[4] A. Buckley, H. Hoeth, H. Lacker, H. Schulz, and J. E. von Seggern, Eur. Phys. J. C **65**, 331 (2010).
[5] T. Sjöstrand, S. Mrenna, and P. Skands, J. High Energy Phys. **05**, 026 (2006).
[6] H. Jung *et al.*, Eur. Phys. J. **C70**, 1237 (2010).
[7] K. Charchula, G. Schuler, and H. Spiesberger, Comput. Phys. Commun. **81**, 381 (1994).
[8] H1 Collaboration, H1prelim-13-033, http://www-h1.desy.de/psfiles/confpap/DIS2013/H1prelim-13-031.pdf.
[9] H1 Collaboration, H1prelim-13-031, http://www-h1.desy.de/psfiles/confpap/DIS2013/H1prelim-13-031.pdf.

Low-energy exclusive cross sections and inclusive production of identified charged hadrons with Babar

J. William Gary

Department of Physics and Astronomy
University of California, Riverside, CA, 92521 USA

Recent measurements of exclusive hadronic cross sections from the Babar Collaboration at SLAC are presented. Specifically, we present results on the $e^+e^- \to K^+K^-(\gamma)$, $p\bar{p}$, K_SK_L, $K_SK_L\pi^+\pi^-$, $K_SK_S\pi^+\pi^-$, and $K_SK_SK^+K^-$ cross sections performed using events with initial-state photon radiation, which allows the cross sections to be measured at low energy and over an extended energy range. In addition, we present results on the inclusive momentum spectra of identified charged pions, kaons, and protons at the fixed center-of-mass energy of 10.54 GeV, allowing new tests of QCD.

1. Introduction

The Babar experiment operated at the PEP-II asymmetric-energy e^+e^- collider at SLAC from 1999-2008. The data analysis is still very active, with around 30 physics publications expected in 2013. Most data were collected at the energy of the $\Upsilon(4S)$ resonance, just above the threshold to produce a $B\overline{B}$ bottom-quark meson pair. The $B\overline{B}$ event sample was (and still is being) used to study CP violation and to probe the physics of the Cabibbo-Kobayashi-Maskawa quark-mixing matrix. Babar also collected large samples of $e^+e^- \to c\bar{c}$ and $e^+e^- \to \tau^+\tau^-$ events and has many results on charm meson and tau lepton physics. The topics of the current presentation are something yet different, however: events with initial-state photon radiation (ISR), which give access to measurements of low-energy exclusive e^+e^- cross sections, and recent results on the inclusive production of identified charged hadrons ($\pi^\pm$, $K^\pm$, p) at the fixed center-of-mass energy of 10.54 GeV.

2. The $e^+e^- \to K^+K^-(\gamma)$ cross section and $K^\pm$ form factor

Our recent measurement of the $e^+e^- \to K^+K^-(\gamma)$ cross section [1] fits into a broad Babar ISR program to provide a precise low-energy measurement of the inclusive $e^+e^- \to$ *hadrons* cross section by summing exclusive

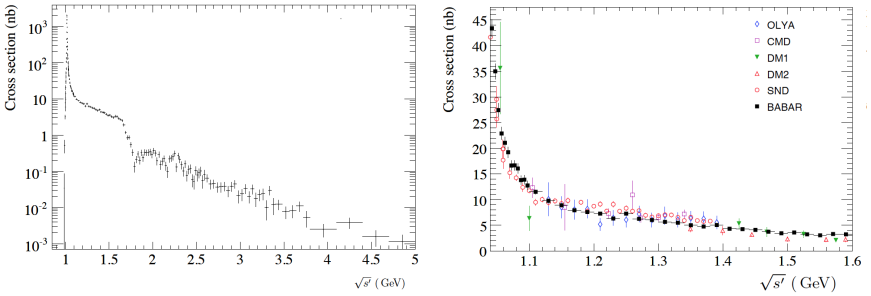

Fig. 1. Babar results for the $e^+e^- \to K^+K^-(\gamma)$ cross section, (left) over the full energy range probed and (right) in the $1.04 \leq \sqrt{s'} \leq 1.60$ GeV region.

channels. One measures the $\sigma(e^+e^- \to X\,\gamma_{ISR})$ cross section, with "X" the exclusive state, as a function of the mass $\sqrt{s'} = m_X$ of the state, where $\sqrt{s'}$ is the effective c.m. energy. The sum of exclusive channels provides a more accurate determination of the cross section than a measurement based on the inclusive recoil against the ISR photon γ_{ISR} because it yields better mass ($\sqrt{s'}$) resolution. With the K^+K^- results presented here, Babar covers essentially the complete set of significant exclusive channels.

The low-energy $e^+e^- \to$ *hadrons* inclusive cross section is needed for the calculation of the hadronic correction to the vacuum polarization contribution to the muon magnetic anomaly a_μ, namely for the standard model prediction of the muon $g-2$ value. Note that a_μ cannot be calculated perturbatively. Instead one uses the measured low-energy $e^+e^- \to$ *hadrons* inclusive cross section in conjunction with dispersion relations.

We measure the number of $K^+K^-(\gamma)$ events in intervals of $\sqrt{s'}$. We allow the possibility of an additional photon "(γ)," beyond the ISR photon, in order to keep the uncertainty of the event acceptance below 10^{-3}. The luminosity is monitored by measuring the number of $\mu^+\mu^-(\gamma)$ events within the same data sample. Thus knowledge of the absolute luminosity is not necessary and there is no reliance on theoretical expressions for radiator functions, reducing systematic uncertainties.

Events are required to contain two charged tracks consistent with a K^+K^- pair. The photon with highest energy is identified as the ISR photon. The ISR photon must have at least 3 GeV in the c.m. frame and lie within 0.3 radians of the missing momentum vector formed from all other reconstructed particles in the event (this last requirement strongly suppresses non-ISR events). Background events, which mostly arise from other ISR processes, are subtracted, and the data are corrected to account for finite detector resolution.

The measured cross section is shown in Fig. 1 (left). The Babar results

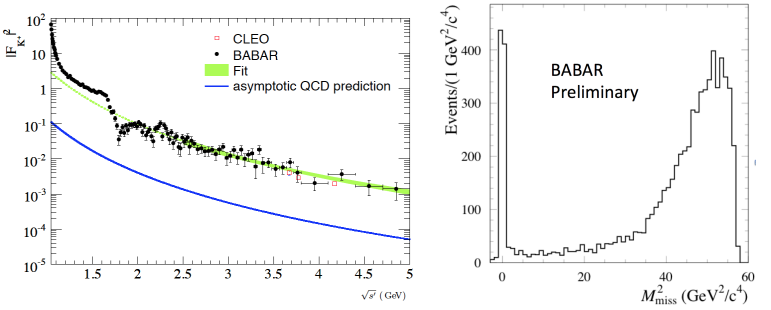

Fig. 2. (left) The charged kaon form factor measurement from Babar. The solid green line shows the result of a fit of the QCD shape $\alpha_S(s')/s'$ to the data. The solid blue line shows the QCD result including the predicted absolute normalization. (right) The missing-mass-squared distribution (preliminary) for untagged γ_{ISR} events in the $e^+e^- \to p\overline{p}$ channel.

cover a large energy range compared with previous experiments and six orders of magnitude in cross section. The precision of the results is emphasized in Fig. 1 (right), which shows the Babar results in a zoomed energy range in comparison with results from other experiments. Concerning the muon anomaly, the Babar results yield $a_\mu^{KK,LO} = 22.93 \pm 0.18(\text{stat.}) \pm 0.22(\text{syst.})$, compared with the previous result $a_\mu^{KK,LO} = 21.63 \pm 0.27(\text{stat.}) \pm 0.68(\text{syst.})$, and thus improve the precision of the KK contribution to a_μ by about a factor of three.

We also extract the charged kaon form factor, shown in Fig. 2 (left). For $\sqrt{s'} \geq 2.5$ GeV, in the region above the hadron resonances, the shape of the QCD prediction $\alpha_S(s')/s'$ (with α_S the strong coupling strength) agrees with the data. However the predicted normalization is wrong by an order of magnitude. The Babar measurements agree with those from the CLEO experiment [2], shown by the three red squares in Fig. 2 (left). CLEO has results at three energy points only because they use fixed c.m. energies rather than the ISR method.

3. The proton form factor

A similar ISR technique to that described above for $e^+e^- \to K^+K^-(\gamma)$ events is used to select $e^+e^- \to p\overline{p}$ events. Babar has two recent studies of the $p\overline{p}\gamma_{ISR}$ channel: one where the photon is reconstructed in the detector ("tagged") [3] and one where it is not ("untagged") [4]. The tagged analysis updates a previous Babar publication [5] using twice as much data and improved analysis techniques. In the untagged analysis, which is preliminary,

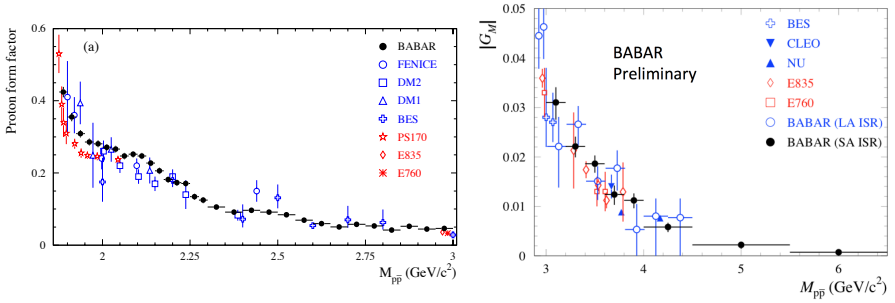

Fig. 3. The proton form factor measurement from the (left) tagged-$\gamma_{\rm ISR}$ $p\bar{p}$ analysis at low $\sqrt{s'}$ and (right) from the untagged (preliminary) and tagged analyses at high $\sqrt{s'}$, in comparison with the results from other experiments.

the ISR photon is colinear with the beam axis, leading to a p and $\overline{\rm p}$ that can be widely separated in phase space and thus to events with a large $p\overline{p}$ invariant mass. The untagged analysis greatly improves the precision of the results for $\sqrt{s'} > 3$ GeV.

For the untagged analysis, the key selection variables are the summed transverse momentum of the identified p and $\overline{\rm p}$ and the missing-mass-squared $M^2_{\rm miss}$ recoiling against the $p\overline{p}$ pair (both quantities should be about zero for signal events). Figure 2 (right) shows the measured $M^2_{\rm miss}$ distribution after all selection criteria for the analysis are applied except for that on $M^2_{\rm miss}$: a clear signal peak with little background is seen at $M^2_{\rm miss} \approx 0$.

Figure 3 shows our measurements of the proton form factor. The left plot, from the tagged analysis (large angle "LA" $\gamma_{\rm ISR}$), confirms the enhancement of the $e^+e^- \to p\overline{p}$ cross section just above the $p\overline{p}$ threshold and demonstrates the precision of the Babar results over a wide energy range. The right plot, from the untagged analysis (small angle "SA" $\gamma_{\rm ISR}$) illustrates the much increased precision achieved at high mass values with the untagged sample.

4. The $e^+e^- \to K_SK_L$, $K_SK_L\pi^+\pi^-$, $K_SK_S\pi^+\pi^-$, and $K_SK_S K^+K^-$ channels

These studies, currently all preliminary, are also based on the ISR technique. For the $e^+e^- \to K_SK_L$ analysis, we require events to contain exactly one $K_S \to \pi^+\pi^-$ candidate that is consistent with arising from the primary interaction point (IP) and to have no charged tracks consistent with the IP. The K_L detection efficiency is measured from data using events in the dominant $e^+e^- \to \phi\gamma_{\rm ISR} \to K_SK_L\gamma_{\rm ISR}$ channel: a clean K_L signal is seen, even though no explicit K_L selection criteria are applied. We then apply

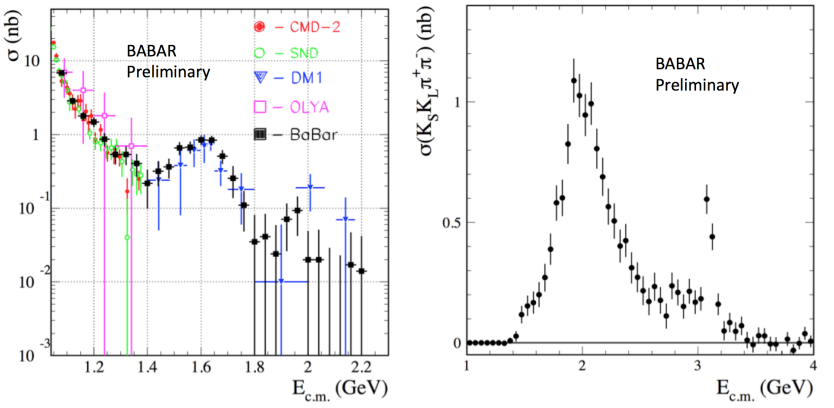

Fig. 4. Cross section measurements of the (left) $e^+e^- \to K_S K_L$ and (right) $e^+e^- \to K_S K_L \pi^+\pi^-$ processes (preliminary).

K_L selection criteria to this sample, identifying a K_L candidate as an isolated cluster in the electromagnetic (EM) calorimeter with energy larger than 0.2 GeV and within 0.5 radians of the expected K_L direction based on the event kinematics. The K_L detection efficiency is thereby measured to be around 48%, about 6% lower than predicted by the simulation. Corresponding corrections are subsequently applied to the simulated K_L detection efficiency as a function of the K_L energy and direction.

We then study the non-resonant $e^+e^- \to K_S K_L$ channel ($K_S K_L$ invariant mass larger than 1.06 GeV). Contributions from $e^+e^- \to K_S K_L(n\pi^0)$ events with $n \geq 1$ are suppressed by requiring the energy of additional EM clusters in the event to be less than 0.5 GeV. Sidebands in the data are used to evaluate and subtract residual background. The results for the $e^+e^- \to K_S K_L$ cross section are shown in Fig. 4 (left). The Babar data are seen to be precise and to cover a larger energy range than previous experiments, as for the K^+K^- and $p\bar{p}$ analyses presented above. Clear evidence is obtained for production through the $\phi(1600)$ resonance: we observe around 1000 events in the $\phi(1600)$ region, compared to 58 events for the only previous measurement in this region, from the DM1 experiment in 1981 [6].

Similar techniques are used to study the $e^+e^- \to K_S K_L \pi^+\pi^-$, $K_S K_S \pi^+\pi^-$, and $K_S K_S K^+K^-$ channels. These are the first measurements ever for these three cross sections. As an example, the results for the $e^+e^- \to K_S K_L \pi^+\pi^-$ cross section are shown in Fig. 4 (right). A clear J/ψ meson peak is observed. Clear J/ψ peaks are also seen in the $K_S K_S \pi^+\pi^-$ and $K_S K_S K^+K^-$ channels. From the J/ψ results, we extract the first measurements of the corresponding J/ψ branching fractions, which are summarized

Table 1. J/ψ branching fractions from the $e^+e^- \to K_S K_L \pi^+\pi^-$, $K_S K_S \pi^+\pi^-$, and $K_S K_S K^+ K^-$ analyses.

Branching fraction ($\times 10^{-3}$)	Babar (preliminary)	PDG (2012)
$\mathcal{B}_{J/\psi \to K_S K_L \pi^+\pi^-}$	$3.7 \pm 0.6 \pm 0.4$	No entry
$\mathcal{B}_{J/\psi \to K_S K_S \pi^+\pi^-}$	$1.68 \pm 0.16 \pm 0.08$	No entry
$\mathcal{B}_{J/\psi \to K_S K_S K^+ K^-}$	$0.42 \pm 0.08 \pm 0.02$	No entry

in Table 1.

5. Identified charged hadron production

The final topic is not about ISR events but rather about the inclusive production of identified charged pions, kaons, and protons at $E_{c.m.} = 10.54$ GeV [7], with $E_{c.m.}$ the c.m. energy. The multiplicity and momentum spectra of identified charged hadrons provide a basic characterization of multihadronic events as well as information on how hadronization depends on hadron mass, strangeness, and baryon number.

Precise measurements of identified charged hadron spectra at energies around 91 GeV were provided by the LEP and SLD experiments. However, until the present work and and roughly contemporaneous results from the Belle Collaboration [8], the only e^+e^- annihilation results on identified charged hadrons at $E_{c.m.} \approx 10$ GeV were from the ARGUS experiment [9]. The BES experiment presented distributions of inclusive charged particle multiplicity and momentum for c.m. energies between around 2 and 5 GeV [10], but not results for identified hadrons.

The Babar analysis makes use of 0.91 fb^{-1} of data collected in the e^+e^- continuum region at 10.54 GeV. This represents only about 0.2% of the total Babar data sample but is sufficient because the uncertainties are dominated by systematic terms. Charged tracks are required to have momenta above 200 MeV so that the particle identification (PID) efficiencies are well determined. In total, 2.2 million events are selected. As for all the studies discussed above, Monte-Carlo-(MC)-simulation-derived track-selection and PID efficiencies are corrected to account for data-MC discrepancies using control samples in the data. The background, which primarily arises from $e^+e^- \to \tau^+\tau^-$ events, is subtracted. We mostly use prompt particles in presenting results, which means that the decay products of K_S mesons and weakly decaying baryons are not included. This differs from the convention generally used by the LEP and SLD experiments.

The results for the inclusive identified charged hadron spectra are shown in Fig. 5 (left). The data are displayed in bins of $x_p = 2p^*/E_{c.m.}$, where p^* is the c.m. particle momentum. The results are shown (from top to

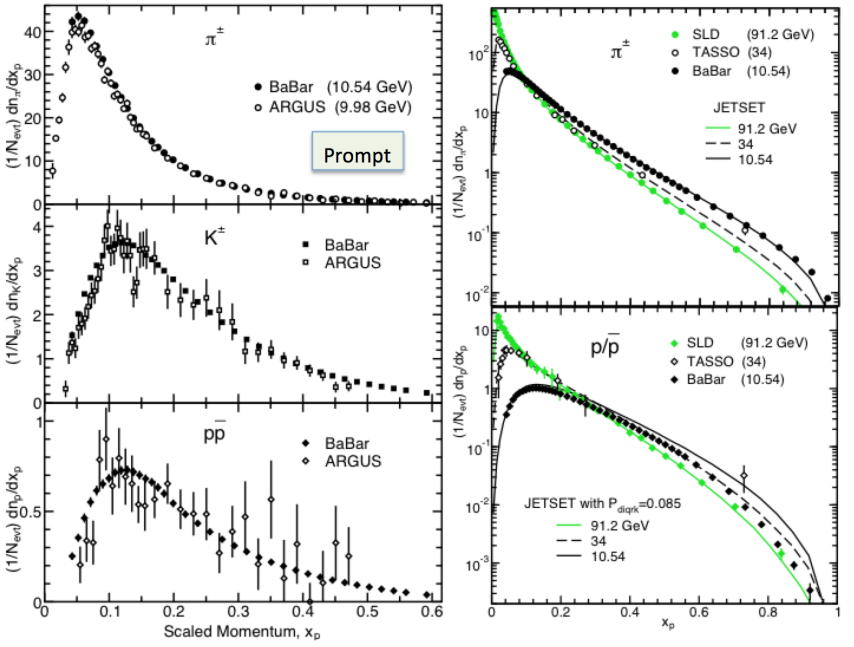

Fig. 5. (left) Scaled momentum spectra for charged pions, kaons, and protons; (right) Comparison of the scaled momentum spectra of charged pions and protons for the SLD, TASSO, and Babar experiments.

bottom) for charged pions, kaons, and protons. The corresponding results from ARGUS are also shown. The Babar and ARGUS data agree once the small difference in c.m. energy is accounted for. The Babar data for kaons and protons are seen to be far more precise than those of ARGUS.

The precise low $E_{c.m.}$ Babar data allow the scaling behavior to be investigated. Figure 5 (right) shows the Babar data (black points) for charged pions (top) and protons (bottom) in comparison with the corresponding results from SLD at 91.2 GeV [11] (green points). Intermediate-energy results from the TASSO experiment [12] are also shown. Clear scaling violations are observed, i.e., the Babar and SLD data do not agree with each other. At large values of x_p, the scaling violation is attributed to the running of the strong coupling strength α_S, while at small x_p it is a hadron-mass effect. Shown in comparison with the data are predictions from the Jetset [13] MC event generator. The green and black Jetset curves correspond to $E_{c.m.} = 10.54$ and 91.2 GeV, respectively. For charged pions (top right plot of Fig. 5), the black curve goes through the black points and the green curve through the green points, so the scaling behavior is well described.

For protons, however (bottom right plot of Fig. 5), the black curve lies above the black points, indicating that the scaling violation is overestimated by the simulation.

6. Summary

Babar has a strong and comprehensive program in the measurement of exclusive $e^+e^- \to$ *hadrons* cross sections using the ISR method. Summing the exclusive channels yields improved results for the inclusive cross section, which is important for the precision of the standard model prediction for the muon anomaly a_μ. The ISR method allows precise measurements of exclusive cross sections over an extended effective c.m. energy range. Recent Babar results based on the ISR method are presented for the the $e^+e^- \to K^+K^-(\gamma)$, $p\overline{p}$, K_SK_L, $K_SK_L\pi^+\pi^-$, $K_SK_S\pi^+\pi^-$, and $K_SK_SK^+K^-$ processes.

In addition, precise measurements of the inclusive momentum spectra of identified charged pions, kaons, and protons at $E_{c.m.} = 10.54$ GeV are presented. These results allow new tests of QCD predictions, both for scaling violations and MLLA calculations (the comparison of data with MLLA results is omitted from this report due to length constraints).

References

[1] J.P. Lees *et al.* (Babar Collaboration), Phys. Rev. D **88**, 032013 (2013).
[2] T.K. Pedlar *et al.* (CLEO Collaboration), Phys. Rev. Lett. **95**, 261803 (2005).
[3] J.P. Lees *et al.* (Babar Collaboration), Phys. Rev. D **87**, 092005 (2013).
[4] J.P. Lees *et al.* (Babar Collaboration), arXiv:1308.1795.
[5] B. Aubert *et al.* (Babar Collaboration), Phys. Rev. D **73**, 012005 (2006).
[6] F. Mané *et al.* (DM1 Collaboration), Phys. Lett. B **99**, 261 (1981).
[7] J.P. Lees *et al.* (Babar Collaboration), Phys. Rev. D **88**, 032011, 2013.
[8] M. Leitgab *et al.* (Belle Collaboration), Phys. Rev. Lett.**111**, 062002 (2013).
[9] H. Albrecht *et al.* (ARGUS Collaboration), Z. Phys. C **44**, 547 (1989).
[10] J.Z. Bai *et al.* (BES Collaboration), Phys. Rev. D **69**, 072002 (2004).
[11] K. Abe *et al.* (SLD Collaboration), Phys. Rev. D **59**, 052001 (1999).
[12] W. Braunschweig *et al.* (TASSO Collaboration), Z. Phys. C **42**, 189 (1989).
[13] T. Sjöstrand, Comput. Phys. Commun. **82**, 74 (1994).

Stochastic mechanism of color confinement

V. Kuvshinov †

Joint Institute for Power and Nuclear Research - Sosny
National Academy of Sciences of Belarus
Krasin str. 99, Minsk, Belarus

It is shown that in stochastic QCD a vacuum color quark is confined due to the interaction with environment, chaotic dynamics of Yang-Mills-Higgsfields, decoherence of pure color state into mixed white (colorless) state and also squeezed, and entangled states appearance. Critical energy of order-chaos transition is obtained which depends on Higgs boson mass. Stochasticity is the root of color confinement disappearing of color at confinement radius.

1. Stochasticity

Let us take a heavy spinless color particle ("quark") in the QCD vacuum, for example inside a hadron or deconfined QGP. QCD vacuum is the environment for color quantum particles whose properties are averaging over all external QCD vacuum implementations [1–5]. Interactions with the environment result in decoherence and relaxation of quantum superpositions [6, 7]. Interactions of some quantum system with the environment can be effectively represented by additional stochastic terms in the Hamiltonian of the system. QCD vacuum represents itself namely as a stochastic (not coherent one) system. Stochastic means that only the second order correlators in the QCD vacuum are dominated (Gauss domination). It has been confirmed by lattice calculation. The most important evidence for this is Casimir scaling [8]. The model of the QCD stochastic vacuum is one of the popular phenomenological models which exhibits quark confinement, string tension and field configurations around static charges [9–12]. When considering a QCD stochastic vacuum as the environment for color quantum particles with the averaging over external QCD stochastic vacuum implementations, we obtain as consequences decoherence, relaxation of quantum superpositions, loss of information, and confinement of color states.

† Email: kuvshinov2003@gmail.com

2. Density matrix

In the situation of a quantum system (quark) in the environment (stochastic QCD vacuum) a density matrix is the most adequate formalism. The color particle density matrix of the system taking into account both color particle and QCD stochastic vacuum as environment is obtained by averaging with respect to the stochastic terms [1–5]

$$\rho(\text{loop}, 1\ 2) =< |\phi(1)\rangle\langle\phi(2)| >, \tag{1}$$

here we average over all implementations of stochastic gauge field (environment degrees of freedom). In the model of QCD stochastic vacuum only expectation values of path ordered exponents over closed paths are defined. The amplitude is obtained by parallel transport [1–5]

$$|\phi(1)\rangle = \mathcal{P} \exp\left(i \int dx^{\mu} \hat{A}_{\mu}\right) |\phi_{in}\rangle, \tag{2}$$

Closed path corresponds to a process in which the particle-antiparticle pair is created, propagates and finally annihilates. With the help of (1) and (2) we can obtain the next expression

$$\rho(\text{loop}, 1\ 2) = N_c^{-1} + (|\phi_{in}\rangle\langle\phi_{in}| - N_c^{-1}) W_{adj}(\text{loop}, 1\ 2). \tag{3}$$

Here N_c is a number of colors, $W_{adj}(\text{loop}, 1\ 2)$ is the Wilson loop in the adjoint representation, and we have used the property that color density matrix in color neutral stochastic vacuum can be decomposed into the pieces transformed under trivial and adjoint representations [4].

As is known due to Casimir scaling, decay rates of Wilson loops in different representations are proportional to each other , in particular W_{fund}(loop, 1 2) and W_{adj}(loop, 1 2). Decay of W_{fund}(loop, 1 2) points at confinement of color charges. Simultaneously we have decay of W_{adj}(loop, 1 2) that means from Eq. (3) that the color density matrix obtained as a result of parallel transport along the (loop, 1 2) tends under the confinement regime to the color density matrix of white (colorless) mixture $\rho = N_c^{-1}$. Here all color states are mixed with equal probabilities and all information on initial color state is lost. The stronger the color states are confined the stronger their states transform into the white mixture.

So, as the Wilson area law holds for the Wilson loop (confinement criterion), we can obtain an explicit expression for the density matrix if we choose for example the rectangular (loop 1 2) spanned in terms of time T and distance R [2, 4]. When R or T are of order of 1 fm (for SU(3) theory), the Wilson loop decays exponentially with the area spanned on (loop 1 2)

$$\rho(\text{loop}, 1\ 2) = N_c^{-1} + (\rho_{in} - N_c^{-1}) \exp(-\sigma_{adj} RT), \tag{4}$$

where $\sigma_{adj} = \sigma_{fund} G_{adj} G_{fund}^{-1}$ is string tension in the adjoint representation and G_{adj}, G_{fund} are the eigenvalues of quadratic Casimir operators. Under the condition of Gaussian dominance, string tension is $\sigma_{fund} = g^2 l_{corr}^2 F^2/2$, where g is the coupling constant, l_{corr} is the correlation length in the QCD stochastic vacuum, and F^2 is the average of the second cumulant of curvature tensor when $g^2 l_{corr}^2 F^2 \ll 1$ [12].

The decoherence rate of transition from pure color states to white mixture can be estimated on the base of purity [6] $P = \mathrm{Tr}\ \rho^2$ [4]

$$P = N_c^{-1} + (1 - N_c^{-1}) \exp(-2\sigma_{fund} G_{adj} G_{fund}^{-1} RT). \tag{5}$$

When T or R tend to 0, $P \to 1$, that corresponds to pure state with the density matrix $\rho_{in} = |\phi_{in}\rangle\langle\phi_{in}|$. When composition RT tends to infinity the purity tends to N_c^{-1}, that corresponds to the white mixture state with the density matrix N_c^{-1}. The rate of purity decreasing is $T_{dec}^{-1} = 2\sigma_{fund} G_{adj} G_{fund}^{-1}$, where T_{dec} is the characteristic time of decoherence proportional to QCD string tension and distance R. It can inferred from (3) and (4) that the stronger is particle-antiparticle pair coupled by QCD string or the larger is the distance between particle and antiparticle the quicker information about color state is lost as a result of interaction with the QCD stochastic vacuum. Thus white states can be obtained as a result of decoherence process which allows to conjecture analogy with color particle confinement. Information on quark color states in confinement region is lost due to interactions between quarks and confining non-Abelian gauge fields (stochastic QCD vacuum).

3. Confinement, fidelity, critical energy of order-chaos transition and mass of the Higgs boson

The Wilson loop definition in QCD is similar [13] to the definition of fidelity [8], the quantity which describes the stability of quantum motion of the particles [14]. Using the analogy between the theory of gauge fields and the theory of holonomic quantum computations [13, 15, 16] we can define the fidelity of quark motion. We consider the motion of color particles in different paths from the point x to the point y. In the initial point x state vectors are $|\phi_{in}\rangle$. For large particle mass and taking into account that because of Hermitian character of $\hat{A}_\mu$ operator (1) is unitary. We can rewrite fidelity as integral over the closed loop, traveling from point x to the point y

$$f = < \langle\phi_{in}| \mathcal{P} \exp\left(i \int dx^\mu \hat{A}_\mu \right) |\phi_{in}\rangle > \tag{6}$$

in the path 1 and back to the point x in the path 2 and obtain integral proportional to the identity due to the color neutrality of stochastic vacuum.

The final expression for the fidelity of the particle moving in the Gaussian-dominated stochastic vacuum is

$$f = \exp\left(-\frac{1}{2} g^2 l_{corr}^2 F^2 S\right), \tag{7}$$

where S is the area of the surface spanned over the contour (loop, 1 2). Thus the fidelity for color particle moving along contour decays exponentially with the surface spanned over the contour S the decay rate being equal to the string tension is $\sigma_{fund} = g^2 l_{corr}^2 F^2/2$. Another situation, more close to the standard treatment of the fidelity, is realised when 1 and 2 are two random paths in Minkowski space, closed to each other. The corresponding expression for the fidelity is similar, but now the averaging is performed with respect to all random paths which are close enough. If the unperturbed path is parallel to the time axis in Minkowski space, the particle moves randomly around some point in three dimensional space. The fidelity in this case also decays exponentially with time. Thus we have close connection between confinement and instability of color particle motion.

The increasing of instability of motion in the confinement region is also connected with existence of chaotic solutions of Yang-Mills field [1, 17], possible chaos onset [18]. Yang-Mills fields already on classical level show inherent chaotic dynamics and have chaotic solutions [17, 18]. It was shown that the Higgs boson and its vacuum quantum fluctuations regularize the system and lead to the emergence of order-chaos transition at some critical energy [13, 19–21]

$$E_c = \frac{3\mu^4}{64\pi^2} \exp(1 - \frac{\lambda}{g^4}). \tag{8}$$

Here μ is mass of Higgs boson, λ is its self-interaction coupling constant, g is the constant coupling gauge and Higgs fields. Very important here is the value of mass of Higgs boson. From Ref. [22]: "Higgs mass lower than some critical value and potential is unstable, and the universe can phase transition to another vacuum." On the other hand, in the region of confinement there exists the boundary of order-chaos transition where the fidelity decreases exponentially and which is equal to string tension $\sigma_{fund} = g^2 l_{corr}^2 F^2/2$. This connects the properties of stochastic QCD vacuum, Higgs boson mass and coupling constants.

4. Squeezed and entangled color states

The instability of motion in the confinement region is also connected with possible phenomena of quantum entanglement and squeezing of color states [23–27].

Color particles moving through QCD vacuum with large momentum transfered develop quark-gluon jets. Both perturbative and nonperturbative (with sub-Poissonian multiplicity distributions) stages of the jet evolution are important [28]. Gluon multiplicity distribution at the end of the perturbative cascade in the range of the small transverse momenta (thin ring of jet) is Poissonian one [29]. Multiplicity distribution for the whole jet at the end of the perturbative cascade can be represented as a combination of Poissonian distributions (coherent states.). Gluon coherent states under the influence of the nonlinearities of QCD Hamiltonian transform into the squeezed and entangled states with sub-(super-)Poissonian multiplicity distributions [24–26]. Within local parton-hadron duality we can estimate nonperturbative contribution of the gluon squeezed states to the pion correlation functions in the jet narrow ring [30].

The emergence of entangled and squeezed states in QCD becomes possible due to the four-gluon self-interaction, the three-gluon self-interaction does not lead to the effects [24–26]. In principle, these effects are possible even for quadratic Hamiltonians in the quantum theory under certain conditions. Moreover we may amplify or, on the contrary, weaken both the squeezing effect and the system instability [31].

Two mode gluon squeezed and entangled states with two different colors can lead to quark-antiquark entangled states, the role of which could be important for of the confinement and hadronization phenomena [25, 26].

Quantum entanglement for cubits and Yang-Mills-Higgs fields was considered in [27] in terms of the original quasiclassical formalism developed in [31]. The concept of quantum entanglement was found to be very useful as a model-independent characteristic of the structure of the ground state of quantum field theories which exhibit strong long range correlations, most notably lattice spin systems near the critical points and the corresponding conformal field theories [32].

Quantum entanglement was also considered as an alternative way to probe the confining properties of large-N gauge theories [33, 34]. Quantum entanglement between the states of static quarks in the vacuum of pure Yang-Mills theory was analyzed in Ref. [33].

The Hilbert space of physical states of the fields and the charges is endowed with a direct product structure by attaching an infinite Dirac string to each charge. Tracing out the gauge degrees of freedom yields the density matrix which depends on the ratio of Polyakov and Wilson loops spanned on quark world lines. In the confinement regime, the entanglement of quark color states is maximal [35].

5. Conclusions

We have shown that a stochastic (not coherent) vacuum of quantum chromodynamics for which only correlators of the second order are important can be considered as the environment (in the sense of quantum optics) for color particles (quarks and gluons), where the Wilson loop corresponds to the fidelity of quantum color particle motion and confinement to the instability (chaoticity) of motion and to decoherence of pure color states into mixed white states. The Wilson loop, fidelity and purity decay exponentially with decay rate equal to the string tension. The dynamics of Yang-Mills fields, which is inherently chaotic one already at the classical level, can be partly regularized by interaction with Higgs fields and by quantum fields fluctuations. The critical point of an order-chaos transition appears which corresponds to the point of fidelity exponential decreasing. Squeezinq, entanglement, decoherence and instability accompany nonperturbative evolution of colour particles in QCD vacuum and confinement phenomenon.

References

[1] V. Kuvshinov and A. Kuzmin, *Gauge Fields and Theory of Deterministic Chaos* (Belorussian Science, Minsk, 2006, p. 1-268, in Russian).

[2] V. Kuvshinov and P. Buividovich, Nonlinear Phenomena in Complex Systems **8**, 313 (2005).

[3] P.V. Buividovich and V.I. Kuvshinov, Phys. Lett. B **634**, 262 (2006).

[4] V. Kuvshinov and P. Buividovich, Acta Physica Pol. B (Proceedings Supplement) **1**, 579 (2008).

[5] V.I. Kuvshinov, Acta Physica Pol. B (Proceedings Supplement) **6**, 661 (2013).

[6] F. Haake, *Quantum Signatures of Chaos* (Springer-Verlag, Berlin, 1991).

[7] A. Peres, *Quantum Theory: Concepts and Methods* (Kluwer, Dordrecht, 1995).

[8] G. Bali, Nucl. Phys. B: Proc. Suppl. **83**, 422 (2000).

[9] J. Ambjørn and P. Olesen, Nucl. Phys. B, **170**, 60 (1980).

[10] Y.A. Simonov, Uspekhi Fizicheskih Nauk **166**, 337 (1996) (in Russian).

[11] A.D. Giacomo, H. Dosch, V.I. Shevchenko, and Y.A. Simonov. Phys. Rep. **372**, 319 (2002).

[12] D.S. Kuzmenko, Y.A. Simonov *et al.*, Uspekhi Fizicheskih Nauk **174** (2004) (in Russian).

[13] V. Kuvshinov and A. Kuzmin, Phys. Lett. A **316**, 391 (2003).

[14] P. Reineker, *Exciton Dynamics in Molecular Crystals and Aggregates* (Springer-Verlag, Berlin, 1991).
[15] V. Kuvshinov and A. Kuzmin, J. Nonl. Math. Phys. **9**, 382 (2002).
[16] V.I. Kuvshinov and P.V. Buividovich, Acta Physica Pol. **36**, 195 (2005).
[17] G.K. Savvidy, Phys. Lett. B **71**, 133 (1977).
[18] T. Kawabe, Phys. Rev. D **41**, 1983 (1990).
[19] S.G. Matinyan *et al.*, JETP Lett. **34**, 613 (1981).
[20] T. Kawabe, Phys. Lett. B **334**, 127 (1994).
[21] V. Kuvshinov and A. Kuzmin, Nonlinear Phenomena in Complex Systems **2**, 100 (1999).
[22] J. Wells, talk at Workshop CLIC 2013, CERN, 28.01–01.02.2013.
[23] V.I. Kuvshinov and V.A. Shaporov, Acta Physica Pol. B **30** (1999).
[24] V.I. Kuvshinov and V.A. Shaparau, Phys. Atom. Nucl. **65**, 309 (2002).
[25] V.I. Kuvshinov and V.A. Shaparau, Nonlinear Phenomena in Complex Systems **6**, 898 (2003).
[26] V.I. Kuvshinov and V.A. Shaparau, Acta Physica Pol. B **35**, 443 (2004).
[27] V. Kuvshinov and V. Marmish, Letters in EPAN, v. 2, 23 (2005).
[28] E.S. Kokoulina and V.I. Kuvshinov, Acta Physica Pol. B **13**, 553 (1982).
[29] S. Lupia, W. Ochs, and J. Wosiek, Nucl. Phys. B **540**, 05 (1999).
[30] V.I. Kuvshinov and V.A. Shaparau, Nonlinear Dynamics and Applications: Proceedings of the Annual Seminar NPCS'2011, vol. 18, 210 (2011).
[31] V. Kuvshinov, V. Marmish, and V. Shaporov, Theor. Math. Phys. **139**, 477 (2004).
[32] P. Calabrese and J. Cardy, Int. J. Quant. Inf. **4**, 429 (2006).
[33] T. Nashioka and T. Takayanagi, J. High Energy Phys. **01**, 090 (2007).
[34] L.R. Klebanov, D. Kutasov, and A. Murugan, http://arxiv.org/abs/0709.2140 (2007).
[35] V.I. Kuvshinov and P.V. Buividovich, Nonlinear Phenomena in Complex Systems **13**, 149 (2010).

Future physics: A personal view

James Bjorken

SLAC National Accelerator Laboratory, Menlo Park, CA 94025

A personal view of the future of particle physics is presented.

1. Introduction

It is a great pleasure to be back at an ISMD meeting, and to again meet so many old friends and colleagues, as well as members of the new generation. Because it has been a long time since I have been active in this field, this talk will not be a summary. I have instead chosen to touch briefly on a variety of topics of special interest to me. I will begin with a revisit of the parton model and continue with a look at the Higgs sector. This will be followed by a quick look at the problems of dark matter and dark energy, along with a few remarks regarding how future experimental programs might best address the above issues. Finally, I have added a few comments relevant to the material which was presented during the meeting.

2. The Kindergarten Parton Model

To most people, the phrase "parton model" nowadays is almost synonymous with the phrase "inclusive distributions." But in principle there is, even at the original kindergarten level, much more to the parton model than that. A single energetic left-moving hadron is to be viewed as a configuration of many partons, each of which is labeled by its internal quantum numbers, its longitudinal fraction, and its location in the transverse impact plane. During its collision with a right-moving hadron (or lepton), the internal motion is frozen due to relativistic time dilation. Furthermore, Lorentz contraction of the valence components of the left-mover and right-mover means that the collision evolution is local in the impact plane until the momentum scale of the final-state evolution becomes of order the QCD scale, of order 1 GeV or so.

Because of this localization in the impact plane, I like to subdivide the transverse impact-plane into pixels, of diameter of order 0.2–0.3 fermi. To each pixel we may assign, event by event, a left-moving longitudinal

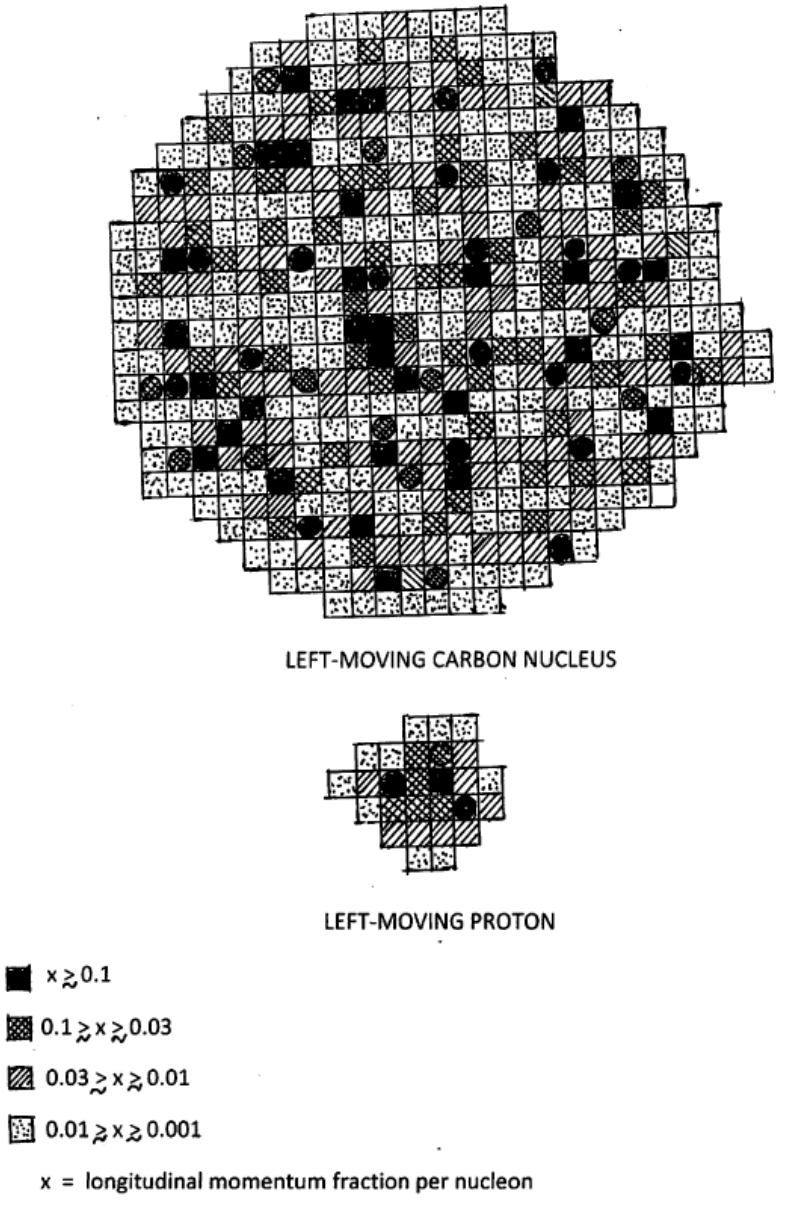

Fig. 1. Pixelized beams-eye views of impact- plane parton momentum fractions for a typical left-moving carbon ion and for a typical left-moving proton.

momentum fraction, a right-moving longitudinal-momentum fraction, a left-moving baryon number, etc. (Fig. 1). Consequently, each pixel can also be assigned a subenergy and a central rapidity for the collision products. Therefore the early stages of the evolution of the overall collision can be described in terms of the evolution of the sub-collisions occurring within the sundry pixels. I am tempted to label these pixels Vegas, because, as they often say, what happens in Vegas stays in Vegas. However this is not strictly true. While hard processes occur within Vegas, the information eventually does spread beyond.

When viewed this way, it is of course interesting to question whether, event-by-event, information regarding the distribution across the impact plane of the subenergies within the sundry pixels is reflected in the observed properties of the ultimate collision products. The answer is, of course, yes. Such effects are by now commonplace in noncentral heavy-ion collisions. The "hot" pixels, i.e. those containing large subenergies, typically comprise an almond-shaped region in the impact plane. This leads to azimuthal asymmetry of the collision products ("ellipticity") which is robust, event-by-event, with respect to longitudinal boosts of a few rapidity units (at LHC energies). The approximate boost invariance of this effect should be rather intuitively obvious, because qualitatively the impact-plane picture is itself quite robust with respect to moderate boosts of the left-moving and right-moving incident projectiles. All that is needed to defend this view is to argue that the distribution of produced entropy within a pixel is broad in rapidity, at least as broad as given, say, by Landau hydrodynamics. This boost-invariance of the initial-state configuration-dependence (e.g. ellipticity) goes by the name "ridge structure."

In the early days of the parton model, the hypothesis that all correlations are short-range in rapidity led to the notion of a universal central-rapidity plateau. This in turn led to the expectation that event-by-event configuration-dependent effects would be observable, if at all, in the fragmentation regions of the left and right movers. However, with the advent of QCD this is no longer true. We now see a dramatic rise in the gluon inclusive distribution at very small x, with a concomitant power-law rise in central multiplicities of produced hadrons. The opposite extreme of a Landau-like dependence of multiplicity on energy is at the least a credible option for phenomenology. If this hypothesis is defensible, it is easy to show that it leads to a significant amount of contrast in the distribution of entropy across the impact plane, even for typical central rapidities.

A reasonable starting point for this picture is to assign to a pixel the same entropy distribution (here assumed to be proportional to the final-state hadron multiplicity distribution) as for an electron-positron annihilation event occurring at the same cms energy as the pixel subenergy. I have

scratched out an example of an LHC noncentral ion-ion collision with this assumption. It is shown in Fig. 2(a).

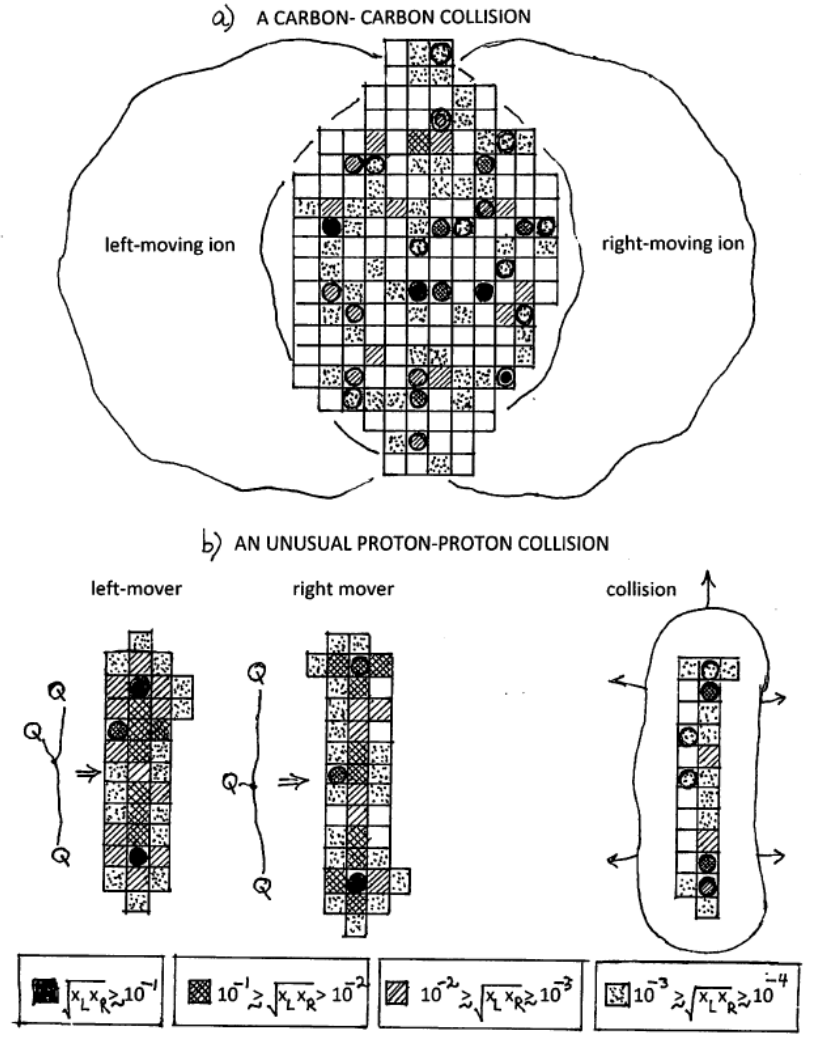

Fig. 2. Pixelized beams-eye views of the subenergy distribution in the impact plane for (a) a non-central carbon-carbon collision and for (b) an unusual LHC proton-proton collision.

Fred Goldhaber, Stan Brodsky, and I have explored an extreme example of configuration dependence [1]. It is shown in Fig. 2(b). Not infrequently the valence-quark configuration in the impact plane for an incident proton will be a compact diquark plus a quark connected by a color string. If both projectiles are in that configuration and are aligned, the hot pixels in the impact plane will lie along a line, and there should be not only high multiplicity but very large ellipticity and ridge structure.

Before moving on, I should emphasize that the above impact-plane picture has a long history, which I have not tried to cite. And present-day theoretical approaches, from BFKL to hydrodynamics to glasma [2], exploit the above ideas in one way or another. But I have included it here in kindergarten language because I believe its usefulness may still be undervalued. But there are problems. As I see it, the biggest problem with experimental searches for configuration dependence is that the theory is best expressed in terms of impact-plane properties, while the experiments are necessarily described in terms of the transverse momenta of the collision products within a given rapidity interval. There is a Fourier transform in between, which appears to create a serious barrier. We may need a good idea to effectively overcome this obstacle.

3. Family Symmetry and the Higgs Sector

Since the discovery at the LHC of the Higgs boson, I too have acquired a serious case of Higgsteria. It is wonderful how firm knowledge of the existence of the Higgs, even when its mass and properties were anticipated quite accurately years ago, can focus the mind and energize ones thinking about the problem. There is no good substitute for experimental facts.

For me, the focus has been on the role of the family group within the Higgs sector. I prefer the word "family" here. Long ago, Gell-Mann introduced a chiral $SU(3) \times SU(3)$ flavor group, with u, d, and s quarks forming a flavor triplet. The generalization appropriate nowadays is a chiral $SU(6) \times SU(6)$ flavor group, with the six quarks forming chiral sextet representations. Within this group is found not only the electroweak group, but also the chiral family group $SU(3) \times SU(3)$, with a family triplet, e.g., consisting of u, c, and t quarks.

Electroweak symmetry demands that d, s, and b also comprise a family triplet. And while it did not have to be so, the charged leptons e, μ, and τ also comprise a family triplet. Again electroweak symmetry demands that the three left-handed Dirac neutrino degrees of freedom are also family triplets. And we know that the photon, the gluons, the W's, and the Z are all family singlets.

But what about the Higgs sector? The default choice is that it consists of

the "vanilla" Higgs, plus its three Goldstone-boson partners that are eaten by the W's and Z, and nothing more. This single electroweak doublet evidently is necessarily assigned to be family singlet. The MSSM extension, as do the majority of other more elaborate models, retains this assumption. To me this assignment of family singlet seems less than reasonable. After all, the notorious family-related problem of the origin of quark and lepton masses and mixings can be directly traced to the properties assigned to the Higgs sector itself. Why should the Higgs sector itself transform trivially under the family group?

It is not that the alternative option has not been explored. Serious technical difficulties were encountered long ago. However, much of that history precedes the important phenomenology associated with the very heavy top quark and with large neutrino mixing. Furthermore, the popularity of electroweak-scale SUSY also seems to have diluted efforts in this direction. But there exists at present very interesting work on the spontaneous breaking of family symmetry [3].

What are the simplest assignments for Higgs multiplets? On the electroweak side, it is singlet or complex doublet. On the family side, it is singlet, triplet, or octet/nonet. This gives six options to explore. I have chosen to assign the observed Higgs and its three Goldstone partners to components of an electroweak-doublet, family nonet. This option allows a Yukawa coupling to the quarks and leptons, and gives $4 \times 9 = 36$ Higgs degrees of freedom in all, 32 of which await discovery. I assume these 32 are heavier than the top quark but no heavier than, say, 1 TeV. A nomenclature and some basic properties of these particles (which predominantly decay, either directly or indirectly, final states containing top quarks plus jets) is given in Fig. 3.

In the absence of first and second generation masses and their concomitant mixings, working out the Higgs mechanism and the phenomenology of the production and decay of these sundry bosons is rather straightforward. Production of the new Higgs states via couplings to the W, Z, and photon appear to give yields too small to be easily detected at present at the LHC. However, certain "coset states" can be singly produced in quark-gluon subprocesses, leading to final states consisting of a top-antitop pair plus a first-generation quark. The same coset states turn out to easily account for the CDF top-antitop angular asymmetry observed a few years ago at Fermilab. Because of this, there have already been specific searches for such particles at the LHC [4, 5]. The bounds on the coupling constant are close to what I specify from the model, but do not appear to rule anything out yet.

On the theoretical side, there are at present serious deficiencies. The above phenomenology is defined in the limit of vanishing first and second

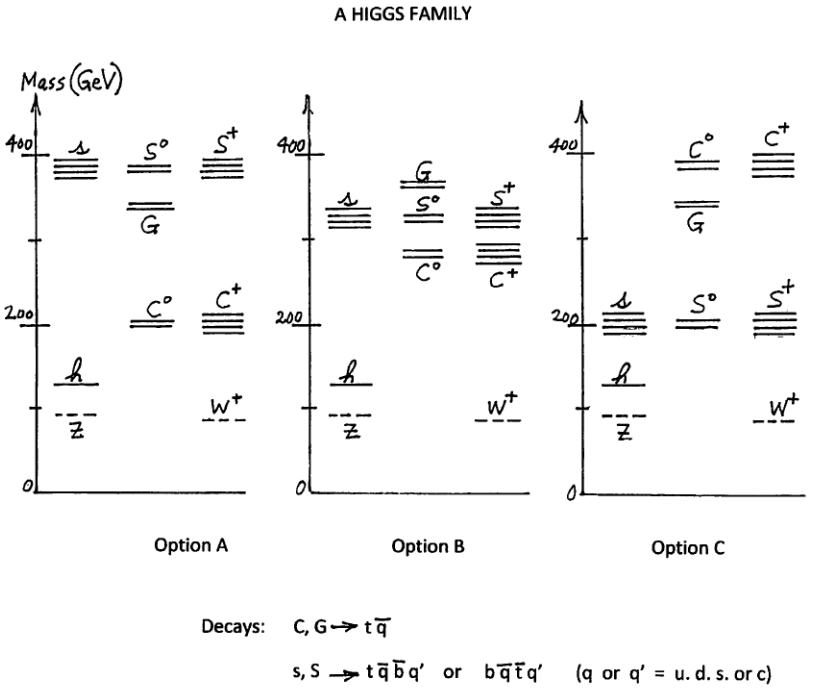

Fig. 3. Three candidate level schemes for the proposed electroweak-doublet, family nonet Higgs multiplet.

generation masses and mixings of the quarks and leptons. What I am looking for is a description in which these effects are generated by spontaneous breaking of the family symmetry group. For a while I thought I had such a model, at least for mixings of the second generation with the third. But I discovered mistakes - conceptual as well as algebraic. However, the parameter of difficulty is small: $(m_b/m_t)^2 \times V_{cb}$. So getting a satisfactory description is still a work in progress. But if there were to be success, I do not think that the LHC phenomenology of production and decay would be modified very much; the phenomenology sketched above, in my opinion, appears to be robust.

There is a message here to you, members of the QCD phenomenology community. The signal for these Higgs-sector candidates is buried in a large background of QCD top-antitop events. And the shape of the signal turns out to be not so different from the shape of the background [6]. Therefore there is a high premium on accurately controlling the background estimates. In addition, there is a second message. As the LHC upgrades energy and

luminosity, most of the attention will rightfully be focused on searching for new physics at mass scales exceeding 1 TeV. What I anticipate is a lot of new physics on mass scales of order 200–500 GeV, but immersed in QCD background. This new-physics window deserves just as much scrutiny as the high-end region. In this regard, I was pleased to hear similar appeals from other speakers at this meeting, in particular by Patrick Meade and by Alan White.

4. Dark Matter and the Higgs Sector

Given the above approach, what seems to be essential for obtaining a satisfactory description of the Higgs sector — one that includes creation of the appropriate masses and mixings of quarks and leptons — is that it should include other family representations, in particular some that are electroweak-singlet. Such components of the Higgs sector – electrically neutral and colorless — appear to me to be attractive dark matter candidates. And it is not politically incorrect to assume that at least some of the members of this "dark Higgs sector" need not have large masses [7]. I myself have worked with others on elaborating this possibility [8].

While assuming a large Higgs sector might seem extravagant, I do not see it that way. For example, if one accepts $SO(10)$ grand unification (without SUSY) as a reasonable hypothesis, then it is reasonable that the 36 massive gauge bosons contained within the adjoint representation (all but the photon and the 8 gluons) get their masses via the Higgs mechanism. This puts 36 Goldstone modes into the Higgs sector, making it at least reasonable that those 36 are accompanied, at the very least, by a few dozen massive Higgs modes.

From the GUT point of view, I therefore find it reasonable to presume that, at the electroweak scale, the effective field theory of the Higgs sector may consist of a considerable number of shattered fragments which have descended down from the GUT scale, and have all the aesthetic deficiencies of its strong-interaction counterpart, namely the Gasser-Leutwyler effective action describing the hadronic sector of QCD. Consequently, I have spent this year contemplating what the Higgs sector might look like at the GUT scale, prior to its devastation via a sequence of symmetry breaking scales. There are of course many options. I have chosen to investigate orthogonal groups larger than $SO(10)$, and have settled for the moment on $SO(16)$. The 120 gauge bosons of that group break down into the 45 within the usual GUT $SO(10)$, plus 15 within the complementary "dark" $SO(6)$. All 15 "dark gluons" are by construction colorless, electrically neutral, and electroweak singlet. The remaining 60 gauge degrees of freedom are "coset" fields, which have both "dark" and "visible" properties. Almost all of these 120 bosons

will have masses very large compared to the electroweak scale. But it is not impossible that there are some massless or almost massless "dark gluons," and/or others that have masses no larger than the electroweak scale.

For this to happen, the Higgs sector has to be quite large. There must be of order 100 Goldstone modes which are eaten by the large number of gauge bosons that do have mass. This suggests that there could be several hundred Higgs degrees of freedom in all. While from a bottoms-up point of view this may seem extravagant, one should keep in mind that from a top-down viewpoint a la string theory this is still modest. For example, the $E(8) \times E(8)$ heterotic string picture suggests the existence of many multiplets. Each one must have a dimensionality no smaller than 248.

The scenario I nowadays entertain contains 120 Higgs fields in the adjoint representation, plus another 256 "frame fields," which transform as vectors under the (spontaneously broken) "gauge $SO(16)$," as well as transforming as vectors under an auxiliary "frame $SO(16)$" (which is explicitly broken). This allows a lot of design flexibility, while keeping the fraction of Higgs fields which are massive relatively small. (I view this as a grotesque deformation of Occam's razor in action.) This notion of utilizing the frame field came to me via the work of Hong-Mo Chan and his collaborators on their "rotating mass matrix" description of fermion masses and mixings [9]. They create, via difficult-to-understand algorithms, an interesting and rather successful phenomenology of such masses and mixings, especially for the second generation. And underlying their ideas is a vision of the Higgs sector (largely unrealized in detail) in terms of such frame fields. As we will mention in the next section, the notion of frame fields also occurs in general relativity.

This is hardly the place to go further into this, which in any case is only work in progress. The reason I mention it at all is that I strongly believe that integration of family symmetry and its breaking (ideally only spontaneously) with Higgs-sector properties, and the integration of both with the dark-matter problem, is a fertile area for theoretical research. I find a lot of present theoretical phenomenology considerably more unfocused, as well as increasingly detached from the natural Big Picture architecture that hints from grand unification suggest.

5. Dark Energy and Darkness

Since retirement, the physics problem that has consumed me the most is that of dark energy. It is an ideal subject for a geriatric like me. Because I assume the default option of dark energy as due to a cosmological constant, all the direct data (a single number!) are in, and it is up to theory to do something about it. I have neither any excuse nor any motivation for pro-

crastination. The two parameters of the Einstein-Hilbert action (Newton constant and cosmological constant) define two extreme distance scales — the Planck scale l_{Pl} of 10^{-33} cm and the Hubble scale H of 10^{28} cm. (The constant H is defined as $H^2 = \Lambda/3$.) All of phenomenologically relevant physics is bracketed by these very fundamental parameters. But taken together, these two parameters define an intermediate scale which is halfway in between, logarithmically speaking. This is the dark energy scale, defined by the value of the (negative) pressure possessed by regions of space (e.g. cosmic voids) whose spacetime curvature is dominated by the cosmological constant, and not by nearby matter. The numbers associated with this scale are 80 microns, or 2.4 meV, a scale associated with life itself.

I have become over the years quite persuaded that this is not the only intermediate scale induced by these two fundamental parameters. The other is what I call [10] the Zeldovich, or darkness, scale [11]. It is two thirds of the way from the cosmological scale to the Planck scale, logarithmically speaking. The value comes out somewhere around 10^{-12} cm, or 20 MeV. While the dark-energy scale is defined by vacuum pressure and vacuum energy, the darkness scale is defined (given that the idea makes sense!) by vacuum topology. By analogy with the density of vacuum energy that defines the dark-energy scale, the darkness scale is defined by a density of vacuum topological structures, roughly 10^{39} per liter.

This assertion is dependent on a certain version of general relativity called the MacDowell-Mansouri extension of the first-order Einstein-Cartan formalism. The Einstein-Cartan formalism replaces the 10 degrees of freedom (metric tensor) of the Einstein-Hilbert action with 40. It is a Yang-Mills gauge theory, with an $O(3,1)$ gauge group living in Minkowski spacetime. The gauge potentials, generally labeled ω, account for 24 degrees of freedom. These are supplemented by 16 frame fields (the "vierbein", generally labeled e) which are spacetime vectors as well as vector gauge-fields. The metric tensor of the usual (Einstein-Hilbert) textbook version is recovered in terms of a quadratic form in the vierbein fields. The Einstein-Cartan action depends on all 40 degrees of freedom. For most macroscopic applications, a few lines of computation exhibit the equivalence of the two formalisms. An exception occurs when Dirac particles are included in the gravitational action. Then it is imperative that the first-order Einstein-Cartan formalism be used [12].

The MacDowell-Mansouri extension of the first order formalism [13] generalizes the $O(3,1)$ gauge group to $O(4,1)$. The 16 vierbein variables e and the 24 gauge-potential variables ω are synthesized into the 40 gauge potentials A of the $O(4,1)$ group. A field strength F is constructed in the usual way, and an action, quadratic in the field strength F, is posited. When this, to my eyes, rather elegant form of the action is decomposed all the way back

to the Einstein-Hilbert description, one finds three terms. One is the original Einstein-Hilbert term, and another is the cosmological-constant term (with necessarily a nonvanishing value, and with the correct sign, corresponding to a positive dark energy density). The third term is a well-known structure called the Euler or Gauss-Bonnet topological invariant. It is a quadratic form built from the Riemann curvature tensor, and its Lagrangian is a total time derivative. It therefore does not affect the Einstein field equations at all. However, what is interesting about this term is its coefficient, which is a pure number. That coefficient turns out to be the notorious factor of 10^{120} which pervades all discussions of the deep problems associated with dark energy.

In a formal sense, this Gauss-Bonnet term is the leading term when expanding out the MacDowell-Mansouri action. In a more practical sense, it is a totally irrelevant term. This ambivalence makes it hard to draw conclusions without pursuing the relevant issues more deeply. There is a rough QCD analogy. I think most of us believe that understanding the topological structure of the QCD vacuum is very important and fundamental. Even after decades of work, a small army of lattice QCD theorists still debate what that topological structure is: chromoelectric strings vs. monopoles vs. center vortices, etc., etc. Nevertheless, despite these deep unresolved issues, QCD phenomenology moves ahead, mostly unconcerned about the ultimate outcome.

Anyway, I choose to take this Gauss-Bonnet topological term seriously, and write its action in standard form, namely $S = 2\pi dN/dt$, with N an integer valued quantity. It is then possible to learn more about how N behaves in simple geometries, even without understanding in microscopic terms what it means. I find that, in FRW cosmology, this quantity is indeed extensive, and that in a cosmic void the density of topology or darkness, defined as $n = N/V$, is indeed proportional to HM_{Pl}^2. In the early universe, n was larger than that. It was Planckian when the universe was radiation-dominated, with a temperature of order 10 MeV. Likewise, upon adding a simple matter source to empty space, with nuclear matter density (proton, lead nucleus, neutron star), one finds that the darkness density varies in proportion to the inverse 9/2 power of the distance from the source. The darkness density becomes Planckian just outside the radius of the source, independent of the mass of the source.

These results, and other related issues, strongly suggest that at best the MacDowell-Mansouri action is an effective action, usable only at distance scales larger than the darkness scale of 10^{-12} cm. This does not mean that this formalism predicts that the Einstein equations of motion are invalid below that scale. It only means that the formalism itself is inappropriate to use at distance scales smaller than the darkness scale. A rough analogy

might be QCD. Use of quarks and gluons to describe phenomena at distance scales large compared to the confinement scale is usually inappropriate. But this does not mean there is something fundamentally wrong with the QCD Lagrangian at such distance scales. And there are elements of the short-distance description, such as the weak and electromagnetic currents built from the quark fields, which can be used productively in the large-distance limit of the theory.

But the bottom line question is whether this concept of darkness can be put to work in other ways. I am tempted to speculate that there is a link to the confinement scale of QCD and the mass scale of the quarks and leptons. These scales did not in principle have to be close to the darkness scale. But they are. Perhaps the QCD vacuum texture somehow communicates with this gravitational topological vacuum texture. The QCD vacuum and the gravitational vacuum are in the same place at the same time, with arguably the same energy. Therefore, even a tiny coupling may persuade the two vacuum scales to converge to a common value. Likewise, the quark and lepton masses and mixings depend on the structure of the "Dirac sea" and of the Higgs vacuum condensate. So a similar argument may also apply in that case.

This line of argument provides me with a guidepost in my present search for patterns of symmetry breaking, etc. in the Higgs sector. I envisage an infrared, "darkness" scale characterized by a mass parameter m which controls first and second generation masses and mixings. Were this parameter m to be set to zero, all such effects vanish. In other words, many of the most difficult "family problems" resolve themselves, not at very high mass scales, but at mass scales no larger than the electroweak scale. While this is not at all what is anticipated by the vast majority of experts, I feel that the scenario I sketched out in the previous sections may just possibly be consistent with this notion. So I keep it in as a working hypothesis, which helps constrain the myriad of alternative scenarios that I face in dealing with the family problem.

I even have a candidate value for the small parameter — 7 MeV. I have created my own rough reconstruction of the aforementioned "rotating mass matrix" scheme of Hong-Mo Chan et al., with output values of masses and mixings as given in Fig. 4. In my version [10], this parameter m is explicit, and clearly plays a central role. In the original version [9] this low mass scale is also present, but in a less overt way.

6. Concluding Comments Beyond the QCD material

Most of this talk has not been hard science, but merely an outline of a personal belief system. The main features of this set of beliefs (or, more

MASSES AND MIXINGS

First generation:

$m_u \lesssim m = 7$ MeV (2.3 ± 0.6 MeV)

$m_d \lesssim m = 7$ MeV (4.8 ± 0.5 MeV)

$m_e = m^2/m_\mu = .44$ MeV * (0.51 MeV)

Second generation:

$m_c = \sqrt{m\, m_t} = 1.1$ GeV ** (1.3 GeV)

$m_s = \sqrt{m\, m_b} = 170$ MeV ** (100 ± 30 MeV)

$m_\mu = \sqrt{m\, m_\tau} = 110$ MeV ** (106 MeV)

CKM mixing:

$|V_{cb}| = \sqrt{m / m_b} = .040$ ** (.041)

$|V_{ts}| = m/\sqrt{m_b m_s} = .0080$ * (.0081)

$|V_{ub}| = m/\sqrt{m_b m_c} = .0032$ * (.0039)

Unitarity-triangle vertex angle:

$\alpha = \pi/2$ ($89^\circ \pm 4^\circ$)

Fig. 4. Masses and mixings of quarks and leptons according to the electroweak-doublet, family-nonet model. The asterisks are "Michelin star" ratings, according to the quality (or lack thereof) of the theoretical arguments leading to the prediction.

respectably, working hypotheses) are as follows:

1. The problem of family symmetry (why three generations of quarks and leptons?) deserves as much detailed attention as, for example, the much more popular one having to do with the presence or absence of electroweak-scale supersymmetry.

2. A natural setting for addressing this problem is the issue of nontrivial family structure within the Higgs sector.

3. Given the reasonableness of an $SO(10)$ GUT, it is reasonable that the Higgs sector is quite large, with perhaps hundreds of degrees of freedom having masses below the GUT scale, and with a significant fraction being Goldstone. This feature makes it even more reasonable that nontrivial family multiplets of Higgs bosons exist.

4. It is not unreasonable to gauge the family group, thereby embedding the usual GUT $SO(10)$ within a larger unifying group. This opens up the possibility of the existence of a set of "dark gluons", which may be massless and/or nearly massless, with a concomitant "dark confinement" mass scale.

5. This also leads to a corresponding "dark sector" component of the Higgs sector, the members of which are also electroweak singlet, zero charge, and colorless. They, together with the "dark gluons," are candidates for the sector of the standard model responsible for dark matter. A significant fraction of this set of states may have masses no larger than the electroweak scale. Some might even be axion-like familons, with the extremely small mass scale appropriate to present-day axion searches.

6. The pattern of third generation masses suggests an origin connected to the GUT mass scale, because the sundry fermions get their masses via different group structures at the level of $SU(5)$: top via $5 \times (10 \times 10)$, bottom and tau via $5 \times (\bar{10} \times 5)$, Dirac neutrino via $5 \times (\bar{5} \times 1)$. However, the first and second generation masses are conjectured by me to come from a mechanism tied, either completely or largely, to an "infrared" scale, somewhere between a few Mev and tens of MeV. Explication of this mechanism will require, in all likelihood, a quite detailed understanding of nontrivial family multiplets beyond the one containing the recently discovered Higgs boson.

7. The origin of such a mysterious infrared scale may be tied to an equally mysterious "darkness" scale associated with topological structures within the "gravitational vacuum." This darkness scale might control not only the scale of quark and lepton masses, but also the value of the QCD confinement scale. It may also imply existence of dark matter degrees of freedom within the same mass scale.

8. Progress in developing the above ideas depends upon management of many details and the devils therein. In principle, the pattern of

masses and mixings may provide enough clues to allow data-driven progress. Many theorists, especially the landscapers, assert that there is no pattern at all, and that all of these mass and mixing parameters are determined anthropically. While I personally am sympathetic to anthropic reasoning and the multiverse hypothesis, this does not preclude the existence of a pattern. We should be very careful not to give up too soon. For better or worse, I do claim to see a pattern (Fig. 4) and try to build from it.

Many of the above items are not at all novel. Some are quite politically correct. Others will be regarded by most critics as rather outrageous. But, for better or worse, this is my personal belief system. I think that such belief systems at the individual level — even though they go far beyond the discipline of the scientific method — are a great asset. They energize us. They make us work much harder. But at the societal level, institutionalization of such belief systems is dangerous, both within science and beyond. I present mine not as advocacy, but as an encouragement to the community to maximize its tolerance of those viewpoints which do lack political correctness.

What do these beliefs have to say about the experimental future of our field?

1. There remains a high level of potential at the LHC for discovering members of the extended Higgs sector at the "low" mass scale of 200–500 GeV. This region deserves continued careful scrutiny.

2. If such states exist, they create an extremely strong case for an ILC.

3. A rich sector of dark-matter states with masses small compared to the electroweak scale invites a broad variety of non-accelerator searches (along with others at low-energy, high-intensity accelerators), with plenty of room for new creative ideas.

Were the political climate to improve to the level existing in, say, the 1970's, existing technology would by itself guarantee a healthy future for many decades, perhaps culminating in a 100 TeV-scale proton-proton collider. The homework for such big initiatives should be done as soon as possible, so that if and when the politics improves, the field is ready to move ahead expeditiously.

I have in this talk wandered far afield from QCD phenomenology. Nevertheless, I need not elaborate here, of all places, on how central QCD remains in all of the above issues. It is our best quantum field theory. It is the underpinning of a large fraction of all particle-physics experiments. And it contains important fundamental features shared by other gauge theories —

including general relativity. Thorough, data-driven studies of QCD in all its aspects should never go out of fashion.

7. Acknowledgments

Thanks go to many colleagues at SLAC, Stanford, and elsewhere for much helpful criticism of these ideas. Thanks also go to Sergei Chekanov, Zack Sullivan, and their able assistants for organizing such an interesting and successful meeting.

8. Addendum

During the meeting, I could not help but react to the interesting material which was presented. In this addendum is a short summary of some primary reactions:

A. Underlying Events and Hole Fragmentation: Simulations of minimum-bias physics and of underlying-event structure have by now become very sophisticated. Nevertheless, there will always be room for improvement. With that in mind, it seems to me that a targeted approach is appropriate, with the individual targets being the dozen or so distinct regions of the lego plot present in a typical LHC hard-collision event (cf. Fig 5(a)). Most of these regions are already well-identified and studied. Beam fragmentation regions are challenging, but difficult to access experimentally. I suspect that a relatively underappreciated region is the "hole fragmentation" region, namely that portion of the lego plot which contained the initial state partons that participated in the hard process. In order to most expeditiously examine its properties and to compare with simulations, it would seem to be advantageous to place a hole fragmentation region in the barrel region of the detector, centered at zero rapidity (Fig. 5(b)). The trigger is a symmetric pair of "endwall jets."

B. Boosted Jets and Plumbing: There was considerable discussion of new physics searches involving "boosted jets." While well-isolated conventional jets can be defined as the contents within a circle of radius 0.7 in the lego plot, "boosted" configurations cannot. This "overlapping jet" problem requires more sophisticated approaches to the kinematics, some of which were on display during the meeting. Long ago I worked on this problem, and came up with a general method for untangling overlapping jets (SLAC-PUB-5593). Alas, it never received much attention. But I still think it has possible merit, and would like to see it applied, at the very least, to Monte Carlo data.

C. PDF's at very small x: During the meeting there was no discussion or display of PDF's at values of the deep-inelastic scaling variable $x \ll 10^{-4}$.

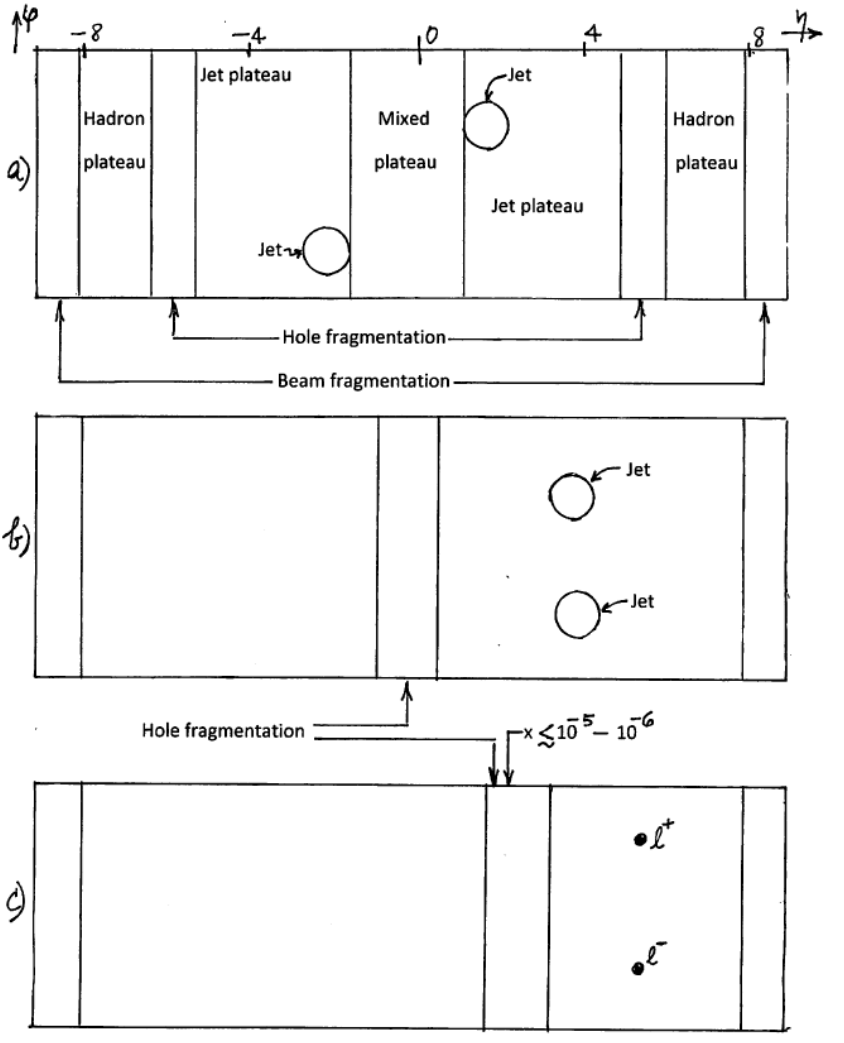

Fig. 5. Lego plots at the LHC energy scale for (a) a typical dijet event, for (b) a boosted dijet event appropriate for the detailed study of hole fragmentation, and for (c) probing parton distributions via the Drell-Yan process at values of $x < 10^{-5}$–10^{-6}.

Kinematically one can reach another factor of 10–100 at the LHC via "end-wall Drell-Yan dileptons" with masses in the 5–10 GeV range (Fig. 5(c)). After my talk, I learned that LHCb has published some data (LHCb-CONF-2012-013). But the resultant PDF's still deserve to be catalogued — it is an important frontier measurement.

References

[1] J. Bjorken, S. Brodsky, and A. Goldhaber, arXiv:1308.1435 [hep-ph].

[2] A nice introduction to these ideas is given by Y. Kovchegov, AIP Conference Proceedings 1520 (2013).

[3] J. Espinosa, C.S. Fong, and E. Nardi, arXiv:1211.6428 [hep-ph], and references therein; cf. C.S. Fong and E. Nardi, arXiv:1307.4412 [hep-ph].

[4] M. Gresham, I.W. Kim, and K. Zurek, Phys. Rev. D **85**, 014022 (2012); Phys. Rev. D **83**, 114027 (2011), and references therein.

[5] ATLAS Collaboration, Phys. Rev. D **86**, 091103 (2012).

[6] See in particular Fig. 2 of reference Ref. [5].

[7] An up-to-date review of this very active subfield is about to emerge, thanks to the Snowmass process.

[8] J. Bjorken, R. Essig, P. Schuster, and N. Toro, Phys. Rev. D **80**, 075018 (2009).

[9] M. Baker, H.M. Chan, and S.T. Tsou, arXiv:1206.0199 [hep-ph], and references therein.

[10] J. Bjorken, Annalen der Physik **525**, A67 (2013).

[11] Y. Zeldovich, JETP Lett. **6**, 316 (1967).

[12] A nice introduction to the first-order formalism is given by J. Magueijo, T. Ziosnik, and T. Kibble, Phys. Rev. D **87**, 063504 (2013), and references therein.

[13] My favorite source is that of L. Friedel and A. Starodubtsev, hep-th/0501191, and references therein.